

**COLLECTED PAPERS on  
Dressed Photon Science and  
Technology**

**Vol. 27**

**August 2011 – July 2012**

**Prof. Motoichi OHTSU**

# MEMBERS

(From April 1, 2012)

## *[I] The University of Tokyo\**

### **Professor**

Motoichi OHTSU<sup>(a-c)</sup> (Dr. Eng.)

### **Associate Professor**

Takashi YATSUI (Dr. Eng.)

### **Researcher**

Makoto NARUSE (Dr. Eng.)  
Senior Researcher, National Institute of Information and  
Communications Technology (NICT)

### **Research Assistant**

Kiyomi MATSUE

### **Graduate Students (Doctor Candidate)**

Yang LIU  
Ryoma OYAMA

### **Graduate Students (Master Course)**

Takuro HAYASHI  
Takahiro MOCHIZUKI  
Hajime TANAKA  
YU Byungho  
Tsubasa IMOTO  
Naoki WADA

### **Undergraduate Students**

TRAN Anh Minh  
Nabila TANJEEM  
Maiku YAMAGUCHI  
Yasuyuki WATANABE

## **Manager**

Kazuhiko TAMAKI

## **Secretary**

Sachiyo KOJIMA

- a) Also a director “Nanophotonics Research Center, The Institute of Engineering Innovation, School of Engineering The University of Tokyo”
- b) Also a director, “Preparatory research phase, Research and Development Program of Innovative Energy Efficiency Technology, and NEDO (New Energy and Industrial Technology Development Organization)
- c) Also a director, NPO-Research Institute of Nanophotonics

(\*)

Department of Electronics Engineering and Information Systems,

Graduate School of Engineering,

The University of Tokyo

(Room 215, Bldg. Eng. 9)

2-11-16 Yayoi, Bunkyo-ku, Tokyo 113-8656, Japan

Phone: +81-3-5841-1189

FAX: +81-3-5841-1140

E-mail: ohtsu@ee.t.u-tokyo.ac.jp

URL:<http://uuu.t.u-tokyo.ac.jp/>

東京大学大学院 工学系研究科 電気系工学専攻

〒113-8656 東京都文京区弥生 2-11-16 工学部 9 号館 215 号室

電話: 03-5841-1189, ファックス: 03-5841-1140

E-mail: ohtsu@ee.t.u-tokyo.ac.jp

URL: <http://uuu.t.u-tokyo.ac.jp/>

***[II] Preparatory research phase,  
Research and Development Program of Innovative Energy  
Efficiency Technology,  
NEDO project\****

**Professor**

Motoichi OHTSU (Dr. Eng.)

**Associate Professor**

Takashi YATSUI (Dr. Eng.)

**Researcher**

Tadashi KAWAZOE (Dr. Sci.)

Wataru NOMURA (Dr. Eng.)

Naoya TATE (Dr. Info. Sci.)

**Research Assistant**

Ayako MIZUSHIMA

Etsuko OTA

**Secretary**

Noriko KUROKI

Kumiko NOZAWA

(\*)

Department of Electronics Engineering and Information Systems,

Graduate School of Engineering,

The University of Tokyo

(Room 219, Bldg. Eng. 9)

2-11-16 Yayoi, Bunkyo-ku, Tokyo 113-8656, Japan

Phone: +81-3-5841-1670

FAX: +81-3-5841-1140

E-mail: info@nanophotonics.t.u-tokyo.ac.jp

URL: <http://uuu.t.u-tokyo.ac.jp/>

東京大学大学院 工学系研究科 電気系工学専攻  
〒113-8656 東京都文京区弥生 2-11-16 工学部 9 号館 219 号室  
電話 : +81-3-5841-1670, ファックス: +81-3-5841-1140  
E-mail: info@nanophotonics.t.u-tokyo.ac.jp  
URL: <http://uuu.t.u-tokyo.ac.jp/>

## ***[IV] Nanophotonics Research Center\****

### **Director**

Motoichi OHTSU, Professor (core member)

### **Members**

Kazuo HOTATE, Professor (core member)

Hitoshi TABATA, Professor (core member)

Masaki TANAKA, Professor (core member)

Takao SOMEYA, Professor

Shinji YAMASHITA, Professor

Yuichiro KATO, Associate Professor

Shinobu OHYA Associate Professor

Masakazu SUGIYAMA, Associate Professor

Takashi YATSUI, Associate Professor

Munetoshi SEKI, Assistant Professor

Masanori KUBOTA, Assistant Professor

Makoto NARUSE, Senior Researcher, (NICT)

Tadashi KAWAZOE, Researcher

Wataru NOMURA, Researcher

Naoya TATE, Researcher

(\*)

Institute of Engineering Innovation,

School of Engineering, The University of Tokyo

(Room 219, Bldg. Eng. 9)

2-11-16 Yayoi, Bunkyo-ku, Tokyo 113-8656, Japan

Phone: +81-3-5841-1670

FAX: +81-3-5841-1140

E-mail: [info@nanophotonics.t.u-tokyo.ac.jp](mailto:info@nanophotonics.t.u-tokyo.ac.jp)

URL: <http://www.npc.t.u-tokyo.ac.jp/>

東京大学大学院 工学系研究科 総合研究機構

〒113-8656 東京都文京区弥生 2-11-16 工学部 9 号館 219 号室

電話 : +81-3-5841-1670, ファックス: +81-3-5841-1140

E-mail: [info@nanophotonics.t.u-tokyo.ac.jp](mailto:info@nanophotonics.t.u-tokyo.ac.jp)

URL: <http://www.npc.t.u-tokyo.ac.jp/>

### ***[III] Research Institute of Nanophotonics\****

#### **Director**

Motoichi OHTSU

(\*)

Research Institute of Nanophotonics,

Nonprofit Organization

1-20-10 Sekiguchi, Bunkyo-ku, Tokyo 112-0014, Japan

Phone: +81-3-3267-6790. Fax: +81-3-5261-9788

E-mail: ohtsu-rinps@nanophotonics.t.u-tokyo.ac.jp

URL: <http://www.nanophotonics.info/>

特定非営利法人 ナノフォトンクス工学推進機構

〒112-0014 東京都文京区関口 1-20-10

電話: 03-3267-6790, ファックス: 03-5261-9788

E-mail: ohtsu-rinps@nanophotonics.t.u-tokyo.ac.jp

URL: <http://www.nanophotonics.info/>

## LIST OF PAPERS

[(pp. XX-XX); pages in this issue of the COLLECTED PAPERS]

### [I] ORIGINAL PAPERS

- [1] N. Wada, T. Kawazoe, and M. Ohtsu, “An optical and electrical relaxation oscillator using a Si homojunction structured light emitting diode” Appl. Phys. B-Lasers and Optics, Vol. 108, No.1, July 2012, pp. 25-29.

**(pp. 1-5)**

- [2] H. Tanaka, T. Kawazoe, and M. Ohtsu, “Increasing Si photodetector photosensitivity in near-infrared region and manifestation of optical amplification by dressed photons” Appl. Phys. B-Lasers and Optics, Vol. 108, No.1, July 2012, pp. 51-56.

**(pp. 7-12)**

- [3] M. Ohtsu, “Dressed photon technology,” Nanophotonics, Vol. 1, Issue 1, July 2012, pp. 83-97.

**[Invited paper]**

**(pp. 13-27)**

- [4] M. Naruse, N. Tate, and M. Ohtsu, “Optical security based on near-field processes at the nanoscale,” Journal of Optics, Vol. 14, No. 9, July 2012, pp. 094002 1-13.

**[Invited paper]**

**(pp. 29-41)**

- [5] T. Yatsui, K. Nakanishi, K. Kitamura, and M. Ohtsu, “Room-temperature growth of high-quality ZnO nanocrystals using a dressed-photon-assisted near-field process,” Appl. Phys. B-Lasers and Optics, Vol. 107, No.3, June 2012, pp. 637-641.

**(pp. 43-47)**

- [6] T. Yatsui, A. Ishikawa, K. Kobayashi, A. Shojiguchi, S. Sangu, T. Kawazoe, M. Ohtsu, J. Yoo, and G.-C. Yi, “Superradiance from one-dimensionally aligned ZnO nanorod multiple-quantum-well structures,” Appl. Phys. Lett., Vol. 100, Issue 23, June 2012, pp. 233118 1-4.

**(pp. 49-52)**



- [7] T. Kawazoe, M. Ohtsu, K. Akahane, and N. Yamamoto, “Si homojunction structured near-infrared laser based on a phonon-assisted process,” *Appl. Phys. B-Lasers and Optics*, Vol. 107, No.3, June 2012, pp. 659-663.

**(pp. 53-57)**

- [8] M. Naruse, P. Holmstrom, T. Kawazoe, K. Akahane, N. Yamamoto, L. Thylen, and M. Ohtsu, “Energy dissipation in energy transfer mediated by opticalnear-field interactions and their interfaces with optical far-fields,” *Appl. Phys. Lett.*, Vol. 100, Issue 24, June 2012, pp. 241102 1-4.

**(pp. 59-62)**

- [9] K. Kitamura, T. Kawazoe, and M. Ohtsu, “Homojunction-structured ZnO light-emitting diodes fabricated by dressed-photon assisted annealing,” *Appl. Phys. B-Lasers and Optics*, Vol. 107, No. 2, May 2012, pp. 293-299.

**(pp. 63-69)**

- [10] T. Yatsui, M. Tsuji, Y. Liu, T. Kawazoe, and M. Ohtsu, “Emission from a dipole-forbidden energy state in a ZnO quantum dot induced by a near-field interaction with a fiber probe,” *Appl. Phys. Lett.*, Vol. 100, Issue 22, May 2012, pp. 223110 1-4.

**(pp. 71-74)**

- [11] M. Naruse, Y. Liu, W. Nomura, T. Yatsui, M. Aida, L. B. Kish, and M. Ohtsu, “Stochastic processes in light-assisted nanoparticle formation,” *Appl. Phys. Lett.*, Vol. 100, Issue 19, May 2012, pp. 193106 1-5.

**(pp. 75-79)**

- [12] W. Nomura, T. Yatsui, T. Kawazoe, E. Runge, C. Lienau, and M. Ohtsu, “Direct observation of optical excitation transfer based on resonant optical near-field interaction,” *Appl. Phys. B-Lasers and Optics*, Vol. 107, No. 2, May 2012, pp. 257-262

**(pp. 81-86)**

- [13] M. Mascheck, S. Schmidt, M. Silies, T. Yatsui, K. Kitamura, M. Ohtsu, D. Leipold, E. Runge, and C. Lienau, “Observing the localization of light in space and time by ultrafast second-harmonic microscopy,” *Nature Photonics*, Vol. 6, No. 5, May 2012, pp. 293-298.

**(pp. 87-92)**

- [14] M. Naruse, F. Peper, K. Akahane, N. Yamamoto, T. Kawazoe, N. Tate, and M. Ohtsu, “Skew Dependence of Nanophotonic Devices Based on Optical Near-Field Interactios,” *ACM Journal on Emerging Technologies in Computing Systems*, Vol. 8, No. 1, February 2012, pp. 4:1-4:12

**(pp. 93-104)**

- [15] T. H. H. Le, K. Mawatari, Y. Pihosh, T. Kawazoe, T. Yatsui, M. Ohtsu, M. Tosa, and T. Kitamori, "Optical near-field induced visible response photoelectrochemical water splitting on nanorod TiO<sub>2</sub>," *Appl. Phys. Lett.*, Vol. 99, Issue 21, November 2011, pp. 213105 1-3.

**(pp. 105-107)**

- [16] M. Naruse, K. Leibnitz, F. Peper, N. Tate, W. Nomura, T. Kawazoe, M. Murata, and M. Ohtsu, "Autonomy in excitation transfer via optical near-field interactions and its implications for information networking," *Nano Communication Networks*, Vol. 2, No. 4, December 2011, pp. 189-195

**(pp. 109-115)**

- [17] M. Naruse, T. Kawazoe, T. Yatsui, N. Tate, and M. Ohtsu, "A stochastic modeling of morphology formation by optical near-field processes," *Appl. Phys. B-Lasers and Optics*, Vol. 105, No. 4, October 2011, pp. 185-190

**(pp. 117-122)**

- [18] H. Matsui, W. Nomura, T. Yatsui, M. Ohtsu, and M. Tabata, "Optical dynamics of energy-transfer from a CdZnO quantum well to a proximal Ag nanostructure," *Optics Letters*, Vol. 36, Issue 19, September 2011, pp. 3735-3737

**(pp. 123-125)**

- [19] T. Kawazoe, M. A. Mueed, and M. Ohtsu, "Highly efficient and broadband Si homojunction structured near-infrared light emitting diodes based on the phonon-assisted optical near-field process," *Appl. Phys. B-Lasers and Optics*, Vol. 104, No. 4, September 2011, pp. 747-754

**(pp. 127-134)**

- [20] N. Tate, M. Naruse, W. Nomura, T. Kawazoe, T. Yatsui, M. Hoga, Y. Ohyagi, Y. Sekine, H. Fujita, and M. Ohtsu, "Demonstration of modulatable optical near-field interactions between dispersed resonant quantum dots," *Optics Express*, Vol. 19, Issue 19, September 2011, pp. 18260-18271

**(pp. 135-146)**

### **[II] PRESENTATIONS IN INTERNATIONAL CONFERENCES**

- [1] T. Yatsui, K. Iijima, K. Kitamura, and M. Ohtsu, "Phonon-assisted near-field activation of electron transfer between a solution and an electrode," Schedule and Abstracts of XIV International Conference on Phonon Scattering in Condensed Matter (PHONONS 12), University of Michigan, July 9-12, 2012, Ann Arbor, MI, USA, pp. 234-235.

**(pp. 147-148)**

- [2] T. Mochizuki, K. Kitamura, T. Yatsui, and M. Ohtsu, "Visible-light-induced water splitting by phonon-assisted optical near fields in ZnO nanorods," Schedule and Abstracts of XIV International Conference on Phonon Scattering in Condensed Matter (PHONONS 12), University of Michigan, July 9-12, 2012, Ann Arbor, MI, USA, pp. 236-237.

**(pp. 149-150)**

- [3] Y. Miyauchi, M. Iwamura, S. Mouri, T. Kawazoe, M. Ohtsu, and K. Matsuda, "Luminescence Properties of Oxygen-Doped Carbon Nanotubes," Abstracts(WEB) of Thirteenth International Conference on the Science and Application of Nanotubes, NT12 Organising Committee, June, 24-29, 2012, Brisbane, Australia, P. 5.

**(pp. 151-152)**

- [4] T. Yatsui, W. Nomura, and M. Ohtsu, "Nanophotonic polishing of substrate with angstrom scale," CCMR 2012 Program and Abstract, Springer, June 15-29, 2012, Seoul, South Korea, pp. 12-13.

**[Invited presentation]**

**(pp. 153-154)**

- [5] M. Ohtsu, "Concepts of dressed photon science and technology," Workshop Program of The 2<sup>nd</sup> Sweden-Japan Workshop on Nanophotonics and Related Technologies, Royal Institute of Technology (KTH), June 18-19, 2012, Kista, Sweden, paper number Mo2.

**(pp. 155-156)**

- [6] T. Yatsui, M. Tsuji, Y. Liu, T. Kawazoe, and M. Ohtsu, "Nanophotonic device utilizing a dipole-forbidden energy state," Workshop Program of The 2<sup>nd</sup> Sweden-Japan Workshop on Nanophotonics and Related Technologies, Royal Institute of Technology (KTH), June 18-19, 2012, Kista, Sweden, paper number Mo4.

**(pp. 157-158)**

- [7] T. Kawazoe and M. Ohtsu, "Highly efficient Si homojunction infrared LED based on the dressed photon-assisted process," Workshop Program of The 2<sup>nd</sup> Sweden-Japan Workshop on Nanophotonics and Related Technologies, Royal Institute of Technology (KTH), June 18-19, 2012, Kista, Sweden, paper number Mo6.

**(pp. 159-160)**

- [8] W. Nomura, T. Yatsui, T. Kawazoe, M. Naruse, and M. Ohtsu, "Dynamic properties of optical near-field signal transfer in random array of quantum dots," Workshop Program of The 2<sup>nd</sup> Sweden-Japan Workshop on Nanophotonics and Related Technologies, Royal Institute of Technology (KTH), June 18-19, 2012, Kista, Sweden, paper number Mo10.

**(pp. 161-162)**

- [9] T. Yatsui, M. Tsuji, Y. Liu, T. Kawazoe, and M. Ohtsu, "Evaluation of a dipole-forbidden energy state in ZnO quantum dots induced by the optical near-field interaction," Programme of European Materials Research Society (E-MRS) 2012 Spring meeting, European Materials Research Society, May 14-28, 2012, Strasbourg, France, paper number N50.

**(p. 163)**

- [10] Y. Liu, T. Yatsui, and M. Ohtsu, "Controlling the size of ZnO quantum dots via dressed photon-phonon states," Programme of European Materials Research Society (E-MRS) 2012 Spring meeting, European Materials Research Society, May 14-28, 2012, Strasbourg, France, paper number N55.

**(pp. 165-166)**

- [11] T. Yatsui and M. Ohtsu, "Nanophotonic device utilizing a dipole-forbidden energy state," Program & Abstracts of 2012 Energy, Materials and Nanotechnology (EMN) meeting, Open-Access House of Science and Technology (OAHOST), April 16-20, 2012, Orlando, FL, USA, pp. 103-104, paper number A51.

**[Invited presentation]**

**(pp. 167-168)**

- [12] R. Teki, A. J. Kadaksham, M. House, J. H. Jones, A. Ma, S. V. Babu, A. Hariprasad, P. Dumas, R. Jenkins, J. Provine, A. Richmann, J. Stowers, S. Meyers, U. Dietze, T. Kusumoto, T. Yatsui, M. Ohtsu, and F. Goodwin, "Alternative Smoothing Techniques to Mitigate EUV Substrate Defectivity," Proceedings of the Society of Photo-optical Instrumentation Engineers (SPIE), SPIE, February 12-16, 2012, San Jose, CA, USA, Vol. 8322, pp. 1-12.

**(pp. 169-179)**

- [13] M. Ohtsu, "Dressed Photon Technology for Novel Devices and Fabrications,"

Proceedings of Global COE International Symposium on Secure-Life Electronics, The University of Tokyo, January 17-18, 2012, Tokyo, Japan, pp. 120-124.

**(pp. 181-185)**

- [14] T. Yatsui, H. Fujita, and M. Ohtsu, "Self-assembled QD based nanophotonic device," Proceedings of International Display Workshop (IDW)'11, The Institute of Image Information and Television Engineers (ITE) and the Society for Information Display (SID), December 7-9, 2011, Nagoya, Aichi, Japan, pp. 1189 -1190.

**[Invited presentation]**

**(pp. 187-188)**

- [15] M. Naruse, N. Tate, and M. Ohtsu, "Nanophotonic system based on localized and hierarchical optical near-field processes," Abstracts of The 1st European Optical Society (EOS) Topical Meeting on Micro- and Nano-Optoelectronic Systems, European Optical Society, December 7-9, Bremen, Germany, paper number 4730.

**(pp. 189-190)**

- [16] M. Ohtsu, "Dressed Photon Technology," Abstracts, Symposium on Global Research in Advanced Photonics and Energy (GRAPE), University of Yamanashi, December 6, 2011, Kofu, Yamanashi, Japan, p. 9.

**[Invited presentation]**

**(pp. 191-192)**

- [17] T. Yatsui, W. Nomura, and M. Ohtsu, "Nanophotonic Fabrication Using a Dressed Photon," Proceedings of The 9th International Displays Research Workshop (IDRW'11), Research Institute of Electronics, Shizuoka University, December 5-6, 2011, Hamamatsu, Shizuoka, Vol. 2, pp. S3-1-1- S3-1-18.

**[Invited presentation]**

**(pp. 193-210)**

- [18] T. Kawazoe and M. Ohtsu, "Efficient light emitting diodes using indirect-transition semiconductors driven by dressed photons," Technical Digest of The 2nd France-Japan Workshop on Nanophotonics, The University of Tokyo, November 7-9, 2011, Toba, Mie, Japan, pp. 13-14.

**(pp. 211-212)**

- [19] T. Yatsui, M. Tsuji, Y. Liu, T. Kawazoe, A. Neogi, and M. Ohtsu, "Emission from a dipole-forbidden energy state in ZnO quantum dots induced by the near-field interaction Photo-Assisted Sol-Gel Method," Technical Digest of The 2nd France-Japan Workshop on Nanophotonics, The University of Tokyo, November 7-9, 2011, Toba, Mie, Japan, pp. 38-39.

**(pp. 213-214)**

[20] M. Ohtsu, "The Magic of the Dressed Photon," Technical Digest & Conference Program, 30<sup>th</sup> International Congress on Applications of Lasers & Electro-Optics (ICALEO), Laser Institute of America, October, 23-27, 2011, Orlando, FL., USA, pp. 58.

**[Plenary presentation]**

**(p. 215)**

[21] M. Naruse, T. Kawazoe, T. Yatsui, N. Tate, and M. Ohtsu, "Stochastic Modeling of Morphology Formation by a Phonon-Assisted Optical Near-Field Process," Abstract book of The 8th Asia-Pacific Workshop on Nanophotonics and Near-Field Optics (APNFO-8), McLaren University, August 25-26, 2011, St. McLaren Vale, S.A., Australia, p. 3.

**(p. 217)**

[22] Y. Liu, T. Yatsui, T. Kawazoe, and M. Ohtsu, "Controlling the size and variance of ZnO quantum dot diameter using photo-assisting sol-gel method," Abstract book of The 8th Asia-Pacific Workshop on Nanophotonics and Near-Field Optics (APNFO-8), McLaren University, August 25-26, 2011, St. McLaren Vale, S.A., Australia, p. 5.

**(p. 219)**

[23] N. Tate, Y. Liu, T. Kawazoe, M. Naruse, T. Yatsui, and M. Ohtsu, "Nanophotonic droplet: Autonomous capsulation of sort-selective quantum dot pairs based on phonon-assisted process," Abstract book of The 8th Asia-Pacific Workshop on Nanophotonics and Near-Field Optics (APNFO-8), McLaren University, August 25-26, 2011, St. McLaren Vale, S.A., Australia, p. 6.

**(p. 221)**

[24] Y. Fujiyoshi, M. Haraguchi, T. Okamoto, T. Yatsui, M. Ohtsu, K. Hirata, and Y. Tabata, "Numerical simulation for non-adiabatic optical near-field etching," Abstract book of The 8th Asia-Pacific Workshop on Nanophotonics and Near-Field Optics (APNFO-8), McLaren University, August 25-26, 2011, St. McLaren Vale, S.A., Australia, p. 7.

**(p. 223)**

[25] W. Nomura, T. Yatsui, T. Kawazoe, M. Naruse, and M. Ohtsu, "Long-range optical energy transfer between randomly distributed resonant quantum dots," Abstract book of The 8th Asia-Pacific Workshop on Nanophotonics and Near-Field Optics (APNFO-8), McLaren University, August 25-26, 2011, St. McLaren Vale, S.A., Australia, p. 19.

**(p. 225)**

### [III] REVIEW PAPERS

- [1] M. Naruse, T. Kawazoe, and M. Ohtsu, “Innovative Optical Functional Devices by Dressed Photon Interactions,” The Journal of Institute of Electronics Information and Communication Engineers, Vol. 95, No.4, April, 2012, pp. 330-334.

【成瀬誠、川添忠、大津元一、「ナノ領域の光と物質との相互作用を用いた新機能デバイス」、電子情報通信学会誌、第95巻、第4号、2012年4月、pp. 330-334】

**(pp. 227-231)**

- [2] M. Ohtsu, “Overview,” OPTRONICS, Vol. 31, No.363, March, 2012, pp. 76-79.

【大津元一、「総論」、オプトロニクス、Vol. 31、No. 363、2012年3月、pp. 76-79】

**(pp. 233-236)**

- [3] T. Kawazoe and M. Ohtsu, “A high-efficiency and high-power light emitting diode by a bulk Si crystal,” OPTRONICS, Vol. 31, No. 363, March, 2012, pp. 85-88.

【川添忠、大津元一、「バルク結晶シリコンを用いた高効率・高出力発光ダイオード」、オプトロニクス、Vol. 31、No. 363、2012年3月、pp. 85-88】

**(pp. 237-240)**

---

#### **[IV] PUBLISHED BOOKS**

- [1] Gyu-Chul Yi (ed.), *Semiconductor Nanostructures for Optoelectronic Devices*, T. Yatsui, G.-C. Yi, and M. Ohtsu, chapter 10, pp. 279-296, “Nanophotonic Device Application Using Semiconductor Nanorod Heterostructures,” Springer Verlag, Berlin, Germany, January 2012, (1726 pages)  
**(pp. 241-251)**
- [2] F. Tragaer (ed.), *Handbook of Lasers and Optics*, -2<sup>nd</sup> Editions- M. Ohtsu, chapter 19, “Nanooptics,” Springer Verlag, Berlin, Germany, May 2012, (349 pages)  
**(pp. 253-255)**
- [3] I. Naydenova (ed.), “*Holograms - Recording Materials and Applications*, N. Tate, M. Naruse, T. Yatsui, T. Kawazoe, M. Hoga, Y. Ohyagi, Y. Sekine, T. Fukuyama, M. Kitamura, and M. Ohtsu, chapter 15, “Nanophotonic Hierarchical Holograms: Demonstration of Hierarchical Applications Based on Nanophotonics,” *Holograms - Recording Materials and Applications*, InTech, Rijeka, Croatia, open access publisher, November 2011, pp. 341-356.  
**(pp. 257-260)**
- [4] M. Ohtsu (ed.), *Progress in Nanophotonics I*, Springer-Verlag, Berlin, September. 2011. (236 pages)  
**(pp. 261-265)**



## [VI] AWARDS

- [1] M. Naruse (NICT), N. Tate (Univ. Tokyo), Y. Sekine (DNP), Y. Ohyagi (DNP), M. Hoga (DNP), T. Matsumoto (Yokohama Natl. Univ.), M. Ohtsu (Univ. Tokyo), Grand Prize for Frontier Technology: Pave a New Way for Creativity Research and Development of Information Security by Nanophotonics

成瀬誠、豎直也、関根陽子、大八木康之、法元盛久、松本勉、大津元一、「ナノ寸法の光を用いたナノフォトニックセキュリティの研究開発」, 第 26 回(2012 年度)独創性を拓く 先端技術大賞、企業・産学部門、フジサンケイビジネスアイ賞、フジサンケイビジネスアイ、2012 年 6 月

# [I] ORIGINAL PAPERS



# An optical and electrical relaxation oscillator using a Si homojunction structured light emitting diode

N. Wada · T. Kawazoe · M. Ohtsu

Received: 22 May 2012 / Published online: 4 July 2012  
© Springer-Verlag 2012

**Abstract** We propose an optical and electrical relaxation oscillator making use of an S-shaped negative resistance characteristic of a recently developed light-emitting diode using a bulk silicon crystal homojunction. From simulations, we found that the voltage and optical power oscillated synchronously, and their oscillation frequency increased with increasing injection current. The synchronous oscillation was also confirmed by experimental measurements. The amplitude of the voltage was  $50 V_{p-p}$ , the amplitude of the optical power was  $3 \text{ mW}_{p-p}$ , and the maximum oscillation frequency was 34 kHz. The measured value of the spontaneous emission lifetime of a Si wafer was 900 ps, which was as short as that of direct transition-type semiconductors.

## 1 Introduction

Optical pulse oscillators have been widely used in the fields of optical communication, optical data storage, optical fabrication, spectroscopy, and so on. Semiconductor lasers driven by pulsed current and mode-locked lasers are popular examples of such devices [1]. Although the former are compact, they need to be driven by an electrical trigger, and thus require an electronic driving circuit. The latter are large and

have high power consumption because they consist of numerous electronic parts and optical elements.

To realize a novel optical and electrical relaxation oscillator for solving these problems, here we propose the use of a light-emitting diode formed of a bulk silicon (Si) crystal homojunction (Si-LED) developed by the authors [2]. Because the device is operated by connecting it only to a DC power supply, and no optical elements are required, it is expected to solve the problems mentioned above.

In this paper, the principle of the device operation will be introduced in Sect. 2. Then simulation design and measurement results of the spontaneous emission lifetime are described in Sect. 3. The simulation results and results of measuring the dynamic characteristics are described in Sect. 4. Finally, this paper concludes with Sect. 5.

## 2 Device fabrication and principle of oscillation

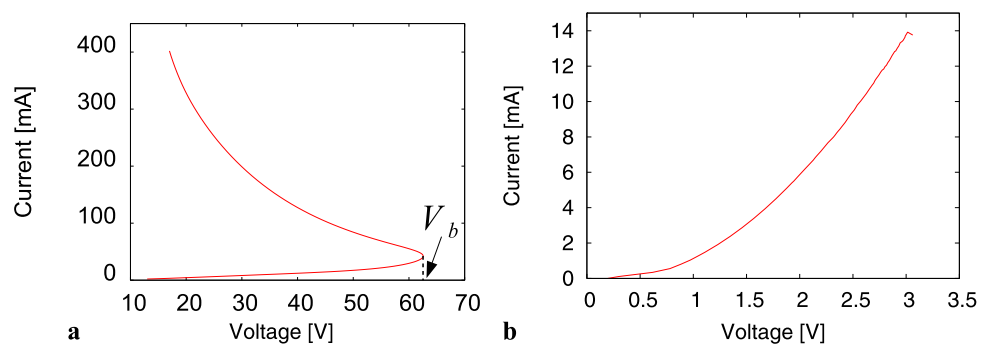
### 2.1 Fabrication method

In order to fabricate a Si-LED using Si, which is an indirect transition-type semiconductor, boron (B) was implanted in an arsenic (As)-doped n-type Si wafer with a thickness of 650  $\mu\text{m}$  and an electrical resistivity of  $10 \Omega \text{ cm}$  by ion implantation (implantation energy 700 keV, dose density  $5 \times 10^{13} \text{ cm}^{-2}$ ) to form a p-type region, thus realizing a p–n homojunction. From secondary ion mass spectrometry (SIMS), the thickness of the p-type layer was about 2  $\mu\text{m}$ , the B concentration in the p-type layer was about  $10^{19} \text{ cm}^{-3}$ , and the As concentration in the n-type layer was less than  $10^{15} \text{ cm}^{-3}$ . An indium tin oxide (ITO) film with a thickness of 150 nm was deposited on the p-layer side, and an aluminum (Al) film with a thickness of 80 nm was deposited on the n-layer side, both by RF sputtering, and these were

N. Wada (✉) · T. Kawazoe · M. Ohtsu  
Department of Electrical Engineering and Information Systems,  
Graduate School of Engineering, The University of Tokyo,  
2-11-16 Yayoi, Bunkyo-ku, Tokyo 113-8656, Japan  
e-mail: [wada@nanophotonics.t.u-tokyo.ac.jp](mailto:wada@nanophotonics.t.u-tokyo.ac.jp)  
Fax: +81-3-58411140

T. Kawazoe · M. Ohtsu  
Nanophotonics Research Center, Graduate School of  
Engineering, The University of Tokyo, 2-11-16 Yayoi,  
Bunkyo-ku, Tokyo 113-8656, Japan

**Fig. 1** Relation between the current  $I$  and the voltage  $V$  ( $I$ – $V$  characteristic) in a Si-LED, for (a) a device with an area of  $9 \text{ mm}^2$  and a thickness of  $650 \text{ }\mu\text{m}$  (Si-LED1), and (b) a device with an area of  $0.6 \text{ mm}^2$  and a thickness of  $120 \text{ }\mu\text{m}$



used as positive and negative electrodes, respectively. Devices with an area of about  $9 \text{ mm}^2$  were made by cleaving the Si wafer.

Next, the devices were subjected to phonon-assisted annealing described in Ref. [2]; namely, they were annealed with Joule heat by applying a current. During this process, the substrate surface was irradiated with light having a photon energy  $h\nu = 0.95 \text{ eV}$  (wavelength  $1.3 \text{ }\mu\text{m}$ ), which is smaller than the bandgap energy of Si ( $E_g = 1.12 \text{ eV}$ , wavelength  $1.1 \text{ }\mu\text{m}$ ), so as to control the spatial distribution of the B concentration at the p–n junction in a self-organized manner. As a result, dressed photon–phonons were efficiently generated in the B regions, by which electrons and holes recombined, producing spontaneous emission. A dressed photon–phonon is a quasiparticle which represents the coupled state of a dressed photon and a phonon [2]. A dressed photon is also a quasi-particle representing the coupled state of a photon and an electron. This Si-LED fabrication process is called a phonon-assisted process since it requires dressed photon–phonons.

In this study, two Si-LEDs were fabricated:

1. Si-LED1: fabricated by phonon-assisted annealing by applying a voltage of about 10 V and an injection current of about 420 mA for 30 minutes under laser light irradiation (power 500 mW)
2. Si-LED2: fabricated by phonon-assisted annealing by applying a voltage of about 7.2 V and an injection current of about 700 mA for 30 minutes under laser light irradiation (power 200 mW)

Si-LED1 was mainly used for simulation and measurement of the spontaneous emission lifetime, described in Sect. 3, whereas Si-LED2 was mainly used for quantitative characterization of the oscillation, described in Sect. 4.

The Si-LEDs fabricated by this method emit high-power near infrared light whose emission spectrum has a peak that corresponds to the wavelength of the irradiated laser light, as shown in Fig. 6(d) of [2]. In addition, because of the considerable inhomogeneous spatial distribution of the B concentration in the Si-LED, the current density also becomes inhomogeneous when the device has a size as large as  $9 \text{ mm}^2$

in area and  $650 \text{ }\mu\text{m}$  in thickness [3]. As a result, as shown in Fig. 1(a), the current–voltage ( $I$ – $V$ ) characteristic exhibits S-shaped negative resistance, where the voltage  $V_b$  at the bending point of the S-shaped curve is the breakover voltage. In contrast, when the device has a size as small as  $0.6 \text{ mm}^2$  in area and  $120 \text{ }\mu\text{m}$  in thickness, the  $I$ – $V$  characteristic does not exhibit such a negative resistance but exhibits the same  $I$ – $V$  characteristic of ordinary LEDs using direct transition-type semiconductors, as shown in Fig. 1(b). In the following, the S-shaped negative resistance characteristic in Fig. 1(a) is expressed as  $I = f(V)$ . This negative resistance characteristic was utilized to realize an optical and electrical relaxation oscillator.

## 2.2 Principle of oscillation

The  $I$ – $V$  characteristic of Fig. 1(a) is shown again in Fig. 2(a). The Si-LED can be treated as a circuit in which the Si-LED is connected in parallel with a capacitor and a constant current source, as shown in Fig. 2(b), where the capacitor can be regarded as the stray capacitance of the Si-LED and/or the circuit wiring. Here,  $C$  is the capacitance of the capacitor,  $I_1$  and  $I_2$  are the currents that flow through the Si-LED and the capacitor, respectively,  $V_1$  and  $V_2$  are the voltages applied to them, and  $I_0$  is the current from the constant current source. By setting  $I_0 > f(V_b)$  and  $V_1 = V_2 = 0$  as the initial conditions, it is expected that the voltage and optical power will exhibit periodic and oscillatory temporal behaviors due to sequential processes 1–4 described below and schematically explained in Fig. 2(a).

1.  $V_1$  increases as electric charges flow into  $C$ , and the current flows into the Si-LED simultaneously.
2. At the moment when  $V_1$  reaches  $V_b$ ,  $V_2$  increases because the current  $I_0 - f(V_b)$  flows into  $C$ . However, because  $V_1$  cannot exceed  $V_b$ , the difference between  $V_1$  and  $V_2$  increases.
3.  $I_1$  increases and, as a result,  $V_1$  decreases because the electric charge is released from  $C$  due to this voltage difference between  $V_1$  and  $V_2$ . This accelerates the release of the charge and, as a result, the optical output power increases rapidly.

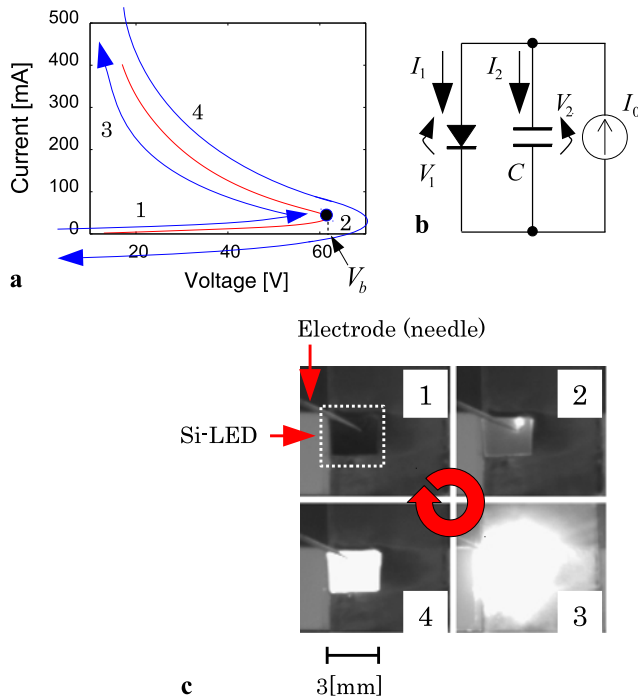


**Fig. 2** Explanation of oscillating behavior. (a) Four processes are represented by 1–4 on the  $I$ – $V$  characteristic. (b) A circuit for the oscillator. (c) Images of output light spots corresponding to the processes 1–4

- The values of  $V_1$  and  $V_2$  return to the initial state around zero due to the decrease of the electric charge in  $C$ . Then process 1 starts again.

The temporal behavior of  $V_1$  exhibits a sawtooth-like profile due to the instantaneous electric discharge. On the other hand, that of the optical power exhibits a pulse-like profile due to the rapid increase of  $I_1$  occurring right after the electric discharge. Because of a slight time difference between the electric discharge and the increase of  $I_1$ , there is a phase delay in the periodic pulse profile of the optical power with respect to the peak value of the voltage  $V_1$ . Since these temporal profiles are due to electrical and optical power dissipation based on the difference between  $V_1$  and  $V_2$ , this circuit is regarded as a nonequilibrium open system. Thus, the temporal behavior of the voltage and optical power described above is called relaxation oscillation [3]. Figure 2(c) shows images of a light spot emitted from the Si-LED in case of  $C = 100 \mu\text{F}$ , captured by an infrared camera. Images 1–4 correspond to processes 1–4 above. An output light spot can be clearly seen in process 3.

### 3 Simulation methods and measurement of spontaneous emission lifetime

#### 3.1 Modeling of the device

Figure 3 shows a simplified equivalent circuit of a Si-LED [4, 5], which is composed of a p-type layer, an n-type layer,

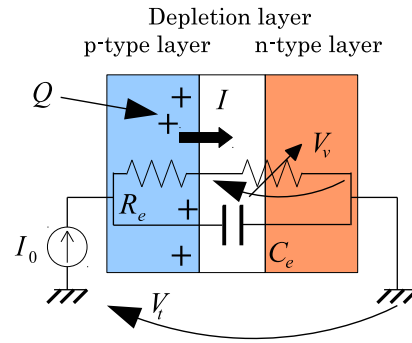


**Fig. 3** Equivalent circuit of a Si-LED

and a depletion layer. For simplicity, carriers are assumed to recombine only in the depletion layer.  $C_e$  is the equivalent capacitance representing the capability of storing electric charge  $Q$  in the Si-LED,  $R_e$  is the resistance at the p-type layer,  $I_0$  is the current from the constant current source,  $I$  is the current injected into the depletion layer,  $V_v$  is the difference in the voltage between the anode-side and the cathode-side of the depletion layer, and  $V_t$  is the total voltage applied to the Si-LED.

The variations in the number of carriers in the Si-LED,  $n$ , and the number of photons in the depletion layer,  $p$ , with respect to time are represented by the following rate equations [6]:

$$\frac{dn}{dt} = \frac{f(V)}{q} - \frac{n}{\tau} - G(n - n_{th})p, \tag{1}$$

and

$$\frac{dp}{dt} = \frac{n}{\tau} + BG(n - n_{th})p - Ap. \tag{2}$$

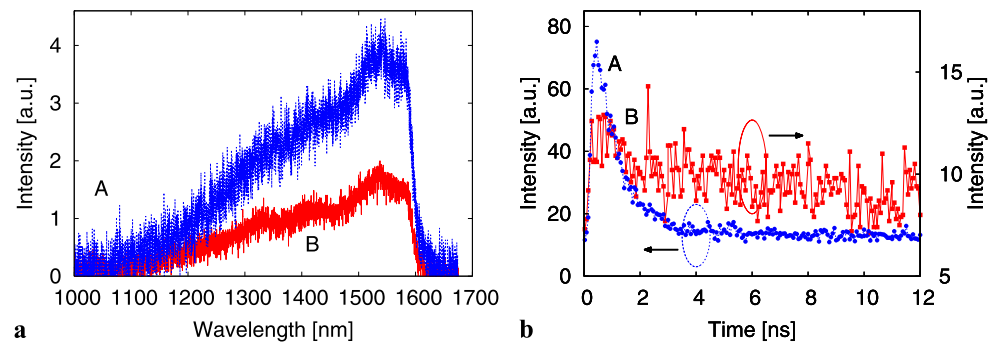
The first, second, and third terms on the right side of Eq. (1) represent electron injection, spontaneous emission, and stimulated emission, respectively. Those in Eq. (2) represent spontaneous emission, stimulated emission, and light emission from the Si-LED, respectively. Here,  $q$  is the electron charge,  $\tau$  is the spontaneous emission lifetime,  $G$  is the stimulated emission coefficient,  $n_{th}$  is the transparency carrier number in the depletion layer (transparency carrier density  $\times$  depletion layer volume),  $B$  is the coefficient of electron confinement, and  $A$  is the rate of photon dissipation from the depletion layer to the outside. For simplicity, the carrier injection efficiency is assumed to be unity.

The simulation was performed using Eqs. (1), (2), and circuit equations for the equivalent circuit shown in Fig. 3. The values of  $n$  and  $p$  were derived iteratively with the time increment  $dt$  by the following steps:

- Process that is rate-limited by charging of  $C_e$ :

In the processes 1 and 2 shown in Fig. 2(a), the charge  $Q$  at time  $t + dt$  was derived using  $Q(t + dt) = Q(t) + (I_0 - I)dt$ . Then  $V_t$ ,  $V_v$ , and  $I$  were derived by

**Fig. 4** Light emission characteristics. **(a)** Curves A and B show photoluminescence spectra of Si-LED1 and a nonannealed Si wafer, respectively. **(b)** Time variation of photoluminescence intensities. Curves A and B are for Si-LED1 and the nonannealed Si wafer, respectively



$V_t = Q/C_e$ ,  $V_v = V_t - R_e I$ , and  $I = f(V_t)$ . After substituting  $f(V_t)$  into Eq. (1), Eqs. (1) and (2) were approximated as difference equations to derive the values of  $n$  and  $p$  at time  $t + dt$ .

## 2. Process that is rate-limited by discharging of $C_e$ :

2-1. If  $V_t > V_b$  in the process 1, the capacitor  $C_e$  started discharging. Thus,  $V_t$ ,  $V_v$ , and  $I$  were set to  $V_t = V_v = V_b$  and  $I = I_0$ . Then  $n$  and  $p$  at time  $t + dt$  were derived using Eqs. (1) and (2).

2-2. If the discharging of  $C_e$  continued,  $V_t$  and  $V_v$  were derived using  $V_t = f^{-1}(I)$  and  $V_v = Q/C_e$ . Then  $Q(t + dt)$  and  $I(t + dt)$  were derived using  $Q(t + dt) = Q(t) - (V_t - V_v)dt/R_e$  and  $I(t + dt) = I_0 + (V_t - V_v)/R_e$ . This calculation continued until  $V_2 > V_b$  or  $I < 0$  was satisfied.

## 3.2 Measurement of the spontaneous emission lifetime

The values of physical quantities  $R_e$ ,  $C_e$ ,  $f(V)$ ,  $\tau$ ,  $G$ ,  $n_{th}$ ,  $B$ , and  $A$  in Sect. 3.1 have to be determined to perform the simulation. Among them, known values were employed for  $R_e$ ,  $C_e$ ,  $n_{th}$ ,  $B$ , and  $A$ , as will be shown later. The curve in Fig. 1(a) was used for  $f(V)$ . However, the spontaneous emission lifetime  $\tau$  must be found through measurements because electroluminescence from an indirect transition-type Si semiconductor has never been realized, and hence the value of  $\tau$  for a bulk Si crystal is unknown.

The method used for the direct measurement of  $\tau$  and the measurement results are presented in this subsection. The Si-LED1 was used for the measurement, and a nonannealed Si wafer was also used as a reference specimen. As an excitation light source, the second-harmonic pulsed light from a Ti-sapphire mode-locked laser (2 ps pulse width, 80 MHz pulse repetition rate, 454 nm wavelength, 30 mW power) was used. The light passed through a longpass filter with a cutoff wavelength of 850 nm or 1000 nm, as required, before reaching the Si-LED and nonannealed Si wafer specimens. The specimens were placed in a vacuum chamber and cooled down to about 6 K. The emitted photoluminescence was measured using an infrared photomultiplier tube (PMT; Hamamatsu Photonics, H10840-68MOD), a single photon counting module (Boston Electronics Corporation, SPC-600), and a monochromator.

Curves A and B in Fig. 4(a) represent the acquired spectral profiles of the Si-LED1 and the nonannealed Si wafer, respectively. Neither curve clearly shows band-edge emission at wavelengths around 1100 nm, which corresponds to the bandgap energy of Si. On the contrary, the spectra were broadened and extended to the longer-wavelength region, due to a multistep deexcitation inherent to the phonon-assisted process. Temporal decreases in the photoluminescence intensity were measured for the Si-LED1 and the nonannealed Si wafer after optical pulse irradiation, as shown by the curves A and B in Fig. 4(b). An exponential function of the spontaneous emission lifetime  $\tau$  was used for least squares fitting to the measured values:

$$y(t) = y_0 + y_1 \exp(-t/\tau). \quad (3)$$

As a result, the value  $\tau = 0.90 \pm 0.02$  ns was obtained from the curve A. This value was used for the simulation. Curve B, on the other hand, shows the measured result for the nonannealed Si wafer. In this case, the spontaneous emission probability was very low since the nonannealed Si wafer remained an indirect transition-type semiconductor. As a result, the values of curve B were very small, which made it difficult to estimate the value of  $\tau$ .

Comparing the curves A and B, the remarkable increase in the spontaneous emission probability and the decrease in the value of  $\tau$  enabled the first successful estimation of  $\tau$  by this method. The value of  $\tau$  derived above is as short as that of direct transition-type semiconductors [7–9].

The values of the other physical quantities used for the simulations were:  $R_e = 5 \Omega$ ,  $C_e = 1.5 \times 10^{-10}$  F,  $n_{th} = 7.0 \times 10^{13}$ , and  $B = 0.1$ . For A, an equation  $A = 1 - r^{1/t_0} \text{ s}^{-1}$  was used, where  $r = 0.0002$  is the Fresnel reflection coefficient at the boundary between the depletion layer and the p-type/n-type layer, and  $t_0 = 31$  fs is the time for the light to traverse the depletion layer. The value of  $G$  was used as a fitting parameter for the simulation.

## 4 Results of the simulation and characterization of the oscillator

The results of the simulation described in Sect. 3.1 are shown by curves A and B in Fig. 5(a). The voltage and

**Fig. 5** Results of the simulation. **(a)** Variation of photon number (curve A) and voltage (curve B) for  $I_0 = 1$  A and  $G = 1.8 \times 10^{-10} \text{ s}^{-1}$ . **(b)** Relationship between injection current and oscillation frequency

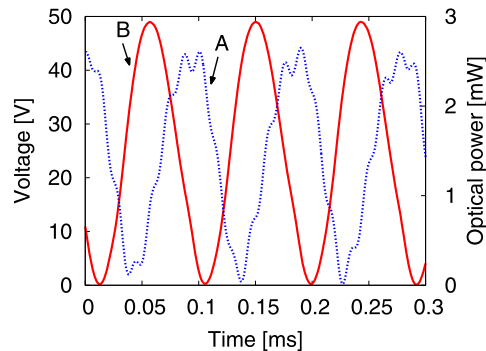
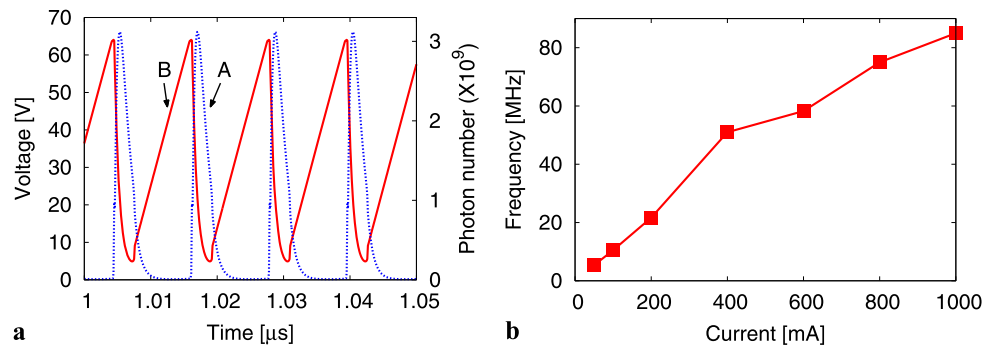


**Fig. 6** Experimental results of the temporal behaviors of optical power (curve A) and voltage (curve B) for Si-LED2

photon number varied synchronously. The temporal behavior of the voltage (curve B) exhibited a sawtooth-like profile, whereas that of the photon number (curve A) was pulse-like. The pulse width of curve A for the optical power depended on the spontaneous emission lifetime,  $\tau$ . The amplitude of the curve A decreased and exhibited relaxation oscillation with increasing  $G$ . As shown by Fig. 5(b), the oscillation frequency increased with increasing injection current  $I_0$ , and the increase rate was 80 MHz/A.

The curves A and B in Fig. 6 show the measured results of the temporal profiles of the optical power and the voltage of the Si-LED2, acquired at room temperature. The voltage was measured using an oscilloscope, and the optical power was measured using a photodiode. Comparing the two curves, they varied synchronously, and the oscillation frequency was 10 kHz. The amplitudes of the curves A and B were about 3 mW<sub>p-p</sub> and 50 V<sub>p-p</sub>, respectively. The optical energy integrated over one period of oscillation was 0.14  $\mu\text{J}$ .

When injection current was applied to Si-LED1 without connecting any external capacitor, the oscillation was caused by stray parasitic capacitance in the circuit and/or the Si-LED. The maximum oscillation frequency was 34 kHz. Comparing the two curves in Fig. 6, the voltage and optical power oscillated synchronously, and the optical power takes the maximum value at a time slightly after the voltage takes the maximum value. This agrees with the simulation result shown in Fig. 5(a). The reason why the two curves in Fig. 6

change more slowly than those of Fig. 5(a) is due to stray capacitance, stray inductance, and parasitic resistance of the circuit.

## 5 Conclusion

We proposed an optical and electrical relaxation oscillator making use of an S-shaped negative resistance characteristic of a recently developed LED using a bulk Si crystal homojunction. We validated the device operation and characterized its relaxation oscillation via simulations and measurements.

From the simulations, we found that the voltage and optical power oscillated synchronously, and their oscillation frequency increased with increasing injection current. The synchronous oscillation was also experimentally confirmed using a device with an area of 9 mm<sup>2</sup>. We also confirmed that the optical power took the maximum value at a time slightly delayed from the maximum voltage value. The amplitude of the voltage was 50 V<sub>p-p</sub>, the amplitude of the optical power was 3 mW<sub>p-p</sub>, and the maximum oscillation frequency was 34 kHz. The measured value of the spontaneous emission lifetime of a Si wafer was 900 ps, which is as short as that of direct transition-type semiconductors.

## References

1. O. Svelto, *Principles of Lasers*, 2nd edn. (Plenum, New York, 1982)
2. T. Kawazoe, M.A. Mueed, M. Ohtsu, *Appl. Phys. B* **104**, 747 (2011)
3. E. Shl, *Nonequilibrium Phase Transitions in Semiconductors* (Springer, Berlin, 1987)
4. M. Meier, S. Karg, W. Riess, *J. Appl. Phys.* **82**, 1961 (1997)
5. J. Katz, S. Margalit, C. Harder, D. Wilt, A. Yariv, *IEEE J. Quantum Electron.* **17**, 4 (1981)
6. G. Björk, Y. Yamamoto, *IEEE J. Quantum Electron.* **27**, 2386 (1991)
7. E. Finkman, M.D. Sturge, R. Bhat, *J. Lumin.* **35**, 235 (1986)
8. V. Zwiller, T. Aichele, W. Seifert, J. Persson, O. Benson, *Appl. Phys. Lett.* **82**, 1509 (2003)
9. K. Okamoto, I. Niki, A. Scherer, Y. Narukawa, T. Mukai, Y. Kawakami, *Appl. Phys. Lett.* **87**, 071102 (2005)

# Increasing Si photodetector photosensitivity in near-infrared region and manifestation of optical amplification by dressed photons

H. Tanaka · T. Kawazoe · M. Ohtsu

Received: 22 March 2012 / Published online: 24 May 2012  
© The Author(s) 2012. This article is published with open access at Springerlink.com

**Abstract** We fabricated a novel photodetector by subjecting a Si crystal having a p–n homojunction to phonon-assisted annealing. The photosensitivity of this device for incident light having a wavelength of 1.16  $\mu\text{m}$  or greater was about three times higher than that of a reference Si-PIN photodiode. The photosensitivity was increased for incident light with a wavelength of 1.32  $\mu\text{m}$  by applying a forward current. When the forward current density was 9  $\text{A}/\text{cm}^2$ , a photosensitivity of 0.10  $\text{A}/\text{W}$  was achieved. This value is at least 4000 times higher than the zero-bias photosensitivity. This remarkable increase was due to the manifestation of optical amplification cause by the forward current injection. For a forward current density of 9  $\text{A}/\text{cm}^2$ , the small-signal gain coefficient of the optical amplification was  $2.2 \times 10^{-2}$ , and the saturation power was  $7.1 \times 10^2$  mW.

## 1 Introduction

Silicon (Si) is an abundant material in the Earth's crust and has low toxicity, and it is widely used as a material for many electronic and optical devices. For example, Si photodetectors (Si-PDs) are widely used photoelectric conversion

devices; however, their photosensitivity limit at the long-wavelength side is limited by the bandgap energy,  $E_g$ , of Si ( $= 1.12$  eV) [1], and the photosensitivity drops rapidly at wavelengths above 1.11  $\mu\text{m}$ . Because of this, materials such as Ge [2], InGaAsP [3], and InGaAs [4] that have a smaller  $E_g$  than Si have been used in optical fiber communications. However, Ge photodetectors have a large dark current, and cooling is required in many cases. In addition, InGaAs photodetectors suffer from problems such as the use of highly toxic metal-organic materials in their fabrication, high cost, and so forth, and recently, depletion of resources, such as In, has also been a problem. If the photosensitivity limit of Si-PDs could be extended past the 1.11  $\mu\text{m}$  wavelength into the near-infrared region at 1.3  $\mu\text{m}$  and above, these problems could be overcome. An additional benefit of Si-PDs is their high compatibility with electronic devices. For this reason, photoelectric conversion devices exploiting effects such as mid-bandgap absorption [5–7], surface-state absorption [8, 9], internal photoemission absorption [10, 11], and two-photon absorption [12, 13] in Si have been reported in the literature. However, in the case of mid-bandgap absorption, for example, the photosensitivity at a wavelength of 1.3  $\mu\text{m}$  is limited to only 50  $\text{mA}/\text{W}$  [5].

In this research, we realized a novel Si-PD with increased photosensitivity. We applied the same fabrication method and light emission principle of a silicon light emitting diode (Si-LED) based on a phonon-assisted process that we previously proposed [14, 15]. Specifically, while radiating light, Joule-heat annealing was performed to control the spatial distribution of the impurity (boron) concentration in a Si crystal in a self-organized manner, to efficiently generate dressed photons. The photocurrent of the novel Si-PD fabricated by this method was varied by a stimulated emission process driven by the incident light. Because this stimulated emission process caused optical amplification, the photosen-

H. Tanaka · T. Kawazoe (✉) · M. Ohtsu  
Department of Electrical Engineering and Information Systems,  
Graduate School of Engineering, The University of Tokyo,  
2-11-16 Yayoi, Bunkyo-ku, Tokyo 113-8656, Japan  
e-mail: kawazoe@ee.t.u-tokyo.ac.jp  
Fax: +81-3-58411140

T. Kawazoe · M. Ohtsu  
Nanophotonics Research Center, Graduate School of  
Engineering, The University of Tokyo, 2-11-16 Yayoi,  
Bunkyo-ku, Tokyo 113-8656, Japan



sitivity of this Si-PD was remarkably increased. The operating principle of the Si-PD is described in Sect. 2, the fabrication method is described in Sect. 3, device characterization and evaluation results are presented in Sect. 4, and the paper concludes with Sect. 5.

## 2 Operating principle

The operating principle of the Si-PD fabricated in this research is based on a phonon-assisted process caused by dressed photons [16–20]. A dressed photon is a quasi-particle representing a coupled state between a photon and an electron at the nanoscale. The phonon-assisted process originates in the property of a dressed photon to couple with a phonon. By using this property, it is possible to create an electron–hole pair via a two-step excitation even with photons having an energy smaller than the bandgap energy,  $E_g$ , of the semiconductor. Therefore, the Si-PD can exhibit photosensitivity even for infrared light with a photon energy smaller than  $E_g$ . This principle has already been applied to photochemical vapor deposition [16], photovoltaic devices [17], photolithography [18], subnanometer polishing of a glass surface [19], optical frequency up-conversion [20], and other applications.

Electrons in the Si-PD experience a two-step excitation via processes (1) and (2) described below. (These processes (1) and (2), as well as processes (1′) and (2′) described later, are the same as those in the Si-LED previously proposed by the authors; for details, refer to Ref. [14] and Fig. 1 therein.)

- (1) First step: The electron is excited from the initial ground state  $|E_g; el\rangle \otimes |E_{\text{exthermal}}; phonon\rangle$  to intermediate state  $|E_g; el\rangle \otimes |E_{\text{ex}}; phonon\rangle$ . Here,  $|E_g; el\rangle$  represents the ground state (valence band) of the electron, and  $|E_{\text{exthermal}}; phonon\rangle$  and  $|E_{\text{ex}}; phonon\rangle$  respectively represent the excited state of the phonon determined by the crystal lattice temperature and the excited state of the phonon determined by the dressed photon energy. The symbol  $\otimes$  represents the direct product of the ket vectors. Because this is an electric-dipole–forbidden transition, a dressed photon is essential for the excitation.
- (2) Second step: The electron is excited from the intermediate state  $|E_g; el\rangle \otimes |E_{\text{ex}}; phonon\rangle$  to the final state  $|E_{\text{ex}}; el\rangle \otimes |E_{\text{ex}'}; phonon\rangle$ . Here,  $|E_{\text{ex}}; el\rangle$  represents the excited state (conduction band) of the electron, and  $|E_{\text{ex}'}; phonon\rangle$  represents the excited state of the phonon. Because this is an electric-dipole–allowed transition, the electron is excited not only by the dressed photon but also by propagating light. After this excitation, the phonon in the excited state relaxes to a thermal equilibrium state having an occupation probability determined by the crystal lattice temperature,

which completes excitation to the electron excited state  $|E_{\text{ex}}; el\rangle \otimes |E_{\text{exthermal}}; phonon\rangle$ .

Because a phonon is involved in the above excitation of the electron, this excitation process is known as a phonon-assisted process [16–20]. When light having a photon energy smaller than  $E_g$  is incident on the Si-PD, electrons are excited by the two-step excitation described above, generating a photocurrent. Photosensitivity to this incident light is manifested by means of the above process.

Note that applying a forward current to the Si-PD causes the two-step stimulated emission described by processes (1′) and (2′) below [17].

- (1′) First step: When a forward current is applied, an electron is injected from the external circuit to the conduction band, and therefore, the state  $|E_{\text{ex}}; el\rangle \otimes |E_{\text{exthermal}}; phonon\rangle$  is the initial state. During this time, driven by a dressed photon generated in the p–n junction of the Si-PD by the incident light, the electron transitions from the initial state  $|E_{\text{ex}}; el\rangle \otimes |E_{\text{exthermal}}; phonon\rangle$  to an intermediate state  $|E_g; el\rangle \otimes |E_{\text{ex}}; phonon\rangle$ , creating a dressed photon and propagating light via stimulated emission. Because Si is an indirect-transition–type semiconductor, there are almost no transitions caused by spontaneous emission.
- (2′) Second step: The electron transitions from the intermediate state  $|E_g; el\rangle \otimes |E_{\text{ex}}; phonon\rangle$  to a final state  $|E_g; el\rangle \otimes |E_{\text{ex}'}; phonon\rangle$ , causing stimulated emission. Because this is an electric-dipole–forbidden transition, only a dressed photon is generated. After this transition, the phonon in the excited state relaxes to a thermal equilibrium state determined by the crystal lattice temperature, which completes the transition to the electron ground state  $|E_g; el\rangle \otimes |E_{\text{exthermal}}; phonon\rangle$ .

Here, if the electron number densities occupying the initial state  $|E_{\text{ex}}; el\rangle \otimes |E_{\text{exthermal}}; phonon\rangle$  and the intermediate state  $|E_g; el\rangle \otimes |E_{\text{ex}}; phonon\rangle$ ,  $n_{\text{ex}}$  and  $n_{\text{inter}}$ , satisfy the Bernard–Duraffourg inversion condition ( $n_{\text{ex}} > n_{\text{inter}}$ ) [21], the number of photons created by stimulated emission exceeds the number of photons annihilated by absorption. In other words, optical amplification occurs. Because the amplified light brings about processes (1′) and (2′) again via dressed photons, the photosensitivity of the Si-PD in the case where a forward current is applied far exceeds the photosensitivity based on only processes (1) and (2).

## 3 Fabrication method

To realize the optical amplification described in Sect. 2, it is essential to efficiently generate dressed photons in the p–n junction of the Si-PD. To do so, we adopted a Si-LED fabrication method that we previously proposed [14]. In this

method, Joule-heat annealing was performed while radiating 1.32  $\mu\text{m}$ -wavelength light.

First, an n-type silicon substrate with an electrical resistivity of 10  $\Omega\text{ cm}$  and a thickness of 625  $\mu\text{m}$ , doped with arsenic (As), was used as the Si-PD material. This substrate was doped with boron (B) via ion implantation to form a p-layer. For the B doping, the implantation energy was 700 keV, and the ion dose density was  $5 \times 10^{13}\text{ cm}^{-2}$ . After forming a p–n homojunction in this way, an indium tin oxide (ITO) film with a thickness of 150 nm was deposited at the p-layer side, a chromium film and an aluminum film with thicknesses of 5 nm and 80 nm were deposited at the n-substrate side, all by RF sputtering, and these were used as positive and negative electrodes. Then, the silicon substrate with these electrodes attached was diced with a dicer to form a single Si-PD. The area was about 2  $\text{mm}^2$ .

Next, annealing was performed by applying a forward current to the Si-PD to generate Joule heating, causing the B to diffuse and changing the spatial distribution of the B concentration. During this time, the device was irradiated, from the ITO electrode side, with laser light having a photon energy smaller than  $E_g$  of Si ( $E_g$  of 0.9 eV, corresponding to a wavelength of 1.32  $\mu\text{m}$ , and optical power of 120 mW). This induced the phonon-assisted process, and the B diffusion due to the annealing was controlled. As a result, a B concentration with a spatial distribution suitable for efficiently generating dressed photons was formed in a self-organized manner.

The above method is the same as the method of fabricating Si-LEDs previously reported by the authors [14, 15]. Here, however, in order to make use of the stimulated emission process described in Sect. 2 for the Si-PD to be fabricated, it is necessary to make the probability of generating stimulated emission larger than the probability of generating spontaneous emission. To do so, the forward current density for annealing was kept smaller than that in Ref. [14], namely, 1.3  $\text{A}/\text{cm}^2$ . Determining the number of injected electrons per unit time and per unit area on this basis gives a value of  $8.1 \times 10^{18}\text{ s}^{-1}\text{ cm}^{-2}$ , which corresponds to the probability of generating spontaneous emission. On the other hand, the generation probability of stimulated emission corresponds to the number of photons per unit time and per unit area, which is  $3.9 \times 10^{19}\text{ s}^{-1}\text{ cm}^{-2}$  in the case of the laser power mentioned above (120 mW). Comparing this with the number of injected electrons confirms that the probability of generating stimulated emission is sufficiently large.

When performing Joule-heat annealing under laser irradiation in practice, the surface temperature of the Si-PD, measured by thermography, showed a temporal variation similar to Fig. 2(c) in Ref. [14]. Specifically, immediately after applying the forward current, the surface temperature rose to 40.7  $^\circ\text{C}$ , then dropped due to the generation of stimulated emission and dissipation of its associated Joule energy,

and reached an almost stable temperature (38.6  $^\circ\text{C}$ ) after about 10 minutes, at which point the annealing was completed.

## 4 Device characterization

In this section we present the results of evaluating the spectral sensitivity characteristics, the voltage–current characteristics, and the optical amplification characteristics of the fabricated device.

### 4.1 Spectral sensitivity characteristics

First, we measured the spectral sensitivity characteristics when a forward current was not applied to the device. Photoelectric conversion in this case is based on the two-step excitation described by processes (1) and (2) in Sect. 2. As the light source, we used a xenon lamp, for wavelength selection we used a monochromator, and for photocurrent detection we used a lock-in amplifier. The optical power at each wavelength was measured with an InGaAs photodiode (Hamamatsu Photonics, G8370). The measurement wavelength range was 1.00–1.20  $\mu\text{m}$ . The spectral sensitivity characteristics measured in the infrared region are shown by curves A to C in Fig. 1. Curve A shows the values obtained with a Si-PD fabricated by annealing using the phonon-assisted process described in Sect. 3. For comparison, curve B shows values obtained with a Si-PD fabricated without annealing. Curve C shows the values obtained with a Si-PIN photodiode (Hamamatsu Photonics, S3590) used as a reference. Comparing curves A and C, the photosensitivities of both of them were reduced in the wavelength region longer than a cutoff wavelength  $\lambda_c = 1.11\text{ }\mu\text{m}$  determined by  $E_g$  of Si, although in curve A the reduction was more gentle, and at wavelengths above 1.16  $\mu\text{m}$ , the photosensitivity was about three times higher than that of curve C. In addition, the photosensitivity values for curve A were larger than the values for curve B. This was due to the spatial distribution of the B concentration being controlled in a self-organized manner so that dressed photons are efficiently generated by annealing using the phonon-assisted process. Also, the higher photosensitivity values for curve B compared with the values for curve C indicates that dressed photons are readily generated inside the Si-PD compared with the case of curve C, as a result of implantation of a high concentration of B.

Because Joule-heat annealing was performed while radiating 1.32  $\mu\text{m}$ -wavelength light for fabricating the Si-PD (see Sect. 3), when light having the same wavelength (1.32  $\mu\text{m}$ ) is incident on the device, it is expected that the photosensitivity will be selectively increased. This wavelength-selective photosensitivity increase has already been observed in the case of photovoltaic devices that we

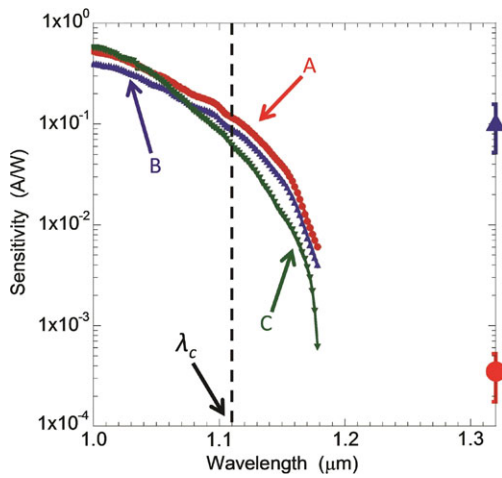


**Fig. 1** Wavelength dependency of photosensitivity. Curve A: device fabricated by phonon-assisted annealing. Curve B: device fabricated without annealing. Curve C: commercially available photodiode (S3590, Hamamatsu Photonics). The red circles and blue triangles show the photosensitivity to incident light (wavelength 1.32  $\mu\text{m}$ ) for forward current densities of 60  $\text{mA}/\text{cm}^2$  and 9  $\text{A}/\text{cm}^2$ , respectively

developed using the phonon-assisted process [17]. Therefore, photosensitivity for incident light with a wavelength of 1.32  $\mu\text{m}$  in particular is discussed in the following. We made a constant forward current flow in the device and evaluated the photosensitivity for incident light with a wavelength of 1.32  $\mu\text{m}$ . Photoelectric conversion in this case involved not only the two-step excitation described by processes (1) and (2) in Sect. 2, but also processes (1') and (2'), but the contribution of the latter was sufficiently large. A semiconductor laser was used as the light source, and the output beam was made incident on the Si-PD after being intensity-modulated with a chopper. We obtained the current variation  $\Delta I = V/R$  from the ratio of the voltage variation  $V$  produced at that time and the resistance  $R$  of the Si-PD, and we divided this by the incident light power  $P$  to obtain the photosensitivity  $\Delta I/P$ . The results are indicated by the red circles and the blue triangles in Fig. 1. These are the measured values for cases where the forward current densities of the fabricated Si-PD were 60  $\text{mA}/\text{cm}^2$  and 9  $\text{A}/\text{cm}^2$ , respectively. The photosensitivity for the current density of 9  $\text{A}/\text{cm}^2$  was 0.10  $\text{A}/\text{W}$ . This is as much as two times higher than the case using mid-bandgap absorption [5–7] described in Sect. 1, demonstrating that we achieved our objective of increasing the photosensitivity. This value is about 300 times higher than the 60  $\text{mA}/\text{cm}^2$  case, and shows the same large values as curve C at a wavelength of 1.09  $\mu\text{m}$ . This photosensitivity is sufficiently high for use in long-distance optical fiber communication systems [22]. The increase in photosensitivity with increasing forward current at a wavelength of 1.32  $\mu\text{m}$  is due to the higher stimulated emission gain as well as the higher number of recombining electrons.

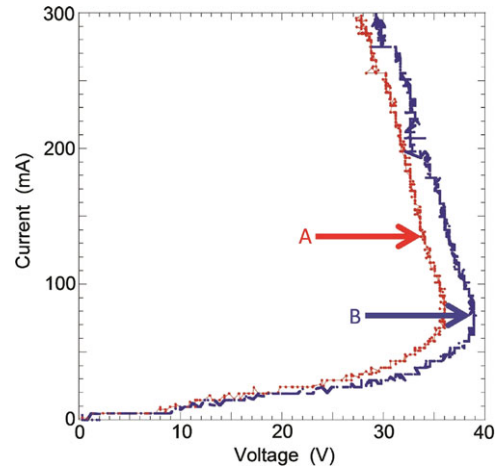


**Fig. 2** Voltage–current characteristics. Curves A and B are measurement results obtained with and without light irradiation

#### 4.2 Voltage–current characteristics and optical amplification characteristics

First, we measured the voltage–current characteristics for cases where the Si-PD was irradiated and not irradiated with 1.32  $\mu\text{m}$ -wavelength, 120  $\text{mW}$ -power laser light. The measurement results are shown by curves A and B in Fig. 2. Both curves show negative-resistance characteristics at forward currents of 80  $\text{mA}$  and higher, similarly to the case of a Si-LED (see Fig. 4 in Ref. [14]). Also, curve A is shifted toward lower voltages compared with curve B. This shift was particularly remarkable when the forward current was 30  $\text{mA}$  and higher. The reason for this is that the electron number density in the conduction band is reduced because a population inversion occurs around a forward current of 30  $\text{mA}$  and electrons are consumed for stimulated emission, and as a result, the voltage required for injecting the same number of electrons is decreased. On the other hand, when the forward current is increased further, the amount of shift is reduced. This is because the probability of stimulated emission recombination driven by spontaneous emission is increased as the forward current increases, and as a result, the voltage drop due to stimulated emission recombination caused by incident light becomes relatively small.

Next, we measured the relationship between the incident light power  $P$  and the current variation  $\Delta I$ . For this measurement, we used forward current densities of 60  $\text{mA}/\text{cm}^2$  and 9  $\text{A}/\text{cm}^2$ , and we varied the incident light power by using neutral density filters. In a conventional Si-PD, only absorption of light is used for photoelectric conversion. In our Si-PD, however, because stimulated emission is also used, the current variation  $\Delta I$  depends on the number of electron–hole pairs that recombine due to stimulated emission and is given by  $\Delta I = (eP/h\nu)(G - 1)$ . Here,  $e$  is the electron

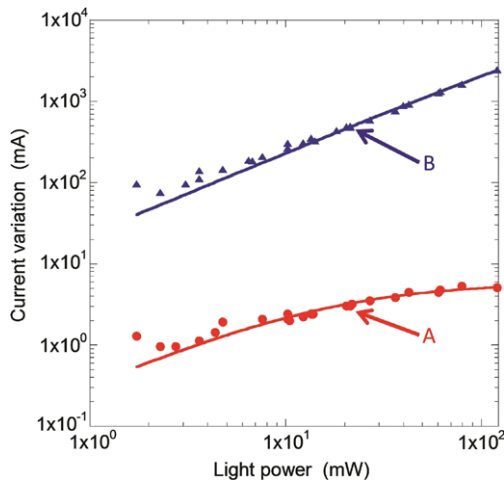


**Fig. 3** Relationship between incident light power (wavelength 1.32  $\mu\text{m}$ ) and current variation. Curves A and B are for forward current densities of 60  $\text{mA}/\text{cm}^2$  and 9  $\text{A}/\text{cm}^2$ , respectively

charge,  $h\nu$  is the photon energy, and  $G$  is the stimulated emission gain.

The relationship between the incident light power at a wavelength of 1.32  $\mu\text{m}$  and the current variation  $\Delta I$  is shown in Fig. 3. Similarly to Fig. 1, the red circles and blue triangles show the measurement results for forward current densities of 60  $\text{mA}/\text{cm}^2$  and 9  $\text{A}/\text{cm}^2$ , respectively. For the forward current density of 60  $\text{mA}/\text{cm}^2$ ,  $\Delta I$  saturated as the incident light power increased; whereas for the forward current density of 9  $\text{A}/\text{cm}^2$ ,  $\Delta I$  did not saturate but continued to increase linearly. The curves A and B show calculation results fitted to the experimental results using the above relationship  $\Delta I = (eP/h\nu) \times (G - 1)$ . The stimulated emission gain  $G$  depends on the incident light power as  $\exp[g/(1 + P/P_s)]$  [23], where  $g$  is the small-signal gain coefficient, and  $P_s$  is the saturation power. For the fitted results, these values were  $g = 3.2 \times 10^{-4}$  and  $P_s = 17$  mW in the case of curve A, and  $g = 2.2 \times 10^{-2}$  and  $P_s = 7.1 \times 10^2$  mW in the case of curve B. The increases in  $g$  and  $P_s$  as the forward current increased were due to the increasing number of electrons recombining. The experimental values and calculated values showed good agreement in Fig. 3, confirming that the remarkable increase in photosensitivity shown by the red circles and blue triangles in Fig. 1 was due to optical amplification as a result of stimulated emission.

#### 4.3 Photosensitivity characteristics with reverse bias

In Sects. 4.1 and 4.2 above, it was shown that the remarkable increase in photosensitivity when a forward current was applied is due to optical amplification based on stimulated emission. In this subsection, in order to verify this,

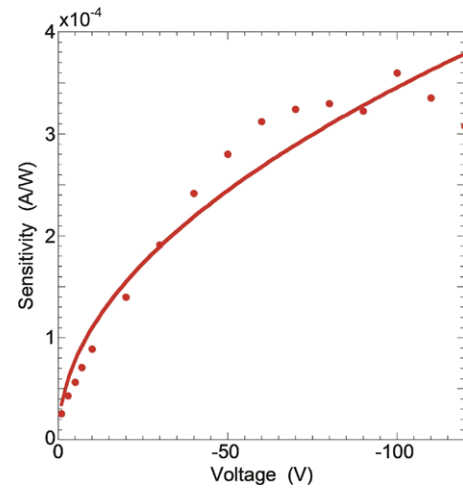


**Fig. 4** Relationship between reverse-bias voltage and photosensitivity. The wavelength of the incident light was 1.32  $\mu\text{m}$

we measured the photosensitivity when a reverse bias voltage  $V_r$  was applied, while keeping the incident light power fixed. The photoelectric conversion in this case is based on the two-step excitation described by processes (1) and (2) in Sect. 2. For these measurements, we set the stabilized power supply to a constant-voltage mode and measured the voltage variation across both ends of a 1  $\text{k}\Omega$  load resistor. The red circles in Fig. 4 are the measurement results of the relationship between the reverse bias voltage and the photosensitivity. The maximum photosensitivity was about  $3 \times 10^{-4}$  A/W, which is about 1/300 of the value (0.10 A/W) indicated by the blue triangles in Fig. 1 (a forward current density of 9  $\text{A}/\text{cm}^2$ ). When  $V_r = 0$ , the photosensitivity was too low to be measured. When the reverse bias voltage was low, for example,  $V_r = -1$  V, the photosensitivity was about  $2.5 \times 10^{-5}$  A/W, and therefore, the value of 0.10 A/W above shows that the photosensitivity at  $V_r = 0$  was amplified by a factor of at least 4000.

This figure shows that the photosensitivity increases as the reverse bias voltage increased, and then saturated. Electron-hole pairs created by light absorption are extracted from the depletion layer, generating photocurrent, and the photocurrent is proportional to the width  $w$  of the depletion layer; therefore, we used the expression  $w = A\sqrt{-V_r}$  [24] representing the relationship between the width  $w$  and the reverse bias voltage  $V_r$ , and the curve in this figure shows the calculation results fitted to the measured values. Because the photosensitivity saturates as the reverse bias voltage increases, no electron avalanche effect [25] occurs. This means that there is no contribution from an avalanche effect in the remarkable increase in photosensitivity observed when a forward current was applied (see Sects. 4.1 and 4.2). Therefore, it was confirmed that this remarkable increase in photosensitivity was due to optical amplification based on stimulated emission.

## 5 Conclusion

We fabricated a new photodetector by subjecting a Si crystal having p–n homojunction to a phonon-assisted annealing process. For incident light with a wavelength of 1.16  $\mu\text{m}$  and higher, this device showed a photosensitivity about three times higher than a Si-PIN photodiode used as a reference. The photosensitivity for 1.32  $\mu\text{m}$ -wavelength incident light was increased by applying a forward current, and we obtained a photosensitivity of 0.10 A/W for a forward current density of 9 A/cm<sup>2</sup>. This value is at least 4000 times greater than the zero-bias photosensitivity, and the remarkable increase was due to the manifestation of optical amplification caused by the forward current injection. For a forward current density of 9 A/cm<sup>2</sup>, the small-signal gain coefficient for optical amplification was  $2.2 \times 10^{-2}$ , and the saturation power was  $7.1 \times 10^2$  mW. There was no contribution from an electron avalanche effect in this behavior. In a future paper, we plan to report details of other characteristics, such as the photosensitivity for incident light in the infrared region at wavelengths other than 1.32  $\mu\text{m}$ , the signal-to-noise ratio, and the frequency response band.

**Open Access** This article is distributed under the terms of the Creative Commons Attribution License which permits any use, distribution, and reproduction in any medium, provided the original author(s) and the source are credited.

## References

1. M. Levinshtein, S. Rumyantsev, M. Shur, *Handbook Series on Semiconductor Parameters*, vol. 1 (World Scientific, Singapore, 1996)
2. A. Loudon, P.A. Hiskett, G.S. Buller, *Opt. Lett.* **27**, 219 (2002)
3. C. Cremer, N. Emeis, M. Schier, G. Heise, G. Ebbinghaus, L. Stoll, *IEEE Photonics Technol. Lett.* **4**, 108 (1992)
4. A.F. Phillips, S.J. Sweeney, A.R. Adams, P.J.A. Thijs, *IEEE J. Sel. Top. Quantum Electron.* **5**, 401 (1999)
5. J.E. Carey, C.H. Crouch, M. Shen, E. Mazur, *Opt. Lett.* **30**, 1773 (2005)
6. M.W. Geis, S.J. Spector, M.E. Grein, R.T. Schulein, J.U. Yoon, D.M. Lennon, C.M. Wynn, S.T. Palmacci, F. Gan, F.X. Kärtner, T.M. Lyszczarz, *Opt. Express* **15**, 16886 (2007)
7. M.W. Geis, S.J. Spector, M.E. Grein, R.T. Schulein, J.U. Yoon, D.M. Lennon, F. Gan, F.X. Kärtner, T.M. Lyszczarz, *IEEE Photonics Technol. Lett.* **19**, 152 (2007)
8. T. Baehr-Jones, M. Hochberg, A. Scherer, *Opt. Express* **16**, 1659 (2008)
9. H. Chen, X. Luo, A.W. Poon, *Appl. Phys. Lett.* **95**, 171111 (2009)
10. M. Lee, C. Chu, Y. Wang, *Opt. Lett.* **26**, 160 (2001)
11. M. Cassalino, L. Sirloto, L. Moretti, M. Gioffrè, G. Coppola, *Appl. Phys. Lett.* **92**, 251104 (2008)
12. T. Tanabe, K. Nishiguchi, E. Kuramochi, M. Notomi, *Appl. Phys. Lett.* **96**, 101103 (2010)
13. B. Shi, X. Liu, Z. Chen, G. Jia, K. Cao, Y. Zhang, S. Wang, C. Ren, J. Zhao, *Appl. Phys. B* **93**, 873 (2008)
14. T. Kawazoe, M.A. Mueed, M. Ohtsu, *Appl. Phys. B* **104**, 747 (2011)
15. T. Kawazoe, M. Ohtsu, K. Akahane, N. Yamamoto, *Appl. Phys. B* (2012, in press)
16. T. Kawazoe, K. Kobayashi, S. Takubo, M. Ohtsu, *J. Chem. Phys.* **122**, 024715 (2005)
17. S. Yukutake, T. Kawazoe, T. Yatsui, W. Nomura, K. Kitamura, M. Ohtsu, *Appl. Phys. B, Lasers Opt.* **99**, 415 (2010)
18. T. Kawazoe, M. Ohtsu, Y. Inao, R. Kuroda, *J. Nanophotonics* **1**, 011595 (2007)
19. T. Yatsui, K. Hirata, W. Nomura, Y. Tabata, M. Ohtsu, *Appl. Phys. B* **93**, 55 (2008)
20. T. Kawazoe, H. Fujiwara, K. Kobayashi, M. Ohtsu, *IEEE J. Sel. Top. Quantum Electron.* **15**, 1380 (2009)
21. M.G.A. Bernard, G. Duraffourg, *Phys. Status Solidi* **1**, 699 (1961)
22. J.D. Schaub, *J. Lightwave Technol.* **19**, 272 (2001)
23. T. Saitoh, T. Mukai, *IEEE J. Quantum Electron.* **23**, 1010 (1987)
24. N.W. Ashcroft, N.D. Mermin, *Solid State Physics* (Brooks Cole, Singapore, 1976)
25. R.J. McIntyre, *IEEE Trans. Electron Devices* **13**, 164 (1966)

# Dressed photon technology

Motoichi Ohtsu<sup>1,2</sup>

<sup>1</sup>Graduate School of Engineering, University of Tokyo,  
2-11-16 Yayoi, Bunkyo-ku, Tokyo 113-8656, Japan

<sup>2</sup>Nanophotonics Research Center, University of Tokyo,  
2-11-16 Yayoi, Bunkyo-ku, Tokyo 113-8656, Japan,  
e-mail: ohtsu@ee.t.u-tokyo.ac.jp

## Abstract

This paper reviews the theoretical picture of dressed photons used to describe the electromagnetic interactions between nanometric particles located in close proximity to each other. The coupling between a dressed photon and multi-mode coherent phonons is also presented, revealing the presence of a novel phonon-assisted process in light-matter interactions. Applications of this novel process to innovative optical devices, fabrication technologies, energy conversion, and hierarchical systems are demonstrated.

**Keywords:** (45.20.dh) Energy conversion; (42.50.-p) Quantum optics; (42.79.Nv) Optical frequency converters; (42.82.Cr) Fabrication techniques; (4.282.Gw) Other integrated-optical elements and systems; (78.67.Hc) Quantum dots; (78.68.+m) Optical properties of surfaces.

## 1. Introduction

Nanophotonics, proposed by the author in 1993 [1–3], is a novel optical technology that utilizes the electromagnetic fields localized in nanometric space. These fields have been named optical near-fields due to their non-propagating features. Nanophotonics enables the realization of qualitative innovations in optical devices, fabrication techniques, energy conversion, and hierarchical systems by exploiting the novel functions and phenomena enabled by optical near-field interactions that would otherwise be impossible if only conventional propagating light were used. In this sense, the principles and concepts of dressed photon technology are quite different from those of conventional wave-optical technology encompassing photonic crystals [4], plasmonics [5], metamaterials [6, 7], silicon photonics [8], and quantum-dot photonic devices [9]. This is because these devices use propagating light even though the materials or particles used may be nanometer-sized. Advancing these innovations has required a deeper understanding of optical near-fields. The theoretical picture of dressed photons has been proposed to describe the electromagnetic interactions between nanometric particles located in close proximity to each other, giving birth to a new field known as dressed photon technology.

This article reviews the unique features of dressed photons and demonstrates examples of the innovations that can be achieved [10].

## 2. Principles

The optical near-field is a virtual cloud of photons that always exists around an illuminated nanometric particle. A naïve wave-optical picture of the optical near-field has been given [11]. This picture, however, is not adequate for use as a theoretical basis for realizing qualitative innovations; to do so requires a quantum optical approach and quantum field theory. A real photon (also called a free photon, i.e., conventional propagating scattered light) can be emitted from an electron in an illuminated nanometric particle. Independently of the real photon, another photon is emitted from the electron, and this photon can be re-absorbed within a short duration. This photon, i.e., a virtual photon, is nothing more than the optical near-field, and its energy is localized at the surface of the nanometric particle. Since the virtual photon remains in the proximity of the electron, it can couple with the electron in a unique manner. This coupled state, called a dressed photon, is a quasi-particle from the standpoint of photon energy transfer. It is the dressed photon, not the free photon, that carries the material excitation energy. The dressed photon has been theoretically described by assuming a multipolar quantum electrodynamic Hamiltonian in a Coulomb gauge and single-particle states in a finite nano-system [12]. After a unitary transformation and some simple calculations, the creation and annihilation operators of the dressed photon are expressed as the sum of the operators of the free photon and an electron-hole pair.

The real system is more complicated because the nanometric subsystem (composed of nanometric particles and dressed photons) is buried in a macroscopic subsystem composed of the macroscopic substrate material and the macroscopic incident and scattered light fields. A novel theory was developed to avoid describing all of the complicated behaviors of these subsystems rigorously, since we are interested only in the behavior of the nanometric subsystem. In this theory, the projection operator method is effectively employed for describing the quantum mechanical states of the system [13]. As a result of this projection, the local electromagnetic interaction in the nanometric subsystem is expressed by a screened potential using a Yukawa function, which represents the dressed photons around the nanometric particles. The decay length of this potential is equivalent to the particle size.

A real nanometric material is composed not only of electrons but also of a crystal lattice. In this case, after a dressed photon is generated on an illuminated nanometric particle, its energy can be exchanged with the crystal lattice. By this exchange, the crystal lattice can excite the vibration mode

coherently, creating a multi-mode coherent phonon state. As a result, the dressed photon and the coherent phonon can form a coupled state. The creation operator of this quasi-particle, representing the coupled state, is expressed as the product of the creation operator of the dressed photon and a displacement operator of the phonon, which represents the creation of the coherent phonon state [14, 15]. This coupled state (the dressed photon carrying the coherent phonon energy, or DP-CP for short) is a quasi-particle and is generated only when the particle size is small enough to excite the crystal lattice vibration coherently.

### 3. Devices

To realize optical devices with innovative operating principles while decreasing their sizes beyond the diffraction limit and reducing the energy consumption required for their operation, novel dressed photon devices and their associated integrated circuits have been proposed [16]. As a first example of a basic device, an AND gate using three different-sized cubic quantum dots (QDs) – used as two input ports and one output port – has been demonstrated [17]. By fixing their size ratio to  $1:\sqrt{2}:2$ , they satisfy the resonant condition for energy transfer by dressed photon exchange. In that study, AND gate operation was experimentally confirmed at a temperature of 5 K by using cubic copper chloride (CuCl) QDs with sizes of 4 nm, 6 nm, and 8 nm, separated from each other by 3 nm. The rise time of the output signal is 25 ps, which is determined by the time constant of the dressed photon exchange and is inversely proportional to the dressed photon interaction energy represented by the Yukawa function. The fall time is 4 ns, which is determined by the carrier lifetime. A decrease in the fall time is expected by extracting the energy of the lowest exciton energy level of the input QD into the other energy levels in the other QDs placed adjacent to it. The second example is a NOT gate, for which two different-sized QDs are used as input and input ports. NOT gate operation was experimentally confirmed by using CuCl QDs, as in the case of the AND gate [10].

In another study, two layers of InAs QDs were grown on a substrate by molecular beam epitaxy in a size- and position-controlled manner for room-temperature operation of logic gates, and the substrate was processed to form a two-dimensionally aligned array of mesa structures (Figure 1) [18]. The mesa dimensions were  $300\text{ nm} \times 300\text{ nm} \times 85\text{ nm}$ , and the areal density was  $1 \times 10^8$  units/cm<sup>2</sup>. Devices that operate as AND gates and NOT gates were implemented by adjusting the characteristics of the energy transfer via dressed photons between two InAs QDs in the upper and lower layers of the mesa structures. One hundred and thirty-three devices were fabricated, of which 53 devices operated successfully as AND gates and 50 devices operated as NOT gates. Figure 2 shows the NOT gate operation at room temperature. The Au nanoparticle plays the role of improving the output efficiency of propagating light serving as an output signal of the device. That is, since the gallium arsenide (GaAs) constituting the barrier layer has a large refractive index, optical signals emitted by the device are scattered backward in the direction of

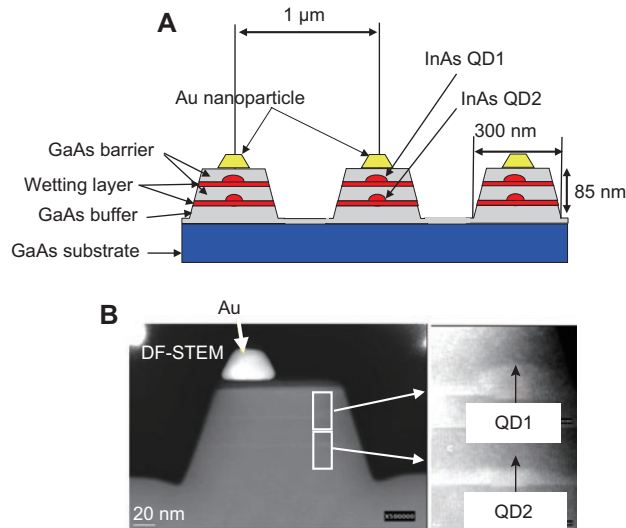


**Figure 1** (A) Cross-sectional profiles of mesa-structured NOT gate devices and (B) SEM images. QD1 and QD2 are the larger and smaller quantum dots, respectively.

the substrate [19]. The Au nanoparticle shown in Figure 1 allows a greater portion of the scattered light to be released to the outside of the device. By combining AND and NOT gates, NOR, OR, and NAND gates can be assembled, allowing a complete set of logic gates to be realized for application to future information processing systems.

Two kinds of optical pulse generators have also been invented: One uses cooperative behavior of the induced electric dipoles in a chain of closely spaced QDs to realize Dicke's super-radiant photon emission [20]. The other uses two QD systems, each consisting of a combination of smaller and larger QDs [21]. With an architecture in which the two QD systems take the role of a timing delay and frequency up-conversion, sustained pulsation with an oscillation period of several nano-seconds was numerically confirmed.

A novel device named an optical nano-fountain has been devised as an input terminal to convert incident propagating light to dressed photons. Its operation is similar to that of the light-trapping antennae in light-harvesting bacteria [22]. Proper device operation has been experimentally confirmed by using CuCl QDs at low temperature. The output optical spot diameter was  $<10\text{ nm}$ , and the time required for energy transfer to the central largest QD was about 1 ns, which is governed by the time constant for dressed photon exchange. For room-temperature operation of this device, multi-layered InAs QDs were grown by molecular beam epitaxy, as in the case of Figure 1 [23]. A layer of large QDs was sandwiched by 30 layers of small QDs. As a result of optical energy transfer, the photoluminescence intensity emitted from the large QDs was confirmed to be 40 times larger than that from a solitary layer of large QDs.

An output terminal, i.e., efficient energy conversion from dressed photons to propagating light, has been realized by fixing a metallic nanometric particle in close proximity to the output QD of a dressed photon device, as was demonstrated in Figure 1.

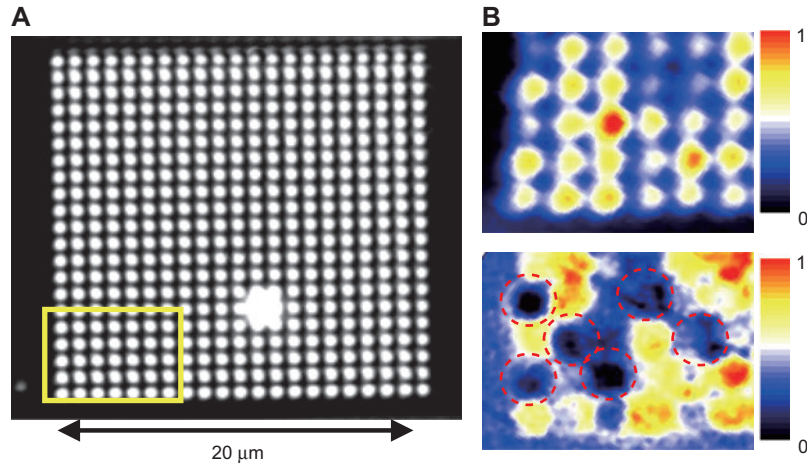


**Figure 2** Images of the two-dimensional array of NOT gates. (A) Image taken with an optical microscope. (B) Spatial profile of the output optical signals emitted from the area surrounded by the white lines in (A), which were acquired by microspectroscopic measurements. Upper and lower images show the profile without and with the input optical signal, respectively. The areas surrounded by the dashed circles in the lower figure correspond to the output optical signals from the mesa-structures reliably operating as NOT logic gates.

An optical buffering operation has been confirmed by using multiple-quantum wells in a zinc oxide (ZnO) nanorod [24] and by utilizing the time-delayed energy concentration feature of an optical nano-fountain [25]. A nano-dot coupler using a chain of cadmium selenide (CdSe) QDs [26] has also been devised.

The dressed photon devices reviewed above have several unique features that establish their superiority over conventional wave-optical devices [5–9] for application to next-generation information processing systems. One feature is undoubtedly their nanometer-scale dimensions reaching down beyond the diffraction limit, which is an example of a quantitative innovation in optical technology. However, it should be noted that the true nature of dressed photon devices involves their ability to realize qualitative innovations, originating from their unique features, listed below.

1. Low heat generation and low energy dissipation: A dressed photon device dissipates energy only through the relaxation from an upper electric-dipole-forbidden energy level to a lower electric-dipole-allowed energy level. It was found that the bit error rate of a device remained lower than  $10^{-6}$  if the magnitude of the energy dissipation due to the relaxation in the large QD was larger than  $25 \mu\text{eV}$  [27]. This small value of energy dissipation suggests that the heat generation of dressed photon devices could be substantially lower than that of conventional electronic logic devices [28]. In fact, this low energy dissipation could be as low as that of the computational operations in biological systems [29].
2. Single photon operation: The capability of dressed photon devices to operate based on single photons has been confirmed by the Hanbury Brown and Twiss method [30], where two closely spaced CuCl QDs were used at 15 K [31]. Single photon emission was guaranteed by three blockade mechanisms: tuning the incident light to the smaller QD and using an electric-dipole-forbidden energy level in the larger QD, using the dressed photon

interaction to transfer energy from the smaller QD to the larger QD, and using a single exciton emission level in the larger QD. These mechanisms are supported by the large binding energy of the exciton molecule. A 99.3% plausibility of single-photon emission was confirmed with 99.98% accuracy.

3. Resistance to non-invasive attacks: Conventional electronic and optical devices need electrical or optical wires to dissipate their energies toward the external macroscopic loads in order to fix the output signal intensity. Since it is straightforward to monitor the signals transmitted through these wires by using electrical or optical sensing probes, non-invasive attacks are possible [32]. In contrast, a dressed photon device dissipates energy only through relaxation from the higher to lower energy levels in the QD. Because the energy is dissipated by non-radiative relaxation to the crystal lattice vibration in the QD and also because its magnitude is very low, non-invasive attacks are extremely difficult, and thus, tamper resistance is high [33].

Based on the three unique features outlined above, dressed photon devices have already been employed for demonstrating novel information processing systems. One example is a highly integrated content addressable memory of an optical router system [34].

## 4. Fabrication technologies

Novel fabrication technologies have been developed utilizing dressed photons. Some examples are reviewed in this section.

### 4.1. Photochemical vapor deposition

Photochemical vapor deposition (PCVD) involves depositing particles or films on a substrate by photo-dissociating organic



molecules. In the case of metallic Zinc (Zn) deposition as an example, a popularly employed metal-organic molecule is gaseous diethylzinc (DEZ), which has been employed as a parent gas due to its strong optical absorption [35]. Its photo-absorption energy,  $E_{abs}$ , and dissociation energy,  $E_{dis}$ , are 4.59 eV and 2.26 eV, respectively. In a novel PCVD method using a DP-CP, the molecule can be excited from  $|E_g;el\rangle\otimes|E_i;vib\rangle$  to  $|E_g;el\rangle\otimes|E_h;vib\rangle$  by absorbing the DP-CP energy, even though this transition is electric-dipole-forbidden. Here,  $|E_g;el\rangle$ ,  $|E_i;vib\rangle$ , and  $|E_h;vib\rangle$  represent the ground electronic state, the lowest molecular vibrational energy state, and a high molecular vibrational energy state, respectively. Such processes are named phonon-assisted processes. If the incident photon energy  $h\nu$  is higher than  $E_{dis}$ , transfer of a single DP-CP from the fiber probe tip to the molecule is sufficient for dissociation. On the other hand, when  $h\nu < E_{dis}$ , a two-step DP-CP transfer, i.e.,  $|E_g;el\rangle\otimes|E_i;vib\rangle \rightarrow |E_g;el\rangle\otimes|E_h;vib\rangle \rightarrow |E_{ex};el\rangle\otimes|E_i;vib\rangle$ , is required for dissociation, by which the molecule can be excited to the excited electronic state  $|E_{ex};el\rangle$ . One technical advantage of these phonon-assisted processes is that a high-power-consumption short-wavelength light source is not required. In principle, one can use a longer-wavelength light source even if its photon energy is lower than  $E_{dis}$ , which represents a qualitative innovation of this novel PCVD method.

Figures 3(A), (B), and (C) show AFM images of the nanometric Zn particles deposited on a sapphire substrate as a result of dissociating DEZ molecules by phonon-assisted PCVD using ultraviolet ( $h\nu=3.81$  eV; wavelength=325 nm), blue ( $h\nu=2.54$  eV; wavelength=488 nm), and red ( $h\nu=1.81$  eV; wavelength=684 nm) light sources, respectively, for generating the DP-CP at the fiber probe tip [36].

Figure 3(D) shows the relation between the photon flux,  $I$ , of the light incident on the fiber probe tip for generating the DP-CP and the deposition rate,  $R$ , of the Zn nanometric particles on the substrate, which can be expressed as  $R=aI+bl^2+cl^3+\dots$ , where the first, second, and third terms represent single-, two-, and three-step excitation by the DP-CP,

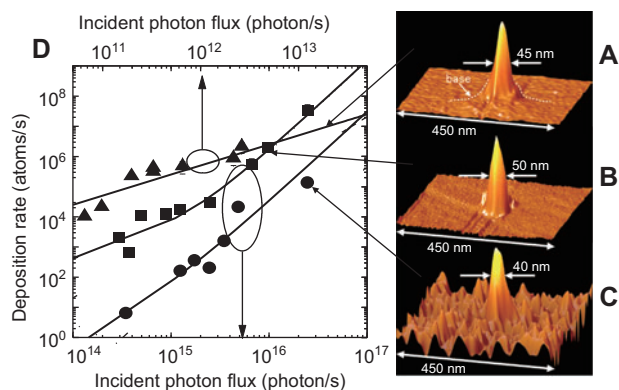


**Figure 3** Experimental results of depositing nanometric Zn particles on a sapphire substrate by phonon-assisted PCVD. (A), (B), (C) AFM images of the deposited nanometric Zn particles using ultraviolet, blue, and red light sources, respectively. (D) Relation between the incident photon flux and the deposition rate.

respectively. Since the relation  $h\nu > E_{dis}$  holds in the case of the ultraviolet light source [Figure 3(A)], single-step excitation is sufficient to dissociate the DEZ molecules. Thus, the experimental results are fitted by  $R=aI$ . Since  $h\nu > E_{dis}$  also holds in the case of the blue light [Figure 3(B)], single-step excitation is sufficient here, too. However, by increasing the incident light intensity  $I$ , two-step excitation becomes possible. Thus, the experimental results are fitted by  $R=aI+bl^2$ . Since  $h\nu < E_{dis}$  holds in the case of the red light [Figure 3(C)], two-step excitation is essential for dissociation. By increasing  $I$ , even three-step excitation becomes possible. Thus, the experimental results are fitted by  $R=bI^2+cI^3$ . Theoretical studies have shown that the ratios between the coefficients  $a, b, c, \dots$  satisfy the relation  $b/a=c/b=\dots$ . This relation was confirmed experimentally by measuring the values of  $b/a$  and  $c/b$ , which were found to be on the order of  $10^{-15}$  [37]. It should be pointed out that a nanometric Zn particle can be deposited even by dissociating optically inactive zinc-bis(acetylacetonate) [ $Zn(acac)_2$ ] molecules [37].

## 4.2. Photolithography

Conventional photolithography is well-established and has matured as information technology has moved towards miniaturization with the associated exponential increase in the density of transistors that can be fabricated on computer chips. In a laboratory setting, lithographic patterns with a line resolution of about 100 nm have been obtained using 193 nm-wavelength UV radiation [38]. Although several studies of optical near-field lithography have recently been reported [39], it is unlikely to find industrial applications and can be considered only as a complementary method to other photolithographic techniques. To solve these problems, the phonon-assisted process described above has been applied also to photolithography to pattern widely available commercial photoresists by using a visible light source, even though such photoresists are sensitive only to UV light. To confirm this patterning ability, a film of commercial photoresist (OFPR) was coated on a substrate, and a photomask having a sub-wavelength sized aperture was mounted on it. Irradiating the photomask and photoresist with visible light generated a DP-CP at the edge of the aperture of the photomask, and its energy was transferred to the photoresist, thereby activating and patterning the photoresist by the phonon-assisted process [40]. Figure 4(A) shows an AFM image of the linear pattern formed on the OFPR photoresist. The linewidth of the fabricated pattern was as narrow as 90 nm, which is equivalent to the width of the aperture and is much narrower than the wavelength (550 nm) of the incident visible light. For comparison with conventional photolithography, which is based on an adiabatic process, the same OFPR photoresist and the same photomask were used. Here, they were illuminated by UV light, to which the OFPR photoresist was sensitive. As shown in Figure 4(B), the resultant linewidth of the pattern was as wide as 300 nm, which is much broader than that of Figure 4(A). The broader linewidth was due to diffraction of the propagating UV light passing through the aperture.

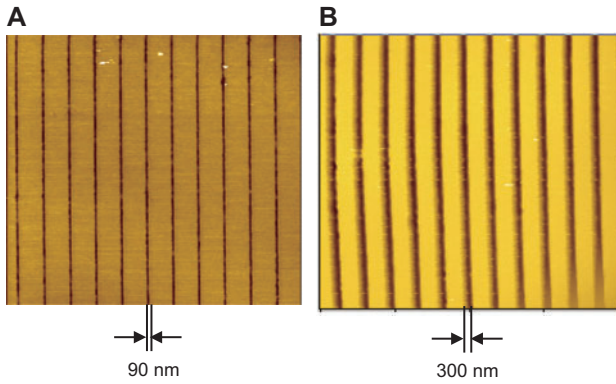


**Figure 4** Photolithography by phonon-assisted process and conventional adiabatic process. (A), (B) AFM images of OFPR photoresist patterned by visible and UV light, respectively.

Based on the results outlined above, a prototype machine has been constructed for producing commercial patterned devices [41]. It occupies an area as small as 1 m<sup>2</sup>. It uses a conventional xenon (Xe) lamp as a light source and is operated by computer-controlled robotics. A resolution of 20–50 nm is guaranteed for a substrate area of 50 mm×60 mm. It should be pointed out that a metallic photomask may degrade the resolution due to diffraction of the plasmonic wave. To solve this problem, the plasmonic wave on the photomask surface must be suppressed; it has been confirmed that Si is a suitable photomask material for this purpose.

A linear pattern with a minimum linewidth of 22 nm has been realized by using high-resolution photoresist [41]. Other examples of fabricated structures include diffraction gratings and Fresnel zone plates for soft X-rays with a wavelength of 0.5–1.0 nm. These devices were fabricated by using green light, whose wavelength is more than 500 times longer than that of soft X-rays. For the diffraction gratings, corrugations of 7600 lines/mm were patterned on a Si substrate, as shown in Figure 5(A), and were then coated with molybdenum/silicon dioxide (Mo/SiO<sub>2</sub>) multilayer films. The evaluated diffraction efficiency was as high as 3% in the soft X-ray wavelength range of 0.5–1.0 nm. This is higher than that of a commercially available diffraction grating fabricated using a Potassium Hydrogen Phthalate (KAP) crystal lattice [42]. For Fresnel zone plates, concentric circular patterns were fabricated on a tantalum (Ta) film [43]; SEM images are shown in Figure 5(B). The outer diameter, linewidth at the rim, and number of rings were 400 μm, 420 nm, and 230, respectively. The thickness of the Ta was 65 nm. By evaluating the contrast of the pattern as a function of the order of the rings [Figure 5(C)], it was confirmed that the phonon-assisted photolithography realized higher contrast than the conventional photolithography, especially for rings of higher order. A notable advantage of this method of fabricating soft X-ray devices is its mass-production capability. For example, with an exposure of several minutes, a pattern consisting of a two-dimensional array of Fresnel zone plates prepared on the photomask was transferred to the photoresist, allowing 49 Fresnel zone plates to be fabricated simultaneously.

### 4.3. Self-proceeding smoothing

Novel methods of smoothing surfaces are reviewed in this subsection, which are high-throughput fabrication technologies because neither a fiber probe nor a photomask is required. The key to these methods is to exploit the fact that DP-CPs can always be generated on a nanometrically rough material surface when it is illuminated with propagating light. The generated DP-CPs cause smoothing of locally rough parts, which then become flat, and the smoothing stops spontaneously because DP-CPs are no longer generated. Thus, they are called self-proceeding processes. Two methods are reviewed here.

1. Etching [44]: Substrates with ultra-flat surfaces of sub-nanometer roughness are required for various applications, including the manufacture of high-quality, extreme-UV optical components, high-power lasers, ultra-short-pulse lasers, and future optical devices with dimensions at the sub-100-nm scale. It is estimated that the required surface roughness,  $R_a$ , will be <0.1 nm [45]. Conventionally, chemical-mechanical polishing (CMP) has been used to flatten the surface [46]. However, CMP has difficulties in reducing  $R_a$  to <0.2 nm because the polishing pad roughness is as large as 10 μm, and the diameters of the polishing particles in the slurry are as large as 100 nm. In addition, polishing causes scratches or digs due to the contact between the polishing particles and/or impurities in the slurry and the substrate. To solve these problems, phonon-assisted photochemical etching was developed for smoothing the surface of glass. In this process, a quartz glass substrate with nanometric surface roughness is installed in a vacuum chamber filled with gaseous chlorine (Cl<sub>2</sub>) molecules. Although the absorption band edge wavelength of these molecules is 400 nm, green propagating light with a wavelength as long as 532 nm is used for photochemical etching. The Cl<sub>2</sub> molecules remain stable above the flat glass surface because of the absence of DP-CPs. However, when DP-CPs are generated at the tips of bumps on the illuminated rough surface, by the exchange of DP-CPs between the bumps and the Cl<sub>2</sub> molecules, the Cl<sub>2</sub> molecules are dissociated (as in Subsection 4.1) to produce chlorine (Cl) radicals, which etch the tips of the bumps. By this phonon-assisted process, the photochemical etching starts spontaneously to remove the bumps when the glass surface is illuminated with incident propagating light, and it stops spontaneously when the glass surface becomes so flat that DP-CPs are no longer generated.

As shown in Figure 6, the magnitude of the roughness,  $R_a$ , evaluated by atomic force microscopic measurements, decreased to 0.13 nm after 30 min of photochemical etching. In order for *in situ* real-time monitoring of the change in surface roughness during the photochemical etching, red CW laser light (wavelength=633 nm) was radiated onto the substrate surface in addition to the green CW laser light used for etching, and the scattered red light intensity was monitored [47]. As shown in Figure 6, the monitored results are consistent with the results of the  $R_a$  measurements.

After the photochemical etching, high-reflectivity films were coated on the glass substrate to produce a mirror suitable for

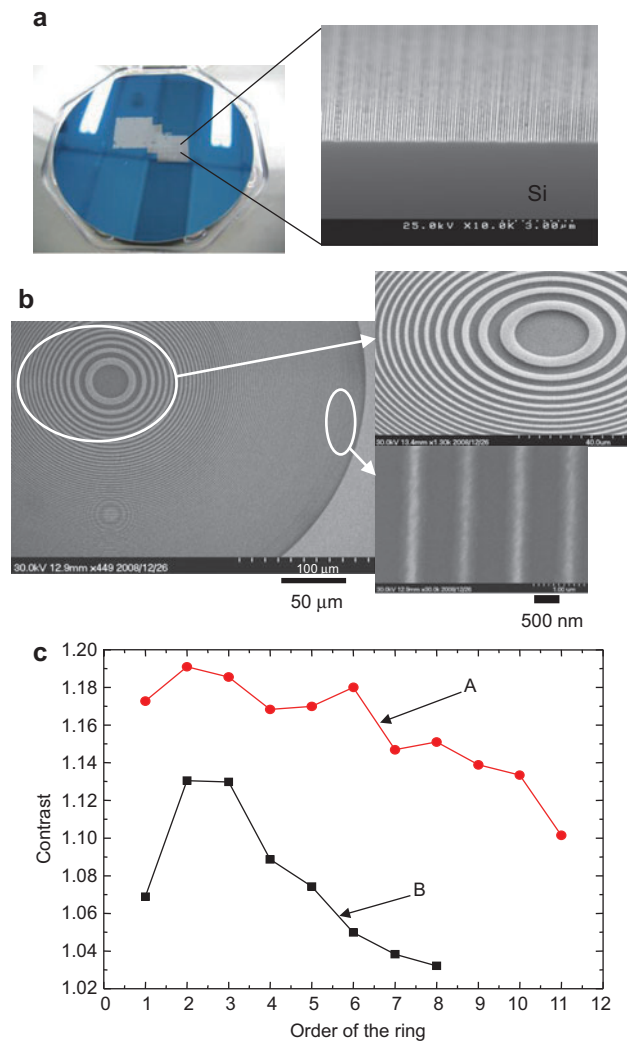


**Figure 5** Fabricated soft X-ray devices. (a) SEM image of the diffraction grating. (b), (c) SEM image of the Fresnel zone plate and the relation between the order of the rings and the contrast, respectively. Zigzag lines A and B represent the contrasts of the Fresnel zone plates fabricated by phonon-assisted and conventional adiabatic lithography, respectively.

high-power lasers [48]. Its laser damage threshold was evaluated by shooting the mirror with 355 nm laser pulses, which is a standard evaluation method (the “200 on 1” method in compliance with the international standard ISO 11254). The damage threshold was 14.0 J/cm<sup>2</sup>, which was 1.7 times higher than that of a mirror made from a conventional CMP substrate.

The methods reviewed above can be applied not only to planar substrates but also to convex and concave substrates. They can also be applied to the inner surface of a cylinder if it can be illuminated by propagating light. Side-walls of the corrugations of a diffraction grating pattern in soda lime glass have been also polished with this technique [49]. Furthermore, they can also be applied to a variety of materials, such as glasses, crystals, ceramics, metals, plastics, and so on. They can be used to polish surfaces of magnetic disks, photomasks for high-resolution photolithography, and so on.

2. Desorption [50]: Transparent polycrystalline ceramics are attracting interest for applications in optical technology [51–54], particularly for use as gain media for solid state lasers or optical windows [55–58]. To realize higher lasing efficiency or to reduce the scattering loss in optical windows, it is necessary to decrease the surface roughness. To meet this requirement, CMP is difficult to apply to polycrystalline ceramics because of their anisotropic interaction with the polishing medium. A key problem with CMP is that it may cause scratches because of collisions with the abrasive grains in the slurry. Furthermore, CMP may cause bumps on the surface, due to the difference in etching rates between adjacent grains and the polycrystal. To solve these problems, phonon-assisted desorption has been developed for smoothing the surface of transparent alumina (Al<sub>2</sub>O<sub>3</sub>), which is a hard polycrystalline ceramic, with the aim of fabricating low-loss gain media for ceramic lasers to be used in laser-driven spark plugs for the ignition systems in automobile engines. It is expected that the surface roughness, including the scratches formed in the preliminary grinding by diamond abrasive grains, will be repaired by sputtering Al<sub>2</sub>O<sub>3</sub> particles and phonon-assisted desorption. For this purpose, Al<sub>2</sub>O<sub>3</sub> particles are deposited on the substrate by RF sputtering. The substrate is illuminated with visible light (power density, 400 mW/cm<sup>2</sup>) whose wavelength (473 nm) is longer than that of the absorption band edge wavelength (260 nm) of the Al<sub>2</sub>O<sub>3</sub> particles. By this illumination, DP-CPs are generated on the ridges of the scratches, which causes the Al<sub>2</sub>O<sub>3</sub> particles to be activated, increasing the migration length, or which causes them to be desorbed from the ridges. By this phonon-assisted process, the deposition at the ridges is suppressed, whereas the bottoms of the scratches are filled by the Al<sub>2</sub>O<sub>3</sub> particles, and finally, the scratches are repaired. Experimental results are shown in Figure 7, which shows a drastic change in the surface profile. Statistical analysis using a Hough transform revealed that the average width of the scratches decreased from 128 nm to 92 nm using this method. The average depth decreased from 3 nm to 1 nm.

## 5. Energy conversion

This section reviews novel methods of conversion between optical and electrical energies by using DP-CPs.

### 5.1. Optical to optical energy

Frequency up-conversion of infrared light is advantageous for many applications, such as expanding the effective bandwidth of photodetectors or imaging sensors. Although second harmonic generation (SHG) [59] and phosphorescence using a multistep transition [60] are popular alternatives, SHG requires high-power, coherent light or a built-up cavity for high efficiency, and phosphorescence suffers from problems with saturation of the emitted light intensity. To increase the frequency up-conversion efficiency and to avoid these problems, a novel optical energy up-conversion method has been

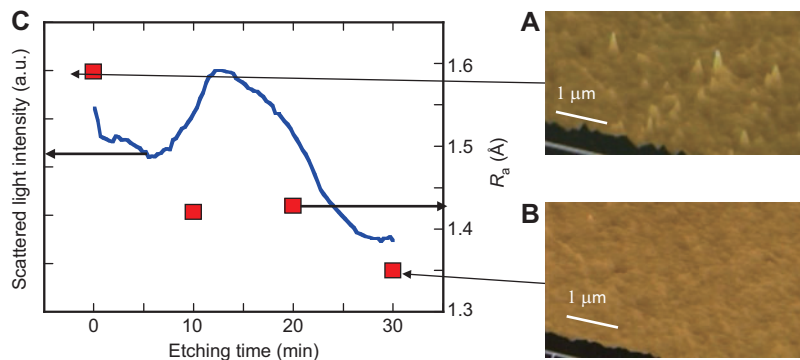


**Figure 6** Results of phonon-assisted photochemical etching of a glass substrate surface. (A), (B) AFM images of the glass surfaces before and after the etching. (C) Relation between the etching time, the surface roughness,  $R_a$ , and scattered light intensity.

realized by using powdery grains of 4-dicyanomethylene-2-methyl-6-*p*-dimethylaminostyryl-4H-pyran (DCM) organic dye molecules as a test specimen [61]. Although the absorption band-edge wavelength of the DCM is as short as 670 nm, the grains are illuminated by near-infrared light with a wavelength of 805 nm. This illumination generates DP-CPs at the edges of the grains, which are then exchanged between adjacent grains. As a result of this exchange, an electron in an adjacent grain is excited by a phonon-assisted process and then emits photons whose energies are higher than that of the incident light due to the contribution of the phonon energy.

Curve A in Figure 8 shows the spectral profile of the frequency up-converted light. For comparison, curve B is the spectral profile of the conventional fluorescence excited by the 402 nm-wavelength light. The spectral profiles show similar shapes in the wavelength range shorter than 660 nm,

which means that the up-converted light is emitted from the electrons in the same excited state as that involved in emitting the fluorescence. The spectral intensity of curve A in the longer wavelength range is as high as that of its spectral peak, which means that the longer wavelength light is emitted from a long-lived electronic excited state to which the electron relaxes after the phonon-assisted excitation. Inset images in this figure show optical microscope images of the frequency up-converted light and conventional fluorescence. The lower image shows an inhomogeneous spatial distribution of the emitted light intensity because the light was emitted selectively from the edges of the grains, showing the phonon-assisted process due to the DP-CPs. In the upper image, the spatial distribution of the fluorescence intensity is homogenous, in contrast to that of the lower image. Figure 9(A) shows the relation between the incident photon flux used for excitation and the frequency

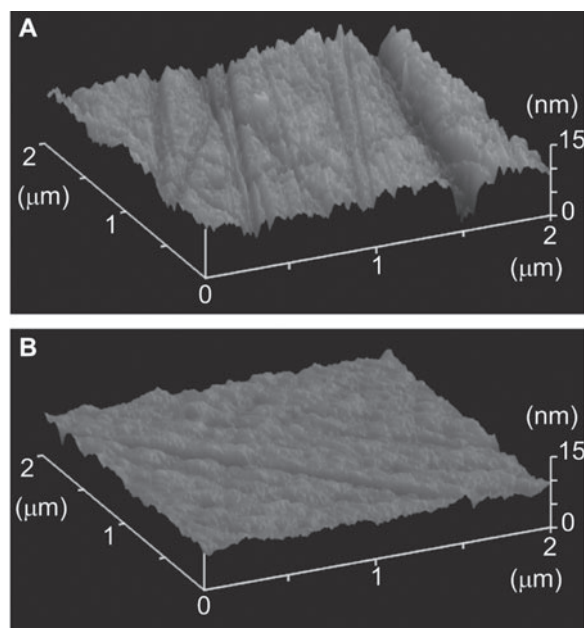


**Figure 7** AFM images of alumina substrate surface (A) before and (B) after RF sputtering under visible light illumination.

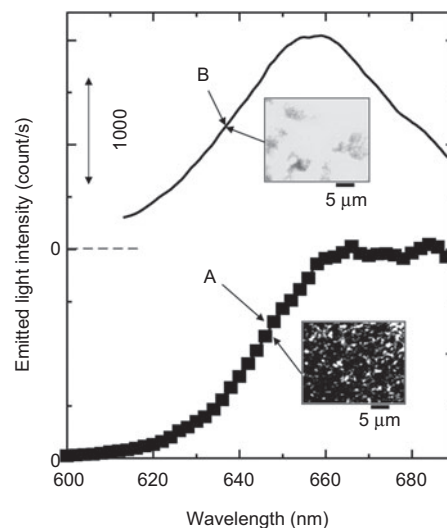


**Figure 8** Spectral profiles of frequency up-converted light. Curve A is the spectrum obtained by applying near-infrared light with a wavelength of 805 nm. Curve B is the conventional fluorescence spectrum. The inset photos show optical microscope images of the up-converted light and conventional fluorescence.

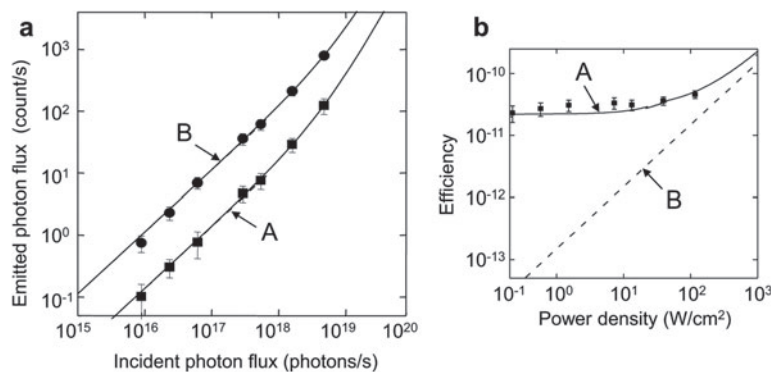


**Figure 9** Frequency up-converted light intensity and the efficiency of conversion. (a) Relation between the incident photon flux and the emitted photon flux. Curves A and B represent the intensity of the wavelength components of 650 nm and 690 nm, respectively. (b) Efficiency of the frequency up-conversion as a function of the incident light power density (curve A). For comparison, the efficiency of the second harmonic generation from a KDP crystal is also shown (line B).

up-converted photon flux emitted from the DCM. Experimental results are presented for the wavelength components of 650 nm and 690 nm, to which the second-order curve was least-squares fitted. The fitted results are represented by solid curves A and B. These curves show that the frequency up-conversion is due to the two-step excitation by the DP-CPs [62]. The curve A in Figure 9(B) shows the relation between the incident light power density and the efficiency of the frequency up-conversion. For comparison, the line B shows the efficiency of conventional second harmonic generation from a popular Potassium Dihydrogen Phosphate (KDP) crystal, which has the same optical thickness as that of the powdery grains of DCM. It is easily found that the efficiency of the frequency up-conversion is more than 100 times greater than that of the second harmonic generation for an incident light power density lower than 1 W/cm<sup>2</sup>. By increasing the incident light power density, the second-step excitation of the phonon-assisted process becomes dominant, and thus, the conversion efficiency increases in proportion to the incident light power density. Therefore, the conversion efficiency remains higher than that of the second harmonic generation even at higher incident power density.

It has been found that non-degenerate two-step excitation can also emit higher-frequency light by using two mutually independent light beams with different wavelengths [63]. Using this excitation, a novel system for optical pulse shape measurement has been developed: Due to the two non-degenerate optical pulses, the DCM is excited by the two-step phonon-assisted process. By measuring the emitted light intensity with a conventional visible-light photodetector as a function of the time delay of the incident reference optical pulse, the optical pulse shape to be measured can be acquired. Using the DCM, the shape of the 800 nm-wavelength optical pulse was measured with a temporal resolution of 0.8 ps, which was limited by the lifetime of the intermediate state involved in the two-step excitation. The measured optical pulse shape has low jitter because the measurement system employs only optical processes, unlike the conventional streak-camera system employing electro-optical processes. By using other commercially available dye molecules, such as Coumarin, the

measurable wavelength range can be extended to 1.3–1.55  $\mu\text{m}$  with a temporal resolution of 0.8 ps, which enables optical pulse shape measurement for optical fiber transmission systems.

## 5.2. Optical to electrical energy

A key issue in the progress of optical technologies is improving the performance of semiconductor photovoltaic devices, for example, increasing their conversion efficiency. Although it is also essential to expand their working wavelength range, the long-wavelength cutoff,  $\lambda_c$ , is governed by the bandgap energy,  $E_g$ , of the semiconductor material used as the active medium for these devices. To expand the wavelength range, lower  $E_g$  is required, which can be achieved by exploring novel semiconductor materials or structures. This subsection reviews a novel method of expanding the working wavelength range of a photovoltaic device beyond the one limited by  $E_g$ , even though the semiconductor materials remain untreated. It utilizes a phonon-assisted process to convert optical energy to electrical energy with frequency up-conversion to realize selective photocurrent generation in the transparent wavelength range of the photovoltaic device material [64]. This frequency up-conversion can extend the photo-detection bandwidth of photovoltaic devices, which has been confirmed by using a poly(3-hexylthiophene) (P3HT) organic thin film as a p-type semiconductor and a ZnO film as an n-type semiconductor. The absorption band-edge wavelength, i.e., the long-wavelength cutoff,  $\lambda_c$ , is 570 nm, which is governed by the bandgap energy,  $E_g$ , of the P3HT. An ITO layer and an silver (Ag) layer were used as electrodes of the device.

The phonon-assisted process is used twice: once for efficient photocurrent generation in the wavelength range beyond the one limited by  $E_g$ , and once for fabricating a metallic electrode for the device, in which the morphology of the Ag electrode surface can be controlled in a self-organized manner [65] so that the phonon-assisted process is efficiently induced for photocurrent generation. For this self-organized control, Ag is deposited by RF-sputtering under light illumination

on a previously deposited Ag thin film while the P3HT/ZnO pn-junction is reversely biased with a DC voltage  $V_b$ . Here,  $V_b$  was fixed to -1.5 V, and the wavelength,  $\lambda_0$ , of the incident light was 660 nm, which is longer than  $\lambda_c$  of the P3HT. It is expected that this deposition with light illumination controls the morphology of the Ag film as a result of the phonon-assisted process induced by the DP-CPs. When the Ag film with this controlled morphology is used as an electrode of the photovoltaic device, it is also expected that a conspicuous phonon-assisted process will be induced for photocurrent generation.

The mechanism of controlling the morphology is as follows: Under light illumination, a dressed photon is generated on the Ag surface. This dressed photon excites a coherent phonon at the pn-junction, resulting in generation of a DP-CP. By the two-step phonon-assisted process, induced by the DP-CP, electrons can be excited to create electron-hole pairs at the pn-junction even though the photon energy of the incident light is lower than  $E_g$ . The created electron-hole pairs disappear because the electrons and positive holes are separated from each other due to the electric field of the reverse bias voltage. As a result, the positive holes are injected into the deposited Ag. Since the sputtered Ag is positively ionized due to the transmission of the Ag through the argon plasma or due to the collision of the argon plasma with the Ag target used for RF-sputtering, these positively ionized Ag particles are repulsed from the area of the positively charged Ag film into which the positive holes have been injected in the manner described above. This means that subsequent deposition of Ag is suppressed in the area in which the DP-CP energy density is higher than in other areas. As a result, a unique granular Ag film is formed, which depends on the spatial distribution of the DP-CP energy density. This granular Ag film grows in a self-assembled manner with increasing RF-sputtering time, resulting in the formation of a unique morphology.

By using this morphology-controlled Ag film as an electrode of the photovoltaic device and by applying the incident light from the rear surface of the sapphire substrate, it is expected that the DP-CPs can be efficiently generated on the electrode. Thus, electron-hole pairs can be created efficiently by the phonon-assisted process if this device is illuminated by light with the same wavelength,  $\lambda_0$ , as the one used for controlling the morphology. On the other hand, if it is illuminated by light of a different wavelength,  $\lambda_1$ , the efficiency of the electron-hole pair creation should be lower because the spatial profile and the photon energy of the generated DP-CPs are different from those in the case where wavelength  $\lambda_0$  is used. Thus, this device should exhibit wavelength-selectivity in the photocurrent generation, which should take a maximum at the wavelength  $\lambda_0$ . Furthermore, since this wavelength is longer than  $\lambda_c$ , the working wavelength becomes longer than that limited by  $E_g$ .

By depositing Ag on the previously fabricated Ag film by RF sputtering, a first device (Device 1) was fabricated without applying the bias voltage,  $V_b$ , or the incident light power,  $P$ , which was used as a reference to evaluate the performance of a second device (Device 2). For Device 2,  $V_b$  and  $P$  were -1.5 V and 70 mW, respectively. Inset photos

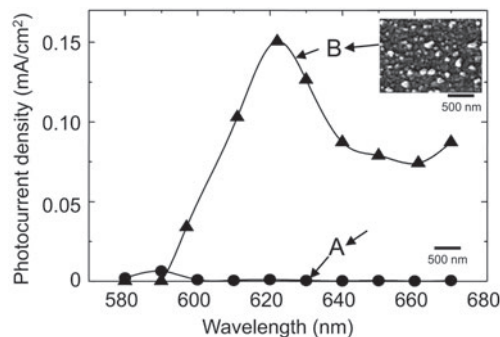


**Figure 10** Dependence of the generated photocurrent densities on the wavelength of the incident light. Curves A and B are for Devices 1 and 2, respectively. Inset photos show SEM images of Ag film surfaces for Devices 1 and 2.

in Figure 10 show SEM images of the Ag film surfaces of Devices 1 and 2. By comparing them, it is clear that the Ag surface of Device 2 was very rough, with larger grains than those of Device 1. The average and standard deviation of the grain diameters of Device 2 were 86 nm and 32 nm, respectively. Since the sum of the thicknesses of the Ag and P3HT was estimated to be <70 nm, it is expected that the DP-CPs generated on the Ag grains of Device 2 can extend to the pn-junction. As a result, it is expected that these DP-CPs efficiently create electron-hole pairs at the pn-junction by the phonon-assisted process.

The wavelength dependences of the photocurrent generation in the longer wavelength range beyond  $E_g$  of P3HT are shown in Figure 10. Based on a linear relation between the incident light power and the generated photocurrent density, the power density of the incident light, which was radiated through the transparent ITO electrode, was fixed to 125 mW/cm<sup>2</sup> (optical power=1 mW). The photocurrent density from Device 1 was very low, but it is shown by curve A as a reference. Curve B represents the measured photocurrent densities from Device 2, generated by incident light with wavelengths up to  $\lambda_i=670$  nm, which clearly demonstrates the extension of the working wavelength range beyond that limited by  $E_g$  of P3HT. The photocurrent of curve B was the highest at  $\lambda_{ip}^g=620$  nm. Thus, Device 2 effectively functions as a wavelength-selective photovoltaic device for incident light with a wavelength beyond that limited by  $E_g$ . The wavelength  $\lambda_{ip}$  is 40 nm shorter than  $\lambda_0$ , which is attributed to the DC Stark effect induced by the reverse bias voltage,  $V_b$ , applied in the process of controlling the morphology. The photocurrent density was 0.15 mW/cm<sup>2</sup> at the peak of curve B, which corresponds to a quantum efficiency of 0.24%, which is as high as that of a conventional heterojunction photovoltaic device using P3HT [66]. However, it should be pointed out that Device 2 realized such high quantum efficiency even for wavelengths longer than the one limited by  $E_g$  of P3HT. This morphology-controlling technology using DP-CPs can be applied not only to the device described here using the organic P3HT thin film but also to a variety of other photovoltaic devices, including solar cell batteries.

The morphology was analyzed, and a stochastic model was constructed in order to understand the principles behind the

self-organized pattern formation process [67]. The modeling includes the geometrical characteristics of the structures, their associated dressed photons, and the matter that flows in and out of the system. The numerical simulation exhibited behavior consistent with the experimental results. These phenomena can be regarded as a new kind of self-organized criticality taking account of dressed photons.

### 5.3. Electrical to optical energy

Although silicon (Si) is a semiconductor having low toxicity and no concerns about depletion of resources, its photon emission efficiency is low because it is an indirect transition type semiconductor. However, because of the growing concern over environmental issues, light emitting diodes (LEDs) using Si have recently been investigated. For example, in the visible region, porous Si [68], silicon/silicon dioxide (Si/SiO<sub>2</sub>) superlattice structures [69, 70], and Si nanoprecipitates in SiO<sub>2</sub> [71] have been used, and in the infrared region, erbium-doped Si [72] and silicon-germanium (Si-Ge) [73] have been used. However, their emission efficiencies are still lower than 1% [74].

In this subsection, a novel fabrication technology and operation of a highly efficient, broadband LED using a bulk crystal Si having a simple homojunction structure are reviewed. The spatial distribution of the dopant density in the Si is varied by annealing using a phonon-assisted process induced by a dressed photon [36]. By this process, an electron-hole pair is created even if light having a photon energy smaller than the Si bandgap energy,  $E_g$ , is incident. The reason for this is that it is possible for electrons in the valence band to be excited to the conduction band via an electric-dipole-forbidden transition to the phonon level. This excitation is a two-step transition, as in the cases described in Subsections 5.1 and 5.2.

There is an inverse process to this process, namely, the two-step spontaneous emission process [64]. Some of the DP-CPs spontaneously emitted by this two-step process are converted to observable propagating light, allowing an LED to be realized. The emission wavelength of this device depends not on the bandgap energy,  $E_g$ , but on the energy of the DP-CP generated in the vicinity of the p-n junction.

It is well-known that a phonon is needed for an indirect transition type semiconductor to spontaneously emit propagating light. This is because, for spontaneous emission, the wavenumber must be conserved. A DP-CP, however, has multiple modes that satisfy the wavenumber conservation law because the photons are strongly coupled with multi-mode phonons [36, 75], and thus, the probability of spontaneous emission due to the DP-CP is extremely high. In addition, this phonon-assisted process can also involve a two-step stimulated emission process.

To realize an LED device, the two-step phonon-assisted process involving DP-CPs was used twice: once for operating the device to obtain spontaneously emitted light, and once for fabricating the device, in other words, for self-organized control of the spatial distribution of the dopant density suitable for high-efficiency spontaneous emission. The second usage method is described in the following.

To fabricate the device, an arsenic (As)-doped n-type Si crystal wafer was used, which was then doped with boron (B) by ion implantation to form a p-layer. After forming a p-n homojunction in this way, an ITO layer and an Al layer were deposited, to be used as positive and negative electrodes, respectively. Finally, a forward bias voltage of 16 V was applied to generate Joule heating for performing annealing, which diffuses the B and varies the spatial distribution of its concentration. During this process, laser light (optical power density=10 W/cm<sup>2</sup>) with a photon energy ( $h\nu_{\text{anneal}}=0.95$  eV, wavelength=1.30  $\mu\text{m}$ ) smaller than the bandgap energy of Si ( $E_g=1.12$  eV) [76] was radiated from the ITO electrode side.

This radiation induced a phonon-assisted process, modifying the B diffusion by annealing, and forming characteristic minute inhomogeneous domain boundaries in a self-organized manner. This was due to the following three reasons: Because the forward bias voltage (16 V) is much higher than  $E_g$  (=1.12 eV), the difference between the quasi-Fermi energies of the conduction and valence bands is higher than  $E_g$ , thus satisfying the Bernard-Duraffourg inversion condition. Also, when light with a photon energy  $h\nu_{\text{anneal}}$  below  $E_g$  is radiated, this light propagates in the substrate without being absorbed in the Si and generates dressed photons at the domain boundaries of the inhomogeneous distribution of B [77]. These dressed photons excite coherent phonons close to the p-n junction, forming DP-CPs. Because the DP-CP energy is the sum of the dressed photon energy and the energy of the induced phonon, this energy is large enough to cause stimulated emission of photons even though  $h\nu_{\text{anneal}} < E_g$ . Thus, a part of the Joule heating energy due to the forward bias is spent in the stimulated emission of photons, and therefore, the annealing rate is decreased. That is, at sites where the phonon-assisted stimulated emission is easily generated, the shape and dimensions of the inhomogeneous domain boundaries of B become more difficult to change. However, it is expected that the shapes and distribution of the domain boundaries formed in this way will be optimal for efficiently inducing the phonon-assisted process during device operation.

After the surface temperature suddenly increased to 154°C by the Joule heating due to the bias current, it dropped and reached a stable value (140°C) after about 6 min. This temperature variation is consistent with the above discussion related to annealing under light irradiation. Specifically, once the DP-CPs are generated in the domain boundary and commence stimulated emission, part of the Joule heating is dissipated in the form of light, and the temperature drops, soon reaching the stationary state. The forward bias was applied for 30 min while irradiating the device with light, which completes the fabrication of the device.

Figures 11(A) and (B) show photographs of the external appearance of the non-biased and forward-biased (current density=4.2 A/cm<sup>2</sup>) device taken with an infrared CCD camera (photosensitive band=0.73–1.38 eV, wavelength=0.90–1.70  $\mu\text{m}$ ) at room temperature. Figure 11(B) reveals strong emitted light, for which the applied electrical power was 11 W, and the emitted power reached as high as 1.1 W. Curve A in Figure 12 shows the extremely weak emission spectrum when an injected current density of 0.2 A/cm<sup>2</sup> was

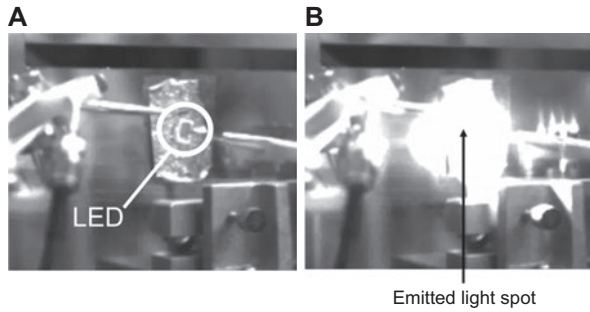


**Figure 11** Photograph of emitted light at room temperature, captured with an infrared camera under fluorescent light illumination: (a) current density  $I_d=0$ ; (b) current density  $I_d=4.2$  A/cm<sup>2</sup>.

made to flow in a commercially available Si photodiode. In this graph, like the results in Ref. [74], the emission spectrum was distributed on the high-energy side of  $E_g$  ( $=1.12$  eV). This is due to phonon scattering in the indirect band structure of the Si. Curves B–D are the emission spectra of devices fabricated by annealing for 1 min, 7 min, and 30 min, respectively. The injected current density was  $1.5\pm0.5$  A/cm<sup>2</sup>. Unlike curve A,

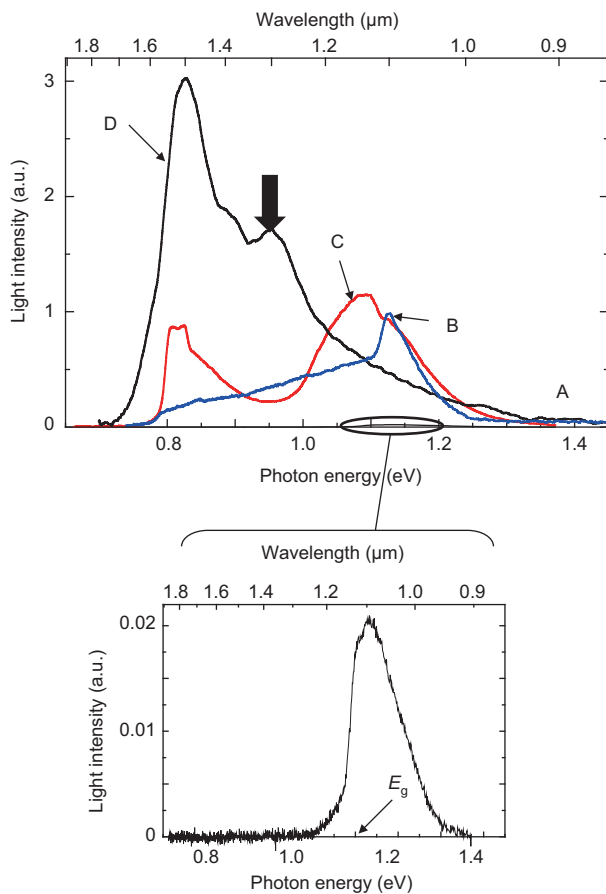


**Figure 12** Emission spectra. Curve A: Emission spectrum of commercially available Si photodiode. Curves B–D: Emission spectra of fabricated devices. Annealing times were 1 min, 7 min, and 30 min, respectively. The downward pointing arrow on curve D indicates the photon energy of the light irradiated during annealing.

the emission spectrum extended to energies lower than  $E_g$ . The decrease in the emission spectral intensity in the energy region below 0.8 eV was due to the sensitivity limit of the photo-detector. The 1-min annealed device had an intense emission peak close to  $E_g$ , which extended as far as 0.75 eV (wavelength=1.65  $\mu\text{m}$ ), as shown in curve B. A new emission peak appeared close to 0.83 eV (wavelength=1.49  $\mu\text{m}$ ) in the emission spectrum of the 7-min annealed device (curve C). In the 30-min annealed device (curve D), there was no intense emission peak at  $E_g$ ; however, a peak (downward pointing arrow in the figure) appeared in the region corresponding to the photon energy ( $h\nu=0.95$  eV, wavelength=1.3  $\mu\text{m}$ ) of the light irradiated during annealing. In addition, the peak in the low-energy region (0.83 eV) was higher than in curve C.

Figure 13(A) shows the relationship between the output optical power and the electrical driving power of the 30-min annealed device. When 11 W of electrical power was supplied, the external power conversion efficiency was 1.3%. The differential external power conversion efficiency was 5.0%, which was derived from the gradient of the straight broken line in this figure. To obtain the quantum efficiency, Figure 13(B) shows the relationship between the emitted optical power density  $P_d$  and the current density  $I_d$  of the 30-min annealed device. The measured values, indicated by the closed squares, were fitted by the quadratic curve  $P_d=0.04I_d^2$  shown by the solid curve. In other words,  $P_d$  is proportional to  $I_d^2$  in this device, in contrast to conventional devices in which  $P_d$  is proportional to  $I_d$ . This is because the two-step spontaneous emission process is dominant; in other words, a single electron is converted to two photons. The external quantum

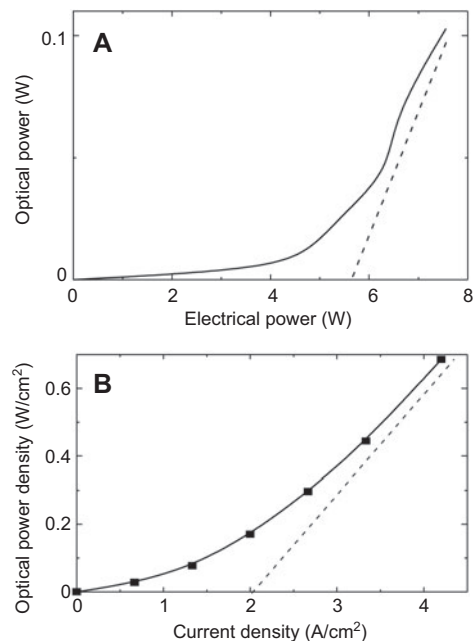


**Figure 13** Relations between electrical and optical energies. (A) Relation between applied electrical power and emitted optical power. (B) Relation between injected current density and emitted optical power density.



efficiency is 15% at  $I_d=4.0$  A/cm<sup>2</sup>, and the differential external quantum efficiency is 40% at  $I_d=3.0$ – $4.0$  A/cm<sup>2</sup>.

It should be possible to realize an LED in the visible wavelength region by using other indirect transition type semiconductors. This approach can also be applied to laser oscillators.

## 6. Hierarchy and its applications

There are multiple layers associated with the physical scale between the macro-scale world and the atomic-scale world, which are primarily governed by propagating light and electron interactions, respectively. Between those two extremes, typically in scales ranging from a few nanometers to the wavelength scale, dressed photon interactions play a crucial role, and they exhibit hierarchical properties [66, 78].

We can make use of physical differences in optical near-field and far-field effects for a wide range of applications. The behavior of conventional optical elements, such as diffractive optical elements, holograms, or glass components, is associated with their optical responses in the optical far-field. Nanostructures can exist in such optical elements as long as they do not affect the optical responses in the far-field. Therefore, designing nanostructures that are accessible only via DP-CPs can provide additional, or hidden, information recorded in those optical elements while maintaining the original optical responses in the far-field. A “hierarchical hologram” and a “hierarchical diffraction grating” have been experimentally demonstrated [79, 80].

There is hierarchy at scales smaller than the optical wavelengths [66]. The electromagnetic interactions between two nano-materials are maximized when these sizes are comparable. Based on this principle, hierarchical memory retrieval was demonstrated using an array of Au nanoparticles, each with a diameter of 80 nm, distributed over a SiO<sub>2</sub> substrate in a 200 nm-radius ring. The output signal increased linearly corresponding to the number of nanoparticles, demonstrating successful hierarchical memory retrieval from nanostructures via dressed photon interactions.

Such a hierarchical property has also been applied to nanofabrication. By inducing fabrication processes selectively at the positions where dressed photons are generated, a smaller-scale structure can be generated even from a larger-scale one via dressed photon interactions. The principle has been experimentally confirmed by using ZnO nanoneedles fabricated through metal-organic vapor phase epitaxy (MOVPE) followed by a photo-induced MOVPE procedure, where smaller-scale generated structures were clearly observed with the help of light irradiation [81].

Shape-engineering of metal nanostructures is a promising asset in realizing hierarchical optical responses thanks to the progress of technologies in fabricating fine nanostructures [82, 83]. Optical near- and far-field responses from metal nanostructures can be understood in a unified manner by examining induced electric currents in individual nanostructures and their associated DP-CPs between the nanostructures [84]. Based on this picture, a quadrupole-dipole transform has been theoretically and experimentally demonstrated by using two stacked layers of nanostructures [85, 86]. Such

functionality is useful in ensuring product authentication or certification, where a system should work only when the two nanostructures match, just like a lock and key.

## 7. Conclusion

Dressed photons have allowed the realization of qualitative innovations in optical technologies, i.e., enabling novel optical devices, fabrication technologies, energy conversion, and hierarchical systems that would be unrealizable if only conventional propagating light were used. For example, in the case of fabrication technologies, it should be noted that large, expensive, high-power-consumption, short-wavelength light sources are not required; the fabrication equipment has low power consumption, as discussed in Section 4. The phonon-assisted photochemical etching described in Subsection 4.3 does not involve the use of rare-earth metals, in contrast to the conventional CMP method which uses a large amount of cerium dioxide (CeO<sub>2</sub>), a typical rare-earth metal, for polishing quartz glass. It should also be noted that silicon, used for the energy conversion described in Subsection 5.3, has low toxicity and no concerns about depletion of resources. These notable features, realized by using dressed photon technology, are advantageous for energy saving and environmental protection for future society.

## Acknowledgements

The author sincerely thanks Prof. M. Tsukada, Dr. H. Tamura (Tohoku Univ.), Profs. H. Hori, K. Kobayashi, I. Banno (University of Yamanashi), Dr. M. Naruse (National Institute for Communication Technology and University of Tokyo), Prof. T. Yatsui, Drs. T. Kawazoe, W. Nomura, N. Tate, and K. Kitamura (University of Tokyo) for their collaboration.

## References

- [1] Ohtsu M, Kawazoe T, Yatsui T, Naruse M. Nanophotonics: application of dressed photons to novel photonic devices and systems. *IEEE J Sel Top Quantum Electron* 2008;14(6):1404–17.
- [2] Ohtsu M, Kobayashi K, Kawazoe T, Yatsui T, Naruse M. *Principals of nanophotonics*. Florida: Taylor and Francis; 2008, pp. ix-x.
- [3] Ohtsu M. (ed.), *Progress in Nano-Electro-Optics V* (Springer, Berlin, 2006), pp. VII-VIII.
- [4] Yablonovitch E. Inhibited spontaneous emission in solid-state physics and electronics. *Phys Rev Lett* 1987;58(20):2059–62.
- [5] Podolskiy VA, Sarychev AK, Shalaev VM. Plasmon modes and negative refraction in metal nanowire composites. *Opt Exp* 2003;11(7):735–45.
- [6] Selby RA, Smith DR, Schultz S. Experimental verification of a negative index of refraction. *Science* 2001;292(5514):77–9.
- [7] Pendrey JB. Negative refraction makes a perfect lens. *Phys Rev Lett* 2000;85(18):3966–9.
- [8] Rong H, Liu A, Nicolaescu R, Paniccia M. Raman gain and nonlinear optical absorption measurements in a low-loss silicon waveguide. *Appl Phys Lett* 2004;85(12):2196.
- [9] Eberl K. Quantum-dot lasers. *Physics World* 1997:47–50.

- [10] Ohtsu M. (ed.), *Progress in nanophotonics 1*. Berlin: Springer; 2011: pp. 1–58.
- [11] Leviatan Y. Study of near-zone fields of a small aperture. *J Appl Phys* 1986;60(5):1577.
- [12] Kobayashi K, Sangu S, Ito H, Ohtsu M. Near-field optical potential for a neutral atom. *Phys Rev A* 2001;63(1):013806.
- [13] Ohtsu M, Kobayashi K. *Optical near fields*. Berlin: Springer; 2004: pp. 109–120.
- [14] Tanaka Y, Kobayashi K. Optical near field dressed by localized and coherent phonons. *J Microsc* 2008;229(2):228–32.
- [15] Sato A, Tanaka Y, Minami F, Kobayashi K. Photon localization and tunneling in a disordered nanostructure. *J Lumin* 2009;129(12):1718–21.
- [16] Ohtsu M, Kobayashi K, Kawazoe T, Sangu S, Yatsui T. *Nanophotonics: design, fabrication, and operation of nanometric devices using optical near fields*. *IEEE J Sel Top Quantum Electron* 2002;8(4):839–62.
- [17] Kawazoe T, Kobayashi K, Sangu S, Ohtsu M. Demonstration of a nanophotonic switching operation by optical near-field energy transfer. *Appl Phys Lett* 2003;82(18):2957. <http://dx.doi.org/10.1063/1.15.71977> (3 pages).
- [18] Kawazoe T, Ohtsu M, Aso S, Sawado Y, Hosoda Y, Yoshizawa K, Akahane K, Yamamoto N, Naruse M. Two-dimensional array of room-temperature nanophotonic logic gates using InAs quantum dots in mesa structures. *Appl Phys B* 2011;103(3):537–46.
- [19] Zwiller V, Blom H, Jonsson P, Panev N, Jeppesen S, Tsegaye T, Goobar E, Pistol ME, Samuelson L, Bjork G. Single quantum dots emit single photons at a time: Antibunching experiments. *Appl Phys Lett* 2001;78(17):2476–8.
- [20] Shojiguti A, Kobayashi K, Sangu S, Kitahara K, Ohtsu M. Superradiance and dipole ordering of an  $N$  two-level system interacting with optical near fields. *J Phys Soc Jpn* 2003;72(11):2984–3001.
- [21] Naruse M, Hori H, Kobayashi K, Kawazoe T, Ohtsu M. Optical pulsation mechanism based on optical near-field interactions. *Appl Phys B* 2011;102(4):717–23.
- [22] Kawazoe T, Kobayashi K, Ohtsu M. Optical nanofountain: a biomimetic device that concentrates optical energy in a nanometric region. *Appl Phys Lett* 2005;86(10):103102. <http://dx.doi.org/10.1063/1.1875734> (3 pages).
- [23] Akahane K, Yamamoto N, Naruse M, Kawazoe T, Yatsui T, Ohtsu M. “Energy transfer in multi-stacked InAs quantum dots”. *Jpn J Appl Phys* 2011;50(4):04DH05 1–4.
- [24] Yatsui T, Sangu S, Kawazoe T, Ohtsu M, An SJ, Yoo J, Yi G-C. Nanophotonic switch using ZnO nanorod double-quantum-well structures. *Appl Phys Lett* 2007;90(22):223110. <http://dx.doi.org/10.1063/1.2743949> (3 pages).
- [25] Ohtsu M. (ed.), *Progress in nanophotonics 1*. Berlin: Springer; 2011: p. 19.
- [26] Nomura W, Yatsui T, Kawazoe T, Ohtsu M. Observation of dissipated optical energy transfer between CdSe quantum dots. *J Nanophotonics* 2007;1(1):011591.
- [27] Naruse M, Hori H, Kobayashi K, Holmstrom P, Thylen L, Ohtsu M. Lower bound of energy dissipation in optical excitation transfer via optical near-field interactions. *Opt Express* 2010;18(S4):A544–53.
- [28] Kish LB. Moore’s law and the energy requirement of computing versus performance. *IEE Proc Circuits Devices Syst* 2004;151(2):190.
- [29] Carey VP, Shah AJ. The exergy cost of information processing: a comparison of computer-based technologies and biological systems. *J Electron Packag* 2006;128(4):346.
- [30] Hambury Brown R, Twiss RQ. The question of correlation between photons in coherent light rays. *Nature* 1956;178(4548):1447–8.
- [31] Kawazoe T, Tanaka S, Ohtsu M. Single-photon emitter using excitation energy transfer between quantum dots. *J Nanophotonics* 2008;2(1):029502.
- [32] Kocher P, Jaffe J, Jun B. Introduction to differential power analysis and related attacks. <http://www.cryptography.com/public/pdf/DPAtechInfo.pdf>. Accessed April 1, 2012.
- [33] Naruse M, Hori H, Kobayashi K, Ohtsu M. Tamper resistance in optical excitation transfer based on optical near-field interactions. *Opt Lett* 2007;32(12):1761–3.
- [34] Naruse M, Miyazaki T, Kubota F, Kawazoe T, Kobayashi K, Sangu S, Ohtsu M. Nanometric summation architecture based on optical near-field interaction between quantum dots. *Opt Lett* 2005;30(2):201–3.
- [35] Krchnavek RR, Gilgen HH, Chen JC, Shaw PS, Licata TJ, Osgood RM Jr., Photodeposition rates of metal from metal alkyl. *J Vac Sci Technol B* 1987;5(1):20.
- [36] Kawazoe T, Kobayashi K, Takubo S, Ohtsu M. Nonadiabatic photodissociation process using an optical near field. *J Chem Phys* 2005;122(2):024715.
- [37] Kawazoe T, Kobayashi K, Ohtsu M. Near-field optical chemical vapor deposition using  $\text{Zn}(\text{acac})_2$  with a non-adiabatic photochemical process. *Appl Phys B* 2006;84(1–2):247–51.
- [38] Savas TA, Schattenburg ML, Carter JM, Smith HI. Large-area achromatic interferometric lithography for 100 nm period gratings and grids. *J Vac Sci Technol B* 1996;14(6):4167–70.
- [39] Rogers JA, Paul KE, Jackman RJ, Whitesides GM. Using an elastomeric phase mask for sub-100 nm photolithography in the optical near field. *Appl Phys Lett* 1997;70(20):2658.
- [40] Yonemitsu H, Kawazoe T, Kobayashi K, Ohtsu M. Nonadiabatic photochemical reaction and application to photolithography. *J Photolumin* 2007;122:230–3.
- [41] Ito Y, Nakasato S, Kuroda R, Ohtsu M. Near-field lithography as prototype nano-fabrication tool. *Microelectronic Eng* 2007;84(5–8):705–10.
- [42] Ohtsu M. (ed.), *Nanophotonics and nanofabrication*. Weinheim: Wiley-VCH; 2009: pp. 179–191.
- [43] Kawazoe T, Takahashi T, Ohtsu M. Evaluation of the dynamic range and spatial resolution of nonadiabatic optical near-field lithography through fabrication of Fresnel zone plates. *Appl Phys B* 2010;98(1):5–11.
- [44] Yatsui T, Hirata K, Nomura W, Tabata Y, Ohtsu M. Realization of an ultra-flat silica surface with angstrom-scale average roughness using nonadiabatic optical near-field etching. *Appl Phys B* 2008;93(1):55–7.
- [45] Wua B, Kumar A. Extreme ultraviolet lithography: a review. *J Vac Sci Technol B* 2007;25(6):1743.
- [46] Cook LM. Chemical processes in glass polishing. *J Non-Cryst Solids* 1990;120(1–3):152–71.
- [47] Yatsui T, Hirata K, Tabata Y, Nomura W, Kawazoe T, Naruse M, Ohtsu M. *In Situ* real-time monitoring of changes in the surface roughness nonadiabatic optical near-field etching. *Nanotechnol* 2010;21(35):355303.
- [48] Hirata K. In: *Proceedings of the 2011 Photonics West, Realization of high-performance optical element by optical near-field etching*, San Francisco, CA, USA, 22–27 January 2011, Vol. 7921, Bellingham: SPIE; 2011, pp. 79210M1–13.
- [49] Yatsui T, Hirata K, Tabata Y, Miyake Y, Akita Y, Yoshimoto M, Nomura W, Kawazoe T, Naruse M, Ohtsu M. Self-organized near-field etching of the sidewalls of glass corrugations. *Appl Phys B* 2011;103(3):527–30.

- [50] Nomura W, Yatsui T, Yanase Y, Suzuki K, Fujita M, Kamata A, Naruse M, Ohtsu M. Repairing nanoscale scratched grooves on polycrystalline ceramics using optical near-field assisted sputtering. *Appl Phys B* 2010;99(1–2):75–8.
- [51] Ikesue A, Furusato I. Fabrication of polycrystal line, transparent YAG ceramics by a solid-state reaction method. *J Am Ceram Soc* 1995;78(1):225–8.
- [52] Ikesue A, Kinoshita T, Kamata K, Yoshida K. Fabrication and optical properties of high-performance polycrystalline Nd:YAG ceramics for solid-state lasers. *J Am Ceram Soc* 1995;78(4):1033–40.
- [53] Lu J, Son J, Prabhu M, Xu J, Ueda K, Yagi H, Yanagitani T, Kudryashov A. High-power Nd:Y<sub>3</sub>Al<sub>5</sub>O<sub>12</sub> ceramic laser. *Jpn J Appl Phys* 2000;39(Part 2, No. 10b):L1048–50.
- [54] Tanaka N. Transparent Dielectric Ceramics, *Bull Ceram Soc Jpn* 2003;38(12):967–9.
- [55] Krell A, Brank P, Ma H, Hutzler T. Transparent sintered corundum with high hardness and strength. *J Am Ceram Soc* 2003;86(1):12–18.
- [56] Lu J, Ueda K, Yagi H, Yanagitani T, Akiyama Y, Kaminskii AA. Neodymium doped yttrium aluminum garnet (Y<sub>3</sub>Al<sub>5</sub>O<sub>12</sub>) nanocrystalline ceramics – a new generation of solid state laser and optical materials. *J Alloys Compd* 2002;341(1–2):220–5.
- [57] Ikesue A. Polycrystalline Nd:YAG ceramics lasers. *Opt Mater* 2002;19(1):183–7.
- [58] Graham-Rowe D. Lasers for engine ignition. *Nat Photonics* 2008;2(9):515–7.
- [59] Yariv A. Introduction to optical electronics, 1st edn. New York: Holt, Reinhert and Winston; 1985: pp. 177–221.
- [60] Atkins PW. Physical chemistry, 6th edn. Oxford: Oxford University Press; 1998: pp. 497–526.
- [61] Kawazoe T, Fujiwara H, Kobayashi K, Ohtsu M. Visible light emission from dye molecular grains via infrared excitation based on the nonadiabatic transition induced by the optical near field. *IEEE J Sel Top Quantum Electron* 2009;15(5):1380–6.
- [62] Fujiwara H, Kawazoe T, Ohtsu M. Nonadiabatic multi-step excitation for the blue-green light emission from dye grains induced by the near-infrared optical near-field. *Appl Phys B* 2010;98(2–3):283–9.
- [63] Fujiwara H, Kawazoe T, Ohtsu M. Nonadiabatic nondegenerate excitation by optical near-field and its application to optical pulse-shape measurement. *Appl Phys B* 2010;100(1):85–91.
- [64] Yukutake S, Kawazoe T, Yatsui T, Nomura W, Kitamura K, Ohtsu M. Selective photocurrent generation in the transparent wavelength range of a semiconductor photovoltaic device using a phonon-assisted optical near-field process. *Appl Phys B* 2010;99(3):415–22.
- [65] Yatsui T, Nomura W, Ohtsu M. Self-assembly of size- and position-controlled ultralong nanodot chains using near-field optical desorption. *Nano Lett* 2005;5(12):2548–51.
- [66] Guenes S, Neugebauer H, Sariciftci S. Conjugated polymer-based organic solar cells. *Chem Rev* 2007;107(4):1324–38.
- [67] Naruse M, Kawazoe T, Yatsui T, Tate N, Ohtsu M. A stochastic modeling of morphology formation by optical near-field processes. *Appl Phys B* 2011;105(2):185–90.
- [68] Hirschman KD, Tysbekov L, Duttgupta SP, Fauchet PM. Silicon-based visible light-emitting devices integrated into microelectronic circuits. *Nature* 1996;384(6607):338–41.
- [69] Lu ZH, Lockwood DJ, Baribeau J-M. Quantum confinement and light emission in SiO<sub>2</sub>/Si superlattices. *Nature* 1995;378(6554):258–60.
- [70] Dal Negro L, Li R, Warga J, Basu SN. Sensitized erbium emission from silicon-rich nitride/silicon superlattice structures. *Appl Phys Lett* 2008;92(18):181105.
- [71] Komoda T. Visible photoluminescence at room temperature from microcrystalline silicon precipitates in SiO<sub>2</sub> formed by ion implantation. *Nucl Instrum Methods B* 1995;96(1–2):387–91.
- [72] Yerci S, Li R, Dal Negro L. Electroluminescence from Er-doped Si-rich silicon nitride light emitting diodes. *Appl Phys Lett* 2010;97(8):081109.
- [73] Ray SK, Das S, Singha RK, Manna S, Dhar A. Structural and optical properties of germanium nanostructures on Si(100) and embedded in high-k oxides. *Nanoscale Research Lett* 2011;6(1):224.
- [74] Green MA, Zhao J, Wang A, Reece PJ, Gal M. Efficient silicon light-emitting diodes. *Nature* 2001;412(6849):805–8.
- [75] Tanaka Y, Kobayashi K. Spatial localization of an optical near field in one-dimensional nanomaterial system. *Physica E* 2007;40(2):297–300.
- [76] Van Overstraeten RJ, Mertens RP. Heavy doping effects in silicon. *Solid State Electron* 1987;30(11):1077–87.
- [77] Van den Berg JA, Mertens RP. Heavy doping effects in silicon. *Solid-State Electron* 1987;30(11):1077–87.
- [78] Naruse M, Yatsui T, Nomura W, Hirose N, Ohtsu M. Hierarchy in optical near-fields and its application to memory retrieval. *Opt Exp* 2005;13(23):9265–71.
- [79] Naruse M, Inoue T, Hori H. Analysis and synthesis of hierarchy in optical near-field interactions at the nanoscale based on angular spectrum. *Jpn J Appl Phys* 2007;46(9A):6095–103.
- [80] Tate N, Nomura W, Yatsui T, Naruse M, Ohtsu M. Hierarchical hologram based on optical near- and far-field responses. *Opt Exp* 2008;16(2):607–12.
- [81] Naruse M, Yatsui T, Hori H, Kitamura K, Ohtsu M. Generating small-scale structures from large-scale ones via optical near-field interactions. *Opt Express* 2007;15(19):11790–7.
- [82] Tate N, Naruse M, Yatsui T, Kawazoe T, Hoga M, Ohayagi Y, Fukuyama T, Kitamura M, Ohtsu M. Nanophotonic code embedded in embossed hologram for hierarchical information retrieval. *Opt Exp* 2010;18(7):7497–505.
- [83] Naruse M, Yatsui T, Kawazoe T, Akao Y, Ohtsu M. Design and simulation of a nanophotonic traceable memory using localized energy dissipation and hierarchy of optical near-field interactions. *IEEE Trans Nanotechnol* 2008;7(1):14–19.
- [84] Naruse M, Yatsui T, Kim JH, Ohtsu M. Hierarchy in optical near-fields by Nano-scale Shape engineering and its application to traceable memory. *Appl Phys Exp* 2008;1:062004.
- [85] Naruse M, Yatsui T, Hori H, Yasui M, Ohtsu M. Polarization in optical near and far fields and its relation to shape and layout of nanostructures. *J Appl Phys* 2008;103(11):113525.
- [86] Tate N, Sugiyama H, Naruse M, Nomura W, Yatsui T, Kawazoe T, Ohtsu M. Quadrupole-dipole transform based on optical near-field interactions in engineered nanostructures. *Opt Express* 2009;17(13):11113–21.

Received December 6, 2011; accepted March 8, 2012.



Motoichi Ohtsu received his Dr. E. degree in Electronics Engineering from the Tokyo Institute of Technology, Tokyo in 1978. He was first appointed as Research Associate, then an Associate professor, and finally a Professor at the Tokyo Institute of Technology. From 1986 to 1987, while on leave from the Tokyo Institute of Technology, he joined the Crawford Hill Laboratory, AT&T Bell Laboratories, Holmdel, NY, USA.

In 2004, he moved to the University of Tokyo as a professor. He has been the leader of the “Photon Control” project (1993–1998: the Kanagawa Academy of Science and Technology, Kanagawa, Japan), the “Localized Photon” project (1998–2003: ERATO, JST, Japan), “Terabyte Optical Storage Technology” project (2002–2006: NEDO, Japan), “Near Field Optical Lithography System” project (2004–2006: Ministry of Education, Japan), and “Nanophotonics” team (2003–2009: SORST, JST, Japan). He is concurrently the leader of the “Innovative Nanophotonics

Components Development” project (2006–2011: NEDO, Japan) and “Nanophotonics Total Expansion: Industry-University Cooperation and Human Resource Development” project (2006–2011: NEDO, Japan). He has written over 470 papers and received 83 patents. He is the author, co-author, and editor of 62 books, including 27 in English. In 2000, he was appointed as the President of the IEEE LEOS Japan Chapter. From 2000, he has been an executive director of the Japan Society of Applied Physics. His main field of interests are the nanophotonics and dressed photon technology. Dr. Ohtsu is a Fellow of the Optical Society of America, and a Fellow of the Japan Society of Applied Physics. He is also a Tandem Member of the Science Council of Japan. He has been awarded 14 prizes from academic institutions, including the Issac Koga Gold Medal of URSI in 1984, the Japan IBM Science Award in 1988, two awards from the Japan Society of Applied Physics in 1982 and 1990, the Inoue Science Foundation Award in 1999, the Japan Royal Medal with a Purple Ribbon from the Japanese Government in 2004, the H. Inoue Award from JST in 2005, the Distinguished Achievement Award from the Institute of Electronics, Information and Communication Engineering of Japan in 2007, and the Julius Springer Prize for Applied Physics in 2009.

# Optical security based on near-field processes at the nanoscale

Makoto Naruse<sup>1,2</sup>, Naoya Tate<sup>2,3</sup> and Motoichi Ohtsu<sup>2,3</sup>

<sup>1</sup> National Institute of Information and Communications Technology, 4-2-1 Nukui-kita, Koganei, Tokyo 184-8795, Japan

<sup>2</sup> Nanophotonics Research Center, School of Engineering, The University of Tokyo, 2-11-16 Yayoi, Bunkyo-ku, Tokyo 113-8656, Japan

<sup>3</sup> Department of Electrical Engineering and Information Systems, School of Engineering, The University of Tokyo, 2-11-16 Yayoi, Bunkyo-ku, Tokyo 113-8656, Japan

E-mail: [naruse@nict.go.jp](mailto:naruse@nict.go.jp)

Received 16 January 2012, accepted for publication 10 April 2012

Published 11 July 2012

Online at [stacks.iop.org/JOpt/14/094002](http://stacks.iop.org/JOpt/14/094002)

## Abstract

Optics has been playing crucial roles in security applications ranging from authentication and watermarks to anti-counterfeiting. However, since the fundamental physical principle involves optical far-fields, or propagating light, diffraction of light causes severe difficulties, for example in device scaling and system integration. Moreover, conventional security technologies in use today have been facing increasingly stringent demands to safeguard against threats such as counterfeiting of holograms, requiring innovative physical principles and technologies to overcome their limitations. Nanophotonics, which utilizes interactions between light and matter at the nanometer scale via optical near-field interactions, can break through the diffraction limit of conventional propagating light. Moreover, nanophotonics has some unique physical attributes, such as localized optical energy transfer and the hierarchical nature of optical near-field interactions, which pave the way for novel security functionalities. This paper reviews the physical principles and describes some experimental demonstrations of systems based on nanophotonics with respect to security applications such as tamper resistance against non-invasive and invasive attacks, hierarchical information retrieval, hierarchical holograms, authentication, and traceability.

**Keywords:** optical security, nanophotonics, optical near-field, nanostructure, quantum dot, energy transfer

(Some figures may appear in colour only in the online journal)

## 1. Introduction

The security aspects of optics have been studied extensively, and some of them have been commercialized, such as in optical document security [1]. The physical attributes of light, such as spatial parallelism, amplitude, phase, polarization, and so forth, have been successfully exploited in optical security [2]. However, since all of the existing optical security principles and technologies, such as Fourier optics [3], are based on optical far-fields, or propagating light, they suffer from associated limitations such as the difficulty of miniaturizing devices and systems beyond dimensions limited

by the diffraction of light [4]. Moreover, the conventional security technologies in use today have been required to safeguard against even greater security threats, such as side-channel attacks [5], counterfeiting of holograms [6], etc, necessitating innovative physical principles and technologies to overcome their limitations.

Nanophotonics, which utilizes interactions between light and matter at the nanometer scale via optical near-field interactions, can break through the diffraction limit of light [7]. Moreover, nanophotonics has unique physical attributes, such as localized optical energy transfer via optical near-field interactions and the hierarchical

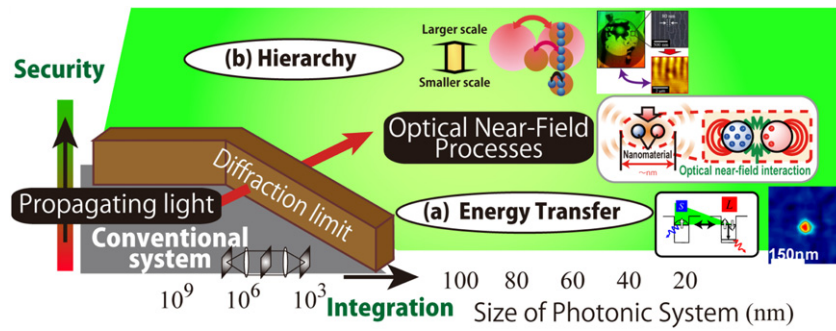


**Figure 1.** Optical security based on near-field processes. We can utilize optical energy transfer and hierarchical properties enabled by optical near-field interactions, not just for overcoming the diffraction limit of propagating light.

nature of optical near-fields [8, 9], which pave the way for novel security functionalities [10–17]. More generally speaking, there is wide scope for nanoscale optical near-field processes to be exploited in optical security applications. This paper reviews the physical principles and describes some experimental demonstrations of systems based on nanophotonics, with regard to security applications such as tamper resistance against non-invasive and invasive attacks [10], hierarchical information retrieval or information hiding [11], hierarchical holograms [12, 13], authentication [14, 15], and traceability [16, 17].

Technologically, the geometry of nanostructures, such as their size, position, shape, and layout, should be well controlled to obtain the intended optical near-field interactions. The rapid progress of technologies for fabricating nanostructures, such as size-controlled InAlAs quantum dots (QDs) [18], ZnO QDs [19, 20], shape-controlled QDs [21], shape-controlled metal nanostructures [22, 23], and so forth, has enabled even room-temperature operation of nanophotonic devices [24], and further advancements in nanotechnology are inevitable. The issue to consider is the design of novel means of optical security based on nanophotonics which will meet the even higher security demands that will be vitally important in the future. Also, the hierarchical nature of nanophotonics allows the co-existence of optical security aspects both in the propagating-light regime and in the subwavelength regime. This concept is schematically summarized in figure 1.

This paper is organized as follows. Section 2 discusses the tamper resistance of optical excitation transfer via optical near-field interactions. The contents of sections 3–6 are based on the hierarchical properties of optical near-fields and their security applications. Section 3 considers hierarchical information retrieval. Section 4 presents hierarchical holograms. Section 5 discusses authentication or certification functions based on shape-engineering of nanostructures. Section 6 discusses traceability based on nanophotonics. Section 7 concludes the paper.

## 2. Secure signal transfer via optical near-field interactions

One of the most critical security threats in present electronic devices is so-called side-channel attacks, by

which information is tampered with either invasively or non-invasively. This may be achieved, for instance, merely by monitoring their power consumption patterns [5]. In this section, we briefly introduce the physics of optical excitation transfer via near-field interactions, and show that the nanoscale devices mediated by optical near-field interactions are more tamper-resistant than their conventional electronic counterparts. We note that the flow of information in nanoscale devices cannot be completed unless they are appropriately coupled with their environment [25], which could possibly be the weakest link in terms of their tamper resistance. We present a theoretical approach to investigate the tamper resistance of optical excitation transfer, including a comparison with electrical devices, for example a single charge tunneling device [26], and we describe numerical calculations based on a theoretical model of optical near-fields [27].

### 2.1. Optical excitation transfer via optical near-field interactions

Here, we define tampering with information as involving simple signal transfer processes, since our primary focus is on their fundamental physical properties. We begin with the interaction Hamiltonian between an electron and an electric field, which is given by

$$\hat{H}_{\text{int}} = - \int \hat{\psi}^\dagger(\vec{r}) \vec{\mu} \hat{\psi}(\vec{r}) \cdot \hat{D}(\vec{r}) d\vec{r}, \quad (1)$$

where  $\vec{\mu}$  is the dipole moment,  $\hat{\psi}^\dagger(\vec{r})$  and  $\hat{\psi}(\vec{r})$  are, respectively, the creation and annihilation operators of the electron at  $\vec{r}$ , and  $\hat{D}(\vec{r})$  is the operator of electric flux density. In usual light-matter interactions the operator  $\hat{D}(\vec{r})$  is a constant since the electric field of propagating light is considered to be constant on the nanoscale. Therefore, as is well known, we can derive optical selection rules by calculating a transfer matrix of an electrical dipole. As a consequence, in the case of cubic quantum dots for instance, transitions to states containing an even quantum number are prohibited. In the case of optical near-field interactions, on the other hand, thanks to the steep electric field of optical near-fields in the vicinity of nanoscale material, an optical

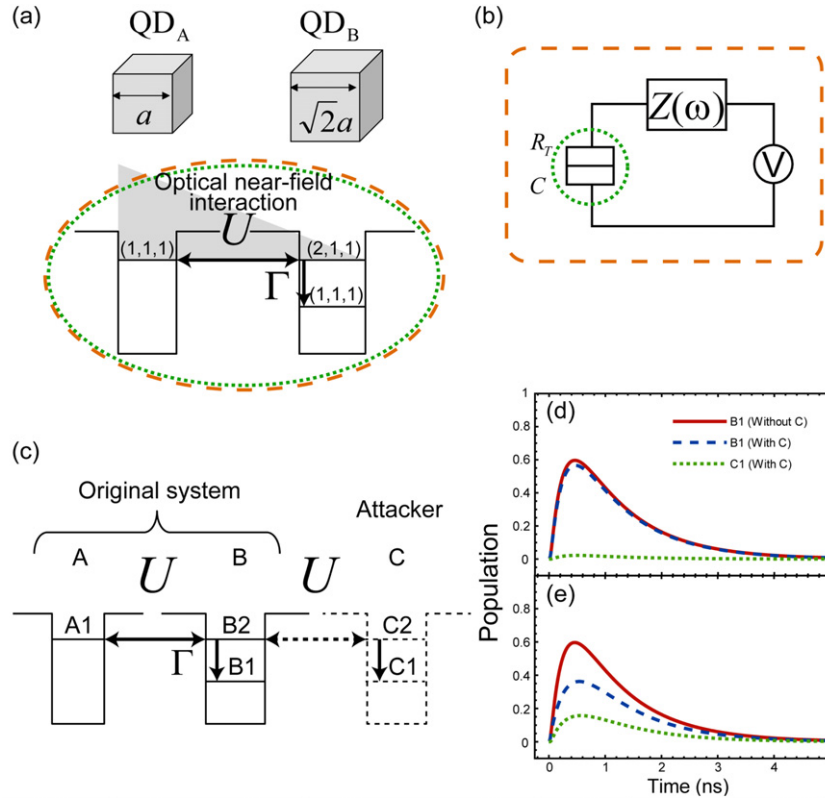


**Figure 2.** Model of tamper resistance in devices based on (a) optical excitation transfer and (b) single charge tunneling. Dotted curves show the scale of a key device, and dashed curves show the scale of the environment required for the system to work. (c) A model of an invasive attack by an attacker. (d), (e) Evolution of the population of the B1-level without QD C (solid curve), the B1-level with QD C (dashed curve), and the C1-level (dotted curve).

transition that violates conventional optical selection rules is allowed. The detailed theory can be found in [9, 28].

Using near-field interactions, optical excitations in nanostructures, such as quantum dots, can be transferred to neighboring ones [28–30]. For instance, assume two cubic quantum dots whose side lengths  $L$  are  $a$  and  $\sqrt{2}a$ , which we call  $QD_A$  and  $QD_B$ , respectively, as shown in figure 2(a). Suppose that the energy eigenvalues for the quantized exciton energy level specified by quantum numbers  $(n_x, n_y, n_z)$  in a QD with side length  $L$  are given by

$$E_{(n_x, n_y, n_z)} = E_B + \frac{\hbar^2 \pi^2}{2ML^2} (n_x^2 + n_y^2 + n_z^2), \quad (2)$$

where  $E_B$  is the energy of the bulk exciton, and  $M$  is the effective mass of the exciton. According to equation (2), there exists a resonance between the level of quantum number (1, 1, 1) for  $QD_A$  and that of quantum number (2, 1, 1) for  $QD_B$ . There is an optical near-field interaction, denoted by  $U$ , due to the steep electric field in the vicinity of  $QD_A$ . Therefore, optical excitation in  $QD_A$  can move to the (2, 1, 1)-level in  $QD_B$ . Note that such a transfer is prohibited in propagating light since the (2, 1, 1)-level in  $QD_B$  contains an even number. In  $QD_B$ , the excitation sees a sublevel energy relaxation, denoted by  $\Gamma$ , which is faster than the near-field interaction, and so the excitation goes to the (1, 1, 1)-level of  $QD_B$ . We should also note that the sublevel relaxation

determines the uni-directional optical excitation transfer from  $QD_A$  to  $QD_B$ .

### 2.2. Tamper resistance of optical excitation transfer

In order to compare the tamper resistance capability, we introduce here an electronic system based on single charge tunneling, where a tunnel junction with capacitance  $C$  and tunneling resistance  $R_T$  is coupled to a voltage source  $V$  via an external impedance  $Z(\omega)$ , as shown in figure 2(b). In order to achieve single charge tunneling, in addition to the condition that the electrostatic energy  $E_C = e^2/2C$  of a single excess electron be greater than the thermal energy  $k_B T$  the environment must fulfill appropriate conditions [26]. For instance, with an inductance  $L$  in the external impedance, the fluctuation of the charge is given by  $\langle \delta Q^2 \rangle = e^2/4\rho \coth(\beta \hbar \omega_S/2)$  where  $\rho = E_C/\hbar \omega_S$ ,  $\omega_S = (LC)^{-1/2}$ , and  $\beta = 1/k_B T$ . Therefore, charge fluctuations cannot be small even at zero temperature unless  $\rho \gg 1$ . This means that a high-impedance environment is necessary, which makes tampering technically easy, for instance by adding another impedance circuit.

Here we define two scales to illustrate tamper resistance: (I) the scale associated with the key device size, and (II) the scale associated with the environment required to operate the system, which are respectively indicated by the dotted and dashed curves in figures 2(a) and (b). In the case of figure 2(b),

scale I is the scale of a tunneling device, whereas scale II covers all of the components. It turns out that the low tamper resistance of such wired devices is due to the fact that scale II is typically the macro-scale, even though scale I is the nanometer scale.

In contrast, in the case of the optical excitation transfer shown in figure 2(a), the two QDs and their surrounding environment are governed by scale I; it is also important to note that scale II is the same as scale I. More specifically, the transfer of an optical excitation from QD<sub>A</sub> to QD<sub>B</sub> is completed due to the non-radiative relaxation process occurring at QD<sub>B</sub>, which is usually difficult to tamper with. Theoretically, the sublevel relaxation constant is given by

$$\Gamma = 2\pi |g(\omega)|^2 D(\omega), \quad (3)$$

where  $\hbar g(\omega)$  is the exciton–phonon coupling energy at frequency  $\omega$ ,  $\hbar$  is Planck’s constant divided by  $2\pi$ , and  $D(\omega)$  is the phonon density of states. Therefore, tampering with the relaxation process would require somehow ‘stealing’ the exciton–phonon coupling, which would be extremely difficult technically.

We should also note that the energy dissipation occurring in the optical excitation transfer, derived theoretically as  $E_{(2,1,1)} - E_{(1,1,1)}$  in QD<sub>B</sub> based on equation (2), should be larger than the exciton–phonon coupling energy of  $\hbar\Gamma$ , otherwise the two levels in QD<sub>B</sub> cannot be resolved. This is similar to the fact that the condition  $\rho \gg 1$  is necessary in the electron tunneling example, which means that the mode energy  $\hbar\omega_s$  is smaller than the required charging energy  $E_C$ . By regarding  $\hbar\Gamma$  as a kind of mode energy in the optical excitation transfer, the difference between the optical excitation transfer and a conventional wired device is the physical scale at which this mode energy is realized: the nanoscale for the optical excitation transfer, and the macro-scale for electrical circuits.

Another possible method of attack is to use a probe, i.e. an invasive attack, to tamper with the excitation transfer. This is modeled by the system shown in figure 2(c), where the original two quantum dots are denoted as A and B, and the attacker is represented by C. Based on a theoretical model of optical near-fields [8, 27], the solid curves shown in figures 2(d) and (e) show the calculated evolution of the population of the lower level of B (=B1) in the absence of the attacker dot C. The interdot interaction time is assumed to be 100 ps ( $U^{-1}$ ), and the sublevel relaxation at B is assumed to be 10 ps ( $\Gamma^{-1}$ ), as typical parameters. Now, in the presence of C, the dashed curve and the dotted curve in figure 2(d) respectively show the evolution of the lower levels of B (B1) and C (C1). It is clear that there is little population in C1, meaning that tampering is difficult, since the sublevel relaxation at B is faster than the interaction between B2 and C2. Now, suppose that the interaction between B2 and C2 could be made faster (for example, 30 ps); then the attacker could have a higher population, as shown by the dotted curve in figure 2(e). However, at the same time, the population of B1 (dashed curve) is degraded accordingly, meaning that the attack is detectable from the performance degradation of the original system.

### 2.3. Remarks

One additional remark regarding optical excitation transfer is that the lower bound of energy dissipation occurring at QD<sub>B</sub> has also been investigated by considering possible interferences among adjacent signal transfer channels [31], which turns out to be about 25  $\mu\text{eV}$ , a significantly small value. Another remark is that using different ratios of the number of QD<sub>A</sub> and QD<sub>B</sub> in a unit area leads to different patterns of optical excitation flow, leading to different spectral characters [32]. Also, modifying the distances between QD<sub>A</sub> and QD<sub>B</sub> results in different photoluminescence spectra [33], or different points in a chromaticity diagram [1]. The ratio of the numbers of QDs or distances between QDs, or generally speaking a network of optical near-field interactions, are other resources allowing optical excitation transfer to be used for security applications.

## 3. Hierarchical information retrieval

### 3.1. Hierarchy in optical near-field interactions and the architecture of hierarchical nanophotonic systems

Another notable feature in optical near-field interactions is their inherent hierarchy, meaning that the interactions behave differently at different scales, as indicated in the inset of figure 3(a). The interactions are theoretically analyzed based on dipole–dipole interactions [34], described in section 3.2 below, a quantum mechanical model [35], and an angular spectrum representation of an electromagnetic field at the nanoscale [36].

Such hierarchical properties allow *hierarchical nanophotonic architectures* where multiple functions are associated with the physical scales involved, as schematically represented in figure 3(b). Hierarchical information retrieval, discussed in section 3.2 below, is one realization of such an architecture, exploiting the fact that different information is retrievable at different physical scales. For security applications, multiple-level security information can be embedded; for example, less-critical security information can be retrieved at a coarser scale, while higher security information is associated with a finer scale. This is also called multi-level information hiding using optical near-field interactions. The contents of sections 4–6 are all based on such a hierarchical architecture.

In particular, the hierarchical hologram shown in section 4 utilizes the physical differences between optical near-fields and far-fields. The behavior of usual optical elements, for instance diffractive optical elements, holograms, or glass components, is associated with their optical responses in the far-field. Nanostructures can exist in these optical elements as long as they do not affect the optical responses in the far-field. Designing nanostructures that are accessible only via optical near-fields allows additional, or hidden, watermark information to be recorded in those optical elements while maintaining the original optical responses in the far-field.



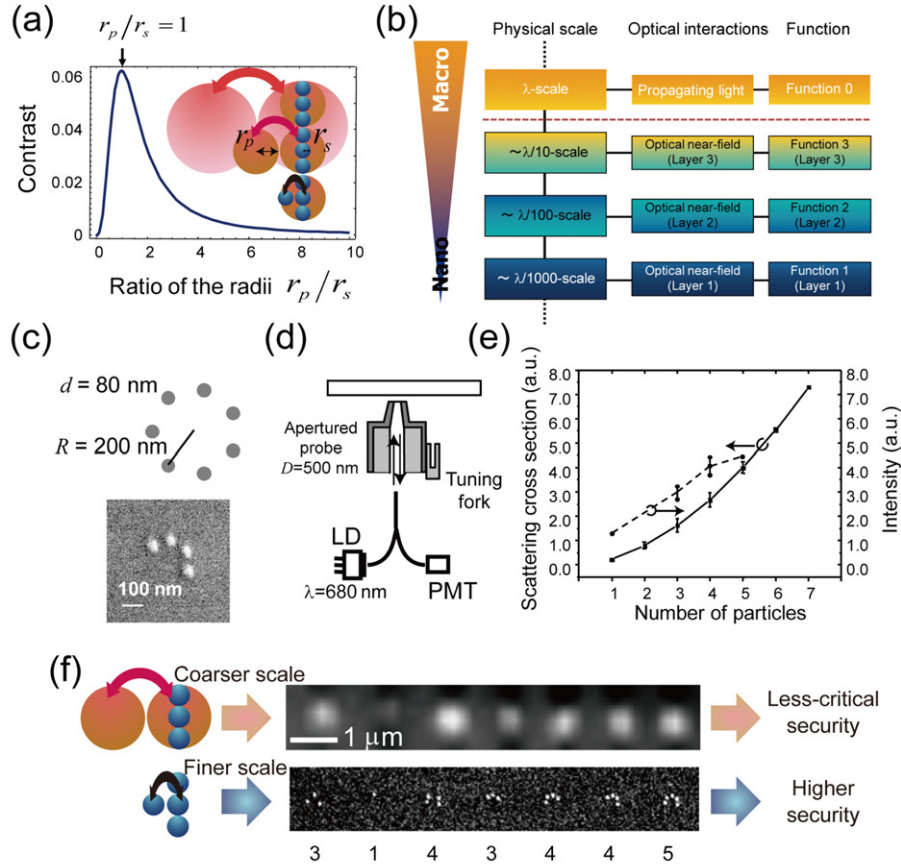


**Figure 3.** (a) Hierarchy in optical near-field interactions. (b) Hierarchical nanophotonic architecture. (c) Signal contrast as a function of the ratio of the radii of the sample and the probe based on dipole–dipole interactions. (d)–(g) Hierarchical information retrieval, or hierarchical information hiding. (d) Each section consists of small particles. (e) Experimental setup. (f) SEM image of a Au particle array and intensity pattern captured by a fiber probe having a 500 nm diameter aperture. (g) Calculated scattering cross-sections depending on the number of particles in each section (square marks), and peak intensity of each section in intensity profile shown in (f).

### 3.2. Hierarchical information retrieval in optical near-fields

Here we briefly describe a physical model of hierarchy in optical near-field interactions based on dipole–dipole interactions [34]. It should be noted that a quantum optical model has also demonstrated hierarchy [35]. Suppose that a probe, which is modeled by a sphere of radius  $r_p$ , is placed close to a sample to be observed, which is modeled as a sphere of radius  $r_s$ . The inset in figure 3(a) shows three different sizes for the probe and the sample. When they are illuminated by incident light whose electric field is  $E_0$ , electric dipole moments are induced in both the probe and the sample; these moments are respectively denoted by  $p_p = \alpha_p E_0$  and  $p_s = \alpha_s E_0$ . The electric dipole moment induced in the sample,  $p_s$ , then generates an electric field, which changes the electric dipole moment in the probe by an amount  $\Delta p_p = \Delta \alpha_p E_0$ . Similarly,  $p_p$  changes the electric dipole moment in the sample by  $\Delta p_s = \Delta \alpha_s E_0$ . These electromagnetic interactions are called dipole–dipole interactions. The scattering intensity induced by these electric dipole moments is given by

$$I = |p_p + \Delta p_p + p_s + \Delta p_s|^2 \approx (\alpha_p + \alpha_s)^2 |E_0|^2 + 4\Delta\alpha(\alpha_p + \alpha_s) |E_0|^2 \quad (4)$$

where  $\Delta\alpha = \Delta\alpha_s = \Delta\alpha_p$ . The second term in equation (4) represents the intensity of the scattered light generated by the dipole–dipole interactions, containing the information of interest, which is the relative difference between the probe and the sample. The first term in equation (4) is the background signal for the measurement. Therefore, the ratio of the second term to the first term of equation (4) corresponds to a signal contrast, which will be maximized when the sizes of the probe and the sample are the same ( $r_p = r_s$ ), as shown in figure 3(a) [34]. Thus, one can see a scale-dependent physical hierarchy in this framework, where a small probe can nicely resolve objects with a comparable resolution, whereas a large probe cannot resolve detailed structure but can resolve structure with a resolution comparable to the probe size. Therefore, although a large-diameter probe cannot detect smaller-scale structure, it could detect certain features associated with its scale.

Based on the above simple hierarchical mechanism, hierarchical information retrieval was demonstrated [11]. Consider, for example, a maximum of  $N$  nanoparticles distributed in a region of subwavelength scale. Those nanoparticles can be nicely resolved by a scanning near-field microscope if the size of its fiber probe tip is comparable to the size of individual nanoparticles. In this way, the

*first-layer* information associated with each distribution of nanoparticles is retrievable, corresponding to  $2^N$ -different codes. By using a larger-diameter fiber probe tip instead, although the distribution of the particles cannot be resolved, a mean-field feature with a resolution comparable to the size of the probe can be extracted, namely, the number of particles within an area comparable to the size of the fiber probe tip. Thus, the *second-layer* information associated with the number of particles, corresponding to  $(N + 1)$ -different level of signals, is retrievable. Therefore, one can access a different set of signals, either  $2^N$  or  $N + 1$ , depending on the scale of observation. This leads to hierarchical data retrieval by associating this information hierarchy with the distribution and the number of nanoparticles by using an appropriate coding strategy. For example, in encoding  $N$ -bit information,  $(N - 1)$ -bit signals can be encoded by distributions of nanoparticles while associating the remaining 1 bit with the number of nanoparticles [11].

In order to experimentally demonstrate such principles, an array of Au particles, each with a diameter around 80 nm, was distributed over a SiO<sub>2</sub> substrate in a 200 nm radius circle, as shown in figure 3(c). These particles were fabricated by a liftoff technique using electron-beam (EB) lithography with a Cr buffer layer. The groups of Au particles were 2  $\mu$ m apart. A scanning electron microscope (SEM) image is shown in the lower side of figure 3(f), in which the values indicate the number of particles within each group. In order to illuminate all Au particles in each group and collect the scattered light from them, a near-field scanning optical microscope (NSOM) with a metallized fiber probe having a large-diameter aperture (500 nm) was used in an illumination–collection setup, as schematically shown in figure 3(d). The light source used was a laser diode with an operating wavelength of 680 nm. The distance between the substrate and the probe was maintained at 750 nm. The upper side of figure 3(f) shows an intensity distribution captured by the probe, from which the second-layer information is retrieved. The solid circles in figure 3(e) indicate the peak intensity of each section, which increased linearly and agrees with the scattering cross-sections as a function of the number of particles calculated based on a finite-difference time-domain (FDTD) simulation indicated by solid circles in figure 3(e). These results show the validity of hierarchical memory retrieval from nanostructures.

#### 4. Hierarchical hologram

Holography, which generates natural three-dimensional images, is one of the most common anti-counterfeiting techniques [1]. In the case of a volume hologram, the surface is ingeniously formed into microscopic periodic structures which diffract incident light in specific directions. A number of diffracted light beams can form an arbitrary three-dimensional image. Generally, these microscopic structures are recognized as being difficult to duplicate, and therefore holograms have been widely used in the anti-counterfeiting of bank notes, credit cards, etc. However, conventional anti-counterfeiting methods based on the physical appearance

of holograms are nowadays not completely secure [6]. Nanophotonic solutions, utilizing light–matter interactions on the nanoscale, would provide higher anti-counterfeiting capability as well as potentially enabling other applications, such as artifact-metric systems [37].

The hierarchical hologram works in both optical far-fields and near-fields, the former being associated with conventional holographic images (figure 4((a) (i)) and the latter being associated with the optical intensity distribution based on a nanometric structure (figure 4((a) (ii)) that is accessible only via optical near-fields (figure 4((a) (iii)). In principle, a structural change occurring at the subwavelength scale does not affect the optical response functions, which are dominated by propagating light. Therefore, the visual aspect of the hologram is not affected by such a small structural change on the surface. Additional data can thus be written by engineering structural changes in the subwavelength regime so that they are only accessible via optical near-field interactions without having any influence on the optical responses obtained via the conventional far-field light. By applying this hierarchy, new functions can be added to conventional holograms.

There are at least two strategies for realizing a hierarchical hologram.

One strategy is to apply nanometric structural changes to the surface structure of a conventional hologram. In [12], a thin metal layer is coated on a conventional hologram and diffraction grating, followed by nanostructure patterning by a focused ion-beam machine. Additional information corresponding to the fabricated nanostructures was successfully retrieved while preserving the macroscopic view of the original hologram or the diffraction efficiency of the diffraction grating.

The other strategy, employed in the case of embossed holograms composed of diffraction gratings, is to locally engineer the original patterns of the hologram from the beginning, that is, to embed nanostructures *within* the original patterns of the hologram [13]. In this case, since the original hologram is basically composed of one-dimensional grating structures, evident polarization dependence is obtained in retrieving the nanostructures via optical near-fields, as detailed below. There are some additional benefits with this approach: one is that we can fully utilize the existing industrial facilities and fabrication technologies that have been developed for conventional holograms, yet provide additional information in the hologram. Another is that the polarization dependence facilitates the readout of nanostructures via optical near-fields, as mentioned below.

As shown in figure 4(a), we created a sample device to experimentally demonstrate retrieval of the nanostructures embedded within an embossed hologram. The entire device structure, whose size was 15 mm  $\times$  20 mm, was fabricated by electron-beam lithography on a Si substrate, followed by sputtering a 50 nm thick Au layer. The cross-sectional profile is shown in figure 4(b).

As indicated in figure 4((a) (i), we can observe a three-dimensional image of the earth reconstructed from the device. More specifically, the device was based on the design of a *Virtuagram*<sup>®</sup>, developed by Dai Nippon

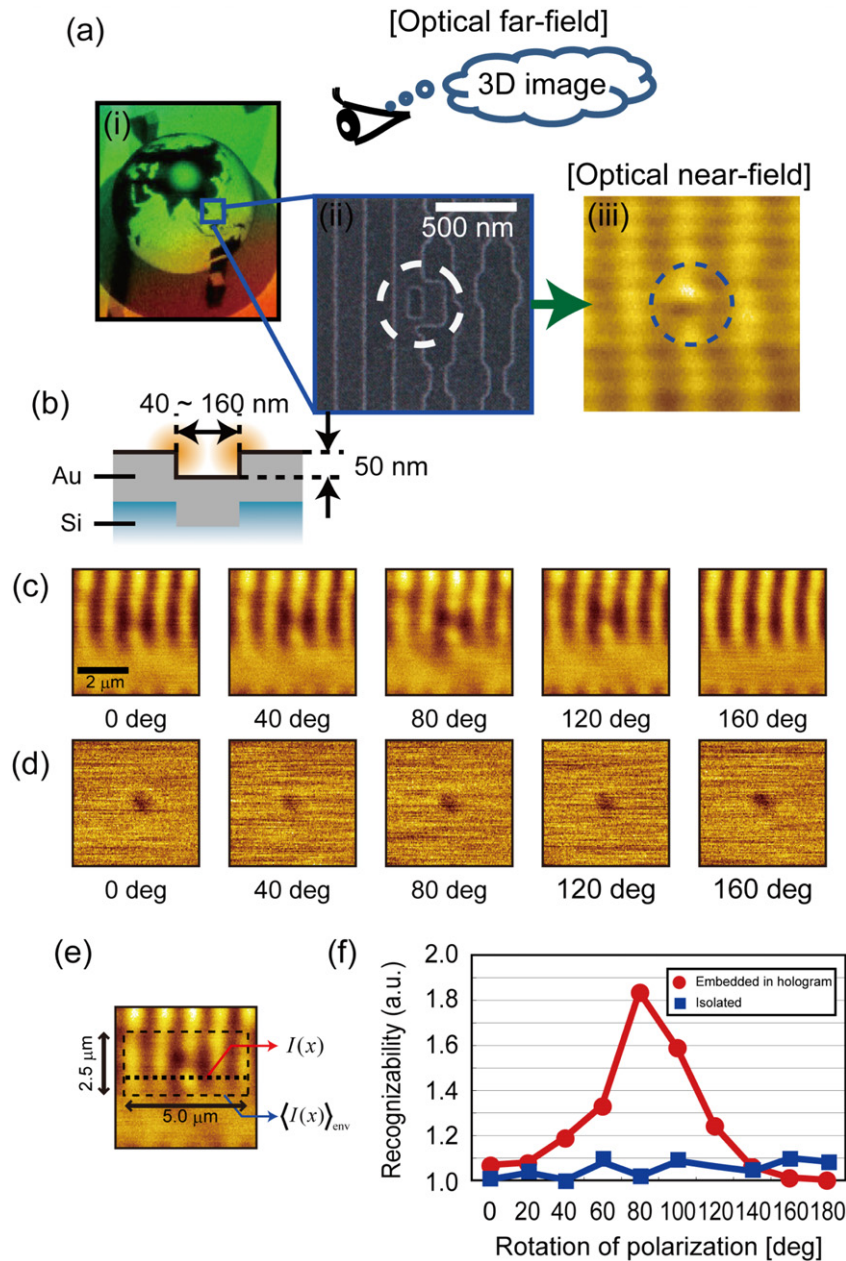


**Figure 4.** Hierarchical hologram. ((a) (i) Far-field view of the fabricated hierarchical hologram. Its design is based on a Virtuagram®. ((a) (ii) Nanometric square- or rectangular-shaped patterns are embedded in the hologram. A discontinuity is induced along the one-dimensional grating structure. ((a) (iii) A retrieved near-field scanning optical microscope (NSOM) image. (b) Cross-sectional optical profile of the device. (c), (d) Polarization dependences in obtained NSOM images. (e) Explanation of  $I(x)$  and  $\langle I(x) \rangle_{\text{env}}$  used to evaluate recognizability figure-of-merit. (f) Recognizability of the nanostructures measured by NSOM. Evident polarization dependency was exhibited in nanostructures embedded in hologram, unlike isolated nanostructures, which showed little dependency.

Printing Co., Ltd, Japan, which is a high-definition computer-generated hologram composed of binary-level one-dimensional modulated gratings, as shown in the scanning electron microscope image in figure 4((a) (ii)). Within the device, we slightly modified the shape of the original structure of the hologram so that the nanostructural change was accessible only via optical near-field interactions. As shown in figure 4((a) (ii)), square- or rectangular-shaped structures, whose associated optical near-fields correspond to the additional or hidden information, were embedded in the original hologram structures. The unit size of

the nanostructures ranged from 40 to 160 nm. Note that the original hologram was composed of arrays of one-dimensional grid structures, spanning along the vertical direction in figure 4((a) (ii)). To embed the nanophotonic codes, the grid structures were partially modified in order to implement the nanophotonic codes. Nevertheless, the grid structures remained topologically continuously connected along the vertical direction. On the other hand, the nanostructures were always isolated from the original grid structures. These geometrical characteristics provide interesting polarization dependence.

The input light induces oscillating surface charge distributions due to the coupling between the light and electrons in the metal. Note that the original 1D grid structures span along the vertical direction. The  $y$ -polarized input light induces surface charges along the vertical grids. Since the grid structure continuously exists along the  $y$ -direction, there is no chance for the charges to be concentrated. However, in the area of the embedded nanophotonic code, we can find structural discontinuity in the grid; this results in higher charge concentrations at the edges of the embedded nanostructure. On the other hand, the  $x$ -polarized input light sees structural discontinuity along the horizontal direction due to the vertical grid structures, as well as in the areas of the embedded nanostructures. It turns out that charge concentration occurs not only in the edges of the embedded nanostructures but also at other horizontal edges of the environmental grid structures. When square-shaped nanophotonic codes are *isolated* in a uniform plane, both  $x$ - and  $y$ -polarized input light have equal effects on the nanostructures. These mechanisms indicate that the nanostructures embedded in holograms could exploit these polarization dependences.

In the experimental demonstration, optical responses in near-mode observation were detected using a near-field scanning optical microscope (NSOM) operated in an illumination–collection mode with an optical fiber tip with a radius of curvature of 5 nm. The observation distance between the tip of the probe and the sample device was set at less than 50 nm. The light source used was a laser diode (LD) with an operating wavelength of 785 nm, and scattered light was detected by a photomultiplier tube (PMT).

We examined NSOM images in the vicinity of nanostructures that were embedded in the hologram and nanostructures that were not embedded in the hologram using a linearly polarized radiation source from  $0^\circ$ - to  $180^\circ$ -rotated polarizations at  $20^\circ$  intervals, as summarized in figures 4(c) and (d), respectively. (In the figure, the NSOM images obtained at  $40^\circ$  intervals are shown.) In the case of nanostructures embedded in the hologram, clear polarization dependence was observed; for example, from the area of the nanophotonic code located in the center, a high-contrast signal intensity distribution was obtained with polarizations around  $80^\circ$ . To quantitatively evaluate the polarization dependence of the embedded nanophotonic code, we adopted a figure-of-merit, what we call *recognizability*, for the observed NSOM images, defined as follows. Let the horizontal intensity profile along the dashed line in figure 4(e), which crosses the area of the nanostructure, be denoted by  $I(x)$ , where  $x$  represents the horizontal position. Also, let the average intensity along the vertical direction at the horizontal position  $x$  within a range of  $2.5 \mu\text{m}$  be denoted by  $\langle I(x) \rangle_{\text{env}}$ , which indicates the environmental signal distribution. When a higher intensity is obtained selectively from the area of the nanostructure, the difference between  $I(x)$  and  $\langle I(x) \rangle_{\text{env}}$  should be large. On the other hand, if the intensity distribution is uniform along the vertical direction, the difference between  $I(x)$  and  $\langle I(x) \rangle_{\text{env}}$  should be small. Thus, the difference between  $I(x)$  and  $\langle I(x) \rangle_{\text{env}}$  indicates the *recognizability* of the

nanostructures. With respect to the polarization angle  $\theta$ , we evaluate the *recognizability*  $R(\theta)$  as

$$R(\theta) = \sum_x |I(x) - \langle I(x) \rangle_{\text{env}}|. \quad (5)$$

The square and circular marks in figure 4(f) respectively show  $R(\theta)$  based on the NSOM images of isolated nanostructures and those embedded in the hologram. Clear polarization dependence is observed in the case of the nanostructures embedded in the holograms, facilitating near-field information retrieval.

## 5. Authentication function based on near-field processes

### 5.1. Principles

In this section we demonstrate that two metal nanostructures, called shape A and shape B hereafter, can be designed to exhibit far-field radiation only when their shapes are appropriately configured and when they are closely stacked [14, 15]. Such functionality is useful in ensuring product authentication or certification, where a system should work only when the two nanostructures match, just like a *lock* and *key*. We explain the operating principle by observing induced electrical currents and their associated optical near-fields, and also describe experimental demonstrations.

We have previously proposed a theoretical scheme that is useful for examining the relation between the shapes of nanostructures and the resulting light polarization in their optical near-field and far-field [38]. In that study, the geometry of a given nanostructure can be understood in terms of ‘individual element’ and ‘layout’ factors, where the former represents the shapes of individual elements, and the latter their spatial arrangement. There are two important physical aspects in analyzing their corresponding optical responses. One is that input light induces electric currents within individual elements of the metal nanostructure. The other is the optical near-fields between those individual elements. We can understand those two processes in a unified manner as vectorial elements in the system [38].

Shape A and shape B were designed as aligned rectangular units on an  $xy$ -plane at constant intervals horizontally (along the  $x$ -axis) and vertically (along the  $y$ -axis), as respectively shown in figures 5(a) and (b). When we irradiate shape A with  $x$ -polarized light, surface charges are concentrated at the horizontal edges of each of the rectangular units. The relative phase difference of the oscillating charges between the horizontal edges is  $\pi$ , which is schematically represented by  $+$  and  $-$  marks in figure 5(a). Now, consider the  $y$ -component of the far-field radiation from shape A, which is associated with the charge distributions induced in the rectangle. When we draw arrows from the  $+$  marks to the  $-$  marks along the  $y$ -axis, we find that adjacent arrows are always directed oppositely, indicating that the  $y$ -component of the far-field radiation is externally small. In other words, shape A behaves as a quadrupole regarding the  $y$ -component of the far-field radiation. It should also be noted

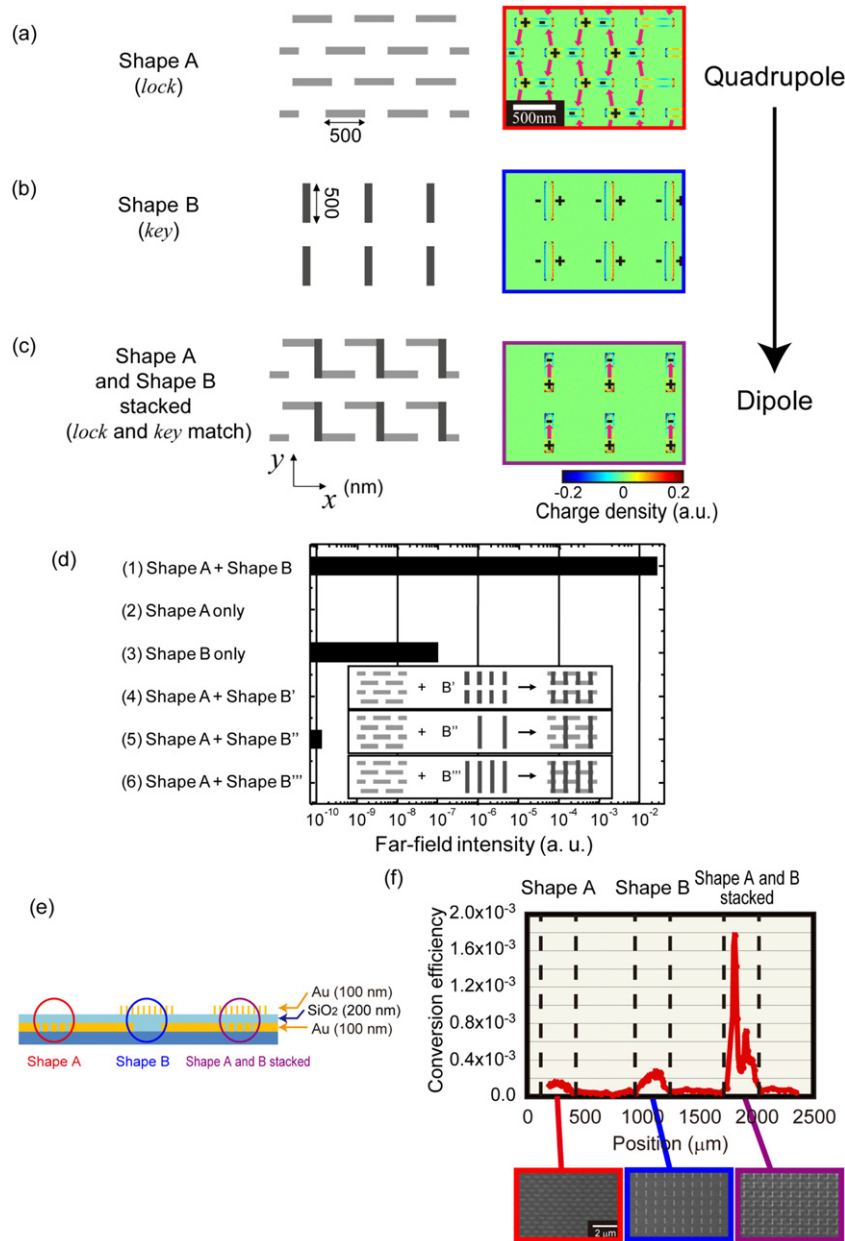


**Figure 5.** Authentication, or lock and key, based on nanophotonics. (a)–(c) The shape and the distribution of induced charge density: (a) shape A, (b) shape B, and (c) stacked structure of shapes A and B. (d) Comparison of calculated far-field intensity for various combinations of shapes. Far-field intensity appears strongly only when shape A matches the appropriate shape B, that is to say, when lock and key match. (e) A schematic cross-sectional diagram of the fabricated device. (f) Measured polarization conversion efficiency for three areas of the fabricated device. Conversion efficiency exhibited a larger value specifically in the areas where the stacked structure of shapes A and B was located. SEM images of each area are also shown.

that near-field components exist in the vicinity of the units in shape A. With this fact in mind, we put the other metal nanostructure, shape B, on top of shape A. Through the optical near-fields in the vicinity of shape A, surface charges are induced on shape B. What should be noted here is that the arrows connecting the + and – marks along the y-axis are now aligned in the same direction, and so the y-component of the far-field radiation appears; that is, the stacked structure of shape A and shape B behaves as a dipole (figure 5(c)). Also, shape A and shape B need to be closely located to invoke such effects since the optical near-field interactions between shape

A and shape B are critical. In other words, far-field radiation appears only when shape A and shape B are correctly stacked; that is to say, a *quadrupole–dipole transform* is achieved through shape-engineered nanostructures and their associated optical near-field interactions.

In order to verify this mechanism, we numerically calculated the surface charge distributions induced in the nanostructures and their associated far-field radiation based on FDTD electromagnetic simulations. The designs of shape A and shape B consist of arrays of gold rectangular units; each unit has a length of 500 nm, and a width and a height

of 100 nm, which are identical to the dimensions of the experimental devices discussed later below. As the material, we assumed the Drude model of gold with a refractive index of 0.16 and an extinction ratio of 3.8 at a wavelength of 688 nm [39].

When irradiating these three structures with continuous-wave  $x$ -polarized input light at a wavelength of 688 nm, the right-hand side of figures 5(a)–(c) shows the induced surface charge density distributions (simply called surface charge hereafter) obtained by calculating the divergence of the electric fields. For the shape A-only structure (figure 5(a)), we can find a local maximum and local minimum of the surface charges, denoted by plus and minus signs. When we draw arrows from the plus signs to the minus signs between adjacent rectangular units, as already introduced above, we can see that adjacent arrows are always directed opposite to each other, meaning that the shape A-only structure behaves as a quadrupole for the  $y$ -component of the far-field radiation. For the shape B-only structure (figure 5(b)), the electron charges are concentrated at the horizontal edges of each of the rectangular units, and there are no  $y$ -components that could contribute to the far-field radiation. Figure 5(c) shows the surface charge distributions induced in shape B when it is stacked on top of shape A. We can clearly see that the electron charges are induced at the vertical edges of each of the rectangular units, and they are arranged in the same directions. In other words, a dipole arrangement is accomplished with respect to the  $y$ -component, leading to a drastic increase in the far-field radiation.

In figure 5(d), we also consider the output signals when we place differently shaped structures on top of shape A, instead of shape B. With shape B', shape B'', and shape B''', whose shapes are respectively represented in the insets of figure 5(d), the output signals do not appear, as shown from the fourth to the sixth row in figure 5(d), since the condition necessary for far-field radiation is not satisfied with those shapes; namely, the correct *key* is necessary to unlock the *lock*.

## 5.2. Experiment

We fabricated structures consisting of (i) shape A-only, (ii) shape B-only, and (iii) shape A and shape B stacked. Although the stacked structure should ideally be provided by combining the individual single-layer structures, in the following experiment the stacked structure was integrated in a single sample as a solid two-layer structure to avoid the experimental difficulty in precisely aligning the individual structures mechanically. The fabrication process was detailed in [15].

Figure 5(e) schematically represents cross-sectional profiles of these fabrication processes, where (i) shape A-only structures were fabricated in the first layer, (ii) shape B-only structures were fabricated in the second layer, and (iii) stacked structures had shapes A and B in the first and second layers, respectively. The lower part in figure 5(f) also shows SEM images of fabricated samples of (i)–(iii). Because the stacked structure was fabricated as a single sample, the gap between shape A and shape B was fixed at 200 nm.

The performance was evaluated in terms of the polarization conversion efficiency by radiating  $x$ -polarized light on each of the areas (i)–(iii) and measuring the intensity of the  $y$ -component in the transmitted light. The light source was a laser diode with an operating wavelength of 690 nm. Two sets of Glan–Thompson prisms (extinction ratio  $10^{-6}$ ) were used to extract the  $x$ -component for the input light and to extract the  $y$ -component in the transmitted light. The intensity was measured by a lock-in controlled photodiode. The position of the sample was controlled by a stepping motor with a step size of 20  $\mu\text{m}$ .

Figure 5(f) shows the polarization conversion efficiency as a function of the position on the sample, where it exhibited a larger value specifically in the areas where the stacked structure of shapes A and B was located, which agrees well with the theoretically predicted and calculated results.

## 6. Traceability using nanophotonics

### 6.1. Principle

As mentioned in section 3.1, different functions can be associated with different physical scales. In this section, we associate one of the hierarchical layers with energy dissipation processes. Specifically, a two-layer system is demonstrated, where (i) at smaller scale, called *scale 1*, the system should exhibit a unique response, and (ii) at a larger scale, called *scale 2*, the system should output two different signals. Such a hierarchical response can be applied to functions like *traceability* or *tamper evidence* in combination with a localized energy dissipation process at scale 1 [16]. Optical access to this memory will be automatically recorded due to energy dissipation occurring locally in scale 1, while at the same time, information will be read out based on the scale 2 behavior, as depicted in figure 6(a). These functions will be useful in applications such as tamper-evident or high-security optical memory (confidentiality can be ensured), managing digital content, or privacy protection [40].

Shape-engineered metal nanostructures can exhibit hierarchical features like those described above, where the finer scale is used for implementing traceability [17]. Here, two types of shapes were assumed. The first one (*shape I*) had two triangular metal plates aligned in the same direction, and the other one (*shape II*) had them facing each other, as shown in figure 6(a). The metal was gold, the gap between the two apices was 50 nm, the horizontal length of one triangular plate was 173 nm, the angle at the apex was  $30^\circ$ , and the thickness was 30 nm. An incident uniform plane wave with a wavelength of 680 nm was assumed for input light. The polarization was parallel to the  $x$ -axis in the inset of figure 6(b). Now, scale 1 is associated with the scale around the gap of the triangles, and scale 2 is associated with the scale covering both of the triangles, as shown in figure 6(a).

Regarding the optical response at scale 1, as shown in figure 6(b), the electric field near the surface (1 nm away from the metal surface) showed an intensity nearly five orders of magnitude higher than the surrounding area. It should also be noted that nearly comparable electric field enhancements

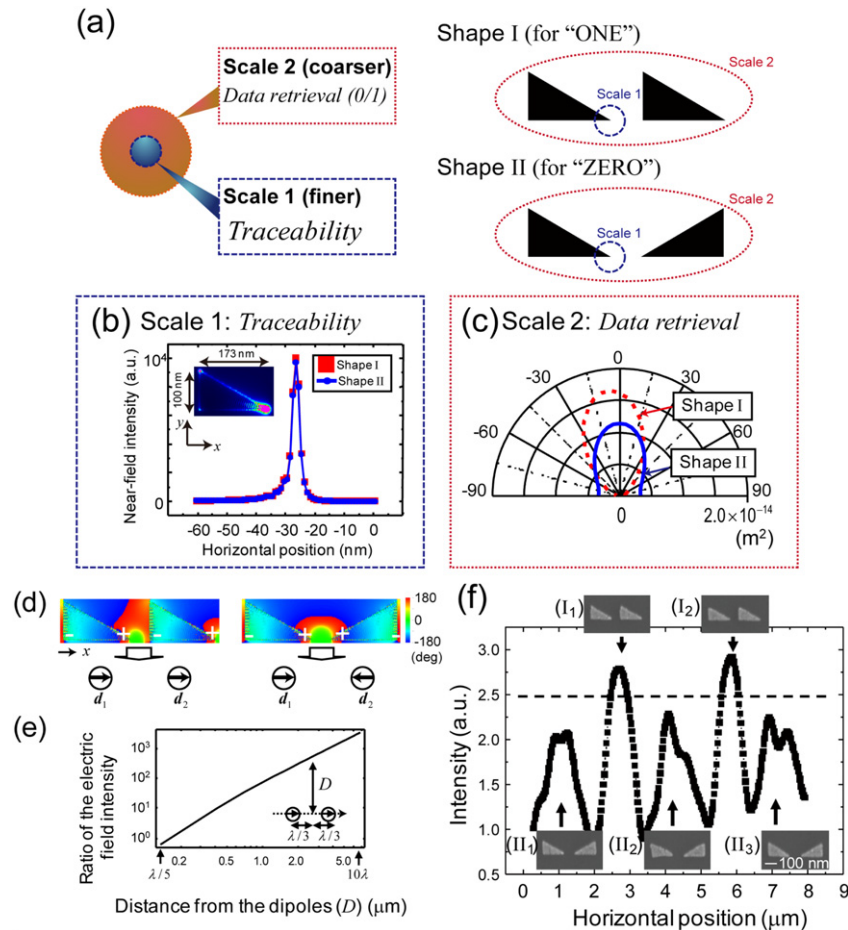


**Figure 6.** (a) Traceability using hierarchy in optical near-fields based on shape-engineered nanostructures. (b) In scale 1, both shape I and shape II exhibit comparable electric field enhancement, whereas (c) in scale 2, they exhibit different responses. (d) Profiles of the  $x$ -component of phase in the electric fields. (e) Ratio of the electric field intensity from identically oriented dipoles to that of dipoles facing each other. (f) Experimental intensity profiles for scale 2 signals for both shapes I and II.

were observed near the apices of shapes I and II, which are respectively denoted by the squares and circles in figure 6(b).

On the other hand, shapes I and II exhibited different responses at scale 2. As shown in figure 6(c), shape I exhibited a larger scattering cross-section compared with shape II. This indicates that a digital output is retrievable by observing the scattering from the entire structure (scale 2), where, for example, digital 1 and 0 are respectively associated with shape I and shape II.

One physical reason behind such a character is the following. As shown in Figure 6(d), the phases of the  $x$ -component of the electric field inside the metal differ by almost  $180^\circ$  between the apex and the opposite side. Therefore, the system is approximated by two dipoles orientated in the same direction for shape I and in opposite directions for shape II, which are schematically indicated by two dipoles  $d_1$  and  $d_2$  in figure 6(d). Based on the formula describing an electric field from oscillating dipoles, figure 6(e) demonstrates that the electric field intensity from the identically oriented dipoles increases rapidly compared with that from the oppositely oriented dipoles as the distance between the dipoles and the observation position, denoted by  $D$  in the inset, increases. In other words, we see that shapes

I and II effectively behave as a dipole and a quadrupole, respectively. Figure 6(e) also indicates that comparable intensities are obtained for both shapes when the observation position is close to the dipoles, which is the intended system response at scale 1.

### 6.2. Experiment

In order to experimentally demonstrate the principle, shapes I and II were fabricated in gold metal plates on a glass substrate by a liftoff technique using electron-beam lithography. A NSOM was used in an illumination–collection setup with a fiber probe having an aperture of diameter 500 nm. The light source used was a laser diode with an operating wavelength of 780 nm. The distance between the substrate and the probe was maintained at 375 nm. Figure 6(f) shows the electric field intensity depending on the shape of the metal plates, where the shape I series exhibited larger values compared with the shape II series, as expected.

## 7. Summary

In summary, this paper describes the physical principles and numerical and experimental demonstrations of systems

based on nanophotonics, with regards to security-related applications, such as tamper resistance against non-invasive and invasive attacks, hierarchical information retrieval, hierarchical holograms, authentication, and traceability. In addition to overcoming the limitations faced by conventional propagating light, such as the diffraction limit, we can make use of the unique attributes of optical near-field interactions on the nanoscale, namely optical excitation transfer and hierarchy, for security applications. As is clear with the hierarchical hologram demonstration, nanophotonic security principles could co-exist with various existing optical security technologies, which would provide qualitatively new functions and/or offer a higher level of security. It should be emphasized that we need more detailed characterizations, including detailed quantitative performance analysis [41], and technological improvements, both in the design of systems and in fabricating nanostructures, for future deployment. Also, there are many other unique attributes offered by nanophotonics, such as phonon-assisted processes [42, 43], based on a theoretical dressed photon model [44], that can potentially contribute to security applications. Further exploration of nanophotonics may lead to *nano-intelligence* and contribute to security in our lives and society, and is also expected to establish novel dressed photon science and technologies.

## Acknowledgments

This work was supported in part by the Strategic Information and Communications R&D Promotion Programme (SCOPE) of the Ministry of Internal Affairs and Communications, and Grants-in-Aid for Scientific Research from the Japan Society for the Promotion of Science. The authors acknowledge Dai Nippon Printing Co., Ltd, for fabrication of the hierarchical hologram.

## References

- [1] van Renesse R L 2005 *Optical Document Security* (Boston, MA: Artech House Publishers)
- [2] Javidi B 2005 *Optical and Digital Techniques for Information Security* (New York: Springer)
- [3] Goodman J W 2004 *Introduction To Fourier Optics* (Colorado: Roberts and Company)
- [4] Pohl D W and Courjon D (ed) 1993 *Near Field Optics* (Dordrecht: Kluwer Academic)
- [5] Kocher P, Jaffe J and Jun B 1998 Introduction to differential power analysis and related attacks *Cryptogr. Res.* [www.cryptography.com/public/pdf/DPATechInfo.pdf](http://www.cryptography.com/public/pdf/DPATechInfo.pdf)
- [6] McGrew S P 1990 Hologram counterfeiting: problems and solutions *Proc. SPIE* **1210** 66–76
- [7] Ohtsu M and Hori H 1999 *Near-Field Nano-Optics* (New York: Kluwer Academic/Plenum)
- [8] Ohtsu M, Kawazoe T, Yatsui T and Naruse M 2008 Nanophotonics: application of dressed photons to novel photonic devices and systems *IEEE J. Sel. Top. Quantum Electron.* **14** 1404–17
- [9] Ohtsu M, Kobayashi K, Kawazoe T, Yatsui T and Naruse M 2008 *Principles of Nanophotonics* (Boca Raton, FL: Taylor and Francis)
- [10] Naruse M, Hori H, Kobayashi K and Ohtsu M 2007 Tamper resistance in optical excitation transfer based on optical near-field interactions *Opt. Lett.* **32** 1761–3
- [11] Naruse M, Yatsui T, Nomura W, Hirose N and Ohtsu M 2005 Hierarchy in optical near-fields and its application to memory retrieval *Opt. Express* **13** 9265–71
- [12] Tate N, Nomura W, Yatsui T, Naruse M and Ohtsu M 2008 Hierarchical hologram based on optical near- and far-field responses *Opt. Express* **16** 607–12
- [13] Tate N, Naruse M, Yatsui T, Kawazoe T, Hoga M, Ohayagi Y, Fukuyama T, Kitamura M and Ohtsu M 2010 Nanophotonic code embedded in embossed hologram for hierarchical information retrieval *Opt. Express* **18** 7497–505
- [14] Naruse M, Yatsui T, Kawazoe T, Tate N, Sugiyama H and Ohtsu M 2008 Nanophotonic matching by optical near-fields between shape-engineered nanostructures *Appl. Phys. Express* **1** 112101
- [15] Tate N, Sugiyama H, Naruse M, Nomura W, Yatsui T, Kawazoe T and Ohtsu M 2009 Quadrupole-dipole transform based on optical near-field interactions in engineered nanostructures *Opt. Express* **17** 11113–21
- [16] Naruse M, Yatsui T, Kawazoe T, Akao Y and Ohtsu M 2008 Design and simulation of a nanophotonic traceable memory using localized energy dissipation and hierarchy of optical near-field interactions *IEEE Trans. Nanotechnol.* **7** 14–9
- [17] Naruse M, Yatsui T, Kim J H and Ohtsu M 2008 Hierarchy in optical near-fields by nano-scale shape engineering and its application to traceable memory *Appl. Phys. Express* **1** 062004
- [18] Akahane K, Yamamoto N and Tsuchiya M 2008 Highly stacked quantum-dot laser fabricated using a strain compensation technique *Appl. Phys. Lett.* **93** 041121
- [19] Huang M H, Mao S, Feick H, Yan H, Wu Y, Kind H, Weber E, Russo R and Yang P 2001 Room-temperature ultraviolet nanowire nanolasers *Science* **292** 1897–9
- [20] Yatsui T, Ohtsu M, An S J, Yoo J and Yi G-C 2005 Near-field measurement of spectral anisotropy and optical absorption of isolated ZnO nanorod single-quantum-well structures *Appl. Phys. Lett.* **87** 033101
- [21] Mano T and Koguchi N, Nanometer-scale GaAs ring structure grown by droplet epitaxy *J. Cryst. Growth* **278** 108–12
- [22] Ueno K, Mizeikis V, Juodkazis S, Sasaki K and Misawa H 2005 Optical properties of nanoengineered gold blocks *Opt. Lett.* **30** 2158–60
- [23] Valentine J, Zhang S, Zentgraf T, Ulin-Avila E, Genov D A, Bartal G and Zhang X 2008 Three-dimensional optical metamaterial with a negative refractive index *Nature* **455** 376–9
- [24] Kawazoe T, Ohtsu M, Aso S, Sawado Y, Hosoda Y, Yoshizawa K, Akahane K, Yamamoto N and Naruse M 2011 Two-dimensional array of room-temperature nanophotonic logic gates using InAs quantum dots in mesa structures *Appl. Phys. B* **103** 537–46
- [25] Hori H 2001 Electronic and electromagnetic properties in nanometer scales *Optical and Electronic Process of Nano-Matters* ed M Ohtsu (Dordrecht: Kluwer Academic) pp 1–55
- [26] Ingold G-L and Nazarov Y V 1992 Charge tunneling rates in ultrasmall junctions *Single Charge Tunneling* ed H Grabert and M H Devoret (New York: Plenum) pp 21–107
- [27] Sangu S, Kobayashi K, Shojiguchi A, Kawazoe T and Ohtsu M 2003 Excitation energy transfer and population dynamics in a quantum dot system induced by optical near-field interaction *J. Appl. Phys.* **93** 2937–45
- [28] Ohtsu M, Kobayashi K, Kawazoe T, Sangu S and Yatsui T 2002 Nanophotonics: design, fabrication, and operation of nanometric devices using optical near fields *IEEE J. Sel. Top. Quantum Electron.* **8** 839–62



- [29] Franzl T, Klar T A, Schietinger S, Rogach A L and Feldmann J 2004 Exciton recycling in graded gap nanocrystal structures *Nano Lett.* **4** 1599–603
- [30] Maier S A, Kik P G, Atwater H A, Meltzer S, Harel E, Koel B E and Requicha A A G 2003 Local detection of electromagnetic energy transport below the diffraction limit in metal nanoparticle plasmon waveguides *Nature Mater.* **2** 229–32
- [31] Naruse M, Hori H, Kobayashi K, Holmstrom P, Thylen L and Ohtsu M 2010 Lower bound of energy dissipation in optical excitation transfer via optical near-field interactions *Opt. Express* **18** A544–53
- [32] Naruse M, Kawazoe T, Ohta R, Nomura W and Ohtsu M 2009 Optimal mixture of randomly dispersed quantum dots for optical excitation transfer via optical near-field interactions *Phys. Rev. B* **80** 125325
- [33] Tate N, Naruse M, Nomura W, Kawazoe T, Yatsui T, Hoga M, Ohayagi Y, Sekine Y, Fujita H and Ohtsu M 2011 Demonstration of modulatable optical near-field interactions between dispersed resonant quantum dots *Opt. Express* **19** 18260–71
- [34] Ohtsu M and Kobayashi K 2004 *Optical Near Fields* (Berlin: Springer)
- [35] Sangu S, Kobayashi K and Ohtsu M, Optical near fields as photon-matter interacting systems *J. Microsc.* **202** 279–85
- [36] Naruse M, Inoue T and Hori H 2007 Analysis and synthesis of hierarchy in optical near-field interactions at the nanoscale based on angular spectrum *Japan. J. Appl. Phys.* **46** 6095–103
- [37] Matsumoto H and Matsumoto T 2003 Clone match rate evaluation for an artifact-metric system *IPSI J.* **44** 1991–2001
- [38] Naruse M, Yatsui T, Hori H, Yasui M and Ohtsu M 2008 Polarization in optical near- and far-field and its relation to shape and layout of nanostructures *J. Appl. Phys.* **103** 113525
- [39] Lynch D W and Hunter W R 1985 Comments on the optical constants of metals and an introduction to the data for several metals *Handbook of Optical Constants of Solids* ed E D Palik (Orlando: Academic) pp 275–367
- [40] Garfinkel S L, Juels A and Pappu R 2005 RFID privacy: an overview of problems and proposed solutions *IEEE Secur. Priv. Mag.* **3** 34–43
- [41] Naruse M, Hori H, Kobayashi K, Ishikawa M, Leibnitz K, Murata M, Tate N and Ohtsu M 2009 Information theoretical analysis of hierarchical nano-optical systems in the subwavelength regime *J. Opt. Soc. Am. B* **26** 1772–9
- [42] Fujiwara H, Kawazoe T and Ohtsu M 2010 Nonadiabatic multi-step excitation for the blue–green light emission from dye grains induced by the near-infrared optical near-field *Appl. Phys. B* **98** 283–9
- [43] Naruse M, Kawazoe T, Yatsui T, Tate N and Ohtsu M 2011 A stochastic modeling of morphology formation by optical near-field processes *Appl. Phys. B* **105** 185–90
- [44] Ohtsu M 2011 Nanophotonics: dressed photon technology for qualitatively innovative optical devices, fabrication, and systems *Progress in Nanophotonics 1* ed M Ohtsu (Berlin: Springer) pp 1–58

# Room-temperature growth of high-quality ZnO nanocrystals using a dressed-photon-assisted near-field process

T. Yatsui · K. Nakanishi · K. Kitamura · M. Ohtsu

Received: 19 April 2012 / Published online: 24 May 2012  
© Springer-Verlag 2012

**Abstract** Single-crystalline ZnO nanocrystals were fabricated by room-temperature photo-chemical vapor deposition (PCVD). We further enhanced the growth of high-quality single-crystalline ZnO nanocrystals using dressed photons and phonons (DPPs). This resulted in greater position control and the growth of high-quality ZnO nanocrystals. The ZnO nanocrystals produced with DPPs had excellent cathodoluminescence characteristics, indicating that the near-field PCVD process could be a promising technique for nanophotonic integrated circuit production.

## 1 Introduction

Future optical transmission systems require nanometer-scale photonic devices (nanophotonic devices [1]) composed of quantum dots (QDs) to increase data transmission rates and capacity. One representative device studied by the authors is a nanophotonic switch [2, 3]. Recently, Kawazoe et al., succeeded in fabricating AND-gate and NOT-gate devices that operated at room temperature using InAs QD pairs [4], in which switching dynamics are controlled by a dipole-forbidden optical energy transfer among resonant energy levels in QDs via an optical near field.

To fabricate nanophotonic devices and their integrated circuits, QDs must be deposited on a substrate with nanoscale position control. To achieve this level of control,

we have demonstrated the feasibility of nanoscale chemical vapor deposition (CVD) by scanning a near-field fiber probe [5] as well as the deposition of 60-nm Zn dots with nanoscale control [6]. Although selective growth of semiconductor QDs via a self-assembly has recently been demonstrated by either metal catalyst-assisted [7, 8] or catalyst-free methods [9, 10], only limited semiconductor nanomaterials, substrates, and growth temperatures were used.

## 2 Dressed-photon-assisted near-field process

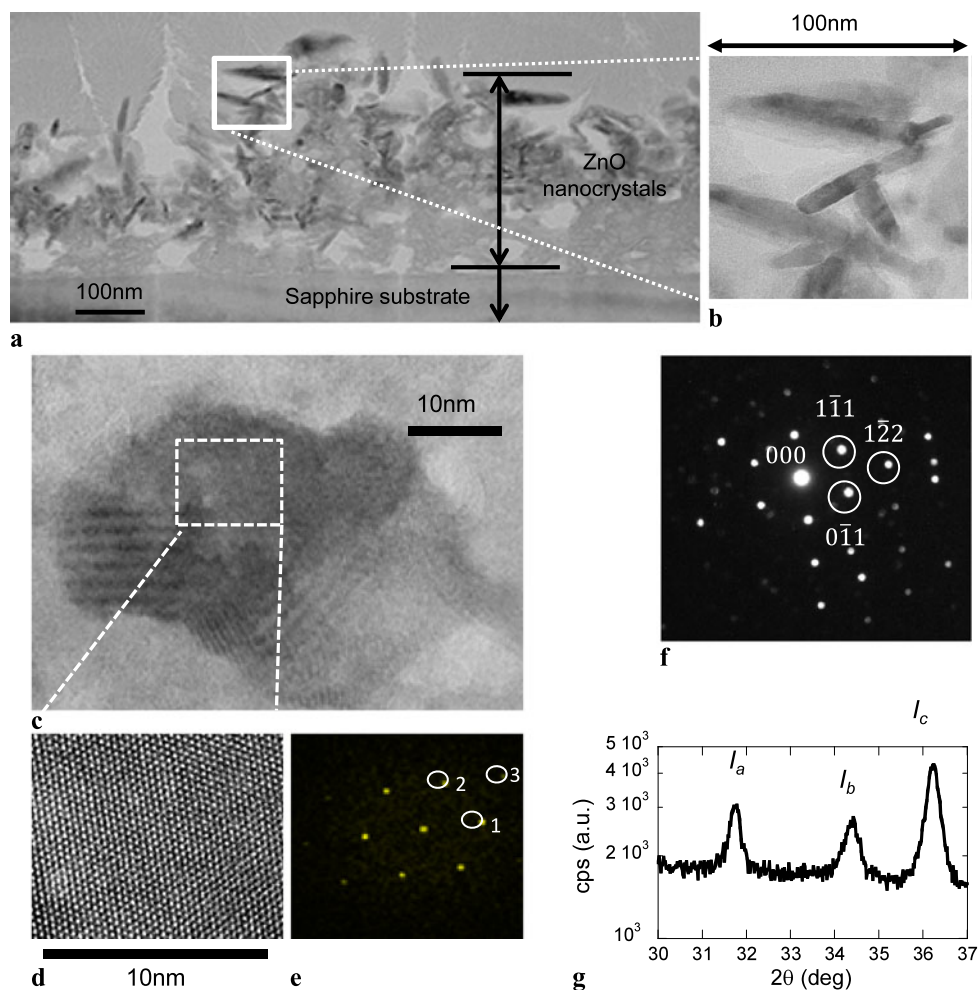
To achieve greater position control, we used the optical near-field. The optical near-field is a virtual photon that couples with an excited electron. The quasiparticle representing this coupled state is called a dressed photon (DP) [11]. The energy of a dressed photon is larger than the energy of a free photon due to the contribution from coupling with the excited electron energy. In addition to excite electron coupling, the DP interacts with the crystal lattice structure of the nanomaterial by coupling with the multimodes of the phonons. As a result, the DP can dress the energy of phonons in a coherent state [12]. The coupled state of the DP and the coherent phonon (dressed photon and phonon or DPP) is a quasiparticle. The energy of the DPP is larger than that of the DP and the incident free photon, contributed from the electron and phonon. The use of DPPs has facilitated novel nanoscale technology [13, 14].

The ZnO nanocrystal is potentially ideal for room-temperature nanophotonic device production due to its high exciton-binding energy [15–17] and great oscillator strength [18]. For this reason, ZnO was used to demonstrate the feasibility of room-temperature nanocrystal growth by DPPs.

T. Yatsui (✉) · K. Nakanishi · K. Kitamura · M. Ohtsu  
School of Engineering, University of Tokyo, Bunkyo-ku, Tokyo,  
113-8656, Japan  
e-mail: [yatsui@ee.t.u-tokyo.ac.jp](mailto:yatsui@ee.t.u-tokyo.ac.jp)

T. Yatsui · M. Ohtsu  
The Nanophotonics Research Center, University of Tokyo,  
Bunkyo-ku, Tokyo, 113-8656, Japan

**Fig. 1** (a) TEM image of the ZnO nanocrystals deposited on a sapphire substrate. (b) Magnified TEM image in the area indicated by the white open square in (a). (c) and (d) high-resolution TEM images. (e) FFT image of (d). (f) The selection area diffraction (SAD) pattern of (d) taken from the (011) direction. (g) XRD  $\theta$ - $2\theta$  scan result of (a)



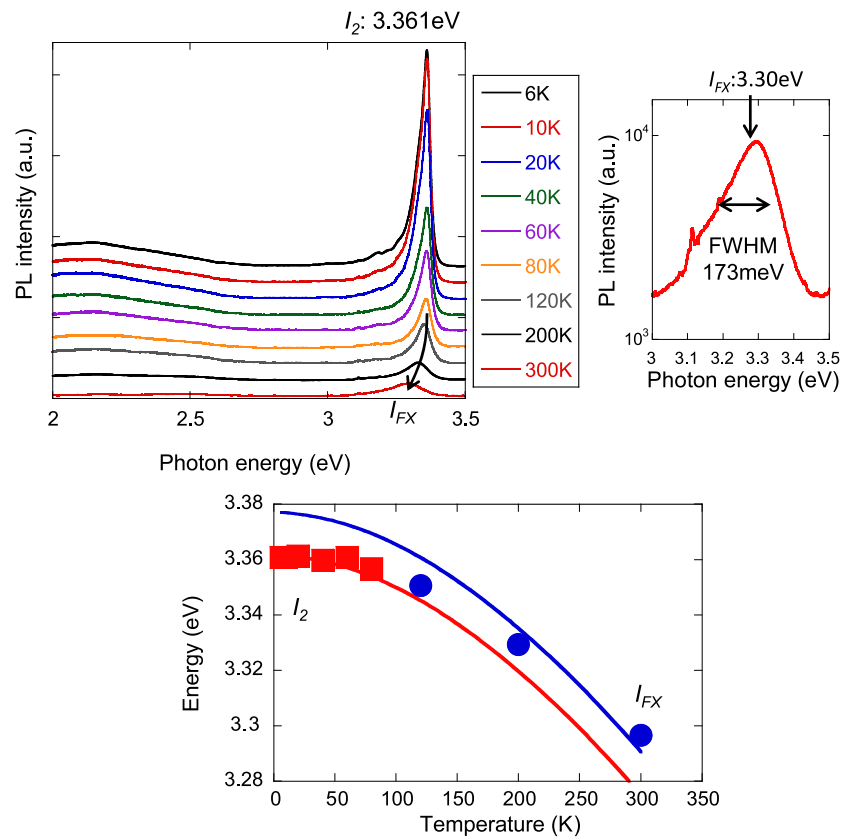
ZnO nanocrystals grown using photochemical vapor deposition (PCVD). PCVD reduces the growth temperature by producing reactive radicals via the photolysis of their precursors [19]. As a result, higher position alignment can be realized due to the reduction in the thermal diffusion of the nanoparticles deposited on the substrate.

### 3 Room temperature growth of ZnO nanocrystal using photochemical vapor deposition

As a preliminary study of the position selective growth of nanocrystals by DPPs, we carried out conventional PCVD for ZnO nanocrystal growth. Diethyl zinc (DEZn) and oxygen were used as II and VI sources. Argon was used as the carrier gas for DEZn. The II/VI ratio was 9/20,000. The total pressure in the reaction chamber was 5.0 Torr. Q-switch pulsed laser light (5.82 eV,  $\lambda = 213$  nm, 20 Hz, pulse width = 5 ns) was used as the light source for PCVD growth. The photon energy of the light source exceeds the absorption band-edge energy of DEZn (4.59 eV) [20]. The growth time was 3 hours.

Low-magnification transmission electron microscopy (TEM), shown in Figs. 1(a) and 1(b), revealed rod-shaped structures with 50–100 nm in length and 5–10 nm in diameter. High-resolution TEM images (Figs. 1(c) and 1(d)) and the corresponding fast Fourier transform (FFT) pattern (Fig. 1(e)) revealed a periodic structure indicating single-crystalline formation. Using inverse FFT, we determined that the lattice spacing (0.280, 0.280, 0.163 nm) matched the ZnO wurtzite planes; 0.284 nm along the (100) plane, 0.281 nm along the (010) plane, and 0.165 nm along the (110) plane. From these results, the TEM images of Figs. 1(c) and 1(d) are of the wurtzite ZnO crystal from the (001) direction. These results were also confirmed by selection area diffraction (SAD) patterns obtained from the (011) direction (Fig. 1(f)), where the selective spot indicated by the white open circles matched the lattice spacing of wurtzite ZnO ( $1\bar{1}1$ ), ( $1\bar{2}2$ ), and ( $0\bar{1}1$ ). The X-ray diffraction (XRD)  $\theta$ - $2\theta$  scans, shown in Fig. 1(g), indicate three peaks at 31.77 ( $I_a$ ), 34.42 ( $I_b$ ), and 36.25 ( $I_c$ ) degrees, corresponding to ZnO (100), ZnO (001), and ZnO (101), respectively. These results confirm that the obtained structure

**Fig. 2** (a) Temperature-dependent PL spectra of deposited ZnO nanocrystals. (b) Room-temperature (300 K) PL spectrum. (c) Temperature dependence of the emission peak energy. *Solid lines* show the calculated temperature-dependent PL peak position using Varshni's equation



was a wurtzite ZnO single crystal and deposited with random direction with respect to the substrate.

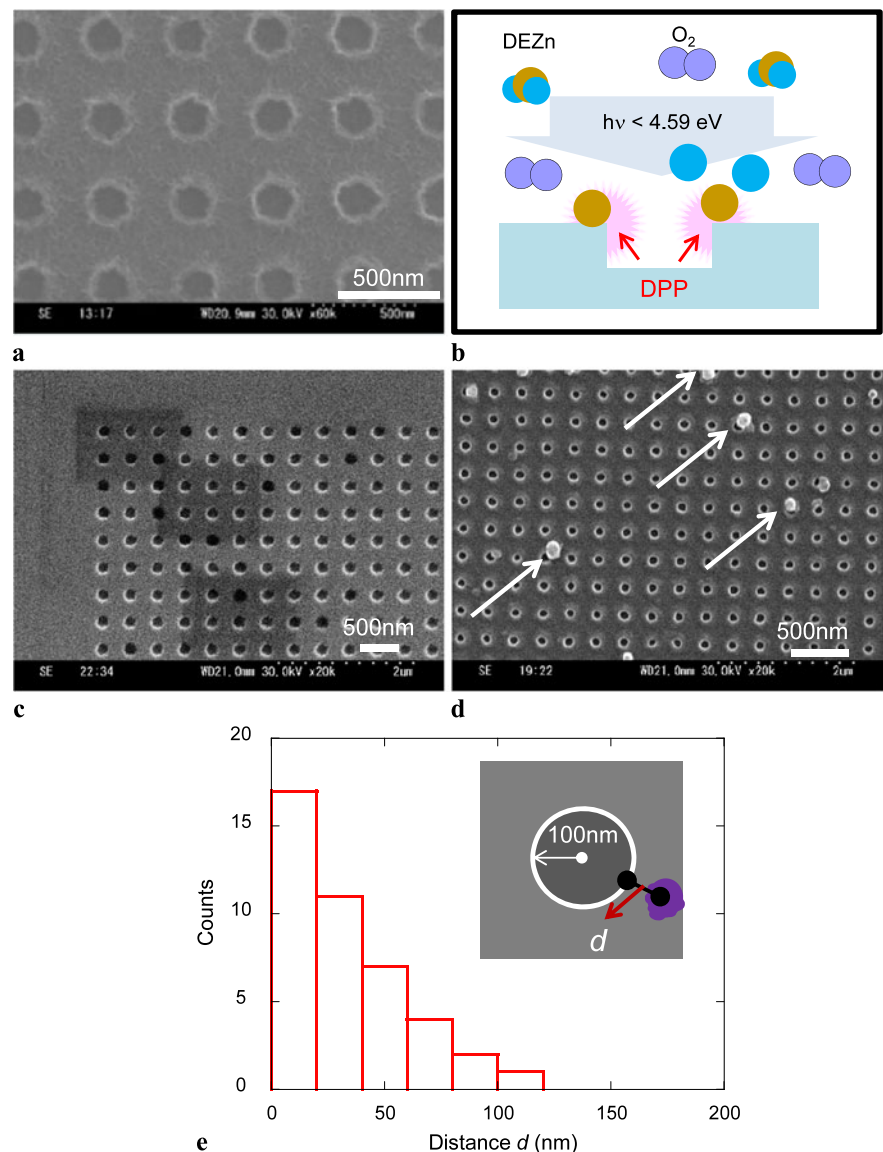
Photoluminescence (PL) was used to evaluate the optical properties of the deposited nanocrystals. We used a continuous-wave He–Cd laser ( $\lambda = 325$  nm) as the excitation light source. The temperature-dependent PL spectrum (Fig. 2(a)) shows a strong sharp peak at 3.361 eV ( $I_2$ ) at 6 K. This PL peak originates from the bound exciton in wurtzite ZnO [18]. As the temperature increased, the PL intensity of this peak decreased dramatically. In addition, a new peak (labeled  $I_{FX}$ ) emerged at temperatures above 100 K;  $I_{FX}$  remained visible even at room temperature. Figure 2(b) shows the magnified PL spectrum at room temperature (300 K) with a sharp peak at 3.30 eV. Its full width at half maximum (FWHM) is 173 meV, which is comparable to that of a single-crystalline ZnO nanorod (158 meV) grown by metal-organic vapor phase epitaxy (MOVPE) under 450 °C high-growth temperature conditions [21]. These characteristics presumably resulted from the recombination of the neutral donor-bound exciton to the free exciton in wurtzite ZnO. The temperature dependence of the energy at the peaks  $I_2$  and  $I_{FX}$  is fitted using Varshni's equation (solid curves in Fig. 2(c)) [22], which defines the temperature dependence of the band gap. These results indicated that the ZnO nanocrystals synthesized by PCVD at room temperature were as high

quality as the ZnO synthesized using MOVPE with a high growth temperature of 450 °C.

#### 4 Room temperature growth of ZnO nanocrystal using dressed-photon-assisted near-field process

Based on the experimental results of the conventional PCVD described above, we proceeded to grow ZnO nanocrystals at room temperature using the DPP process. To generate DPPs, a patterned substrate with 200-nm-diameter holes and a 400-nm center-to-center period was fabricated on a 40-nm-thick SiO<sub>2</sub> film (Fig. 3(a)). A Q-switched pulsed laser with lower energy (3.49 eV,  $\lambda = 355$  nm, 20 Hz, pulse width = 5 ns) was used to prevent DEZn dissociation at the free space. DEZn can be selectively dissociated at the pattern edge by the DPP (Fig. 3(b)). Although no nanoparticles were deposited after 10-minute gas flow without irradiation (Fig. 3(c)), the deposition of nanoparticles at the rim of the hole (indicated by the white arrows) was confirmed after 10-minute gas flow with light irradiation of 3.49-eV (Fig. 3(d)). The nanoparticle deposition sites were sparse, despite the fact that the spot irradiated by the 3.49-eV light source was 1 mm in diameter. We evaluated the distance  $d$  between the nearest edge of the 100-nm hole and the nanoparticle center. The shapes of the nanoparticles were approximated by

**Fig. 3** (a) SEM image of the hole array substrate. (b) Schematic of ZnO-nanocrystal deposition using a DPP. SEM images the substrate after (c) 10-minutes without irradiation and (d) 10-minutes with irradiation. (e) Histogram of the obtained distance  $d$ . (Inset: schematic of the distance  $d$  between the nearest edge of the hole and the center of the nanoparticle)



circles of equal area. Figure 3(e) shows the histogram of  $d$ . From this result, 40-% of the nanoparticles were deposited within 20 nm of the edge, indicating that deposition was realized by DPPs generated at the rim of the hole structure. The results have shown the potential of DPPs for higher position-selective alignment.

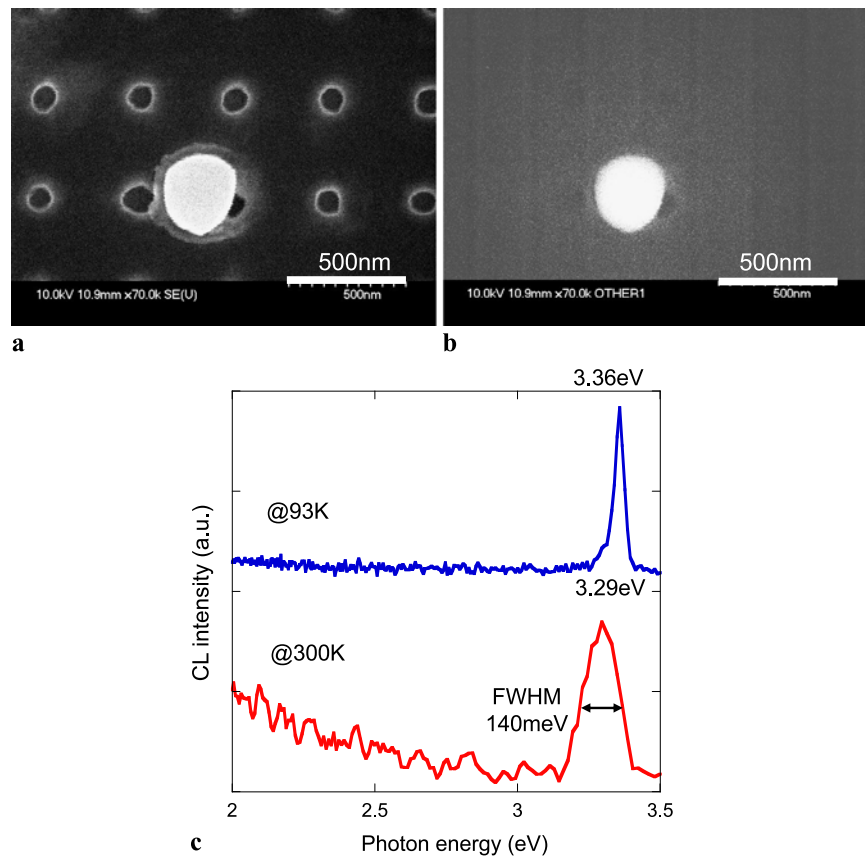
We used cathodoluminescence (CL) to evaluate the optical properties of the deposited nanoparticles. Figures 4(a) and 4(b) show the scanning electron microscopy (SEM) image of the deposited nanoparticles and the corresponding CL mapping at 3.36 eV taken at 93 K, which corresponds to the energy of the free exciton emission peak of wurtzite ZnO nanocrystals (blue solid curve in Fig. 4(c)). In addition, the room-temperature CL spectrum has a high peak at 3.29 eV with a width of 140-meV (red solid curve in Fig. 4(c)), which is comparable to that fabricated using MOVPE un-

der high growth temperature (450 °C). From these results, we confirmed that the deposited nanoparticles were high-quality wurtzite ZnO.

## 5 Conclusion

The use of PCVD allowed room-temperature growth of single-crystalline ZnO nanocrystals. Additionally, using a DPP generated in the nanoscale structure, we realized room-temperature growth of high-quality ZnO nanocrystals. We confirmed their excellent CL characteristics at room temperature. Because the deposition technique uses a photochemical reaction at room temperature, it can be applied to other materials and other substrates.

**Fig. 4** (a) Typical SEM image of the deposited ZnO nanocrystal and (b) the corresponding CL image at 3.36 eV obtained at 93 K. (c) CL spectra obtained at 93 K (blue solid curve) and 300 K (red solid curve)



**Acknowledgements** This work was partially supported by a Grant-in-Aid for Young Scientists (A), Grants-in-Aid for Scientific Research, Japan Society for the Promotion of Science (JSPS), and a Research Grant (Basic Research) from the TEPCO memorial foundation.

## References

- M. Ohtsu, T. Kawazoe, T. Yatsui, M. Naruse, *IEEE J. Sel. Top. Quantum Electron.* **14**, 1404 (2008)
- T. Kawazoe, K. Kobayashi, S. Sangu, M. Ohtsu, *Appl. Phys. Lett.* **82**, 2957 (2003)
- T. Yatsui, S. Sangu, T. Kawazoe, M. Ohtsu, S.J. An, J. Yoo, G.C. Yi, *Appl. Phys. Lett.* **90**, 223110 (2007)
- T. Kawazoe, M. Ohtsu, S. Aso, Y. Sawado, Y. Hosoda, K. Yoshizawa, K. Akahane, N. Yamamoto, M. Naruse, *Appl. Phys. B* **103**, 537 (2011)
- T. Yatsui, S. Takubo, J. Lim, W. Nomura, M. Kourogi, M. Ohtsu, *Appl. Phys. Lett.* **83**, 1716 (2003)
- J. Lim, T. Yatsui, M. Ohtsu, *IEICE Trans. Electron.* **E88c**, 1832 (2005)
- L.E. Jensen, M.T. Bjork, S. Jeppesen, A.I. Persson, B.J. Ohlsson, L. Samuelson, *Nano Lett.* **4**, 1961 (2004)
- A.I. Hochbaum, R. Fan, R.R. He, P.D. Yang, *Nano Lett.* **5**, 457 (2005)
- J. Noborisaka, J. Motohisa, T. Fukui, *Appl. Phys. Lett.* **86**, 213102 (2005)
- S.D. Hersee, X.Y. Sun, X.T. Wang, *Nano Lett.* **6**, 1808 (2006)
- K. Kobayashi, S. Sangu, H. Ito, M. Ohtsu, *Phys. Rev. A* **63**, 013806 (2001)
- A. Sato, Y. Tanaka, F. Minami, K. Kobayashi, *J. Lumin.* **129**, 1718 (2009)
- T. Yatsui, K. Hirata, W. Nomura, Y. Tabata, M. Ohtsu, *Appl. Phys. B* **93**, 55 (2008)
- T. Kawazoe, T. Takahashi, M. Ohtsu, *Appl. Phys. B* **98**, 5 (2010)
- A. Ohtomo, K. Tamura, M. Kawasaki, T. Makino, Y. Segawa, Z.K. Tang, G.K.L. Wong, Y. Matsumoto, H. Koinuma, *Appl. Phys. Lett.* **77**, 2204 (2000)
- M.H. Huang, S. Mao, H. Feick, H.Q. Yan, Y.Y. Wu, H. Kind, E. Weber, R. Russo, P.D. Yang, *Science* **292**, 1897 (2001)
- H.D. Sun, T. Makino, Y. Segawa, M. Kawasaki, A. Ohtomo, K. Tamura, H. Koinuma, *J. Appl. Phys.* **91**, 1993 (2002)
- D.C. Reynolds, D.C. Look, B. Jogai, C.W. Litton, G. Cantwell, W.C. Harsch, *Phys. Rev. B* **60**, 2340 (1999)
- S. Yamazaki, T. Yatsui, M. Ohtsu, *Appl. Phys. Express* **1**, 061102 (2008)
- R.R. Krchnavek, H.H. Gilgen, J.C. Chen, P.S. Shaw, T.J. Licata, R.M. Osgood, *J. Vac. Sci. Technol. B* **5**, 20 (1987)
- K. Kitamura, T. Yatsui, M. Ohtsu, G.C. Yi, *Nanotechnology* **19**, 175305 (2008)
- Y.P. Varshni, *Physica* **34**, 149 (1967)

## Superradiance from one-dimensionally aligned ZnO nanorod multiple-quantum-well structures

T. Yatsui, A. Ishikawa, K. Kobayashi, A. Shojiguchi, S. Sangu et al.

Citation: *Appl. Phys. Lett.* **100**, 233118 (2012); doi: 10.1063/1.4725514

View online: <http://dx.doi.org/10.1063/1.4725514>

View Table of Contents: <http://apl.aip.org/resource/1/APPLAB/v100/i23>

Published by the [American Institute of Physics](#).

---

### Related Articles

Two-photon-pumped optical gain in dye-polymer composite materials  
[Appl. Phys. Lett.](#) **100**, 133305 (2012)

Two-photon-pumped optical gain in dye-polymer composite materials  
[APL: Org. Electron. Photonics](#) **5**, 83 (2012)

Stimulated emission in AlGaIn/AlGaIn quantum wells with different Al content  
[Appl. Phys. Lett.](#) **100**, 081902 (2012)

Microwave-induced spin-flip scattering of electrons in point contacts  
[Low Temp. Phys.](#) **37**, 925 (2011)

Direct observation of amplified spontaneous emission of surface plasmon polaritons at metal/dielectric interfaces  
[Appl. Phys. Lett.](#) **98**, 261912 (2011)

---

### Additional information on *Appl. Phys. Lett.*

Journal Homepage: <http://apl.aip.org/>

Journal Information: [http://apl.aip.org/about/about\\_the\\_journal](http://apl.aip.org/about/about_the_journal)

Top downloads: [http://apl.aip.org/features/most\\_downloaded](http://apl.aip.org/features/most_downloaded)

Information for Authors: <http://apl.aip.org/authors>

## ADVERTISEMENT

**AIPAdvances**

Special Topic Section:  
**PHYSICS OF CANCER**

Why cancer? Why physics? [View Articles Now](#)

## Superradiance from one-dimensionally aligned ZnO nanorod multiple-quantum-well structures

T. Yatsui,<sup>1,2,a)</sup> A. Ishikawa,<sup>3</sup> K. Kobayashi,<sup>3</sup> A. Shojiguchi,<sup>4</sup> S. Sangu,<sup>5</sup> T. Kawazoe,<sup>1,2</sup> M. Ohtsu,<sup>1,2</sup> J. Yoo,<sup>6,7</sup> and G.-C. Yi<sup>6</sup>

<sup>1</sup>*School of Engineering, University of Tokyo, Bunkyo-ku, Tokyo 113-8656, Japan*

<sup>2</sup>*The Nanophotonics Research Centre, University of Tokyo, Bunkyo-ku, Tokyo 113-8656, Japan*

<sup>3</sup>*Department of Electrical and Electronic Engineering, University of Yamanashi, Kofu, Yamanashi 400-8511, Japan*

<sup>4</sup>*Green Platform Lab., NEC Corp., Kawasaki, Kanagawa 211-8666, Japan*

<sup>5</sup>*Device and Module Technology Development Centre, Ricoh Co., Ltd., Yokohama, Kanagawa 224-0035, Japan*

<sup>6</sup>*National Creative Research Initiative Centre for Semiconductor Nanorods and Department of Physics and Astronomy, Seoul National University, Seoul, Gwanak-gu 151-747, South Korea*

<sup>7</sup>*Center for Integrated Nanotechnologies, Los Alamos National Laboratory, Los Alamos, New Mexico 87545, USA*

(Received 8 March 2012; accepted 16 May 2012; published online 7 June 2012)

Using one-dimensionally aligned ZnO nanorod multiple-quantum-well structures (MQWs), we observed a superradiance, i.e., a cooperative spontaneous emission. We confirmed that the excitation power dependence of the emissions from the MQWs originated from the coherent coupling of the QWs due to the well organization at nanoscale. We identified two QWs with cooperative emission. Additionally, we evaluated the number of coherently coupled QWs sets of four that resulted in the superradiance. Our findings provide criteria for designing nanoscale synergetic devices without the use of an external cavity. © 2012 American Institute of Physics. [<http://dx.doi.org/10.1063/1.4725514>]

Cooperative spontaneous emission from coherently coupled two-level systems was predicted by Dicke,<sup>1</sup> and this work was followed by several theoretical investigations.<sup>2-7</sup> When two-level systems in the optical-wavelength region coherently interact via a single radiation field and all of them are excited to a population inversion as an initial condition, the result is a pulsed emission that originates from the quantum fluctuation of the radiation field. This phenomenon is called superfluorescence,<sup>5,6</sup> and the observations were in an atomic<sup>8</sup> and molecular<sup>9</sup> systems. More recently, superfluorescence was observed in solid samples consisting of ensemble quantum dots (QDs).<sup>10</sup>

Dicke's cooperative emission was not limited to superfluorescence. An additional cooperative emission, superradiance, does not start with the initial population inversion condition but originates from the giant initial polarization when the two-level systems are coherently coupled.<sup>1,3,4</sup> In superradiance, the number of initially excited two-level systems depends on the excitation power. If more than half of the two-level systems are excited (high-excitation power-condition), pulsed single-peak emission is obtained rather superfluorescence. Conversely, if fewer than half of the two-level systems are excited (low-excitation power-condition), emission with an exponentially decayed profile is obtained, which has a faster decay time and greater emission intensity compared with independent spontaneous emission. Recent observations of superradiance from single QD<sup>11</sup> J-aggregate,<sup>12</sup> and ensemble QDs<sup>13</sup> were realized under low-excitation-power conditions. Because the cooperative phenomenon is thought to be suppressed by dephasing in the disordered

system, we introduced a well-organized nanoscale structure so we could control the initial interactions among all the elements and thereby overcome the dephasing and obtain superradiance. By performing time-resolved spectroscopy of ZnO nanorod quantum-well structures (QWs) aligned in one dimension and found that multiple-QWs (MQWs) exhibited higher emission intensities and faster decay times than did single-QWs (SQWs). We confirmed that the excitation-power dependence of the emissions exceeding the spontaneous emission originated from the coherent coupling of the QWs due to the well-organization at nanoscale. Our findings provide criteria for designing nanoscale synergetic devices without the use of an external cavity, which provides a route for miniaturization below the operating wavelength.

To observe the interaction among ZnO/ZnMgO quantum structures, two samples were prepared using metal-organic vapor-phase epitaxy<sup>14</sup> (Fig. 1(a)): (1) SQWs with a well-layer thickness  $L_w$  of 3.25 nm and (2) MQWs with  $L_w=3.25$  nm (consisting of nine QWs separated by  $S=9$  nm). Figure 1(b) shows the Z-contrast transmission electron microscopic (TEM) image of the MQWs, in which it is clear that the ZnO QWs were aligned in one dimension. The far-field photoluminescence (PL) spectra were obtained using a continuous-wave, 3.81 eV photon energy, He-Cd laser and the emission signal was collected using an achromatic lens ( $f=50$  mm). In addition to the spectral peak at 3.380 eV from the ZnO stem ( $I_{ZnO}$ ), a blue-shifted PL peak was observed at 3.420 eV ( $I_{QW}$ ) (Figs. 1(c) and 1(d)). We believe that the peak energy  $I_{QW}$  originated from the exciton ground-state emission of the ZnO QWs because their energy was consistent with the ZnO well-layer thickness of 3.25 nm (3.433 eV), calculated using a finite square-well potential for

<sup>a)</sup>Electronic mail: yatsui@ee.t.u-tokyo.ac.jp.



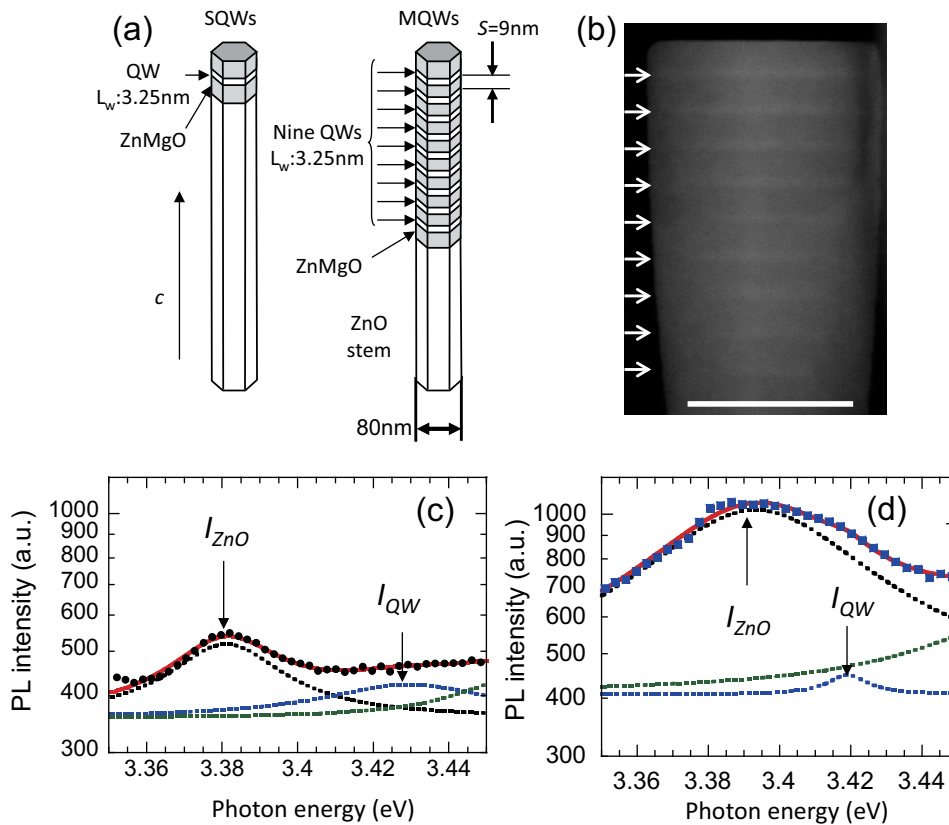


FIG. 1. ZnO/ZnMgO nanorod quantum-well-structures.  $c$ :  $c$ -axis of the ZnO stem. (a) Schematic of ZnO/ZnMgO single-quantum-well structures (SQWs) and multiple-quantum-well structures (MQWs). (b) Z-contrast TEM image of MQWs, clearly showing the compositional variation, with the bright layers indicated by white arrows representing the ZnO well layers. Scale bar: 50 nm. PL spectra of SQWs (c) and MQWs (d).

the quantum confinement effect in ZnO SQWs.<sup>15</sup> The theoretical calculation used  $0.28 m_0$  and  $1.8 m_0$  for the effective electron and hole masses in ZnO, respectively, a ratio of conduction and valence band offsets ( $\Delta E_c/\Delta E_v$ ) of 9, and a band gap offset ( $\Delta E_g$ ) of 250 meV. Taking into account those parameters, the carrier penetration depth from QWs was 0.7 nm. Therefore, the large separation between adjacent QWs (9 nm) prevented carrier tunneling and resultant electron interactions. This is, the excitons between adjacent QWs coupled via optical interactions only.<sup>16</sup>

Figures 2(a) and 2(b) show the time-resolved PL (TRPL) for the SQWs and MQWs, respectively, using the third harmonic of a mode-locked Ti:sapphire laser (4.025 eV photon energy, 80-MHz frequency, 1-ps pulse duration, and 100- $\mu$ m beam-spot size). Although the decay time was similar, the SQWs peak intensity increased as the excitation-power density increased (solid squares in Figs. 3(a) and 3(b)). The decay time of SQWs remained constant, with an average decay time of 383 ps ( $\tau_{SQW}$ ), and the peak intensity of the SQWs became saturated over time as the excitation-power density increased; this supports the conclusion that the emission originated from isolated SQWs. However, although the MQWs peak intensity increased as the excitation-power density increased, a faster decay time was observed as the excitation-power density increased (solid circles in Figs. 3(a) and 3(b)).

Based on these results, we evaluated the number of QWs ( $m$ ) with cooperative emission in  $M$ -QWs ( $M$  is the number of coherently coupled QWs). Given that the time evolution of the emission peak intensity is given by the time

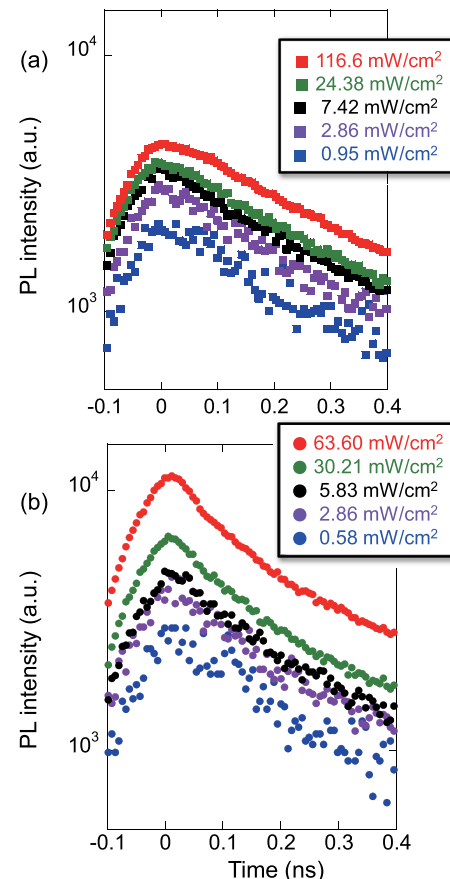


FIG. 2. The excitation-power-density dependence of time-resolved PL (TRPL) signals of (a) SQWs and (b) MQWs.

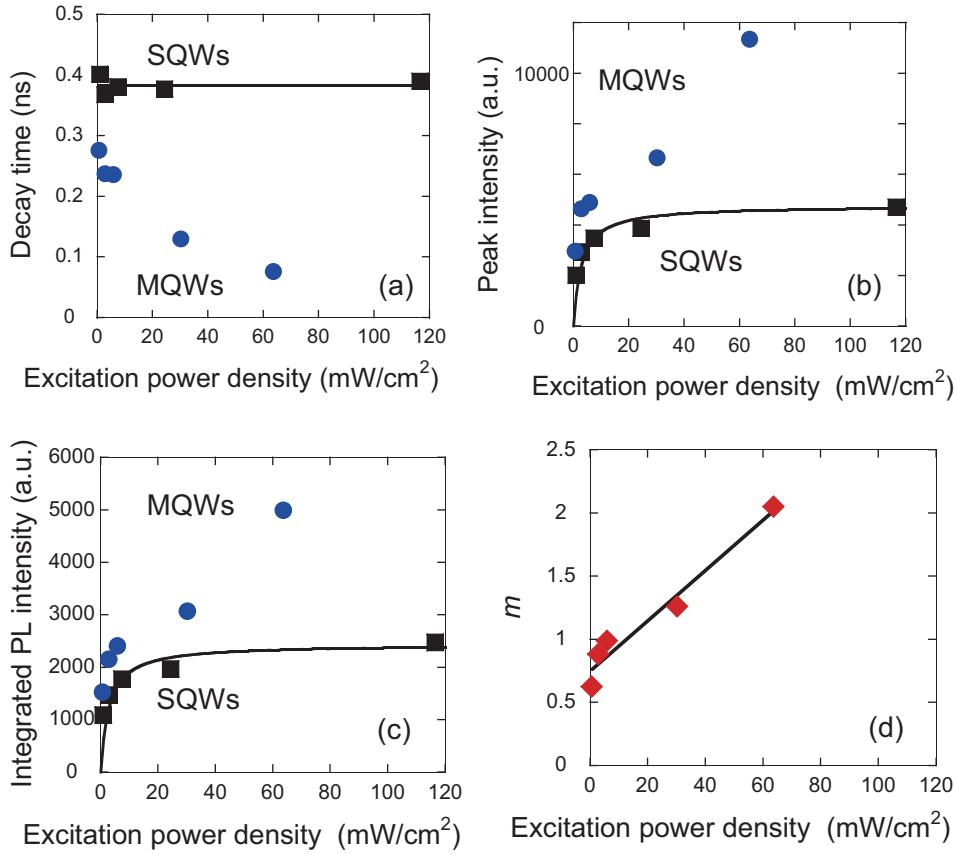


FIG. 3. Excitation power dependence of (a) decay time and (b) PL peak intensity (solid squares: SQWs, solid circles: MQWs). (c) Time-integrated of SQWs (solid squares) and MQWs (solid circles). (d) Evaluated value of the number of excited QWs,  $m$ .

differential of the emitted photon number, the time-integrated PL intensity is proportional to the number of excited QWs,  $m$ . Figure 3(c) shows the excitation-power density dependence of the time-integrated PL intensity, indicating that the time-integrated PL intensity did not saturate as observed for SQWs. The solid curve in Fig. 3(c) shows the fitted integrated PL intensity for the SQWs. Using this result, we determined the value of  $m$ . As shown in Fig. 3(d), the value of  $m$  increased to 2 at an excitation power density of 60 mW/cm<sup>2</sup>.

Based on the above evaluation, we determined the value of  $M$  by the Dicke theory.<sup>1</sup> An isotropic system is assumed,

and the position dependence of the QWs is neglected. The emission intensity of  $M$  coherently coupled two-level systems is given by

$$I(t) = 2\pi \sum_{m=0}^{M-1} (m+1)(M-m)G^2 n_{m+1,M}(t), \quad (1)$$

where  $G$  is the interaction coefficient and is obtained from  $G = \left(\frac{c^3}{8\pi^2 \omega_{ex}^2 \tau_{SQW}}\right)^{\frac{1}{2}}$ ,  $\tau_{SQW}$  is the average decay time of SQWs (Fig. 3(a)),  $n_{m,M}$  is the population of the  $m$  excited state in the  $M$  coherently coupled two-level systems, and  $\omega_{ex}$  is

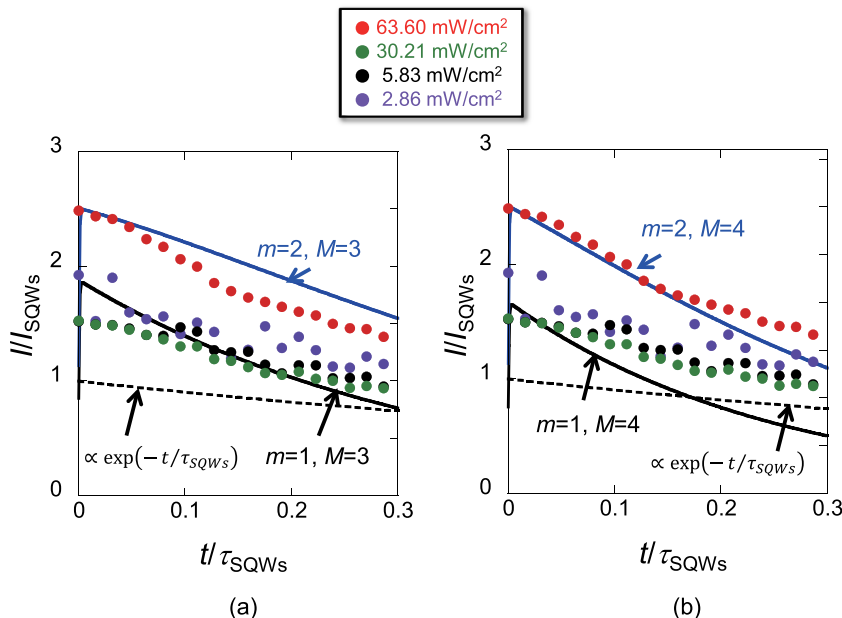


FIG. 4. Time-resolved PL intensity of numerical simulation (solid curves) and experimental results (solid circles) of MQWs. The PL intensity for MQWs was normalized by the PL intensity for SQWs,  $I_{SQWs}$ , which was obtained from fitting curve (solid black curve) for SQWs in Fig. 3(b). Calculated results for MQWs ( $I/I_{SQWs}$ ) for (a)  $M=3$  (solid black curve:  $m=1$ , solid blue curve:  $m=2$ ) and (b)  $M=4$  (solid black curve:  $m=1$ , solid blue curve:  $m=2$ ), respectively, using Eqs. (1) and (2).  $\tau_{SQWs} = 383$  ps. Dashed curves in (a) and (b) are proportional to  $\exp(-t/\tau_{SQWs})$ , corresponds to the results for SQWs.

resonant frequency of a two-level system. In this system, all QWs are approximated as two-level systems that interact with the photon field only. From Eq. (1), the emission intensity is determined by the population, which is determined by following hierarchical rate equation:

$$\begin{aligned} \frac{\partial}{\partial t} n_{m,M}(t) &= \frac{8\pi^2}{c^3} \omega_{ex}^2 (m+1)(M-m) G^2 n_{m+1,M}(t) \\ &\quad - \frac{8\pi^2}{c^3} \omega_{ex}^2 m(M-m+1) G^2 n_{m,M}(t). \end{aligned} \quad (2)$$

The solid curves in Figs. 4(a) and 4(b) show the calculated time evaluation of the PL intensity for  $M=3$  and 4, respectively, using Eqs. (1) and (2). In Figs. 4(a) and 4(b), the experimental PL intensity for MQWs was also plotted. Since the experimental excitation power density for MQWs and SQWs were different, the PL intensity for MQWs was normalized by the PL intensity for SQWs,  $I_{SQWs}$ , which was obtained from fitting curve (solid black curve) for SQWs in Fig. 3(b). From these results, it is reasonable to consider that the initial condition of  $m=2$  and  $M=4$  is comparable to the experimental results at the high-excitation power density of  $63.60 \text{ mW/cm}^2$ . The coherent exciton length in ZnO is estimated to be  $30 \text{ nm}$ ,<sup>17</sup> which is consistent with the length of QWs exhibiting coherently coupling with  $M=4$  ( $9 \times 3 + 3.25 \times 4 = 40 \text{ nm}$ ). From these results, it was concluded that the superradiance effect originated from the coherent coupling of the populations among the QWs. The slow decay component at  $t/\tau_{SQWs} > 0.2$  should originate from the decoherence, leading to the conclusion that the emission profile follows spontaneous emission, as described by  $\exp(-t/\tau_{SQWs})$ , at  $t/\tau_{SQWs} > 0.2$ .

In conclusion, we observed a superradiance from one-dimensionally aligned ZnO MQWs in nanorod. We evaluated the number of coherently coupled QWs, as achieved by the well-alignment of the QWs. For larger numbers of excitons with cooperative emission, a decrease in the separation of the QWs is required to avoid exciton decoherence. To reduce the separation, a higher Mg concentration in the barrier layers is required, so that the wave-functions of adjacent quantum wells do not overlap. This can be achieved using an Mg concentration of 50% with a band-gap offset ( $\Delta E_g$ ) of  $680 \text{ meV}$ .<sup>18</sup> Under these conditions, the separation between

QWs can be as small as  $1 \text{ nm}$  without a wave-function overlap. It is estimated that this would increase the number of cooperative radiation excitons  $m$  to 8 ( $1 \times 7 + 3.25 \times 8 = 33 \text{ nm}$ ). Because the emission intensity of the superradiance increases as  $N(N/2 + 1)/2$ , a 20-fold increase in intensity would be expected using MQWs. Nanoscale devices have low output efficiencies due to their small volume, so this type of cooperative radiation can play a significant role at nanoscale light sources without the use of an external cavity, greatly facilitating the miniaturisation process.<sup>19</sup>

T.Y. was financially supported by a grant from the Grant-in-Aid for Young Scientists (A) from MEXT, and by a research grant (Basic Research) from The TEPCO Memorial Foundation. G.-C.Y. and J.Y. were financially supported by the National Creative Research Initiative Project (R16-2004-004-01001-0) of the National Research Foundation of Korea (NRF).

<sup>1</sup>R. Dicke, *Phys. Rev.* **93**, 99 (1954).

<sup>2</sup>N. E. Rehler and J. H. Eberly, *Phys. Rev. A* **3**, 1735 (1971).

<sup>3</sup>R. Bonifacio, P. Schwendimann, and F. Haake, *Phys. Rev. A* **4**, 302 (1971).

<sup>4</sup>R. Bonifacio, P. Schwendimann, and F. Haake, *Phys. Rev. A* **4**, 854 (1971).

<sup>5</sup>R. Bonifacio and L. Lugiato, *Phys. Rev. A* **11**, 1507 (1975).

<sup>6</sup>R. Bonifacio and L. Lugiato, *Phys. Rev. A* **12**, 587 (1975).

<sup>7</sup>D. Polder, M. F. H. Schuurmans, and Q. H. F. Vrethen, *Phys. Rev. A* **19**, 1192 (1979).

<sup>8</sup>H. Gibbs, Q. Vrethen, and H. Hiksloops, *Phys. Rev. Lett.* **39**, 547 (1977).

<sup>9</sup>N. Skribanowitz, I. Herman, J. MacGillivray, and M. Feld, *Phys. Rev. Lett.* **30**, 309 (1973).

<sup>10</sup>K. Miyajima, Y. Kagotani, S. Saito, M. Ashida, and T. Itoh, *J. Phys. Condens. Matter* **21**, 195802 (2009).

<sup>11</sup>T. Itoh, M. Furumiya, T. Ikehara, and C. Gourdon, *Solid State Commun.* **73**, 271 (1990).

<sup>12</sup>H. Fidler, J. Knoester, and D. A. Wiersma, *Chem. Phys. Lett.* **171**, 529 (1990).

<sup>13</sup>M. Scheibner, T. Schmidt, L. Worschech, A. Forchel, G. Bacher, T. Passow, and D. Hommel, *Nature Phys.* **3**, 106–110 (2007).

<sup>14</sup>W. I. Park, G. C. Yi, M. Y. Kim, and S. J. Pennycook, *Adv. Mater.* **15**, 526 (2003).

<sup>15</sup>W. I. Park, S. J. An, J. L. Yang, G.-C. Yi, S. Hong, T. Joo, and M. Kim, *J. Phys. Chem. B* **108**, 15457 (2004).

<sup>16</sup>T. Yatsui, S. Sangu, T. Kawazoe, M. Ohtsu, S. J. An, J. Yoo, and G.-C. Yi, *Appl. Phys. Lett.* **90**, 223110 (2007).

<sup>17</sup>B. Gil and A. V. Kavokin, *Appl. Phys. Lett.* **81**, 748–750 (2002).

<sup>18</sup>W. I. Park, G. C. Yi, and H. M. Jang, *Appl. Phys. Lett.* **79**, 2022 (2001).

<sup>19</sup>A. Shojiguchi, K. Kobayashi, S. Sangu, K. Kitahara, and M. Ohtsu, *J. Phys. Soc. Jpn.* **72**, 2984 (2003).

## Si homojunction structured near-infrared laser based on a phonon-assisted process

T. Kawazoe · M. Ohtsu · K. Akahane · N. Yamamoto

Received: 18 April 2012 / Published online: 25 May 2012  
© The Author(s) 2012. This article is published with open access at Springerlink.com

**Abstract** We fabricated several near-infrared Si laser devices (wavelength  $\sim 1300$  nm) showing continuous-wave oscillation at room temperature by using a phonon-assisted process induced by dressed photons. Their optical resonators were formed of ridge waveguides with a width of  $10 \mu\text{m}$  and a thickness of  $2 \mu\text{m}$ , with two cleaved facets, and the resonator lengths were  $250\text{--}1000 \mu\text{m}$ . The oscillation threshold currents of these Si lasers were  $50\text{--}60$  mA. From near-field and far-field images of the optical radiation pattern, we observed the high directivity which is characteristic of a laser beam. Typical values of the threshold current density for laser oscillation, the ratio of powers in the TE polarization and TM polarization during oscillation, the optical output power at a current of  $60$  mA, and the external differential quantum efficiency were  $1.1\text{--}2.0$  kA/cm<sup>2</sup>,  $8:1$ ,  $50 \mu\text{W}$ , and  $1\%$ , respectively.

Because silicon (Si) is an indirect-transition-type semiconductor, it is difficult to use it as a material for optical devices

such as light-emitting diodes (LEDs) and lasers. Nevertheless, Si has been the subject of extensive research for use in fabricating lasers since it shows excellent compatibility with electronic devices [1]. For example, there are reports in the literature on Raman lasers [2] and lasers utilizing quantum size effects [3]; however, parameters such as the operating temperature, efficiency, wavelength and so forth are still not adequate for practical adoption of these devices. To solve these problems, in the research described here, we developed a Si laser showing continuous-wave operation at room temperature. To do so, we applied the same fabrication method and operating principle used for a Si-LED that we previously developed, which used a Si crystal having a p–n homojunction [4]. We report the results here.

Similar to the fabrication of Si LEDs that we have already reported, in this work, first we formed a p–n homojunction by introducing a p dopant into an n-type Si substrate by ion implantation. Then, while irradiating the structure with light, we applied an electrical current to generate Joule heating, causing annealing. Stimulated emission was produced via a two-step transition process driven by the light irradiation. This process is described below [4, 5].

- (i) First step: Dressed photons are generated by the light irradiation in regions where the dopant concentration in the p–n junction has a non-uniform spatial distribution. A dressed photon is a quasi-particle representing a coupled state due to the mutual interaction between a photon and an electron on the nanometer scale. The dressed photon then couples with a multi-mode phonon, generating stimulated emission that causes a conduction-band electron to transition from an initial state  $|E_{\text{ex}}; el\rangle \otimes |E_{\text{ex,thermal}}; phonon\rangle$  to an intermediate state  $|E_g; el\rangle \otimes |E_{\text{ex}}; phonon\rangle$ . Here,  $|E_{\text{ex}}; el\rangle$  and  $|E_g; el\rangle$  respectively represent the excited state (conduction band) and ground state (valence band) of the

---

T. Kawazoe (✉) · M. Ohtsu  
Department of Electrical Engineering and Information Systems,  
Graduate School of Engineering, The University of Tokyo,  
2-11-16 Yayoi, Bunkyo-ku, Tokyo 113-8656, Japan  
e-mail: kawazoe@ee.t.u-tokyo.ac.jp  
Fax: +81-3-58411140

T. Kawazoe · M. Ohtsu  
Nanophotonics Research Center, Graduate School  
of Engineering, The University of Tokyo, 2-11-16 Yayoi,  
Bunkyo-ku, Tokyo 113-8656, Japan

K. Akahane · N. Yamamoto  
National Institute of Information and Communications  
Technology, Koganei, Tokyo 184-8795, Japan

electron;  $|E_{\text{ex,thermal}}; \text{phonon}\rangle$  and  $|E_{\text{ex}}; \text{phonon}\rangle$  respectively represent the thermal equilibrium state and excited state of the phonon; and the symbol  $\otimes$  represents the direct product of the ket vectors. Because this transition is an electric-dipole-allowed transition, propagating light and a dressed photon are generated.

- (ii) Second step: A transition from the intermediate state  $|E_g; el\rangle \otimes |E_{\text{ex}}; \text{phonon}\rangle$  to the final state  $|E_g; el\rangle \otimes |E_{\text{ex}'}; \text{phonon}\rangle$  occurs, producing stimulated emission. Here,  $|E_{\text{ex}'}; \text{phonon}\rangle$  is the excited state of the phonon, but it differs from  $|E_{\text{ex}}; \text{phonon}\rangle$  in process (i) above. Because this is an electric-dipole-forbidden transition, only a dressed photon is generated. After this transition, the phonon relaxes to the thermal equilibrium state.

The two-step transition process described above, referred to as a phonon-assisted process, has already been applied to photochemical vapor deposition [6], photolithography [7], photoetching [8], optical frequency up-conversion [9], photovoltaic devices [10], and so on.

When the electron number densities in the initial state  $|E_{\text{ex}}; el\rangle \otimes |E_{\text{ex,thermal}}; \text{phonon}\rangle$  and the intermediate state  $|E_g; el\rangle \otimes |E_{\text{ex}}; \text{phonon}\rangle$ ,  $n_{\text{ex}}$  and  $n_{\text{inter}}$ , satisfy the Bernard–Duraffourg inversion condition ( $n_{\text{ex}} > n_{\text{inter}}$ ) [11], optical amplification gain occurs. In Si, which is an indirect-transition-type semiconductor, the spontaneous emission probability is low, and the probability of the first-step transition in process (i) occurring in the absence of externally incident light is low. However, if the fabricated devices have an optical cavity structure for confining the emission energy in the p–n junction, and if the optical amplification gain is larger than the cavity loss, there is a possibility of laser oscillation occurring as a result of spontaneous emission.

To examine this possibility, we fabricated Si lasers by the following method. We used an As-doped n-type Si crystal with an electrical resistivity of 10  $\Omega$  cm and a thickness of 625  $\mu\text{m}$  as a device substrate. This substrate was doped with boron (B) by ion implantation to form a p-type layer. The implantation energy for the B doping was 700 keV, and the ion dose density was  $5 \times 10^{13} \text{ cm}^{-2}$ . After forming a p–n homojunction, an indium tin oxide (ITO) film with a thickness of 150 nm was deposited on the p-layer side of the Si substrate, and an aluminum (Al) film with a thickness of 80 nm was deposited on the n-substrate side, both by RF sputtering, for use as electrodes. Next, the Si substrate was diced to form the device. The device area was about 400  $\text{mm}^2$ . Similarly to [4], the substrate was irradiated with laser light having a wavelength of 1320 nm and a power density of 200  $\text{mW}/\text{cm}^2$ , during which annealing was performed by applying a forward-bias current of 1.2 A to generate Joule heating, causing the B to disperse.

With this method, the spatial distribution of the B concentration changes, forming microdomain boundaries in a self-organized manner, which allows efficient generation of

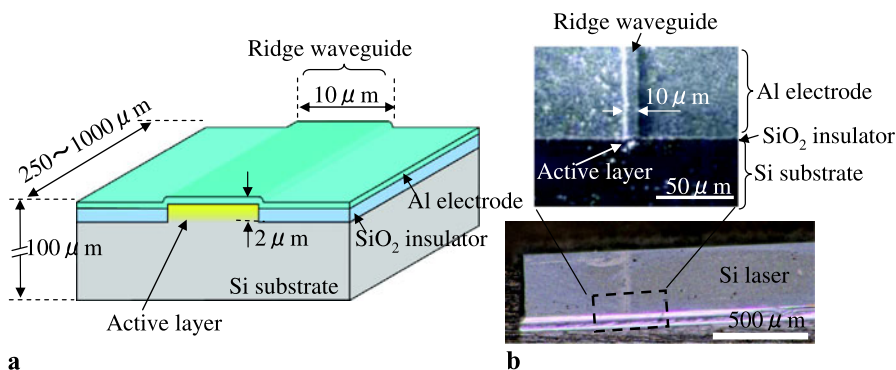
the phonon-assisted process. These domain boundaries have a shape and distribution suitable for efficiently inducing the phonon-assisted process described above during light emission [4, 5].

Next, to fabricate a Si laser, the ITO electrode and the Al electrode on the Si substrate were removed by etching. Then, the ridge waveguide structure was fabricated by using conventional photolithography. An  $\text{SiO}_2$  film, used as a mask in wet chemical etching of Si by KOH, was deposited by means of tetraethyl orthosilicate chemical vapor deposition (TEOS-CVD). After transferring the mask pattern, with a line width of 10  $\mu\text{m}$ , to the  $\text{SiO}_2$ , KOH etching was conducted to fabricate a ridge waveguide structure with a depth of 2  $\mu\text{m}$ . Then, an  $\text{SiO}_2$  film for isolating the Si wafer and the electrode was deposited by TEOS-CVD, and a contact window was formed on top of the ridge waveguide. After that, an Al electrode was deposited by DC sputtering. The substrate was then polished to a thickness of 100  $\mu\text{m}$ , and Al was deposited on the reverse side of the Si substrate. The sample was cleaved to various cavity lengths, and the cleaved facets served as mirrors. We fabricated several Si laser devices with the above method. Note that all of the experiments described below were conducted at room temperature (15–25  $^\circ\text{C}$ ).

Figure 1(a) illustrates the device structure. From secondary ion mass spectrometry (SIMS) measurements, we confirmed that the active layer formed in the p–n junction was located at a depth of 1.5–2.5  $\mu\text{m}$  from the surface of the Si substrate. This corresponds to the bottom of the ridge waveguide. Figure 1(b) shows optical micrographs of a fabricated Si laser. The width and thickness of the ridge waveguide constituting the resonator were 10  $\mu\text{m}$  and 2  $\mu\text{m}$ , respectively. We fabricated several Si lasers with resonator lengths of 250–1000  $\mu\text{m}$ . The guiding loss in the ridge waveguide and the optical scattering loss at the cleaved facets were estimated to be about 70 % for the TE-polarization component. Because this ridge waveguide does not exhibit optical confinement in the thickness direction, the guiding loss is large; it can be estimated to be 90 % or more. However, because an active layer that efficiently generates dressed photons is formed in the p–n junction by the phonon-assisted annealing process, the effective refractive index of the active layer is higher than the refractive index of the surrounding area. Therefore, the actual guiding loss is smaller than the above value. We measured the current density dependency of the optical amplification gain resulting from irradiating the Si laser with 1320 nm-wavelength laser light and obtained a transparent current density of  $J_{\text{tr}} = 26.3 \text{ A}/\text{cm}^2$ . This value is about 1/10 of that for a conventional laser device made using a direct-transition-type semiconductor [12], demonstrating the possibility that this ridge waveguide with the p–n homojunction structure has adequate performance for use as a laser.

Of the several Si lasers that we fabricated, the current–voltage characteristic for the laser with a resonator length

**Fig. 1** (a) Schematic diagram for explaining structure of fabricated Si lasers. (b) Optical micrographs



of 750  $\mu\text{m}$  is shown in Fig. 2(a). The red squares and the blue circles are the results of measurements obtained while increasing the current and decreasing the current, as shown by the red and blue arrows, respectively. In both cases, the voltage value showed a large change at a current value of 50 mA, which corresponds to the threshold current for laser oscillation. This can be explained using the optical radiation pattern of the Si laser. Far-field images of the optical radiation pattern are shown next to numerals ① to ⑤ in Fig. 2(a). A near-field image is also shown next to numeral ③. There is a ridge waveguide with a width of 10  $\mu\text{m}$  at the center of the circle indicated with the white dotted line in this near-field image. At an injection current of 50 mA and above, the optical radiation pattern was concentrated inside the ridge waveguide, and the optical power was increased. This concentration indicates that the directivity of the optical radiation pattern was high due to the laser oscillation. At an injection current below 50 mA, on the other hand, the directivity was low; this is because the main components of the optical radiation pattern are spontaneous emission and amplified spontaneous emission (ASE).

The left side of Fig. 2(b) shows near-field images for the TM- and TE-polarization components forming the optical radiation pattern at ③ in Fig. 2(a). The right side of Fig. 2(b) shows the cross-sectional light intensity profiles taken along the white dotted lines in these near-field images. From these figures, the TM-polarization component from the Si laser was spread over the entire device, whereas the TE-polarization component was concentrated at the location of the ridge waveguide. Because the output beam from a conventional semiconductor laser during oscillation contains the TE-polarization [13], this measurement result also confirms that laser oscillation occurred. In this measurement, the intensity ratio of the TE-polarization and the TM-polarization was 8:1. On the other hand, in a usual semiconductor laser, the intensity ratio of the two polarizations is 100:1 or greater [13]. The reason for the difference between our result and this value is that there is no optical confinement structure in the thickness direction of the ridge waveguide, and also because the spectral wavelength bands of the spontaneous emission and ASE are extremely wide.

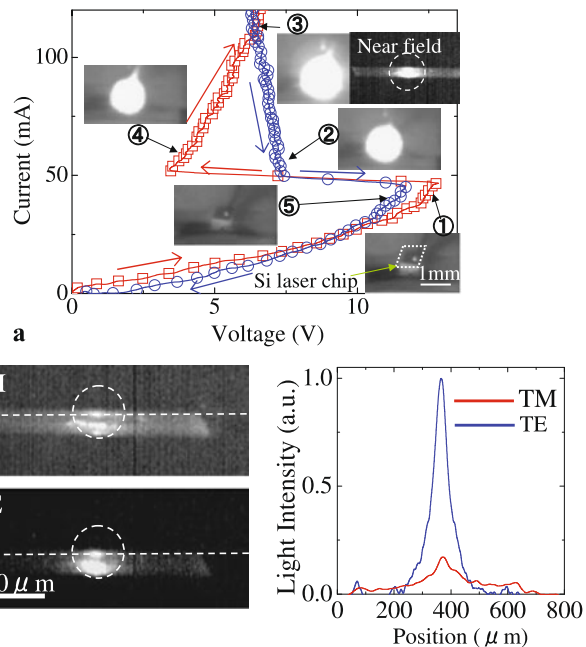


**Fig. 2** Images of optical radiation pattern from Si laser (resonator length 750  $\mu\text{m}$ ). (a) Current–voltage characteristic of Si laser. *Red squares* and *blue circles* are results measured while increasing and decreasing the current, as shown by the *red* and *blue* arrows, respectively. Far-field images of the output optical radiation pattern are shown beside numerals ① to ⑤. A near-field image is also shown beside numeral ③. The *circle* indicated with the white dotted white line shows the ridge waveguide structure. (b) The left-hand side shows near-field images of the TM-polarization and TE-polarization in the output light from the Si laser. These correspond to ③ in (a). The *circle* indicated with the white dotted white line shows the ridge waveguide structure. The right-hand side shows the cross-sectional light intensity profiles taken along the white dotted lines in the near-field images at the left

Figure 3(a) shows the output light spectral characteristics of the Si laser. In these measurements, in order to separately observe each longitudinal mode, we used a device having a shorter resonator (resonator length 250  $\mu\text{m}$ ) than that in Fig. 2. A sharp peak showing laser oscillation at an injection current of 60 mA was observed at 1356 nm (the position indicated by the upward-pointing arrow in the figure); however, the tip of the peak went off the top edge of the graph

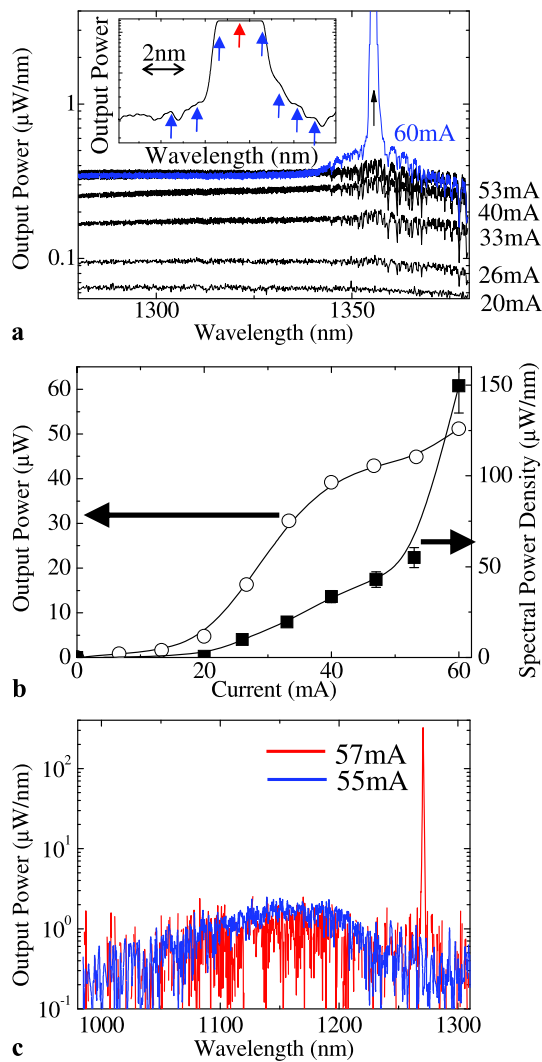


**Fig. 3** Spectral characteristics of output light from Si laser. (a) Current dependency of output light spectrum (resonator length = 250  $\mu\text{m}$ ). The inset shows an enlarged view in the vicinity of the peak in the oscillation spectrum during laser oscillation (current = 60 mA). The upward-pointing arrows show the positions of the longitudinal modes. (b) Current dependency of output optical power. The white circles are values obtained by integrating the optical power with respect to wavelength, in the wavelength range 1220–1380 nm. The black squares are values of the spectral power density at a wavelength of 1356 nm. (c) Output light spectra from Si laser (resonator length 500  $\mu\text{m}$ ) above the oscillation threshold (current 57 mA) and below the oscillation threshold (55 mA)

due to saturation of the photo-receiver sensitivity of the measurement equipment. The inset shows a magnified view of the vicinity of the oscillation spectral peak during laser oscillation, where several longitudinal modes (positions indicated by the upward-pointing arrows in the inset) were observed at a wavelength spacing of 1.0 nm, corresponding to the resonator length (250  $\mu\text{m}$ ). Figure 3(b) shows the current dependency of the output light power. The white circles are values obtained by integrating the optical power with re-

spect to wavelength in the wavelength range 1220–1380 nm. At an injection current of 60 mA, the optical output power was 50  $\mu\text{W}$ , and the external differential quantum efficiency was 1 %. This value is as high as that reported for a 1.3  $\mu\text{m}$ -wavelength double heterojunction laser using InGaAsP/InP, which is a direct-transition-type semiconductor [14]. The black squares are values of the spectral power density at a wavelength of 1356 nm. At the injection current of 60 mA, the spectral power density was 150  $\mu\text{W}/\text{nm}$ . Because this device had a wide emission wavelength band, as the current increases, the optical power of the spontaneous emission and ASE also increase; therefore, the measurement results indicated by the white circles do not show a sudden increase in the optical output power due to laser oscillation. The black squares, on the other hand, do show this, and the threshold current for laser oscillation was found to be 50 mA, giving a threshold current density of 2.0  $\text{kA}/\text{cm}^2$ .

To measure the optical power and spectral linewidth at the peak wavelength in the laser oscillation spectrum, we measured the output spectrum during laser oscillation (current = 57 mA) using a different Si laser (resonator length = 500  $\mu\text{m}$ ) from that used in Figs. 3(a) and 3(b). The results are shown in Fig. 3(c). The vertical axis of this graph is a logarithmic scale. At an injection current of 55 mA or less, only a wide emission spectrum was measured; however, above the threshold current (about 56 mA), a sharp laser oscillation spectrum was observed, with a center wavelength of 1271 nm. The full width at half maximum (FWHM) was the wavelength resolution (0.9 nm) or less. In addition, from these measurement results, we confirmed that the threshold current density for laser oscillation was 1.1  $\text{kA}/\text{cm}^2$ .

In summary, we fabricated several near-infrared Si lasers (1300 nm wavelength band) showing continuous-wave oscillation at room temperature. For the fabrication and operation of these Si lasers, we used a phonon-assisted process induced by dressed photons. The optical resonators of these lasers were formed of a 10  $\mu\text{m}$ -wide, 2  $\mu\text{m}$ -thick ridge waveguide with two cleaved facets, and the resonator lengths were 250–1000  $\mu\text{m}$ . The oscillation threshold currents of these Si lasers were 50–60 mA. From near-field and far-field images of the optical radiation patterns, we observed the high directivity which is characteristic of a laser beam. Typical values of the threshold current density for laser oscillation, the ratio of powers of the TE-polarization and the TM-polarization during oscillation, the optical output power for a current of 60 mA, and the external quantum efficiency were 1.1–2.0  $\text{kA}/\text{cm}^2$ , 8:1, 50  $\mu\text{W}$ , and 1 %, respectively.

**Open Access** This article is distributed under the terms of the Creative Commons Attribution License which permits any use, distribution, and reproduction in any medium, provided the original author(s) and the source are credited.

## References

1. D. Liang, J.E. Bowers, *Nat. Photonics* **4**, 511 (2010)
2. H. Rong, R. Jones, A. Liu, O. Cohen, D. Hak, A. Fang, M. Paniccia, *Nature* **433**, 725 (2005)
3. S. Saito, Y. Suwa, H. Arimoto, N. Sakuma, D. Hisamoto, H. Uchiyama, J. Yamamoto, T. Sakamizu, T. Mine, S. Kimura, T. Sugawara, M. Aoki, *Appl. Phys. Lett.* **95**, 241101 (2009)
4. T. Kawazoe, M.A. Mueed, M. Ohtsu, *Appl. Phys. B* **104**, 747 (2011)
5. K. Kitamura, T. Kawazoe, M. Ohtsu, *Appl. Phys. B* (2012). doi:[10.1007/s00340-012-4991-z](https://doi.org/10.1007/s00340-012-4991-z)
6. T. Kawazoe, K. Kobayashi, S. Takubo, M. Ohtsu, *J. Chem. Phys.* **122**, 024715 (2005)
7. T. Kawazoe, M. Ohtsu, Y. Inao, R. Kuroda, *J. Nanophotonics* **1**, 011595 (2007)
8. T. Yatsui, K. Hirata, W. Nomura, Y. Tabata, M. Ohtsu, *Appl. Phys. B* **93**, 55 (2008)
9. T. Kawazoe, H. Fujiwara, K. Kobayashi, M. Ohtsu, *IEEE J. Sel. Top. Quantum Electron.* **15**, 1380 (2009)
10. S. Yukutake, T. Kawazoe, T. Yatsui, W. Nomura, K. Kitamura, M. Ohtsu, *Appl. Phys. B* **99**, 415 (2010)
11. M.G.A. Bernard, G. Duraffourg, *Phys. Status Solidi* **1**, 699 (1961)
12. W.J. Choi, P.D. Dapkus, J.J. Jewell, *IEEE Photonics Technol. Lett.* **11**, 1572 (1999)
13. T. Tanbun-Ek, N.A. Olsson, R.A. Logan, K.W. Wecht, A.M. Sergent, *IEEE Photonics Technol. Lett.* **3**, 103 (1991)
14. Zh.I. Alferov, *Semiconductors* **32**, 1 (1998)



## Energy dissipation in energy transfer mediated by optical near-field interactions and their interfaces with optical far-fields

Makoto Naruse, Petter Holmström, Tadashi Kawazoe, Kouichi Akahane, Naokatsu Yamamoto et al.

Citation: *Appl. Phys. Lett.* **100**, 241102 (2012); doi: 10.1063/1.4729003

View online: <http://dx.doi.org/10.1063/1.4729003>

View Table of Contents: <http://apl.aip.org/resource/1/APPLAB/v100/i24>

Published by the [American Institute of Physics](http://www.aip.org).

---

### Related Articles

Optical switch based on electrowetting liquid lens

*J. Appl. Phys.* **111**, 103103 (2012)

Thermo-optic switch based on transmission-dip shifting in a double-slot photonic crystal waveguide

*Appl. Phys. Lett.* **100**, 201102 (2012)

Complementary cellophane optic gate and its use for a 3D iPad without glasses

*Rev. Sci. Instrum.* **83**, 043710 (2012)

A nanomachined optical logic gate driven by gradient optical force

*Appl. Phys. Lett.* **100**, 113104 (2012)

Thermo-optic plasmo-photonic mode interference switches based on dielectric loaded waveguides

*Appl. Phys. Lett.* **99**, 241110 (2011)

---

### Additional information on *Appl. Phys. Lett.*

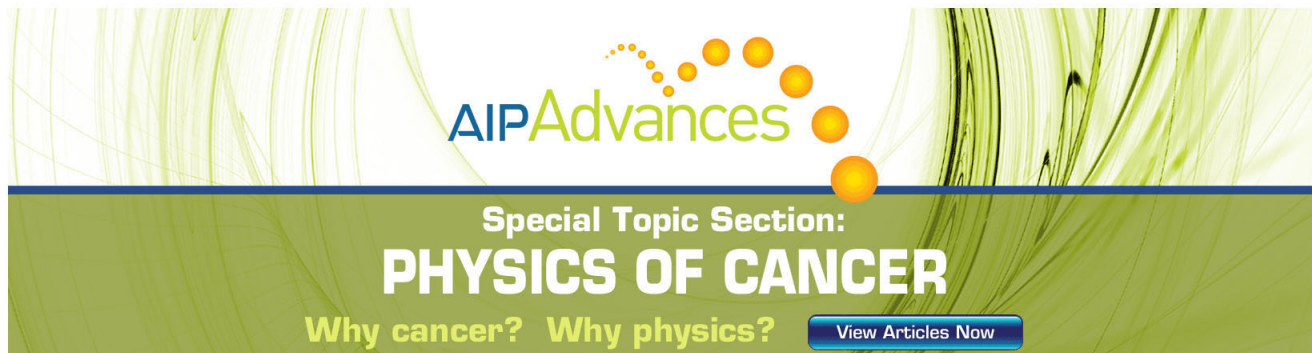
Journal Homepage: <http://apl.aip.org/>

Journal Information: [http://apl.aip.org/about/about\\_the\\_journal](http://apl.aip.org/about/about_the_journal)

Top downloads: [http://apl.aip.org/features/most\\_downloaded](http://apl.aip.org/features/most_downloaded)

Information for Authors: <http://apl.aip.org/authors>

## ADVERTISEMENT

The advertisement features a green and white background with a pattern of thin, vertical lines. At the top, the text 'AIP Advances' is written in a green, sans-serif font. To the right of this text is a decorative graphic consisting of several orange and yellow circles of varying sizes, arranged in a curved path. Below the main text, the words 'Special Topic Section:' are written in a smaller, white font. Underneath that, the words 'PHYSICS OF CANCER' are written in a large, bold, white font. At the bottom left, the phrase 'Why cancer? Why physics?' is written in a green font. At the bottom right, there is a blue button with the text 'View Articles Now' in white.

## Energy dissipation in energy transfer mediated by optical near-field interactions and their interfaces with optical far-fields

Makoto Naruse,<sup>1,2,a)</sup> Petter Holmström,<sup>3</sup> Tadashi Kawazoe,<sup>2,4</sup> Kouichi Akahane,<sup>1</sup>  
Naokatsu Yamamoto,<sup>1</sup> Lars Thylén,<sup>3,5</sup> and Motoichi Ohtsu<sup>2,4</sup>

<sup>1</sup>Photonic Network Research Institute, National Institute of Information and Communications Technology, 4-2-1 Nukui-kita, Koganei, Tokyo 184-8795, Japan

<sup>2</sup>Nanophotonics Research Center, Graduate School of Engineering, The University of Tokyo, 2-11-16 Yayoi, Bunkyo-ku, Tokyo 113-8656, Japan

<sup>3</sup>Laboratory of Photonics and Microwave Engineering, Royal Institute of Technology (KTH), SE-164 40 Kista, Sweden

<sup>4</sup>Department of Electrical Engineering and Information Systems, Graduate School of Engineering, The University of Tokyo, 2-11-16 Yayoi, Bunkyo-ku, Tokyo 113-8656, Japan

<sup>5</sup>Hewlett-Packard Laboratories, Palo Alto, California 94304, USA

(Received 6 April 2012; accepted 22 May 2012; published online 11 June 2012)

We theoretically and experimentally evaluated energy dissipation of nanophotonic devices based on energy transfer via near-field interactions and their interfaces with optical far-fields. The lower bound is about  $10^4$  times more energy-efficient than electronic devices. We also examined some fundamental differences between near-field-mediated optical energy transfer logic and electrical logic in terms of energy dissipation. © 2012 American Institute of Physics. [<http://dx.doi.org/10.1063/1.4729003>]

Energy efficiency is one of the most important aspects of today's optical technologies.<sup>1-4</sup> Energy efficiency of optical processes has been highlighted in the context of exploiting the low-loss, wavelength-multiplexed, high-bandwidth nature of optical communications.<sup>4</sup> Another feature of photons for efficient energy usage is their unique attributes exhibited on the nanometer scale, namely, energy transfer mediated by optical near-field interactions between quantum nanostructures.<sup>1</sup> Nanophotonic devices based on optical near-field interactions have been experimentally demonstrated at room temperature based on stacked quantum dots (QDs).<sup>5</sup> Previously, we have theoretically analyzed the lower bound of energy dissipation required for elemental optical excitation transfer from a smaller QD to a larger one by analyzing the energy dissipation occurring at the destination quantum dot.<sup>1</sup> The purpose of the study described in this letter is to analyze the energy dissipation in energy transfer via optical near-field interactions as a total system, including the energy dissipation of the input and output interfaces with optical far-fields, while considering the number of photons required for photodetection. The lower bound of total energy dissipation was estimated to be 138 eV theoretically and 155 eV experimentally, which are both about  $10^4$  times more energy-efficient than electrically wired devices, as discussed below. The tradeoff between device redundancy and operating speed is also evaluated. We also examined some fundamental differences between near-field-mediated optical energy transfer logic and electrical logic in terms of energy dissipation.

Optical energy transfer occurs from a smaller quantum dot, denoted by  $QD_S$  in Fig. 1(a), to a larger one ( $QD_L$ ) via optical near-field interactions in the resonant energy sublevels.<sup>1,6</sup> The energy dissipation occurring in the larger dot, namely, relaxation from  $L_2$  to  $L_1$  in Fig. 1(a), allows uni-directional

signal flow from  $QD_S$  to  $QD_L$ . Such energy transfer enables versatile functionality, such as nanophotonic logic gates<sup>5</sup> or energy concentration.<sup>6,7</sup> When we operate these nanophotonic devices, input and output interfaces are needed in practice. Figure 1(b) schematically represents a system model considered in this letter, composed of (i) an input interface converting an optical far-field to an optical near-field, (ii) a nanophotonic logic device (e.g., a NOT gate), and (iii) an output interface converting the optical near-field to the optical far-field, followed by a photodetector.

The input interface can be realized by multiple combinations of energy transfer, called an optical nanofountain<sup>7</sup> or cascaded energy transfer (CET),<sup>6</sup> as schematically shown in the left hand side of Fig. 1(b). The conversion efficiency from the input optical energy to the largest QD in the system is known to be high, similarly to a light harvesting antenna.<sup>8</sup> The energy dissipation associated with such input interfaces involves inter-sublevel relaxations occurring in the larger QD. Here  $\eta_{in}$  denotes the transmission efficiency at the input interface, that is, the efficiency of the conversion from the optical far-field to the optical near-field at the input. The input signal is then transferred to a nanophotonic logic gate (e.g., NOT gate), which consists of one smaller and one larger QD, as shown in the middle of Fig. 1(b). The output optical near-field is scattered by a metal nanoparticle located in the vicinity of the quantum dot, is converted to an optical far-field, and is captured by a photodetector, as depicted in the right hand side of Fig. 1(b). Here, the output conversion efficiency from the optical near-field to the optical far-field is denoted by  $\eta_{out}$ , which is analyzed in detail later below. Also, we need to take into account the number of photons per time slot arriving at the photodetector, denoted by  $n_p$ , which should yield sufficiently low error rate in the photodetection. The operating speed of the total system depends on the architecture of the system, as discussed at the end of this letter.

<sup>a)</sup>Electronic mail: naruse@nict.go.jp.

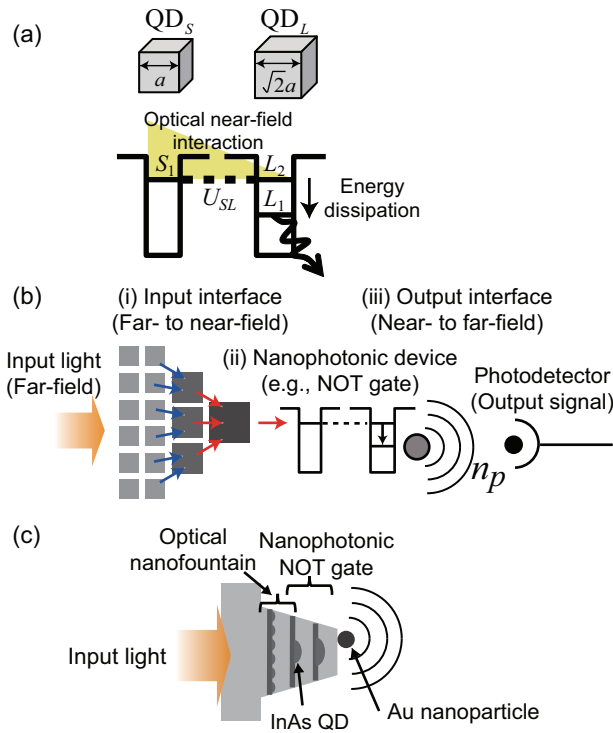


FIG. 1. (a) Energy transfer from a smaller QD to a larger one via optical near-field interactions. (b) Total system model of nanophotonic device including input and output interfaces. (c) The design of an experimental nanophotonic device shown in (b) based on stacked QDs.

We evaluate each of the parameters based on theoretical and experimental data. The architecture discussed in Fig. 1(b) will be experimentally fabricated as shown in Fig. 1(c), which is based on the technology of stacked quantum dots in which energy transfer occurs from smaller QDs to larger ones.<sup>5</sup>

**[Input interface]** The energy dissipation associated with the input interface is given by  $\eta_{in} = 1 - \varepsilon_d$ , where  $\varepsilon_d$  is the overall inter-sublevel relaxation occurring in the optical excitation transfer via optical near-field interactions. As discussed above, the transfer efficiency is high, similarly to light harvesting antennae in nature. Here, we assume that  $\varepsilon_d < 0.1$ , meaning that  $\eta_{in}$  is greater than 0.9.

**[Logic gate]** The energy dissipation associated with the logic gate based on energy transfer via the near-field interaction is the inter-sublevel energy dissipation, whose lower bound is theoretically derived to be  $E_{d(th)} = 25 \mu\text{eV}$  (Ref. 1) and experimentally estimated to be  $E_{d(exp)} = 65 \text{meV}$  in the case of a nanophotonic NOT gate based on two layers of InAs QDs.<sup>5</sup>

**[Output interface]** The efficiency of the output interface is estimated based on experimental data in two layers of InAs QDs working as a NOT gate.<sup>5</sup> It is evaluated by the following three steps. In the two layers of QDs, the size of the QDs in the first layer is smaller than those in the second layer, which is achieved by optimizing the parameters in the molecular beam epitaxy (MBE) process used to fabricate them.<sup>5</sup> First, consider the system shown in Fig. 2(a), where InAs QDs are encapsulated in GaAs barrier layers. Let the radiation from the output QD ( $QD_L$ ) in this setup be given by  $P_{emit}$ . Due to Fresnel refraction, the ratio of the optical power extracted from the QD,  $P_{extract}$ , is given by  $P_{extract}/P_{emit} = [(n_G - 1)/(n_G + 1)]^2$ ,

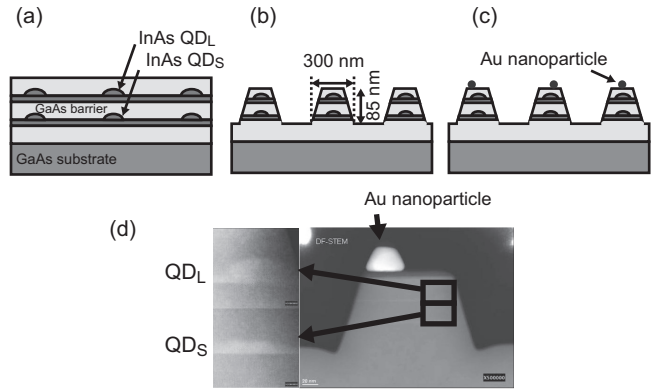


FIG. 2. (a)–(d) Experimental device structures based on two-layer, different-sized stacked InAs QDs.

where  $n_G$  is the refractive index of GaAs. Second, as shown in Fig. 2(b), the device is fabricated in a mesa structure. We experimentally evaluated that the optical power from the mesa device,  $P_{mesa}$ , is half of that in the system shown in Fig. 2(a); that is,  $P_{mesa}/P_{extract} = 0.5$ . Third, by placing a metal nanoparticle on top of the mesa structure (Fig. 2(c)), whose emitted optical power is denoted by  $P_m$ , we can expect enhanced light scattering compared with the system shown in Fig. 2(b). Figure 2(d) shows a cross-sectional image of the system shown in Fig. 2(d) taken by a scanning transmission electron microscope.<sup>5</sup> The interactions between semiconductor QDs and metal nanostructures have been studied in depth,<sup>9–13</sup> but they have still not been clearly understood, particularly regarding the upper bound of the enhancement; for instance, a more than fivefold increase, as well as quenching in certain conditions, has been observed in CdSe/ZnS nanocrystals on metal surfaces by various groups,<sup>10–12</sup> while modest increases have been reported in InGaAs QD/metal composites.<sup>13</sup> In Ref. 5, thanks to the placement of an Au nanoparticle, the enhancement factor was experimentally estimated at 3. Based on this experimental value, which we also consider modest, in this letter we assume  $P_m/P_{mesa} = 3.0$ . Summing up, the output interface efficiency is given by

$$\eta_{out} = P_m/P_{emit} = (P_m/P_{mesa}) \times (P_{mesa}/P_{extract}) \times (P_{extract}/P_{emit}), \quad (1)$$

which yields 0.45 based on the numerical values evaluated in the three steps discussed above.

We assume that 100 photons ( $n_p = 100$ ) are required in order to obtain an error rate of  $10^{-9}$ , assuming that an optical preamplifier is employed,<sup>14</sup> which we consider one realistic operation. Thus, the energy required for the detector, denoted by  $E_{det}$ , is given by  $E_{det} = n_p h\nu$ , where  $\nu$  is the optical frequency of the output beam and  $h$  is Planck's constant. Taking into account the efficiencies at the input, internal, and output stages, the required optical input energy,  $E_{in}$ , is given by  $E_{in} = n_p(h\nu + E_d)/(\eta_{in}\eta_{out})$ , which was estimated to be 235 eV (theoretical) and 251 eV (experimental, wavelength 1.3  $\mu\text{m}$ ). Therefore, the total energy dissipation in the system is given by  $E_{d,total} = E_{in} - E_{det}$ , which is 140 eV (22.4 aJ) (theoretical) and 156 eV (25 aJ) (experimental). Figure 3(a)

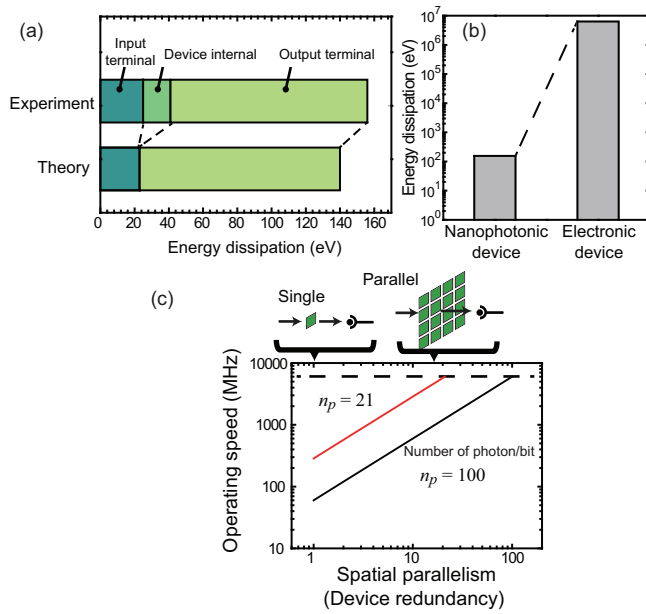


FIG. 3. (a) Energy dissipation breakdown. (b) Comparison of energy dissipation. (c) Evaluation of possible operating speed of the system based on the spatial parallelism of the internal logic gates, or device redundancy, and the number of photons/bit.

represents the breakdown of energy dissipation. We can find that the energy dissipation is dominated by the output interface, whereas that for the input interface, which is given by  $\epsilon_d E_{in}$ , is small, and that for energy transfer, given by  $n_p E_d / \eta_{in} \eta_{out}$ , is nearly negligible. This indicates that developing an improved output interface would significantly improve the energy efficiency. The energy dissipation of electronic wired devices, including interfacing, is estimated to be 6.3 MeV,<sup>15</sup> indicating that the energy dissipation of nanophotonic devices is about  $10^4$  times more energy-efficient than their electrical counterparts (Fig. 3(b)).

The operating speed of the total system depends on the architecture of the device. First, suppose that there is one logic gate in the system, as shown in Fig. 1(b) and at the upper left in Fig. 3(c). Since the energy transfer time from the smaller dot to the large one is estimated to be  $\tau = 50$  ps,<sup>5</sup> the minimum duration of the time slot required to determine a single bit, requiring 100 photons ( $n_p = 100$ ), i.e.,  $n_p / \eta_{out}$  excitons passing the device, is given by  $n_p \tau / \eta_{out}$ , which is about 17 ns, corresponding to a total system operating frequency of about 60 MHz. However, when we assume multiple identical devices operating in parallel or device redundancy, as schematically shown at the upper right in Fig. 3(c), the minimum duration for a single information bit could be shortened, enabling a higher operating speed. The tradeoff between such device redundancy and operating speed was also evaluated when  $n_p = 21$ , which is the quantum limit of detection yielding an error rate of  $10^{-9}$ ,<sup>14</sup> providing higher operating speed with the same parallelism compared with  $n_p = 100$ .

Finally, we make a few additional remarks. First, assuming electrical circuits with 30 nm feature size gives subpicosecond gate time and a dissipated switching energy of  $\sim 50$  aJ.<sup>16</sup> The comparison above considers energy dissipation including interfacing,<sup>15</sup> which leads to  $10^4$  times higher

energy efficiency with optical energy transfer. Superficially, however, the 50 aJ switching energy in electronics and the total energy dissipation for optical energy transfer in logic gates are comparable.

Second, when we consider multiple-input devices based on optical energy transfer, for instance, NOT gates or AND gates as in Ref. 5, we make use of energy resonance or off-resonance between quantum dots or state filling effects induced at larger quantum dots. It should be noted that the near-field-mediated optical energy transfer logic demonstrated in Ref. 5 and references therein is quite different in concept from other attempts in the field.<sup>17</sup> In particular, it should be noted that additional input light, denoted by  $E_a$ , is needed for inducing energy-resonance in implementing a NOT gate, for example, leading to additional input energy, but this does not result in negligible energy dissipation ( $\epsilon_d \times E_a$ ) or heat generation within the device; namely, almost all of the energy is dissipated from the device under study as photon radiation. This is another unique mechanism inherent in logic based on optical energy transfer, in contrast to electronic devices, where the energy contributes to heat generation, which is the most severe issue in state-of-the-art electronics.

One final remark is that system architectures and applications based on optical energy transfer could be very different from those based solely on silicon electronics. For example, the parallel and autonomous features of optical energy transfer<sup>18</sup> and optical interfaces with the real-world, including light energy inputs (wireless connections to power supplies) and sensors, would provide unique architectures and applications<sup>19–21</sup> for nanophotonic devices and systems.

In summary, we theoretically and experimentally analyzed the energy dissipation in energy transfer mediated by optical near-field interactions and their interfaces with optical far-fields. Our findings provide insights that will aid in the further development of nanophotonic devices and systems.

This work was supported in part by the Japan–Sweden Bilateral Joint Project supported by the Japan Society for the Promotion of Science (JSPS) and the Swedish Agency for Innovation Systems (VINNOVA). This work was also supported in part by the Strategic Information and Communications R&D Promotion Programme (SCOPE) of the Ministry of Internal Affairs and Communications, and Grants-in-Aid for Scientific Research from the Japan Society for the Promotion of Science.

<sup>1</sup>M. Naruse, H. Hori, K. Kobayashi, P. Holmström, L. Thylén, and M. Ohtsu, *Opt. Express* **18**, A544 (2010).

<sup>2</sup>D. C. Kilper, D. Neilson, D. Stiliadis, D. Suvakovic, and S. Goyal, in Proceedings of 36th European Conference and Exhibition on Optical Communication (ECOC), 19–23 September 2010, Torino, Italy, pp. 437–442.

<sup>3</sup>D. A. B. Miller, *Proc. IEEE* **97**, 1166 (2009).

<sup>4</sup>R. S. Tucker, R. Parthiban, J. Baliga, K. Hinton, R. W. A. Ayre, and W. V. Sorin, *J. Lightwave Technol.* **27**, 243–252 (2009).

<sup>5</sup>T. Kawazoe, M. Ohtsu, S. Aso, Y. Sawado, Y. Hosoda, K. Yoshizawa, K. Akahane, N. Yamamoto, and M. Naruse, *Appl. Phys. B* **103**, 537 (2011).

<sup>6</sup>T. Franzl, T. A. Klar, S. Schietinger, A. L. Rogach, and J. Feldmann, *Nano Lett.* **4**, 1599 (2004).

<sup>7</sup>T. Kawazoe, K. Kobayashi, and M. Ohtsu, *Appl. Phys. Lett.* **86**, 103102 (2005).

<sup>8</sup>H. Imahori, *J. Phys. Chem. B* **108**, 6130 (2004).

<sup>9</sup>G. Sun and J. B. Khurgin, *IEEE J. Sel. Top. Quantum Electron.* **17**, 110 (2011).

- <sup>10</sup>O. Kulakovich, N. Strekal, A. Yaroshevich, S. Maskevich, S. Gaponenko, I. Nabiev, U. Woggon, and M. Artemyev, *Nano Lett.* **2**, 1449 (2002).
- <sup>11</sup>K. T. Shimizu, W. K. Woo, B. R. Fisher, H. J. Eisler, and M. G. Bawendi, *Phys. Rev. Lett.* **89**, 117401 (2002).
- <sup>12</sup>K. Matsuda, Y. Ito, and Y. Kanemitsu, *Appl. Phys. Lett.* **92**, 211911 (2008).
- <sup>13</sup>A. Urbańczyk, G. J. Hamhuis, and R. Nötzel, *Nanoscale Res. Lett.* **5**, 1926–1929 (2010).
- <sup>14</sup>Y. Yamamoto, *Lecture notes on “Fundamentals of noise processes.”* See <http://www.qis.ex.nii.ac.jp/qis/lecturenotes.html>.
- <sup>15</sup>F. Moll, M. Roca, and E. Isern, *Microelectronics J.* **34**, 833 (2003).
- <sup>16</sup>M. T. Bohr, *IEEE Trans. Nanotechnol.* **1**, 56 (2002).
- <sup>17</sup>D. A. B. Miller, *Nat. Photonics* **4**, 3 (2010).
- <sup>18</sup>M. Naruse, K. Leibnitz, F. Peper, N. Tate, W. Nomura, T. Kawazoe, M. Murata, and M. Ohtsu, *Nano Commun. Networks* **2**, 189 (2011).
- <sup>19</sup>C. Pistol, C. Dwyer, and A. R. Lebeck, *IEEE Micro* **28**, 7–18 (2008).
- <sup>20</sup>M. Naruse, T. Miyazaki, T. Kawazoe, S. Sangu, K. Kobayashi, F. Kubota, and M. Ohtsu, *IEICE Trans. Electron.* **E88-C**, 1817 (2005).
- <sup>21</sup>M. Naruse, F. Peper, K. Akahane, N. Yamamoto, T. Kawazoe, N. Tate, and M. Ohtsu, *ACM J. Emerging Technol. Comput. Syst.* **8**, 4 (2012).

# Homojunction-structured ZnO light-emitting diodes fabricated by dressed-photon assisted annealing

K. Kitamura · T. Kawazoe · M. Ohtsu

Received: 9 March 2012 / Published online: 5 April 2012  
© The Author(s) 2012. This article is published with open access at Springerlink.com

**Abstract** We formed a p–n homojunction by implanting nitrogen ions, serving as a p-type dopant, into an n-type ZnO crystal. A forward bias current was injected into the crystal while irradiating it with light, bringing about Joule heating which annealed the crystal and changed the spatial distribution of the N-dopant concentration. This activated the N-dopant, causing its concentration distribution to be modified in a self-organized manner so as to be suitable for generating dressed photons. A light-emitting diode fabricated by this dressed-photon assisted annealing method showed electroluminescence at room temperature. In a device fabricated by annealing under irradiation with 407 nm-wavelength light, at a forward bias current of 20 mA, the peak wavelength of the electroluminescence was 436 nm, the optical output power was 6.2  $\mu$ W, and the external quantum efficiency was  $1.1 \times 10^{-4}$ . The emission spectral profile depended on transitions from intermediate phonon states.

## 1 Introduction

ZnO is a direct-transition, wide bandgap semiconductor and is expected to be used as a material for fabricating optical devices such as UV light-emitting diodes and laser diodes [1].

In general, using a semiconductor that can form p–n junctions allows straightforward fabrication of light-emitting diodes and laser diodes [2–5]; however, this is difficult in the case of ZnO. The reason why is that it is difficult to form a p-type crystal because the acceptors are compensated due to the numerous oxygen vacancies and interstitial zinc in the ZnO crystal acting as donors [6]. Therefore, despite the numerous efforts that have been made [7–13], until now there have been very few reports of EL emission at room temperature [11, 12]. Because the radius of N ions is approximately the same as that of oxygen ions, they are promising candidates to serve as p-type dopants in ZnO [1], and N doping by, for example, ion implantation has been examined [14]. However, the large number of lattice defects generated in normal ion implantation cannot be removed even with thermal annealing, and therefore, no p-type crystals of sufficient quality for fabricating devices have been obtained [14].

On the other hand, according to recent research by the authors, the possibility of fabricating p-type ZnO has been increased by employing annealing using dressed photons [15], a technique known as dressed-photon assisted annealing. This annealing method has already been applied to Si, an indirect-transition semiconductor, to realize high-efficiency p–n homojunction-structured LEDs using bulk Si crystal [16]. Also, processing methods based on the same principle have been applied to organic thin-film photovoltaic devices [17], frequency up-conversion via organic dye grains [18], photolithography [19], and subnanometer polishing of glass surfaces [20].

In this study, we successfully fabricated a p–n homojunction-structured LED that emits at room temperature by applying dressed-photon assisted annealing to a bulk ZnO crystal. The principle of the annealing technique, the device fabrication method, and the characteristics of the fabricated devices are described in the following.

---

K. Kitamura · T. Kawazoe (✉) · M. Ohtsu  
Department of Electrical Engineering and Information Systems,  
Graduate School of Engineering, The University of Tokyo,  
2-11-16 Yayoi, Bunkyo-ku, Tokyo 113-8656, Japan  
e-mail: kawazoe@ee.t.u-tokyo.ac.jp  
Fax: +81-3-58411140

T. Kawazoe · M. Ohtsu  
Nanophotonics Research Center, Graduate School  
of Engineering, The University of Tokyo, 2-11-16 Yayoi,  
Bunkyo-ku, Tokyo 113-8656, Japan

## 2 Principle of dressed-photon assisted annealing

In this study, we used an n-type bulk ZnO crystal implanted with N ions (N dopant) serving as a p-type dopant. In previous work by the authors, when a bulk Si crystal was implanted with boron (B) serving as a p-type dopant, the B was readily activated to form acceptors, thus creating a p–n homojunction [16]; in the present study, however, where we employed ZnO, the N dopant was not readily activated [6]. Therefore, first we tried to activate the N dopant.

Specifically, Joule heating brought about by a forward bias current was used to anneal the crystal, activating the N dopant. An overview of this principle is as follows: if a forward bias current is applied directly after implanting the N dopant, the N is not activated much; therefore, only electrons, which are majority carriers, carry the electrical current. Also, because no holes exist, recombination emission does not take place either. Therefore, the p–n junction remains highly resistive, and when a constant current is applied, the voltage applied across the p–n junction is high. As a result, a high level of Joule heating occurs, diffusing the N dopant and considerably changing the concentration distribution, causing the N dopant to be activated. Therefore, because holes also become current carriers, the resistance decreases. Because ZnO is a direct-bandgap semiconductor, a part of the electrical energy is converted to spontaneous emission optical energy through recombination of electrons and holes, and this is radiated from the crystal. The Joule heating drops due to this energy dissipation and the decrease in resistance mentioned above and, therefore, the concentration distribution of the N dopant eventually reaches a steady state. This completes the N dopant activation process.

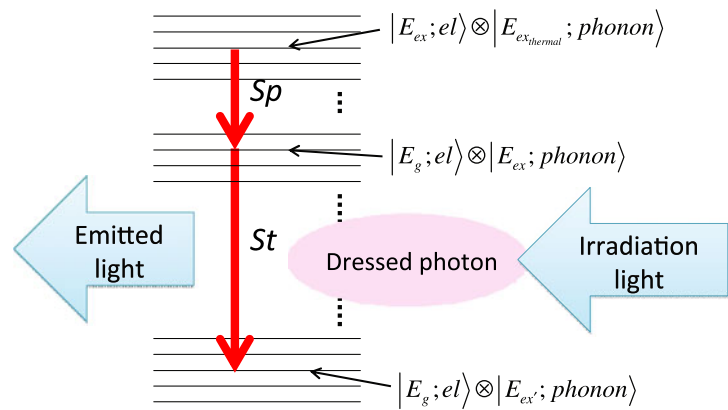
Next, we use dressed-photon assisted annealing simultaneously with the activation described above. The process can be explained as follows: a p–n homojunction is formed in the ZnO crystal by implanting N ions; however, because this structure is simple, the electrons and holes both exhibit wide spatial distributions. Therefore, their recombination probability is low, and the emission intensity is also low. The dressed-photon assisted process is used to increase the emission intensity. Specifically, while applying a forward bias current during the annealing, the crystal surface is irradiated with light having a low photon energy compared with the band gap energy. This light is not absorbed in the ZnO crystal and reaches the p–n junction in the form of exciton polaritons. Because the N dopant present in the p–n junction is introduced by ion implantation, its concentration distribution is not homogeneous [21], and centers of localization of electrons and holes are formed at regions of high concentration. Therefore, when these centers of localization are irradiated with the above exciton polaritons, the exciton polaritons are localized. As a result, localized dressed photons are generated in the vicinity of the localized exciton polaritons. These dressed photons can excite multimode coherent

phonons in the vicinity of the p–n junction [22], resulting in a state where the dressed photons and phonons are coupled; in other words, dressed-photon phonons are created. On the other hand, because it is difficult to form centers of localization in regions where the N dopant concentration is low, dressed photons and dressed-photon phonons are not created there.

When Joule heating is generated by the forward bias current, the N dopant in the p–n junction is diffused; however, at regions where dressed photons are generated by the process described above, stimulated emission occurs, driven by the dressed photons. Furthermore, in the p–n junction, because an electron population inversion is formed between the conduction band and the valence band, the stimulated emission light produced is amplified by this population inversion. Therefore, part of the electrical energy given by the forward bias current is efficiently converted to the stimulated emission photon energy and is radiated from the crystal. At the same time, spontaneously emitted light is also radiated externally, similar to the case where activation is performed, as described above. Therefore, the amount of thermal energy produced in these regions is small compared with regions where dressed photons are not generated, and thus the N dopants are not easily diffused. As a result, at regions where dressed photons are generated with high efficiency, the concentration distribution of the N dopant hardly changes, maintaining the high dressed-photon generation efficiency.

The electronic transitions related to the above process will now be explained using Fig. 1. A dressed-photon phonon is created by light irradiation, which means that an intermediate state  $|E_g; e\rangle \otimes |E_{ex}; \text{phonon}\rangle$  represented by the direct product of the valence band electronic state  $|E_g; e\rangle$  and the phonon excited state  $|E_{ex}; \text{phonon}\rangle$  is created. At this time, an electron transitions from the upper state  $|E_{ex}; e\rangle \otimes |E_{ex_{\text{thermal}}}; \text{phonon}\rangle$ , represented by the direct product of the conduction band electronic state  $|E_{ex}; e\rangle$  and the phonon thermal equilibrium state  $|E_{ex_{\text{thermal}}}; \text{phonon}\rangle$ , to the above mentioned intermediate state  $|E_g; e\rangle \otimes |E_{ex}; \text{phonon}\rangle$ , and a photon is generated by spontaneous emission (arrow *Sp* in Fig. 1). Then the electron transitions to the lower state  $|E_g; e\rangle \otimes |E_{ex'}; \text{phonon}\rangle$  represented by the direct product of the valence band electronic state  $|E_g; e\rangle$  and the phonon low-energy state  $|E_{ex'}; \text{phonon}\rangle$ , during which another photon is generated by stimulated emission driven by a dressed photon (arrow *St* in Fig. 1). As a result, because the concentration distribution of the N dopant is maintained at regions where dressed photons are generated with high efficiency, as described above, Joule-heating annealing and stimulated emission proceed there, eventually forming, in a self-organized manner, a concentration distribution that is suitable for inducing the dressed-photon assisted process with the optimum efficiency. Af-

**Fig. 1** Principle of stimulated emission driven by a dressed photon. Arrows  $Sp$  and  $St$  represent spontaneous emission and stimulated emission, respectively



ter the annealing, the number of regions with a high efficiency of generating dressed photons is higher than that before the annealing. Hence, considering that the spontaneous emission probability is proportional to the stimulated emission probability, a light-emitting diode that efficiently generates spontaneous emission can be fabricated by using this dressed-photon assisted annealing process.

### 3 Device fabrication

In this study, we used an n-type ZnO single crystal fabricated by the hydrothermal growth method [23]. The crystal axis direction was (0001), the thickness was 500  $\mu\text{m}$ , and the electrical resistivity was 50–150  $\Omega\text{cmN}^{2+}$  ions were implanted into the crystal at an energy of 600 keV and an ion dose density of  $1.0 \times 10^{15}\text{ cm}^{-2}$ . The implantation depth was confirmed to be about 3  $\mu\text{m}$  by secondary ion mass spectrometry (SIMS). This allowed the N dopant to be distributed in the vicinity of the crystal surface, forming a p-type ZnO layer. As a result, we realized a p–n homojunction structure. Using RF sputtering, a 150 nm-thick indium tin oxide (ITO) film was deposited on the surface of the p-type ZnO layer, and a 5 nm-thick Cr film and a 100 nm-thick Al film were deposited on the surface of the n-type ZnO layer to serve as electrodes. Then, the crystal was diced to form a device with an area of about 9  $\text{mm}^2$ .

Annealing was performed by causing a forward bias current to flow through the device to generate Joule heating. To do so, the current was made to flow by bringing a W probe into contact with the positive electrode and attaching a Cu film to the negative electrode.

We fabricated the following two types of devices.

**Device 1:** A device fabricated by annealing with a forward bias current alone, without light irradiation, to activate the N dopant.

**Device 2:** A device fabricated by dressed-photon assisted annealing. (To do so, during annealing with the forward

bias current, the device was irradiated with laser light having a photon energy  $h\nu = 3.05\text{ eV}$  ( $\lambda = 407\text{ nm}$ ) lower than the bandgap energy of ZnO (3.4 eV), from the ITO electrode side.)

The forward bias current density for annealing both devices was made as high as possible without causing thermal destruction of the device, namely 0.22  $\text{A}/\text{cm}^2$ . For Device 2, the irradiation power was set as high as possible without causing the crystal temperature to rise, namely, about 1/10 of the input power, or about 2.2  $\text{W}/\text{cm}^2$ . Figure 2(a) shows a thermographic image of the surface of Device 2 about 1 minute after commencing annealing. Figure 2(b) shows the change in surface temperature with time at the center of the device. The surface temperature rose to 100  $^\circ\text{C}$  when annealing commenced, and then dropped, reaching a constant temperature of 74  $^\circ\text{C}$  after about 60 minutes. This temperature drop was caused by the generation of dressed photons as annealing progressed, bringing about stimulated emission, and by part of the electrical energy added to produce Joule heating being dissipated in the form of optical energy. To confirm this stimulated emission effect, Fig. 2(c) shows the results of measuring the change in surface temperature with time for another identical sample of Device 2, when the irradiated light power was turned on and off every 5 minutes. The temperature during light irradiation dropped, confirming the stimulated emission effect.

### 4 Device characterization

Based on the results in Fig. 2(b), we fabricated the two devices described above via dressed-photon assisted annealing for 60 minutes.

First, the characteristics of Device 1 will be described. The three curves in Fig. 3(a) are EL emission spectra of Device 1 at room temperature. These spectra are formed of a high-intensity, narrow-band emission component in the ultraviolet region close to a wavelength of 382 nm and a



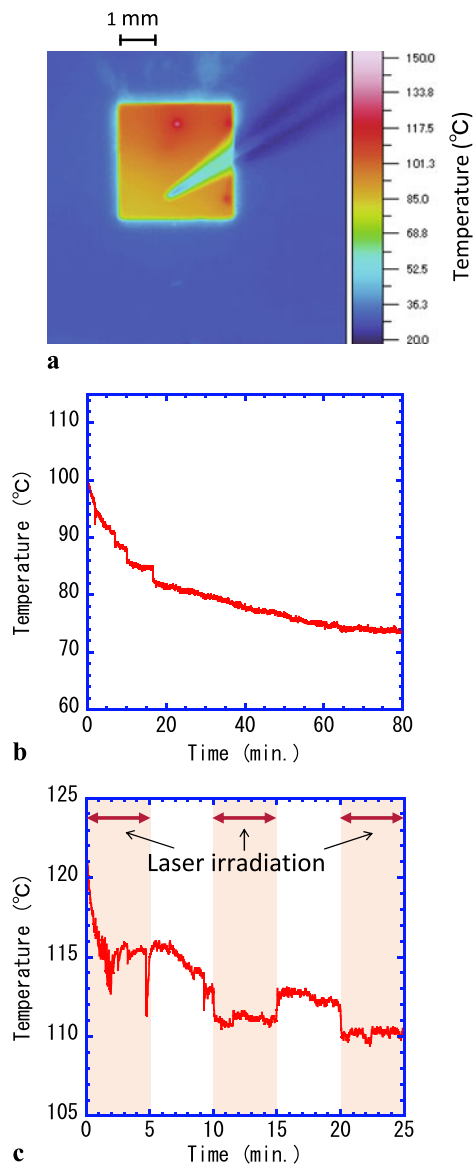


**Fig. 2** Surface temperature of ZnO crystal annealed while being irradiated with light, showing (a) surface temperature distribution one minute after commencing annealing; (b) change in surface temperature with time at center of crystal surface; and (c) change in surface temperature with time at center of crystal surface when laser irradiation during annealing was turned on and off every 5 minutes

low-intensity, wide-band emission component in the visible region above 490 nm. The former is attributed to the band edge transition in ZnO, and the latter is attributed to emission from defect levels [24]. The emission from the defect levels is not related to the dressed-photon assisted process in the case of Device 2, described below, and depends on the substrate quality. In other words, from these spectra, the emission from Device 1 was confirmed to be mainly due to the band edge transition. As shown in Fig. 3(b), the  $I$ - $V$  characteristic of this device showed the same rectifying properties as an ordinary diode, confirming

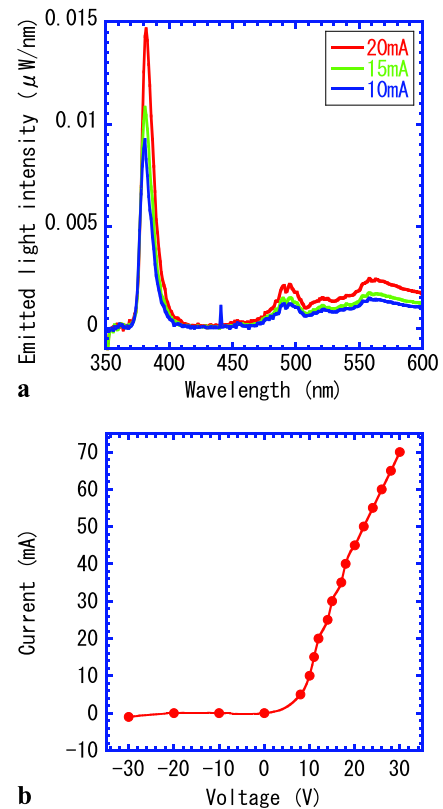
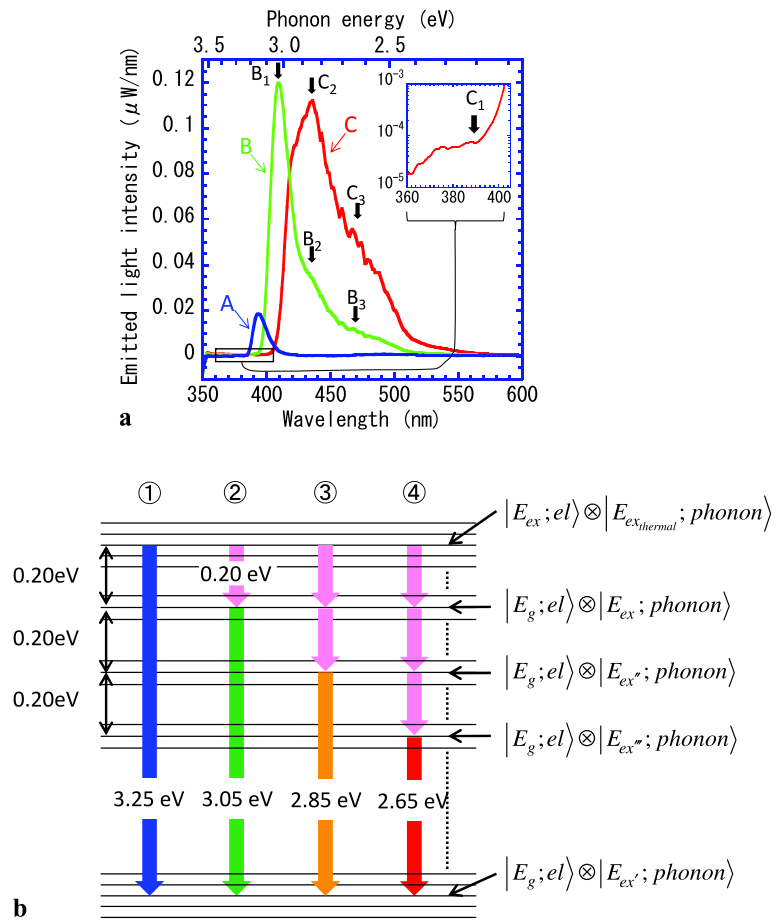


**Fig. 3** Characteristics of Device 1, showing (a) EL emission spectra and (b)  $I$ - $V$  characteristic

that a suitable p-n homojunction was formed by the annealing.

Next, the characteristics of Device 2 will be described. EL emission spectra of Device 2 at room temperature are shown by the three curves A, B, and C in Fig. 4(a). Curves A, B, and C show the results obtained with forward bias currents of 10 mA, 15 mA, and 20 mA, respectively. The emission peak wavelength of curve A was 393 nm, which is attributed to the band edge transition, similar to the case of Device 1 (Fig. 3(a)). Comparing curves B and C with curve A, the spectral centroid of the emission spectrum of Device 2 shifted to the long wavelength side as the forward bias current was increased. However, this shift was not attributed to a change in the bandgap energy induced by Joule heating [25], because the emission peak attributed to the band edge transition in Device 1 did not show this kind of shift. Furthermore, as shown in the inset, the emission (arrow  $C_1$ ) attributed to the band edge transition, although weak, was also found in curve C (20 mA). Therefore, we can ignore the long-wavelength shift of the emission spectra attributed to Joule heating at forward bias currents in the range of 10–20 mA. Attributing this long-wavelength shift to stimulated emission driven by dressed photons, not Joule heating, is explained as follows.

**Fig. 4** Characteristics of Device 2. **(a)** EL emission spectra, where curves A, B, and C are for forward bias currents of 10, 15, and 20 mA, respectively. *Inset* is a magnified view of curve C around the photon energy corresponding to the band edge transition. Arrows  $B_1$ ,  $B_2$ , and  $B_3$  show the positions of the peak and two bumps in curve B, respectively. Arrow  $C_1$  in the *inset* shows the position of a bump in curve C. Arrows  $C_2$  and  $C_3$  show the positions of the peak and a bump in curve C, respectively. **(b)** Diagram for explaining transitions involving phonons during light emission



A dressed-photon assisted process is involved not only in the device fabrication described in Sect. 3 but also during device operation. Light emission during LED operation, like the stimulated emission process during annealing (Fig. 1), is attributed to a two-step transition, i.e., from  $|E_{ex}; el\rangle \otimes |E_{ex_{thermal}}; phonon\rangle$  to  $|E_g; el\rangle \otimes |E_{ex}; phonon\rangle$  (the pink arrow at ② in Fig. 4(b)) and from  $|E_g; el\rangle \otimes |E_{ex}; phonon\rangle$  to  $|E_g; el\rangle \otimes |E_{ex'}; phonon\rangle$  (the green arrow at ② in Fig. 4(b)). Because the second-step transition is an electric-dipole-forbidden transition, only dressed photons are emitted, and these dressed photons are scattered by the inhomogeneous N dopant concentration and are converted to propagating light. The photon energy of the emitted dressed photons is determined by the photon energy of the light radiated during annealing (3.05 eV, wavelength 407 nm). This is because the N dopant concentration distribution is formed in a self-organized manner by the dressed-photon assisted annealing described in Sect. 3, with the result that, in Device 2, a transition via the intermediate phonon level corresponding to the photon energy of the irradiation light easily occurs. Therefore, in curve B in Fig. 4(a), the peak photon energy of 3.03 eV (409 nm; arrow  $B_1$ ) is the same as the photon energy of the irradiation light.

On the other hand, the photon energy of light generated in the first-step transition is given by the energy difference between  $|E_{ex}; el\rangle \otimes |E_{ex_{thermal}}; phonon\rangle$  and  $|E_g; el\rangle \otimes |E_{ex}; phonon\rangle$ . Comparing the blue arrow at ① in Fig. 4(b) and the green arrow at ② in Fig. 4(b), this photon energy is 0.20 eV. (The blue arrow at ① represents the band edge transition of ZnO, whose energy is 3.25 eV (382 nm) according to Fig. 3(a).) This first-step transition is an electric-dipole-allowed transition; however, because the occupation probability of such high-energy phonons is low, propagating light is not emitted, and only dressed photons, which can couple with multimode coherent phonons, are generated. In addition, when the stimulated emission driven by the dressed photons emitted in the first-step transition is repeated one more time and two more times, new intermediate phonon levels  $|E_g; el\rangle \otimes |E_{ex''}; phonon\rangle$  (③ in Fig. 4(b)) and  $|E_g; el\rangle \otimes |E_{ex'''}; phonon\rangle$  (④ in Fig. 4(b)) are formed whose eigenenergies are lower by amounts corresponding to an integer multiple of the photon energy of the dressed photons. Thus, the energies of the photons emitted via these new intermediate phonon levels are lower by amounts corresponding to the energy of the dressed photons emitted in the first-step transition (0.20 eV). In the case of ③ and ④, these photon energies are 2.85 eV (435 nm) and 2.65 eV

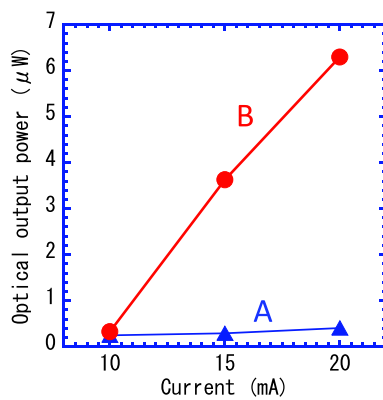


**Fig. 5** Dependence of EL emission intensity on forward bias current. Curves A and B show Devices 1 and 2, respectively

(468 nm), respectively, as shown by the yellow arrow and the red arrow in Fig. 4(b). These are similar to the emission peaks measured in the conventional optical transition of bulk ZnO crystal, which are an integer multiple of the LO phonon energy (72 meV) [24]. However, unlike the conventional optical transition, in the transition driven by dressed photons, the energy that is exchanged is an integer multiple of the energy determined by dressed-photon phonons among the multiple phonon modes involved, rather than a material-specific phonon mode. The slope of curve B (forward bias current of 15 mA) shows two bumps (arrows B<sub>2</sub> and B<sub>3</sub> in curve B), whose positions were found to be 2.84 eV (436 nm) and 2.64 eV (470 nm), respectively, by the curve fitting based on the second-derivative spectroscopy method [26]. These agree well with the photon energies indicated by the yellow and red arrows at ③ and ④ in Fig. 4(b). In addition, curve C (20 mA) also shows a peak (arrow C<sub>2</sub>) and one bump (arrow C<sub>3</sub>) at 2.84 eV (436 nm) and 2.63 eV (471 nm), respectively. These also agree well with the photon energies indicated by the yellow and red arrows at ③ and ④ in Fig. 4(b).

Light emission via the intermediate phonon levels occurs not only due to single- or two-step stimulated emission at ③ and ④ in Fig. 4(b) but also due to multistep stimulated emission, therefore, when the forward bias current is increased, the emission intensity at the low-energy side also increases, which explains the long-wavelength shift in Fig. 4(a). Note that the emission intensity due to the band gap transition in curve B is small; this is attributed to the fact that the transition ① involving stimulated emission is faster than the transition ② involving only spontaneous emission, because electrons in the conduction band for stimulated emission relax to the intermediate phonon level.

To compare the performance of Devices 1 and 2, curves A and B in Fig. 5 respectively show how the optical output power of the two devices depended on the forward bias current. The optical output power was obtained by integrating the curves A, B, and C in Fig. 4 in the wavelength range

350–600 nm. For curve B, at the forward bias current of 20 mA (current density 0.22 A/cm<sup>2</sup>), the optical output power from Device 2 was 6.2 μW, which was about 15 times higher than the optical output power from Device 1, shown in curve A. The external quantum efficiency was  $1.1 \times 10^{-4}$ .

From the above results, we showed that dressed-photon assisted annealing, which has been used for fabricating indirect-bandgap semiconductor optical devices, is effective even for direct-transition semiconductors. At present, the maximum forward bias current that can be injected is determined by the thermal destruction limit of the device. Therefore, it should be possible to achieve further increases in the optical output power and emission efficiency by improving the electrical and thermal properties of the bulk ZnO crystals to be used.

## 5 Conclusion

We succeeded in fabricating a light-emitting diode having a p–n homojunction structure by applying dressed-photon assisted annealing to an n-type ZnO crystal doped with N ions by ion implantation. The device showed good EL emission characteristics at room temperature. Specifically, annealing was achieved by Joule heating alone, without irradiating the device with light, activating the N dopant. The emission peak wavelength of the fabricated device was 382 nm. As for the device fabricated by dressed-photon assisted annealing while radiating light, the emission peak wavelength at a forward bias current of 20 mA was 436 nm, the optical output power was 6.2 μW, and the external quantum efficiency was  $1.1 \times 10^{-4}$ . The emission spectral profile was found to be dependent on transitions from intermediate phonon states.

**Open Access** This article is distributed under the terms of the Creative Commons Attribution License which permits any use, distribution, and reproduction in any medium, provided the original author(s) and the source are credited.

## References

1. Y.-S. Choi, J.-W. Kang, D.-K. Hwang, S.-J. Park, *IEEE Trans. Electron Devices* **57**, 26 (2010)
2. T.M. Quist, R.H. Rediker, R.J. Keyes, W.E. Krag, B. Lax, A.L. McWhorter, H.J. Ziegler, *Appl. Phys. Lett.* **1**, 91 (1962)
3. N. Holonyak, S.F. Bevacqua, *Appl. Phys. Lett.* **1**, 82 (1962)
4. R.N. Hall, G.E. Fenner, J.D. Kingsley, T.J. Soltys, R.O. Carlson, *Phys. Rev. Lett.* **9**, 366 (1962)
5. M.I. Nathan, W.P. Dumke, G. Burns, F.H. Dill, G. Lasher, *Appl. Phys. Lett.* **1**, 62 (1962)
6. D. Seghier, H.P. Gislason, *J. Mater. Sci., Mater. Electron.* **19**, 687 (2008)
7. A. Tsukazaki, A. Ohtomo, T. Onuma, M. Ohtani, T. Makino, M. Sumiya, K. Ohtani, S.F. Chichibu, S. Fuku, Y. Segawa, H. Ohno, H. Koinuma, M. Kawasaki, *Nat. Mater.* **4**, 42 (2005)

8. A. Tsukazaki, M. Kubota, A. Ohtomo, T. Onuma, K. Ohtani, H. Ohno, S.F. Chichibu, M. Kawasaki, *Jpn. J. Appl. Phys.* **44**, L643 (2005)
9. W.Z. Xu, Z.Z. Ye, Y.J. Zeng, L.P. Zhu, B.H. Zhao, L. Jiang, J.G. Lu, H.P. He, S.B. Zhang, *Appl. Phys. Lett.* **88**, 173506 (2006)
10. Z.P. Wei, Y.M. Lu, D.Z. Shen, Z.Z. Zhang, B. Yao, B.H. Li, J.Y. Zhang, D.X. Zhao, X.W. Fan, Z.K. Tang, *Appl. Phys. Lett.* **90**, 042113 (2007)
11. J. Kong, S. Chu, M. Olmedo, L. Li, Z. Yang, J. Liu, *Appl. Phys. Lett.* **93**, 132113 (2008)
12. A. Nakagawa, T. Abe, S. Chiba, H. Endo, M. Meguro, Y. Kashiwaba, T. Ojima, K. Aota, I. Niikura, Y. Kashiwaba, T. Fujiwara, *Phys. Status Solidi C* **6**, S119 (2009)
13. F. Sun, C.X. Shan, B.H. Li, Z.Z. Zhang, D.Z. Shen, Z.Y. Zhang, D. Fan, *Opt. Lett.* **36**, 499 (2011)
14. Z.Q. Chen, T. Sekiguchi, X.L. Yuan, M. Maekawa, A. Kawasuso, *J. Phys., Condens. Matter* **16**, S293 (2004)
15. T. Kawazoe, K. Kobayashi, S. Takubo, M. Ohtsui, *J. Chem. Phys.* **122**, 024715 (2005)
16. T. Kawazoe, M.A. Mueed, M. Ohtsu, *Appl. Phys. B* **104**, 747 (2011)
17. S. Yukutake, T. Kawazoe, T. Yatsui, W. Nomura, K. Kitamura, M. Ohtsu, *Appl. Phys. B* **99**, 415 (2010)
18. T. Kawazoe, H. Fujiwara, K. Kobayashi, M. Ohtsu, *IEEE J. Sel. Top. Quantum Electron.* **15**, 1380 (2009)
19. T. Kawazoe, M. Ohtsui, Y. Inao, R. Kuroda, *J. Nanophotonics* **1**, 011595 (2007)
20. T. Yatsui, K. Hirata, W. Nomura, Y. Tabata, M. Ohtsu, *Appl. Phys. B* **93**, 55 (2008)
21. W.L. Ng, M.A. Lourenco, R.M. Gwilliam, S. Ledain, G. Shao, K.P. Homewood, *Nature* **410**, 192 (2001)
22. Y. Tanaka, K. Kobayashi, *Physica E* **40**, 297 (2007)
23. T. Sekiguchi, S. Miyashita, K. Obara, T. Shishido, N. Sakagami, *J. Cryst. Growth* **214/215**, 72 (2000)
24. Ü. Özgür, Y.I. Alivov, C. Liu, A. Teke, M.A. Reshchikov, S. Doğan, V. Avrutin, S.-J. Cho, H. Morkoç, *J. Appl. Phys.* **98**, 041301 (2005)
25. M.S. Kim, K.G. Yim, J.Y. Leem, D.Y. Lee, J.S. Kim, J.S. Kim, *J. Korean Phys. Soc.* **58**, 821 (2011)
26. H. Mach, C.R. Middaugh, *Anal. Biochem.* **222**, 323 (1994)

## Emission from a dipole-forbidden energy state in a ZnO quantum dot induced by a near-field interaction with a fiber probe

T. Yatsui, M. Tsuji, Y. Liu, T. Kawazoe, and M. Ohtsu

Citation: *Appl. Phys. Lett.* **100**, 223110 (2012); doi: 10.1063/1.4723574

View online: <http://dx.doi.org/10.1063/1.4723574>

View Table of Contents: <http://apl.aip.org/resource/1/APPLAB/v100/i22>

Published by the [American Institute of Physics](http://www.aip.org).

---

### Related Articles

Excitonic origin of enhanced luminescence quantum efficiency in MgZnO/ZnO coaxial nanowire heterostructures  
*Appl. Phys. Lett.* **100**, 223103 (2012)

Quality improvement of ZnO thin layers overgrown on Si(100) substrates at room temperature by nitridation pretreatment  
*AIP Advances* **2**, 022139 (2012)

Thermally activated below-band-gap excitation behind green photoluminescence in ZnO  
*J. Appl. Phys.* **111**, 093525 (2012)

Photoluminescence quenching in cobalt doped ZnO nanocrystals  
*J. Appl. Phys.* **111**, 094310 (2012)

Enforced c-axis growth of ZnO epitaxial chemical vapor deposition films on a-plane sapphire  
*Appl. Phys. Lett.* **100**, 182101 (2012)

---

### Additional information on *Appl. Phys. Lett.*

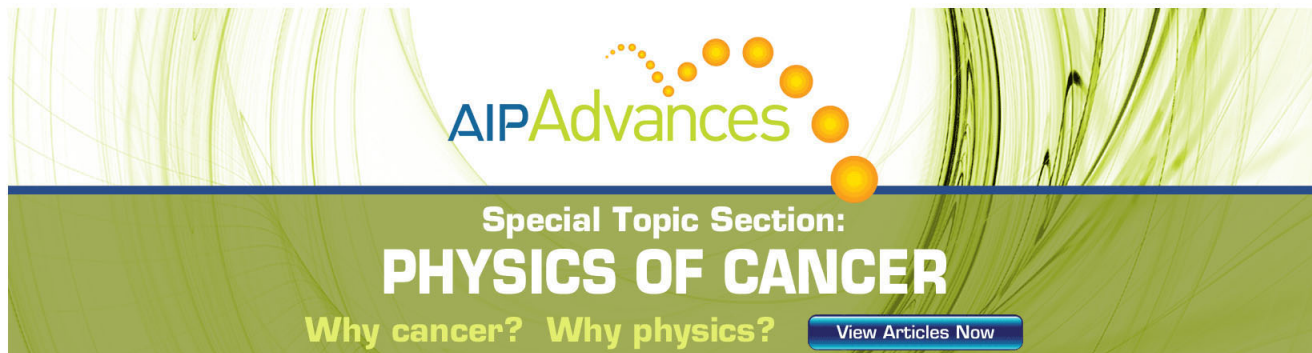
Journal Homepage: <http://apl.aip.org/>

Journal Information: [http://apl.aip.org/about/about\\_the\\_journal](http://apl.aip.org/about/about_the_journal)

Top downloads: [http://apl.aip.org/features/most\\_downloaded](http://apl.aip.org/features/most_downloaded)

Information for Authors: <http://apl.aip.org/authors>

## ADVERTISEMENT

The advertisement features a green and white background with a pattern of thin, vertical, wavy lines. At the top, the 'AIP Advances' logo is displayed, with 'AIP' in blue and 'Advances' in green, accompanied by a series of orange and yellow dots. Below the logo, the text 'Special Topic Section: PHYSICS OF CANCER' is written in white, with 'PHYSICS OF CANCER' in a larger, bold font. At the bottom, the phrase 'Why cancer? Why physics?' is written in white, and a blue button with the text 'View Articles Now' is positioned to the right.

# Emission from a dipole-forbidden energy state in a ZnO quantum dot induced by a near-field interaction with a fiber probe

T. Yatsui,<sup>1,2,a)</sup> M. Tsuji,<sup>1</sup> Y. Liu,<sup>1</sup> T. Kawazoe,<sup>1,2</sup> and M. Ohtsu<sup>1,2</sup>

<sup>1</sup>School of Engineering, University of Tokyo, Bunkyo-ku, Tokyo 113-8656, Japan

<sup>2</sup>The Nanophotonics Research Center, University of Tokyo, Bunkyo-ku, Tokyo 113-8656, Japan

(Received 7 March 2012; accepted 12 May 2012; published online 31 May 2012)

The emission intensity from the dipole-forbidden state in a spherical quantum dot (QD) was enhanced by introducing an aperture fiber probe close to the ZnO QD to induce a near-field interaction between the probe tip and the QD. The cross-sectional profiles of the photoluminescence intensities of the ground exciton state and the excited exciton states varied spatially in an anti-correlated manner. © 2012 American Institute of Physics. [<http://dx.doi.org/10.1063/1.4723574>]

Continued innovation in optical technology is required to continue the progress in the advancement of information-processing systems. It is particularly important to reduce both the size and energy consumption of photonic devices to be successfully integrated. To reduce the size of photonic devices beyond the diffraction limit, we have proposed nanophotonic devices that consist of semiconductor quantum cubes,<sup>1,2</sup> quantum dots (QDs),<sup>3</sup> and quantum wells.<sup>4</sup> More recently, Kawazoe *et al.* have shown the room temperature operation of AND-gate and NOT-gate devices using InAs QD pairs.<sup>2</sup> In a nanophotonic device, near-field energy-transfer via a dipole-forbidden energy state, which is unattainable in conventional photonic device, is used.<sup>5</sup> The near-field energy-transfer originates from an exchange of virtual photons between the resonant energy states,<sup>6</sup> where the virtual photons on a nanoparticle activate the dipole-forbidden energy state. Although emission from the dipole-forbidden energy state cannot be detected in the far field, it can be observed when a detector is installed in close proximity to the nanoparticle. Therefore, to evaluate the dipole-forbidden energy state, we used near-field spectroscopy to study ZnO QDs.

We chose ZnO QDs because, due to their exciton binding energy,<sup>7</sup> they exhibit a high emission intensity at room temperature. Our ZnO colloidal QDs were synthesized using the sol-gel method,<sup>8,9</sup> and an average diameter of 4 nm was confirmed from transmission electron microscopic (TEM) images. To observe their optical properties, the QDs were dispersed over a sapphire substrate. The average 5-nm thickness of the dispersed ZnO QDs was determined by their absorption coefficient. The photoluminescence (PL) spectra were obtained with 300-nm diameter apertured fiber probe coated with 100 nm of aluminium [see inset, Fig. 1(a)].<sup>10</sup> To excite the exciton states of ZnO QDs through the substrate, we used continuous-wave He-Cd laser with a photon energy of 3.81 eV ( $E_{ex}$ , wavelength of 325 nm), far beyond the ground state of the 4-nm diameter (3.423 eV) ZnO QDs. The red open circles in Fig. 1(a) and the blue open circles in Fig. 1(b) represent the far-field and near-field spectra obtained

with a probe-to-QD distances,  $d$ , of 6  $\mu\text{m}$  and 5 nm, respectively.

To evaluate the difference in the profiles between far- and near-field spectra, we analyzed the ZnO QD quantized energy states. Given that the 1.4-nm exciton Bohr radius of ZnO is small compared to the 4-nm diameter QD size, we

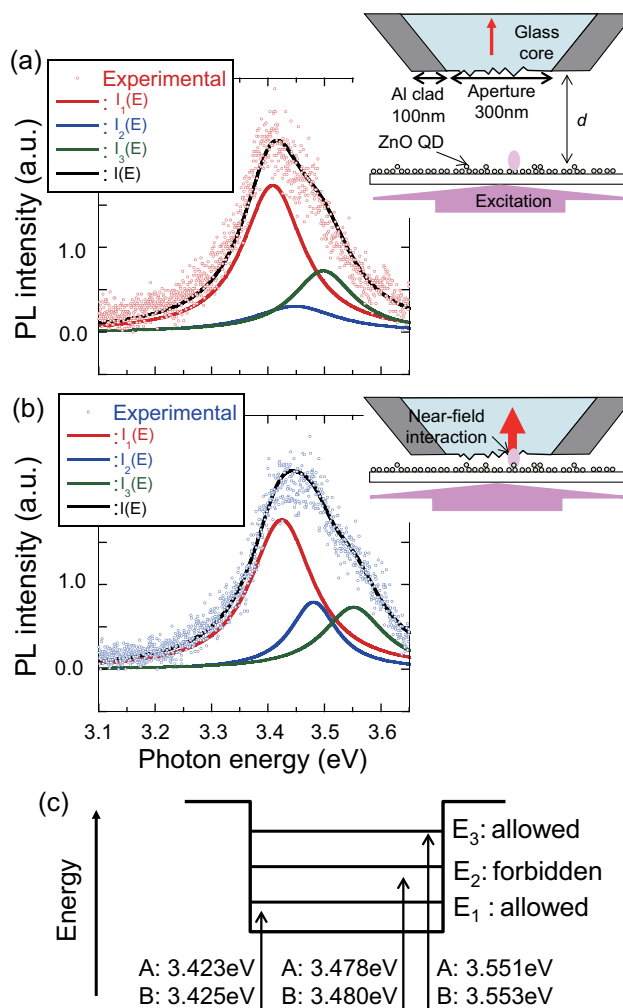


FIG. 1. (a) Far-field (red open circles) and (b) near-field PL spectra of ZnO QDs. The respective separation,  $d$ , between the fiber and the ZnO QD was (a) 1  $\mu\text{m}$  and (b) 5 nm. (c) Energy states in 4-nm-diameter, spherical ZnO QDs. A: The quantized energies for (a). B: The quantized energies for (b).

<sup>a)</sup> Author to whom correspondence should be addressed. Electronic mail: yatsui@ee.t.u-tokyo.ac.jp.

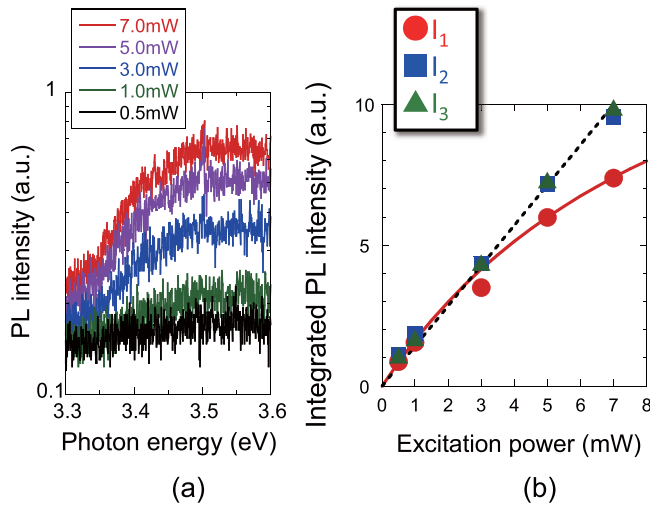


FIG. 2. (a) Excitation-power dependence of the near-field PL spectra. (b) Excitation power dependence of the integrated PL intensity.

considered energy states using the exciton notation, i.e., the optical selection rules in QDs are determined by the wave function of the exciton by considering the constant electric field in the QD.<sup>11</sup> QDs synthesized by the sol-gel method are known to be spherical and are of a single crystalline wurtzite structure.<sup>12</sup> Therefore, the quantized energies of exciton are calculated by

$$E(n, l) = E_B + \frac{\hbar^2 \pi^2}{2(m_e + m_h)eR^2} \zeta_{n,l}^2 - \frac{13.6\mu}{m_0 \varepsilon^2}, \quad (1)$$

where  $E_B$  is the band gap energy of bulk material (3.37),  $m_e$  and  $m_h$  are the effective mass of electron and hole as  $m_e = 0.32 m_0$  and  $m_h = 0.42 m_0$ ,<sup>9</sup>  $m_0$  is the electron mass,  $\mu$  is the translation mass described by  $m_e m_h / (m_e + m_h)$ ,  $e$  is elementary electric charge,  $\varepsilon$  is permittivity (5.8),  $R$  is the QD radius, and  $\pi \zeta_{n,l} = \rho_{n,l}$  is the  $n$ th root of the  $l$ th-order

TABLE I. The ratio between near-field and far-field intensity in each energy state.

	Far [Fig. 1(a)]	Near [Fig. 1(b)]	Near/far ratio
$A_1$	$0.76 \pm 0.27$	$0.72 \pm 0.05$	0.95
$A_2$	$0.13 \pm 0.07$	$0.32 \pm 0.1$	2.46
$A_3$	$0.21 \pm 0.09$	$0.28 \pm 0.10$	1.33

spherical Bessel function. The third term in Eq. (1) is the correction term. The principal quantum number  $n$  and the angular-momentum quantum number  $l$  take values  $n = 1, 2, 3, \dots$  and  $l = 0, 1, 2, \dots$ , respectively.  $\zeta_{n,l}$  takes values  $\zeta_{1,0} = 1$ ,  $\zeta_{1,1} = 1.43$ ,  $\zeta_{1,2} = 1.83$ ,  $\zeta_{2,0} = 2$ , and so on.<sup>13,14</sup> To fit the experimental data, we set the quantized energies of  $E_1$  ( $\zeta_{1,0} = 1$ , dipole-allowed) as 3.423 eV [Fig. 1(a)] and 3.425 eV [Fig. 1(b)]. Consequently, using  $\zeta_{1,1} = 1.43$  (dipole-forbidden) and  $\zeta_{1,2} = 1.83$  (dipole-allowed) in Eq. (1), the values of  $E_2$  and  $E_3$  were determined, respectively [see Fig. 1(c)].<sup>14</sup> The obtained values of  $E_1$  obtained Eq. (1),<sup>9</sup> 3.478 eV [Fig. 1(a)] and 3.480 eV [Fig. 1(b)], correspond to  $R = 2.00$  and 1.98 nm, respectively, which is in good agreement with the values determined via TEM measurement. Since the variance of the peak energy of  $E_1$  was small as 2 meV in this area, we assumed the spectral width of 150 meV to have originated from the homogeneous line width at room temperature. Therefore, using these energy values, we fit the PL spectra by the linear superposition of three Lorentzian functions ( $I_i(E)$  ( $i = 1-3$ )) at 95% statistical confidence. The spectral components,  $I_i(E)$ , are shown as solid red ( $i = 1$ ), blue ( $i = 2$ ), and green ( $i = 3$ ) curves, respectively, in Figs. 1(a) and 1(b). These fitted spectra were used to determine the near/far ratios, i.e., the ratio between the peak intensities  $A_i$  of each of the near/far spectra (see Table I). The results indicated that the peak intensity  $A_2$  increased drastically as the fiber probe approached the ZnO QDs, whereas the peak intensity  $A_1$  remained constant. The

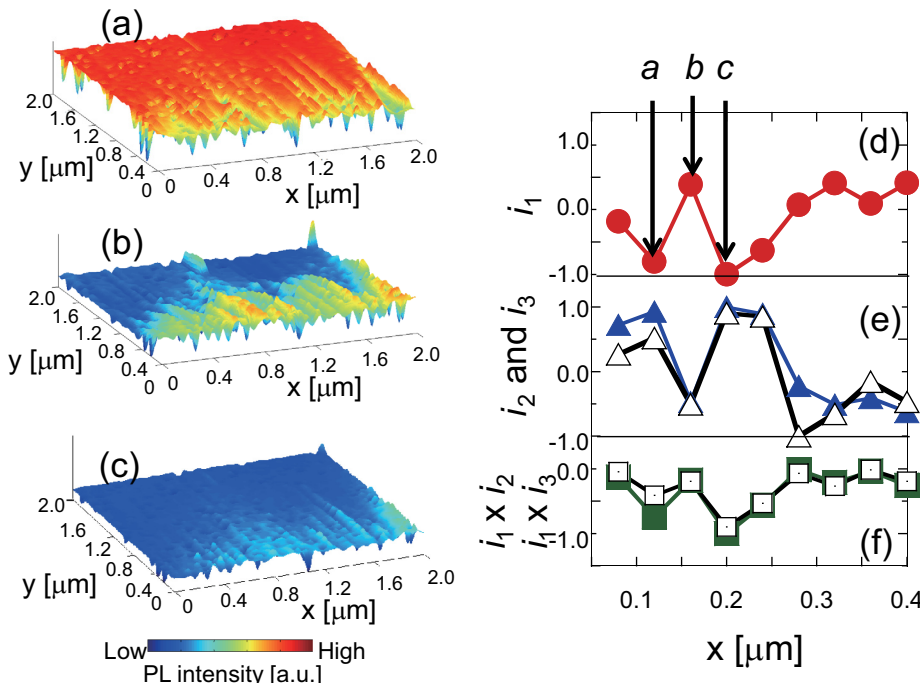


FIG. 3. Near-field intensity mappings at (a) 3.423 eV ( $I_1$ ), (b) 3.4780 eV ( $I_2$ ), and (c) 3.551 eV ( $I_3$ ). Cross-sectional profiles of normalized PL intensity of (d)  $i_1$  and (e)  $i_2$  and  $i_3$  ( $i_i = \frac{\Delta I_i}{|\Delta I_i|_{\max}} = \frac{I_i(x) - \langle I_i(x) \rangle}{|\Delta I_i|_{\max}}$ ) at  $y = 0.8 \mu\text{m}$  in (a) and (b). (f) Cross-sectional profile of  $i_1 \times i_2$  and  $i_1 \times i_3$ .

increase in the peak intensity of  $A_3$  at photon energy of 3.551 eV ( $E_3$ ) as the probe-to-QD distance  $d$  decreased was due to the fact that higher excitation photon energy of 3.81 eV ( $E_{ex}$ ) was higher than  $E_3$ . Therefore, the incident photons coupled with continuous band first, and most of the photons were dissipated and emitted from the ground state of  $E_1$ . On the other hand, when the  $d$  decreased, the coupling efficiency between excited state and the fiber probe increased, and consequently the peak intensity of excited state increased.

In addition to the spectral change depending on  $d$ , the excitation-power dependence of the near-field PL spectra was also investigated with  $d$  held at 5 nm [see Fig. 2(a)], we obtained the integrated PL intensity  $I_i = \int I_i(E) dE$  ( $i = 1, 2, 3$ ) from the three excited states:  $E_1 = 3.423$  eV (solid circles),  $E_2 = 3.4780$  eV (solid squares), and  $E_3 = 3.551$  eV (solid triangles), respectively [see Fig. 2(b)]. As can be seen in Fig. 2(b), where they are fit by the dashed line,  $I_2$  and  $I_3$  increased linearly as excitation power increased.  $I_1$ , however, increased almost linearly up to 5 mW and then gradually saturated. Its excitation-power dependence was fit by the saturation function  $I_1 = \frac{\alpha I_{ex}}{1 + I_{ex}/\beta}$  ( $I_{ex}$ : excitation power,  $\alpha$ ,  $\beta$ : constant) and is

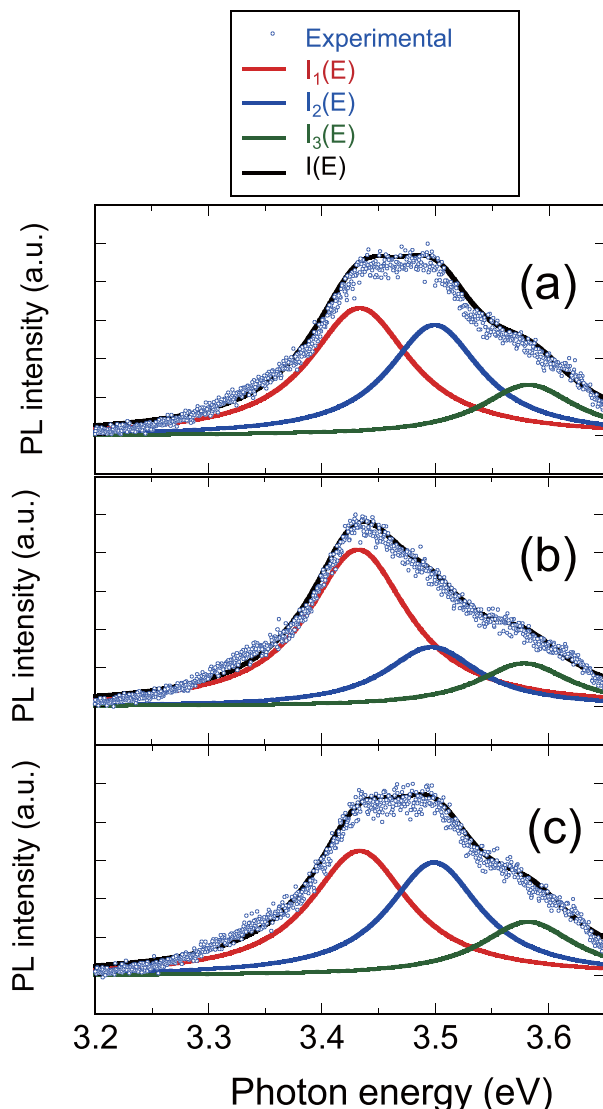


FIG. 4. (a)–(c) PL spectra at  $x = 0.120 \mu\text{m}$  (a),  $0.160 \mu\text{m}$  (b), and  $0.20 \mu\text{m}$  (c) in Fig. 3(d).

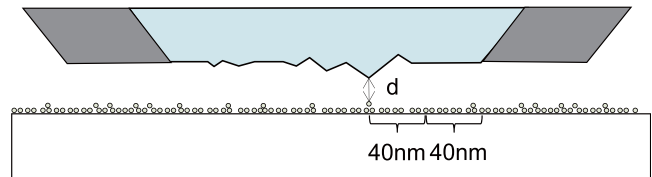


FIG. 5. Schematic representation of the fiber probe scanning over the dispersed ZnO QDs.

represented by the solid curve in Fig. 2(b). This strongly implies that the  $E_1$  energy state originated from the recombination of the ground state of the ZnO QDs, and the saturation suggests band-filling.<sup>15</sup>

Based on the above assignment of the energy states, we measured the spatial distributions of  $I_i$  of the near-field PL spectra of the dispersed ZnO QDs; these are shown in Figs. 3(a)–3(c). Figures 3(d) and 3(e) show the cross-sectional profiles of the normalized PL intensities of  $i_k$  ( $i_k = \frac{\Delta I_k}{|\Delta I_k|_{\max}} = \frac{I_k(x) - \langle I_k(x) \rangle}{|\Delta I_k|_{\max}}$ ,  $k = 1, 2, 3$ ) along the  $x$ -axis at  $y = 0.8 \mu\text{m}$  in Figs. 3(a)–3(c), respectively. These results indicate that the PL intensities of  $I_2$  and  $I_3$  vary spatially in the same manner. To find the relationship between the energy states of  $E_1$ ,  $E_2$ , and  $E_3$ , we obtained the value of  $i_1 \times i_2$  and  $i_1 \times i_3$  as shown in Fig. 3(f), in which all the values were less than zero and in fact reached  $-1$  at positions  $a$  ( $x = 0.12 \mu\text{m}$ ) and  $c$  ( $x = 0.20 \mu\text{m}$ ). This result indicates that the PL intensities  $I_2$  and  $I_3$  vary spatially in an anti-correlated manner with the PL intensity  $I_1$ .

The spatial dependence of the emission peak intensities  $A_i$  was supported by the PL spectra. Figures 4(a)–4(c) show the PL spectra at positions  $a$ – $c$  as indicated in Fig. 3(d). The three positions were laterally separated by 40 nm. However, it must be noted that although the fiber probe was scanned in constant-distance mode, the distance is not truly constant because fiber probe including the metal cladding was as large as 500 nm, some 125 times larger than the 4-nm diameter QD. Therefore, because the thickness of the dispersed ZnO QDs was not uniform and the surface of the fiber probe had nanoscale roughness (see Fig. 5), the probe-to-QD distance  $d$  varied depending on position. Thus, the spectral changes at the different positions are considered as originating from the variability of  $d$  during fiber-probe scanning.

In conclusion, we directly observe emission from an optically forbidden state in ZnO QDs. By introducing a near-field fiber probe in close proximity to the QDs, we observed increased emission intensity from the dipole-forbidden state. Because the decay time of the dipole-forbidden state is  $10^6$  times longer than that of the dipole-active state,<sup>16</sup> the dipole-forbidden state can be used to realize novel devices such as optical buffer memory and signal-transmission devices.

This work was partially supported by The University of Tokyo Global COE Program “Secure-Life Electronics,” a Grant-in-Aid for Young Scientists (A), Grants-in-Aid for Scientific Research, Japan Society for the Promotion of Science (JSPS), and a Research Grant (Basic Research) from the TEPCO memorial foundation. The authors gratefully acknowledge Dr. Tony Llopi and Professor A. Neogi,



University of North Texas, for their useful advice and discussions.

- <sup>1</sup>T. Kawazoe, K. Kobayashi, J. Lim, Y. Narita, and M. Ohtsu, *Phys. Rev. Lett.* **88**, 067404 (2002).
- <sup>2</sup>T. Kawazoe, M. Ohtsu, S. Aso, Y. Sawado, Y. Hosoda, K. Yoshizawa, K. Akahane, N. Yamamoto, and M. Naruse, *Appl. Phys. B - Lasers Opt.* **103**, 537 (2011).
- <sup>3</sup>T. Yatsui, H. Jeong, and M. Ohtsu, *Appl. Phys. B - Lasers Opt.* **93**, 199 (2008).
- <sup>4</sup>T. Yatsui, S. Sangu, T. Kawazoe, M. Ohtsu, S. J. An, J. Yoo, and G.-C. Yi, *Appl. Phys. Lett.* **90**, 223110 (2007).
- <sup>5</sup>K. Mukai, S. Abe, and H. Sumi, *J. Phys. Chem. B* **103**, 6096 (1999).
- <sup>6</sup>M. Ohtsu, T. Kawazoe, T. Yatsui, and M. Naruse, *IEEE J. Sel. Top. Quantum Electron.* **14**, 1404 (2008).
- <sup>7</sup>M. H. Huang, S. Mao, H. Feick, H. Yan, Y. Wu, H. Kind, E. Weber, R. Russo, and P. Yang, *Science* **292**, 1897 (2001).
- <sup>8</sup>E. M. Hendriks, *Zeitschrift für Physik B Condensed Matter* **57**, 307 (1984).
- <sup>9</sup>Y. Liu, T. Morishima, T. Yatsui, T. Kawazoe, and M. Ohtsu, *Nanotechnology* **22**, 215605 (2011).
- <sup>10</sup>T. Saiki, S. Mononobe, M. Ohtsu, N. Saito, and J. Kusano, *Appl. Phys. Lett.* **68**, 2612 (1996).
- <sup>11</sup>Z. K. Tang, A. Yanase, T. Yasui, Y. Segawa, and K. Cho, *Phys. Rev. Lett.* **71**, 1431 (1993).
- <sup>12</sup>L. Zhang, L. Yin, C. Wang, N. Lun, and Y. Qi, *Appl. Mater. Interfaces* **2**, 1769 (2010).
- <sup>13</sup>A. D. Yoffe, *Adv. Phys.* **51**, 799 (2002).
- <sup>14</sup>N. Sakakura and Y. Masumoto, *Phys. Rev. B* **56**, 4051 (1997).
- <sup>15</sup>T. Yatsui, J. Lim, M. Ohtsu, S. J. An, and G.-C. Yi, *Appl. Phys. Lett.* **85**, 727 (2004).
- <sup>16</sup>C. Garcia, B. Garrido, P. Pellegrino, R. Ferre, J. A. Moreno, J. R. Morante, L. Pavesi, and M. Cazzanelli, *Appl. Phys. Lett.* **82**, 1595 (2003).

## Stochastic processes in light-assisted nanoparticle formation

Makoto Naruse, Yang Liu, Wataru Nomura, Takashi Yatsui, Masaki Aida et al.

Citation: *Appl. Phys. Lett.* **100**, 193106 (2012); doi: 10.1063/1.4711808

View online: <http://dx.doi.org/10.1063/1.4711808>

View Table of Contents: <http://apl.aip.org/resource/1/APPLAB/v100/i19>

Published by the [American Institute of Physics](#).

---

### Related Articles

Nucleation of Ge clusters at high temperatures on Ge/Si(001) wetting layer

*J. Appl. Phys.* **111**, 094307 (2012)

Impact of the Ga/In ratio on the N incorporation into (In,Ga)(As,N) quantum dots

*J. Appl. Phys.* **111**, 083530 (2012)

Dimensional transition and carrier dynamics in  $\text{Cd}_x\text{Zn}_{1-x}\text{Te}/\text{ZnTe}$  nanostructures on Si substrates

*Appl. Phys. Lett.* **100**, 171905 (2012)

Identification of visible emission from ZnO quantum dots: Excitation-dependence and size-dependence

*J. Appl. Phys.* **111**, 083521 (2012)

Internal structure of tunable ternary  $\text{Cd}_x\text{Se}_{1-x}\text{S}_x$  quantum dots unraveled by x-ray absorption spectroscopy

*Appl. Phys. Lett.* **100**, 163113 (2012)

---

### Additional information on *Appl. Phys. Lett.*

Journal Homepage: <http://apl.aip.org/>

Journal Information: [http://apl.aip.org/about/about\\_the\\_journal](http://apl.aip.org/about/about_the_journal)

Top downloads: [http://apl.aip.org/features/most\\_downloaded](http://apl.aip.org/features/most_downloaded)

Information for Authors: <http://apl.aip.org/authors>

## ADVERTISEMENT



GET YOUR COPY TODAY >>

**FREE CD with 700  
Multiphysics Presentations**

COMSOL

## Stochastic processes in light-assisted nanoparticle formation

Makoto Naruse,<sup>1,a)</sup> Yang Liu,<sup>2</sup> Wataru Nomura,<sup>2</sup> Takashi Yatsui,<sup>2</sup> Masaki Aida,<sup>3</sup> Laszlo B. Kish,<sup>4</sup> and Motoichi Ohtsu<sup>2</sup>

<sup>1</sup>Photonic Network Research Institute, National Institute of Information and Communications Technology, 4-2-1 Nukui-kita, Koganei, Tokyo 184-8795, Japan

<sup>2</sup>Department of Electrical Engineering and Information Systems and Nanophotonics Research Center, Graduate School of Engineering, The University of Tokyo, 2-11-16 Yayoi, Bunkyo-ku, Tokyo 113-8656, Japan

<sup>3</sup>Tokyo Metropolitan University, 6-6 Asahigaoka, Hino, Tokyo 191-0065, Japan

<sup>4</sup>Department of Electrical and Computer Engineering, Texas A&M University, College Station, Texas 77843-3128, USA

(Received 16 February 2012; accepted 20 April 2012; published online 8 May 2012)

Recently, light-assisted nanofabrication have been introduced, such as the synthesis of quantum dots using photo-induced desorption that yields reduced size fluctuations or metal sputtering under light illumination resulting in self-organized, nanoparticle chains. The physical mechanisms have originally been attributed to material desorption or plasmon resonance effects. However, significant stochastic phenomena are also present that have not been explained yet. We introduce stochastic models taking account of the light-assisted processes that reproduce phenomenological characteristics consistent with the experimental observations. © 2012 American Institute of Physics. [<http://dx.doi.org/10.1063/1.4711808>]

Nanophotonic devices and systems have been intensively studied for use in a wide range of applications, such as information and communication, energy and environment, etc.<sup>1,2</sup> Precision control of the geometrical features of materials on the nanometer scale, such as the sizes and positions, are important factors in obtaining the intended functionalities of nanophotonic devices and systems in which multiple nanostructures are mediated by optical near-field interactions<sup>1</sup> and also for plasmonic devices.<sup>2</sup> To satisfy such requirements, light-assisted, self-organized nanostructure fabrication principles and techniques have been developed.<sup>3,4</sup> One example is the sol-gel synthesis of ZnO quantum dots (QDs) using photo-induced desorption, which yields reduced QD diameter fluctuations.<sup>3</sup> (In Ref. 3, they are called “variations.” We use the term “fluctuations” throughout the paper with the same meaning.) From an application standpoint, the sizes of QDs should be well-controlled to ensure that the quantized energy levels are resonant between adjacent QDs, facilitating efficient optical near-field interactions.<sup>5</sup> Another example of light-assisted nanostructure fabrication is metal sputtering with light irradiation, which yields self-organized, size- and position-controlled metal nanoparticle chains.<sup>4</sup> Arrays of nanoparticles are important in various applications, such as nanophotonic devices,<sup>1</sup> optical far-field to near-field converters,<sup>6</sup> plasmonic light transmission lines,<sup>7</sup> etc. We should also emphasize that common advantages of these light-assisted, self-organized fabrication techniques are their relatively simple experimental setups and superior production throughput compared with, for instance, scanning-based methods, such as those based on electron beams<sup>8</sup> or scanning probes.<sup>9</sup>

The physical mechanisms behind the light-assisted nanostructure formation have been attributed to material desorption<sup>3,10,11</sup> or plasmon resonance between light and matter.<sup>4</sup>

However, stochastic physical processes are also involved, as observed in the experimental data reported below. Also, we consider that stochastic approaches are indispensable to take account of the emergence of ordered structures and the wide range of phenomena observed on the nanoscale in general.<sup>12,13</sup> For example, Söderlund *et al.* demonstrated lognormal size distributions in particle growth processes with a simple statistical model,<sup>12</sup> and Kish *et al.* demonstrated the lognormal distribution of single-molecule fluorescence bursts in micro- and nano-fluidic channels based on a stochastic analysis.<sup>13</sup> Also, a study<sup>14</sup> of the stochastically driven growth of self-organized structures indicates that the spatio-temporal distribution functions have a key role in controlling the shape and width of size distributions within the formations. Cutting the log tails of such distribution functions can contribute to narrower size distributions.

In this Letter, we approach light-assisted nanofabrication from a stochastic standpoint. We build stochastic models taking account of the light-assisted processes that reproduce tendencies consistent with experimental observations. Through such considerations, we obtain critical insights into the order formation on the nanometer scale, which will contribute to the design of nanophotonic devices and systems. Before the discussion, note that the term “size” is used when it is relevant to general indications of physical size, including diameter, whereas the term “diameter” is used when it is relevant to specific experimental results discussed in this Letter.

First, we characterize the light-assisted, self-organized ZnO quantum dot formation, which was experimentally demonstrated in Ref. 3, with a stochastic approach. We first briefly review the experimental observations that have been reported.

Among various methods of fabricating ZnO QDs, synthetic methods using liquid solutions are advantageous because of their need for simple facilities and their high productivity<sup>15</sup> compared with those based on laser ablation,<sup>16</sup>

<sup>a)</sup>Author to whom correspondence should be addressed. Electronic mail: naruse@nict.go.jp.

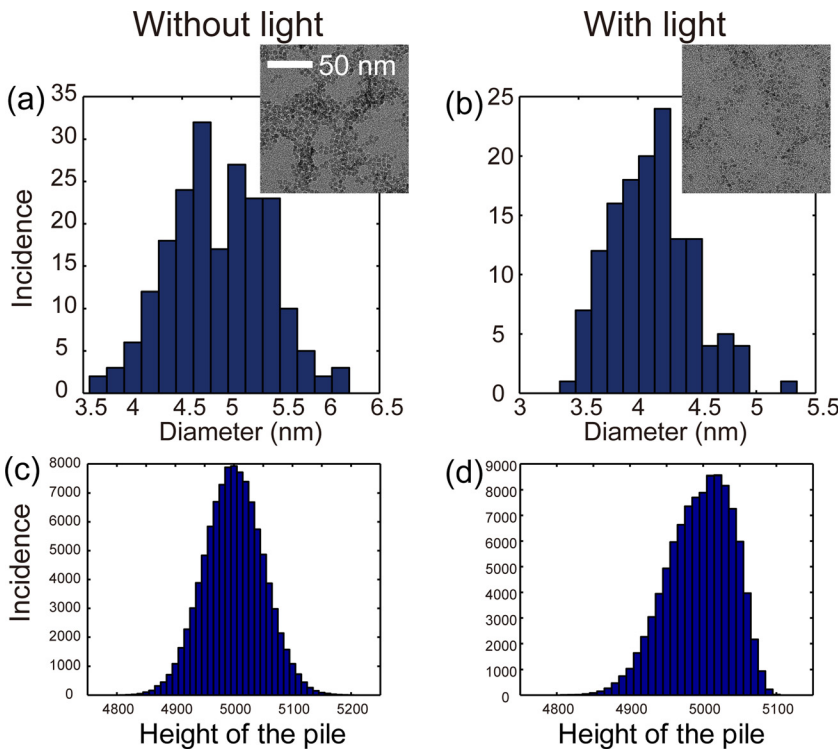


FIG. 1. (a) and (b) Incidence patterns of the diameters of fabricated ZnO QDs formed by a sol-gel method (a) without light illumination and (b) with light irradiation. Insets in (a) and (b), respectively, are transmission electron microscope images of QDs without and with light illumination. With light irradiation, the incidences of the larger-diameter QDs are reduced, i.e., the diameter distribution is skewed. (c) and (d) Incidence patterns of the size distribution generated with the proposed stochastic models. The patterns are consistent with the experimental observations in (a) and (b).

reactive electron beam evaporation,<sup>17</sup> etc. Although the size of the QDs, which is precisely the diameter of the QDs, fluctuates by as much as 25% in conventional sol-gel methods,<sup>15</sup> the light-assisted sol-gel method demonstrated in Ref. 3 reduced the QD diameter fluctuations. When light with a photon energy higher than the bandgap energy is radiated during the ZnO QD formation process, electron-hole pairs could trigger an oxidation-reduction reaction in the QDs, causing the ZnO atoms depositing on the QD surface to be desorbed. In addition, such desorption is induced with a high probability when the formed QDs reach a particular diameter. This light-dependent QD size regulation has also been reported in other material systems, such as CdSe<sup>10</sup> and Si.<sup>11</sup>

The insets in Figs. 1(a) and 1(b), respectively, show transmission electron microscope (TEM) images of fabricated ZnO QDs without and with continuous-wave (CW) light illumination at a wavelength of 325 nm with a power density of 8 mW cm<sup>-3</sup>. The experiments are detailed in Ref. 3. Figures 1(a) and 1(b), respectively, summarize the incidence rate of nanoparticles as a function of their diameter. The diameter fluctuations decreased from 23% to 18% with light irradiation.

What we particularly address in this Letter is that the diameter distributions are different between these two cases. It exhibits behavior similar to a normal distribution without light illumination (Fig. 1(a)), whereas the distribution is skewed with light irradiation; in particular, the incidences at larger diameters decreased (Fig. 1(b)). We investigate the different behavior by means of stochastic modeling, as described below.

First, in the absence of light illumination, we represent the formation process as a statistical pile-up model, as schematically shown in Fig. 2(a). An elemental material that constitutes a nanoparticle is represented by a square-shaped block. Such blocks are grown, or stacked one after another,

with a piling success probability  $p$ ; accordingly, the piling fails with a probability of  $1 - p$ . In other words, if we let the length of the pile at step  $t$  be  $s(t)$ , the piling probability is given by

$$\begin{aligned} P[s(t+1) = s(t) + 1 | s(t)] &= p, \\ P[s(t+1) = s(t) | s(t)] &= 1 - p. \end{aligned} \tag{1}$$

Since this is equivalent to a random walk with drift, after repeating this process with an initial condition  $s(0) = 0$ , the resultant lengths of the piles exhibit a normal distribution, as shown in Fig. 1(c). Specifically, the statistics shown in Fig. 1(c) were obtained by repeating 10 000 steps for 100 000 different trials.

On the other hand, we model the effect of light irradiation in the formation process in the stochastic model as follows. As described above, since the material desorption is likely induced at a particular diameter of nanoparticle,<sup>5</sup> we consider that the piling success rate  $p$  is a function of the diameter, namely the height of the pile. For simplicity, we consider that  $p$ , which represents the deposition success

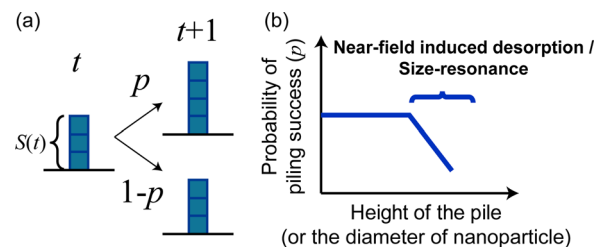


FIG. 2. A stochastic model of light-assisted nanoparticle formation. (a) The growth of the QD is characterized with a one-dimensional pile-up model. The success of the piling depends on probability  $p$ . (b) The effect of light irradiation is modeled by a decrease in the probability  $p$  beyond a certain size of pile, which corresponds to the diameter in the experiment.

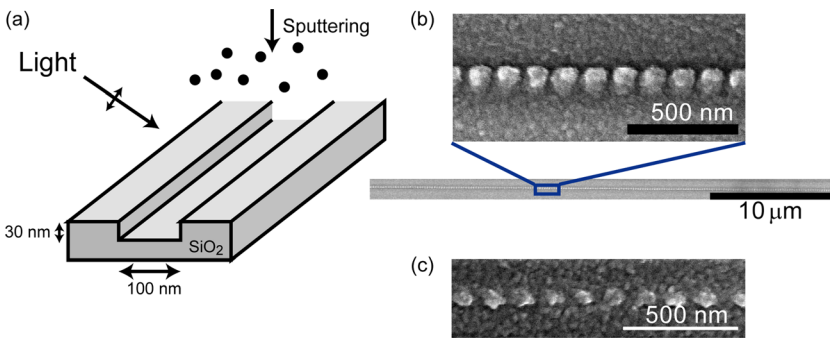


FIG. 3. (a) Schematic diagram of the experimental setup of Al sputtering on a SiO<sub>2</sub> substrate in which a 100 nm-wide, 30 nm-deep groove is formed. During the sputtering, the substrate is irradiated with light having a polarization perpendicular to the direction of the groove. (b) and (c) An array of uniform-diameter, uniform-separation Al nanoparticles is self-organized along the groove, with (b) 2.33 eV light irradiation and (c) 2.62 eV light irradiation.

probability, decreases linearly beyond a certain total height of a pile, as schematically shown in Fig. 2(b). In other words, the material desorption is more likely to be induced beyond a certain pile size due to the resonant effect mentioned above. That is, the probability  $p$  in Eq. (1) is replaced with the following size-dependent probability:

$$p(s(t)) = \begin{cases} c & s(t) \leq R \\ c - \alpha s(t) & s(t) > R \end{cases} \quad (2)$$

where  $c$  and  $\alpha$  are constants. With such a stochastic model, the resultant incidence distributions of the piles is skewed or reduced at larger sizes. In the calculated results shown in Fig. 1(d), we assume  $c = 1/2$  and  $\alpha = 1/250$ . The numerical results obtained through the statistical modeling are consistent with the experimental observations.

Second, in Ref. 4, self-organized formation of an array of ultralong nanoparticle chains was demonstrated based on near-field optical desorption. We first briefly describe our experimental observations. With conventional radio-frequency (RF) sputtering, we deposited aluminum on a glass substrate. A 100 nm-wide and 30 nm-deep groove was formed in the substrate, as schematically shown in Fig. 3(a). Also, the substrate was illuminated with light linearly polarized perpendicularly to the direction of the groove during the RF sputtering. Thanks to the edge of the groove, a strong optical near-field was generated in its vicinity.

A metallic nanoparticle has strong optical absorption because of plasmon resonance,<sup>18–20</sup> which depends strongly on the particle size. This can induce desorption of a deposited metallic material when it reaches the resonant diameter.<sup>21,22</sup> It turns out that as the deposition of the metallic material proceeds, the growth is governed by a tradeoff between deposition and desorption, which determines the particle diameter, depending on the photon energy of the incident light. Consequently, an array of metallic nanoparticles is aligned along the groove, as shown in Fig. 3(b). While radiating CW light with a photon energy of 2.33 eV (wavelength: 532 nm) during the deposition of aluminum, 99.6 nm-diameter, 27.9 nm-separation nanoparticles were formed in a region as long as 100  $\mu\text{m}$ , as shown in Fig. 3(b).

As described above, the origin of the size regulation of the nanoparticles was attributed to the resonance between the nanoparticles and the illuminated light, similarly to the case discussed earlier. At the same time, we consider that although this physical mechanism indeed plays a crucial role, it is not enough to explain the formation of the uniformly formed array structure. To explain such an observa-

tion, we need to extend the stochastic model described above as follows.

In the modeling, we assume a one-dimensional horizontal system that mimics the groove on the substrate. More specifically, it consists of an array of  $N$  pixels with their identity represented by an index  $i$  ranging from 1 to  $N$ . An elemental material to be deposited onto the system, experimentally by the RF sputtering described above, is schematically represented by a square-shaped block. As depicted in Fig. 4(a), the initial condition is a flat structure without any blocks.

At every iteration cycle, the position at which a block arrives is randomly chosen, which we denote  $x$ . We determine the success of the deposition at  $x$  by the following rules. We denote the occupation by a block at position  $x$  of the groove by  $S(x)$ :  $S(x) = 1$  when a block occupies a position  $x$ , and  $S(x) = 0$  when there is no block at position  $x$ . Also, we use the term “cluster” to mean multiple blocks consecutively located along the groove. We also call a single, isolated block in the system a “cluster.”

- (1) When the randomly chosen position  $x$  belongs to one of the cluster(s), namely,  $S(x) = 1$ , we maintain  $S(x) = 1$ . (Fig. 4(b-i))
- (2) Even if  $S(x) = 0$ , when the chosen position  $x$  belongs to a “neighbor” of a cluster with a size greater than a particular number  $B_{th1}$ , the deposition is inhibited. That is, we maintain  $S(x) = 0$  (Fig. 4(b-ii)).
- (3) Even if  $S(x) = 0$ , when the chosen position  $x$  has blocks at both its left and right sides and the total

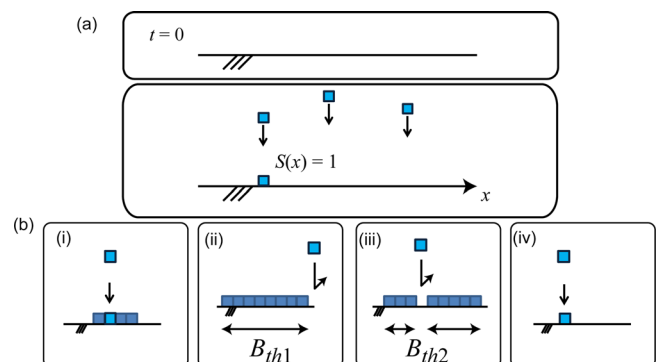


FIG. 4. A stochastic model of the nanoparticle array formation. (a) One-dimensional array in which an elemental block could be deposited at position  $x$ . (b) Rules for successful deposition at a randomly chosen position  $x$ . (b-ii) Deposition is inhibited in neighboring clusters whose size is larger than  $B_{th1}$ . (b-iii) Deposition is inhibited at positions where they see clusters at both the left- and right-hand sides and when the total size of both clusters is larger than  $B_{th2}$ .

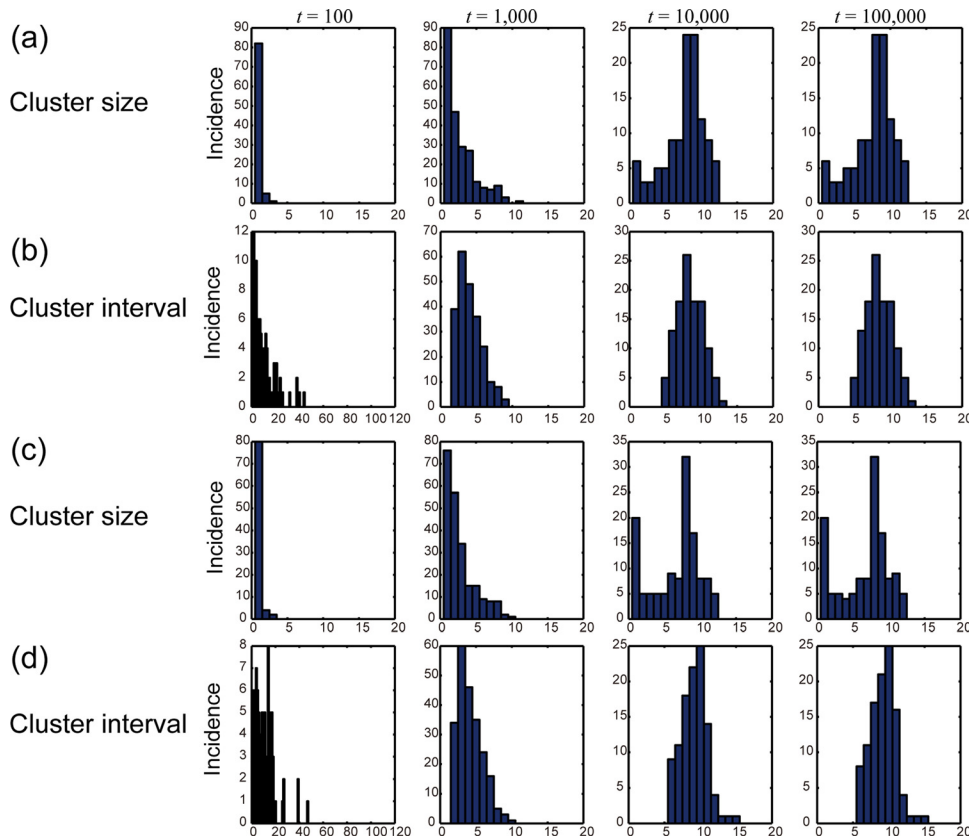


FIG. 5. Evolution of (a) the cluster size and (b) the cluster interval based on a stochastic model. Both the size and the interval converge to incidence patterns that exhibit their maximum at a particular value, which reproduced the size- and separation-controlled, nanoparticle array formations observed experimentally. (c) and (d) Note that the separation of the nanoparticles is greater with higher photon energy (Fig. 3(c), Table I). By modifying rule (ii) of the stochastic modeling, the cluster interval increases, which is consistent with the experimental observations.

number of connected blocks is greater than  $B_{th2}$ , the deposition is inhibited. That is, we maintain  $S(x) = 0$ . (Fig. 4(b-iii))

- (4) In other cases, the deposition at the position  $x$  succeeds; namely,  $S(x) = 1$ . (Fig. 4(b-iv)).

The rules (2) and (3) correspond to the physical effect of the resonance between the material and the light illumination that facilitates desorption of the particle. The optical near-field intensity in the vicinity of a nanostructure follows a Yukawa function,<sup>3</sup> which depends on the material size. Therefore, the optical near-fields promote material desorption or, in effect, inhibit material deposition, beyond a certain size of nanoparticles, which is characterized as rule (2) above. Also, even when a single cluster size is small, meaning that the corresponding near-fields are small, when several such clusters are located in close proximity, a material desorption effect should be induced overall. Such an effect is represented as rule (3) above. One remark here is that we do not pile more than two blocks at a single position  $x$ ; that is to say,  $S(x)$  takes binary values only, since our concern is how the clusters are formed in the 1D system.

Figure 5 shows a numerical demonstration assuming a 1D array with  $N = 1000$ . As statistical values in the simulations, we evaluated the incidence of the cluster size and the center-to-center interval between two neighboring clusters. Figures 5(a) and 5(b) summarize the evolution of these two values at  $t = 100$ ,  $t = 1000$ ,  $t = 10\,000$ , and  $t = 100\,000$ . In the numerical calculations, for the threshold values in rules (2) and (3), we assumed  $B_{th1} = 8$  and  $B_{th2} = 12$ , respectively. We clearly observed that the size and the interval converged to representative values, which are consistent with the experimental observations shown in Fig. 3(b).

Furthermore, as reported in Ref. 4, a similar experiment was conducted with a higher photon energy of 2.62 eV (473 nm) and an optical power of 100 mW, which yielded a 84.2 nm-diameter, 48.6 nm-separation nanoparticle formation. As summarized in Table I, the diameter is slightly reduced, and the nanoparticle distance is enlarged compared with the previous case of lower photon energy (2.33 eV (532 nm)). The reduced diameter of the nanoparticles is attributed to the fact that the higher photon energy leads to desorption at smaller diameters.<sup>4,18</sup> The larger separation between adjacent nanoparticles is, however, not obviously explained.

We presume that a stronger light-matter resonance is induced at a higher photon energy, which more strongly induces material desorption, or inhibits the deposition of materials, in the neighboring clusters. We can take account of this effect by modifying the stochastic model described above. Instead of blocking the deposition at the neighboring positions by rule (2), we consider that distant neighbors are also inhibited (2') Even if  $S(x) = 0$ , when  $x$  sees a cluster with a size greater than a particular number  $B_{th1}$ , within a area (a) between  $x - 3$  and  $x - 1$  or (b) between  $x + 1$  and  $x + 3$ , the deposition is inhibited. That is, we maintain  $S(x) = 0$ .

TABLE I. The diameter and the interval of the nanoparticles obtained with light-assisted Al sputtering.

Assist light	Diameter (nm)	Nanoparticle interval (nm)
2.33 eV (532 nm)	99.6	127.5
2.62 eV (473 nm)	84.2	132.8

While preserving  $B_{th1}$  and  $B_{th2}$  values with the previous example, the cluster size statistics evolve as shown in Fig. 5(c). At the iteration cycles  $t = 10\,000$  and  $100\,000$ , the incidences of single-sized clusters are large. This is due to the strict inhibition rule (2') above, which reduces the chance of clusters growing. Treating such a single-sized cluster as an artifact, or a virtually ignorable element, in the system, we evaluate the cluster-to-cluster interval except for single-sized clusters. The cluster interval converges to a maximum of 10, as shown in Fig. 5(d), which is larger than the previous case, which converged to 8, as shown in Fig. 5(a). This is consistent with the experimental observations. Finally, we make one remark about the dimensions of the models concerned in this Letter. We consider that the 1D models described above characterize the physical principles behind the experimental demonstrations of ZnO QD formation and the Al nanoparticle array formation.

In summary, we developed stochastic models taking account of the optical near-field-based material desorption/deposition between light and matter on the nanometer scale. By using a simple model, the observed behavior of skewed diameter distributions of ZnO quantum dots with light irradiation, and self-organized nanoparticle array formation along a groove were reproduced in the stochastic modeling, providing greater insights into the order formation occurring on the nanometer scale. We consider that such modeling will be applicable to other light-assisted material formation processes and will be beneficial in the design of future nanophotonic devices and systems. For example, phonon-assisted near-field processes generated characteristic surface morphology.<sup>23</sup> Further investigation based on a stochastic viewpoint will be more important in the future.

This work was supported in part by Grants-in-Aid for Scientific Research from the Japan Society for the Promotion of Science (JSPS) and the Strategic Information and Com-

munications R&D Promotion Programme (SCOPE) of the Ministry of Internal Affairs and Communications, Japan.

- <sup>1</sup>M. Ohtsu, T. Kawazoe, T. Yatsui, and M. Naruse, *IEEE J. Sel. Top. Quantum Electron.* **14**, 1404 (2008).
- <sup>2</sup>E. Ozbay, *Science* **311**, 189 (2006).
- <sup>3</sup>Y. Liu, T. Morishima, T. Yatsui, T. Kawazoe, and M. Ohtsu, *Nanotechnology* **22**, 215605 (2011).
- <sup>4</sup>T. Yatsui, W. Nomura, and M. Ohtsu, *Nano Lett.* **5**, 2548 (2005).
- <sup>5</sup>M. Naruse, T. Kawazoe, R. Ohta, W. Nomura, and M. Ohtsu, *Phys. Rev. B* **80**, 125325 (2009).
- <sup>6</sup>W. Nomura, M. Ohtsu, and T. Yatsui, *Appl. Phys. Lett.* **86**, 181108 (2005).
- <sup>7</sup>L. A. Sweatlock, S. A. Maier, H. A. Atwater, J. J. Penninkhof, and A. Polman, *Phys. Rev. B* **71**, 235408 (2005).
- <sup>8</sup>T. Ishikawa, S. Kohmoto, and K. Asakawa, *Appl. Phys. Lett.* **73**, 1712 (1998).
- <sup>9</sup>T. Yatsui, T. Kawazoe, M. Ueda, Y. Yamamoto, M. Kouroggi, and M. Ohtsu, *Appl. Phys. Lett.* **81**, 3651 (2002).
- <sup>10</sup>T. Torimoto, S. Murakami, M. Sakuraoaka, K. Iwasaki, K. Okazaki, T. Shibayama, and B. Ohtan, *J. Phys. Chem. B* **110**, 13314 (2006).
- <sup>11</sup>H. Koyama and N. Koshida, *J. Appl. Phys.* **74**, 6365 (1993).
- <sup>12</sup>J. Söderlund, L. B. Kiss, G. A. Niklasson, and C. G. Granqvist, *Phys. Rev. Lett.* **80**, 2386 (1998).
- <sup>13</sup>L. L. Kish, J. Kameoka, C. G. Granqvist, and L. B. Kish, *Appl. Phys. Lett.* **99**, 143121 (2011).
- <sup>14</sup>J. Kertesz and L. B. Kiss, *J. Phys. A* **23**, L433 (1990).
- <sup>15</sup>E. A. Meulenkaamp, *J. Phys. Chem. B* **102**, 5566 (1998).
- <sup>16</sup>S. Besner, A. V. Kabashin, F. M. Winnik, and M. Meunier, *Appl. Phys. A* **93**, 955 (2008).
- <sup>17</sup>H. Z. Wu, D. J. Qiu, Y. J. Cai, X. L. Xu, and N. B. Chen, *J. Cryst. Growth* **245**, 50 (2002).
- <sup>18</sup>T. Yatsui, S. Takubo, J. Lim, W. Nomura, M. Kouroggi, and M. Ohtsu, *Appl. Phys. Lett.* **83**, 1716 (2003).
- <sup>19</sup>A. Wokaun, J. P. Gordon, and P. F. Liao, *Phys. Rev. Lett.* **48**, 957 (1982).
- <sup>20</sup>G. T. Boyd, T. Rasing, J. R. R. Leite, and Y. R. Shen, *Phys. Rev. B* **30**, 519 (1984).
- <sup>21</sup>J. Bosbach, D. Martin, F. Stietz, T. Wenzel, and F. Träger, *Appl. Phys. Lett.* **74**, 2605 (1999).
- <sup>22</sup>K. F. MacDonald, V. A. Fedotov, S. Pochon, K. J. Ross, G. C. Stevens, N. I. Zheludev, W. S. Brocklesby, and V. I. Emel'yanov, *Appl. Phys. Lett.* **80**, 1643 (2002).
- <sup>23</sup>M. Naruse, T. Kawazoe, T. Yatsui, N. Tate, and M. Ohtsu, *Appl. Phys. B* **105**, 185 (2011).

# Direct observation of optical excitation transfer based on resonant optical near-field interaction

W. Nomura · T. Yatsui · T. Kawazoe · M. Naruse ·  
E. Runge · C. Lienau · M. Ohtsu

Received: 21 February 2012 / Published online: 21 April 2012  
© Springer-Verlag 2012

**Abstract** This article reports the direct observation of long-distance optical excitation transfer based on resonant optical near-field interactions in randomly distributed quantum dots (QDs). We fabricated optical excitation transfer paths based on randomly distributed QDs by using CdSe/ZnS core-shell QDs and succeeded for the first time in obtaining output signals resulting from a unidirectional optical excitation transfer length of 2.4  $\mu\text{m}$ . Furthermore, we demonstrate that the optical excitation transfer occurs via the resonant excited levels of the QDs with a comparative experiment using non-resonant QDs. This excitation-transfer mechanism allows for intersecting, non-interacting nano-optical wires.

## 1 Introduction

Novel optical devices, nanofabrication technologies, and systems utilizing energy transfer between nanomaterials by means of optical near field have been developed during recent years [1]. Several theoretical studies performed in parallel with the advancements in near-field technologies describe the optical near field as a field in which a material excitation is coupled with photons and which may be appropriately viewed as photons carrying a material excitation (dressed photons) [2]. According to the dressed photon theory, optical near-field interactions, i.e. the transfer of electromagnetic energy through near-field interactions between nanomaterials, is interpreted as the exchange of dressed photons. Since dressed photons that occur in nanomaterials are localized in nanometric dimensions [3], the long-wavelength approximation that has been used for conventional light–electron interactions does not hold. In particular, it is possible to excite electrons and excitons to energy levels that are dipole-forbidden [4]. This has brought about qualitative innovations in optical devices and their applications. One example of a recently developed practical nanophotonic device that operates based on this property is a nanodimensional logic gate array that operates at room temperature [5].

In order to utilize optical near-field excitation transfer based on the exchange of dressed photons for a device or a system, it is necessary to pay sufficient care to the transfer of optical signals between functional elements. In order to ensure stability of a nanophotonic device, which operates based on very weak signals, wiring (we use the term to include optical signal connections) that does not involve signal reflections from the subsequent stage is required. In general, it is difficult to eliminate such signal reflections in optical waveguides, such as those using surface plasmon polaritons or photonic crystals [6, 7]. A substantial challenge consists

---

W. Nomura (✉) · T. Yatsui · T. Kawazoe · M. Ohtsu  
School of Engineering, The University of Tokyo, Bunkyo-ku,  
Tokyo 113-8656, Japan  
e-mail: [nomura@nanophotonics.t.u-tokyo.ac.jp](mailto:nomura@nanophotonics.t.u-tokyo.ac.jp)

W. Nomura · T. Yatsui · T. Kawazoe · M. Ohtsu  
The Nanophotonics Research Center, The University of Tokyo,  
Bunkyo-ku, Tokyo 113-8656, Japan

M. Naruse  
National Institute of Information and Communications  
Technology, 4-2-1 Nukui-kita, Koganei, Tokyo 184-8795, Japan

E. Runge  
Institut für Physik, Technische Universität Ilmenau,  
98693 Ilmenau, Germany

C. Lienau  
Institut für Physik, Carl von Ossietzky Universität,  
26111 Oldenburg, Germany



in enabling signal transfer over long distances, exceeding the wavelength, for the purpose of connecting between a macrodimensional external system and a nanodimensional device [8], etc.

A promising nanophotonic signal transfer path satisfying this demand is an optical energy transfer path (nanophotonic signal transfer device) based on the exchange of dressed photons between quantum dots (QDs) having discrete excited energy levels [9]. In this signal transfer device, optical signals exist as optical excitations in QDs and are transferred by successive optical near-field interactions between QDs. In such devices, the optical signals do not exhibit wave-like behavior since near-field exchange occurs on time scales exceeding the QD dephasing time. Therefore, operation is possible with a wiring width less than the diffraction limit, and unidirectional light transfer is possible by inter-sublevel relaxation at the output QD.

Our previous research demonstrated experimentally and through numerical calculations that long-distance optical excitation transfer is possible by using randomly distributed QDs with the same diameters (QD1) and a larger-diameter QD having a resonant level (QD2) [10]. At that time, we did not fabricate or evaluate any nanophotonic signal transfer device having an output terminal. However, using CdSe/ZnS core-shell QDs as an example we succeeded to demonstrate optical excitation transfer at a distance greater than  $5\ \mu\text{m}$  by measuring the excitation picked up by a dot QD2 fixed to a fiber probe as a function of the distance from the excitation spot where the QD1 were illuminated. Presumably, the optical excitation is transferred efficiently since it reaches the output dot QD2 via a path with particularly short distances between the randomly positioned QDs, along which optical near-field interactions are intense. Based on this principle, arbitrarily shaped optical wirings can be implemented with very low energy consumption, in contrast with other spatial excitation transfer schemes such as via GaAs quantum wells [11]. This optical excitation transfer based on a random distribution is a very promising technology for implementing the nanophotonic signal transfer device described above.

In the research reported here, we designed and fabricated a structure for the purpose of a quantitative study of guided optical excitation transfer based on optical near-field interactions between quantum dots of different size randomly distributed in certain areas on a substrate. Measuring the intensity of emission from QD2 outside of the device, we succeeded in obtaining an output signal that had been transferred over a distance of several wavelengths, in the form of propagating light. Furthermore, we confirmed the selectivity of the optical excitation transfer through a comparative experiment using a QD pair not having resonant energy levels.

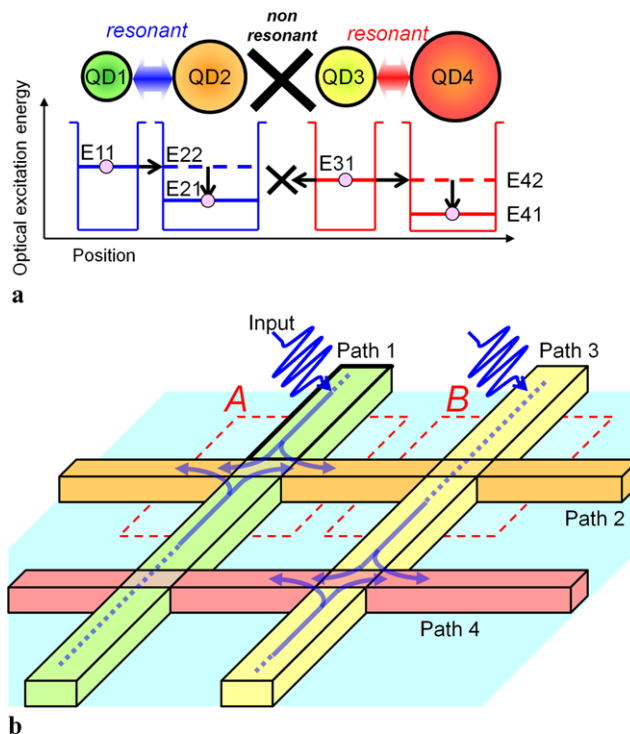


**Fig. 1** Schematic illustrations of (a) energy levels and (b) selective transfer at intersections of optical excitation transfer paths

## 2 Principles of optical near-field excitation transfer in QDs

Figure 1a shows the principles of energy transfer using resonant energy levels: a quantum dot QD1 having diameter  $d_1$  and a quantum dot QD2 having diameter  $d_2$  larger than  $d_1$  are disposed in proximity to each other, and optical excitation occurs in the quantum dot QD1. The ground level E11 of the excitons of QD1 and the first excited level E22 of the excitons of QD2 are resonant with each other, enabling optical excitation transfer via optical near-field interactions. This is the case, e.g., for spherical QDs if the ratio of the diameters of the QDs is approximately  $d_2 = 1.43 \times d_1$  [12]. The optical excitation transferred from E11 to E22 immediately relaxes to a more stable predetermined level E21 in QD2, preventing reverse flow of the optical excitation to QD1.

Based on this principle, long-distance optical energy transfer is possible by using a structure in which a large number of quantum dots QD1 are arranged in a line and a quantum dot QD2, used as an optical marker, is provided at the end of this line [10]. Since the intensity of optical near-field interactions is represented by a Yukawa function of the distance between QDs, the intensity of direct transfer changes exponentially with the distance. Therefore, the transfers via the QDs with the shortest distance among the randomly distributed quantum dots QD1, i.e. via the QDs

with the highest efficiency of optical near-field energy transfer, contribute dominantly to the optical excitation transfer. Furthermore, although optical near-field excitation transfer between the quantum dots QD1 occurs bidirectionally, the optical excitation transfer is unidirectional at the quantum dot QD2 as a terminal, so that the destination of optical excitation transfer by all QDs is fixed. By utilizing this property, it is expected that an optical excitation transfer path can be readily fabricated since it is not necessary to precisely position either QD1 or QD2.

In addition, since optical near-field interactions occur only between resonant levels, selectivity of optical excitation transfer is expected: now, assume the presence of another resonant QD pair, QD3 and QD4, with diameters  $d_3$  and  $d_4$  (see Fig. 1a). If the diameters satisfy the condition  $d_1 < d_3 < d_2 < d_4$ , QD3 does not have an energy level that is resonant with QD1 or QD2. Therefore, optical near-field interactions are very weak, even if QD3 is placed in proximity to QD1 or QD2; thus, optical excitation transfer does not occur. Therefore, QD3 and QD4 can exchange optical excitation independently of QD1 and QD2. That is, optical excitation introduced into the quantum dots QD1 is not transferred even if QD3 or QD4 is located in proximity to them, and the optical excitation is finally transferred only to QD2. Thus, an optical excitation transfer path through QDs with well-chosen parameters can exhibit selectivity of the signal transfer destination.

As an example, Fig. 1b shows a schematic illustration of optical excitation transfer paths consisting of two channels of QDs with intersections. Referring to the figure, quantum dots QD1 to QD4 are individually distributed at random in proximity to each other in the areas of paths 1 to 4, so that two types of QDs coexist at the path intersections. In this device, when optical excitation is introduced to QD1 on path 1, as described earlier, an optical signal is transferred through path 1 by optical near-field interactions among the quantum dots QD1. At the intersection with path 2, unidirectional energy transfer from QD1 to QD2 occurs, so that the optical signal is transferred to path 2 (part A in the figure). At the intersection between paths 1 and 4, however, the signal does not transfer since QD1 and QD4 are non-resonant. Similarly, an optical signal introduced into path 3 is transferred to path 4 but is not transferred to path 2 (part B in the figure). Hence, each optical excitation in the different QDs autonomously selects its transfer destination. Optical excitations in non-resonant QDs do not interfere with each other and it is therefore expected that wires can be crossed without any interactions.

The properties of the above-described optical excitation transfer paths are unique to optical near-field interactions and seem difficult to be realized with all-optical waveguides.

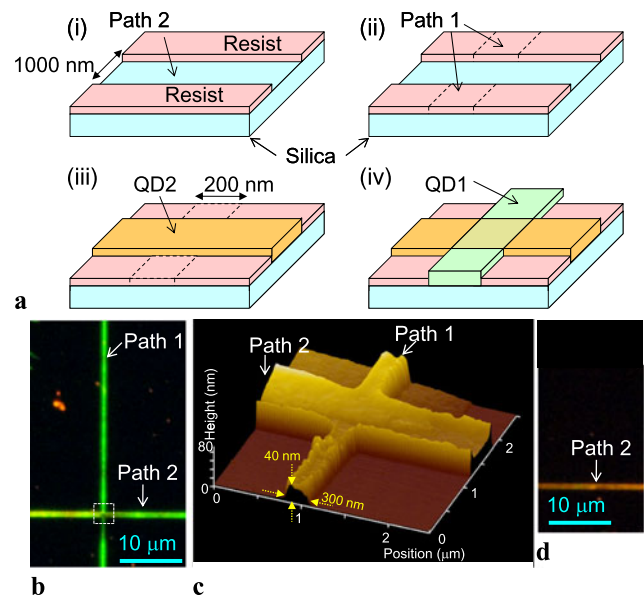


**Fig. 2** (a) Schematic illustration of the procedure for fabricating samples. (b) Fluorescence microscope image of sample A. (c) Atomic force microscope image of sample A. (d) Fluorescence microscope image of sample C

### 3 Experiments and discussion

In order to evaluate the above-described optical excitation transfer properties of QDs, we conducted an experiment for actually confirming the difference in optical excitation transfer behavior in parts A and B shown in Fig. 1b. For the purpose of this experiment, we used CdSe/ZnS core-shell QDs (manufactured by Quantum Design, Inc.). As materials for QD1, QD3, and QD2 described above, those with central emission wavelengths of  $\lambda_1 = 537$  nm,  $\lambda_3 = 547$  nm, and  $\lambda_2 = 585$  nm were used. The outside of the shells was modified with an organic molecule carboxyl group. A sample in which QDs were placed in proximity to each other with gaps between them was obtained by drying drops of a solution. Using a transmission electron microscope, we estimated that the average distance between the centers of QDs closest to each other was about 10.4 nm. The distance is well within the effective field of optical near-field interactions calculated with Yukawa-function parameters appropriate for CdSe/ZnS core-shell QDs [3]. Yet, it is far too large to expect significant tunnel coupling between adjacent QDs.

We fabricated sample A, corresponding to part A in Fig. 1b, by the procedure described below and shown in Fig. 2a.

1. Electron-beam resist (ZEP-520A) was spin coated to a thickness of about 100 nm on a synthetic silica substrate and was baked at 180 °C for 240 s.
2. Path 2 with a width of 1000 nm was drawn by an electron-beam (EB) lithography system.

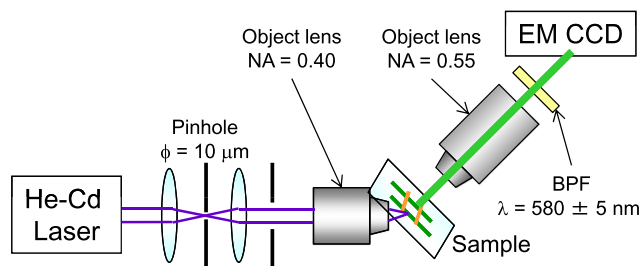


**Fig. 3** Schematic illustration of the experimental measurement system

3. Path 2 was developed by immersing it in a developer (Fig. 2a (i)).
4. By using the EB lithography system, path 1 with a width of 200 nm was drawn so as to perpendicularly intersect path 2 (Fig. 2a (ii)).
5. Drops of QD2 solution were dropped onto the substrate and were left for one minute, and then the remaining drops on the resist were blown away (Fig. 2a (iii)).
6. Path 1 was developed by immersing it in a developer.
7. Drops of QD1 solution were dropped onto the substrate and were left for one minute, and then the remaining drops on the resist were blown away (Fig. 2a (iv)).
8. The sample was immersed in resist cleaner (solvent ZEP-A) to remove the electron-beam resist.

Since the ZEP-520A film was hardly wetted with the QD solution, QDs were obtained almost exclusively on the paths in steps 5 and 7 (Fig. 2a (iii) and (iv)). Note that the QD1 which were distributed in path 2, where QD2 were already distributed in step 5, do not affect the optical excitation transfer properties since the optical excitation that reaches path 2 is all transferred to QD2, which is more stable.

Figure 2b shows a fluorescence microscopic image of the fabricated sample A excited with a mercury lamp. QD1 were randomly distributed in proximity to each other on path 1 and are seen to emit in green color. QD2 on the other hand were randomly distributed on top of a QD1 layer in path 2, shifting the emission in this region towards yellow. Figure 2c shows the result of scanning the area indicated by a white dotted line in Fig. 2b by an atomic force microscope (AFM). The result revealed that QDs were distributed in a region with a width of 300 nm and a height of 40 nm in the section of path 1. Furthermore, by using QD3 solution instead of QD1 solution in step 7 in a similar process, we fabricated sample B corresponding to part B in Fig. 1b. In addition, as a comparative example, we fabricated sample C in which only path 2 was present. Figure 2d shows a fluorescence microscopic image of sample C, revealing the yellow emission of QD2 only.

These samples were then used to experimentally study optically induced near-field energy transfer processes. The experimental setup is shown in Fig. 3. The sample substrate was irradiated by CW He-Cd laser light (wavelength

$\lambda = 325$  nm) from the back side of the substrate at oblique incidence. The laser beam was beforehand shaped by a pinhole with a diameter of 10  $\mu\text{m}$  and excited QD1 by irradiating path 1 with an objective lens with NA = 0.4. The objective lens was scanned in a range of  $-2 \mu\text{m} < L < 15 \mu\text{m}$ , where  $L$  denotes the distance between the irradiation spot and the intersection of paths 1 and 2. The laser power was 450 nW, and the diameter of the irradiation spot was 2  $\mu\text{m}$ . The optical excitation generated by the excitation light was transferred along path 1 and was transferred to QD2 in part A, emitting light from the ground level E21 of QD2 ( $\lambda_2 = 585$  nm). The light emission from E21 was observed with an electron-multiplying CCD camera (Hamamatsu ImageEM C9100-13H, Hamamatsu Photonics K.K.) by using an objective lens with NA = 0.55 and a band-pass filter with a center wavelength of  $580 \pm 5$  nm, i.e. near  $\lambda_2$ . The format of acquired images was  $512 \times 512$  pixels, 16-bit grayscale, with a resolution of 0.37  $\mu\text{m}/\text{pixel}$ .

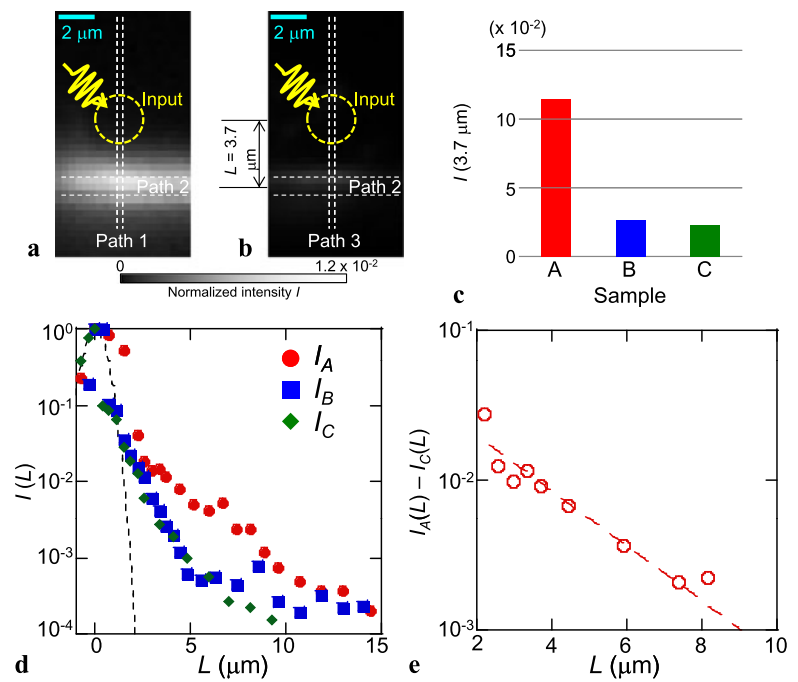
We evaluated the efficiency of the optical excitation transfer by studying the dependence of the intensity  $I$  of light emission from QD2 as a function of its distance  $L$  from the excitation spot. More specifically,  $I$  is the peak value in CCD images which is observed at the path intersection. A difference in the density of QD2 among the samples was compensated for by normalization by the value at  $L = 0 \mu\text{m}$ . Finally, we define as a performance metric the distance  $L_0$  at which the light emission intensity  $I(L)$  has decreased to  $1/e$  (see below).

As examples of the measurement results, Fig. 4a and b show CCD images of sample A (the intersection between paths 1 and 2, where QD1 and QD2 are resonant) and sample B (the intersection between paths 3 and 2, where QD3 and QD2 are non-resonant) obtained at  $L = 3.7 \mu\text{m}$ . The color scale was normalized in the previously discussed manner. Since a band-pass filter transparent at E21 was used, light emission is not observed in paths 1 and 3 and is observed mainly at the intersections.

Comparing samples A and B, we find generally much stronger light emission from sample A having a resonant level with, e.g.,  $I_A(3.7 \mu\text{m}) = 1.1 \times 10^{-2}$  and  $I_B(3.7 \mu\text{m}) = 2.6 \times 10^{-3}$ , respectively (Fig. 4c). Furthermore, in a similar measurement performed on sample C, which did not have optical excitation transfer paths corresponding to paths 1 and 3, we obtained  $I_C(3.7 \mu\text{m}) = 2.3 \times 10^{-3}$ , exhibiting essentially the same value as sample B (Fig. 4c). Since QD2 in sample C were directly excited by stray laser light, presumably, direct optical excitation of QD2 was also dominant in sample B and the optical near-field excitation transfer from QD3 through path 3 was very small.

Figure 4d shows the results of plotting the measured values of  $I_A(L)$ ,  $I_B(L)$ , and  $I_C(L)$  evaluated and normalized as described, i.e.  $I_A(0) = I_B(0) = I_C(0) = 1$ . No substantial differences were observed among  $I_A(L)$ ,  $I_B(L)$ , and  $I_C(L)$

**Fig. 4** (a) and (b) CCD images of samples A and B, respectively, observed at  $L = 3.7 \mu\text{m}$ . The *white dotted lines* mark the paths, the *yellow dashed circles* represent the irradiation positions of incident light. (c) Peak value  $I(L)$  of the intensity of light emission from QD2, obtained at  $L = 3.7 \mu\text{m}$ . (d)  $I(L)$  in samples A, B, and C, where the *red circles*, *blue rectangles*, *green rhombuses* represent  $I_A(L)$ ,  $I_B(L)$ , and  $I_C(L)$ , respectively, and the *black dotted line* represents a Gaussian distribution with a width of  $2 \mu\text{m}$ . (e) Component  $I_A(L) - I_C(L)$  of  $I_A(L)$  associated with optical near-field interactions, where the *dashed line* represents a single-exponential attenuation curve



for  $L < 2 \mu\text{m}$ . In this region, the emission profile matches the  $2\text{-}\mu\text{m}$ -diameter Gaussian beam profile of the excitation laser (dashed line in Fig. 4d) rather well and direct optical excitation of QD2 dominates over near-field excitation transfer. In sample C, no excitation transfer occurs and the weak signal for  $L > 2 \mu\text{m}$  in this sample thus represents a background signal reflecting limitations of our setup. The signal recorded in sample B in this region is very similar and we therefore conclude that the effect of energy transfer from path 3 to path 2 in sample B can be disregarded. Thus, we confirmed that optical excitation transfer based on optical near-field interactions is strongly suppressed between QDs not having resonant energy levels, demonstrating selectivity of the optical excitation transfer destination with QDs.

In the range  $L > 2 \mu\text{m}$ ,  $I_A(L)$  clearly exceeds the other two. In order to quantify this effect, Fig. 4e shows the results of subtracting the background-dominated signal  $I_C(L)$  from  $I_A(L)$ . As expected,  $I_A(L) - I_C(L)$  decreases monotonically with increasing  $L$ . It can be approximated by a single-exponential attenuation curve indicated by a dotted straight line in the logarithmic plot of Fig. 4e. From its slope, we obtain the optical excitation transfer distance  $L_0$  at which the optical excitation energy was reduced to  $1/e$  as  $L_0 = 2.4 \mu\text{m}$ . This value shows a good agreement with the transfer distance calculated according to our previous study [10] using a QD-center distance of  $10.4 \text{ nm}$ , a width of  $300 \text{ nm}$ , and a height of  $40 \text{ nm}$  of path 1. This indicates that the optical energy transfer observed in sample A presumably occurred through optical excitation transfer based on optical near-field interactions. Our results demonstrate that sample A, in which QD1 and QD2 were distributed at random, op-

erates as an optical excitation transfer path that can function at dimensions less than or equal to the diffraction limit, that is, with a width of  $300 \text{ nm}$  and a height of  $40 \text{ nm}$ . From these results, we believe that we succeeded in demonstrating that optical excitation transfer in randomly distributed QDs has properties unique to optical near-field interactions between resonant energy levels.

## 4 Conclusion

In summary, we fabricated a structure containing excitation paths formed by randomly distributed QDs and evaluated the optical excitation transfer properties. When two types of CdSe/ZnS core-shell QDs having resonant energy levels, namely, QD1 and QD2, were used, we succeeded in observing a directed optical excitation transferred by optical near-field interactions as propagating light emitted as an output signal from QD2. The transfer distance was estimated to be  $2.4 \mu\text{m}$ . When using QDs with non-resonant energy levels, however, near-field optical excitation transfer was greatly reduced. These results demonstrate that optical excitation transfer in QDs occurs via excited levels of the QDs. Thus, it is possible to readily fabricate an optical excitation transfer path by randomly distributing QDs and to implement the functionality for selecting the signal transfer destination by utilizing non-resonant levels. These properties will be very effective in nanophotonic signal transfer devices, and randomly distributed QDs appear as a promising candidate technology for implementing these features. In order to further increase the optical excitation transfer distance, appropriate QD designs and surface treatments should

be chosen. Specifically, it will be effective to use QDs with a longer exciton lifetime and to change the surface-modifying group on the QDs in order to reduce the interdot distance. Work along those directions is underway in our laboratories.

**Acknowledgements** This work was financially supported by JST and DFG under the Strategic Japanese–German Cooperative Program, and by MEXT under the Special Coordination Funds for Promoting Science and Technology. T. Yatsui was financially supported by a Grant-in-Aid for Young Scientists (A) from MEXT, and by a research grant (Basic Research) from the TEPCO Memorial Foundation.

## References

1. M. Ohtsu, T. Kawazoe, T. Yatsui, M. Naruse, *IEEE J. Sel. Top. Quantum Electron.* **14**, 1404 (2008)
2. Y. Tanaka, K. Kobayashi, *J. Microsc.* **229**, 228 (2008)
3. K. Kobayashi, M. Ohtsu, *J. Microsc.* **194**, 249 (1999)
4. U. Hohenester, G. Goldoni, E. Molinari, *Phys. Rev. Lett.* **95**, 216802 (2005)
5. T. Kawazoe, M. Ohtsu, S. Aso, Y. Sawado, Y. Hosoda, K. Yoshizawa, K. Akahane, N. Yamamoto, M. Naruse, *Appl. Phys. B* **103**, 537 (2011)
6. R. Waele, S.P. Burgos, H.A. Atwater, A. Polman, *Opt. Express* **18**, 12770 (2010)
7. P.I. Borel, A. Harpøth, L.H. Frandsen, M. Kristensen, *Opt. Express* **12**, 1996 (2004)
8. S.A. Maier, P.G. Kik, H.A. Atwater, S. Meltzer, E. Harel, B.E. Koel, A.A.G. Requicha, *Nat. Mater.* **2**, 229 (2003)
9. T. Yatsui, Y. Ryu, T. Morishima, W. Nomura, T. Kawazoe, T. Yonezawa, M. Washizu, H. Fujita, M. Ohtsu, *Appl. Phys. Lett.* **96**, 133106 (2010)
10. W. Nomura, T. Yatsui, T. Kawazoe, M. Naruse, M. Ohtsu, *Appl. Phys. B* **100**, 181 (2010)
11. A. Richter, G. Behme, M. Süptitz, Ch. Lienau, T. Elsaesser, M. Ramsteiner, R. Nötzel, K.H. Ploog, *Phys. Rev. Lett.* **79**, 2145 (1997)
12. N. Sakakura, Y. Masumoto, *Phys. Rev. B* **56**, 4051 (1997)

# Observing the localization of light in space and time by ultrafast second-harmonic microscopy

Manfred Mascheck<sup>1</sup>, Slawa Schmidt<sup>1</sup>, Martin Silies<sup>1</sup>, Takashi Yatsui<sup>2</sup>, Kokoro Kitamura<sup>2</sup>, Motoichi Ohtsu<sup>2</sup>, David Leipold<sup>3</sup>, Erich Runge<sup>3</sup> and Christoph Lienau<sup>1\*</sup>

**Multiple coherent scattering and the constructive interference of certain scattering paths form the common scheme of several remarkable localization phenomena of classical and quantum waves in randomly disordered media<sup>1</sup>. Prominent examples are electron transport in disordered conductors<sup>2,3</sup>, the localization of excitons in semiconductor nanostructures<sup>4,5</sup>, surface plasmon polaritons at rough metallic films<sup>6,7</sup> or light in disordered dielectrics<sup>8–11</sup> and amplifying media<sup>1,12–14</sup>. However, direct observation of the fundamental spatiotemporal dynamics of the localization process remains challenging<sup>15</sup>. This holds true, in particular, for the localization of light occurring on exceedingly short femtosecond timescales and nanometre length scales. Here, we combine second harmonic microscopy with few-cycle time resolution to probe the spatiotemporal localization of light waves in a random dielectric medium. We find lifetimes of the photon modes of several femtoseconds and a broad distribution of the local optical density of states, revealing central hallmarks of the localization of light.**

Multiple coherent scattering of light is both ubiquitous and elusive at the same time. Prominent examples include the colours of opals, random lasers, and the famous Brocken spectres—halo-like glories around shadow images seen on misty mountain clouds. Quite generally<sup>16</sup>, whenever light (or any other classical or quantum-mechanical wave) interacts with a dense collection of static, random scatterers, multiple coherent scattering and wave interference results in an increased probability of it returning to the same point or to be scattered in the back-direction<sup>10,11</sup>. This can lead to pronounced spatial fluctuations of the local density of states (LDOS) and to wavefunctions or optical mode profiles that are exponentially localized and of fractal shape<sup>17,18</sup>. The energies  $\hbar\omega_n$  of modes localized in the same region are strongly correlated and depend sensitively on the dimensionality and geometric size of the system as well as its symmetry with respect to time reversal. The local electric field at position  $\mathbf{r}$  inside the sample can be expressed in terms of the lifetime  $T_{1n}$  and the field profile  $E_n(\mathbf{r})$  of the individual eigen modes:

$$E(\mathbf{r}, t) = \sum_n E_n(\mathbf{r}) \exp(-i\omega_n t) \exp(-t/2T_{1n}) \quad (1)$$

Such field intensities show unusually broad statistical distributions. Various imaging techniques have been used successfully to map field distributions<sup>8,19</sup> and to probe statistical signatures of photon localization<sup>20</sup>. Ultrasound transmission through three-dimensional media, for example, has shown a transition from a Rayleigh to a stretched exponential distribution of speckle intensities<sup>21</sup>. Together with the concomitant increase in fluctuations, this characterizes the transition between weak and strong localization. This is

quantitatively described by predictions<sup>22</sup> based on one-parameter scaling<sup>23</sup> with the dimensionless conductance  $g$  as the natural measure of disorder strength.

Considerably less is known about temporal aspects of light localization on an ultrafast, femtosecond timescale. In the present work, we combine high-resolution nonlinear optical microscopy with few-cycle time resolution to probe the lifetimes of localized photon modes in random dielectric nanostructures. We demonstrate our approach for a densely packed disordered array of zinc oxide nanoneedles (Fig. 1a).

Zinc oxide, a wide-gap semiconductor with a bandgap of 3.3 eV, is an essentially transparent medium throughout the visible and near-infrared. With its large refractive index of  $n = 1.96$  at 800 nm, it is a strong light scatterer and a prototypical random lasing material<sup>13,14</sup>. Moreover, ZnO nanostructures have large second-harmonic coefficients<sup>24</sup>, making them ideal for probing the local electric field inside a sample by means of the emitted second-harmonic radiation.

We investigated randomly distributed arrays of  $\sim 300$ -nm-long ZnO needles with an average separation of 100 nm grown on a base of larger rods on a sapphire substrate (Fig. 1b,c). By controlling the substrate temperature<sup>25</sup>, the needle diameter was reduced to 30–50 nm so that the needles could act as structureless point scatterers, avoiding light localization within individual needles.

We focused linearly  $p$ -polarized ultrashort 6 fs laser pulses (centre wavelength, 800 nm, far below the ZnO bandgap) to a diffraction-limited spot with a diameter of  $\sim 1 \mu\text{m}$  on the sample<sup>26</sup>. Local second-harmonic spectra were recorded in a reflection geometry while raster-scanning the sample through the focus. A two-dimensional map of the total, spectrally integrated second-harmonic intensity (Fig. 2a) shows pronounced spatial fluctuations. The second-harmonic emission  $I_{SH}$  is localized in certain hot spots, randomly distributed across the sample. In some spots the intensity exceeds by a factor of more than 30 the average  $\langle I_{SH} \rangle$ , which is dominated by a weak background, probably from the base layer. The typical diameter of a single emission spot is only 500 nm (Fig. 2b), limited by the microscope resolution. The intensity and spectral shape of the second harmonic both fluctuate from spot to spot (Fig. 2c), another strong signature of photon localization within the ZnO array<sup>6</sup>.

To time-resolve the localized photon field, we used a pair of phase-locked and time-delayed 6 fs pulses focused to a  $1 \mu\text{m}$  spot. The resulting second-harmonic emission was spectrally resolved and monitored as a function of the detection wavelength  $\lambda$  and the time delay  $\tau$ . The resulting interferometric frequency-resolved autocorrelation (IFRAC) trace<sup>27</sup> can be written as

$$I_{\text{IF}}(\lambda, \tau) = \left| \int E_{\text{NL}}(t, \tau) \cdot \exp(-i2\pi ct/\lambda) dt \right|^2$$

<sup>1</sup>Institut für Physik and Center of Interface Science, Carl von Ossietzky Universität, 26129 Oldenburg, Germany, <sup>2</sup>School of Engineering, University of Tokyo, 113-8656 Tokyo, Japan, <sup>3</sup>Institut für Physik, Technische Universität Ilmenau, 98684 Ilmenau, Germany. \*e-mail: christoph.lienau@uni-oldenburg.de

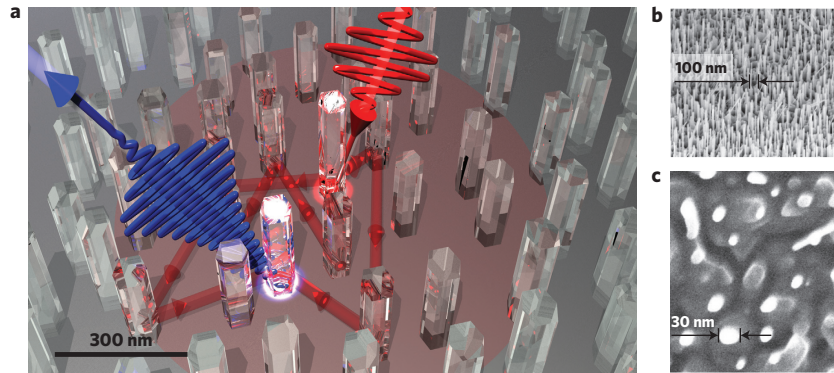


**Figure 1 | Spatiotemporal localization of light in a ZnO nanoneedle array.** **a**, An ultrashort 6 fs laser pulse centred at 800 nm is focused to its diffraction limit of  $\sim 1\ \mu\text{m}$  onto an array of randomly distributed vertically aligned dielectric ZnO nanoneedles. Multiple coherent light scattering inside the array results in field localization in certain hot spots. The concomitant local field enhancement gives rise to pronounced second-harmonic emission from the ZnO needles. Experimentally, the second-harmonic emission is resolved in time, providing a measure of the lifetime of the localized light modes. **b,c**, Side view (**b**) and top view (**c**) scanning electron microscopy images of a needle array with an average separation of  $\sim 100\ \text{nm}$  and a needle diameter of 30 nm.

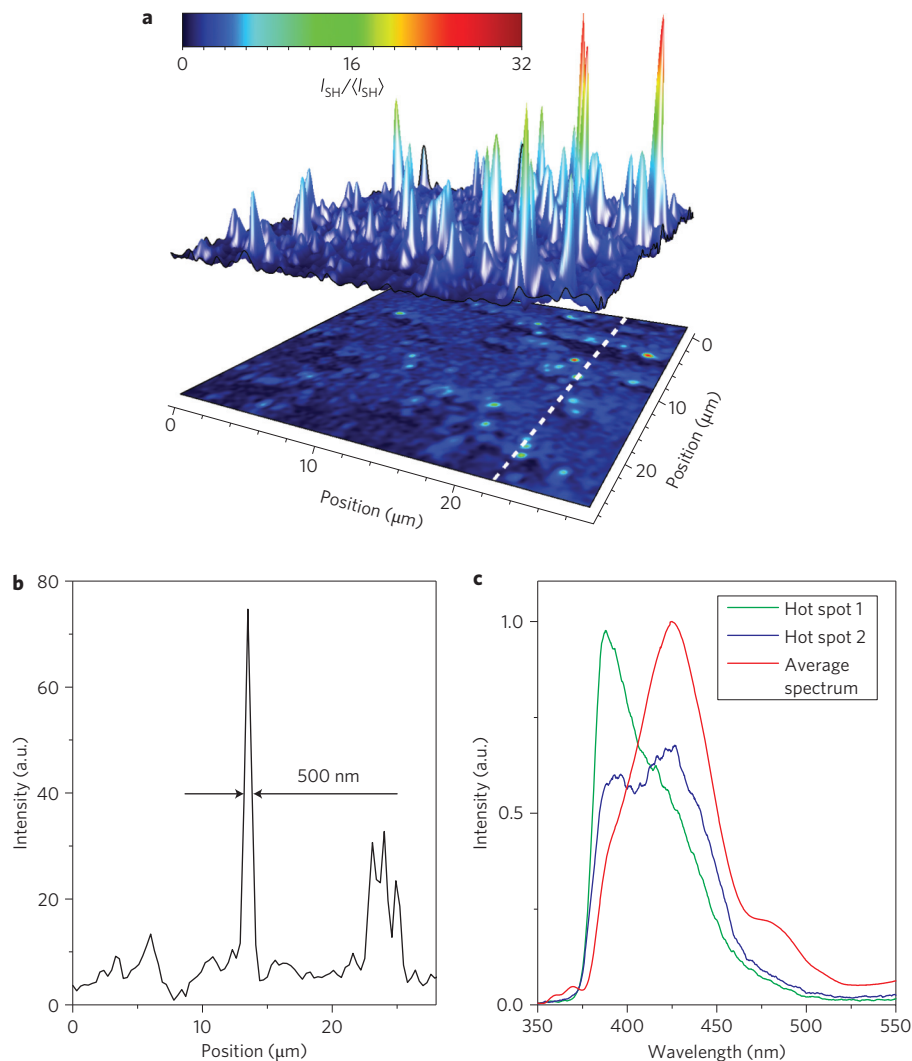


**Figure 2 | Spatial intensity distribution of the second-harmonic emission.** **a**, Confocal second-harmonic microscopy image of the nanoneedle array illuminated with 6 fs pulses at 800 nm. In the most intense local hot spots, the second-harmonic intensity is enhanced by a factor of more than 30 above the average. The overall variation of the second-harmonic intensity throughout the image reflects slight structural variations within the nanoneedle array. **b**, Cross-section along the dashed line in **a** showing that these hot spots are localized to a size of 500 nm, determined by the resolution of the microscope. **c**, Local second-harmonic emission spectra recorded inside different hot spots (green and blue solid lines) in comparison to the spatially averaged second-harmonic spectrum (red line).

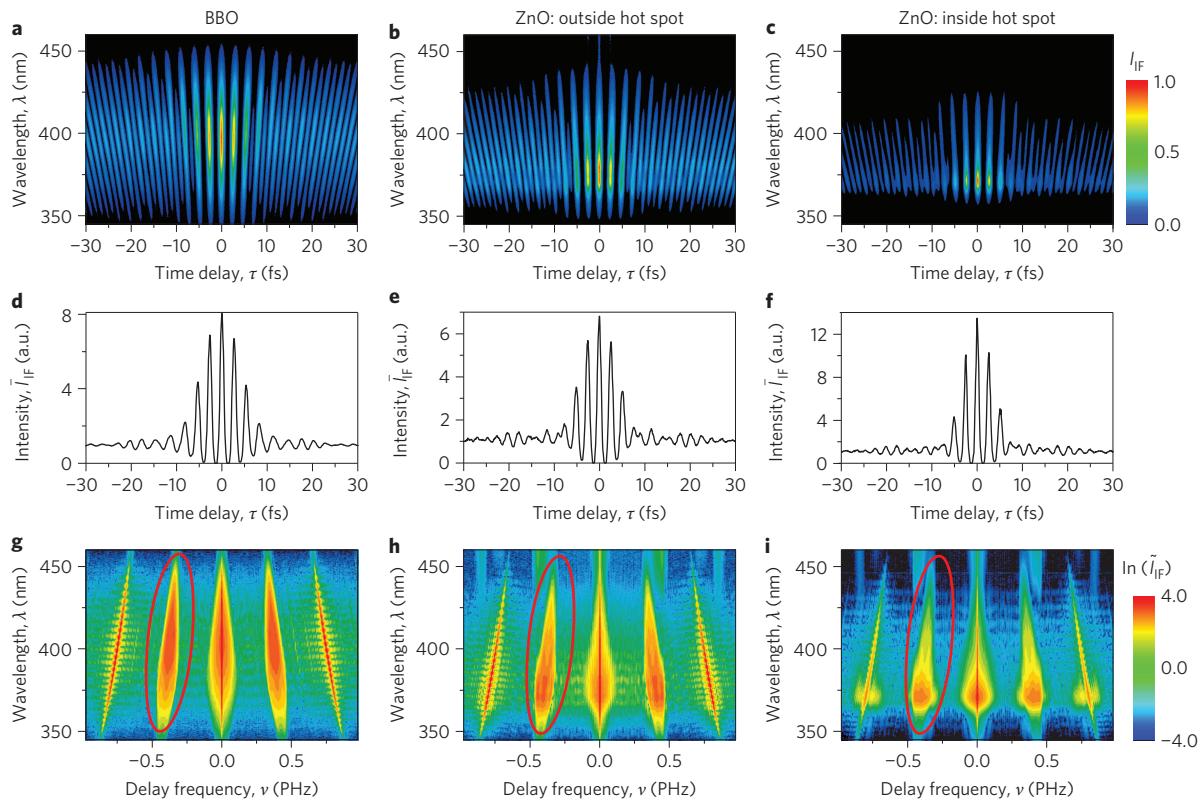


**Figure 3 | IFRAC traces.** **a-c**, The samples are illuminated with a phase-locked pair of 6 fs pulses focused to 1  $\mu\text{m}$ , and IFRAC traces  $I_{IF}(\lambda, \tau)$  are recorded as a function of the pulse delay  $\tau$ . Data are taken from a 10- $\mu\text{m}$ -thick BBO crystal used as reference (**a**) and at positions outside (**b**) and inside (**c**) a local second-harmonic hot spot on the ZnO sample. **d-f**, Corresponding spectrally integrated interferometric autocorrelation traces  $\bar{I}_{IF}(\tau)$ . Slight beatings at delays of  $\pm 10$  and  $\pm 20$  fs reflect the non-Gaussian input spectrum of the 6 fs laser pulses. **g-i**, Fourier transforms  $\bar{I}_{IF}(\lambda, \nu)$  along the time axis of the data in **a-c** plotted on a logarithmic intensity scale, showing distinct peaks at integer multiples of the first sideband  $\nu = \pm c/(2\lambda)$  (marked by red ellipses). The strong reduction in spectral width of the hot spot spectrum in **c** and **i** is the signature of the increased lifetime of the localized light mode.

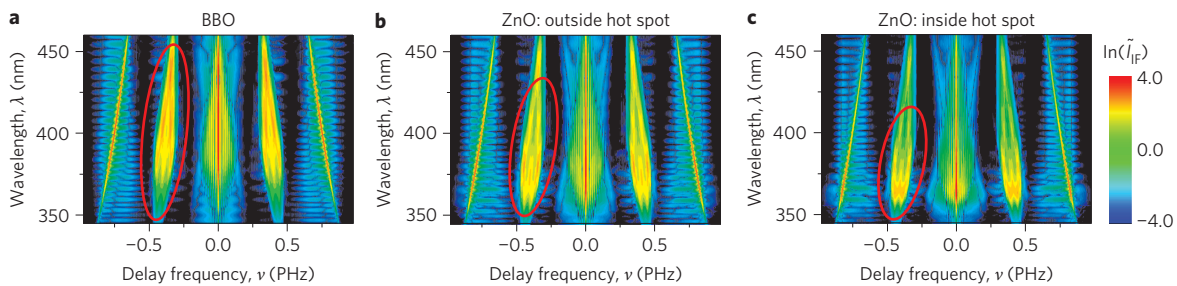


**Figure 4 | Simulated Fourier transforms of IFRAC traces and reconstructed local electric fields.** **a-c**, Fourier transforms  $\bar{I}_{IF}(\lambda, \nu)$  of IFRAC traces obtained from a Bloch equation model, describing the two-photon excitation of a two-level system by an ultrashort laser pulse. The lifetime  $T_1$  of the two-level system is adapted to match the data in Fig. 3g-i. Lifetimes of 1.0 fs for the BBO crystal (**a**), 3.0 fs for a position outside a hot spot (**b**) and 6.5 fs for a position inside a hot spot (**c**) are deduced.

where  $E_{NL}$  is the electric field emitted from the sample illuminated by the pulse pair with field  $E(t) + E(t + \tau)$ . For an instantaneous second-harmonic process,  $E_{NL}(t, \tau) \propto (E(t) + E(t + \tau))^2$ , and the time structure of  $E(t)$  can be reconstructed directly<sup>27</sup>.

We have recorded such spectrograms from a variety of different positions inside the ZnO array. Figure 3 shows representative measurements taken from a 10- $\mu\text{m}$ -thick reference beta barium borate (BBO) crystal (Fig. 3a) and positions outside (Fig. 3b) and inside (Fig. 3c) a hot spot of the ZnO array. The spectrally broad second-harmonic emission from the BBO crystal covers a range of almost 100 nm. In contrast, the spectral second-harmonic bandwidth from the ZnO array is much narrower and decreases even

more when moving from a position outside to inside one of the hot spots in Fig. 2. Spectrally integrated interferometric autocorrelation traces  $\bar{I}_{IF}(\tau) = \int I_{IF}(\lambda, \tau) d\lambda$  are shown in Fig. 3d-f. The marked differences between all three spectrograms are most clearly recognized by comparing Fourier transforms  $\bar{I}_{IF}(\lambda, \nu) = \int I_{IF}(\lambda, \tau) \exp(i2\pi\nu\tau) d\tau$  along the delay axis (Fig. 3g-i). In the reference measurement the spectral bandwidth of all sidebands<sup>27</sup> at  $\nu = \pm nc/(2\lambda)$ ,  $n = 0, 1, 2$ , is substantially larger than in the nanoneedle array data. By far the smallest bandwidth is seen within one of the hotspots (Fig. 3i). This reduction in spectral width is a clear signature of the long lifetime of the localized photon modes.



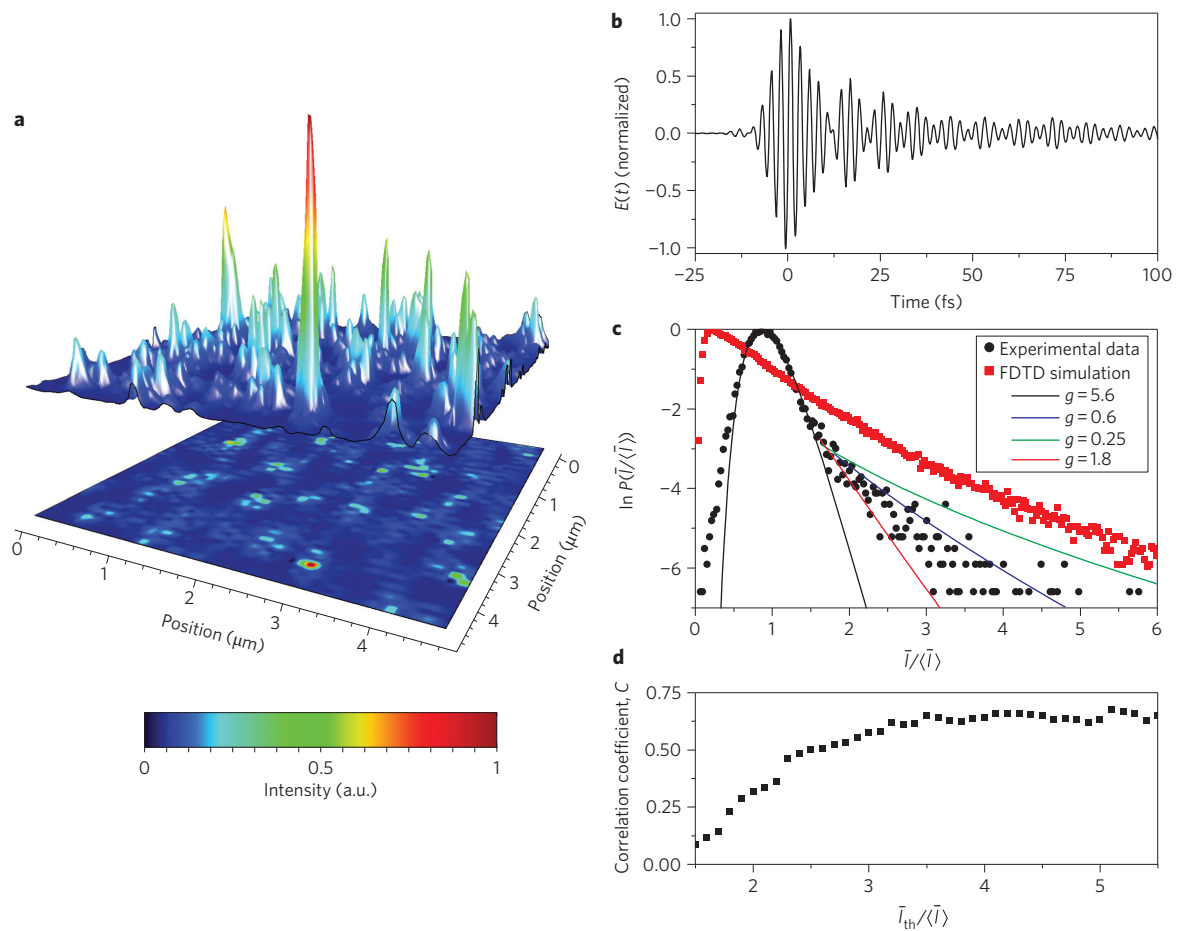


**Figure 5 | Numerical solutions of Maxwell's equations for light localization inside a randomly distributed array of dielectric cylinders.** **a**, Spatial distribution of the time-integrated second-harmonic intensity. **b**, Time structure of the electric field in one of the hot spots, suggesting a lifetime of 20 fs. **c**, Histograms of logarithms of the measured (circles) and simulated (squares) time-averaged local field intensity  $\bar{I}$  at the fundamental laser wavelength. Experimental data  $\bar{I}(\mathbf{r}) = I_{SH}^{1/2}(\mathbf{r})$  are taken from Fig. 2a. Both sets of data show large deviations from a Gaussian distribution at high intensities. The experimental data can be modelled by the sum of two terms given by the analytic expressions of ref. 20 with  $g \approx 0.6$  (blue line) and  $g \approx 5.6$  (black line). Additional curves for  $g = 0.25$  and  $g = 1.8$  illustrate the sensitivity. **d**, Correlation coefficient  $C(I_{th})$  between photon lifetime  $T_1$  and second-harmonic intensity  $I_{SH}$  for the experimental data in Fig. 2a, taking only those data points in **c** with intensity  $\bar{I} > I_{th}$ .

A weak contribution of higher-order coherent components<sup>28</sup> and incoherent multiphoton-induced luminescence background<sup>24,29</sup> to the nonlinear emission from ZnO nanostructures makes the application of direct pulse retrieval techniques<sup>27</sup> difficult, so we use a phenomenological Bloch equation model for data analysis<sup>29</sup>. We model the local nonlinear optical response of the array as that of an effective two-level system interacting with the incident laser by two-photon excitation only. The excited-state lifetime  $T_1$ , reflecting the lifetime of the local photon mode (equation (1)), is the only adjustable parameter to match the experimental data.

Simulated Fourier-transforms of IFRAC traces, shown in Fig. 4 for three different lifetimes— $T_1 = 1$  fs (Fig. 4a), 3.0 fs (Fig. 4b) and 6.5 fs (Fig. 4c)—agree quantitatively with the corresponding experimental data in Fig. 3g–i. This provides a measure of the photon mode lifetime and a reconstruction of the localized electric field  $\mathbf{E}(\mathbf{r}, t)$  at the fundamental laser wavelength. Evidently, multiple coherent scattering within the disordered ZnO nanoneedle array results in a significant increase in the time duration of the local field. In some of the hot spots, the electric field, decaying at  $1/(2T_1)$ , persists for as long as 13 fs. Because the absorption coefficient of the ZnO film at 800 nm is less than  $10 \text{ cm}^{-1}$ , these lifetimes are not limited by absorption but rather reflect radiative out-of-plane losses.

By analysing the spectral width of the coherent second-harmonic emission spectrum, we have constructed a spatial map of the local

photon mode lifetimes (Supplementary Fig. S8b), which displays random fluctuations of the  $T_1$  time between 3 and 8 fs on a scale of 500 nm, limited by the microscope resolution. Considered in total, this map shows a negligible correlation with a simultaneously recorded map of the second-harmonic intensity (correlation coefficient  $C \approx 0.1$ ). The correlation increases dramatically to  $C \approx 0.6$  if only the points with strong second harmonic are included (Fig. 5d). This confirms the visual impression from Fig. 2a that localized states are rare events of little statistical weight at the fundamental laser frequency.

To scrutinize our results, we performed three-dimensional time-resolved simulations of Maxwell's equations for such a nanorod structure, modelled as an array of randomly distributed dielectric cylinders. A plot of the spatial distribution of the time-integrated second-harmonic intensity for a typical simulation run (Fig. 5a) displays pronounced spatial fluctuations in the second-harmonic intensity and local hot spots. The localized modes display a multifractal character<sup>18</sup> with field maxima predominantly located between the cylinders. They show intensity variations on a characteristic scale of 20 nm only, far beyond the experimental resolution. For sufficiently strong disorder, the average distance between adjacent hot spots reaches a few hundreds of nanometres, reflecting again the rare occurrence of strongly localized second-harmonic active modes and indicating indeed that often only an individual hot spot is probed experimentally.

The dynamics of the electric field amplitude, simulated at a distance of  $\sim 1 \mu\text{m}$  above the cylinders, is depicted in Fig. 5b. The overall decay of 20 fs matches the experiment well. At such large distances, the field dynamics display a characteristic beating pattern due to interference of a few neighbouring localized modes. This beating can be suppressed by reducing this distance, restricting the detection to fields from a single hot spot. Such beatings are not observed in Fig. 3b,c, indicating that these measurements indeed mainly probe a single localized mode. Additional arguments supporting this interpretation and ruling out alternatives, such as random lasing, are presented in Supplementary Sections S3 and S8.

Such intensity fluctuations in the LDOS are one hallmark of randomly localized modes. We therefore calculated histograms of the time-averaged local electric field intensity  $\bar{I}(\mathbf{r}) = \int |E(\mathbf{r}, t)|^2 dt$  at the fundamental laser frequency from both experimental and theoretical data (Fig. 5c). Even though analytic expressions for the LDOS exist<sup>21,30</sup>, we are not aware of predictions for the statistics of such spectrally integrated field intensities. For sufficiently strong disorder, we expect a large variance<sup>20</sup> and deviations from Gaussian statistics, specifically at high intensities, governed by strongly localized states. Experimentally we find a broad Gaussian around  $\bar{I}/\langle\bar{I}\rangle = 1$  and a weak but pronounced approximately exponential tail at  $\bar{I}/\langle\bar{I}\rangle \gg 1$ . Separate measurements on the bottom layer of larger rods indicate that the second harmonic from this layer mainly leads to the Gaussian around  $\bar{I}/\langle\bar{I}\rangle = 1$ , confirming that second harmonic generation by modes localized within the top layer of thinner nanoneedles gives rise to the broad exponential tail in Fig. 5c. The statistics of the finite-difference time-domain (FDTD) results show a similar broad tail at  $\bar{I}/\langle\bar{I}\rangle \gg 1$ , decaying even slower than exponentially. The experimentally measured tail follows roughly the predictions of ref. 20 for a dimensionless conductance  $g \approx 0.6$ , that is, at the transition into the strong localization regime. At present, a more quantitative analysis is difficult because the exact shape of the histogram depends on the spatial resolution of the experiment and is also affected by second harmonic generation from the base of larger-diameter nanorods.

Taken together, our experimental and theoretical results present compelling evidence for light localization near the transition into the strong localization regime in an array of randomly disordered ZnO nanoneedles. We have explored the spatial and temporal aspects of this localization using a novel interferometric second-harmonic microscopic technique with few-cycle time resolution, and have directly measured lifetimes of individual localized photon modes of a few femtoseconds. This new experimental approach opens the way to the study of light localization dynamics in a variety of passive and active random media and we specifically expect it to shed new light on random lasing dynamics in ZnO nanoparticles.

## Methods

**ZnO sample preparation.** The ZnO nanorod samples were grown by metal-organic vapour phase epitaxy (MOVPE) on a sapphire substrate<sup>25</sup>. By applying a two-temperature technique, ZnO rods with diameters of 30 nm and height of  $\sim 300$  nm were grown on top of a base of larger rods with diameters of  $\sim 100$  nm and height of  $\sim 100$  nm. The density of the thinner rods was  $\sim 60$  needles per  $\mu\text{m}^2$ , as determined by scanning electron microscopy.

**IFRAC microscope.** Laser pulses with a duration of 6 fs centred at a wavelength of 800 nm were derived from a Ti:sapphire oscillator (Femtolasers Rainbow) operating at a repetition rate of 82 MHz. A phase-locked pair of these pulses was generated in a dispersion-balanced Mach-Zehnder interferometer with an accuracy of  $< 30$  as using a hardware-linearized piezo scanner (Physik Instrumente P-621.1CD PIHera). Pulses with an energy of  $\sim 20$  pJ were focused to their diffraction limit of  $1.0 \mu\text{m}$  using an all-reflective Cassegrain objective with a numerical aperture of 0.5, fully preserving their temporal resolution<sup>26</sup>. The sample was placed at an oblique angle of  $30^\circ$  with respect to the linearly  $p$ -polarized incident beam, maximizing the electric field component along the ZnO needle axis and enhancing the second-harmonic signal<sup>29</sup>. The sample position within the focus was controlled using a three-dimensional piezo scanner (Physik Instrumente NanoCube) with a lateral resolution of 10 nm. The second-harmonic and photoluminescence emission from the sample were collected in reflection geometry, spectrally dispersed in a 0.5 m

monochromator (Acton SpectraPro-2500i) and detected as a function of time delay and lateral position on the sample using a liquid-nitrogen-cooled charge coupled device (Princeton Instruments Spec-10)<sup>29</sup>.

**Optical Bloch equations modelling.** We simulated the time structure of the local second-harmonic emission by solving optical Bloch equations for a two-level system interacting with the laser electric field  $E(t)$  by two-photon excitation with a generalized Rabi frequency  $\Omega(t) = \alpha E(t)^2/\hbar$ . The excited-state lifetime  $T_1$  gives the lifetime of the localized photon mode. Details are described in Supplementary Section S5.

**FDTD simulation.** Maxwell's equations for a model system were solved using a three-dimensional FDTD method using the freely available Maxwell solver Meep. Randomly distributed, vertically aligned cylindrical rods with a refractive index of  $n = 1.96$ , diameter of 100 nm and a randomly varied length between 0.9 and  $1.0 \mu\text{m}$  were placed on top of a dielectric substrate with the refractive index of sapphire ( $n = 0.175$ ). The needle density was chosen to be 60 needles per  $\mu\text{m}^2$  to match the experimental parameters. The local second-harmonic intensity  $I_{SH}(\mathbf{r}, t) = |E(\mathbf{r}, t)|^2$ .

To simulate the incident electromagnetic field, a plane wave source at an incidence angle of  $30^\circ$  and with a Gaussian temporal envelope of 6 fs (full-width at half-maximum) centred at the laser wavelength of 800 nm was used. The time dynamics of the local electric field  $E(\mathbf{r}, t)$  at position  $\mathbf{r}$  inside a sample of area  $4.3 \times 4.3 \mu\text{m}^2$  containing  $\sim 1,000$  cylinders were calculated with a spatial resolution of 10 nm. Perpendicular to the cylinder axis, Bloch periodic boundary conditions were applied. At the boundaries along this axis, strongly absorbing perfectly matched layer areas were used to model open boundary conditions.

Received 24 December 2011; accepted 29 February 2012;  
published online 15 April 2012

## References

1. Abrahams, E. (ed.) *50 Years of Anderson Localization* (World Scientific, 2010).
2. Belitz, D. & Kirkpatrick, T. R. The Anderson-Mott transition. *Rev. Mod. Phys.* **66**, 261–380 (1994).
3. Richardella, A. *et al.* Visualizing critical correlations near the metal-insulator transition in  $\text{Ga}_{1-x}\text{Mn}_x\text{As}$ . *Science* **327**, 665–669 (2010).
4. Hess, H. F., Betzig, E., Harris, T. D., Pfeiffer, L. N. & West, K. W. Near-field spectroscopy of the quantum constituents of a luminescent system. *Science* **264**, 1740–1745 (1994).
5. Intonti, F. *et al.* Quantum mechanical repulsion of exciton levels in a disordered quantum well. *Phys. Rev. Lett.* **87**, 076801 (2001).
6. Gresillon, S. *et al.* Experimental observation of localized optical excitations in random metal-dielectric films. *Phys. Rev. Lett.* **82**, 4520–4523 (1999).
7. Stockman, M. I. Femtosecond optical responses of disordered clusters, composites, and rough surfaces: 'the ninth wave' effect. *Phys. Rev. Lett.* **84**, 1011–1014 (2000).
8. Sapienza, L. *et al.* Cavity quantum electrodynamics with Anderson-localized modes. *Science* **327**, 1352–1355 (2010).
9. Schwartz, T., Bartal, G., Fishman, S. & Segev, M. Transport and Anderson localization in disordered two-dimensional photonic lattices. *Nature* **446**, 52–55 (2007).
10. Albada, M. P. V. & Lagendijk, A. Observation of weak localization of light in a random medium. *Phys. Rev. Lett.* **55**, 2692–2695 (1985).
11. Wolf, P.-E. & Maret, G. Weak localization and coherent backscattering of photons in disordered media. *Phys. Rev. Lett.* **55**, 2696–2699 (1985).
12. Wiersma, D. S., van Albada, M. P. & Lagendijk, A. Coherent backscattering of light from amplifying random media. *Phys. Rev. Lett.* **75**, 1739–1742 (1995).
13. Cao, H. *et al.* Random laser action in semiconductor powder. *Phys. Rev. Lett.* **82**, 2278–2281 (1999).
14. Fallert, J. *et al.* Co-existence of strongly and weakly localized random laser modes. *Nature Photon.* **3**, 279–282 (2009).
15. Wang, J. & Genack, A. Z. Transport through modes in random media. *Nature* **471**, 345–348 (2011).
16. Sheng, P. *Introduction to Wave Scattering, Localization and Mesoscopic Phenomena* (Springer, 2006).
17. Evers, F. & Mirlin, A. D. Anderson transitions. *Rev. Mod. Phys.* **80**, 1355–1417 (2008).
18. Schreiber, M. & Grussbach, H. Multifractal wave functions at the Anderson transition. *Phys. Rev. Lett.* **67**, 607–610 (1991).
19. Riboli, F. *et al.* Anderson localization of near-visible light in two dimensions. *Opt. Lett.* **36**, 127–129 (2011).
20. Chabanov, A. A., Stoytchev, M. & Genack, A. Z. Statistical signatures of photon localization. *Nature* **404**, 850–853 (2000).
21. Hu, H., Strybulevych, A., Page, J. H., Skipetrov, S. E. & van Tiggelen, B. A. Localization of ultrasound in a three-dimensional elastic network. *Nature Phys.* **4**, 945–948 (2008).
22. Nieuwenhuizen, T. M. & van Rossum, M. C. W. Intensity distributions of waves transmitted through a multiple scattering medium. *Phys. Rev. Lett.* **74**, 2674–2677 (1995).

23. Abrahams, E., Anderson, P. W., Licciardello, D. C. & Ramakrishnan, T. V. Scaling theory of localization: absence of quantum diffusion in two dimensions. *Phys. Rev. Lett.* **42**, 673–676 (1979).
24. Djurišić, A. B. & Leung, Y. H. Optical properties of ZnO nanostructures. *Small* **2**, 944–961 (2006).
25. Kitamura, K. *et al.* Fabrication of vertically aligned ultrafine ZnO nanorods using metal–organic vapor phase epitaxy with a two-temperature growth method. *Nanotechnology* **19**, 175305 (2008).
26. Piglosiewicz, B. *et al.* Ultrasmall bullets of light-focusing few-cycle light pulses to the diffraction limit. *Opt. Express* **19**, 14451–14463 (2011).
27. Stibenz, G. & Steinmeyer, G. Interferometric frequency-resolved optical gating. *Opt. Express* **13**, 2617–2626 (2005).
28. Tritschler, T., Mücke, O. D., Wegener, M., Morgner, U. & Kärtner, F. X. Evidence for third-harmonic generation in disguise of second-harmonic generation in extreme nonlinear optics. *Phys. Rev. Lett.* **90**, 217404 (2003).
29. Schmidt, S. *et al.* Distinguishing between ultrafast optical harmonic generation and multi-photon-induced luminescence from ZnO thin films by frequency-resolved interferometric autocorrelation microscopy. *Opt. Express* **18**, 25016–25028 (2010).
30. Mirlin, A. D. Statistics of energy levels and eigenfunctions in disordered systems. *Phys. Rep.* **326**, 259–382 (2000).

### Acknowledgements

This research was supported by the Japan Science and Technology Agency (JST) and the Deutsche Forschungsgemeinschaft (DFG) within the ‘Nanoelectronics’ programme. The authors acknowledge support in Germany by the DFG (priority programme ‘Ultrafast nanooptics’, SPP 1391) and by the Korea Foundation for International Cooperation of Science & Technology (Global Research Laboratory project K20815000003). Support in Japan through a Grant-in-Aid for Young Scientists (A) from MEXT and a research grant (Basic Research) from The TEPCO Memorial Foundation is also acknowledged.

### Author contributions

C.L., E.R. and M.O. conceived the experiment. M.M. and S.S. carried out the measurements and analysed the data, together with M.S. and C.L. The samples were fabricated by K.K. and T.Y. FDTD simulations were performed by D.L. The manuscript was prepared by M.M., M.S., D.L., E.R. and C.L. All authors contributed to finalizing the manuscript.

### Additional information

The authors declare no competing financial interests. Supplementary information accompanies this paper at [www.nature.com/naturephotonics](http://www.nature.com/naturephotonics). Reprints and permission information is available online at <http://www.nature.com/reprints>. Correspondence and requests for materials should be addressed to C.L.

# Skew Dependence of Nanophotonic Devices Based on Optical Near-Field Interactions

MAKOTO NARUSE, National Institute of Information and Communications Technology,  
and The University of Tokyo  
FERDINAND PEPPER, KOUICHI AKAHANE, and NAOKATSU YAMAMOTO,  
National Institute of Information and Communications Technology  
TADASHI KAWAZOE, NAOYA TATE, and MOTOICHI OHTSU, The University of Tokyo

We examine the timing dependence of nanophotonic devices based on optical excitation transfer via optical near-field interactions at the nanometer scale. We theoretically analyze the dynamic behavior of a two-input nanophotonic switch composed of three quantum dots based on a density matrix formalism while assuming arrival-time differences, or skew, between the inputs. The analysis reveals that the nanophotonic switch is resistant to a skew longer than the input signal duration, and the tolerance to skew is asymmetric with respect to the two inputs. The skew dependence is also experimentally examined based on near-field spectroscopy of InGaAs quantum dots, showing good agreement with the theory. Elucidating the dynamic properties of nanophotonics, together with the associated spatial and energy dissipation attributes at the nanometer scale, will provide critical insights for novel system architectures.

Categories and Subject Descriptors: B.6.1 [Logic Design]: Design Styles; C.4 [Performance of Systems]; H.5.3 [Information Interfaces and Presentation]: Group and Organization Interfaces

General Terms: Design, Experimentation, Performance

Additional Key Words and Phrases: Nanophotonics

## ACM Reference Format:

Naruse, M., Peper, F., Akahane, K., Yamamoto, N., Kawazoe, T., Tate, N., and Ohtsu, M. 2012. Skew dependence of nanophotonic devices based on optical near-field interactions. *ACM J. Emerg. Technol. Comput. Syst.* 8, 1, Article 4 (February 2012), 12 pages.  
DOI = 10.1145/2093145.2093149 <http://doi.acm.org/2093145.2093149>

## 1. INTRODUCTION

For information and communications technologies, nanoscale devices, systems, and architectures that are not based on conventional electronic means have been attracting increasing interest even though they have not yet reached the stage of mass production [Collier et al. 1999; Dai et al. 2010; Naruse et al. 2005; Peper et al. 2004;

---

This work was partially supported by the New Energy and Industrial Technology Development Organization (NEDO) under the program of comprehensive activity for personnel training and industry academia collaboration based on NEDO projects.

Authors' addresses: M. Naruse, F. Peper, K. Akahane, and N. Yamamoto, National Institute of Information and Communications Technology, 4-2-1 Nukui-kita, Koganei, Tokyo 184-8795, Japan; T. Kawazoe, N. Tate, and M. Ohtsu, Department of Electrical Engineering and Information Systems and Nanophotonics Research Center, School of Engineering, The University of Tokyo, 2-11-16 Yayoi, Bunkyo-ku, Tokyo 113-8656, Japan; email: naruse@mict.go.jp.

Permission to make digital or hard copies of part or all of this work for personal or classroom use is granted without fee provided that copies are not made or distributed for profit or commercial advantage and that copies show this notice on the first page or initial screen of a display along with the full citation. Copyrights for components of this work owned by others than ACM must be honored. Abstracting with credit is permitted. To copy otherwise, to republish, to post on servers, to redistribute to lists, or to use any component of this work in other works requires prior specific permission and/or a fee. Permissions may be requested from the Publications Dept., ACM, Inc., 2 Penn Plaza, Suite 701, New York, NY 10121-0701, USA, fax +1 (212) 869-0481, or [permissions@acm.org](mailto:permissions@acm.org).

© 2012 ACM 1558-4832/2012/02-ART4 \$10.00

DOI 10.1145/2093145.2093149 <http://doi.acm.org/10.1145/2093145.2093149>

Pistol et al. 2008; Yan et al. 2011]. It should be noted that the ultimate motivations for these novel approaches may not necessarily be replacing or competing with current CMOS-based principles and technologies. The novelties of, for example, nanoscale optical computing [Naruse et al. 2005; Pistol et al. 2008], are their physical interfaces with the real world, leading to interesting biological applications, as one example [Pistol et al. 2008]. Also, the energy transfer mechanism itself, which is one of the primary concerns of this article regarding nanophotonics, provides fundamentally different characters compared with conventional electron transfer and so on, and the insights gained, provide versatile novel characteristics and application systems. For instance, molecular logic gates [Remacle et al. 2001; Yeow and Steer 2003] or artificial materials [Crooker et al. 2002] have been investigated.

Nanophotonics exploits the local optical near-field interactions between nanometer-scale materials as the fundamental mechanism underlying the device operation. Based on the optical excitation transfer between quantum dots (QDs), nanophotonics is not restricted by the diffraction limit of light, and it thus promises ultrahigh integration densities of devices and systems [Franzl et al. 2004; Ohtsu et al. 2008; Unold et al. 2005]. Its theoretical fundamentals have been extensively studied through the development of dressed photon models [Ohtsu et al. 2008] and angular-spectrum analysis [Hori 2001]. Experimental technologies, both in fabrication and characterization of nanostructures, have seen rapid progress, such as in geometry-controlled quantum nanostructures [Akahane et al. 2002, 2008], advanced spectroscopy [Matsuda et al. 2005], and so forth. The principles of versatile nanophotonic devices based on optical excitation transfer have also been demonstrated, such as with logic gates [Kawazoe et al. 2003; Yatsui et al. 2007] and interconnects [Naruse et al. 2006]. Very recently, room-temperature operation of nanophotonic logic gates was demonstrated [Kawazoe et al. 2011].

The energy transfer between nanomaterials, especially semiconductor QDs has been attracting considerable research interest, driven by the importance of realizing subwavelength-scale optical circuits [Kawazoe et al. 2011] as well as other applications such as energy concentration [Franzl et al. 2004; Naruse et al. 2009]. The physical origin of optical energy transfer between semiconductor QDs has been extensively investigated in various disciplines, such as carrier tunneling [Heitz et al. 1998; Mazur et al. 2005; Xu et al. 1996] or dipole–dipole interactions [Kagan et al. 1996]. The detailed physical discussions of the differences among optical near-field interactions and other disciplines are not the primary concern of this article, although partially reviewed in Section 2; but one of the most important attributes from an information processing perspective is their dynamic properties in the time domain. In particular, a fundamental characteristic of optical devices and systems is their performance associated with skew, which is the difference in arrival timing among multiple input channels [Keeler et al. 2000; Naruse et al. 2003]. Elucidating the dynamic properties of nanophotonic devices in this way has implications for novel system architectures, as discussed in Section 5.

In this article, we theoretically analyze the dynamic behavior of a nanophotonic switch composed of three quantum dots, based on a quantum mechanical formulation using a density matrix, while assuming an arrival-time difference, or skew, between two input signals. The device is resistant to a skew longer than the duration of the input signals, and the tolerance to skew is asymmetric, depending on the arrival timing of the two inputs. An experimental demonstration is also shown based on near-field spectroscopy using stacked InGaAs quantum dots, and it is in good agreement with the theory.

## 2. EXCITATION TRANSFER BASED ON OPTICAL NEAR-FIELD INTERACTIONS

Conventionally, the interaction Hamiltonian between an electron and an electric field is given by

$$\hat{H}_{int} = - \int \hat{\psi}^\dagger(\vec{r}) \vec{\mu} \hat{\psi}(\vec{r}) \bullet \hat{D}(\vec{r}) d\vec{r}, \quad (1)$$

where  $\vec{\mu}$  is the dipole moment,  $\hat{\psi}^\dagger(\vec{r})$  and  $\hat{\psi}(\vec{r})$  are respectively creation and annihilation operators of an electron at  $\vec{r}$ , and  $\hat{D}(\vec{r})$  is the operator of electric flux density. In usual light–matter interactions, the operator  $\hat{D}(\vec{r})$  is a constant since the electric field of propagating light is considered to be constant on the nanometer scale. Therefore, one can derive optical selection rules by calculating a transfer matrix of an electric dipole. Consequently, in the case of cubic quantum dots, transitions to states described by quantum numbers containing an even number are prohibited. In the case of optical near-field interactions, on the other hand, there is a steep electric gradient of optical near-fields in the vicinity of nanometer-scale matter, and this facilitates optical transitions that violate conventional optical selection rules. Such an energy transfer to conventionally dipole-forbidden energy levels cannot be explained by carrier tunneling [Heitz et al. 1998; Mazur et al. 2005; Xu et al. 1996] or dipole interactions [Kagan et al. 1996; Pistol et al. 2008].

Optical excitations in nanostructures, such as quantum dots, can be transferred to neighboring structures via optical near-field interactions [Ohtsu et al. 2008]. Assume that two cubic quantum dots,  $QD_S$  and  $QD_M$ , whose side lengths are  $a$  and  $\sqrt{2}a$  respectively, are located close to each other (Figure 1(a)). Suppose that the energy eigenvalues for the quantized exciton energy level specified by quantum numbers  $(n_x, n_y, n_z)$  in the QD with side length  $a$  ( $QD_S$ ) are given by

$$E_{(n_x, n_y, n_z)} = E_B + \frac{\hbar^2 \pi^2}{2M a^2} (n_x^2 + n_y^2 + n_z^2), \quad (2)$$

where  $E_B$  is the energy of the bulk exciton, and  $M$  is the effective mass of the exciton. According to (2), there exists a resonance between the level of quantum number (1,1,1) of  $QD_S$  (denoted by  $S_1$  in Figure 1(a)) and that of quantum number (2,1,1) for  $QD_M$  ( $M_2$ ). There is an optical near-field interaction, denoted by  $U_{S_1, M_2}$ , resulting from the steep gradient of the electric field in the vicinity of  $QD_S$ . It is known that the interdot optical near-field interaction is given by a Yukawa-type potential [Ohtsu et al. 2008]. Therefore, excitons in  $QD_S$  can move to the (2,1,1)-level in  $QD_M$ . Note that such a transfer is prohibited for propagating light since the (2,1,1)-level in  $QD_M$  contains an even number. In  $QD_M$ , the exciton sees a sublevel energy relaxation, denoted by  $\Gamma$ , which is faster than the near-field interaction, so the exciton goes to the (1,1,1)-level of  $QD_M$  ( $M_1$ ).

In the optical excitation transfer as discussed, the energy dissipation occurring in the destination quantum dot,  $QD_M$ , determines the unidirectionality of signal transfer [Naruse et al. 2007]. Therefore, when the lower energy level of the destination quantum dot is filled with another excitation (called state filling), an optical excitation occurring in a smaller QD cannot move to a larger one. As a result, the optical excitation will go back and forth between these dots (optical nutation). This suggests the existence of two different states, which depend on whether the destination quantum dots are occupied or not. An important characteristic in information processing can be exploited to implement digital logic operations [Kawazoe et al. 2003]. Figure 1(b) schematically represents a two-input AND gate formed of three quantum dots.  $QD_S$  and  $QD_L$ , whose sizes are  $a$  and  $2a$ , work as the two input dots, accepting input signals denoted by IN  $S$  and IN  $L$ , respectively, and  $QD_M$ , whose size is  $\sqrt{2}a$ , works as the

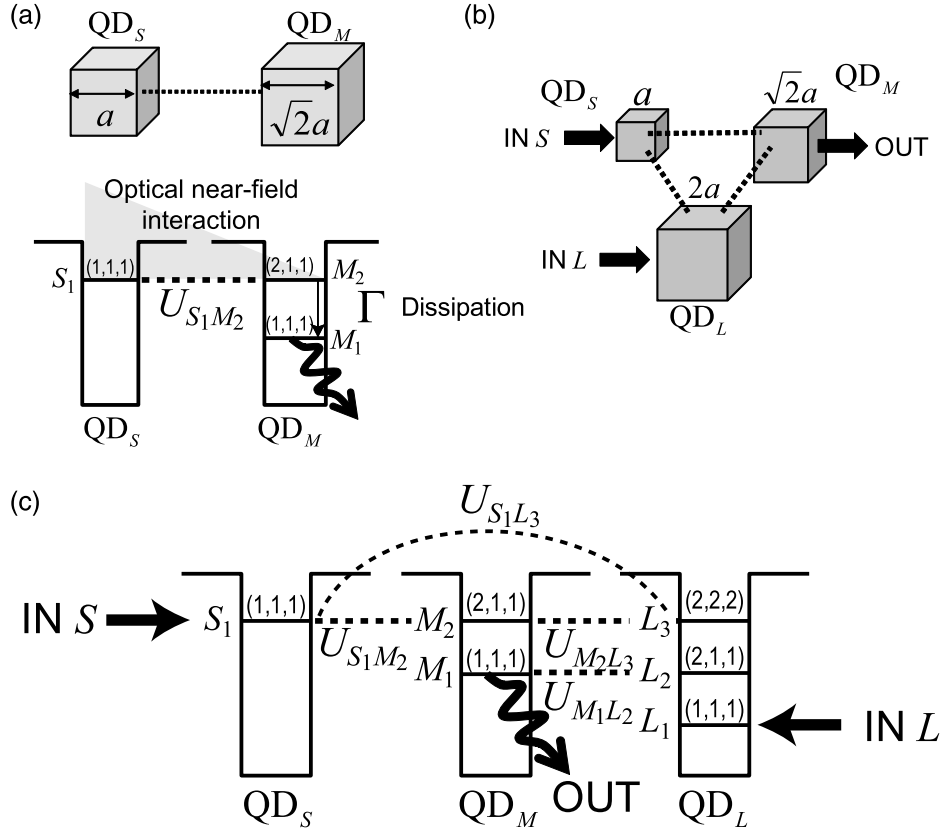


Fig. 1. (a) Optical near-field interaction between a smaller quantum dot ( $QD_S$ ) and a larger one ( $QD_M$ ). (b) Two-input AND gate implemented by three quantum dots with interdot optical near-field interactions. Two inputs are indicated by  $IN\ S$  and  $IN\ L$ , which are applied to  $QD_S$  and  $QD_L$ , respectively. Output is associated with radiation from  $QD_M$ . (c) Energy diagram of the system shown in (b).

output dot. The energy diagram is shown in Figure 1(c), where the optical frequencies of the input signals  $IN\ S$  and  $IN\ L$  are resonant with the  $(1,1,1)$ -level of  $QD_S$  ( $S_1$ ) and the  $(1,1,1)$ -level of  $QD_L$  ( $L_1$ ), respectively.

When both inputs are provided, it is not possible for the optical excitation occurring in  $S_1$ , induced by  $IN\ S$ , to be transferred to  $L_1$  in  $QD_L$  because  $L_1$  is excited by  $IN\ L$ , and it should thus radiatively decay from the  $(1,1,1)$ -level of  $QD_M$  ( $M_1$ ) (logically,  $IN\ S = 1$ ,  $IN\ L = 1 \rightarrow OUT = 1$ ). On the other hand, when only  $IN\ S$  is given, the optical excitation induced in  $QD_S$  should be transferred to  $QD_L$  and radiatively decay from the  $(1,1,1)$ -level of  $QD_L$ , resulting in a lower radiation from  $QD_M$  ( $IN\ S = 1$ ,  $IN\ L = 0 \rightarrow OUT = 0$ ). Finally, there is no output signal from  $QD_M$  when  $IN\ S$  is not given ( $[IN\ S = 0, IN\ L = 1 \rightarrow OUT = 0]$  and  $[IN\ S = 0, IN\ L = 0 \rightarrow OUT = 0]$ ). Therefore, the preceding three-dot configuration, as the logical relation between input and output suggests, provides a logical AND gate operation.

The lower bound of energy dissipation required for optical excitation transfer from a smaller quantum dot to a larger one via optical near-field interactions was theoretically compared with the bit flip energy of an electrically wired device [Naruse et al. 2010]. The former is about  $10^4$  times more energy-efficient than the latter, demonstrating the high energy efficiency of optical excitation transfer. Such an attribute

also contributes to superior tamper resistance against attacks via power consumption monitoring [Naruse et al. 2007].

### 3. DYNAMICS OF THREE-DOT OPTICAL NEAR-FIELD INTERACTIONS

We now analyze the dynamic behavior of the system based on a density matrix formalism assuming optical near-field interactions among these three dots, as well as external inputs to QD<sub>S</sub> and QD<sub>L</sub>. Since there are in total, six energy levels (namely, [S<sub>1</sub> in QD<sub>S</sub>], [M<sub>1</sub> and M<sub>2</sub> in QD<sub>M</sub>], and [L<sub>1</sub>, L<sub>2</sub>, and L<sub>3</sub> in QD<sub>L</sub>]), the number of different states occupying those energy levels is 2<sup>6</sup> (= 64).

In Figure 1(c), the optical near-field interaction between resonant energy levels  $E_i$  and  $E_j$  is represented by  $U_{E_i E_j}$ ; for instance, the interaction between the (1,1,1)-level of QD<sub>S</sub> (S<sub>1</sub>) and the (2,2,2)-level of QD<sub>L</sub> (L<sub>3</sub>) is denoted by  $U_{S_1 L_3}$ . The radiative relaxation rates from S<sub>1</sub>, M<sub>1</sub>, and L<sub>1</sub> are given by  $\gamma_S$ ,  $\gamma_M$ , and  $\gamma_L$ , respectively. The quantum master equation of the total system is then given by [Carmichael 1999]

$$\begin{aligned} \frac{d\rho(t)}{dt} = & -\frac{i}{\hbar} [H_{int} + H_{ext}(t), \rho(t)] + \sum_{i=S_1, M_1, L_1} \frac{\gamma_i}{2} \left( 2R_i \rho(t) R_i^\dagger - R_i^\dagger R_i \rho(t) - \rho(t) R_i^\dagger R_i \right) \\ & + \sum_{i=M_2, L_2, L_3} \frac{\Gamma}{2} \left( 2S_i \rho(t) S_i^\dagger - S_i^\dagger S_i \rho(t) - \rho(t) S_i^\dagger S_i \right), \end{aligned} \quad (3)$$

where the interaction Hamiltonian is given by  $H_{int}$  and the external Hamiltonian  $H_{ext}(t)$ . Let the  $(i, i)$  and  $(j, j)$  elements of  $\rho(t)$  be the probabilities of the two states that are transformable between each other via an optical near-field interaction denoted by  $U$ . Then, the  $(i, j)$  and  $(j, i)$  elements of the interaction Hamiltonian are given by  $U$ . The matrices  $R_i$  ( $i = S_1, M_1, L_1$ ) are annihilation operators that respectively annihilate excitations in S<sub>1</sub>, M<sub>1</sub>, and L<sub>1</sub> via radiative relaxations. The matrices  $R_i^\dagger$  ( $i = S_1, M_1, L_1$ ) are respectively creation operators given by the transposes of the matrices of  $R_i$ . The matrices  $S_i$  ( $i = M_2, L_2, L_3$ ) are annihilation operators that respectively annihilate excitations in M<sub>2</sub>, L<sub>2</sub>, and L<sub>3</sub> via sublevel relaxations. The external Hamiltonian  $H_{ext}(t)$  indicates the Hamiltonian that represents the interaction between the external input light and the quantum dot system, given by

$$H_{ext}(t) = IN_S(t) \times (R_{S_1}^\dagger + R_{S_1}) + IN_L(t) \times (R_{L_1}^\dagger + R_{L_1}), \quad (4)$$

where  $IN_S(t)$  and  $IN_L(t)$  specify the duration and the amplitude of the external input light applied to QD<sub>S</sub> and QD<sub>L</sub>, and which are denoted by IN *S* and IN *L*, respectively.

We assume a rectangular-shaped input signal for both  $IN_S(t)$  and  $IN_L(t)$ , and then characterize the output population relevant to the radiation from QD<sub>M</sub>, i.e., the populations involving the (1,1,1)-level of QD<sub>M</sub> (M<sub>1</sub>). The purpose is to analyze the dependence on the relative arrival-time difference of IN *S* and IN *L*, namely, the skew, as schematically shown in Figure 2(a).

We assume the following parameter values for evaluation: (1) interdot optical near-field interaction  $U^{-1} = 100$ ps, (2) sublevel relaxation  $\Gamma^{-1} = 10$ ps, and (3) radiative decay times  $\gamma_L^{-1} = 1$ ns,  $\gamma_M^{-1} = 2^{3/2} \times 1 \sim 2.83$ ns, and  $\gamma_S^{-1} = 2^3 \times 1 \sim 8$ ns, which are inversely proportional to the volumes of the QDs [Itoh et al. 1990]. The duration of both  $IN_S(t)$  and  $IN_L(t)$  is set to 2ps.

Figure 2(b) shows the evolution of the populations in the output dot under the assumption that (1) there is no skew between the two inputs (solid, blue), (2) IN *L* is advanced by 300ps relative to IN *S* (dash-dot, red), (3) IN *L* is delayed by 300ps relative to IN *S* (dotted, green), and (4) only IN *S* is provided (dashed, black). Comparing cases (1) and (4), we find that the former exhibits a larger population than the latter, which demonstrates behavior typical of a logical AND gate. Note that case (2) exhibits an output population comparable to that of case (1). On the other hand, in case (3), the



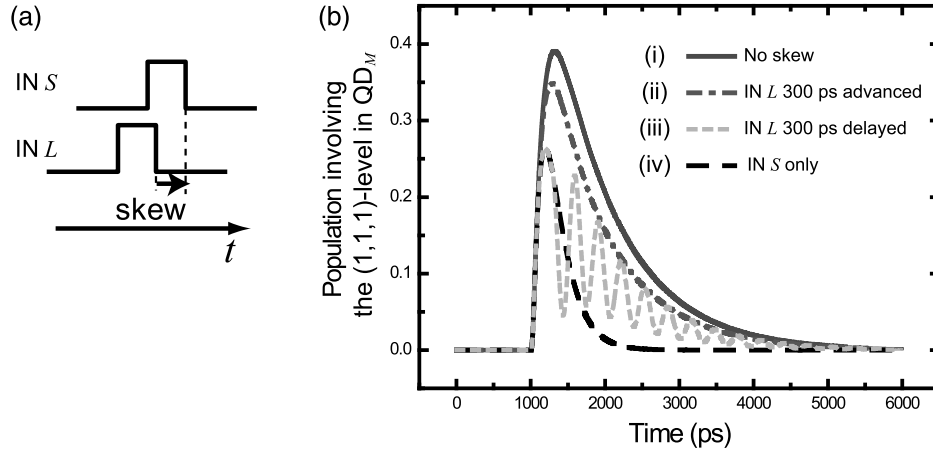


Fig. 2. (a) The arrival-timing difference, or skew, between IN *S* and IN *L*. (b) Time evolution of the output population, that is, the population involving the (1,1,1)-level in QD<sub>*M*</sub>.

curve of the population evolution is greatly deteriorated compared with case (1) due to the optical nutation effect introduced in Section 2. Case (4) should, as an AND gate, exhibit a lower population; however, due to the limited radiation lifetime in QD<sub>*L*</sub>, a nonzero output population still appears.

Next, we evaluate the ON/OFF ratio of the output signal as a function of skew, which is the difference between the arrival times of IN *S* and IN *L*. The ON/OFF ratio is estimated as the time integral of the output population when both IN *L* and IN *S* are applied (ON state), divided by the time integral of the output population when only IN *S* is applied (OFF state). The circular marks in Figure 3 represent the ON/OFF ratio as a function of skew ranging from  $-1$  to  $1$  ns, and the triangular marks represent that for skew ranging from  $-4$  to  $4$  ns. The AND gate shows resistance to the delay of IN *S*: a delay of nearly  $1000$  ps in IN *S* provides an ON/OFF ratio greater than 2. Since the duration of the input signal is  $2$  ps, the system is resistant to a skew much longer than the duration of the input signals. On the other hand, the gate operation is not resistant to a delay of IN *L* relative to IN *S*. This is due to the fact that filling the state of QD<sub>*L*</sub> is crucial for the optical excitation transfer from QD<sub>*S*</sub> to QD<sub>*M*</sub>. Therefore, an early, rather than late, arrival of IN *L* is preferred when AND gate-like behavior is intended.

#### 4. EXPERIMENTAL RESULTS

As explained in Section 2, geometrical conditions, such as the size and position of the quantum dots, play a major role in determining their behavior. In addition, the dynamic behavior of the devices, especially the skew dependence of the two input channels discussed in detail in Section 3, is the primary focus of this article. In the experimental demonstration, we need to carefully consider the technological feasibility of the quantum dot devices and diagnostic equipment. We experimentally examined the skew properties involving optical excitation transfer via optical near-field interactions based on InGaAs QDs and a near-field spectroscopy setup with a two-channel short-pulse system, as described in the following and schematically shown in Figure 4.

##### 4.1. Quantum Dots

Stacked InGaAs QD devices fabricated by molecular beam epitaxy (MBE) based on the Stranski–Krastanow (S–K) growth mode [Akahane et al. 1998] were used in the

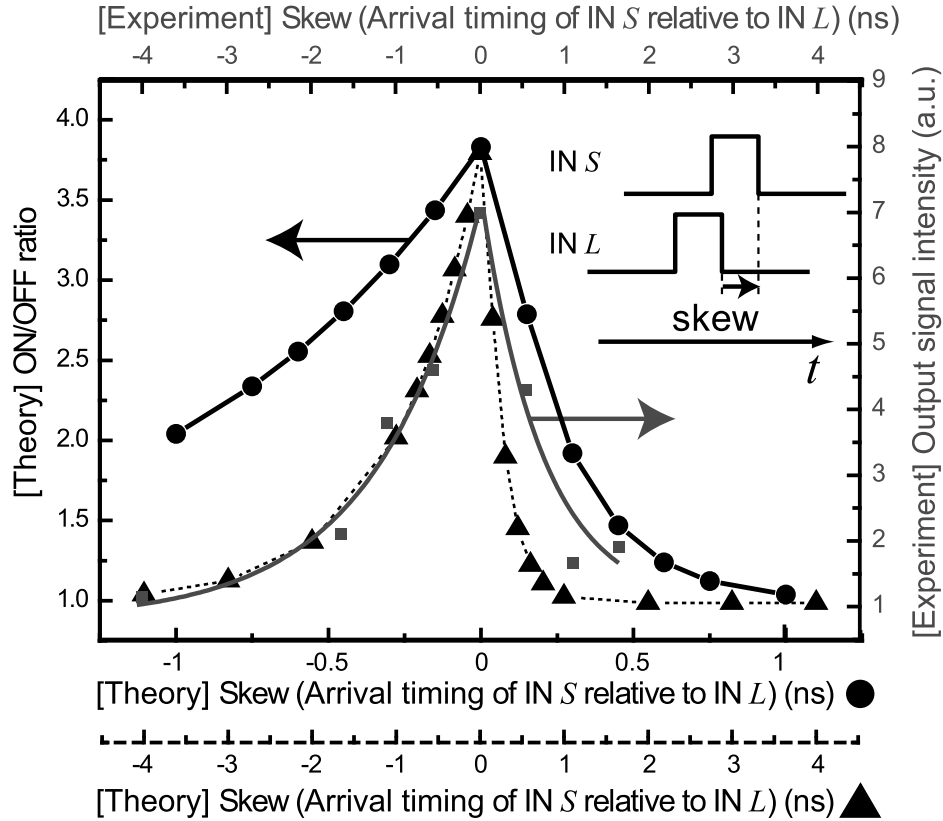


Fig. 3. [Theory: circular and triangular marks] ON/OFF ratio of the output of the AND gate as a function of the skew between the two input signals predicted by theoretical calculations. The skew ranges corresponding to the circular and triangular marks are respectively given by  $\{-1$  to  $1\text{ns}\}$  and  $\{-4$  to  $4\text{ns}\}$ . [Experiment: square marks] Output signal intensity as a function of the skew between the two input signals obtained experimentally by near-field spectroscopy of an InGaAs stacked QD device.

experiment. Figure 4(a) shows a schematic cross-sectional diagram of the InGaAs device sample (more precisely, the fabricated QD is  $\text{In}_{0.4}\text{Ga}_{0.6}\text{As}$ ) used in the experiment, where seven layers of InGaAs QDs with an interlayer distance of 50 nm were fabricated on a GaAs substrate. Figure 4(b) shows a surface profile image of the device, captured with an atomic force microscope (AFM). The average diameter and height of the QDs were around 50nm and 5.5nm, respectively.

Stacked, self-organized QD systems, based on the S–K growth mode in lattice-mismatched materials, have been used in investigating the interactions among QDs, as mentioned in Section 1 [Heitz et al. 1998; Kagan et al. 1996; Mazur et al. 2005; Xu et al. 1996]. In the case of optical excitation transfer via optical near-field interactions, the interlayer QD distances, corresponding to barrier layers, should be thick enough so that the wave functions representing the electronic states of the two QDs do not overlap, but are thin enough so that the optical near-field interactions exist [Ohtsu et al. 2008]; 50 nm satisfies this requirement. Using such stacked QDs, we have demonstrated logic gate operations based on optical near-field interactions [Kawazoe et al. 2006].

In precisely controlling the size of the quantum dots layer-by-layer, Akahane et al. [2002, 2008] developed stacked InAs QDs with InGaAlAs spacer layers on an

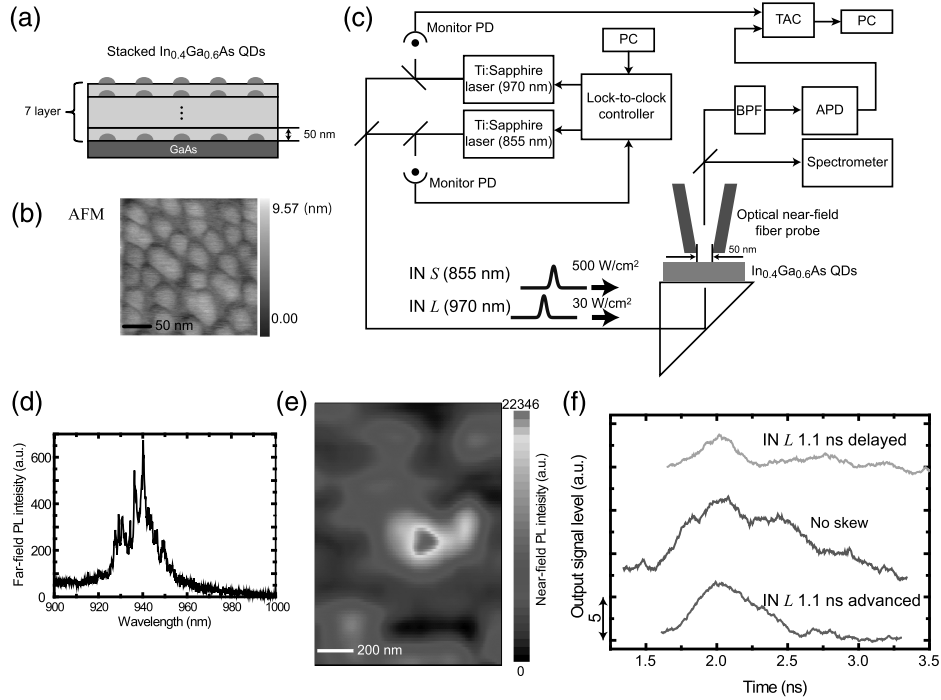


Fig. 4. (a) Cross-sectional profile of the stacked InGaAs QDs used in the experiment. (b) AFM image of the first layer of the InGaAs QD. The average diameter is about 50nm. (c) Schematic diagram of the experimental setup composed of two input optical pulses (wavelengths of 855nm and 970nm) and an optical near-field microscope with a diameter of 50nm. (d) Far-field photoluminescence of the sample. (e) Spatial distribution of the near-field intensity obtained by the near-field fiber probe tip. (f) Time evolution of the output signal when the arrival timing of IN *L* relative to IN *S* was -1.1ns, 0ns, and +1.1ns, respectively.

InP(311)B substrate employing a strain compensation technique, which provides layer-by-layer size-controlled stacked quantum nanostructures. The device used in our experiment was, however, intentionally chosen as InGaAs QDs on a GaAs substrate, where large interlayer strain remains compared with InAs QDs on an InP substrate [Akahane et al. 2002], leading to nonuniformity in the QD sizes. One reason is that the feasible operating wavelengths ( $<1.0\mu\text{m}$ ) of the optical near-field experimental apparatus described in the following are well-matched with InGaAs QDs, whereas InP-based QDs requires wavelengths greater than  $1.0\mu\text{m}$ , which are not well-matched. Another reason is that, as demonstrated in the spatial intensity distribution observed by the near-field spectroscopy in the following, the inhomogeneity of the dot size of the InGaAs QDs enabled interdot optical excitation transfer, and we searched for spatial positions where the InGaAs QDs work as AND gates.

#### 4.2. Spectroscopy Apparatus

The two-channel input signals, IN *S* and IN *L*, were respectively applied to the sample by optical pulses generated by two Ti:Sapphire lasers with wavelengths of 855nm and 970nm, as schematically shown in Figure 4(c). These two lasers were synchronized by a lock-to-clock controller. The pulse duration of both input channels was 2ps, and their repetition rate was 80 MHz. The average optical powers in the IN *S* and IN *L* channels irradiated on the sample were  $500\text{W}/\text{cm}^2$  and  $30\text{W}/\text{cm}^2$ , respectively, which were sufficiently low to avoid multiphoton processes in the sample. One of the input

beams, the IN *S* channel at 855nm, was sampled by a monitoring photodetector and was fed back to the lock-to-clock controller for the purpose of electrical timing control of the 855nm pulses. This allowed a relative timing difference to be produced between IN *S* and IN *L* for the skew evaluation described as follows. As shown in Figure 4(c), the QD sample under study was placed on a prism, and the two input beams irradiated the sample from the back side (facing the substrate).

The photoluminescence of the sample was obtained from the front side (facing the top layer of the QDs) by an optical near-field fiber probing tip with a diameter of 50nm, which conveyed the sampled light to a spectrometer and an avalanche photodiode (APD). Figure 4(d) shows a far-field photoluminescence spectrum of the sample measured at 48.8K, showing inhomogeneous broadening corresponding to the size distributions in the sample. This allowed us to investigate the optical excitation transfer in the region where the transfer conditions were satisfied in the sample.

We then evaluated the near-field intensity distribution of the output signal, corresponding to the radiation from QD<sub>*M*</sub>, as discussed in Section 3, as the integrated photoluminescence between 945nm and 955nm obtained by the spectrometer. Figure 4(e) shows a near-field intensity distribution, for irradiation with 855nm light, corresponding to the output wavelength that exhibits spatial position dependence, indicating that energy transfer occurs among the QDs. There was no polarization-dependence in the experiments we conducted in this study.

### 4.3. Skew Dependences

To evaluate the skew dependence, we employed a time-correlated single photon counting method [Becker 2005]. The photoluminescence of the sample obtained by the near-field probing tip was first filtered by a band-pass filter (945–955nm) to select the output signal, and was detected by an APD. At the same time, input optical pulses at 970nm (IN *L* channel) were monitored by a photodiode. These two signals were provided to a time-to-amplitude converter (TAC) to characterize the time evolution of the output signal. This evaluation was repeated while modifying the relative timing difference between IN *S* and IN *L* using the lock-to-clock laser systems described earlier. Figure 4(f) demonstrates three time evolutions of the output signal, detected through the TAC, when the arrival timing of IN *L* relative to IN *S* was -1.1ns, 0ns, and +1.1ns, respectively. (These three signal traces are represented with different offsets in Figure 4(f) so that we can clearly observe the differences.) The output signal exhibited a higher level when there was no skew between the inputs. The output signal decreased due to the timing difference between IN *L* and IN *S*, but it was more robust to the early arrival of IN *L* rather than the delay of IN *L*, as theoretically discussed in Section 2.

We characterized the output signal intensity as the time integral of the output signal, three examples of which are shown in Figure 4(f), for a duration between 0 and 3ns. The output signal intensity depended on the skew, as indicated by the squares in Figure 3. We observed that they exhibited asymmetric responses with respect to the arrival timing of IN *S* and IN *L*, showing good agreement with the behavior predicted by the theory discussed earlier.

## 5. SUMMARY AND DISCUSSION

We examined the timing dependence of nanophotonic devices based on optical excitation transfer via optical near-field interactions, and analyzed the dynamic behavior of a nanophotonic switch composed of three quantum dots, based on a quantum mechanical formulation using a density matrix, while assuming skew between input signals. The device is resistant to skew longer than the duration of the input signals, and the

tolerance to skew is asymmetric with respect to the arrival timing of the two inputs since the state filling of the largest dot is the key process for the nanophotonic switch operation. Experimental confirmation was also obtained based on near-field spectroscopy using stacked InGaAs quantum dots, showing good agreement with the theory.

Finally, we make a few remarks regarding the content discussed in this article, focusing on the timing properties in nanophotonics. First, elucidating the dynamic properties of nanophotonic devices in this way has implications for novel system architectures. For example, a skew resistance being much longer than the duration of input signals opens up the possibility of asynchronous architectures [Hauck 1995] based on optical excitation transfer. Such architectures are especially useful in situations where the implementation of clock signals poses problems. Asynchronous circuits have been well known for their robustness to timing fluctuations, and in recent years this idea has been extended to the design of asynchronous cellular automata [Lee et al. 2005]. The probabilistic nature of optical near-field interactions, the limited distances over which these interactions take place, and the array-like structures of QDs that are in the realm of fabrication technology, all combine to form a promising basis for the realization of such architectures.

Second, the resistance to timing skew on the order of nanoseconds, at the same time reveals that the nanophotonic system could suffer from the problem of lower bit rate (100 Mbps range), although strict timing management could provide Gbps performance [Ohtsu et al. 2008]. The bit rate also depends on the energy dissipation in the system [Naruse et al. 2010], as well as the signal-to-noise ratio of the detectors and the number of photons per time slot. A unified, total performance evaluation of nanophotonic systems, taking account of architectural, energy dissipation, reliability, and dynamic properties would be a future important research theme.

For the implementation of more advanced nanophotonic devices, as already mentioned in Section 4, Akahane et al. [2008] developed a method of stacking InAs QDs using a strain compensation scheme where spacer layers with a lattice constant slightly smaller than that of the substrate are used to embed the QD layers. Using this method, 150 InAs QD layers were successfully stacked without any degradation in QD quality, leading to the implementation of a versatile arrangement of QDs within a device. Another approach to size- and position-controlled realization of nanophotonic devices includes DNA-based self-assembly technologies [Pistol et al. 2008; Warner and Hutchison 2003]. We have recently developed a self-assembly method of linearly aligning ZnO quantum dots with the help of DNA as a size-controlled template [Yatsui et al. 2010]. With those architectural and experimental insights and technologies, we will continue to broaden our understanding of optical near-field interactions and utilize them for information processing and communications applications.

## REFERENCES

- AKAHANE, K., KAWAMURA, T., OKINO, K., KOYAMA, H., LAN, S., OKADA, Y., KAWABE, M., AND TOSA, M. 1998. Highly packed InGaAs quantum dots on GaAs(311)B. *Appl. Phys. Lett.* 73, 3411, 1–3.
- AKAHANE, K., OHTANI, N., OKADA, Y., AND KAWABE, M. 2002. Fabrication of ultra-high density InAs-stacked quantum dots by strain-controlled growth on InP(3 1 1)B substrate. *J. Cryst. Growth* 245, 31–36.
- AKAHANE, K., YAMAMOTO, N., AND TSUCHIYA, M. 2008. Highly stacked quantum-dot laser fabricated using a strain compensation technique. *Appl. Phys. Lett.* 93, 041121, 1–3.
- BECKER, W. 2005. *Advanced Time-Correlated Single Photon Counting Techniques*. Springer.
- CARMICHAEL, H. J. 1999. *Statistical Methods in Quantum Optics 1*. Springer-Verlag.
- COLLIER, C. P., WONG, E. W., BELOHRADSKY, M., RAYMO, F. M., STODDARD, J. F., KUEKES, P. J., WILLIAMS, R. S., AND HEATH, J. R. 1999. Electronically configurable molecular-based logic gates. *Science* 285, 391–394.

- CROOKER, S. A., HOLLINGSWORTH, J. A., TRETIAK, S., AND KLIMOV, V. I. 2002. Spectrally resolved dynamics of energy transfer in quantum-dot assemblies: Towards engineered energy flows in artificial materials. *Phys. Rev. Lett.* 89, 186802, 1–4.
- DAI, J., WANG, L., AND LOMBARDI, F. 2010. An information-theoretic analysis of quantum-dot cellular automata for defect tolerance. *ACM J. Emerg. Technol. Comput. Syst.* 6, 9, 1–19.
- FRANZL, T., KLAR, T. A., SCHIETINGER, S., ROGACH, A. L., AND FELDMANN, J. 2004. Exciton recycling in graded gap nanocrystal structures. *Nano Lett.* 4, 1599–1603.
- HAUCK, S. 1995. Asynchronous design methodologies: An overview. *Proc. IEEE* 83, 69–93.
- HEITZ, R., MUKHAMEDZHANOV, I., CHEN, P., AND MADHUKAR, A. 1998. Excitation transfer in self-organized asymmetric quantum dot pairs. *Phys. Rev. B* 58, R10151–R10154.
- HORI, H. 2001. Electronic and electromagnetic properties in nanometer scales. In *Optical and Electronic Process of Nano-Matters*. M. Ohtsu Ed., Kluwer Academic, 1–55.
- ITOH, T., FURUMIYA, M., IKEHARA, T., AND GOURDON, C. 1990. Size-dependent radiative decay time of confined excitons in CuCl microcrystals. *Solid State Comm.* 73, 271–274.
- KAGAN, C. R., MURRAY, C. B., NIRMAL, M., AND BAWENDI, M. G. 1996. Electronic energy transfer in CdSe quantum dot solids. *Phys. Rev. Lett.* 76, 1517–1520.
- KAWAZOE, T., KOBAYASHI, K., SANGU, S., AND OHTSU, M. 2003. Demonstration of a nanophotonic switching operation by optical near-field energy transfer. *Appl. Phys. Lett.* 82, 2957–2959.
- KAWAZOE, T., KOBAYASHI, K., AKAHANE, K., NARUSE, M., YAMAMOTO, N., AND OHTSU, M. 2006. Demonstration of nanophotonic NOT gate using near-field optically coupled quantum dots. *Appl. Phys. B* 84, 243–246.
- KAWAZOE, T., OHTSU, M., ASO, S., SAWADO, Y., HOSODA, Y., YOSHIZAWA, K., AKAHANE, K., YAMAMOTO, N., AND NARUSE, M. 2011. Two-dimensional array of room-temperature nanophotonic logic gates using InAs quantum dots in mesa structures. *Appl. Phys. B*, 103, 537–546.
- KEELER, G. A., NELSON, B. E., AGARWAL, D., AND MILLER, D. A. B. 2000. Skew and jitter removal using short optical pulses for optical interconnection. *IEEE Photon. Technol. Lett.* 12, 714–716.
- LEE, J., ADACHI, S., PEPER, F., AND MASHIKO, S. 2005. Delay-insensitive computation in asynchronous cellular automata. *J. Comput. Syst.* 70, 201–220.
- MATSUDA, K., SAIKI, T., NOMURA, S., AND AOYAGI, Y. 2005. Local density of states mapping of a field-induced quantum dot by near-field photoluminescence microscopy. *Appl. Phys. Lett.* 4, 043112, 1–3.
- MAZUR, Y. I., WANG, Z. M., TARASOV, G. G., XIAO, M., SALAMO, G. J., TOMM, J. W., TALALAEV, V., AND KISSEL, H. 2005. Interdot carrier transfer in asymmetric bilayer InAs/GaAs quantum dot structures. *Appl. Phys. Lett.* 86, 063102, 1–3.
- NARUSE, M., MITSU, H., FURUKI, M., IWASA, I., SATO, Y., TATSUURA, S. AND TIAN, M. 2003. Femtosecond timing measurement and control using ultrafast organic thin films. *Appl. Phys. Lett.* 83, 4869–4871.
- NARUSE, M., MIYAZAKI, T., KAWAZOE, T., SANGU, S., KOBAYASHI, K., KUBOTA, F., AND OHTSU, M. 2005. Nanophotonic computing based on optical near-field interactions between quantum dots. *IEICE Trans. Electron. E88-C*, 1817–1823.
- NARUSE, M., KAWAZOE, T., SANGU, S., KOBAYASHI, K., AND OHTSU, M. 2006. Optical interconnects based on optical far- and near-field interactions for high-density data broadcasting. *Opt. Express* 14, 306–313.
- NARUSE, M., HORI, H., KOBAYASHI, K., AND OHTSU, M. 2007. Tamper resistance in optical excitation transfer based on optical near-field interactions. *Opt. Lett.* 32, 1761–1763.
- NARUSE, M., KAWAZOE, T., OHTA, R., NOMURA, W., AND OHTSU, M. 2009. Optimal mixture of randomly dispersed quantum dots for optical excitation transfer via optical near-field interactions. *Phys. Rev. B* 80, 125325, 1–3.
- NARUSE, M., HORI, H., KOBAYASHI, K., HOLMSTRÖM, P., THYLÉN, L., AND OHTSU, M. 2010. Lower bound of energy dissipation in optical excitation transfer via optical near-field interactions. *Opt. Express* 18, A544–A553.
- OHTSU, M., KOBAYASHI, K., KAWAZOE, T., YATSUI, T., AND NARUSE, M. 2008. *Principles of Nanophotonics*. Taylor and Francis.
- PEPER, F., LEE, J., ABO, F., ISOKAWA, T., ADACHI, S., MATSUI, N., AND MASHIKO, S. 2004. Fault-tolerance in nanocomputers: A cellular array approach. *IEEE Trans. Nanotechnol.* 3, 187–201.
- PISTOL, C., DWYER, C., AND LEBECK, A. R. 2008. Nanoscale optical computing using resonance energy transfer logic. *IEEE Micro* 28, 7–18.
- REMACLE, F., SPEISER, S., AND LEVINE, R. D. 2001. Intermolecular and intramolecular logic gates. *J. Phys. Chem. B* 105, 5589–5591.

- UNOLD, T., MUELLER, K., LIENAU, C., ELSAESSER, T., AND WIECK, A. D. 2005. Optical control of excitons in a pair of quantum dots coupled by the dipole-dipole interaction. *Phys. Rev. Lett.* *94*, 137404, 1–3.
- WARNER, M. G. AND HUTCHISON, J. E. 2003. Linear assemblies of nanoparticles electrostatically organized on DNA scaffolds. *Nature Mat.* *2*, 272–277.
- XU, Z. Y., LU, Z. D., YANG, X. P., YUAN, Z. L., ZHENG, B. Z., XU, J. Z., GE, W. K., WANG, Y., WANG, J., AND CHANG, L. L. 1996. Carrier relaxation and thermal activation of localized excitons in self-organized InAs multilayers grown on GaAs substrates. *Phys. Rev. B* *54*, 11528–11531.
- YAN, H., CHOE, H. S., NAM, S., HU, Y., DAS, S., KLEMIC, J. F., ELLENBOGEN, J. C., AND LIEVER, C. M. 2011. Programmable nanowire circuits for nanoprocessors. *Nature* *470*, 240–244.
- YEOW, E. K. L. AND STEER, R. P. 2003. Energy transfer involving higher electronic states: A new direction for molecular logic gates. *Chem Phys. Lett.* *377*, 391–398.
- YATSUI, T., SANGU, S., KAWAZOE, T., OHTSU, M., AN, S. J., YOO, J., AND YI, G.-C. 2007. Nanophotonic switch using ZnO nanorod double-quantum-well structures. *Appl. Phys. Lett.* *90*, 223110 1–3.
- YATSUI, T., RYU, Y., MORISHIMA, T., NOMURA, W., KAWAZOE, T., YONEZAWA, T., WASHIZU, M., FUJITA, H., AND OHTSU, M. 2010. Self-assembly method of linearly aligning ZnO quantum dots for a nanophotonic signal transmission device. *Appl. Phys. Lett.* *96*, 133106 1–3.

Received October 2010; revised March 2011, May 2011; accepted June 2011

## Optical near-field induced visible response photoelectrochemical water splitting on nanorod TiO<sub>2</sub>

Thu Hac Huong Le,<sup>1</sup> Kazuma Mawatari,<sup>1</sup> Yuriy Pihosh,<sup>1</sup> Tadashi Kawazoe,<sup>2</sup> Takashi Yatsui,<sup>2</sup> Motoichi Ohtsu,<sup>2</sup> Masahiro Tosa,<sup>3</sup> and Takehiko Kitamori<sup>1,a)</sup>

<sup>1</sup>Department of Applied Chemistry, Graduate School of Engineering, The University of Tokyo, Hongo 7-3-1, Bunkyo-ku, Tokyo 113-8656, Japan

<sup>2</sup>Department of Electrical Engineering and Information Systems, Graduate School of Engineering, The University of Tokyo, Hongo 7-3-1, Bunkyo-ku, Tokyo 113-8656, Japan

<sup>3</sup>Micro-Nano Component Materials Group, Materials Engineering Laboratory, National Institute for Materials Science (NIMS), Sengen 1-2-1, Tsukuba, Ibaraki 305-0047, Japan

(Received 30 September 2011; accepted 30 October 2011; published online 22 November 2011)

Here we report a way to induce the visible response of non-doped TiO<sub>2</sub> in the photocatalytic electrochemical water splitting, which is achieved by utilizing the optical near-field (ONF) generated on nanorod TiO<sub>2</sub>. The visible response is attributed to the ONF-induced phonon-assisted excitation process, in which TiO<sub>2</sub> is excited by sub-bandgap photons via phonon energy. Our approach directly gets involved in the excitation process without chemical modification of materials; accordingly it is expected to have few drawbacks on the photocatalytic performance. This study may offer another perspective on the development of solar harvesting materials. © 2011 American Institute of Physics. [doi:10.1063/1.3663632]

Among many candidates of semiconductor photocatalyst, TiO<sub>2</sub> has become the most investigated one for overall water splitting for hydrogen production, due to its outstanding chemical stability, low cost, and non-toxicity. There have been significant efforts to improve the visible response of TiO<sub>2</sub> based photocatalyst by chemically manipulating its bandgap. The anionic doping of non-metals such as nitrogen, carbon, or sulfur has been reported to form the mid bandgap states slightly above the intrinsic valence band of TiO<sub>2</sub>, thereby narrowing the bandgap.<sup>1-4</sup> However, these midgap states would lead to the formation of recombination centers that reduce the overall catalytic activity.<sup>5</sup> Another promising approach involves the plasmon-induced enhancement of visible response in TiO<sub>2</sub> loading metal nanoparticles (Au, Ag, etc), yet these materials need a large applied bias or the addition of electron donor in order to obtain hydrogen generation and the stability of the metal is still a problem.<sup>6,7</sup> The lack of materials that meet both the requirements of bandgap energy and stability indicates that the issue has some certain limitations that cannot be solved only by chemical modification.

The nanostructured semiconductors have attracted much attention for their unique optical and electronic properties. Although the nanostructured TiO<sub>2</sub> enhances the catalytic performance at UV region by improving the charge separation and transport properties, the visible response of TiO<sub>2</sub> derived from nanostructures has not been investigated to date. Recently, it has been reported that optical near-field (ONF) generated at the nanostructures can excite the coherent phonons in the nanostructures, together with the ONF; these excited coherent phonons form a coupled state which is called virtual exciton-phonon-polariton. This coupled state contributes to the so-called phonon-assisted process,<sup>8,9</sup> which excites an electron in the valence band of a semicon-

ductor to the conduction band via energy of phonon. Although this excitation is an electric-dipole forbidden, it is allowed by the ONF which can couple with phonons to generate a quasi-particle of exciton-phonon-polariton in a nanomeric space. That is, this quasi-particle can excite the electron to the phonon level and successively to the conduction band. This two-step excitation process is possible even though the incident photon energy lower than the band gap energy. The ONF phonon-assisted excitation has already been experimentally proved and widely applied as photochemical vapor deposition, photolithography,<sup>10</sup> self-organized photochemical etching,<sup>11</sup> optical frequency up-conversion,<sup>12</sup> and semiconductor photovoltaic.<sup>13</sup> This effect has inspired us a physical approach to induce the visible response of semiconductor photocatalysts such as TiO<sub>2</sub> by introducing favorable nanostructure to generate ONF (Scheme 1 in supplemental materials<sup>21</sup>). In this study, we demonstrate the fabrication of specific nanorod TiO<sub>2</sub> that leads to the generation of ONF and confirms the excitation of TiO<sub>2</sub> with sub-bandgap photons by using ONF.

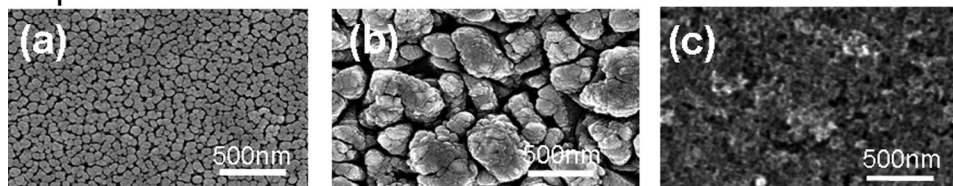
Generally, the generation of ONF strongly depends on the nanomeric structures; hence, the fabrication of favorable nanostructures is crucial to induce the ONF effect. Among the techniques for fabrication of nanostructures, glancing angle deposition (GLAD) allows a viable way to fabricate aligned nanorod with well-controlled diameter, density, and shape.<sup>14,15</sup> Herein, we demonstrate the using of radio frequency magnetron sputtering deposition equipped with GLAD regime to fabricate vertical nanorod TiO<sub>2</sub> with different diameters.

The scanning electron microscopy, top view, and cross sectional images of fabricated films shown in the Fig. 1 reveal the formation of vertical and isolated nanorods. The deposition onto a flat indium tin oxide (ITO) coated glass substrate leads to the growth of nanorod less than 100 nm in diameter, meanwhile the using of pyramid-like nano-patterns

<sup>a)</sup> Author to whom correspondence should be addressed. Electronic mail: kitamori@icl.t.u-tokyo.ac.jp. Tel.: +81-3-5841-7231.



## Top view



## Cross-section

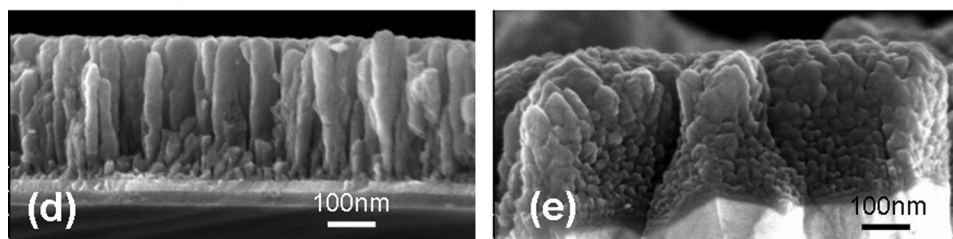


FIG. 1. SEM images of (a) top view of nanorod  $\text{TiO}_2$  fabricated on ITO substrate. The average diameter was estimated by image analysis software to be  $65 \text{ nm} \pm 2 \text{ nm}$ ; (b) top view of nanorod  $\text{TiO}_2$  fabricated on nano-patterned FTO substrate. The average diameter is about  $150 \text{ nm} \pm 15 \text{ nm}$ ; (c) top view of flat film made of Aeroxide P-25 nanoparticles; (d) cross sectional view of 65 nm nanorod sample; (e) cross sectional view of 150 nm nanorods, which themselves have rough surfaces composed of fine nanoscale structure.

on the F-doped tin oxide (FTO) substrate, which serves as nucleation sites for the incoming target flux, allows the growth of rods larger than 100 nm. For the reference purpose, we fabricated the flat film made of Aeroxide P-25 nanoparticles by spin-coating. It should be noted from cross-sectional images that the larger nanorod (150 nm) sample is built from the individual nanorods which themselves have rough surfaces composed of fine nanoscale structure, compared to the flat surface on smaller (65 nm) nanorod one. The analysis on the crystalline structures of nanorod  $\text{TiO}_2$  films after post-annealing carried out by X-ray diffractometry (XRD) shows the single anatase phase.

The photocatalytic performance of  $\text{TiO}_2$  film was evaluated by photoelectrochemical (PEC) measurement with a 3-electrode setup in 0.5 M  $\text{NaClO}_4$  electrolyte and 0.5 V (vs. Ag/AgCl) applied bias. The power dependence of photocurrent in Figs. 2(a) and 2(b) show the photocatalytic performance of fabricated films under ultraviolet (UV, 365 nm) and visible (488 nm) irradiation, respectively. Under UV irradiation, the nanorod  $\text{TiO}_2$  films perform a comparative photo current to the reference P-25 film, while under visible (488 nm) irradiation, more than 2 orders of magnitude enhancement of photocurrents in 150 nm nanorod sample has been observed. The introduction of nanorod structures has led to a significant enhancement only in the visible region that excludes the possibility of the photocurrent derived from enhanced specific surface area or improved charge separation and transport properties. The linear dependence in a wide range of light power density ( $10^1 \sim 10^5 \text{ mW cm}^{-2}$ ) and the slope equal to 1.0 excludes the possibility of the excitation of  $\text{TiO}_2$  by non-linear multi-photon absorption. As described above, although the phonon-assisted excitation is a two-step one and since the second step transition from the energy levels of phonon to the conduction band is a conventional adiabatic transition, the probability of the second step transition is more than  $10^6$  times larger than that of the first transition step from the valence band to phonon levels.<sup>9,12</sup> In addition, the second step transition of a conventional adiabatic transition easily saturates, which results in the linear power dependence as shown in the Fig. 2(b). It is also worthy to note that the photocurrent has been acquired in the range

of  $10^{-5} \text{ A}$  that eliminates the factors of thermal effect or background noise during the measurement.

There is a limited investigation of non-doped  $\text{TiO}_2$  in which its visible response is attributed to the excitation of mid-gap impurities states.<sup>16,17</sup> Generally, photoluminescence (PL) spectroscopy is the common method to study defects states in oxide materials. The absorption spectra of nanorod samples (Fig. 3(a)) show clear interference patterns in visible region which can be attributed to the interference in the thickness of the films ( $\sim 300 \text{ nm}$ ). The slight absorption in visible region has been observed, and this absorption strongly enhances in nanorod samples. The enhancement of the visible absorption can be ascribed to the scattering effect on complex nanorod structures. A strong gain of optical absorption in nanorod samples is in good agreement with

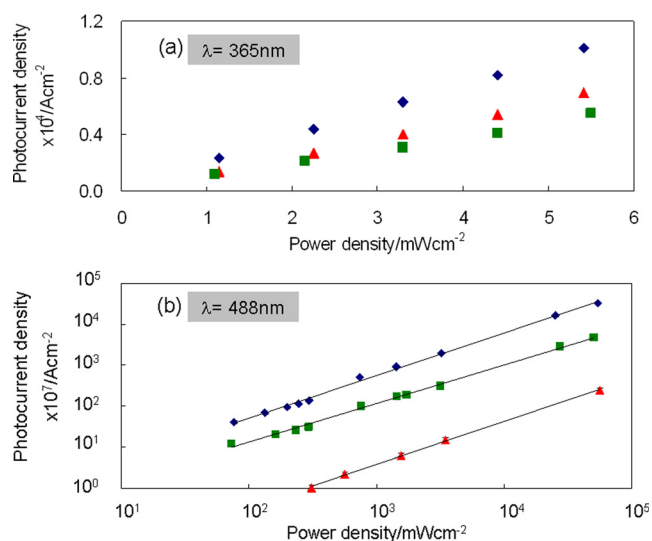


FIG. 2. (Color online) The power dependence of photo current measured by PEC method at 0.5 V applied bias (vs. Ag/AgCl) in 0.5 M  $\text{NaClO}_4$  (a) under 365 nm irradiation and (b) 488 nm irradiation of 150 nm nanorod (blue diamond), 65 nm nanorod (green square), and P-25 film (red triangle). The photoresponse of fabricated nanorod  $\text{TiO}_2$  samples UV irradiation are comparable to the P-25 film; however, (b) under 488 nm irradiation the photocurrents in nanorods samples are more than 2 orders of magnitude larger than that of P-25 film. A linear dependence in a wide range of light power intensity  $10^1 \sim 10^5 \text{ mW cm}^{-2}$ .

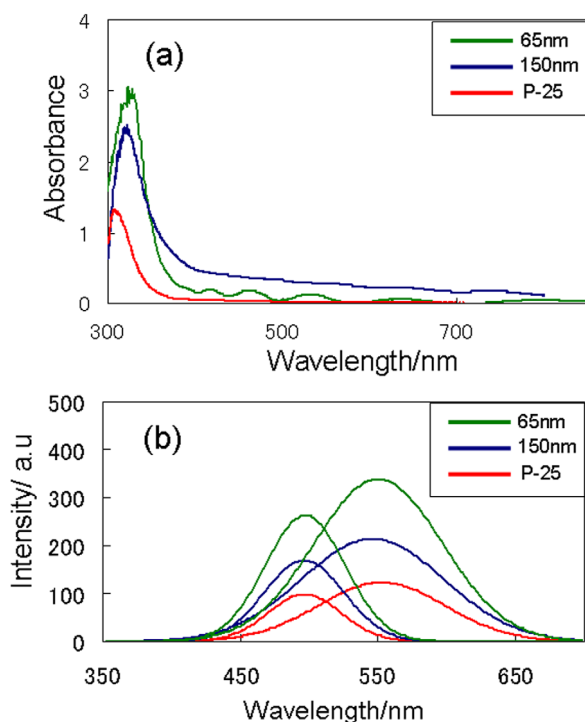


FIG. 3. (Color online) (a) The UV-vis absorption spectra of TiO<sub>2</sub> films with a slight absorption in visible region (>400 nm) of 150 nm nanorod (blue line), 65 nm nanorod (green line), and P-25 (red line) film. The larger enhancement of optical absorption observed in nanorod samples compared to that of flat film with the same thickness can be attributed to the low refraction and cavity effect of dense nanorod structure (b) the Gaussian-fitted PL spectra of 150 nm nanorod (blue line), 65 nm nanorod (green line), and P-25 film (red line) acquired at 12 K with 325 nm excitation. The peak centered at 500 and 550 nm can be attributed to the surface oxygen defects and the intrinsic defects inside the bulk, respectively. The PL intensity of nanorod film is 2-fold larger than that of P-25 film, yet there is no relevant relation between PL intensity and visible response photocurrent.

previous reports on the decrease of refraction index and the consequent increase of light trapping and nanocavity effect in nanostructures.<sup>18,19</sup> The normalized and Gaussian-fitted PL spectra taken at 12 K under 325 nm excitation in Fig. 3(b) show that all the samples have a broad luminescence band composed of two bands centered at 500 and 550 nm, which can be ascribed to the surface oxygen defects and the intrinsic defects inside the bulk, respectively.<sup>20</sup> Interestingly, there is no significant difference of the PL intensity in nanorod TiO<sub>2</sub> samples, while the intensity in nanorod samples is 2 folds higher than that of P-25 flat film. However, the intensity of PL peaks does not reveal any relevant relation with the visible response photocurrent result. It can be concluded from PEC and PL studies that the significant enhancement of visible response in nanorod samples does not relate to the defect states, but the introduction of specific nanostructure does contribute to the enhancement of ONF and consequently induce the visible response of TiO<sub>2</sub> via the

ONF-induced phonon-assisted excitation. Moreover, the visible response photocurrent in 150 nm nanorod sample is about one order larger than that of 65 nm nanorod. We attribute that individual nanorods which themselves have rough surfaces composed of fine nanostructure in 150 nm nanorod sample play a critical role in the enhancement of ONF.

In summary, nanorod TiO<sub>2</sub> has been fabricated by sputtering with GLAD regime. The introduction of nanorod structure and specific morphology on each rod has led to the generation of ONF, which induces the visible response via the phonon-assisted excitation. Our result has confirmed a physical approach to excite semiconductor photocatalyst, while the materials remain untreated. We believe that the present approach can be applied not only to photocatalyst but also other solar-harvesting materials.

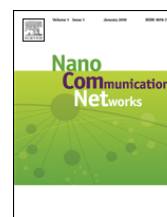
We thank Dr. Makoto Naruse and Dr. Kokoro Kitamura of Ohtsu Laboratory, at the Department of Electrical Engineering and Information Systems, Graduate School of Engineering, The University of Tokyo for useful discussion. We would like to thank Mr. Ivan Khalakhan for help with the SEM measurements. The authors acknowledge the financial support of JSPS specially promoted research.

- <sup>1</sup>K. Maeda and K. Domen, *J. Phys. Chem. C* **111**, 7851 (2007).
- <sup>2</sup>R. Asahi, T. Morikawa, T. Ohwaki, K. Aoki, and Y. Taga, *Science* **293**, 269 (2001).
- <sup>3</sup>H. Irie, Y. Watanabe, and K. Hashimoto, *Chem. Lett.* **32**, 772 (2003).
- <sup>4</sup>S. Kim, S.-Ju. Hwang, and W. Choi, *J. Phys. Chem. B* **109**, 24260 (2005).
- <sup>5</sup>J. Zhang, Y. Wu, M. Xing, S. Leghari, and S. Sajjad, *Energy Environ. Sci.* **3**, 715 (2010).
- <sup>6</sup>Y. Tian and T. Tatsuma, *Chem. Commun.* **2004**, 1810 (2004).
- <sup>7</sup>Y. Tian and T. Tatsuma, *J. Am. Chem. Soc.* **127**, 7632 (2005).
- <sup>8</sup>K. Kobayashi, S. Sangu, H. Ito & M. Ohtsu, *Phys. Rev. A* **63**, 013806 (2001).
- <sup>9</sup>T. Kawazoe, K. Kobayashi, S. Takubo, and M. Ohtsu, *J. Chem. Phys.* **122**, 024715 (2005).
- <sup>10</sup>T. Kawazoe, M. Ohtsu, Y. Inao, and R. Kuroda, *J. Nanophoton.* **1**, 011595 (2007).
- <sup>11</sup>T. Yatsui, K. Hirata, W. Nomura, Y. Tabata, and M. Ohtsu, *Appl. Phys. B* **93**, 55 (2008).
- <sup>12</sup>T. Kawazoe, H. Fujiwara, K. Kobayashi, and M. Ohtsu, *J. Sel. Top. Quantum Electron.* **15**, 1380 (2009).
- <sup>13</sup>S. Yukutake, T. Kawazoe, T. Yatsui, K. Hirata, W. Nomura, K. Kitamura, and M. Ohtsu, *Appl. Phys. B* **99**, 415 (2010).
- <sup>14</sup>K. Robbie and M. Brett, *J. Vac. Sci. Technol. A* **15**, 1460 (1997).
- <sup>15</sup>Y. Pihosh, I. Turkevych, J. Ye, M. Goto, A. Kasahara, M. Kondo, and M. Tosa, *J. Electrochem. Soc.* **156**, 160 (2009).
- <sup>16</sup>A. Gorzkowska-Sobas, E. Kusior, M. Radecka, and K. Zahrzewska, *Surf. Sci.* **600**, 3964 (2006).
- <sup>17</sup>H. Kikuchi, M. Kitano, M. Takeuchi, M. Matsuoka, M. Anpo, and P. V. Kamat, *J. Phys. Chem. B* **110**, 5537 (2006).
- <sup>18</sup>Z. P. Yang, L. Ci, J. A. Bur, S. Y. Lin, and P. M. Ajayan, *Nano Lett.* **8**, 446 (2008).
- <sup>19</sup>W. Han, L. Wu, R. F. Klie, and Y. Zhu, *Adv. Mater.* **19**, 2525 (2007).
- <sup>20</sup>K. Iijima, M. Goto, S. Enomoto, H. Kunugita, K. Ema, M. Tsukamoto, N. Ichikawa, and H. Sakama, *J. Lumin.* **128**, 911 (2008).
- <sup>21</sup>See supplemental material at <http://dx.doi.org/10.1063/1.3663632> for fabrication and evaluation methods.



Contents lists available at SciVerse ScienceDirect

# Nano Communication Networks

journal homepage: [www.elsevier.com/locate/nanocomnet](http://www.elsevier.com/locate/nanocomnet)

## Autonomy in excitation transfer via optical near-field interactions and its implications for information networking

Makoto Naruse<sup>a,b,\*</sup>, Kenji Leibnitz<sup>a,c</sup>, Ferdinand Peper<sup>a</sup>, Naoya Tate<sup>b,d</sup>, Wataru Nomura<sup>b,d</sup>, Tadashi Kawazoe<sup>b,d</sup>, Masayuki Murata<sup>c</sup>, Motoichi Ohtsu<sup>b,d</sup>

<sup>a</sup> National Institute of Information and Communications Technology, 4-2-1 Nukui-kita, Koganei, Tokyo 184-8795, Japan

<sup>b</sup> Nanophotonics Research Center, Graduate School of Engineering, The University of Tokyo, 2-11-16 Yayoi, Bunkyo-ku, Tokyo 113-8656, Japan

<sup>c</sup> Department of Information Networking, Graduate School of Information Science and Technology, Osaka University, 1-5 Yamadaoka, Suita, Osaka 565-0871, Japan

<sup>d</sup> Department of Electrical Engineering and Information Systems, Graduate School of Engineering, The University of Tokyo, 2-11-16 Yayoi, Bunkyo-ku, Tokyo 113-8656, Japan

### ARTICLE INFO

#### Article history:

Received 15 July 2011

Accepted 24 July 2011

Available online 30 July 2011

#### Keywords:

Nanophotonics

Optical excitation transfer

Optical near-fields

Autonomous system

Information network

### ABSTRACT

We demonstrate optical excitation transfer in a mixture composed of quantum dots of two different sizes (larger and smaller) networked via optical near-field interactions. For the optical near-field interaction network based on a density matrix formalism, we introduce an optimal mixture that agrees with experimental results. Based on these findings, we theoretically examine the topology-dependent efficiency of optical excitation transfer, which clearly exhibits autonomous, energy-efficient networking behavior occurring at the nanometer scale. We discuss what we can learn from this optical excitation transfer and its implications for information and communications applications.

© 2011 Elsevier Ltd. All rights reserved.

### 1. Introduction

Optics is expected to play a crucial role in enhancing system performance to handle the continuously growing amount of digital data and new requirements demanded by industry and society [24]. However, there are some fundamental difficulties impeding the adoption of optical technologies in information processing and communication systems [17,16,8,1,2]. One problem is the poor integrability of optical devices in systems due to the diffraction limit of light. This is because the optical wavelength used in a given system is typically around 1  $\mu\text{m}$ , which is about 100 times larger than the gate length of present silicon VLSI hardware.

Nanophotonics, on the other hand, is based on local interactions between nanometer-scale materials via

optical near-fields, which are not restricted by conventional diffraction of light, allowing ultrahigh-density integration [17,16,8]. Optical excitation transfer between quantum dots via optical near-field interactions will be one of the most important mechanisms for realizing novel devices and systems [17,16,25,9,5]. Moreover, qualitatively novel features that are unavailable in conventional optics and electronics will be made possible by such optical excitation transfer [14,12].

In this paper, we demonstrate optical excitation transfer in a mixture composed of different-sized (larger and smaller) quantum dots networked via optical near-fields in their vicinities. We introduce a theoretical model of a mixture of two different-sized quantum dots that is optimal in terms of the optical near-field interaction network. This model is based on a density matrix formalism in which the mixture agrees well with experimental results using CdSe/ZnS quantum dot mixtures with diameters of 2.0 and 2.8 nm. Based on these findings, we theoretically examine the topology-dependent efficiency of

\* Corresponding author. Tel.: +81 42 327 6794; fax: +81 42 327 7035.  
E-mail address: [naruse@nict.go.jp](mailto:naruse@nict.go.jp) (M. Naruse).

optical excitation transfer, which clearly exhibits autonomous, energy-efficient networking behavior at nanometer scales. Such autonomous behavior can also give us valuable insights when we look at network architectures in general or at communication networks in particular. At the stage of designing future communication networks, the operational conditions are usually unknown, so these networks must be planned in such a way that they can adapt to changing environments, for example, caused by link failures, changes in traffic patterns, etc. We hope that our discussion on the implications of this optical excitation transfer will also lead to some new aspects in the design of autonomous, robust, and energy-efficient communication architectures.

This paper is organized as follows. In Section 2, we describe the physical fundamentals of optical excitation transfer between quantum dots, followed by the introduction of a network of optical near-field interactions, whereby we analyze the mixture-dependent optical excitation transfer theoretically and experimentally. In Section 3, we investigate the topology-dependency and autonomy of the excitation transfer. Section 4 reflects on what can be learned from these principles and phenomena physically existing at nanometer scales and discusses their implications for information and communications applications.

## 2. Network of optical near-field interactions

### 2.1. Theoretical background

We briefly review the fundamental principles of optical excitation transfer involving optical near-field interactions [17,16]. The interaction Hamiltonian between an electron and an electric field is given by

$$\hat{H}_{\text{int}} = - \int \hat{\psi}^\dagger(\vec{r}) \vec{\mu} \hat{\psi}(\vec{r}) \bullet \hat{D}(\vec{r}) d\vec{r}, \quad (1)$$

where  $\vec{\mu}$  is the dipole moment,  $\hat{\psi}^\dagger(\vec{r})$  and  $\hat{\psi}(\vec{r})$  are respectively the creation and annihilation operators of the electron at  $\vec{r}$ , and  $\hat{D}(\vec{r})$  is the operator of electric flux density. In usual light-matter interactions, the operator  $\hat{D}(\vec{r})$  is a constant since the electric field of propagating light is considered to be constant at nanometer scales. Therefore, one can derive optical selection rules by calculating a transfer matrix of an electric dipole. In the case of cubic quantum dots, for instance, transitions to states described by quantum numbers containing an even number are prohibited [17]. Contrast this with optical near-field interactions, where due to the steep electric field of optical near-fields in the vicinity of a nanometer-scale structure, such as a quantum dot, an optical transition is allowed that would otherwise violate conventional optical selection rules [17,16].

Optical excitations in nanostructures can be transferred to neighboring nanostructures via optical near-field interactions [17,16,25,9,5,14,12,13,15]. Assume that two cubic quantum dots with side lengths  $a$  and  $\sqrt{2}a$ , which are called  $\text{QD}_S$  and  $\text{QD}_L$ , respectively, are located near to each other, as shown in Fig. 1(a). The energy eigenvalues for the quantized exciton energy level specified by quantum

numbers  $(n_x, n_y, n_z)$  in the quantum dot with side length  $a$  ( $\text{QD}_S$ ) are given by

$$E_{(n_x, n_y, n_z)} = E_B + \frac{\hbar^2 \pi^2}{2Ma^2} (n_x^2 + n_y^2 + n_z^2), \quad (2)$$

where  $E_B$  is the energy of the bulk exciton and  $M$  is the effective mass of the exciton. According to Eq. (2), there exists a resonance between the level of quantum number (1, 1, 1) in  $\text{QD}_S$  and that of quantum number (2, 1, 1) in the quantum dot with side length  $\sqrt{2}a$  ( $\text{QD}_L$ ). There is an optical near-field interaction, which is denoted by  $U_{SL}$ , due to the steep electric field in the vicinity of quantum dots. It is known that the inter-dot optical near-field interaction is given by a Yukawa-type potential [17]. Therefore, excitations in  $\text{QD}_S$  can move to the (2, 1, 1)-level in  $\text{QD}_L$ . Note that such a transfer is prohibited for propagating light since the (2, 1, 1)-level in  $\text{QD}_L$  contains an even number. In  $\text{QD}_L$ , the excitation sees a sublevel energy relaxation, denoted by  $\Gamma$ , which is faster than the near-field interaction, and so the excitation goes to the (1, 1, 1)-level in  $\text{QD}_L$ . In Section 3, we apply these theoretical arguments to systems composed of multiple quantum dots and investigate their impact on fundamental features of optical excitation transfer occurring at nanometer scales.

### 2.2. Network of optical near-field interactions

Consider the quantum dot system in Fig. 1(b), where multiple smaller dots (denoted by  $S_i$ ) can be coupled with one larger dot, denoted by  $L$ . We assume inter-dot interactions between adjacent smaller quantum dots (Fig. 1(c)); that is, (i)  $S_i$  interacts with  $S_{i+1}$  ( $i = 1, \dots, N-1$ ) and (ii)  $S_N$  interacts with  $S_1$ , where  $N$  is the number of smaller quantum dots. For instance the system shown in Fig. 1(d) consists of two smaller quantum dots and one larger quantum dot, denoted by **S2-L1**. Similarly, **S3-L1**, **S4-L1**, **S5-L1** systems are composed of three, four, and five smaller quantum dots in addition to one large quantum dot, which are respectively shown in Fig. 1(e)–(g).

Now, what is of interest is to calculate the flow of excitations from the smaller dots to the larger one. The theoretical and experimental details can be found in Ref. [13]; here we introduce the information necessary for discussing the topology-dependency and autonomy in optical excitation transfer in Section 3.

We deal with the problem theoretically based on a density matrix formalism. In the case of the **S2-L1** system, which is composed of two smaller quantum dots and one larger quantum dot, the inter-dot interactions between the smaller dots and the larger one are denoted by  $U_{S_1L}$ , and the interaction between the smaller dots is denoted by  $U_{S_1S_2}$ , as schematically shown in Fig. 2(a). The radiations from  $S_1$ ,  $S_2$ , and  $L$  are respectively represented by the relaxation constants  $\gamma_{S_1}$ ,  $\gamma_{S_2}$ , and  $\gamma_L$ . We suppose that the system initially has two excitations in  $S_1$  and  $S_2$ . With such an initial state, we can prepare a total of eleven bases where zero, one, or two excitation(s) occupy the energy levels; the state transitions are schematically shown in Fig. 2(b). In the numerical calculation, we assume  $U_{S_1L}^{-1} = 200$  ps,  $U_{S_1S_2}^{-1} = 100$  ps,  $\gamma_L^{-1} = 1$  ns,  $\gamma_{S_1}^{-1} = 2.92$  ns,  $\Gamma^{-1} = 10$

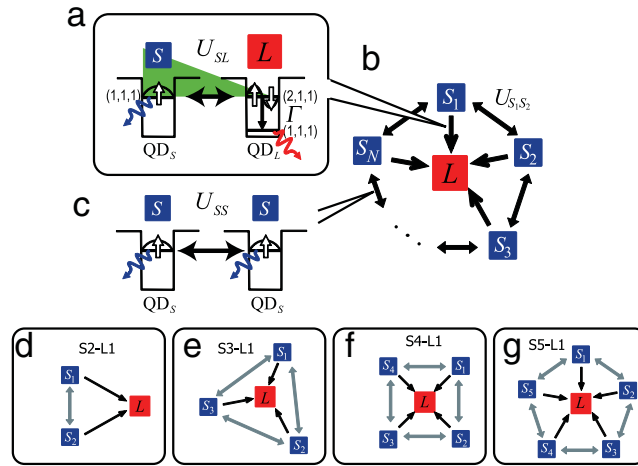


**Fig. 1.** (a) Optical excitation transfer from smaller quantum dot ( $QD_S$ ) to larger quantum dot ( $QD_L$ ) via optical near-field interactions. (b) Multiple-quantum-dot system composed of multiple smaller quantum dots and one large quantum dot networked via optical near-field interactions. (c) Interactions between smaller quantum dots. (d–g) Example systems composed of multiple smaller quantum dots and one large quantum dot.

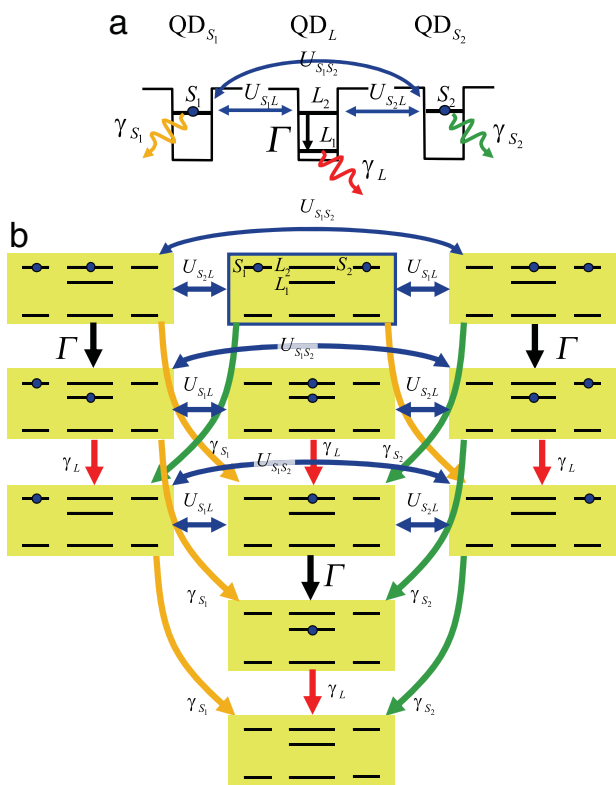


**Fig. 2.** Example of system modeling based on a density matrix formalism. (a) Parameterizations for inter-dot near-field interactions, radiative relaxations, and non-radiative relaxations in the **S2-L1** system. (b) Schematic representation of state transitions in the **S2-L1** system.

ps as parameter values. Following the same procedure, we also derive quantum master equations for the **S3-L1**, **S4-L1**, and **S5-L1** systems that have initial states in which all smaller quantum dots are excited. Finally, we calculate the population of the lower level of a larger quantum dot, of which we regard the time integral as the output signal.

We compare the output signal as a function of the ratio of the number of smaller dots to the number of larger dots assuming that the total number of quantum dots in a given unit area is the same, regardless of their sizes (smaller or

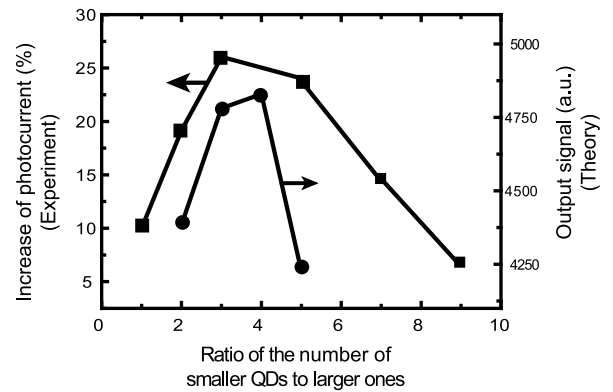


**Fig. 3.** Optimal ratio of the number of smaller quantum dots to larger quantum dots so that the optical excitation transfer is most efficiently induced.

larger). As shown by the circles in Fig. 3, the most efficient transfer is obtained when the ratio of the number of smaller dots to the number of larger dots is 4. In other words, increasing the number of smaller quantum dots beyond a certain level does not necessarily contribute to increased output signals. Because of the limited radiation lifetime of large quantum dots, not all of the initial excitations can be successfully transferred to the large quantum dots due to the states occupying the lower excitation levels of the large quantum dots. Therefore, part of the input populations of smaller quantum dots must decay, which results in a loss in the transfer from the smaller quantum dots to the large quantum dots when there are too many excitations in the smaller quantum dots surrounding one large quantum dot.

An optimal mixture of smaller and larger quantum dots was experimentally demonstrated by using two kinds of CdSe/ZnS core/shell quantum dots whose diameters were 2.0 and 2.8 nm [13,15]. In the experimental details in Ref. [13], the increase of the photocurrent used in the output signal was measured. As shown by the squares in Fig. 3, the maximum increase was obtained when the ratio of the number of smaller quantum dots to larger dots was 3:1, which agrees well with the theoretical optimal ratio discussed above.

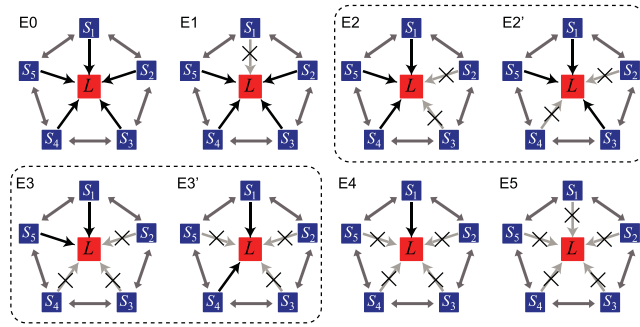


**Fig. 4.** Eight different network topologies in the **S5-L1** system, where some of the interactions between the smaller quantum dots  $QD_S$  and the large quantum dot  $QD_L$  are degraded, or lost. (Degraded interactions are indicated by “X”). The notation  $EN$  indicates that the system contains  $N$  degraded interactions.

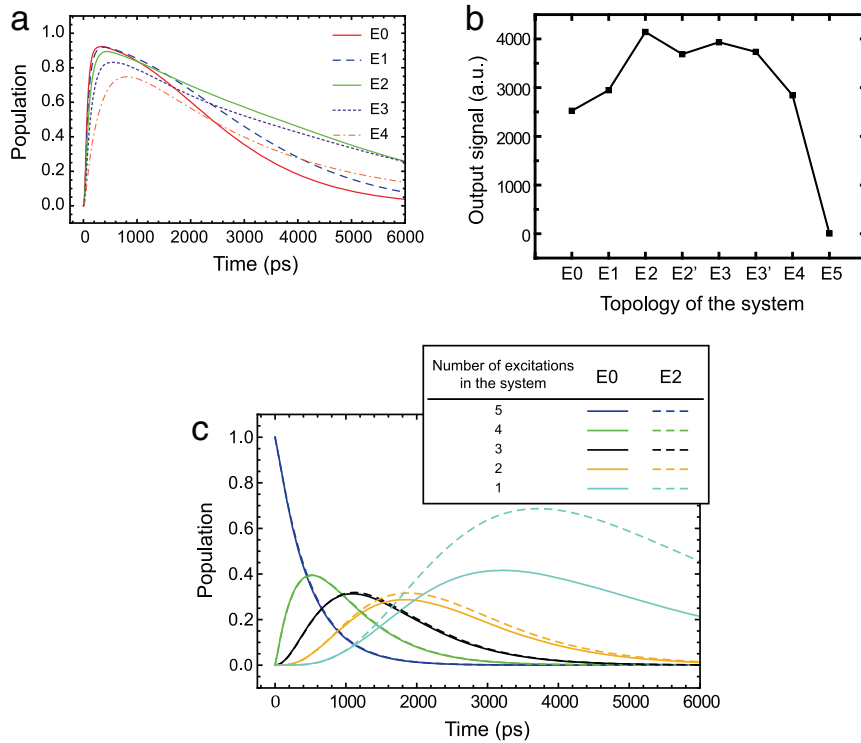


**Fig. 5.** (a) The evolution of the populations associated with the large quantum dot  $QD_L$  in systems **E0**, **E1**, **E2**, **E3**, and **E4** in Fig. 4. (b) Time-integrated populations for the systems in Fig. 4, where systems with certain negligible, or essentially nonexistent, links result in higher output signal levels. (c) The evolution of the populations associated with the number of excitations (ranging from 1 to 5) in systems **E0** and **E2**.

### 3. Topology-dependent, autonomous, efficient optical excitation transfer

In the previous section, we observe that the amount of optical excitation transferred from smaller quantum dots to larger quantum dots depends on the ratio of their numbers. This suggests that we could increase the output by engineering the network structure of the quantum dots. This section takes the **S5-L1** system in Fig. 1(g) as an example, and demonstrates that it is possible to increase the output signal by appropriately configuring the network of quantum dots. We set all of the inter-dot interaction times to 100 ps, while keeping all other parameter values the same as those in Section 2.

Fig. 4 shows the original **S5-L1** system, denoted by **E0**, which is the same as the system shown in Fig. 1(g). Assume that some of the interactions between the smaller

quantum dots (denoted by  $S_1$  to  $S_5$ ) and the large quantum dot surrounded by them are degraded, or lost, due to, for instance, material disorders, such as a violation of the condition represented by Eq. (1). In total there are eight such configurations when symmetries are taken into account; for instance, when one of the five links between the smaller quantum dots on one hand and the large quantum dot on the other hand is degraded, we obtain the system **E1** in Fig. 4. The mark “X” indicates a degraded interaction between  $S_1$  and  $L$ . Similarly, when there are two degraded links, the system should be represented either by the system **E2** or the system **E2'** shown in Fig. 4.

Fig. 5(a) demonstrates the time evolutions of the populations associated with radiation from the large quantum dots. Fig. 5(b) summarizes the integrated populations as a function of the network configurations in Fig. 4. Interestingly, except for the system **E5**, which has no valid links

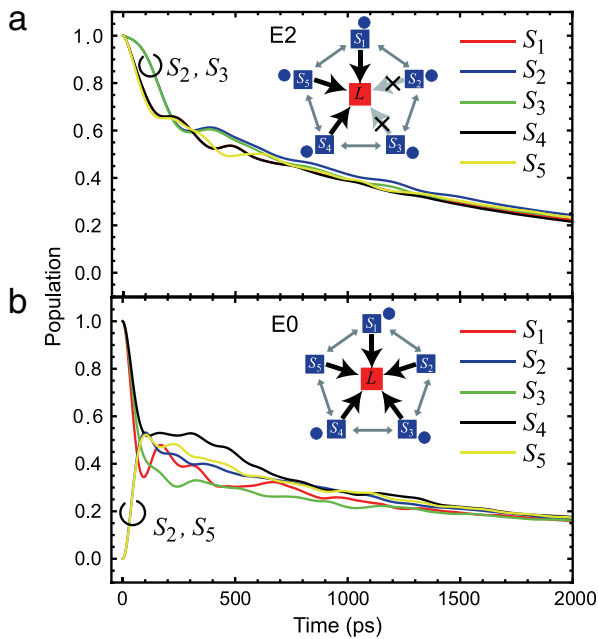


**Fig. 6.** (a) Time evolutions of the populations associated with the smaller quantum dots ( $S_1$  to  $S_5$ ) in system **E2** in Fig. 4 while assuming that all smaller quantum dots contain excitations in the initial setup. (b) Time evolutions of the populations associated with the smaller quantum dots ( $S_1$  to  $S_5$ ) in system **E0** in Fig. 4 while assuming three excitations at  $S_1$ ,  $S_3$ , and  $S_4$ .

between the smaller quantum dots and the large quantum dot, systems with degraded interactions exhibit a higher output signal than the system **E0** without the link defects. System **E2** exhibits an output signal that is about 1.64 times higher than system **E0**. This corresponds to the results described in Section 2, where the output is maximized when the ratio of the number of smaller dots to large dots is 4, meaning that the excessively high number of excitations in the smaller dots cannot be transferred to the large dot they surround. Due to the “limited” interactions between the smaller dots and the large dot, such as in the case of systems **E2** and **E2'**, the excitations located in the smaller dots have a higher probability to be transferred to the larger dot. Fig. 5(c) demonstrates the evolution of populations associated with the total number of excitations contained in the system, ranging from 1 to 5. The solid and dashed curves in Fig. 5(c) respectively refer to systems **E0** and **E2**. The populations containing one excitation increase dramatically in **E2** as compared with **E0**, which is another indication that the excitations can be kept in the system until they are successfully transferred to the destination, exhibiting a topology-dependent efficiency increase.

The autonomous behavior of optical excitation transfer is emphasized by Fig. 6(a), which summarizes the evolutions of populations associated with  $S_1$  to  $S_5$  in system **E2**, where both the interaction between  $S_2$  and  $L$  and the interaction between  $S_3$  and  $L$  are negligible. Initially, all of the smaller dots contain excitations. Note that the populations associated with  $S_2$  and  $S_3$  remain at a higher level for a short initial time, indicating that the excitations in  $S_2$  and  $S_3$  are effectively “waiting” in the smaller dots until they have the opportunity to be transferred to a large dot. Such an autonomous transport is also observed in a “redundant”

situation. Fig. 6(b) characterizes the excitation transfer in system **E0** which contains only the three excitations at  $S_1$ ,  $S_3$ , and  $S_4$ . We can observe that the populations associated with  $S_2$  and  $S_5$  grow instantaneously, whereas they are zero at the start. In other words, we can see that the excitations autonomously exploit the free, usable resources in the system in order to yield efficient transport.

#### 4. Discussion and implications for information and communications systems

Finally, we make a few remarks about how we can apply these findings in nanometer-scale light-matter interaction networks to information and communications technologies (ICTs).

##### 4.1. Autonomous behavior of optical excitations

The first point we should highlight is the autonomous behavior observed in the optical excitations. As we saw from the experiments, there is no “central controller” in the systems, and yet, efficient transport of the optical excitations is realized. Such an intrinsic, seemingly intelligent behavior of the nanometer-scale physical system may also provide valuable lessons for designing self-organizing, distributed, complex ICT systems on the Internet scale.

Currently, great efforts are being made towards designing a new Internet architecture that is capable of supporting the heterogeneity and cooperation among various types of devices and services anticipated in the future [19,7]. While traditional communication technology follows the *client/server* paradigm, new proposals suggest shifting towards fully distributed control mechanisms and network topologies. In a client/server system, clients (e.g., web browsers) make requests for services to servers (e.g., requests for a web page), and the server tightly controls the content and its delivery. On the other hand, distributed network architectures with simple units that exhibit capabilities such as self-organization, self-adaptation, and self-healing have shown benefits in the past when it comes to scalability of the number of requests and robustness to server failures [10]. One popular example is peer-to-peer (P2P) networks, where all network nodes, being equal peers, may simultaneously play the roles of client and server. P2P networks are currently used as application layer overlay networks for content distribution or distributed directory services on the Internet, but it is foreseeable that more and more network architectures will be based on the P2P concept in the future rather than client/server. The benefits of such distributed topologies are that (i) a single point of failure at the server is avoided, (ii) the overall complexity of the system is reduced, and (iii) distributed topologies are more suitable in handling suddenly appearing overload conditions or balancing traffic load and energy consumption.

A recent trend in communication networks also shows that distributed and cooperative methods inspired by biological [3,4] or physical [23] phenomena have gained much attention as flexible and robust mechanisms for autonomous network management and control. Although these nature-inspired autonomous mechanisms often

show inferior performance compared with tightly controlled systems in a static environment, they have great benefits in sustainability and reliability under unknown or changing conditions similar to the autonomous and efficient optical excitation transfer in systems involving missing or failing links discussed in Section 3.

#### 4.2. Robustness against errors

The second important observation is that the increase in the output signal induced by degraded interactions indicates robustness against errors occurring in the system. Such behavior is also of great importance for future communication networks. Since new generation networks are expected to accommodate a large number of heterogeneous end-devices, access technologies, network protocols/services, and traffic characteristics, the consideration of failures or sudden fluctuations in performance seems inevitable. Designing robust mechanisms is, therefore, a key issue, and utilizing such an intrinsic robustness of nanophotonics, which has the potential to provide superior behavior in the presence of errors, while requiring less hardware redundancy than current proposals with redundancies of the order of 10–100 [21], may provide helpful guidelines and principles for constructing efficient future ICT systems.

Let us consider the following simple analogy of a sink node in an arbitrary (wired or wireless) communication network, receiving packets from neighboring source nodes. The node layout follows that of the star topology in Fig. 4, where the sink node corresponds to the large dot and the source nodes resemble the small dots. Our results in Section 3 imply the following. If a source node attempts to transmit a packet, but finds the direct channel to the sink busy or inaccessible, it is promising for this node to attempt a retransmission via a neighboring node since that node may have available resources to forward the packet. Particularly in the case where links may suddenly fail (e.g., due to instantaneous fading on a wireless communication channel), the additional diversity achieved by relaying over a neighboring node results in a higher delivery rate of packets. Furthermore, from the discussion of the best ratios of small quantum dots to large dots, we can see that there is an optimal number of neighboring nodes. Such a value may also exist in communications. There are numerous studies on network topologies using complex network theory, studying the theoretical properties of network connectivity by means of node degree distribution or clustering coefficient. If each node sets its connectivity degree to the ideal number of neighbors depending on their transmission and processing rates, efficient management of distributed ad hoc or P2P networks with less overheads can be achieved.

#### 4.3. Energy-efficiency of optical excitation transfer

Finally, it was demonstrated that a single process of optical excitation transfer is about  $10^4$  times more energy-efficient compared with the single bit flip energy required in current electrical devices [11]. A system-level, comprehensive comparison of energy efficiency is an important and timely subject that should be explored in the future.

On the other hand, energy transfer in light harvesting antennas exhibits superior efficiency [18,22], and these structures have similarities with nanostructures networked via optical near-field interactions. These studies will be extremely helpful for developing energy-efficient strategies to assist in handling the tremendous growth in traffic and required processing energy anticipated in future communication networks [6,20].

#### References

- [1] MONA consortium, A European road map for photonics and nanotechnologies, MONA, Merging Optics and Nanotechnologies Association, consortium, 2008.
- [2] National Research Council, Nanophotonics: Accessibility and Applicability, National Academies Press, Washington, DC, 2008.
- [3] S. Balasubramaniam, D. Botvich, J. Mineraud, W. Donnelly, N. Agoulmine, BiRSM: bio-inspired resource self-management for all IP-networks, *IEEE Netw.* 24 (2010) 20–25.
- [4] S. Balasubramaniam, K. Leibnitz, P. Lio, D. Botvich, M. Murata, Biological principles for future Internet architecture design, *IEEE Commun. Mag.* 49 (2011) 44–52.
- [5] S.A. Crooker, J.A. Hollingsworth, S. Tretiak, V.I. Klimov, Spectrally resolved dynamics of energy transfer in quantum-dot assemblies: toward engineered energy flows in artificial materials, *Phys. Rev. Lett.* 89 (2002) 186802. 1–4.
- [6] M. Gupta, S. Singh, Greening the Internet, in: *Proc. of ACM SIGCOMM '03*, Karlsruhe, Germany, 2003, pp. 19–26.
- [7] H. Harai, K. Fujikawa, V.P. Kafle, T. Miyazawa, M. Murata, M. Ohnishi, M. Ohta, T. Umezawa, Design guidelines for new generation network architecture, *IEICE Trans. Commun.* E93–B (2010) 462–465.
- [8] H. Hori, Electronic and electromagnetic properties in nanometer scales, in: M. Ohtsu (Ed.), *Optical and Electronic Process of Nano-Matters*, Kluwer Academic, 2001, pp. 1–55.
- [9] T.A. Klar, T. Franzl, A.L. Rogach, J. Feldmann, Super-efficient exciton funneling in layer-by-layer semiconductor nanocrystal structures, *Adv. Matter.* 17 (2005) 769–773.
- [10] K. Leibnitz, T. Hoßfeld, N. Wakamiya, M. Murata, Peer-to-peer vs. client/server: reliability and efficiency of a content distribution service, in: *Proc. of 20th International Teletraffic Congress*, Ottawa, Canada, June 2007, pp. 1161–1172.
- [11] M. Naruse, H. Hori, K. Kobayashi, P. Holmström, L. Thylén, M. Ohtsu, Lower bound of energy dissipation in optical excitation transfer via optical near-field interactions, *Opt. Express* 18 (2010) A544–A553.
- [12] M. Naruse, H. Hori, K. Kobayashi, M. Ohtsu, Tamper resistance in optical excitation transfer based on optical near-field interactions, *Opt. Lett.* 32 (2007) 1761–1763.
- [13] M. Naruse, T. Kawazoe, R. Ohta, W. Nomura, M. Ohtsu, Optimal mixture of randomly dispersed quantum dots for optical excitation transfer via optical near-field interactions, *Phys. Rev. B* 80 (2009) 125325. 1–7.
- [14] M. Naruse, T. Miyazaki, F. Kubota, T. Kawazoe, K. Kobayashi, S. Sangu, M. Ohtsu, Nanometric summation architecture based on optical near-field interaction between quantum dots, *Opt. Lett.* 30 (2005) 201–203.
- [15] W. Nomura, T. Yatsui, T. Kawazoe, M. Ohtsu, The observation of dissipated optical energy transfer between CdSe quantum dots, *J. Nanophotonics* 1 (2007) 011591. 1–7.
- [16] M. Ohtsu, T. Kawazoe, T. Yatsui, M. Naruse, Nanophotonics: application of dressed photons to novel photonic devices, and systems, *IEEE J. Sel. Top. Quantum Electron.* 14 (2008) 1404–1417.
- [17] M. Ohtsu, K. Kobayashi, T. Kawazoe, S. Sangu, T. Yatsui, Nanophotonics: design, fabrication, and operation of nanometric devices using optical near fields, *IEEE J. Sel. Top. Quantum Electron.* 8 (2002) 839–862.
- [18] A. Olaya-Castro, C.F. Lee, F.F. Olsen, N.F. Johnson, Efficiency of energy transfer in a light-harvesting system under quantum coherence, *Phys. Rev. B* 78 (2008) 085115. 1–7.
- [19] S. Paul, J. Pan, R. Jain, Architectures for the future networks and the next generation Internet: a survey, *Comput. Commun.* 34 (2011) 2–42.
- [20] A. Qureshi, R. Weber, H. Balakrishnan, J. Guttag, B. Maggs, Cutting the electric bill for Internet-scale systems, *ACM SIGCOMM Comput. Commun. Rev.* 39 (2009) 123–134.
- [21] A.S. Sadek, K. Nikolić, M. Forshaw, Parallel information and computation with restitution for noise-tolerant nanoscale logic networks, *Nanotechnology* 15 (2003) 192–210.



- [22] H. Tamura, J.-M. Mallet, M. Oheim, I. Burghardt, Ab initio study of excitation energy transfer between quantum dots and dye molecules, *J. Phys. Chem. C* 113 (2009) 7458–7552.
- [23] S. Toumpis, Mother nature knows best: a survey of recent results on wireless networks based on analogies with physics, *Comput. Netw.* 52 (2008) 360–383.
- [24] R.S. Tucker, R. Parthiban, J. Baliga, K. Hinton, R.W.A. Ayre, W.V. Sorin, Evolution of WDM optical IP networks: a cost and energy perspective, *J. Lightwave Technol.* 27 (2009) 243–252.
- [25] T. Unold, K. Mueller, C. Lienau, T. Elsaesser, A.D. Wieck, Optical control of excitons in a pair of quantum dots coupled by the dipole-dipole interaction, *Phys. Rev. Lett.* 94 (2005) 137404. 1–4.



**Makoto Naruse** is a Senior Researcher at the Photonic Network Institute in the National Institute of Information and Communications Technology (NICT) and a visiting research fellow at the Nanophotonics Research Center at The University of Tokyo. He received his B.E., M.E., and Ph.D. Degrees from The University of Tokyo in 1994, 1996, and 1999, respectively. After serving as a Research Associate of the Japan Society for the Promotion of Science and The University of Tokyo, he joined NICT in 2002.

From 2001 to 2005, he concurrently served as a researcher of PRESTO of the Japan Science and Technology Agency. From 2006 to 2011, he also served as a Visiting Associate Professor at The University of Tokyo. His research interests include information physics and nanophotonics.



**Kenji Leibnitz** received his masters and Ph.D. Degrees in information science from the University of Würzburg in Germany, where he was also a Research Fellow at the Institute of Computer Science. In May 2004, he joined Osaka University, Japan, as a Postdoctoral Researcher and from 2006 until March 2010 as Specially Appointed Associate Professor at the Graduate School of Information Science and Technology. Since April he is a Senior Researcher at the Brain ICT Laboratory of the National Institute of Information and Communications Technology in Kobe, Japan, and an Invited Associate Professor at Osaka University. His research interests are in modeling and performance analysis of communication networks, especially the application of biologically inspired mechanisms to self-organization in future networks.



**Ferdinand Peper** received both his M.Sc. (1985) and Ph.D. (1989) from Delft University of Technology, the Netherlands, in Theoretical Computer Science. He is a Senior Researcher at the National Institute of Information and Communications Technology (NICT), and he is a member of IEEE and ACM. His research interests include emerging research architectures, cellular automata, nanoelectronics, fluctuation-driven computation, neural science, and networking.



**Naoya Tate** received his B.E. and M.E. degrees in physics and his Ph.D. Degree in information science from Osaka University in 2000, 2002, and 2006, respectively. From 2006 to 2007, he was a Researcher of the Core Research for Evolutional Science and Technology (CREST) at the Japan Science and Technology Agency, Tokyo. In 2007, he joined The University of Tokyo as a Project Assistant Professor. His main field of interest is the implementation and applications of processing systems based on

information photonics. Dr. Tate is a member of the Optical Society of America (OSA) and the Japan Society of Applied Physics.



**Wataru Nomura** received his B.E. and M.E. degrees from Tokyo Institute of Technology in 2002 and 2004, respectively, and Ph.D. degree from The University of Tokyo in 2007. From 2007 to 2011, he was a Project Assistant Professor at the University of Tokyo. In 2011, he joined the University of Tokyo as a Project Researcher. His current research interests are nanophotonic fabrication and optical near-field energy transfer system.



**Tadashi Kawazoe** received his B.S., M.S., and Ph.D. degrees in physics from the University of Tsukuba, Japan, in 1990, 1993, and 1996, respectively. He studied optical nonlinearities in semiconductor quantum dots at the Institute of Physics, University of Tsukuba. In 1996, he joined the faculty of Engineering, Yamagata University, Japan, as a research associate, engaged in research on nonlinear optical materials and devices. In 2000, he joined the Japan Science and Technology Corporation, Japan. Since 2000, he

has studied optical devices and fabrication based on optical near-field interactions. In 2007, he joined The University of Tokyo as a Project Associate Professor. His current research interests are in nanophotonic devices.



**Masayuki Murata** received his M.E. and D.E. degrees in Information and Computer Science from Osaka University, Japan, in 1984 and 1988, respectively. In April 1984, he joined Tokyo Research Laboratory, IBM Japan, as a Researcher. From September 1987 to January 1989, he was an Assistant Professor with the Computation Center, Osaka University. In February 1989, he moved to the Department of Information and Computer Sciences, Faculty of Engineering Science, Osaka University. In April 1999, he

became a Professor of the Cybermedia Center, Osaka University, and is now with the Graduate School of Information Science and Technology, Osaka University since April 2004. He has more than four hundred papers in international and domestic journals and conferences. His research interests include computer communication networks, performance modeling and evaluation. He is a Member of IEEE, ACM and a Fellow of IEICE.



**Motoichi Ohtsu** is a Professor of the Department of Electrical Engineering and Information Systems, Graduate School of Engineering, The University of Tokyo, and the director of the Nanophotonics Research Center at The University of Tokyo. He received his B.E., M.E., and Dr. E. degrees in electronics engineering from the Tokyo Institute of Technology, Tokyo, Japan, in 1973, 1975, and 1978, respectively. In 1978, he was appointed a Research Associate, and in 1982, he became an Associate Professor at the

Tokyo Institute of Technology. From 1986 to 1987, while on leave from the Tokyo Institute of Technology, he joined the Crawford Hill Laboratory, AT&T Bell Laboratories, Holmdel, NJ. In 1991, he became a Professor at the Tokyo Institute of Technology. In 2004, he moved to the University of Tokyo as a Professor. He has been the leader of numerous national projects including "Photon Control" (1993–1998), "Localized Photon" (1998–2003), "Terabyte Optical Storage Technology" (2002–2006), "Near field optical lithography systems" (2004–2006), "Nanophotonics team" (2003–2009), and "Innovative Nanophotonics Components Development" (2006–present), among others. He has written over 380 papers and received 87 patents. He is the author, coauthor, and editor of 51 books, including 22 in English. His main fields of interest are nanophotonics and atom-photonics. He is a Fellow of the Optical Society of America, a Fellow of the Japan Society of Applied Physics, a senior member of IEEE, a Member of the Institute of Electronics, Information and Communication Engineering of Japan, and a Member of the American Physical Society. He is also a Tandem Member of the Science Council of Japan.

# A stochastic modeling of morphology formation by optical near-field processes

M. Naruse · T. Kawazoe · T. Yatsui · N. Tate · M. Ohtsu

Received: 11 July 2011 / Published online: 9 September 2011  
© Springer-Verlag 2011

**Abstract** We previously reported (S. Yukutake et al. in *Appl. Phys. B* 99:415, 2010) that by depositing Ag particles on the electrode of a photovoltaic device composed of poly(3-hexylthiophene) (P3HT) and ZnO under light illumination (wavelength  $\lambda = 660$  nm) while reversely biasing the P3HT/ZnO p–n junction, a unique granular Ag film was formed. The resultant device generated a photocurrent at wavelengths as long as 670 nm, which is longer than the long-wavelength cutoff  $\lambda_c$  ( $=570$  nm) of P3HT. Such an effect originates from a phonon-assisted process induced by an optical near field. In this paper, we analyze the morphological character of the Ag clusters and build a stochastic model in order to understand the principles behind the self-organized pattern formation process. The modeling includes the geometrical character of the material, its associated optical near fields, and the materials that flow in and out of the system. The model demonstrates behavior consistent with that observed in the experiment. We can see these phenomena as a new kind of self-organized criticality taking account of near-field effects, which will provide an insight into the analysis and design of future nanophotonic devices.

---

M. Naruse (✉)

National Institute of Information and Communications Technology, 4-2-1 Nukui-kita, Koganei, Tokyo 184-8795, Japan  
e-mail: [naruse@nict.go.jp](mailto:naruse@nict.go.jp)

M. Naruse · T. Kawazoe · T. Yatsui · N. Tate · M. Ohtsu  
Nanophotonics Research Center, School of Engineering,  
The University of Tokyo, 2-11-16 Yayoi, Bunkyo-ku, Tokyo  
113-8656, Japan

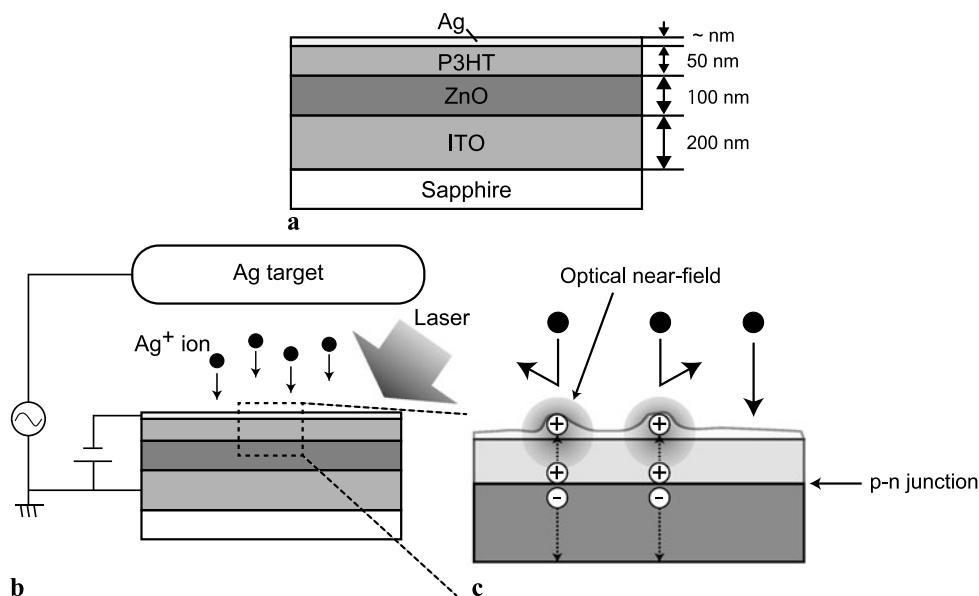
T. Kawazoe · T. Yatsui · N. Tate · M. Ohtsu  
Department of Electrical Engineering and Information Systems,  
School of Engineering, The University of Tokyo, 2-11-16 Yayoi,  
Bunkyo-ku, Tokyo 113-8656, Japan

## 1 Introduction

Nanophotonics, which utilizes local interactions involving light and matter on the nanometer scale, enables a wide range of functions, such as energy harvesting [1], energy concentration [2, 3], signal processing [4, 5], transformation [6], nanofabrication [7, 8], and so forth. Studying nanophotonics also gives us a deeper understanding of the primary processes occurring on the nanometer scale both theoretically, as in the dressed photon model [9], and experimentally, as in wave function mapping via near-field spectroscopy [10], among others. In these processes, the shape and size of the nanomaterials, or the material morphology, play a crucial role in providing the designated functions.

We previously reported in [1] that a unique granular Ag film was formed by depositing Ag particles on the electrode of a photovoltaic device composed of poly(3-hexylthiophene) (P3HT) and ZnO under light illumination (wavelength  $\lambda = 660$  nm) while reversely biasing the P3HT/ZnO p–n junction. The resultant device generated a photocurrent at wavelengths as long as 670 nm, which is longer than the long-wavelength cutoff ( $\lambda_c = 570$  nm) of P3HT. More detail will be summarized later below. This effect originates from a phonon-assisted process induced by an optical near field, as discussed in [1]. We consider that there are two important associated aspects that should be further addressed: one is to investigate the character of the resultant morphology of the devices, as well as to elucidate the physical mechanism of the pattern formation. The other is to reveal the relationship between the morphological character of the material and its associated optoelectronic performance. In this paper, with a view to revealing the former aspect, we analyzed the morphological character of the Ag clusters and constructed a stochastic model in order to understand the principles behind the formation process involving the geometrical character of the material, its

**Fig. 1** Cross-sectional structure of the photovoltaic device made of P3HT and ZnO sandwiched by Ag and ITO electrodes. (b) A schematic diagram of the Ag sputtering process under laser light irradiation and a reverse-bias DC voltage. (c) A close-up of the Ag deposition/repulsion at the surface due to the phonon-assisted optical near-field process



associated optical near fields, and the materials that flow in and out of the system.

The stochastic model described in this paper includes a particle deposition process on the surface while taking account of the repulsion due to the positively charged sputtering particles and the surface of the Ag film, as well as drift processes on the film. The numerical results revealed characteristics consistent with those observed in the previously reported experiment [1] with respect to the incidence patterns of the clusters formed on the surface of the electrode. We can regard this phenomenon as a kind of self-organized criticality [11] that takes into account near-field effects.

This paper is organized as follows. Section 2 reviews the experiment demonstrated in [1] and analyzes the morphology of the surfaces of the fabricated devices. Section 3 demonstrates the stochastic modeling representing the essence of the near-field processes occurring on the nanometer scale and numerical demonstrations. Section 4 concludes the paper.

## 2 Analysis of the morphology

The device structure analyzed in this paper is summarized as follows [1]. A schematic cross section of the device structure is shown in Fig. 1a. A P3HT layer about 50-nm thick was used as a p-type semiconductor material, and a ZnO film about 200-nm thick was used as an n-type semiconductor. P3HT is commonly used as a hole-conduction component [12]. In the experiment [1], photocurrent generation in a P3HT/ZnO thin film was evaluated at wavelengths longer than the cut-off wavelength of P3HT ( $\lambda_c = 570$  nm) which also falls within the wavelength range where the ZnO thin film is transparent (longer than  $\lambda = 400$  nm). An ITO film

about 200-nm thick and an Ag film a few nanometers thick were used as the two electrodes. In the previously reported experiment [1], thin films of these materials were deposited on a sapphire substrate in series. As a result, a multi-layered film with an area of 30 mm<sup>2</sup> was formed on the sapphire substrate. At the last stage of the fabrication process, Ag was deposited on the Ag thin film, which is the key process in differentiating the resultant performance in terms of photocurrent generation. Figures 1b and 1c schematically illustrate the experimental setup used in [1] and the corresponding processes. Briefly, the Ag is deposited by RF sputtering under light illumination while applying a reverse bias DC voltage,  $V_b = -1.5$  V, to the P3HT/ZnO p-n junction. The wavelength of the incident light is 660 nm, longer than the cut-off wavelength of P3HT. Under light illumination, an optical near field is locally generated on the Ag surface, which induces a coherent phonon at the p-n junction, leading to the generation of a virtual exciton-phonon-polariton [1]. This then generates an electron-hole pair at the p-n junction. The electron and holes are separated from each other by the reverse bias voltage. The positive hole is attracted to the Ag film, which makes the Ag film positively charged.

Since the sputtered Ag is positively ionized by passing through the argon plasma or due to the collision of the argon plasma with the Ag target used for RF sputtering [13], these positively ionized Ag particles are repulsed from the positively charged area of the Ag film where the positive holes have been injected, as schematically shown in Fig. 1c. This means that the subsequent deposition of Ag is suppressed in the area where optical near fields are efficiently induced. The processes described here lead to the unique granular structure of the Ag film formed in a self-organized manner, which is the primary focus of the stochastic modeling discussed

**Fig. 2** (a) SEM images of the surfaces of the Ag electrodes in three devices fabricated under the following conditions: (i) no DC bias ( $V_b = 0$ ), no light irradiation ( $P = 0$ ), (ii)  $V_b = -1.5$  V,  $P = 50$  mW, and (iii)  $V_b = -1.5$  V,  $P = 70$  mW. (b) Photocurrent generation in devices (i) to (iii) in a longer wavelength region where the normal device, case (i), exhibited almost no sensitivity, whereas the other two showed evident photocurrent generation

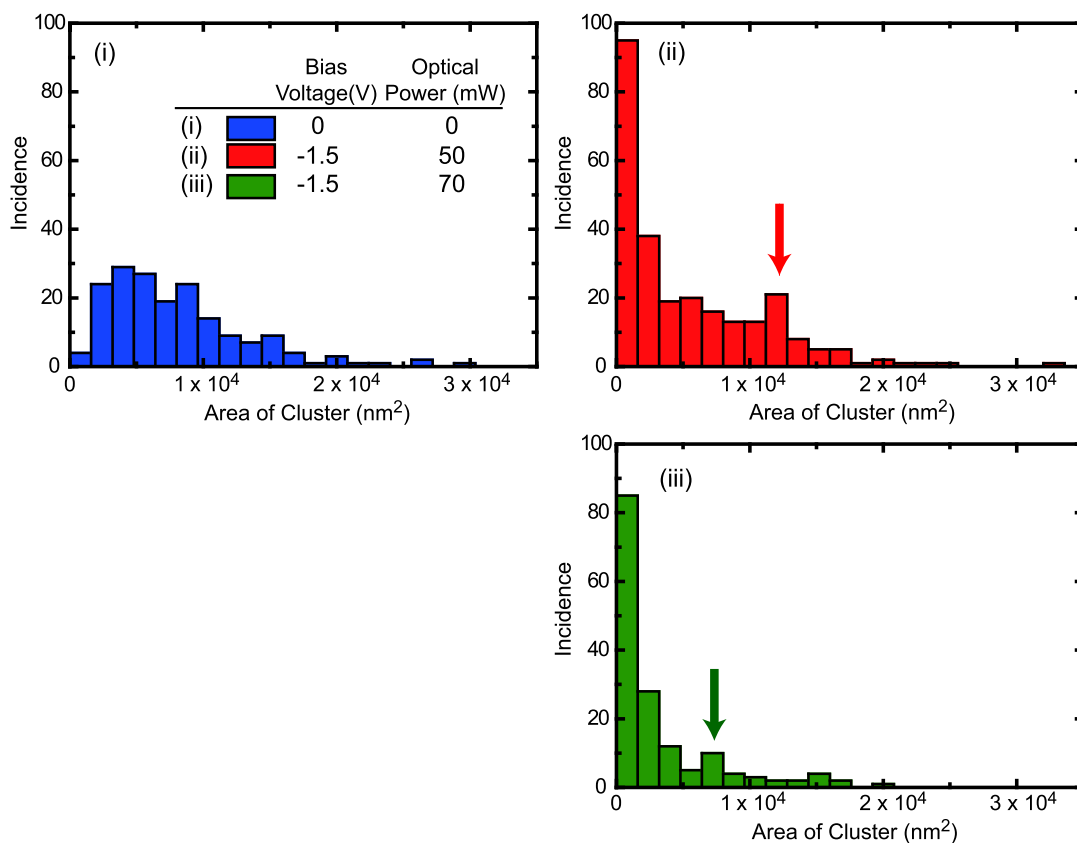
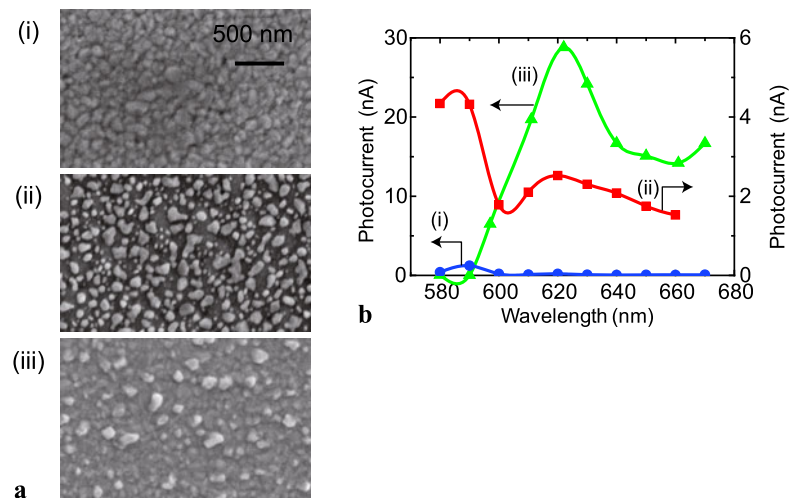


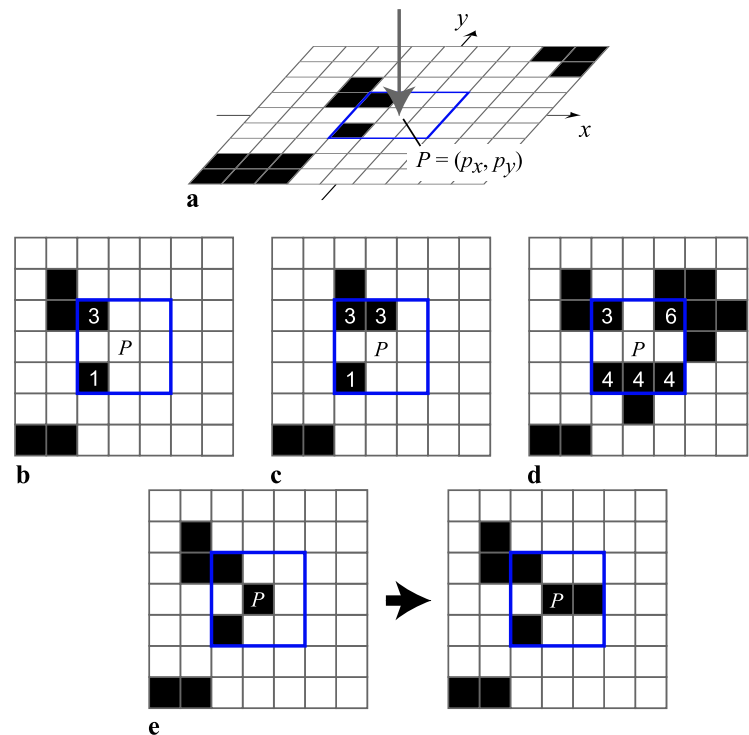
**Fig. 3** Incidence patterns of the cluster areas in cases (i) to (iii) in Fig. 2a

in Sect. 3. Five kinds of devices are discussed in [1], with different combinations of reverse bias voltage and incident light power. In the work described in this paper, we analyzed the following three devices, or cases: (i)  $V_b = 0$  and  $P = 0$ , (ii)  $V_b = -1.5$  V and  $P = 50$  mW, and (iii)  $V_b = -1.5$  V and  $P = 70$  mW. Figure 2a shows SEM images of the Ag film surfaces for cases (i)–(iii). It is evident that unique surface morphologies were obtained in cases (ii) and (iii) with

the light irradiation. As summarized in Fig. 2b, photocurrents were generated in cases (ii) and (iii) in the longer wavelength range, where case (i) exhibited no response.

Figure 3 represents the incidence pattern as a function of the size of the Ag clusters, obtained by analyzing the SEM images in Fig. 2a. A number of small clusters were observed in cases (ii) and (iii), but some of them were large. Also, as depicted by arrows in Figs. 3(ii) and 3(iii), the incidence

**Fig. 4** (a) A two-dimensional (2D) grid cell structure used to model the stochastic pattern formation process. (b–d) Example to calculate the *pseudo footprint* for a cell  $P$ . (e) Simulating a drift process when the pseudo footprint at cell  $P$  is less than the threshold value but cell  $P$  is occupied



showed a local maximum at a particular cluster size. Also note that the maximum appeared at a larger size with lower power light irradiation. On the other hand, case (i) exhibited a different incidence pattern of the cluster area, showing a representative (mode) size of around  $5 \times 10^3 \text{ nm}^2$ . In other words, we can see evident differences in the surface morphologies between the fabrication processes with and without light irradiation and a reverse DC bias.

### 3 Stochastic modeling of the morphology formation

#### 3.1 Stochastic modeling

Taking account of the physical processes of the material formation described above, we constructed a simple stochastic model that preserves the essential characteristics. First we consider a two-dimensional (2D)  $M \times M$  square grid cell structure  $\Lambda_M$  where a cell, also called a pixel, is specified by  $P = (p_x, p_y) \in \Lambda_M$ . In each cell, a variable  $h(P) \in \{0, 1\}$  is assigned so that areas where the Ag film surface has bumps are represented by  $h(P) = 1$ , and areas where the surface is flat are represented by  $h(P) = 0$ . In Fig. 4a, the pixels with  $h(P) = 1$  are indicated by black cells, while those with  $h(P) = 0$  are indicated by white ones. We simulate the material deposition process as follows.

Initially, we assume a completely flat surface, namely,  $h(P) = 0$  for all  $P \in \Lambda_M$ . First, we randomly choose a cell  $P$  in the 2D grid structure and let a particle arrive at  $P$ . Second, we determine if the particle successfully lands on a cell

or is repulsed, that is, deflected out of the system, by taking account of the positively charged Ag to be sputtered and the holes that could appear on the Ag film surface. We calculate a *pseudo footprint* denoted by  $Q_P$ , defined in detail in Sect. 3.2 below, in order to evaluate this effect in the stochastic modeling.

If the calculated value of  $Q_P$  is smaller than or equal to a threshold  $Z$ , and if the flat surface condition is satisfied ( $h(P) = 0$ ), an arriving particle is able to land on the cell  $P$ ; that is,  $h(P) = 0 \rightarrow h(P) = 1$ . In contrast, if  $Q_P$  is larger than  $Z$ , the arriving particle is deflected outside the system, representing repulsion between the positively charged Ag particle and the positively charged clusters on the surface due to the reverse bias. If  $Q_P$  is smaller than or equal to  $Z$  but the point  $P$  is already occupied ( $h(P) = 1$ ), the arriving particle will sit in a free, randomly chosen neighbor, representing a drift process, of which detail is given in Sect. 3.3.

#### 3.2 Pseudo footprint

The pseudo footprint metric in each square grid cell corresponds to the sum of the areas of its eight neighbors. More precisely, the pseudo footprint at  $P$  is given by

$$Q_P = \sum_{i=\{-1,0,1\}, j=\{-1,0,1\}} S_P^{(i,j)}, \quad (1)$$

where  $S_P^{(i,j)}$  represents the total number of occupied cells, or area, connected to the cell  $(p_x + i, p_y + j)$  either in horizontal ( $x$ ) or vertical ( $y$ ) neighbors, as schematically shown

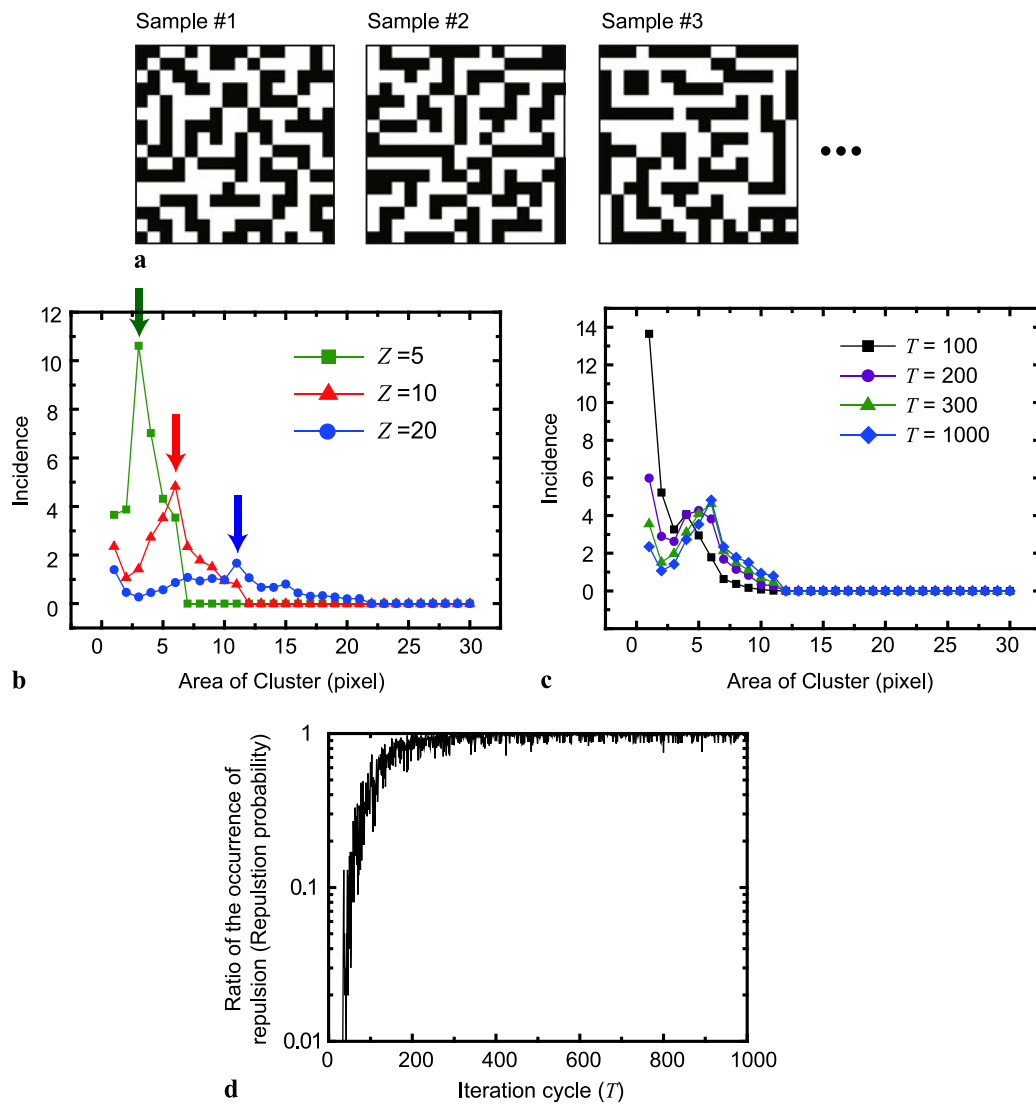


**Fig. 5** (a) Example of generated patterns via the stochastic modeling. (b) Incidence pattern as a function of cluster area, with threshold  $Z$  as a parameter. (c) Evolution of the incidence pattern of the cluster area as a function of iteration cycle  $T$ . (d) Evolution of the ratio of the occurrence of repulsion

in Fig. 4a. For example, in the case shown in Fig. 4b, the area of the top-left corner is  $S_p^{(-1,+1)} = 3$ , and that of the bottom-left one is  $S_p^{(-1,-1)} = 1$ . Therefore, based on (1), the pseudo footprint is given by  $Q_P = S_p^{(-1,+1)} + S_p^{(-1,-1)} = 4$ . In another example shown in Fig. 4c, the areas are given by  $S_p^{(-1,+1)} = 3$ ,  $S_p^{(0,+1)} = 3$ , and  $S_p^{(-1,-1)} = 1$ , which yields  $Q_P = S_p^{(-1,+1)} + S_p^{(0,+1)} + S_p^{(-1,-1)} = 7$ . In another example shown in Fig. 4d,  $Q_P = \sum_{i,j} S_p^{(i,j)} = 21$ .

### 3.3 Drift

When an arriving Ag particle is not repulsed from the system, but the point  $P$  is occupied, the particle lands in a randomly chosen neighboring cell. The left-hand side of

Fig. 4e represents one such example where  $Q_P = 4$ . Suppose that this  $Q_P$  is smaller than the threshold  $Z$ . Since the point  $P$  is occupied, a free neighboring cell is randomly chosen along the  $x$ - or  $y$ -direction with respect to  $P$ . For example, the system is updated as shown in the right-hand side of Fig. 4e, where a newly arriving particle lands to the right of the point  $P$ , in other words,  $h(p_x + 1, p_y) = 0 \rightarrow h(p_x + 1, p_y) = 1$ . Such a rule represents the drift process occurring on the Ag film surface.

### 3.4 Demonstration

By iteratively applying the stochastic process described above in a repeated manner in  $T$  cycles from a flat initial state, a variety of resultant spatial patterns were generated.

They also depended on the threshold  $Z$ . By setting the size of the grid to  $16 \times 16$  cells, that is,  $M = 16$  for the region  $\Lambda_M$ , while setting the threshold at  $Z = 10$  and the number of cycles  $T = 300$ , Fig. 5a represents three examples of the spatial patterns generated in  $N = 100$  different trials. We can clearly observe that a variety of resultant patterns were obtained. To examine the statistical properties, the incidence pattern of the mean number of each cluster in  $N$  different samples was evaluated, as shown in Fig. 5b where the number of repetition cycles was  $T = 1000$ . Squares, triangles, and circles respectively represent the incidence of the clusters in the system with different thresholds  $Z = 5, 10$ , and  $20$ .

The incidence pattern exhibited different characters depending on the threshold value ( $Z = 5, 10$ , and  $20$ ): with smaller  $Z$ , the cluster area yielding the local maximum incidence shifted towards a smaller value in Fig. 5b, which agrees with the experimentally observed character shown in Fig. 3 where larger optical light irradiation produced smaller clusters (peaks are indicated by arrows). In other words, higher power light irradiation more likely induces repulsion, leading to a local maximum at a smaller cluster area for the clusters formed on the surface. This supports the physical interpretation that the pseudo footprint appropriately represents the repulsion due to the optical near-field effect. That is to say, the pseudo footprint reflects the positive holes, and the associated optical near field localized around a cluster, or spatial inhomogeneity, is induced.

Figure 5c shows the evolution of the incidence patterns of the cluster sizes as the number of repetitions  $T$  increases. We can clearly observe that the peak-like incidence clusters emerge as  $T$  increases. Squares, circles, triangles, and diamonds in Fig. 5c respectively show the incidences when  $T$  was 100, 200, 300, and 1000. Also, in the initial cycles, the incidence pattern followed a power-law-like statistical property. In considering the steady-state, converged pattern, Fig. 5d characterizes the ratio of the occurrence of repulsion at cycle  $T$  among  $N = 100$  trials. In other words, it shows the time evolution of the probability of repulsion. The probability increases as the iteration cycle increases; a repulsion probability of 0.8 or higher was observed after the iteration cycle reached around 300. Since the present stochas-

tic model includes a threshold value  $Z$ , strictly speaking, it is *not* so-called self-organized criticality [11]. However, as Fig. 5 indicates, a flat surface converges to various kinds of patterns in a self-organized manner while exhibiting common statistical properties, which is a kind of self-organized critical phenomenon due to near-field effects inherent in the stochastic model described above.

## 4 Conclusion

In summary, in photovoltaic devices made by exploiting an optical phonon-assisted near-field process exhibiting unique photocurrent generation, we analyzed the surface morphology of the Ag electrode of the fabricated devices and constructed a stochastic model to explain the fundamental physical process of the material formation. The numerical simulation results exhibited behavior consistent with the experimental results. The findings reported here will allow us to understand the principles behind the formation process, and to optimize device performance in future.

## References

1. S. Yukutake, T. Kawazoe, T. Yatsui, W. Nomura, K. Kitamura, M. Ohtsu, *Appl. Phys. B* **99**, 415 (2010)
2. T.A. Klar, T. Franzl, A.L. Rogach, J. Feldmann, *Adv. Mater.* **17**, 769 (2005)
3. M. Naruse, T. Kawazoe, R. Ohta, W. Nomura, M. Ohtsu, *Phys. Rev. B* **80**, 125325 (2009)
4. M. Naruse, T. Miyazaki, T. Kawazoe, S. Sangu, K. Kobayashi, F. Kubota, M. Ohtsu, *IEICE Trans. Electron.* **E88-C**, 1817 (2005)
5. C. Pistol, C. Dwyer, A.R. Lebeck, *IEEE MICRO* **28**, 7 (2008)
6. H. Fujiwara, T. Kawazoe, M. Ohtsu, *Appl. Phys. B* **98**, 283 (2010)
7. T. Yatsui, K. Hirata, W. Nomura, Y. Tabata, M. Ohtsu, *Appl. Phys. B* **93**, 55 (2008)
8. S. Yamazaki, T. Yatsui, M. Ohtsu, *Appl. Phys. Express* **2**, 031004 (2009)
9. M. Ohtsu, K. Kobayashi, T. Kawazoe, T. Yatsui, M. Naruse, *Principles of Nanophotonics* (Taylor & Francis, Boca Raton, 2008)
10. K. Matsuda, T. Saiki, S. Nomura, M. Mihara, Y. Aoyagi, S. Nair, T. Takagahara, *Phys. Rev. Lett.* **91**, 177401 (2003)
11. P. Bak, C. Tang, K. Wiesenfeld, *Phys. Rev. A* **38**, 364 (1988)
12. M. Bredol, K. Matras, A. Szatkowski, J. Sanetra, A. Prodi-Schwab, *Sol. Energy Mater. Sol. Cells* **93**, 662 (2009)
13. J. Joo, *J. Vac. Sci. Technol.* **18**, 23 (2000)

# Optical dynamics of energy-transfer from a CdZnO quantum well to a proximal Ag nanostructure

H. Matsui,<sup>1,2,\*</sup> W. Nomura,<sup>2</sup> T. Yatsui,<sup>2</sup> M. Ohtsu,<sup>2</sup> and H. Tabata<sup>1,2</sup>

<sup>1</sup>Department of Bioengineering, School of Engineering, University of Tokyo, Bunkyo-ku, Tokyo 113-8656, Japan

<sup>2</sup>Department of Electrical Engineering and Information Systems, School of Engineering, University of Tokyo, Bunkyo-ku, Tokyo 113-8656, Japan

\*Corresponding author: hiroaki@ee.t.u-tokyo.c.jp

Received May 31, 2011; revised August 5, 2011; accepted August 29, 2011;  
posted August 31, 2011 (Doc. ID 148309); published September 19, 2011

We studied photoluminescence (PL) and energy-transfer dynamics in a hybrid structure comprising a Cd<sub>0.08</sub>Zn<sub>0.92</sub>O quantum well (QW) and an Ag nanostructure. The observed PL quenching was dependent on the electronic states in the QW. Quenching occurred at low temperature where excited carriers recombined radiatively because of excitonic localization, which disappeared with increasing temperature due to delocalization of excitons. Furthermore, nanostructured Ag surfaces produced local surface plasmon (LSP) absorption that was resonant with the PL peak energy of the QW emission. These results indicate that the recombination energy of excitons transfers nonradiatively to induce LSP excitation, which was revealed using time-resolved PL measurements. © 2011 Optical Society of America

OCIS codes: 160.4760, 310.6860.

A semiconductor quantum well (QW) material with a metallic nanostructure is a promising hybrid structure for optical applications based on exciton-plasmon coupling. A surface plasmon (SP) can effectively capture dipole oscillator energy in a QW, which affects the spontaneous decay rate of QW emission [1]. This modulation of the decay rate shows evidence of both enhanced and quenched photoluminescence (PL). Enhanced PL is promoted by a local electric field on a metallic nanostructured surface, whereas quenched PL results from energy-dissipation mechanisms in metals such as electron-hole pair excitation [2] and plasmon excitation [3]. This dissipation is more significant than nonradiative recombination and quenches the PL of a QW.

We recently observed PL quenching in a structure consisting of a CdZnO QW and Ag nanostructure. The PL intensity and lifetime decreased simultaneously with temperature and excitonic localization was observed. Thus far, exciton-plasmon coupling has been observed on the Ag/InGaN QW structure. Some studies have reported PL enhancement [4,5], while others observed PL quenching [6,7]. PL enhancement is due to the local SP field on metallic nanostructures, whereas the influence of plasmon fields on PL quenching has not been extensively reported. In Ag/InGaN QW, PL quenching becomes stronger with increasing excitonic localization in the QWs [8]. Furthermore, the plasmon-enhanced PL properties at room temperature (RT) have no effect at low temperatures [4]. These previous reports led to conjecture that PL quenching is correlated with the electronic states of InGaN QWs.

The electronic states in a QW manifest in the form of either localized or delocalized carriers that depend on temperature, which affects the quantum efficiency of the QW. It is known that high quantum efficiency has been realized by excitonic localization derived from carriers trapped in defect sites and atomic potential fluctuations formed in InGaN and CdZnO QWs. Therefore, we

consider PL quenching to be correlated with the electronic states in a QW.

In this Letter, we focus on the temperature-dependent optical dynamics of PL quenching in a CdZnO QW with an Ag nanostructure. Pulsed optical excitation is used to clarify the dynamics of energy-transfer and other competing processes in carrier recombination in the QW. To investigate exciton-plasmon coupling, we consider two types of relaxation processes: radiative and nonradiative recombination of excited carriers, which are induced alternately by changing the temperature.

A Cd<sub>0.08</sub>Zn<sub>0.92</sub>O/ZnO QW was grown on an O-face ZnO substrate by pulsed laser deposition (PLD). A 5 nm thick Cd<sub>0.08</sub>Zn<sub>0.92</sub>O well layer was embedded between a 150 nm thick ZnO buffer and 5 nm thick ZnO spacer layer. The buffer layer was grown at 570 °C and the well and spacer layers at 260 °C [9]. An Ag layer was then grown by PLD on only half of the sample surface at RT in an Ar gas flow (1.0 Pa). The structural properties were examined by cross-sectional transmittance electron microscopy (X-TEM). An InGaN laser (403 nm) was used as the excitation source for steady-state PL. Luminescence was displayed by a single monochromator. To clarify energy-transfer dynamics, the temporal evolution of the PL of the QW was monitored using a time-correlated single-photon counting system. The sample was excited at 400 nm by the frequency-doublet output of an amplified Ti: sapphire laser (2 ps pulse). PL excitation and emission collection were performed from the substrate side.

X-TEM images of the local structures of the CdZnO QW and the Ag nanostructure are shown in Fig. 1. In Fig. 1(b), the interface between the Ag and ZnO spacer layers showed that the Ag layer consisted of assembled nanoparticles (NPs) with a diameter of 6 nm. The Ag NPs were placed directly on the ZnO spacer layers. No thin-layered Ag structure was evident at the interface. A Z-contrast image of the QW obtained by scanning-TEM (STEM) revealed that spatial separation existed between the QW and the Ag NPs [Fig. 1(c)]. Excited carriers in the



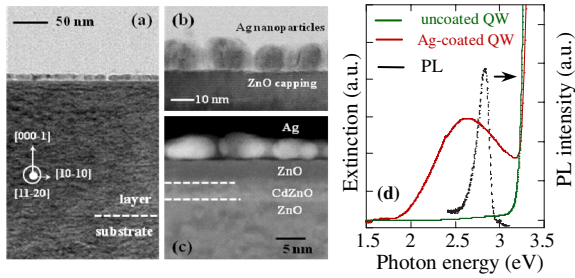


Fig. 1. (Color online) (a) X-TEM image of a CdZnO QW with a proximal Ag nanostructure. (b) High-resolution X-TEM image focused on the Ag/ZnO heterointerface. (c) High-resolution STEM image of the QW with a proximal Ag nanostructure. (d) Extinction spectra of uncoated (green line) and Ag-coated (red line) QWs at RT and a PL spectrum of an uncoated (black dotted line) QW at 10 K.

well layer exhibited a nanoscale spatial separation from the Ag NPs. The extinction spectrum of the Ag layer [Fig. 1(d)] showed a peak at 2.60 eV because of a local surface plasmon (LSP) excited in the gap between the Ag NPs. The photon energies of LSP absorption and QW emission overlapped.

Steady-state PL spectra of uncoated and Ag-coated CdZnO QWs at various temperatures are shown in Fig. 2. At 10 K with the Ag-coated QW, the PL intensity at 2.67 eV decreased by more than an order of magnitude. The PL intensity ratio ( $I_{PL}^*/I_{PL}$ ) of the uncoated ( $I_{PL}$ ) and Ag-coated ( $I_{PL}^*$ ) QWs decreased with the difference between the PL peak energies of the uncoated and Ag-coated QWs at low temperature (<120 K). The PL peak energy of the uncoated QW showed S-shaped temperature dependence, indicating the presence of excitonic localization in the QW [10]. Excited carriers are trapped in localized states and form localized excitons at low temperature (<100 K). In contrast, excited carriers are free to escape from the localized states at high temperature (>100 K) and they therefore cannot form localized excitons. Figure 2(b) shows that strong PL quenching was present in the temperature region in which excitonic localization occurred.

Time-resolved PL (TRPL) signals were measured at the PL peak energies of the uncoated and Ag-coated CdZnO QW [Fig. 3(b)]. TRPL signals at 10 K showed bi-exponential decay that obeyed the relationship:  $I(t) =$

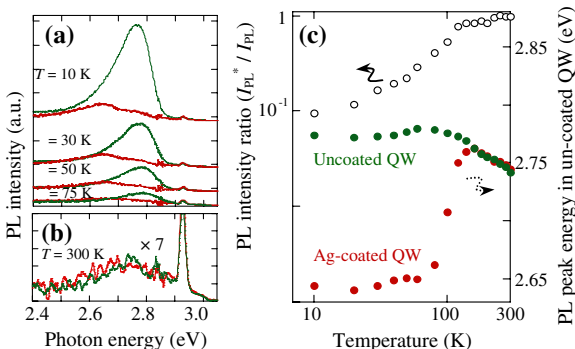


Fig. 2. (Color online) (a) and (b) PL spectra of uncoated (green) and Ag-coated (red) QWs at various temperatures. (c) PL intensity ratio ( $I_{PL}^*/I_{PL}$ ) (left axis, open circles) and PL peak energies (right axis) of uncoated (green) and Ag-coated (red) QWs as a function of temperature.

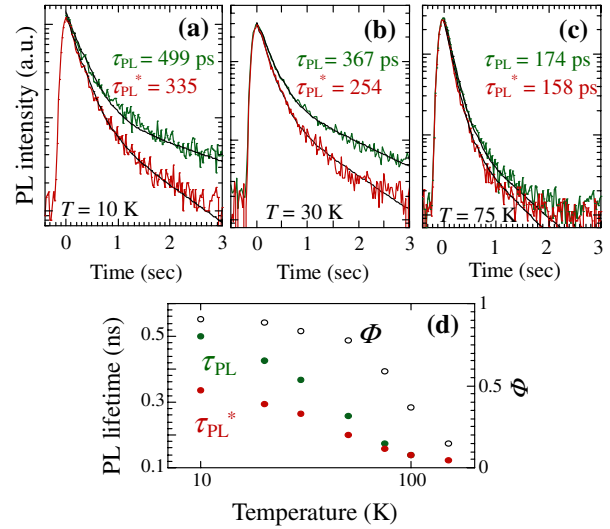


Fig. 3. (Color online) TRPL signals of uncoated (green) and Ag-coated (red) QWs at various temperatures: (a) 10 K, (b) 30 K, and (c) 75 K. (d) PL lifetime as a function of temperature for uncoated ( $\tau_{PL}$ : green) and Ag-coated ( $\tau_{PL}^*$ : red) QWs. Open squares indicate the quantum efficiency ( $\Phi$ ).

$\sum_{i=1,2} I_i \exp(-t/\tau_i)$ , where  $\tau_i^{-1}$  and  $I_i$  are the lifetime and the amplitude, respectively. For the uncoated QW (black lines), the fast decay component  $\tau_1$  (266 ps) corresponds to the radiative lifetime associated with excitonic recombination. In contrast, the slow decay component  $\tau_2$  (2.09 ns) is based on carrier trapping in defect sites and potential fluctuations before the radiative decay, resulting in a long PL lifetime. The values of  $\tau_1$  and  $\tau_2$  for the Ag-coated QW were similarly determined to be 242 ps and 1.75 ns, respectively. PL lifetime estimated by  $((I_1\tau_1 + I_2\tau_2)/(I_1 + I_2))$  was used to represent  $\tau_{PL}$  because the fast and slow decay components were modulated by the presence of the Ag NPs.  $\tau_{PL}^*$  (335 ps) of the Ag-coated QW was shorter than  $\tau_{PL}$  (499 ps) of the uncoated QW. TRPL signals at 30 K exhibited bi-exponential decay with different PL lifetimes for Ag-coated and uncoated QWs [Fig. 3(b)]. However, the difference in PL lifetimes becomes extremely small at 75 K [Fig. 3(c)]. A plot of  $\tau_{PL}$  and  $\tau_{PL}^*$  as a function of temperature showed that the difference in PL lifetime decreased with increasing temperature and vanished at 100 K [Fig. 3(d)]. This behavior was correlated with PL quenching. The values of  $\tau_{PL}$  and  $\tau_{PL}^*$  differed at low temperature (<75 K) where excitonic localization occurred, and both PL lifetimes were equal at high temperature (>75 K) where excitonic delocalization occurred. PL quenching originated from the electronic states in the QW. The changes in PL intensity and lifetime were observed at low temperatures at which high quantum efficiency for the QW was observed.

For the uncoated CdZnO QW, excited carriers in the QW were terminated according to the radiative ( $k_R$ ) or nonradiative ( $k_{NR}$ ) decay rate. Quantum efficiency ( $\Phi$ ) is determined by the ratio of these two decay rates according to  $\Phi = k_R/(k_R + k_{NR})$ . For the Ag-coated QW, a new relaxation process becomes possible owing to the presence of the Ag NPs, which should be effective because of the overlap between the excitonic energy in the QW and the LSP absorption energy [11]. Thus, exciton-plasmon coupling gives rise to the nonradiative

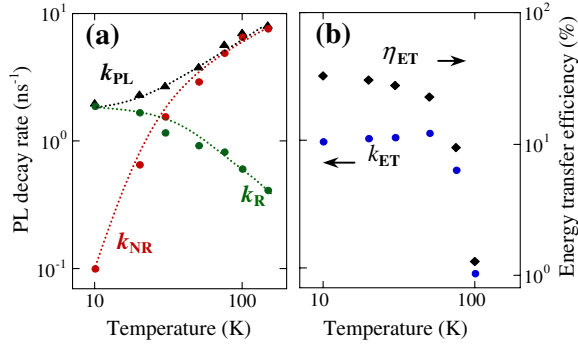


Fig. 4. (Color online) (a) PL decay rate ( $k_{PL}$ : black triangles), radiative decay rate ( $k_R$ : green circles), and nonradiative decay rate ( $k_{NR}$ : red circles) of an uncoated QW as a function of temperature. Dotted lines are drawn as a visual guide. (b) Energy-transfer rate ( $k_{ET}$ : blue circles) and efficiency ( $\eta_{ET}$ : black diamonds) as a function of temperature.

decay rate ( $k_{ET}$ ) in the carrier relaxation of the QW. The value of  $\tau_{PL}^*$  for the Ag-coated QW is described by  $\tau_{PL}^* = 1/k_{PL}^* = 1/(k_R + k_{NR} + k_{ET})$ , where  $k_{ET}$  is the difference in the PL decay rates of the QW in the presence and absence of the Ag layer ( $k_{ET} = k_{PL}^* - k_{PL}$ ). In the plots of  $k_R$  and  $k_{NR}$  as a function of temperature [Fig. 4(a)],  $k_R$  and  $k_{NR}$  can be estimated, respectively, from  $k_R = k_{PL}/\Phi$  and  $k_{NR} = k_{PL}(1 - \Phi)$ , where  $\Phi$  indicates the quantum efficiency of the uncoated QW that was defined as the PL intensity at a particular temperature divided by that at 8 K ( $\Phi = 1.3\%$  at 300 K). At 10 K,  $k_{PL}$  ( $2.01 \text{ ns}^{-1}$ ) was equal to  $k_R$  ( $1.90 \text{ ns}^{-1}$ ). Excited carriers recombined radiatively through excitonic localization. With increasing temperature,  $k_{NR}$  gradually became higher than  $k_R$ , presumably because of nonradiative recombination activated by excitonic delocalization. Between 10 and 50 K,  $k_{ET}$  was in the order of  $1.0 \text{ ns}^{-1}$  [Fig. 4(b)]. The energy-transfer efficiency ( $\eta_{ET}$ ) between the QW and Ag NPs is estimated by  $\eta_{ET} = k_{ET}/(k_{ET} + k_R)$ . The calculated efficiency was as high as 34% at 10 K [Fig. 4(b)]. The carrier relaxation of the CdZnO QW is either radiative or nonradiative, or represents an energy-transfer. For the Ag-coated QW,  $k_{ET}$  is sufficiently fast to compete with  $k_R$ . Therefore, the radiative recombination energy in the QW would be partially consumed by energy-transfer to the Ag NPs, thus quenching PL. The long PL lifetime of QW emission makes QW-LSP coupling highly probable, and it was realized under the high  $\Phi$  at low temperatures.

Studies of PL quenching have mainly described a nanostructure consisting of an Au NP and CdSe quantum dots (QD), resulting from the spectral overlap of the peaks for Au NP plasmon absorption and QD emission [12]. The excitonic energy of the QD is transferred non-radiatively to the Au NP, thus shortening the PL lifetime of QD emission. This situation can apply to the Ag/CdZnO QW because the temperature dependence of the energy-transfer rate is similar to that of the radiative decay rate [Fig. 4]. The observed PL quenching was related to the radiative recombination. In contrast, in Ag/InGaN QWs with PL enhancement, Okamoto *et al.* showed that the

temperature dependence of the energy-transfer rate to an Ag plasmon mode is similar to that of the nonradiative decay rate [4]. Lu *et al.* reported that transfer efficiency to an Ag plasmon mode of trapped carriers is lower than that of free carriers [8]. These reports show a tendency that is opposite to the PL quenching reported in this work because the transfer efficiency for an Ag plasmon mode of trapped carriers was higher than that of free carriers. Therefore, we observed no change in PL at RT in the presence of delocalized free carriers because carrier relaxation in the CdZnO QW was dominated by the nonradiative recombination. A PL intensity of a QW emission can increase or decrease as a result of competition between local field enhancement and nonradiative energy-transfer to a plasmon mode. Analysis of the temperature-dependent PL quenching in this work revealed that we found that excitonic localization in the QW contributed to PL quenching rather than PL enhancement, which was different from optical dynamics of the Ag/InGaN QW with PL enhancement. The prevention of localized excitons in the QW is desired to reduce PL quenching for plasmon-related emitting devices.

In summary, we found remarkable PL quenching in a hybrid structure consisting of a CdZnO QW with Ag NPs, which required a long PL lifetime that gives rise to non-radiative energy-transfer from the QW to Ag NPs due to the spectral overlap of QW emission and Ag NP plasmon absorption. In contrast, a short PL lifetime could not provide a sufficient energy-transfer rate. Therefore, the QW emission did not change at RT.

## References

1. A. Neogi, H. Morkoç, T. Kuroda, and A. Tackeuchi, *Opt. Lett.* **30**, 93 (2005).
2. R. R. Chance, A. Prock, and R. Silbey, *J. Chem. Phys.* **62**, 2245 (1975).
3. X. Li, J. Qian, L. Jiang, and S. He, *Appl. Phys. Lett.* **94**, 063111 (2009).
4. K. Okamoto, I. Niki, A. Scherer, Y. Narukawa, T. Mukai, and Y. Kawakami, *Appl. Phys. Lett.* **87**, 071102 (2005).
5. J. Henson, J. C. Heckel, E. Dimakis, J. Abell, A. Bhattacharyya, G. Chumanov, T. D. Moustakas, and R. Paiella, *Appl. Phys. Lett.* **95**, 151109 (2009).
6. B. Liu, C. W. Cheng, R. Chen, S. A. Ekahana, W. F. Yang, S. J. Wang, T. C. Sum, Z. X. Shen, H. J. Fan, and H. D. Sun, *Appl. Phys. Lett.* **97**, 081107 (2010).
7. C. Y. Chen, D. M. Yeh, Y. C. Lu, and C. C. Yang, *Appl. Phys. Lett.* **89**, 203113 (2006).
8. Y. C. Lu, C. Y. Chen, D. M. Yeh, C. F. Huang, T. Y. Tang, J. J. Huang, and C. C. Yang, *Appl. Phys. Lett.* **90**, 193103 (2007).
9. H. Matsui, T. Osone, and H. Tabata, *J. Appl. Phys.* **107**, 093523 (2010).
10. J. Bai, T. Wang, and S. Sakai, *J. Appl. Phys.* **88**, 4729 (2000).
11. S. Neretina, W. Qian, E. Dreaden, M. A. El-Sayed, R. A. Hughes, J. S. Preston, and P. Mascher, *Nano Lett.* **8**, 2410 (2008).
12. M. Haridas, L. N. Tripathi, and J. K. Basu, *Appl. Phys. Lett.* **98**, 063305 (2011).

# Highly efficient and broadband Si homojunction structured near-infrared light emitting diodes based on the phonon-assisted optical near-field process

T. Kawazoe · M.A. Mueed · M. Ohtsu

Received: 27 April 2011 / Published online: 16 June 2011  
© The Author(s) 2011. This article is published with open access at Springerlink.com

**Abstract** We fabricated a highly efficient, broadband light emitting diode driven by an optical near field generated at the inhomogeneous domain boundary of a dopant in a homojunction bulk Si crystal and evaluated its performance. To fabricate this device, a forward current was made to flow through a Si p–n junction to anneal it. During this process, the device was irradiated with near-infrared light, producing stimulated-emission light using a two-step phonon-assisted process triggered by the optical near field, and the annealing rate was controlled in a self-organized manner. The device emitted light in a wide photon energy region of 0.73–1.24 eV (wavelength 1.00–1.70  $\mu\text{m}$ ). The total power of the emitted light with 11 W of electrical input power was as high as 1.1 W. The external power conversion efficiency of the emitted light was 1.3%, the differential external power conversion efficiency was 5.0%, the external quantum efficiency was 15%, and the differential external quantum efficiency was 40%. The dependency of the emitted light power density on the injected current density clearly showed a characteristic reflecting the two-step phonon-assisted transition process.

## 1 Introduction

The emission wavelength of semiconductor light emitting diodes (LEDs) is determined by the bandgap energy,  $E_g$ , of the materials used. For example, to realize near-infrared LEDs that emit in the wavelength range 1.00–1.70  $\mu\text{m}$  (photon energies 0.73–1.24 eV), which contains the optical fiber communication band, InGaAsP, a direct transition type semiconductor, is used [1, 2]. To achieve high-efficiency light emission, it is necessary to employ a complex double-heterojunction structure that uses an InGaAsP active layer and an InP carrier confinement layer epitaxially grown on an InP substrate. The shortcomings of this approach are that InP is highly toxic [3], and In is a rare material. Silicon (Si), on the other hand, is a semiconductor having low toxicity and no concerns about depletion of resources; however, its emission efficiency is low because it is an indirect transition type semiconductor. Therefore, until now it has been considered unsuitable as a material for use in LEDs. However, because of the growing concern over environmental issues, LEDs using Si have recently been investigated. For example, in the visible region, porous Si [4], Si/SiO<sub>2</sub> superlattice structures [5, 6], and Si nanoprecipitates in SiO<sub>2</sub> [7] have been used, and in the infrared region, erbium-doped Si [8] and Si–Ge [9] have been used. However, their emission efficiencies are still low. For example, the external quantum efficiency and power conversion efficiency of an LED using a sub-bandgap transition in Si [10] are 0.5% and 0.8%, respectively.

In this study, using bulk crystal Si having a homojunction that is extremely simple compared with the structures described above, we varied the spatial distribution of the dopant density in the Si by a novel annealing process using a phonon-assisted process induced by an optical near field [11] to fabricate a highly efficient, broadband LED. The

T. Kawazoe (✉) · M.A. Mueed · M. Ohtsu  
Department of Electrical Engineering and Information Systems,  
Graduate School of Engineering, The University of Tokyo,  
2-11-16 Yayoi, Bunkyo-ku, Tokyo 113-8656, Japan  
e-mail: kawazoe@ee.t.u-tokyo.ac.jp  
Fax: +81-3-58411140

T. Kawazoe · M. Ohtsu  
Nanophotonic Research Center, Graduate School of Engineering,  
The University of Tokyo, 2-11-16 Yayoi, Bunkyo-ku,  
Tokyo 113-8656, Japan

light emission wavelength covered the optical fiber communications band.

## 2 Principles of light emission

The phonon-assisted process [11] originates from the property that an optical near field couples with a phonon; when it is used, however, even if light having a photon energy  $h\nu$  smaller than the bandgap energy  $E_g$  of the semiconductor is incident, an electron–hole pair is created. The reason for this is that it is possible for electrons in the valence band to be excited to the conduction band via an electric dipole forbidden transition to the phonon level, because the optical near field is a quasiparticle representing a virtual exciton–phonon–polariton state in which an exciton polariton and a phonon are coupled in the nano-regime. This excitation is a two-step transition that has already been applied to photochemical vapor deposition [11], photodetectors [12], photolithography [13], subnanometer polishing of glass surfaces [14], frequency up-conversion [15], and so on. This two-step transition is explained as follows (Fig. 1(a)) [11, 16].

- (1) First step: Transition from the ground state  $|E_g; el\rangle \otimes |E_{ex,thermal}; phonon\rangle$ , which is the initial state, to an intermediate state  $|E_g; el\rangle \otimes |E_{ex}; phonon\rangle$ . Here, the ket vector  $|E_g; el\rangle$  represents the electronic ground state, and  $|E_{ex,thermal}; phonon\rangle$  and  $|E_{ex}; phonon\rangle$  respectively represent the phonon excitation state that is determined by the crystal lattice temperature, and the phonon excitation state that is determined by the photon energy of the optical near field. The symbol  $\otimes$  represents the direct product of the ket vectors representing the two states. Because it is an electric dipole forbidden transition, an optical near field is essential in this excitation.
- (2) Second step: Excitation from the intermediate state  $|E_g; el\rangle \otimes |E_{ex}; phonon\rangle$  to the final state  $|E_{ex}; el\rangle \otimes |E_{ex'}; phonon\rangle$ . Here,  $|E_{ex}; el\rangle$  represents the electron excitation state, and  $|E_{ex'}; phonon\rangle$  represents the phonon excitation state. Because this is an electric dipole allowed transition, the excitation occurs via not only an optical near field but also via propagating light. After this excitation, the phonon excitation state relaxes to a thermal equilibrium state with an occupation probability determined by the lattice temperature and ends with excitation to the electron excitation state  $|E_{ex}; el\rangle \otimes |E_{ex,thermal}; phonon\rangle$ .

It should be noted that there is an inverse process to this process, namely, the two-step spontaneous emission process shown below (Fig. 1(b)) [12]:

- (1') First step: Transition from the initial state  $|E_{ex}; el\rangle \otimes |E_{ex,thermal}; phonon\rangle$  of the electron in the conduction band to the intermediate state  $|E_g; el\rangle \otimes |E_{ex}; phonon\rangle$ ,

which generates spontaneously emitted light. Because this is an electric dipole allowed transition, propagating light and an optical near field can both be generated; however, the process of generating propagating light is limited to the transition to  $|E_{ex,thermal}; phonon\rangle$  close to  $|E_g; el\rangle$ . The reason is that the occupation probability of  $|E_{ex}; phonon\rangle$  is low in levels other than those close to  $|E_g; el\rangle$  which has an energy on the order of  $kT$  (where  $k$  is Boltzmann's constant, and  $T$  is the crystal lattice temperature). In other words, this is because the phonon excitation state  $|E_{ex}; phonon\rangle$  is in the thermal equilibrium state since the propagating light does not generate a phonon. On the other hand, the probability of emitting an optical near field does not depend on the occupation probability of the phonon in the thermal equilibrium state, because the optical near field generates a phonon.

- (2') Second step: Transition from the intermediate state  $|E_g; el\rangle \otimes |E_{ex}; phonon\rangle$  to the ground state  $|E_g; el\rangle \otimes |E_{ex'}; phonon\rangle$ . Because this is an electric dipole forbidden transition, only an optical near field is generated. After this transition, the phonon excitation state relaxes to the thermal equilibrium state determined by the crystal lattice temperature and ends with a transition to the electronic ground state  $|E_g; el\rangle \otimes |E_{ex,thermal}; phonon\rangle$ .

Part of the optical near field spontaneously emitted by the above two-step process is converted to observable propagating light, which is observed in the optical far field [12]. Therefore, electrons are excited by current injection, and an LED can be realized utilizing processes (1') and (2') above. The emission wavelength of this device is not the bandgap energy  $E_g$ , but depends on the photon energy of the optical near field in the vicinity of the p–n junction.

It is well known that a phonon is needed for an indirect transition type semiconductor to spontaneously emit propagating light. This is because, for spontaneous emission, the wavenumber must be conserved (this is known as the wavenumber conservation law). An optical near field, however, has multiple modes that satisfy the wavenumber conservation law because the photons are strongly coupled with multi-mode phonons [11, 16], and the probability of spontaneous emission due to the optical near field is extremely high.

In addition, this phonon-assisted process can also involve a two-step stimulated-emission process explained in the following (Fig. 1(c)).

- (1'') First step: When an electron in the conduction band is irradiated with an optical near field, the electron transitions from the initial state  $|E_{ex}; el\rangle \otimes |E_{ex,thermal}; phonon\rangle$  to the intermediate state  $|E_g; el\rangle \otimes |E_{ex}; phonon\rangle$ , and light is emitted via stimulated emission.

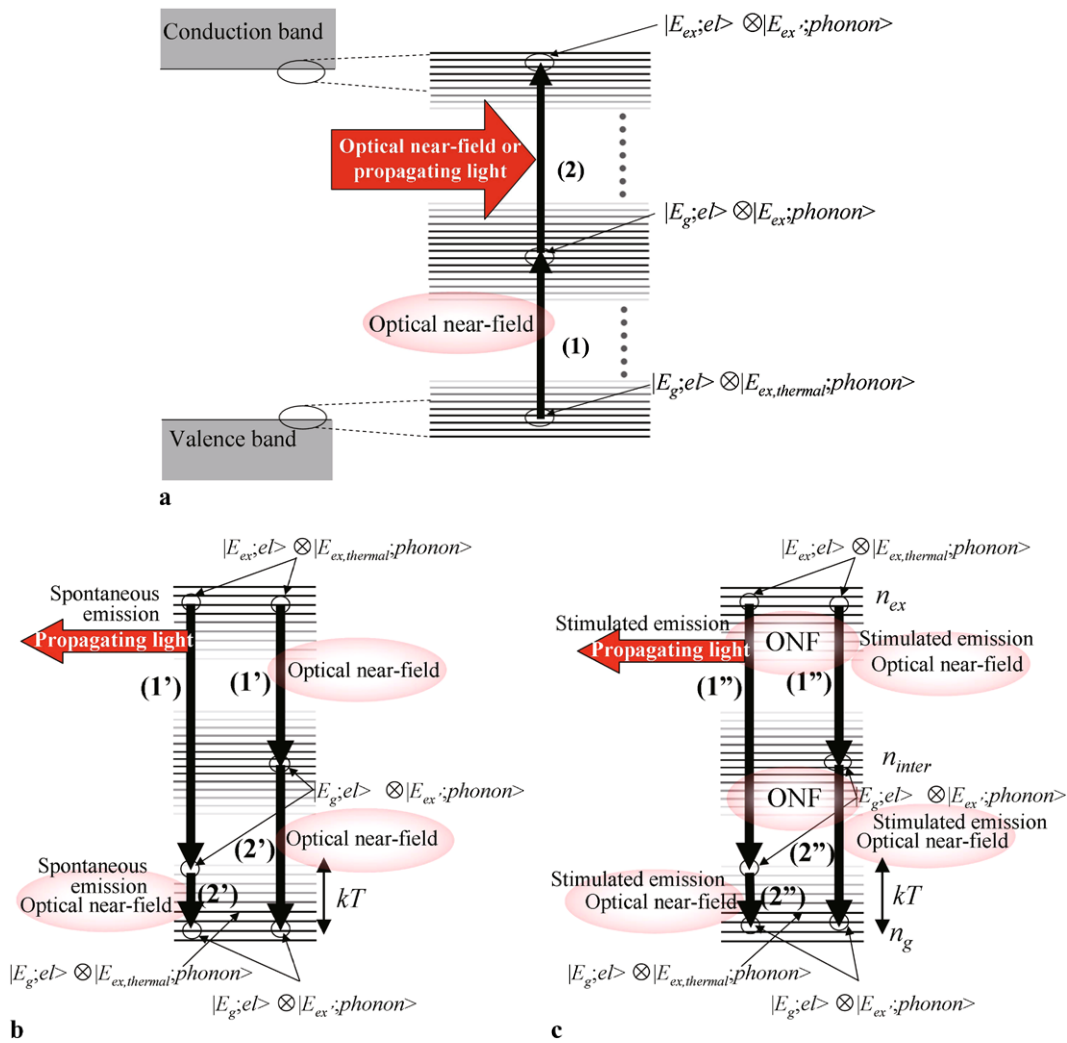


**Fig. 1** Three kinds of two-step phonon-assisted processes. (a) Excitation of an electron: (1) and (2) represent the first and second steps of the excitation, respectively. (b) Spontaneous emission: (1') and (2') repre-

sent the first and second steps of the transition, respectively. (c) Stimulated emission: (1'') and (2'') represent the first and second steps of the transition, respectively. ONF: optical near-field

Similar to the first step (1') of the spontaneous emission described above, the transition processes that generate propagating light are extremely limited. Here, when the electron number densities of occupation in the initial state  $|E_{ex}; el\rangle \otimes |E_{ex,thermal}; phonon\rangle$  and the intermediate state  $|E_g; el\rangle \otimes |E_{ex}; phonon\rangle$ ,  $n_{ex}$  and  $n_{inter}$ , satisfy the Bernard–Duraffourg inversion condition ( $n_{ex} > n_{inter}$ ) [17], the number of photons created by stimulated emission exceeds the number of photons annihilated by absorption.

(2'') Second step: Transition from the intermediate state  $|E_g; el\rangle \otimes |E_{ex}; phonon\rangle$  to the final state  $|E_g; el\rangle \otimes |E_{ex}; phonon\rangle$ , which emits light via stimulated emission. Because this is an electric dipole forbidden transition, only an optical near field is generated. After this transition, the phonon excitation state relaxes to

a thermal equilibrium state determined by the crystal lattice temperature, and ends with a transition to the electronic ground state  $|E_g; el\rangle \otimes |E_{ex,thermal}; phonon\rangle$ .

### 3 Device fabrication

To realize the device proposed in this paper, we used the two-step phonon-assisted process involving optical near fields two times. The first was for operating the device to obtain spontaneously emitted light, and the experimental results of this are reported in the next section. The second was for fabricating the device, in other words, for self-organized control of the spatial distribution of the dopant density suitable for high-efficiency spontaneous emission. The second usage method is described in this section.

To fabricate the device, As-doped n-type Si crystal wafer, with an electrical resistivity of  $10 \Omega \text{ cm}$  and a thickness of  $625 \mu\text{m}$  was used. The Si crystal wafer was then doped with B using ion implantation to form a p-layer. The B implantation energy was  $700 \text{ keV}$ , and the ion dose density was  $5 \times 10^{13} \text{ cm}^{-2}$ . After forming a p–n junction in this way, an indium tin oxide (ITO) layer with a thickness of  $150 \text{ nm}$  was deposited on the p-layer side, and an Al layer with a thickness of  $80 \text{ nm}$  was deposited on the n-layer side, both by RF sputtering, and these were used as positive and negative electrodes. Then, the Si crystal wafer with the electrodes attached was diced into a single device. The surface area was about  $10 \text{ mm}^2$ .

Finally, a forward bias voltage of  $16 \text{ V}$  was applied (current density,  $4.2 \text{ A/cm}^2$ ) to generate Joule heating for performing annealing, diffusing the B and varying the spatial distribution of its concentration. During this process, laser light (optical power density,  $10 \text{ W/cm}^2$ ) with a photon energy ( $h\nu_{\text{anneal}} = 0.95 \text{ eV}$ , wavelength  $1.30 \mu\text{m}$ ) smaller than the bandgap energy of Si ( $E_g = 1.12 \text{ eV}$ ) [18] was radiated from the ITO electrode side. This induced a phonon-assisted process, modifying the B diffusion by annealing, and forming characteristic minute inhomogeneous domain boundaries in a self-organized manner. This was due to the following three reasons:

- (1) Because the forward bias voltage ( $16 \text{ V}$ ) is much higher than  $E_g$  ( $= 1.12 \text{ eV}$ ), the difference ( $E_{F_c} - E_{F_v}$ ) between the quasi-Fermi energy of the conduction band,  $E_{F_c}$ , and the quasi-Fermi energy of the valence band,  $E_{F_v}$ , is higher than  $E_g$ , thus satisfying the Bernard–Durauffourg inversion condition ( $n_{\text{ex}} > n_{\text{inter}}$ ). Also, when light with a photon energy  $h\nu_{\text{anneal}}$  below  $E_g$  is radiated, this light propagates in the substrate without being absorbed in the Si and generates an optical near field at the domain boundaries of the inhomogeneous distribution of B [19]. This optical near field excites coherent phonons close to the p–n junction, forming an optical-near-field–phonon coupled state, that is to say, a virtual exciton–phonon polariton. Because the energy of this quasiparticle is equal to the sum of the photon energy and the energy of the induced phonon, even though  $h\nu_{\text{anneal}} < E_g$ , this energy is large enough to cause stimulated emission. Therefore, the electron transitions from the excitation state to the phonon level via an electric dipole forbidden transition due to the incident light with energy  $h\nu_{\text{anneal}} (< E_g)$ , and a photon is generated during this transition by stimulated emission.
- (2) Part of the Joule heating energy due to the forward bias is spent in the stimulated emission of photons, and therefore, the annealing rate is decreased. That is, at sites where the phonon-assisted stimulated emission in (1) above is easily generated, the shape and dimensions of the B inhomogeneous domain boundaries become more difficult to change. If it is assumed that the shape of the domain boundary is a sphere of radius  $r$ , and that  $r$  is smaller than the thickness of the active layer, the probability of generating stimulated emission in one domain boundary is proportional to the product of the number of photons incident on the domain boundary, the transition probability, and the volume of the spatial distribution of the optical near field. According to [11], these are proportional to  $r^2$ ,  $r^{-2}$ , and  $r^3$ , respectively. Therefore, the probability of stimulated emission (that is, the annealing inhibition rate) is proportional to their product,  $r^3$ . On the other hand, because the generated Joule heating is proportional to the current passing through that domain, the annealing rate is proportional to  $r^2$ . Therefore, the temporal rate of change of the domain boundary size  $r$  ( $dr/dt$ ) is given by  $dr/dt = ar^2 - br^3$  ( $a$  and  $b$  are constants determined by the forward bias current and optical intensity, respectively), and in the stationary state ( $dr/dt = 0$ ), it becomes  $r = a/b$ .
- (3) Process (2) above occurs in all domain boundaries in the device, not just at one domain boundary. In practice, the sizes and shapes of the domain boundaries are inhomogeneous, even after reaching the stationary state, for various reasons, such as the variety of shapes of the domain boundaries, the presence of a large number of domain boundaries, inhomogeneous current density, and so on. Because the probabilities of stimulated emission and spontaneous emission are proportional to each other [20], phonon-assisted spontaneous emission also tends to occur in regions where the phonon-assisted spontaneous stimulated emission process tends to occur. Therefore, as process (2) proceeds, the generated stimulated emission light irradiates the entire device, and therefore, process (2) does not remain in the light-irradiation region but spreads in a self-organized manner to the entire device. It is expected that the shapes and distribution of the domain boundaries formed in this way will be optimal for efficiently inducing the phonon-assisted process during device operation.

Figure 2(a) is a photograph showing the device during annealing. A W probe was contacted to the positive electrode, a  $20 \mu\text{m}$ -thick Al foil was attached to the negative electrode, and electric power was supplied. The electric power applied to the device was  $11 \text{ W}$ . Figure 2(b) is a thermography image of the device surface temperature 1 minute after applying the bias current. The surface temperature of the device was  $110$ – $220^\circ\text{C}$ . The temporal variation of the surface temperature is shown in Fig. 2(c). After a sudden increase to  $154^\circ\text{C}$  by heating due to the bias current, the temperature dropped and reached a stable value ( $140^\circ\text{C}$ ) after about 6 minutes. This temperature variation is consistent with the above discussion related to annealing under light irradiation. Specifically, although the power applied to the device generates Joule heating, raising the temperature, once the optical near field is

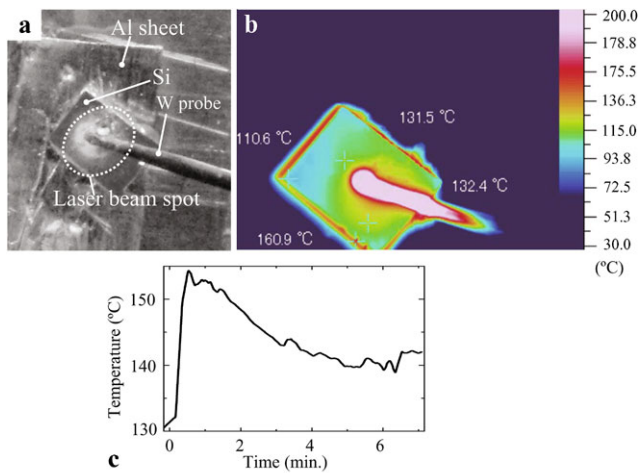


**Fig. 2** Temperature variation due to annealing. (a) Photograph of device during annealing. (b) Surface temperature distribution of device 1 minute after starting annealing. (c) Temporal change in temperature at center of device during annealing

generated in the domain boundary where the B concentration distribution is inhomogeneous, commencing stimulated emission, part of the Joule heating is dissipated in the form of light, and the temperature drops, soon reaching the stationary state. The forward bias was applied for 30 minutes while irradiating the device with light, which completes the fabrication of the device.

#### 4 Device operation

The experimental setup used for evaluating the characteristics of the fabricated device is shown in Fig. 3. We used a spectrometer and an InGaAs linear photodiode array (Spectra-Physics, Inc., OMA-V1024) to observe the emitted light spectrum. We used an InGaAs photodiode (Hamamatsu Photonics K.K., G8370-83) to observe emitted light in the energy region of 0.73 eV (wavelength 1.70  $\mu\text{m}$ ) and above. We used a wideband optical power meter (Spectra-Physics, Inc., 407A) to measure the emitted light intensity in the energy region 0.11–4.96 eV (wavelength 0.25–11.0  $\mu\text{m}$ ).

First, Fig. 4 shows the relationship between the injection current to the device,  $I$ , and the forward bias voltage,  $V$ . In this graph,  $I > 50$  mA indicates a negative resistance, and the break over voltage was 73 V [21]. This was due to the spatially inhomogeneous current density [21] and the generation of filament currents, as shown in the inset of Fig. 4. In other words, the B distribution has a domain boundary, and the current is concentrated in that region. A center of localization where the electrical charge is easily bound is formed in this current concentration region, and an optical near field is easily generated there. That is, the negative resistance is the principle of the device fabrication described in

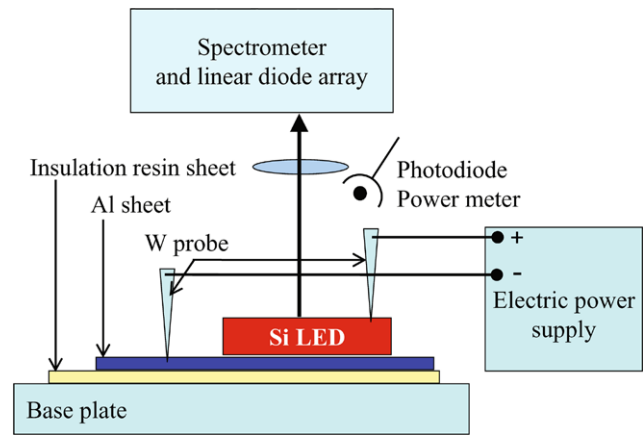


**Fig. 3** Experimental setup for evaluating device characteristics

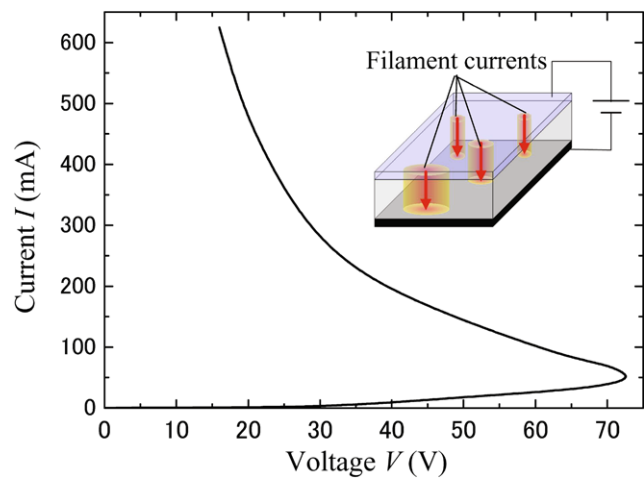


**Fig. 4** Relationship between current  $I$  and forward bias voltage  $V$  applied to device. Inset schematically shows filament currents predicted from the experimental results

the previous section. The reason why the break over voltage is higher than the built-in potential of the Si p–n junction is thought to be because of the high total resistance due to the thick Si crystal wafer, and the large contact resistance between the electrodes and the Si crystal wafer. In addition, although the device surface temperature during annealing (Fig. 2(b)) is too low for diffusing the B, it is thought that localized heating occurs due to the filament currents mentioned above, which makes the temperature inside the device sufficiently high. From secondary ion-microprobe mass spectrometry (SIMS), we confirmed that the B penetration depth was increased to at least 300 nm by the annealing.

Second, Figs. 5(a) and (b) show photographs of the external appearance of the non-biased and forward-biased (current density 4.2 A/cm<sup>2</sup>) device taken with an infrared CCD camera (photoreceptor band 0.73–1.38 eV (wavelength 0.90–1.70  $\mu\text{m}$ )) at room temperature and under fluorescent light illumination. Figure 5(b) reveals strong emit-

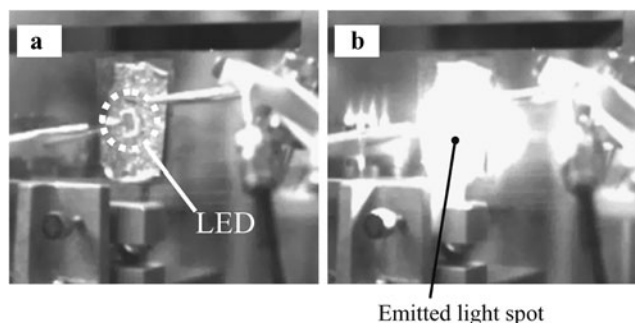


**Fig. 5** Photograph of device emitting light at room temperature, captured with an infrared camera under fluorescent light illumination: (a) current density  $I_d = 0$ ; (b) current density  $I_d = 4.2 \text{ A/cm}^2$

ted light. The injection current at this time was 11 W, and the emitted power reached as high as 1.1 W.

It is well known that commercially available Si photodiodes made by conventional methods emit very small amounts of light. For comparison, therefore, Fig. 6(a) shows the extremely weak emission spectrum when a current density of  $0.2 \text{ A/cm}^2$  was made to flow in a commercially available Si photodiode (Hamamatsu Photonics K.K., S3590). The device was destroyed with a current density higher than this. In this graph, like the results in [10], the emission spectrum was distributed on the high-energy side of  $E_g$  ( $= 1.12 \text{ eV}$ ). This was due to phonon scattering in the indirect band structure of the Si.

In contrast, the shape of the emission spectrum of our device differed from that in Fig. 6(a). Figures 6(b)–(d) are the emission spectra of devices fabricated by annealing for 1 min, 7 min, and 30 min, respectively. The bias current density was  $1.5 \pm 0.5 \text{ A/cm}^2$ . Unlike Fig. 6(a), the emission spectrum extended to energies lower than  $E_g$ . The decrease in the emission spectral intensity in the energy region below  $0.8 \text{ eV}$  was due to the sensitivity limit of the photodetector; in reality, the emission spectrum is thought to extend to even lower energies. The device fabricated by annealing for 1 min had an intense emission peak close to  $E_g$ , which extended as far as  $0.75 \text{ eV}$  (wavelength  $1.65 \mu\text{m}$ ), as shown in Fig. 6(b). A new emission peak appeared close to  $0.83 \text{ eV}$  (wavelength  $1.49 \mu\text{m}$ ) in the emission spectrum of the device fabricated by annealing for 7 min (Fig. 6(c)). The reason for the particularly small spectral intensity at energies lower than this peak was because of the sensitivity limit of the photodetector. There was no intense emission peak at  $E_g$  in the device fabricated by annealing for 30 min (Fig. 6(d)). On the other hand, a peak (downward pointing arrow in the figure) appeared in the region corresponding to the photon energy  $h\nu$  ( $= 0.95 \text{ eV}$ , wavelength  $1.3 \mu\text{m}$ ) of the light radiated during annealing, which indicates that an optical near field was generated by this irradiation light, which restricted the annealing rate. In addition, the peak in the low-energy region ( $0.83 \text{ eV}$ ) was higher than in Fig. 6(c). Specifically, the

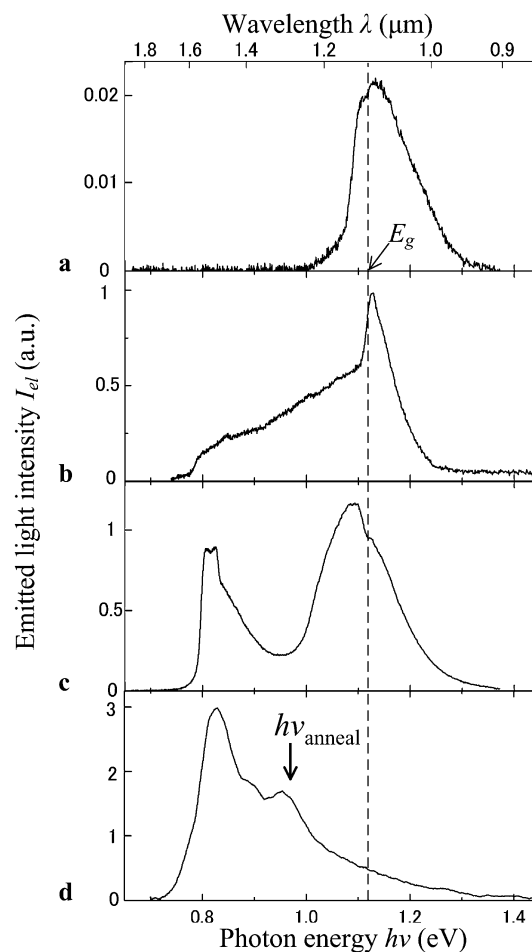


**Fig. 6** Emission spectra. (a) Emission spectrum of commercially available Si photodiode (Hamamatsu Photonics K.K., S3590). (b)–(d) Emission spectra of fabricated devices. Annealing times were 1 minute (b), 7 minutes (c), and 30 minute (d)

emission intensity at this peak position was 14 times higher and 3.4 times higher compared with Figs. 6(b) and (c), respectively. The emission spectrum was distributed over energies  $0.73$ – $1.24 \text{ eV}$  (wavelengths  $1.00$ – $1.70 \mu\text{m}$ ), which covers the optical fiber communication band. The width of this range is  $0.51 \text{ eV}$ , which is at least four times larger than the spectral width of  $0.12 \text{ eV}$  of a commercially available InGaAs LED (Hamamatsu Photonics K.K., L10823) with an emission wavelength of about  $1.6 \mu\text{m}$ .

Third, Figs. 7(a) and (b) show the relationship between the output optical power  $P_o$  and the electrical driving power  $P_e$  of the device fabricated by annealing for 30 min. The gradient of the straight broken line corresponds to the differential external power conversion efficiency. Figure 7(a) shows the results of measuring the power of the emitted light in the energy region higher than the photon energy  $h\nu = 0.73 \text{ eV}$  (wavelength  $1.70 \mu\text{m}$ ). When 11 W of electrical power was applied, the external power conversion efficiency was 1.3%, and the differential external power con-



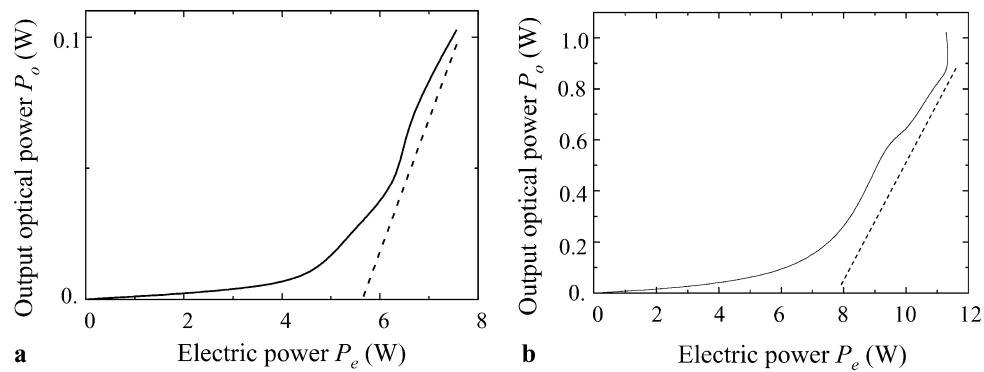


**Fig. 7** Relationship between applied electrical power  $P_e$  and emitted optical power  $P_o$ . (a) Total power of emitted light in photon energy region 0.73 eV and above. Gradient of broken line corresponds to differential external power conversion efficiency of 5.0%. (b) Total

power of emitted light in photon energy region 0.11–4.96 eV. Gradient of broken line corresponds to differential external power conversion efficiency of 40%

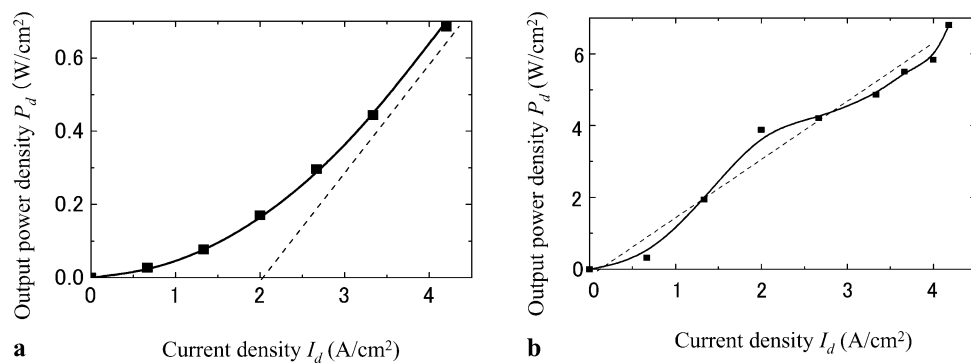


**Fig. 8** Relationship between injected current density  $I_d$  and emitted optical power density  $P_d$ . (a) Squares are measured values of total power density of emitted light in photon energy region 0.73 eV and above. Solid curve represents quadratic curve  $P_d = 0.04I_d^2$ . Gradient

of broken line corresponds to differential external quantum efficiency of 40%. (b) Squares are measured values of total power density of emitted light in photon energy region 0.11–4.96 eV. Gradient of broken line corresponds to external quantum efficiency of 50%

version efficiency was 5.0%. Because of the current limit of the power supply, it was not possible to input a power higher than this; however, even if a higher power could be applied, the device can stably operate without being damaged. Figure 7(b) shows the relationship between  $P_o$  and  $P_e$  in the photon energy region  $h\nu = 0.11$ –4.96 eV (wavelength 0.25–11.0  $\mu\text{m}$ ). An external power conversion efficiency of 10% and an external differential power conversion efficiency of 25% were achieved. However, this also included infrared radiation due to heating of the device, which will be necessary to examine in more detail.

To obtain the quantum efficiency, Fig. 8 shows the relationship between the emitted optical power density ( $P_d$ ) and the current density ( $I_d$ ) of the device fabricated by annealing for 30 min. Figure 8(a) shows the value of  $P_d$  in the energy region higher than the photon energy  $h\nu = 0.73$  eV (wavelength 1.70  $\mu\text{m}$ ). The measured values, indicated by the squares, were fitted by the quadratic curve  $P_d = 0.04I_d^2$  shown by the solid curve. In other words, in contrast to conventional devices in which  $P_d$  is proportional to  $I_d$ , in this

device  $P_d$  is proportional to  $I_d^2$ . This is because the two-step spontaneous emission process described in Sect. 2 is dominant; in other words, a single electron is converted to two photons. When  $I_d$  was 4.0 A/cm<sup>2</sup>, the external quantum efficiency was 15%. When  $I_d$  was 3.0–4.0 A/cm<sup>2</sup>, the differential external quantum efficiency was 40%. Figure 8(b) shows the relationship between  $P_d$  and  $I_d$  in the photon energy region  $h\nu = 0.11$ –4.96 eV (wavelength 0.25–11.0  $\mu\text{m}$ ). The external quantum efficiency reached as high as 150%. The reason why this value is greater than 100% is because a single electron is converted to two photons by the two-step spontaneous emission process, as described above. However, the measured values of  $I_d$  in Fig. 8(b) also include the effects of infrared radiation due to heating of the device, which it will be necessary to examine in more detail.

If the thickness of the high-resistivity Si crystal wafer used in this method could be reduced, the electrical efficiency could be increased even more. Also, because the current density can be increased, if a method of increasing the efficiency of extracting light outside the device could be de-

vised, it should be possible to realize an LED with even higher efficiency and a wider band. This approach can also be applied to laser oscillators, and we plan to publish more details of this in a separate article.

## 5 Conclusion

Using stimulated emission triggered by an optical near field generated at the inhomogeneous domain boundary of B doped in Si, we controlled annealing with current injection and fabricated a high-efficiency, broadband LED. This device emitted light by means of a two-step phonon-assisted process due to the optical near field generated at the inhomogeneous domain boundary of B. Even though we used bulk crystal Si with a simple homojunction structure, the obtained emission band of the device extended over energies 0.73–1.24 eV, and with 11 W of input electrical power, the total optical power was as high as 1.1 W. The external power conversion efficiency was 1.3%, the differential external power conversion efficiency was 5.0%, the external quantum efficiency was 15%, and the differential external quantum efficiency was 40%.

**Open Access** This article is distributed under the terms of the Creative Commons Attribution Noncommercial License which permits any noncommercial use, distribution, and reproduction in any medium, provided the original author(s) and source are credited.

## References

1. T.P. Lee, C.A. Burus, A.G. Dentai, *IEEE J. Quantum Electron.* **17**, 232 (1981)
2. R.A. Milano, P.D. Dapkus, G.E. Stillman, *IEEE Trans. Electron Devices* **29**, 266 (1982)
3. U.S. Department of Health and Human Services, Public Health Service, National Institute of Health, National toxicology program: NTP technical report on the toxicology and carcinogenesis studies of indium phosphide (CAS No. 22398-80-7) in F344/N rats and B6C3F1 mice (inhalation studies), NTP TR 499 (2001)
4. K.D. Hirschman, L. Tysbekov, S.P. Duttagupta, P.M. Fauchet, *Nature* **384**, 338 (1996)
5. Z.H. Lu, D.J. Lockwood, J.-M. Baribeau, *Nature* **378**, 258 (1995)
6. L. Dal Negro, R. Li, J. Warga, S.N. Basu, *Appl. Phys. Lett.* **92**, 181105 (2008)
7. T. Komoda, *Nucl. Instrum. Methods Phys. Res., Sect. B, Beam Interact. Mater. Atoms* **96**, 387 (1995)
8. S. Yerci, R. Li, L. Dal Negro, *Appl. Phys. Lett.* **97**, 081109 (2010)
9. S.K. Ray, S. Das, R.K. Singha, S. Manna, A. Dhar, *Nanoscale Res. Lett.* **6**, 224 (2011)
10. M.A. Green, J. Zhao, A. Wang, P.J. Reece, M. Gal, *Nature* **412**, 805 (2001)
11. T. Kawazoe, K. Kobayashi, S. Takubo, M. Ohtsu, *J. Chem. Phys.* **122**, 024715 (2005)
12. S. Yukutake, T. Kawazoe, T. Yatsui, W. Nomura, K. Kitamura, M. Ohtsu, *Appl. Phys. B, Lasers Opt.* **99**, 415 (2010)
13. T. Kawazoe, M. Ohtsu, Y. Inao, R. Kuroda, *J. Nanophotonics* **1**, 011595 (2007)
14. T. Yatsui, K. Hirata, W. Nomura, Y. Tabata, M. Ohtsu, *Appl. Phys. B* **93**, 55 (2008)
15. T. Kawazoe, H. Fujiwara, K. Kobayashi, M. Ohtsu, *IEEE J. Sel. Top. Quantum Electron.* **15**, 1380 (2009)
16. Y. Tanaka, K. Kobayashi, *Physica E* **40**, 297 (2007)
17. M.G.A. Bernard, G. Duraffourg, *Phys. Status Solidi* **1**, 699 (1961)
18. R.J. Van Overstraeten, R.P. Mertens, *Solid-State Electron.* **30**, 1077 (1987)
19. J.A. Van den Berg, D.G. Armour, S. Zhang, S. Whelan, H. Ohno, T.-S. Wang, A.G. Cullis, E.H.J. Collart, R.D. Goldberg, P. Bailey, T.C.Q. Noakes, *J. Vac. Sci. Technol. B* **20**, 974 (2002)
20. A. Einstein, P. Ehrenfest, *Z. Phys.* **19**, 301 (1923)
21. E. Shl, *Nonequilibrium Phase Transitions in Semiconductors* (Springer, Berlin, 1987), pp. 5–6

# Demonstration of modulatable optical near-field interactions between dispersed resonant quantum dots

Naoya Tate,<sup>1,2,\*</sup> Makoto Naruse,<sup>2,3</sup> Wataru Nomura,<sup>1,2</sup> Tadashi Kawazoe,<sup>1,2</sup> Takashi Yatsui,<sup>1,2</sup> Morihisa Hoga,<sup>4</sup> Yasuyuki Ohyagi,<sup>4</sup> Yoko Sekine,<sup>4</sup> Hiroshi Fujita,<sup>4</sup> and Motoichi Ohtsu<sup>1,2</sup>

<sup>1</sup>Department of Electrical Engineering and Information Systems, School of Engineering, The University of Tokyo, 2-11-16 Yayoi, Bunkyo-ku, Tokyo, 113-8656, Japan

<sup>2</sup>Nanophotonics Research Center, School of Engineering, The University of Tokyo, 2-11-16 Yayoi, Bunkyo-ku, Tokyo, 113-8656, Japan

<sup>3</sup>National Institute of Information and Communications Technology, 4-2-1 Nukuikita, Koganei, Tokyo, 184-8795 Japan

<sup>4</sup>Dai Nippon Printing Co. Ltd., Research and Development Center, 250-1 Wakashiba, Kashiwa, Chiba, 277-0871 Japan

\*[tate@nanophotonics.t.u-tokyo.ac.jp](mailto:tate@nanophotonics.t.u-tokyo.ac.jp)

**Abstract:** We experimentally demonstrated the basic concept of modulatable optical near-field interactions by utilizing energy transfer between closely positioned resonant CdSe/ZnS quantum dot (QD) pairs dispersed on a flexible substrate. Modulation by physical flexion of the substrate changes the distances between quantum dots to control the magnitude of the coupling strength. The modulation capability was qualitatively confirmed as a change of the emission spectrum. We defined two kinds of modulatability for quantitative evaluation of the capability, and an evident difference was revealed between resonant and non-resonant QDs.

©2011 Optical Society of America

**OCIS codes:** (200.3050) Information processing, (200.4740) Optical processing, (230.5590) Quantum-well, -wire, -dot devices, (350.4238) Nanophotonics and photonic crystals.

---

## References and links

1. M. Ohtsu, K. Kobayashi, T. Kawazoe, T. Yatsui, and M. Naruse, eds., *Principles of Nanophotonics*, (Taylor and Francis, 2008).
2. M. Ohtsu and K. Kobayashi, *Optical Near Fields* (Springer-Verlag, 2003), pp. 109–150.
3. K. Kobayashi, S. Sangu, T. Kawazoe, and M. Ohtsu, “Exciton dynamics and logic operations in a near-field optically coupled quantum-dot system,” *J. Lumin.* **112**(1-4), 117–121 (2005).
4. M. Ohtsu, T. Kawazoe, T. Yatsui, and M. Naruse, “Nanophotonics: application of dressed photons to novel photonic devices and systems,” *IEEE J. Sel. Top. Quantum Electron.* **14**(6), 1404–1417 (2008).
5. T. Kawazoe, M. Ohtsu, S. Aso, Y. Sawado, Y. Hosoda, K. Yoshizawa, K. Akahane, N. Yamamoto, and M. Naruse, “Two-dimensional array of room-temperature nanophotonic logic gates using InAs quantum dots in mesa structures,” *Appl. Phys. B* **103**(3), 537–546 (2011).
6. C. R. Kagan, C. B. Murray, and M. G. Bawendi, “Long-range resonance transfer of electronic excitations in close-packed CdSe quantum-dot solids,” *Phys. Rev. B Condens. Matter* **54**(12), 8633–8643 (1996).
7. S. A. Crooker, J. A. Hollingsworth, S. Tretiak, and V. I. Klimov, “Spectrally resolved dynamics of energy transfer in quantum-dot assemblies: towards engineered energy flows in artificial materials,” *Phys. Rev. Lett.* **89**(18), 186802 (2002).
8. M. Achermann, M. A. Petruska, S. A. Crooker, and V. I. Klimov, “Picosecond energy transfer in quantum dot Langmuir-Blodgett nanoassemblies,” *J. Phys. Chem. B* **107**(50), 13782–13787 (2003).
9. T. Franzl, D. S. Koktysh, T. A. Klar, A. L. Rogach, J. Feldmann, and N. Gaponik, “Fast energy transfer in layer-by-layer assembled CdTe nanocrystal bilayers,” *Appl. Phys. Lett.* **84**(15), 2904–2906 (2004).
10. T. Franzl, T. A. Klar, S. Schietinger, A. L. Rogach, and J. Feldmann, “Exciton recycling in graded gap nanocrystal structures,” *Nano Lett.* **4**(9), 1599–1603 (2004).
11. N. Tate, W. Nomura, T. Yatsui, T. Kawazoe, M. Naruse, and M. Ohtsu, “Parallel retrieval of nanometer-scale light-matter interactions for nanophotonic systems,” *Nat. Comput.* **2**, 298–307 (2010).
12. N. Sakakura and Y. Masumoto, “Persistent spectral-hole-burning spectroscopy of CuCl quantum cubes,” *Phys. Rev. B* **56**(7), 4051–4055 (1997).
13. Z. K. Tang, A. Yanase, T. Yasui, Y. Segawa, and K. Cho, “Optical selection rule and oscillator strength of confined exciton system in CuCl thin films,” *Phys. Rev. Lett.* **71**(9), 1431–1434 (1993).

14. T. Kawazoe, K. Kobayashi, J. Lim, Y. Narita, and M. Ohtsu, "Direct observation of optically forbidden energy transfer between CuCl quantum cubes via near-field optical spectroscopy," *Phys. Rev. Lett.* **88**(6), 067404 (2002).
15. H. J. Calmichael, *Statistical Methods in Quantum Optics 1*. (Springer-Verlag, 1999).
16. M. Naruse, H. Hori, K. Kobayashi, P. Holmström, L. Thylén, and M. Ohtsu, "Lower bound of energy dissipation in optical excitation transfer via optical near-field interactions," *Opt. Express* **18**(Suppl 4), A544–A553 (2010).
17. W. Nomura, T. Yatsui, T. Kawazoe, and M. Ohtsu, "The observation of dissipated optical energy transfer between CdSe quantum dots," *J. Nanophotonics* **1**, 011591 (2007).
18. K. Kobayashi, S. Sangu, H. Ito, and M. Ohtsu, "Near-field optical potential for a neutral atom," *Phys. Rev. A* **63**, 013806 (2000).
19. M. Han, X. Gao, J. Z. Su, and S. Nie, "Quantum-dot-tagged microbeads for multiplexed optical coding of biomolecules," *Nat. Biotechnol.* **19**(7), 631–635 (2001).
20. M. Strassburg, M. Dworzak, H. Born, R. Heitz, A. Hoffmann, M. Bartels, K. Lischka, D. Schikora, and J. Christen, "Lateral redistribution of excitons in CdSe/ZnSe quantum dots," *Appl. Phys. Lett.* **80**(3), 473–475 (2002).
21. M. Naruse, T. Kawazoe, R. Ohta, W. Nomura, and M. Ohtsu, "Optimal mixture of randomly dispersed quantum dots for optical excitation transfer via optical near-field interactions," *Phys. Rev. B* **80**, 125325 (2009).

## 1. Introduction

Nanophotonics, which utilizes the local interaction between nanometric materials via optical near-fields, has realized novel photonic devices, fabrication techniques, and systems which will help to meet the requirements of future optical technology [1]. Optical near fields can be viewed as the elementary surface excitations on nanometric materials, which can mediate the local interaction between closely spaced nanometric materials. The interaction potential is expressed by a Yukawa function, which represents the localization of the optical near-field energy around the nanometric particles [2]. Recently, several applications of nanometric, and energy-efficient optical functions have been actively developed by utilizing local energy transfer via optical near-fields and its subsequent dissipation [3–5]. These energy transfer in nanometric materials have been observed in various materials such as [6–10].

The operation of nanophotonic devices described above exhibits a *one-to-one* correspondence with respect to input signals, because the physical properties, size, shape, and alignment of the components for the characteristic optical near-field interactions are built into the substrate and spatially fixed. In order to realize a *one-to-many* correspondence with a single nanophotonic device, it is necessary to implement *modulatable* optical near-field interactions and associated *modulatable* optical functions. Here, we propose a novel concept of *Modulatable Nanophotonics* to realize such a system. It is realized by providing appropriate external controls to modulate the parameters of the components. In our concept, optical far-field retrieval of induced optical near-field interactions is achieved via modulation of the intensity, polarization, and spectrum of the subsequent irradiation. This is an important step toward further exploiting the possibilities of light–matter interactions on the nanometer scale [11].

In this paper, we demonstrate our concept by controlling the magnitude of the optical near-field coupling strength among multiple quantum dots (QDs) randomly dispersed on a flexible substrate. External control is provided by physical flexion of the substrate, whose response can be acquired as a change of the emission spectra in the optical far-field. In Section 2, we describe the basics of local energy transfer via optical near-fields and our experimental concept using QDs on a flexible substrate. Sections 3 and 4 show the concepts and results of numerical and experimental demonstrations, respectively. Quantitative evaluation of each result was performed based on specially defined figure-of-merits. We conclude in Section 5 with a brief summary.

## 2. Modulation of emission spectra of resonant quantum dot pairs

To demonstrate the modulation capability, we utilize *resonant* conditions between appropriate QD pairs on a physically flexible substrate. A conceptual diagram is shown in Fig. 1. Closely positioned resonant QD pairs exhibit high-quantum-efficiency and selective energy transfer via induced optical near-fields between QDs. As a typical case of local energy transfer, here we consider the optical near-field interaction between the exciton of the lowest excited state

$E_{1S}$  in a smaller QD and that of the second-lowest excited state  $E_{2L}$  in a larger QD. These two states are electric dipole allowed and forbidden energy levels, respectively [12,13]. However, energy transfer is allowed via the optical near-field interactions in the case of  $E_{1S} = E_{2L}$  because of the steep gradient field due to the localized nature of the optical near-field. Thus, the excitation energy in the smaller QD is transferred to the larger QD via this optical near-field interaction. The important point is that energy can be successfully transferred from the smaller QD to the larger QD only if  $E_{1S}$  and  $E_{2L}$  are in a resonant condition. Transferred energy is immediately dissipated from  $E_{2L}$  to the lowest excited state  $E_{1L}$  of the larger QD, and a photon is then emitted. Experimental and theoretical results showing good agreement with each other have been discussed in detail in previous papers [6–9,14].

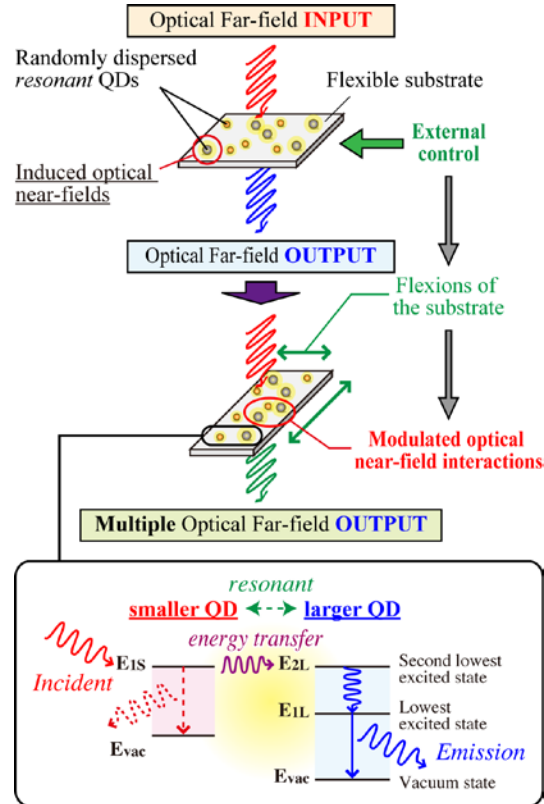


Fig. 1. Conceptual diagram of one-to-many correspondence in nanophotonic device based on concept of Modulatable Nanophotonics using resonant QDs. Induced nanometric modulations should be revealed as multiple outputs in the optical far-field region. [Inset] Schematic of local energy transfer between closely spaced small and large QDs. Energy transfer and subsequent energy dissipation are allowed only via optical near-fields induced between the two QDs.

Here, we consider the case of similar QDs dispersed on a substrate having sufficient physical flexibility. Flexing the substrate can vary the distance between the QDs. Figure 2 shows schematic diagrams comparing the emission processes in resonant and non-resonant QD pairs. In the case of a resonant QDs pair, denoted  $QD_{S-R}$  and  $QD_{L-R}$  in Fig. 2(a), energy transfers occur when the QDs are sufficiently close, because the magnitude of the optical near-field interaction, i.e., the coupling strength between  $QD_{S-R}$  and  $QD_{L-R}$ , depends on the distance  $r$  between them, as represented by the Yukawa function:

$$U = \frac{A \exp(-\mu r)}{r}, \quad (1)$$

where  $\mu$  and  $A$  represent distribution of optical near-fields which determined by exciton energy and amount proportional to the dipole moment, respectively [2]. Thus, emission is preferentially obtained from  $E_{IL}$  of  $QD_{L-R}$ . In contrast, if the separation between  $QD_{S-R}$  and  $QD_{L-R}$  is increased by flexion of the substrate in order to significantly decrease the coupling strength, both  $QD_{S-R}$  and  $QD_{L-R}$  emit independently. This means that the spectral intensities of  $QD_{S-R}$  and  $QD_{L-R}$ , as well as the relative spectral intensity ratio from them, can be modulated by the flexion, i.e., by modulating the coupling strength. Thus, the spectral intensity ratios from  $QD_{S-R}$  and  $QD_{L-R}$  with and without the flexion are evidently different, as shown in Fig. 2(b). On the other hand, in the case of non-resonant QDs, denoted  $QD_{S-NR}$  and  $QD_{L-NR}$  in Fig. 3(a), energy transfer never occurs between the two. Each QD emits individually regardless of whether the substrate is flexed. In this case, only a change in spectral intensity that depends on the areal density of the QDs is obtained. Therefore, the spectral intensity ratios from  $QD_{S-NR}$  and  $QD_{L-NR}$  with and without flexion are equal, as shown in Fig. 3(b).

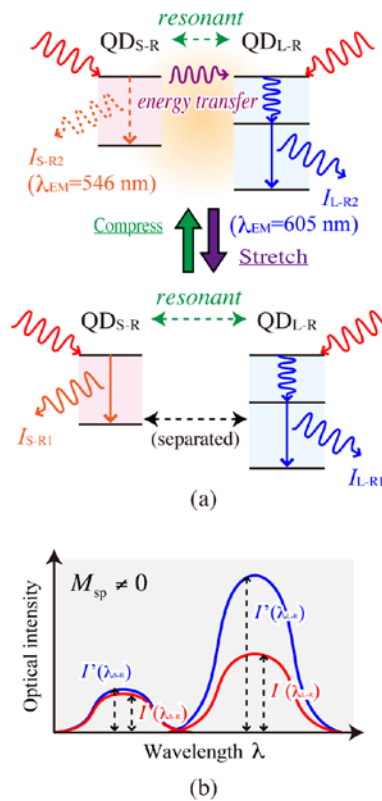


Fig. 2. (a) Schematic diagram of modutable optical near-field interactions between *resonant* QD pairs dispersed on flexible substrates. (b) Definition of sampled optical intensities on emission spectra  $I$  and  $I'$  for quantitative evaluation of systems based on modulability  $M_{sp}$ , by using resonant QD pairs.

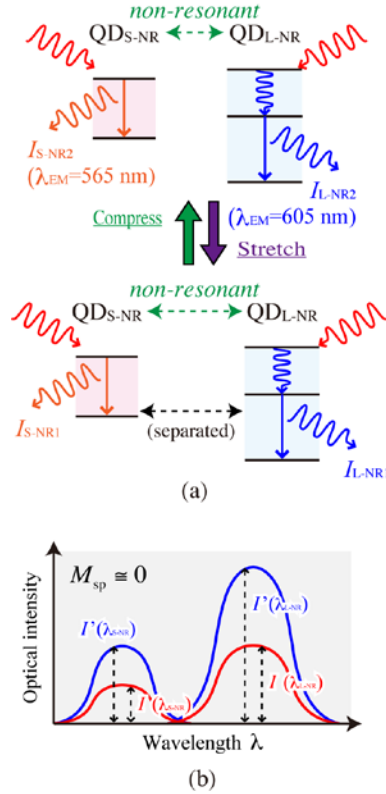


Fig. 3. (a) Schematic diagram of independent emissions from dispersed *non-resonant* QD pairs. (b) Definition of sampled optical intensities on emission spectra  $I$  and  $I'$  for quantitative evaluation of systems based on modulatability  $M_{sp}$ , by using non-resonant QD pairs.

Here, we define *modulatability*  $M_{sp}$  of the emission by using the spectral intensities  $I(\lambda_s)$  and  $I(\lambda_L)$  from the two QDs:

$$M_{sp} = \left| \frac{I'(\lambda_s)}{I(\lambda_s)} - \frac{I'(\lambda_L)}{I(\lambda_L)} \right|, \quad (2)$$

where  $I$  and  $I'$  represent the peak emission intensities of the spectra without and with the flexion, respectively. Wavelengths of peak emission intensities of the spectra of QD<sub>S</sub> and QD<sub>L</sub> are represented as  $\lambda_s$  and  $\lambda_L$ , which are the emissions from  $E_{IS}$  and  $E_{IL}$ , respectively. In the case of the resonant QDs, as shown in Fig. 2(b), the value of  $I'/I$  depends on the magnitude of the coupling strength, governed by the flexion, which means that the modulatability can take a non-zero value ( $M_{sp} \neq 0$ ). On the other hand, in the case of the non-resonant QDs, as shown in Fig. 3(b), the value of  $I'/I$  remains unchanged for all wavelengths because the area density of the QDs is homogeneously modulated by the flexion. Therefore,  $M_{sp}$  is calculated to be nearly zero ( $M_{sp} \equiv 0$ ). One remark regarding Eq. (2) is that singularity may be a problem when denominators therein result in zero. However, as described below in Sections 3 and 4, we can assume that the denominators are non-zero in realistic physical situations, which guarantees the effectiveness as the representation of Eq. (2).

### 3. Numerical demonstration

To numerically estimate the spectral intensity modulation, we assumed a calculation model consisting of four QDs configured as resonant QD pairs, i.e., two small QDs (QD<sub>S-A</sub> and QD<sub>S-C</sub>) and two large QDs (QD<sub>L-B</sub> and QD<sub>L-D</sub>), representing many QDs dispersed on the substrate, as shown in Fig. 4. We simulated the temporal evolution of exciton populations of the relevant excited states in these QDs by quantum master equations [15]. The exciton populations correspond to the intensity of radiation from each QD, and their evolutions are modulated by modulating the magnitude of the optical near-field coupling strength between QDs, by flexion of the substrate. As previously reported in [16], the initial condition is set as a vacuum state, and the duration and the amplitude of the incident light are given by the Hamiltonian representing interactions between the incident light and the QDs. Here, the magnitude of the optical near-field interaction, i.e., the coupling strength, between the two QDs is denoted by the Yukawa function of Eq. (1).

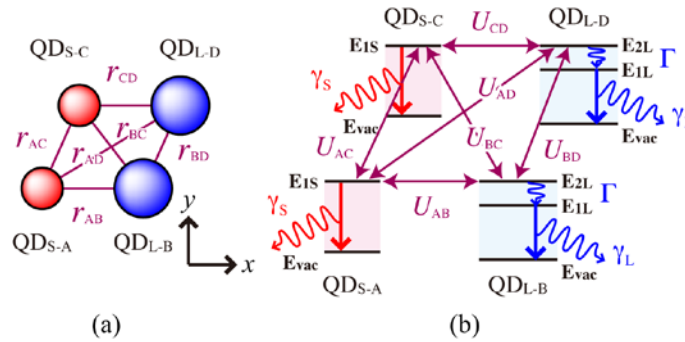


Fig. 4. Schematic diagrams of four-QD calculation model for numerical demonstration of multiple-QD system, showing (a) their geometrical alignment and (b) the conditions of optical near-field interactions between each QD. In our model, each parameter is variable, and their variations are assumed to be imposed by flexion of the substrate.

In this model, the evolution of the exciton population in each QD is calculated for various distances  $r$ , which corresponds to different degrees of coupling, controlled by flexion, as shown by Fig. 4(a). Initial distances between each QD are set on a 2D  $xy$ -surface as  $r_{AB} = r_{BD} = r_{AC} = r_{CD} = 100$  (nm), and the magnitudes of the coupling strengths  $U_{AB}$ ,  $U_{BD}$ ,  $U_{AC}$ ,  $U_{CD}$ ,  $U_{AD}$ , and  $U_{BC}$  depend on these distances, as schematically shown by Fig. 4(b). In our model, the relaxation time constant  $\Gamma^{-1}$  is set at 10 ps, and the radiation lifetimes of QD<sub>S</sub> and QD<sub>L</sub>, denoted as  $\gamma_S^{-1}$  and  $\gamma_L^{-1}$ , are respectively set at 2.83 ns and 1 ns as a typical parameter set for the CdSe/ZnS QDs used for our previous experiments [17], which based on the pattern of conventional energy transfer models between CdSe/ZnS QDs. Based on these setup parameters and proportional relations  $A \propto \mu \propto L^3$  in Eq. (1) [18], the diameter of the smaller QDs,  $L$ , is assumed to be approximately 50 nm, and that of the larger QDs,  $L'$ , satisfies  $L' = \sqrt{2}L$ . Based on theoretically assumed distributions of optical near-fields, which described by the Yukawa function [2], scale of optical near-fields has been proportional to inverse-square of size of the source. Therefore, sufficient energy transfer between QDs via optical near-fields is expected with such model.

First, we assumed *stretching* of the substrate in the  $x$  and  $y$  directions, as shown in Fig. 5(a), and calculated the exciton populations with various stretch lengths  $\delta r$ . In the case of the  $x$ -directional stretching,  $r_{AC}$  and  $r_{BD}$  are constant, as the first-order approximation, and  $r_{AB}$ ,  $r_{CD}$ ,  $r_{AD}$  and  $r_{BC}$  are varied. On the other hand, in the case of the  $y$ -directional stretching,



$r_{AB}$  and  $r_{CD}$  are constant, and  $r_{AC}$ ,  $r_{BD}$ ,  $r_{AD}$  and  $r_{BC}$  are varied. Figure 5(b) shows the calculated results. The horizontal axis represents the relative stretch length, which is defined as  $\delta r / L$ .

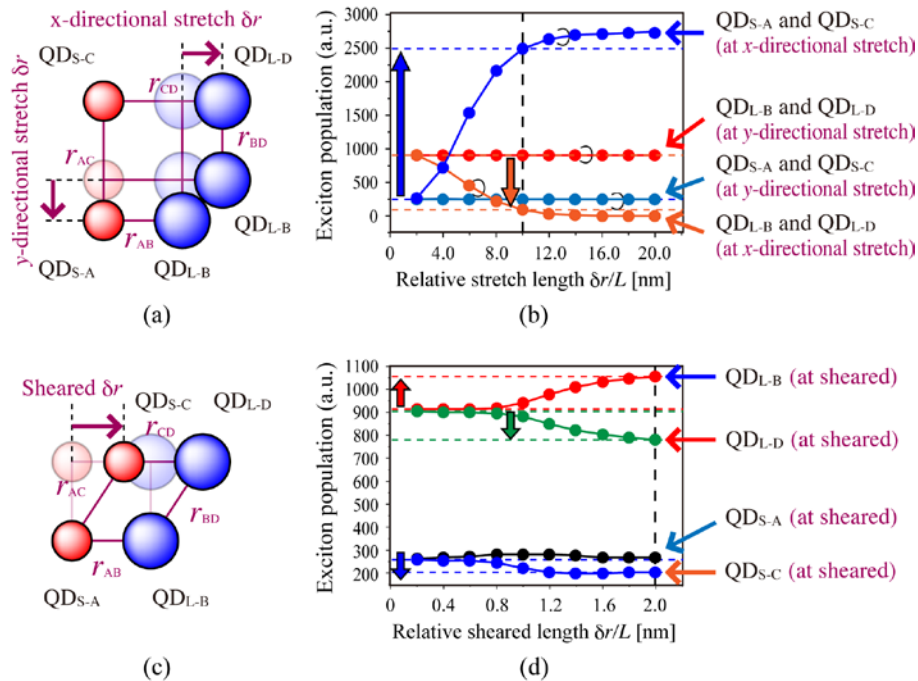


Fig. 5. Schematic diagram of (a) stretch model and (c) shear model, and evolutions of the population of the radiation from four QDs by (b) stretching and (d) shearing the substrate.

Evident changes in the exciton populations are obtained by the  $x$ -directional stretching, because the excitons always preferentially transfer from smaller QDs to larger QDs (from QD<sub>S-A</sub> to QD<sub>L-D</sub>). This result indicates that the coupling strength between the smaller QDs and the larger QDs is decreased by the  $x$ -directional stretching, and they emit independently.

Here we assume that the emission intensity from each QD is proportional to the exciton population at the corresponding QD energy level. Therefore, in the case of the  $x$ -directional stretching, as shown in Fig. 5(a),  $M_{sp}$  is calculated as 9.26 at a stretch length of  $\delta r = 500$  nm. The population in the lowest excited state of the larger QDs finally approaches zero, and  $M_{sp}$  is calculated as infinity. On the other hand,  $y$ -directional stretching gives  $M_{sp} \cong 0$  at the same stretch length. Therefore, only the former model can be said to be a *modulatable nanophotonic system*.

Next, a shear model is assumed for the  $x$ -directional shift of QD<sub>S-C</sub> and QD<sub>L-D</sub>. Its schematic diagram is shown in Fig. 5(c). In the case of the model,  $r_{AB}$  and  $r_{CD}$  are constant, and  $r_{AC}$  and  $r_{BD}$  are increased. Figure 5(d) shows the results of calculations. By increasing the sheared length  $\delta r$ , which is defined by the shifted values of QD<sub>S-C</sub> and QD<sub>L-D</sub>, only the exciton population at QD<sub>L-B</sub> increases, because the magnitude of energy transfer toward QD<sub>L-B</sub> increases not only from QD<sub>S-A</sub> but also from QD<sub>S-C</sub>. In contrast, that to QD<sub>L-D</sub> decreases. This is also because of the increase in the energy transferred from QD<sub>S-C</sub> not only to QD<sub>L-D</sub> but also to QD<sub>L-B</sub>. As a result, the population at QD<sub>S-C</sub> is decreased, whereas that at QD<sub>S-A</sub> remains unchanged, because the main route of energy transfer is from QD<sub>S-A</sub> to QD<sub>L-B</sub>, regardless of the stretching. Here, by these contributions of the exciton populations at the smaller QDs

( $QD_{S-A}$  and  $QD_{S-C}$ ) and the larger QDs ( $QD_{L-B}$  and  $QD_{L-D}$ ), the calculated  $M$  in the shear model shows a non-zero value ( $M_{sp} = 0.11$  for a sheared length of  $\delta r = 100$  nm).

#### 4. Experimental demonstration

We used commercially available CdSe/ZnS spherical QDs (*Evident Technologies*) as a test specimen. QDs are uniformly dispersed in toluene solvents with 10 mg/mL of concentration. Their exciton energy transfer has already been studied [7,19,20], and *resonant* and *non-resonant* conditions via optical near-field interactions have been experimentally verified [17]. The same types of QDs were adopted as  $QD_{L-R}$  and  $QD_{L-NR}$ . Their peak absorption wavelength  $\lambda_{AB}$  and peak emission wavelength  $\lambda_{EM}$  were as given in their technical specifications from the manufacturer, 583 nm and 605 nm, respectively, the latter corresponding to the wavelength of emission from  $E_{1L}$  in Fig. 1. The respective diameters  $D$  of the resonant pair,  $QD_{S-R}$  and  $QD_{L-R}$ , were assumed to be 8.2 nm and 8.7 nm, and those of the non-resonant pair,  $QD_{S-NR}$  and  $QD_{L-NR}$ , were assumed to be 7.7 nm and 8.7 nm. The QDs adopted as  $QD_{S-R}$  have  $\lambda_{AB} = 523$  nm and  $\lambda_{EM} = 546$  nm, and those adopted as  $QD_{S-NR}$  have  $\lambda_{AB} = 565$  nm and  $\lambda_{EM} = 578$  nm. These emission wavelengths  $\lambda_{EM}$  correspond to the wavelengths of emission from  $E_{1L}$ . As the flexible substrate, we used polydimethylsiloxane (PDMS), which is particularly known for its obvious rheological properties. We mixed 5 mL of each QD solution as resonant and non-resonant QD pairs. The mixed QD solutions were dispersed on a 2 cm  $\times$  2 cm square of PDMS substrate and allowed to dry naturally. In our experiments, although evident heterogeneity of the distributions was observed, the average  $r$  was assumed to be approximately 5–10 nm from the thickness of the ZnS shell and the length of the modified ligand to each QD.

Here we consider only 2-D flexion of the substrate. The QDs were excited by a He-Cd laser (wavelength 325 nm) with 5 mW/cm<sup>2</sup> power density. In our experiment, as shown in Fig. 6, the PDMS substrate was set on an aperture formed at the side of a vacuum desiccator and was flexed by evacuation. The flexion brings dispersed QDs close to each other, as represented by  $\delta r < 0$ . The air pressure was decreased and fixed to  $\sim 0.07$  MPa to achieve a 20% in-plane compression ratio of the substrate, which was geometrically determined from the size of the aperture and the depth of the flexed substrate.

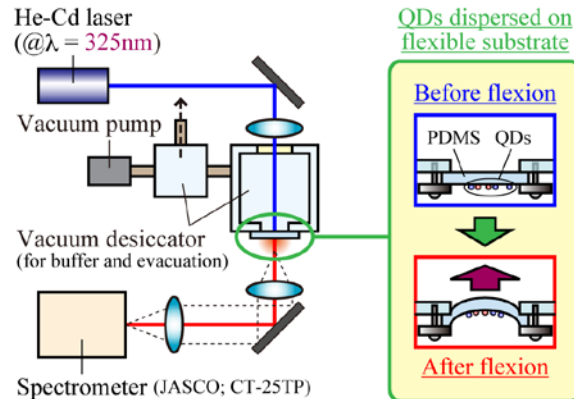


Fig. 6. Schematic diagram of experimental setup for demonstration of modulated nanophotonic system using a flexible substrate on which resonant QD pairs are randomly dispersed. Flexion of the sample substrate is achieved by vacuum evacuation.

We experimentally observed the emission spectra of the resonant and non-resonant QDs without and with flexion by using a spectrometer (JASCO; CT-25TP), as shown in Figs. 7(a) and (b), respectively. The fractional ratio of the numbers of small QDs to large QDs was 1:1. The dashed curves in these figures represent Gaussian curves fitted to the measured spectral profiles. The differences in peak wavelength from those shown in the technical specifications

depend on the variability of each particle's size and the inhomogeneous dispersion of the size distribution. In addition, because all peak wavelengths in Figs. 7 are shifted to red from 5 to 10 nm, the difference can also be explained by re-absorption effect in solid-state QDs on PDMS substrate.

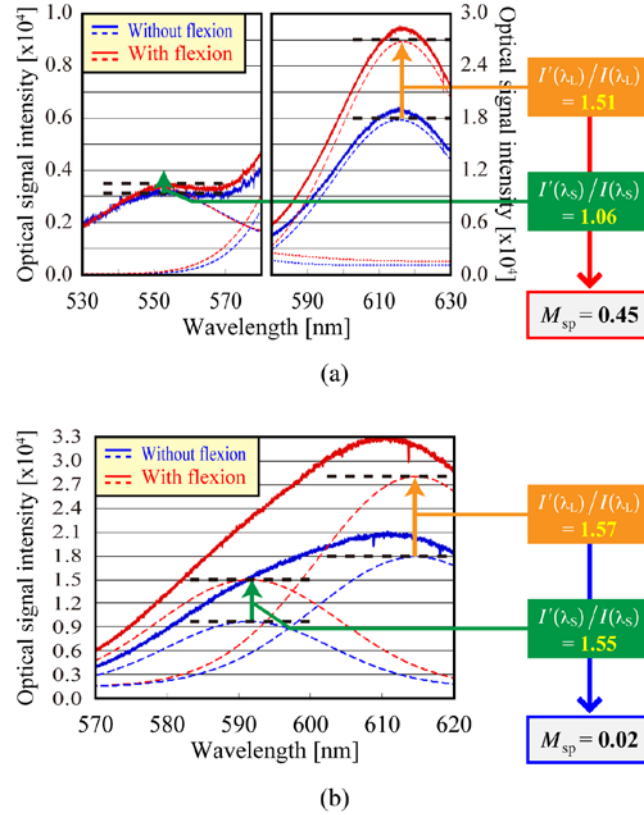


Fig. 7. Obtained emission spectra with (a) resonant and (b) non-resonant samples before (blue curves) and after (red curves) flexion of the substrate. Dashed curves represent results of Gaussian fitting of each spectrum.

As shown, the intensities of the spectra are increased as a whole because the numbers of QDs per unit area are increased by the flexion of each substrate. However, only an increase of the emission intensity from  $QD_{S-R}$  was suppressed. This is because the average distance between  $QD_{S-R}$  to  $QD_{L-R}$  is shortened by the flexion, which induces energy transfer from  $QD_{S-R}$  to  $QD_{L-R}$ . Similar behavior was predicted by our numerical demonstrations described above. For quantitative evaluation of this behavior, we evaluated the intensities at the spectral peak from the fitted curves and calculated the values of  $I'(\lambda_L)/I(\lambda_L)$  and  $I'(\lambda_S)/I(\lambda_S)$ , as shown in Fig. 7. By taking the difference, the modulabilities  $M_{sp}$  obtained with the resonant and non-resonant QDs were 0.45 and 0.02, respectively. Therefore, as in the numerical demonstration in Sec. 3, it was confirmed that the resonant QDs showed a much larger  $M_{sp}$  compared with that of the non-resonant QDs.

Similar experiments were conducted with other resonant samples with various fractional ratios (1:1, 2:1, and 3:1) and dilution rates ( $\times 1$  and  $\times 2$ ). Such parameters control the average distance between dispersed QDs. The assumed average distances in each experimental setup and the calculated modulabilities  $M_{sp}$  were compared (Table 1). Each average distance was calculated from that of the previous experimental setup, which was assumed to be approximately 10 nm. In the cases where resonant QD pairs were used, regardless of the

fractional ratios and dilution rates,  $M_{sp}$  generally showed non-zero values. Moreover, by diluting the QD samples,  $M_{sp}$  decreased. This is because the average distances between QDs were increased by the dilution, and the coupling strength decreased. In Table 1, it was revealed that one-to-many fractional ratios of QDs can show efficient energy transfer and subsequent emission. As previously reported in [21], in a mixture of the equivalent number of larger QDs and smaller QDs, not all of excitons in a smaller QD can be successfully transferred to a neighboring larger QD, because the radiation lifetime of a larger QD is limited as few nanoseconds. So that part of the excitons in smaller QDs must be decayed at each QD and results in loss in the conversion from the input to output. On the other hand, in a mixture of a few larger QDs and a lot of QDs, excitons in smaller QDs can be transferred to neighboring smaller QDs before being radiatively decayed till relaxation at a larger QD. This indicates that the latter case can effectively output radiated excitons at smaller QDs as relaxation at larger QDs.

**Table 1. Calculated Modulabilities  $M_{sp}$  for Several Samples with Various Fractional Ratios and Dilution Rates\***

Fraction ratio [QD <sub>s</sub> :QD <sub>L</sub> ]	Resonant QD pairs						Non-resonant QD pairs
	1:1		2:1		3:1		1:1
Dilution rate	× 1	× 2	× 1	× 2	× 1	× 2	× 1
Average QD distance [nm]	10	14	10	14	10	14	10
$M_{sp}$	0.44	0.21	0.32	0.06	0.86	0.19	0.02

\*Because the average distances between QDs increase by dilution of each sample solution,  $M_{sp}$  takes smaller values by dilution for non-resonant QD pairs.

The difference in the rates of change of each spectral peak intensity of the resonant QD sample corresponds to a difference in color tone of the emission from the sample. Our experimental results indicated that a change in the emitted color tone was successfully obtained by flexion of the substrate on which the resonant QDs were dispersed. From this viewpoint, we constructed a chromaticity diagram based on the color matching functions of each observed emission spectrum and defined another modulability  $M_{ch}$  to directly evaluate the amount of each modulation for several samples. The value of  $M_{ch}$  is defined as a shifted distance between coordinates of each spectrum in the chromaticity diagram due to the modulation. Figure 8 shows chromaticity coordinates of previous experimental results and corresponding values of  $M_{ch}$ . As shown, the resonant QD sample revealed larger  $M_{ch}$  (Fig. 8(a)), whereas the non-resonant QD sample revealed relatively small values of  $M_{ch}$  (Fig. 8(b)). For comparison with  $M_{sp}$  in Table 1, Table 2 shows a list of all values of  $M_{ch}$  for the samples described in Table 1. A similar tendency of the modulabilities  $M_{ch}$  in Table 2 was obtained. Because we used similar types of QD pairs, in our experiment, similar shift vectors from the two coordinates were obtained. That is to say, we can evaluate each modulation, not only in terms of the amount but also the type, based on possible directions of each vector from before modulation to after modulation. Evaluation of the type is a fundamental issue for further discussions on applications utilizing their one-to-many correspondences.

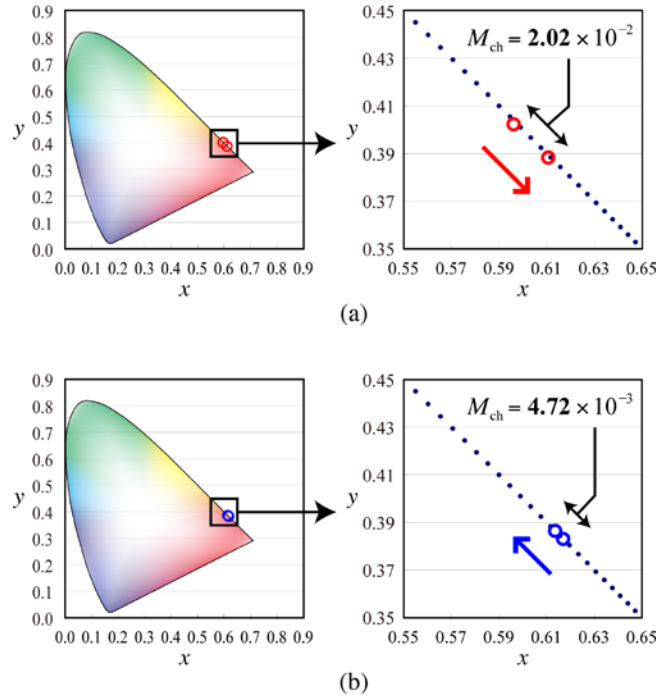


Fig. 8. Calculated modulabilities  $M_{ch}$  with (a) resonant and (b) non-resonant samples. An evident difference in  $M_{ch}$ , defined as the distance between the chromaticity coordinates before and after flexion, was observed.

Table 2. Calculated Modulabilities  $M_{ch}$  for Several Samples with Various Fractional Ratios and Dilution Rates.

	Resonant QD pairs						Non-resonant QD pairs
	1:1		2:1		Fraction ratio [QD <sub>s</sub> :QD <sub>t</sub> ]		1:1
Fraction ratio [QD <sub>s</sub> :QD <sub>t</sub> ]							
Dilution rate	× 1	× 2	Dilution rate	× 1	× 2	Dilution rate	× 1
Average QD distance [nm]	10	14	Average QD distance [nm]	10	14	Average QD distance [nm]	10
$M_{ch}$ [ $\times 10^{-3}$ ]	20.2	6.41	$M_{ch}$ [ $\times 10^{-3}$ ]	20.2	6.41	$M_{ch}$ [ $\times 10^{-3}$ ]	20.2

## 5. Summary

In conclusion, we have described the basic concept of Modulatable Nanophotonics and numerically and experimentally demonstrated the concept by utilizing resonant and non-resonant QD pairs dispersed on flexible substrates. The modulability was qualitatively evaluated by introducing modulabilities  $M_{sp}$  and  $M_{ch}$ . Resonant QD pairs exhibited unique modulability of their emission spectra, which depends on controlling the magnitude of the coupling strength between the QDs via optical near-field interactions. Such modulability cannot be obtained with non-resonant QD pairs.

From the viewpoint of information retrieval, the results of our demonstration indicate that this method can retrieve the effects of optical near-field interactions as a modulation of the optical far-field response. As we demonstrated in this paper, selecting appropriate resonant QD pairs can realize various *modulabilities* of the emission spectrum based on nanophotonics. By developing the concept further and experimentally examining various

implementations, our idea can be applied to a *modulatable multi-spectrum emitting element* whose emission spectrum can be freely switched by applying external modulation.

### **Acknowledgments**

This work was supported in part by a comprehensive program for personnel training and industry-academia collaboration based on projects funded by the New Energy and Industrial Technology Development Organization (NEDO), Japan, as well as the Global Center of Excellence (G-COE) “Secure-Life Electronics” and Special Coordination Funds for Promoting Science and Technology sponsored by the Ministry of Education, Culture, Sports, Science and Technology (MEXT), Japan.

# **[II] PRESENTATIONS IN INTERNATIONAL CONFERENCES**



## Phonon-assisted near-field activation of electron transfer between a solution and an electrode

T. Yatsui, K. Iijima, K. Kitamura, and M. Ohtsu

*School of Engineering, the University of Tokyo, Tokyo 113-8656, Japan*

An optical near-field is expected to realize phonon-assisted multiple excitation in nano-scale structures.<sup>1</sup> Using the phonon-assisted process, higher catalytic activity is expected without heating. Thus, phonon-assisted activation can increase the catalytic activity of nanostructures, in addition to the contribution from increased surface area. To confirm this effect, we observed photo-induced current generation using platinum black electrodes (Fig. 1(a)).<sup>2</sup>

We observed current generation in ferricyanide solution under visible light irradiation (CW,  $\lambda = 532$  nm, Fig. 1(b)). Because the absorption band-edge wavelength of ferricyanide solution is 470 nm, the observed current generation did not originate from the photochemical reaction of the ferricyanide solution. We calculated the heat generation in platinum black, in which all the incident photons were absorbed (solid red line in Fig. 1(b)), and found that the heat generation was negligible with respect to that of the phonon-assisted process. Additionally, higher-order dependencies on the excitation power appeared with increasing current density, which was fitted by the second-order function  $\Delta i / i = aI + bI^2$  (Fig. 1(b)), indicating that these activation of electron transfer originated from the optical near-field effect on the nanostructured surface of the electrode.<sup>1</sup>

### Acknowledgements

This work was financially supported by a Grant-in-Aid for Young Scientists (A) from MEXT, by a research grant (Basic Research) from The TEPCO Memorial Foundation, and by a Research and Development Program of Innovative Energy Efficiency Technology from New Energy and Industrial Technology Development Organization (NEDO).

<sup>1</sup> Arata Sato, Yuji Tanaka, Fujio Minami, and Kiyoshi Kobayashi, *Journal of Luminescence* **129** (12), 1718 (2009).

<sup>2</sup> Lakshmi Krishnan, Steven E. Morris, and Glenn A. Eisman, *Journal of The Electrochemical Society* **155** (9), B869 (2008).



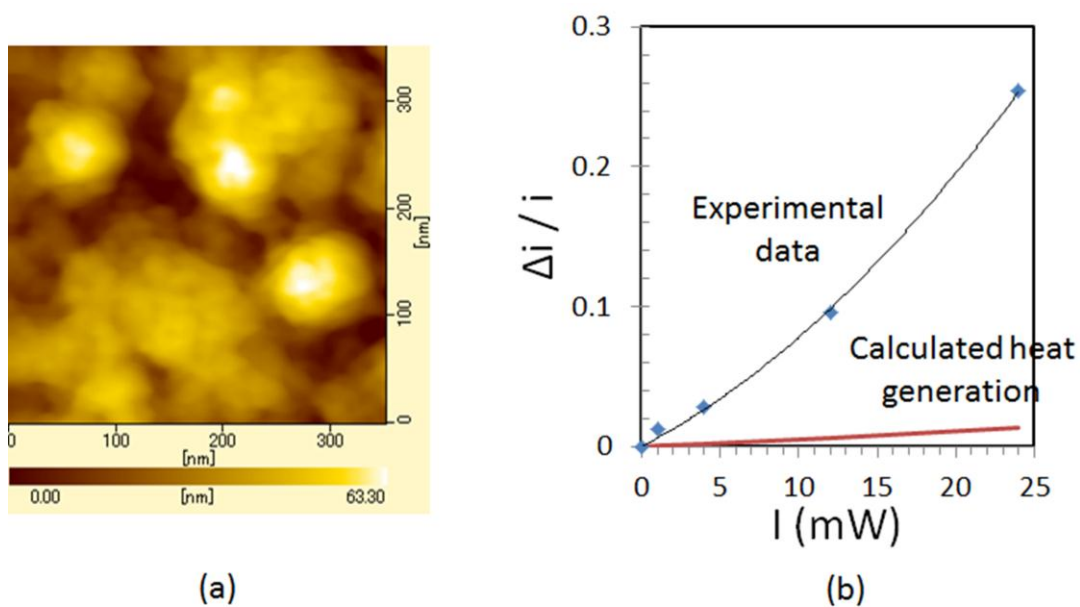


Fig. 1 (a) AFM image of platinum black electrodes. (b) Relationship between irradiation power and current density. Solid diamonds: observed current generation. Black solid curve: fitted curve,  $\Delta i / i = 5.8 \times 10^{-3} I + 2.0 \times 10^{-5} I^2$ . Red solid curve: Calculated heat generation.

## Visible-light-induced water splitting by phonon-assisted optical near fields in ZnO nanorods

Takahiro Mochizuki, Kokoro Kitamura, Takashi Yatsui, and Motoichi Ohtsu

*School of Engineering, the University of Tokyo, Tokyo 113-8656, Japan*

The phonon-assisted optical near-field process was applied to a water-splitting reaction to increase the response of visible light, in which the photon energy was less than the band-gap energy.<sup>1</sup> To generate the optical near field, we used thick (100-nm diameter) and ultra-fine (20-nm diameter) ZnO nanorods. The photocatalytic performance of ZnO was evaluated by photoelectrochemical (PEC) analysis using a three-electrode setup in 0.1 M NaOH electrolyte solution.<sup>2</sup> The power dependence of the photocurrent in Fig. 1(c)–(e) shows the photocatalytic performance under ultraviolet (UV, 325 nm) and visible (473 nm and 532 nm) irradiation, respectively. Under UV irradiation, the photoresponse current of the ZnO nanorods was comparable to that of the reference bulk substrate with a flat surface, whereas under 473-nm irradiation, the photocurrent increased drastically with decreasing nanorod diameter. Compared with the bulk substrate, the ultra-fine nanorods showed a 70-fold enhancement in the photocurrent. Additionally, under 532-nm irradiation, photocurrent generation was observed only for the ultra-fine nanorods. Furthermore, the power dependence was fitted by the second-order function  $PC = aI + bI^2$  ( $PC$ : photocurrent,  $I$ : excitation power) shown by the solid curve in Fig. 1(e), indicating that the photocurrent generated by visible-light irradiation originated from multi-step excitation using the phonon-assisted process.

### Acknowledgements

This work was financially supported by a Grant-in-Aid for Young Scientists (A) from MEXT, by a research grant (Basic Research) from The TEPCO Memorial Foundation, and by a Research and Development Program of Innovative Energy Efficiency Technology from New Energy and Industrial Technology Development Organization (NEDO).

<sup>1</sup> A. Sato, Y. Tanaka, F. Minami, K. Kobayashi, *J. Lumines.* **129**, 1718 (2009).

<sup>2</sup> T. H. H. Le, K. Mawatari, Y. Pihosh, T. Kawazoe, T. Yatsui, M. Ohtsu, M. Tosa, and T. Kitamori, *Appl. Phys. Lett.* **99**, 213105 (2011).

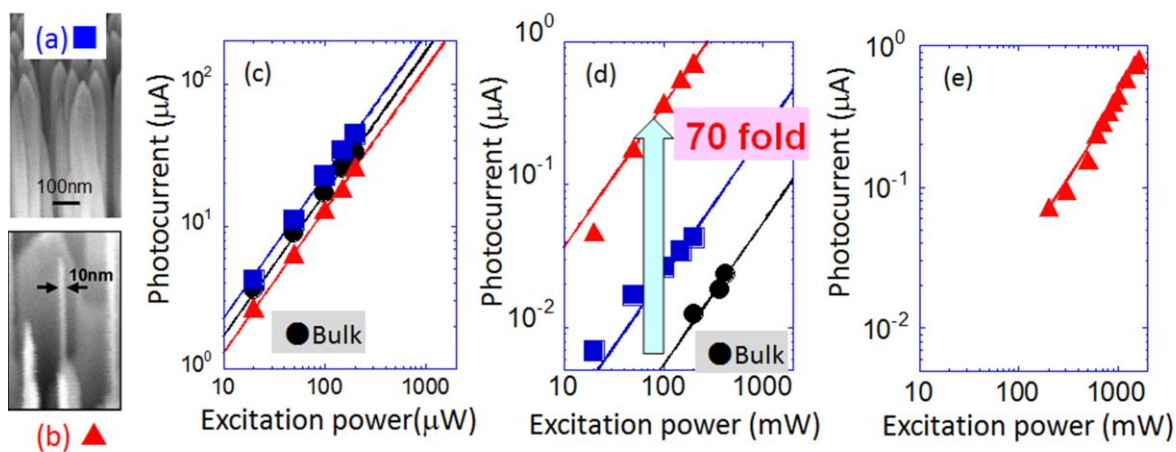


**Fig. 1.** SEM images of (a) thick and (b) ultra-fine ZnO nanorods. The power dependence of the photocurrent measured by PEC analysis in 0.1 M NaOH (c) under 325-nm, (d) 473-nm, and (e) 532-nm irradiation of the bulk ZnO substrate (solid circles), thick nanorods (solid squares), and ultra-fine nanorods (solid triangles).



## Thirteenth International Conference on the Science and Application of Nanotubes

24–29 June 2012

Brisbane Convention & Exhibition Centre, Australia

HOME

HOSTS

SPEAKERS

SYMPOSIA

PROGRAM

PRESENTERS

ABSTRACTS

IMPORTANT DATES

REGISTRATION

ACCOMMODATION

TOURS/TRAVEL

DESTINATION

SPONSORS

GENERAL INFORMATION

COMMITTEES

CONFERENCE CHARTER

## Luminescence Properties of Oxygen-Doped Carbon Nanotubes

- Yuhei Miyauchi, Institute of Advanced Energy, Kyoto University, Japan & Japan Science and Technology Agency, PRESTO, Japan
- Munechiyo Iwamura, Institute of Advanced Energy, Kyoto University, Japan, Japan
- Shinichiro Mouri, Institute of Advanced Energy, Kyoto University, Japan, Japan
- Tadashi Kawazoe, Department of Electrical Engineering and Information Systems, Graduate School of Engineering, The University of Tokyo, Japan, Japan
- Motoichi Ohtsu, Department of Electrical Engineering and Information Systems, Graduate School of Engineering, The University of Tokyo, Japan, Japan
- Kazunari Matsuda, Institute of Advanced Energy, Kyoto University, Japan, Japan

Single-walled carbon nanotubes (SWNTs) have been recognized as promising quasi-one dimensional (1D) materials not only for the fundamental 1D physics researches [1, 2] but also various optoelectronics applications such as light emitters driven by the direct carrier injection [1]. However, the low luminescence quantum yield (QY) of SWNTs at most ~7% even for clean air-suspended SWNTs [3] has limited the potential performance of nanotube-based light emitting devices. Here we demonstrate that the modified excitonic states by oxygen doping in SWNTs ( $E_{11}^*$ ) have enhanced QY because of longer luminescence lifetime and shorter radiative recombination lifetime than the intrinsic  $E_{11}$  excitons in non-doped SWNTs. The oxygen-doped (6, 5) SWNTs used in this work were prepared based on the procedure developed by Ghosh et al. [4]. The effective luminescence lifetime of about 100 ps was observed for the  $E_{11}^*$  states, while the intrinsic  $E_{11}$  excitons in the same SWNTs exhibited the effective lifetimes only less than 20 ps. We also observed temperature dependence of the luminescence intensities of both  $E_{11}$  and  $E_{11}^*$  features. The  $E_{11}^*$  luminescence intensity weakly and monotonically decreased with

decreasing temperature, while the  $E_{11}$  intensity showed the typical 1D behavior nearly proportional to  $T^{-1/2}$ . These results indicate that the mobile quasi-1D  $E_{11}$  exciton is trapped by the localized potential due to the doped oxygen atom, and confined in the quasi-0D state exhibiting the  $E_{11}^*$  luminescence feature.

Furthermore, the radiative recombination lifetime of the quasi-0D excitons is found to be 2-3 times shorter than the  $E_{11}$  excitons, based on the analysis considering exciton diffusion kinetics and successive trapping by the sparsely distributed localized states. The shortened radiative decay lifetime is attributed to the increased oscillator strength reflecting the reduced dimensionality of the  $E_{11}^*$  excitons. The luminescence QY of the  $E_{11}^*$  exciton is determined to be more than one order larger than the  $E_{11}$  excitons in the same SWNTs using the obtained luminescence lifetime and the radiative recombination lifetime of the  $E_{11}^*$  state. [1] P. Avouris, M. Freitag, and V. Perebeinos, *Nature Photon.* 2, 341 (2008). [2] Y. Miyauchi, H. Hirori, K. Matsuda, and Y. Kanemitsu, *Phys. Rev. B* 80, 081410(R) (2009). [3] J. Lefebvre, D. G. Austing, J. Bond, and P. Finnie, *Nano Lett.* 6, 1603 (2006). [4] S. Ghosh, S. M. Bachilo, R. A. Simonette, K. M. Beckingham, and R. B. Weisman, *Science* 330, 1656 (2010).

Email: [nt12@icms.com.au](mailto:nt12@icms.com.au) Homepage: [Thirteenth International Conference on the Science and Application of Nanotubes](http://www.nt12.org).

Conference Organiser: ICMS Pty Ltd, 84 Queensbridge Street, Southbank, Victoria 3006, Australia  
Telephone: +61 3 9682 0244 Fax: +61 3 9682 0288

25-June 2012, 14:00-14:30 PM

**Nanophotonic polishing of substrate with angstrom scale****Takashi Yatsui**<sup>1,2</sup>, Wataru Nomura<sup>1</sup>, Motoichi Ohtsu<sup>1</sup><sup>1</sup>*School of Engineering, University of Tokyo, Bunkyo-ku, Tokyo, Japan**Email: yatsui@ee.t.u-tokyo.ac.jp, web site: [http://www.lux.t.u-tokyo.ac.jp/index\\_e.html](http://www.lux.t.u-tokyo.ac.jp/index_e.html)*<sup>2</sup>*Advanced Low Carbon Technology Research and Development Program (ALCA), Japan Science and Technology**Agency, Kawaguchi-shi, Saitama, Japan*

A reduction of the surface roughness ( $R_a$ ) to less than 1 Å is required in various applications such as hard-disk and optical-disk processing.  $R_a$  is formally defined as the arithmetic average of the absolute values of the surface height deviations from the best-fitting plane. Although chemical-mechanical polishing (CMP) has been used to flatten the surfaces [1], it is generally limited to reducing  $R_a$  to about 2 Å because the polishing pad roughness is as large as 10 μm, and the polishing-particle diameters in the slurry are as large as 100 nm. We therefore developed a new polishing method that uses near-field etching based on an autonomous phonon-assisted process, which does not use any polishing pad, with which we obtained ultraflat silica surface with angstrom-scale average roughness (see Fig. 1) [2,3]. Since this technique is based on photo-chemical process, it can be applicable to other materials, including GaN, PMMA, diamond, and so on. Additionally, it is a non-contact method without a polishing pad, it can be applied not only to flat substrates but also to three-dimensional substrates [4] that have convex or concave surfaces, such as micro-lenses, optical-disk, and the inner wall surface of cylinders. Furthermore, this method is also compatible with mass production.

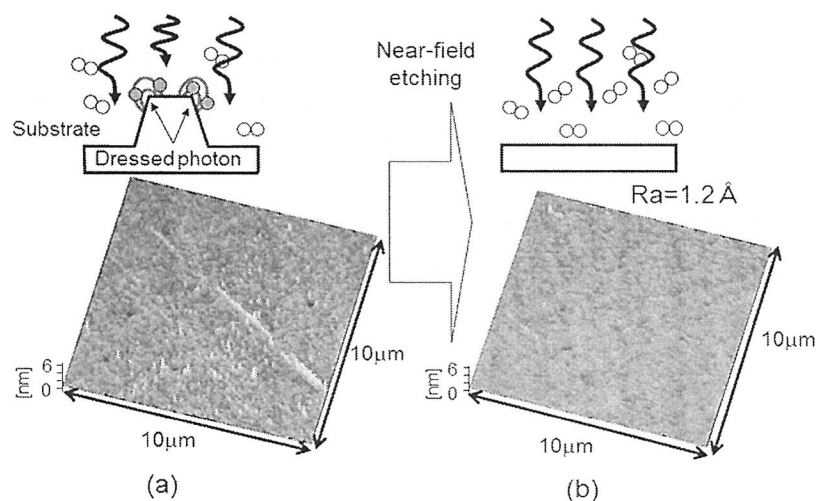


Fig. 1. Schematic of near-field etching. Atomic force microscopic images of (a) before and (b) after the optical near-field etching.

**Refernces**

1. L. M. Cook, J. Non-Crystalline Solids, **120**, 152 (1990).
2. T. Yatsui, K. Hirata, W. Nomura, M. Ohtsu, and Y. Tabata, Appl. Phys. B, **93**, 55 (2008).
3. T. Yatsui, K. Hirata, Y. Tabata, W. Nomura, T. Kawazoe, M. Naruse, and M. Ohtsu, Nanotechnology **21**, 355303 (2010).
4. T. Yatsui, K. Hirata, Y. Tabata, Y. Miyake, Y. Akita, M. Yoshimoto, W. Nomura, T. Kawazoe, M. Naruse, and M. Ohtsu, " Appl. Phys. B- Lasers and Optics, 103, 527 (2011).

# Concepts of dressed photon science and technology

Motoichi Ohtsu

Graduate School of Engineering, the University of Tokyo,

2-11-16 Yayoi, Bunkyo-ku, Tokyo 113-8656, Japan,

also with Nanophotonics Research Center, The University of Tokyo,

2-11-16 Yayoi, Bunkyo-ku, Tokyo 113-8656, Japan,

E-mail: ohtsu@ee.t.u-tokyo.ac.jp

Dressed photon science and technology utilize the electromagnetic fields localized in nanometric space. These fields have been named optical near-fields due to their non-propagating features. Dressed photon science and technology enables the realization of qualitative innovations in optical devices, fabrication techniques, energy conversion, and hierarchical systems by exploiting the novel functions and phenomena enabled by optical near-field interactions. In this sense, the principles and concepts of dressed photon science and technology are quite different from those of conventional wave-optical technology encompassing photonic crystals, plasmonics, metamaterials, silicon photonics, and quantum-dot photonic devices. This is because these devices use propagating light even though the materials or particles used may be nanometer-sized. The theoretical picture of dressed photons has been proposed to describe the electromagnetic interactions between nanometric particles located in close proximity to each other, giving birth to a new field known as dressed photon science and technology. The optical near-field is a virtual cloud of photons that always exists around an illuminated nanometric particle. A real photon (, i.e., conventional propagating scattered light) can be emitted from an electron in an illuminated nanometric particle. Independently of the real photon, another photon is emitted from the electron, and this photon can be re-absorbed within a short duration. This photon, i.e., a virtual photon, is nothing more than the optical near-field, and its energy is localized at the surface of the nanometric particle. Since the virtual photon remains in the proximity of the electron, it can couple with the electron in a unique manner. This coupled state, called a dressed photon, is a quasi-particle from the standpoint of photon energy transfer. It is the dressed photon that carries the material excitation energy. The dressed photon has been theoretically described by assuming a multipolar quantum electrodynamic Hamiltonian in a Coulomb gauge in a finite nano-system [1]. After a unitary transformation, the creation and annihilation operators of the dressed photon are expressed as the sum of the operators of the real photon and an electron-hole pair. A real nanometric material is composed not only of electrons but also of a crystal lattice. In this case, after a dressed photon is generated on an illuminated nanometric particle, its energy can be exchanged with the crystal lattice. By this exchange, the crystal lattice can excite the vibration mode coherently, creating a multi-mode coherent phonon state. As a result, the dressed photon and the coherent phonon can form a coupled state. The creation operator of this quasi-particle, representing the coupled state, is expressed as the product of the creation operator of the dressed photon and a displacement operator of the phonon, which represents the creation of the coherent phonon state [2]. This coupled state is a quasi-particle and is generated only when the particle size is small enough to excite the crystal lattice vibration coherently. Dressed photons have allowed the realization of qualitative innovations in optical technologies. For example, in the case of fabrication technologies, it should be noted that large, expensive, high-power-consumption, short-wavelength light sources are not required. The



photochemical etching by dressed photon-phonons does not involve the use of rare-earth metals for polishing quartz glass. It should also be noted that silicon, used for the energy conversion, has low toxicity and no concerns about depletion of resources. These notable features, realized by using dressed photon science and technology, are advantageous for energy saving and environmental protection for future society.

### References

- [1] K. Kobayashi, S. Sangu, H. Ito, and M. Ohtsu, Phys. Rev. A **63**, 013806 (2001).
- [2] Y. Tanaka and K. Kobayashi, Journal of Microscopy **229**, 228(2008).



**Motoichi Ohtsu** received the Dr. E. degrees in electronics engineering from the Tokyo Institute of Technology, Tokyo in 1978. He was appointed a Research Associate, an Associate professor, a Professor at the Tokyo Institute of Technology. From 1986 to 1987, while on leave from the Tokyo Institute of Technology, he joined the Crawford Hill Laboratory, AT&T Bell Laboratories, Holmdel, NJ. In 2004, he moved to the University of Tokyo as a professor. He has been the leader of several Japanese national projects for academia-industry collaborations. He has written over 470 papers and received 83 patents. He is the author, co-author, and editor of 62 books, including 27 in English. In 2000,

he was appointed as the President of the IEEE LEOS Japan Chapter. From 2000, he is an executive director of the Japan Society of Applied Physics. He is a Fellow of the Optical Society of America, and a Fellow of the Japan Society of Applied Physics. He is also a Tandem Member of the Science Council of Japan. He has been awarded 14 prizes from academic institutions, including the Issac Koga Gold Medal of URSI in 1984, the Japan IBM Science Award in 1988, two awards from the Japan Society of Applied Physics in 1982 and 1990, the Inoue Science Foundation Award in 1999, the Japan Royal Medal with a Purple Ribbon from the Japanese Government in 2004, H. Inoue Award from JST in 2005, the Distinguished Achievement Award from the IEICE of Japan in 2007, and Julius Springer Prize for Applied Physics in 2009.

# Nanophotonic device utilizing a dipole-forbidden energy state

T. Yatsui, M. Tsuji, Y. Liu, T. Kawazoe, and M. Ohtsu

School of Engineering and Nanophotonics Research Center, the University of Tokyo

2-11-16 Yayoi, Bunkyo-ku, Tokyo 113-8656, Japan

Email yatsui@ee.t.u-tokyo.ac.jp

To reduce the size of photonic devices below the diffraction limit, we have proposed nanophotonic devices<sup>1</sup> that consist of semiconductor quantum dots (QDs). In a nanophotonic device, the dipole-forbidden energy-transition<sup>2</sup> can reduce the size of device beyond the diffraction limit of light and achieve the unidirectional energy transfer, which is unattainable in conventional photonic devices. The dipole-forbidden energy transition originates from an exchange of the virtual photons between the resonant energy states. The use of virtual photons activates dipole-forbidden energy state. Although emission from the dipole-forbidden energy state cannot be detected in the far field, it can be utilized when the nanoparticle and detector are in close proximity. Here, we report direct observation of emission from an optically forbidden level in ZnO QDs using the near-field interaction induced by a fiber probe<sup>3</sup>.

ZnO colloidal QD was synthesized using sol-gel method<sup>4</sup>. The average diameter of fabricated ZnO QD was 4 nm. The synthesized ZnO QDs were dispersed uniformly over a sapphire substrate. The red open circles in Fig. 1(a) and the blue open circles in Fig. 1(b) represent the far-field and near-field spectra which were obtained with the probe-to-sample distance of 1  $\mu\text{m}$  and 5nm, respectively.

To observe the changes between far- and near-field spectra, we considered the quantized energy levels in ZnO QDs. QDs synthesized by the sol-gel method are known to be spherical, although the crystalline structure of ZnO QDs is wurtzite<sup>5</sup>. In the present study, the QD shape was assumed to be spherical with radius  $R$ , and the quantized energy levels were calculated [see Fig. 1(c)]<sup>6</sup>. Using these energy values, we fitted the PL spectra using Lorentzian functions, shown as solid red, blue, and green lines, respectively, in Figs. 1(a) and 1(b). The fitted profiles were used to determine near/far ratios, i.e., the ratio between the peak intensities of each near/far spectrum (Table 1). The peak intensity of  $E_2$  increased drastically as the fiber probe approached the ZnO QDs, whereas the peak intensity of  $E_1$  remained constant. The increase in the peak intensity of  $E_3$  was due to the higher excitation photon energy of 3.81 eV.

In conclusion, we achieved direct observation of emission from an optically forbidden level in ZnO QDs. By introducing a near-field fiber probe in close proximity to the QDs, we observed increased emission intensity from the dipole-forbidden. Because the decay time of the dipole-forbidden state is longer than that of the dipole-active state by  $10^6$ , the dipole-forbidden state can be used to realize novel devices such as optical buffer memory, and signal-transmission devices.

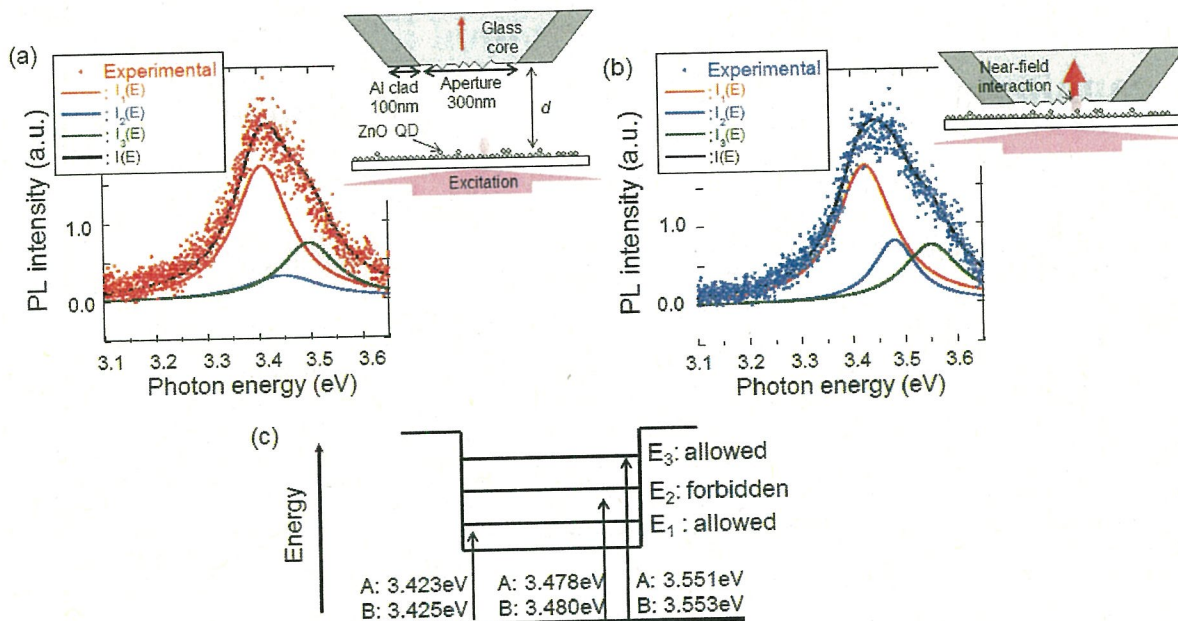


Figure 1. (a) Far-field (red open circles) and (b) near-field PL spectra of ZnO QDs. The respective separation,  $d$ , between the fiber and the ZnO QD was (a) 1  $\mu\text{m}$  and (b) 5 nm. (c) Energy states in 4-nm-diameter, spherical ZnO QDs.

Table I. The ratio between near-field and far-field intensity in each energy state.

	Far (Fig. 1A)	Near (Fig. 1B)	Near/Far ratio
$A_1$	$0.76 \pm 0.27$	$0.72 \pm 0.05$	0.95
$A_2$	$0.13 \pm 0.07$	$0.32 \pm 0.11$	2.46
$A_3$	$0.21 \pm 0.09$	$0.28 \pm 0.10$	1.33

**Reference** [1] M. Ohtsu *et al.*, *IEEE J. Select. Top. Quant. Electron.*, **2008**, *14*, 1404. [2] K. Mukai *et al.*, *J. Phys. Chem. B*, **1999**, *103*, 1. [3] T. Yatsui *et al.*, *Appl. Phys. Lett.*, in press. [4] Y. Liu *et al.*, *Nanotechnology*, **2011**, *22*, 215605. [5] L. Zhang *et al.*, *Appl. Mat. Inter.*, **2010**, *2*, 1769. [6] N. Sakakura and Y. Masumoto, *Phys. Rev. B* **1997**, *56*, 4051



**Takashi Yatsui** was born in Tokyo, Japan, on January 21, 1972. He received his B.E. degree from Keio University, Tokyo, Japan in 1995 and M.E. and D.E. degrees from Tokyo Institute of Technology, Tokyo, Japan in 1997 and 2000, respectively.

From 1999 to 2000, he was a Research Fellow of the Japan Society for the Promotion of Science. From 2000 to 2008, he was a Researcher at the Japan Science and Technology Agency, Tokyo. In 2008, he joined the University of Tokyo as an Associate Professor. His current research interests include nanofabrication using optical near-field and its application to

nanophotonics.

Dr. Yatsui received the Excellent Research Presentation award from the Japan Society of Applied Physics in 2000, Tejima Doctoral Dissertation Award from the Tejima Foundation in 2001, the Gottfried Wagener Prize 2010, and Osaka University Kondo Prize 2012.

# Highly efficient Si homojunction infrared LED based on the dressed photon-assisted process

Tadashi Kawazoe<sup>1,2</sup> and Ohtsu Motoichi<sup>1,2</sup>

<sup>1</sup>Department of Electrical Engineering and Information Systems, Graduate School of Engineering, The University of Tokyo, 2-11-16 Yayoi, Bunkyo-ku, Tokyo 113-8656, Japan

<sup>2</sup>Nanophotonic Research Center, Graduate School of Engineering, The University of Tokyo, 2-11-16 Yayoi, Bunkyo-ku, Tokyo 113-8656, Japan

Email: [kawazoe@ee.t.u-tokyo.ac.jp](mailto:kawazoe@ee.t.u-tokyo.ac.jp)

We fabricated a highly efficient light emitting diode (LED) driven by an optical near field, *i.e.*, a dressed photon, generated at the inhomogeneous domain boundary of a dopant in a homojunction bulk Si crystal[1]. To fabricate this device, a forward current was made to flow through a Si p-n junction to anneal it. During this process, the device was irradiated with near-infrared light, producing stimulated-emission light using a two-step dressed photon-assisted process triggered by the optical near field, and the annealing rate was controlled in a self-organized manner. The device emitted light in a wide photon energy region of 0.73–1.24 eV (wavelength 1.00–1.70  $\mu\text{m}$ ). The total power of the emitted light with 11 W of electrical input power was as high as 1.1 W. The external power conversion efficiency of the emitted light was 1.3%, the differential external power conversion efficiency was 5.0%, the external quantum efficiency was 15%, and the differential external quantum efficiency was 40%. The dependency of the emitted light power density on the injected current density clearly showed a characteristic reflecting the two-step phonon-assisted transition process.

We also propose an optical and electrical relaxation oscillator [2] making use of an S-shaped negative resistance characteristic of an above-mentioned Si-LED. The synchronous oscillation between optical and electric pulses was confirmed by experimental measurements.

The amplitude of the output voltage was 50 V<sub>p-p</sub>, the optical pulse energy was 44 nJ, and the maximum oscillation frequency was 34 kHz. For device simulations, the measured value of the spontaneous emission lifetime of a Si wafer was 900 ps, which was as short as that of direct transition-type semiconductors.

A novel photodetector using a homojunction bulk Si crystal [3] was also realized by controlling the dressed photon-assisted annealing. The photosensitivity of this device for incident light having a wavelength of 1.16  $\mu\text{m}$  or greater was about three-times higher than that of a reference Si-PIN photodiode. The photosensitivity was increased for incident light with a wavelength of 1.32  $\mu\text{m}$  by applying a forward current. When the forward current density was 9 A/cm<sup>2</sup>, a photosensitivity of 0.10 A/W was achieved. This value is at least 4000-times higher than the zero-bias photosensitivity. This remarkable increase was due to the manifestation of optical amplification cause by the forward current injection. For a forward current density of 9 A/cm<sup>2</sup>, the small-signal gain coefficient of the optical amplification was  $2.2 \cdot 10^{-2}$ , and the saturation power was  $7.1 \cdot 10^2$  mW.

The optical amplification of the homojunction bulk Si crystal processed by the dressed photon-assisted annealing can realize Si laser device. The fabricated Si lasers were showing continuous-wave oscillation at room temperature. Their optical resonators were formed of ridge waveguides with a width of 10  $\mu\text{m}$  and a thickness of 2  $\mu\text{m}$ , with two cleaved facets, and the resonator lengths were 250–1000  $\mu\text{m}$ . The oscillation threshold currents of these Si lasers were 50–60 mA. From near-field and far-field images of the optical radiation pattern, we observed the high directivity which is characteristic of a laser beam. Typical values of the threshold current density for laser oscillation, the ratio of powers in the TE polarization and TM polarization during oscillation, the optical output power at a current of 60 mA, and the external differential quantum efficiency were 1.1–2.0  $\text{kA/cm}^2$ , 8:1, 50  $\mu\text{W}$ , and 1%, respectively.

In the presentation, electroluminescences of other homojunction bulk materials, *e.g.*, ZnO [5], fabricated by the dressed photon-assisted annealing are also reviewed.

## References

- [1] T. Kawazoe, M. A. Mueed, and M. Ohtsu, Appl. Phys. B 104, 747 (2011).
- [2] N. Wada, T. Kawazoe, and M. Ohtsu, Appl. Phys. B in press (2012).
- [3] H. Tanaka, T. Kawazoe, and M. Ohtsu, Appl. Phys. B in press (2012).
- [4] T. Kawazoe, M. Ohtsu, K. Akahane, and N. Yamamoto, Appl. Phys. B in press (2012).
- [5] K. Kitamura, T. Kawazoe, M. Ohtsu, Appl. Phys. B, doi:10.1007/s00340-012-4991-z (2012).



**Tadashi Kawazoe** received M.E. and Ph.D. degrees in physics from University of Tsukuba, Tsukuba, Japan, in 1993 and 1996, respectively. He has studied optical nonlinearities in quantum dots at the Institute of Physics, University of Tsukuba. In 1996, he joined the faculty of Engineering, Yamagata University, Japan, as a research associate, engaged in research on nonlinear optical materials and devices. In 2000, he moved to Japan Science and Technology Agency, Japan.

Since 2000, He has studied optical devices and fabrication based on an optical near-field interaction. In 2007, he joined the University of Tokyo as a projected associated professor. From 2010, he has been a projected researcher at the department of electrical engineering and information systems, graduate school of engineering, The University of Tokyo. His current research interests are in the nanophotonic device.

Dr. Kawazoe is a member of the Japan Society of Applied Physics and the Physical Society of Japan.

# Dynamic properties of optical near-field signal transfer in random array of quantum dots

Wataru Nomura<sup>1,2</sup>, Takashi Yatsui<sup>1,2</sup>, Tadashi Kawazoe<sup>1,2</sup>, Makoto Naruse<sup>3</sup> and Motoichi Ohtsu<sup>1,2</sup>

<sup>1)</sup> School of Engineering, The University of Tokyo

Eng. 9-219, 2-11-16 Yayoi, Bunkyo-ku, Tokyo 113-8656, Japan

<sup>2)</sup> Nanophotonic Research Center, The University of Tokyo

Eng. 9-219, 2-11-16 Yayoi, Bunkyo-ku, Tokyo 113-8656, Japan

<sup>3)</sup> National Institute of Information and Communications Technology, 4-2-1 Nukui-kita, Koganei, Tokyo, Japan 184-8795

Email: nomura@nanophotonics.t.u-tokyo.ac.jp

As optical signal wiring for nanophotonic devices [1], we have proposed and developed an optical near-field signal transfer system based on a randomly distributed quantum dot (QD) array. An optical signal is transferred as an optical excitation between neighboring QDs via an optical near-field coupling. In previous work, we have already confirmed the optical excitation transfer efficiency and destination selectivity owing to resonant energy levels [2,3]. In this report, we demonstrate the basic dynamic properties of optical near-field signal transfer in randomly distributed QDs.

Two types of resonant CdSe/ZnS core-shell QDs, called QD1 and QD2, were used for the experiments. Since the diameter of QD2 is about 1.43 times larger than that of QD1, the optical excitation transfers from QD1 to QD2 unidirectionally via an optical near-field interaction [4]. The QDs were dispersed on a SiO<sub>2</sub> substrate, as shown in Fig. 1. QD2s were randomly dispersed in a circular region with 2 μm diameter inside a film of widely dispersed QD1s. Samples A, B and C were prepared with different thicknesses,  $H$ , of the QD1 film:  $H_A = 10$  nm,  $H_B = 25$  nm, and  $H_C = 70$  nm, respectively. We evaluated the time evolution of the emission from QD2 while exciting QD1 located a distance  $L$  away from QD2 using time-correlated single photon counting and a Ti:sapphire laser with a wavelength of 360 nm, a pulse frequency of 80 MHz, and a pulse duration of 2 ps. The acquired time-evolved emission curves were approximated using an integration of a Gaussian function and a single exponential decay. We obtained the emission peak time,  $t_p$ , from the approximation curve for each distance  $L$  (Fig. 2) and found that  $t_p$  increased linearly with increasing  $L$ . Finally, the group velocities,  $v_g$ , of optical signal in samples A to C were estimated from the gradient of  $t_p$  and were found to be  $v_{gA} = 1.2 \times 10^5$  m/s,  $v_{gB} = 1.7 \times 10^5$  m/s, and  $v_{gC} = 3.2 \times 10^5$  m/s, respectively. As shown in Fig. 3,  $v_g$  monotonically increases with increasing  $H$ . This trend agrees with the previously measured energy transfer efficiency of randomly distributed QDs.

## Reference

[1] M. Ohtsu, T. Kawazoe, T. Yatsui, and M. Naruse, IEEE J. Sel. Top. Quantum Electron. **14**, 1404 (2008)

- [2] W. Nomura, T. Yatsui, T. Kawazoe, M. Naruse, and M. Ohtsu, *Appl. Phys. B* **100**, 181 (2010)  
 [3] W. Nomura, T. Yatsui, T. Kawazoe, E. Runge, and C. Lienau, and M. Ohtsu, *Appl. Phys. B* **107**, 257 (2012)  
 [4] N. Sakakura, Y. Masumoto, *Phys. Rev. B* **56**, 4051 (1997)

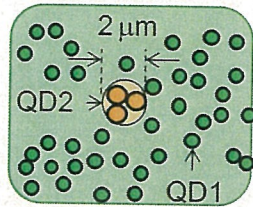


Fig.1 Schematic image of fabricated samples.

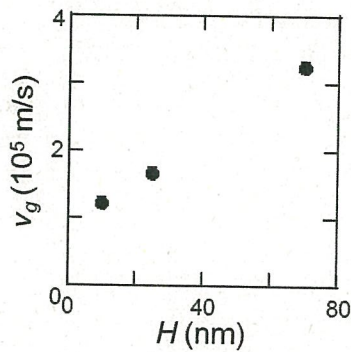


Fig.3 Group velocity  $v_g$  versus height of QD1 film  $H$ .

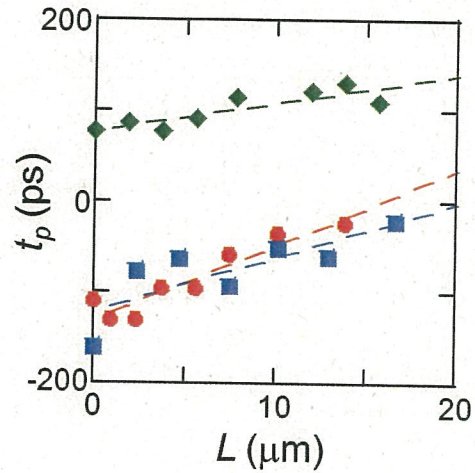


Fig.2 Emission peak time  $t_p$  versus the signal transfer length  $L$ . Red circles, blue squares and green diamonds represent  $t_p$  of samples A, B and C, respectively. Dashed lines represent linear approximations.



**Wataru Nomura**

Project Researcher, Department of Electrical Engineering and Information Systems and Nanophotonics Research Center, Graduate School of Engineering, The University of Tokyo

He received the B.E. and M.E. degrees from Tokyo Institute of Technology in 2002 and 2004, respectively, and the Dr. Eng. degree from The University of Tokyo in 2007. Since 2007, he has been a Project Assistant Professor at the University of Tokyo. He received the JSAP Incentive

Award for Excellent Presentation from the Japan Society of Applied Physics in 2009 and the 6<sup>th</sup> Optics & Photonics Japan Best Presentation Award in 2010.

and explain the origin of dipolar and octupolar contribution to this optical response.

[+](#) add to my program

[↗](#) (close full abstract)

16:15

### **Aluminum for Nonlinear Plasmonics: Resonance-driven Polarized Luminescence of Al, Ag, and Au Nanoantennas.**

**Authors :** Marta Castro-Lopez, Daan Brinks, Riccardo Sapienza, Niek van Hulst

**Affiliations :** ICFO – The Institute of Photonic Sciences, Castelldefels, Barcelona, Spain; ICREA - Inst. Catalana de Recerca i Estudis Avancats, Barcelona, Spain.

**Resume :** Resonant optical antennas are ideal for nanoscale nonlinear optical interactions due to their inherent strong local field enhancement. Indeed second- and third-order nonlinear response of gold nanoparticles has been reported. Here we compare the on- and off-resonance properties of aluminum, silver, and gold nanoantennas, by measuring two-photon photoluminescence (TPPL). Remarkably, aluminum shows 2 orders of magnitude higher luminescence efficiency than silver or gold. Moreover, in striking contrast to gold, the aluminum emission largely preserves the linear incident polarization. We show the systematic resonance control of two-photon excitation and luminescence polarization by tuning the antenna width and length independently. Finally, we analyze this tuning of the polarization with the rod dimensions by measuring the angular emission of TPPL via back focal plane imaging. Our findings point to aluminum as a promising metal for nonlinear plasmonics.

4 2

[+](#) add to my program

[↗](#) (close full abstract)

16:45

### **Evaluation of a dipole-forbidden energy state in ZnO quantum dots induced by the optical near-field interaction**

**Authors :** T. Yatsui, M. Tsuji, Y. Liu, T. Kawazoe, and M. Ohtsu

**Affiliations :** School of Engineering, the University of Tokyo, Japan

**Resume :** To reduce the size of photonic devices, we have proposed nanophotonic devices using semiconductor quantum dots (QDs), in which the dipole-forbidden energy-transition can reduce the size of device beyond the diffraction limit of light and achieve the unidirectional energy transfer. The dipole-forbidden energy transition originates from an exchange of the virtual photons between the resonant energy states, and therefore, the use of virtual photons activates dipole-forbidden energy state. Although emission from the dipole-forbidden energy state cannot be detected in the far field, it can be utilized when the nanoparticle and detector are in close proximity. ZnO QDs with the average diameter of 4 nm were synthesized using sol-gel method. To observe the changes between far- (probe-to-sample distance  $D$  of 6,000 nm) and near-field ( $D$  of 5 nm) spectra, we considered the quantized energy levels in ZnO QDs. Here, the QD shape was assumed to be spherical, and the quantized energy levels were calculated as 3.423 eV (E1, dipole-active state) and 3.4780 eV (E2, dipole-forbidden state), respectively. Using these energy values, we fitted the PL spectra using Lorentzian functions. The peak intensity of E2 increased drastically as probe-to-sample distance  $D$  decreased, whereas the peak intensity of E1 remained constant, indicating that the dipole-forbidden energy state was activated by the near-field interaction induced by a fiber probe.

5 0

[+](#) add to my program

[↗](#) (close full abstract)

16:45

### **Metal-Enhanced Fluorescence (MEF): Developing a Unified Fluorophore Plasmon Model**

**Authors :** Jan O. Karolin, Anatoliy I. Dragan and Chris D. Geddes\*

**Affiliations :** Institute of Fluorescence, University of Maryland Baltimore County, Columbus Center, 701 East Pratt Street, Baltimore, MD, 21202 USA. E-mail: geddes@umbc.edu

**Resume :** In recent years the IoF has described in over 150 peer-reviewed publications the favorable interactions and outcomes of both plasmon supporting particles (Ag, Au, Cu, Zn, Ni, Cr) and substrates with electronically excited states. These favorable effects have included significantly enhanced fluorescence emission from singlet states, S1 and S2 (MEF), as well as enhanced phosphorescence yields from triplet, T1, states (MEP). In addition, we have observed and described plasmon enhanced chemiluminescence intensities (MEC), as well as highly directional surface plasmon coupled Fluorescence (SPCF). As a result of enhanced triplet yields, we have also observed both enhanced singlet oxygen and superoxide anion yields. Our current thinking, describes Metal-Enhanced Fluorescence (MEF) as the near-field coupling of electronic excited states to surface plasmons (a surface mirror dipole), the particle, subsequently radiating the photophysical characteristics of the coupled excited state quanta. In this poster, we

0



accepted that multi-bandgaps are hardly obtained by conventional method involving self-assembly and interference lithography due to the complex process and equipment. In this work, we demonstrate a parallel and scalable method for hierarchical tuning of photonic bandgaps in azopolymer-based inverse opals. Photo-induced movement of azopolymer by directional photofluidization can control the final size and morphology of structure precisely. Therefore, the implementation of hierarchically patterned structures enables the preparation of photonic crystals having multi-bandgaps in a chip.

[+ add to my program](#)

[\(close full abstract\)](#)

16:45

### **Smart Golden NanoCapsules for Controlled Release with Near-Infrared Light**

**Authors :** Mustafa Selman Yavuz\* and Younan Xia

**Affiliations :** Mustafa Selman Yavuz Metallurgy and Materials Science Engineering and Advanced Technology Research and Application Center, Selcuk University, Konya 42075, Turkey. Younan Xia Department of Chemistry & Biochemistry Georgia Institute of Technology, Atlanta,30332 USA

**Resume :** The therapeutic and diagnostic (theragnostic) tools have enhanced over the last few decades, however, spatially and temporally controlled approaches remained as an obstacle. The near-infrared (NIR) radiation is known to have deep tissue penetration with minimum absorption. This outstanding property of NIR, with the aid of strong NIR absorbers, can be utilized to trigger a mechanism in cells for theragnostic purposes. Among other metal nanoparticles that have been extensively studied for such purposes, gold nanoparticles, such as gold nanocages (AuNCs), emerge as ideal tools for these applications since they possess optical tunability, easy functionalization, inertness, non-toxic behavior, accumulation in tissues, and intense absorption of NIR light. During the NIR absorption process, the absorbed energy by AuNCs is transferred into thermal energy that consequently heats the surroundings. Therefore, AuNCs have been employed to destroy the tumor cells in photothermal cancer therapy applications. Furthermore, the surface and pores of AuNCs were covered with a smart polymer to form a hybrid structure, and then the pre-loaded effectors (cancer drug, polymeric dye and enzymes) were successfully released with high spatial and temporal resolutions from AuNCs by controlling with a pulsed NIR laser.

5 3

[+ add to my program](#)

[\(close full abstract\)](#)

16:45

### **Electronic and optical properties of diluted magnetic semiconductors doped cobalt**

**Authors :** Ahmed Neffati\*, Hajer Souissi, Souha Kammoun

**Affiliations :** Université de Sfax, Laboratoire de Physique Appliquée, Groupe de Physique des Matériaux Luminescents, Département de Physique, Faculté des Sciences de Sfax, B.P. 802, 3018 Sfax, Tunisie.

**Resume :** Recently, cobalt doped III-V and II-VI semiconductors attract the greatest interest in electronic, optoelectronic, and electromechanical nanodevices [1-12]. Ligand-field electronic absorption and magnetic circular dichroism (MCD) spectra confirm homogeneous substitutional speciation of Co<sup>2+</sup> in the ZnSe, ZnO and ZnS QDs. In this work, we present a theoretical study of the electronic energy levels of cobalt doped in these semiconductors with a detailed crystal-field analysis based on the Racah theory; we perform a quantum confinement and effects on the linear Zeeman splitting of the electron quantum size energy levels in spherical semiconductor nanocrystals [13-18]. We calculate the size dependence of the electron effective g-values in bare ZnSe, ZnO and ZnS using Kane model. Keywords: Quantum Dots (QDs) ; g-factor; Zeeman effect; Quantum confinement, Crystal field theory.

5 4

[+ add to my program](#)

[\(close full abstract\)](#)

16:45

### **Controlling the size of ZnO quantum dots via dressed photon-phonon states**

**Authors :** Y. Liu, T. Yatsui, and M. Ohtsu

**Affiliations :** Department of Electrical Engineering and Information Systems, the University of Tokyo

**Resume :** Recently, ZnO quantum dot (QD)-based techniques have been actively studied for producing nanometer-sized photonic devices (nanophotonic devices). To realize high-performance devices, reducing the ZnO QD size variance is necessary to resonate the discrete exciton energy levels in ZnO QDs. However, in conventional sol-gel synthesis of ZnO QDs, the QD size distribution is large, and the size variance is greater than 20%. To lessen the size variance, one must decrease the size of QDs that are larger than the peak diameter and increase the size of QDs that are smaller

5 5

than the peak diameter. In previous studies, we demonstrated the feasibility of reducing the size of large ZnO QDs through irradiation with He–Cd laser light, which has a wavelength that is longer than the absorption band-edge of ZnO (380 nm). In the present study, we irradiated ZnO QDs with 671-nm laser light during growth to increase the size of small QDs. Although the irradiating light was not absorbed by the QDs, the dressed photon (DP) around the QDs became excited. Furthermore, DP could couple with multiple phonon modes in ZnO precursors to generate a dressed photon–phonon (DPP) state. Thus, when the ZnO precursors were in close proximity to the QDs, the DPP accelerated ZnO deposition onto QDs. We successfully increased the ZnO QD size by more than 10% with 500-mW irradiation, as determined by the absorption band edge of the QDs. A greater increase in the QD size is expected by increasing the irradiation power.

[+ add to my program](#)

[\(close full abstract\)](#)

16:45

### Calculation of Current Density on Crystalline Silicon Solar Cell with RP-Textured and Double Layer Anti Reflection Coated Surface

**Authors :** Yongwoo Lee<sup>1</sup>, Kyu-Min Him<sup>1,2</sup>, Mi-ju Park<sup>1</sup>, Hi-deok Lee<sup>2</sup>, Jin-su yoo<sup>3</sup>

**Affiliations :** 1DMS CO., LTD 2 Dept. of Electronic Eng, Chungnam National University 3Korea Institute of Energy Research

**Resume :** In this study, double layer anti reflection coating (DLARC) which is popular fabrication technique for high efficiency solar cell will be demonstrated using simulation and short circuit current density (Jsc) calculation. Fabrication of double layer is industrial friendly as well as highly effective on most of silicon based solar cell. However, throughout most studies of DLARC, accurate calculation was difficult to find since there was several obstacles. Which includes calculation of reflectance on textured surface and other than the fact that intensity of light is different on each wavelength. Weight depending on intensity of sun light needs to be considered. Since simulation of reflectance is accurate only with polished surface, reflectance on polished surface was effectively translated into that of textured surface and compared with actual reflectance data under 5% difference. With accurate calculation of reflectance on textured surface, sunlight of AM 1.5 was adapted for Jsc calculation. Double layer ARC was consisted with SiNx on silicon substrate and SiOx as top layer. refractive index was fixed to 2.05 and 1.46 while thickness of both layers were varied from 0 to 150 nm. Achievable current density was 42.87 mA/cm<sup>2</sup> and optimized DLARC get its peak of 42.8 mA/cm<sup>2</sup> at SiNx of 60~80 nm and SiOx of 80~100 nm. Calculation of this method will be easily and widely adapted on most structures of silicon based solar cell using different material with different refractive index.

5 6

[+ add to my program](#)

[\(close full abstract\)](#)

16:45

### Refractometric Sensing with Silicon Quantum Dots Coupled to a Microsphere

**Authors :** Y. Zhi, C.P.K. Manchee, J.W. Silverstone, A. Meldrum

**Affiliations :** Department of Physics, University of Alberta, Edmonton, AB, Canada

**Resume :** Quantum dots (QDs) coupled to an optical microsphere can be used as fluorescent refractometric sensors. The QD emission couples to the whispering gallery mode resonances of the microsphere, leading to sharp, periodic maxima in the fluorescence spectrum. Silicon QDs are especially attractive because of their negligible toxicity and ease of handling. In this work, a thin layer of silicon QDs was coated onto the surface of a microsphere made by melting the end of a tapered glass fiber. Refractometric sensing experiments were conducted using two methods. First, the sphere was immersed directly into a cuvette containing either sucrose or methanol-water mixtures. Second, the sphere was inserted into a glass capillary and the analyte was pumped through the channel. The latter method enables true microfluidic operation, which is otherwise difficult to achieve with a microsphere. In both geometries, high-visibility ( $V=0.57$ ) modes were observed with Q factors up to 1700. The WGM resonances shifted as a function of the refractive index (RI) of the analyte solution, giving sensitivities ranging from 30 – 50 nm per RI unit (RIU) for different microspheres and a detection limit of 0.002 RIU. The coated microsphere structures were simulated using finite difference time domain methods as well as by solving for the roots of the characteristic equations describing layered microsphere, showing that the device sensitivity could be improved to as 80 nm/RIU, depending on the QD film thickness.

5 7

[+ add to my program](#)

[\(close full abstract\)](#)

16:45

### Optimizing the structure of the photonic crystal fibers by using genetic algorithm

5 8

9:00 AM – 9:30 AM

**A51: Nanophotonic device utilizing a dipole-forbidden energy state****Takashi Yatsui<sup>1</sup>** and Motoichi Ohtsu<sup>1</sup><sup>1</sup> School of Engineering, University of Tokyo, Bunkyo-ku, Tokyo, Japan

To reduce the size of photonic devices below the diffraction limit, we have proposed nanophotonic devices [1] that consist of semiconductor quantum dots (QDs). In a nanophotonic device, the dipole-forbidden energy-transition [2] can reduce the size of device beyond the diffraction limit of light and achieve the unidirectional energy transfer, which is unattainable in conventional photonic devices. The dipole-forbidden energy transition originates from an exchange of the virtual photons between the resonant energy states. The use of virtual photons activates dipole-forbidden energy state. Although emission from the dipole-forbidden energy state cannot be detected in the far field, it can be utilized when the nanoparticle and detector are in close proximity. Here, we report direct observation of emission from an optically forbidden level in ZnO QDs using the near-field interaction induced by a fiber probe.

ZnO colloidal QD was synthesized using sol-gel method [3]. The average diameter of fabricated ZnO QD was 4 nm. The synthesized ZnO QDs were dispersed uniformly over a sapphire substrate. The red open circles in Fig. 1A and the blue open circles in Fig. 1B represent the far-field and near-field spectra which were obtained with the probe-to-sample distance of 6  $\mu\text{m}$  and 5 nm, respectively.

To observe the changes between far- and near-field spectra, we considered the quantized energy levels in ZnO QDs. QDs synthesized by the sol-gel method are known to be spherical, although the crystalline structure of ZnO QDs is wurtzite [4]. In the present study, the QD shape was assumed to be spherical with radius  $R$ , and the quantized energy levels were calculated as 3.423 eV ( $E_1$ , dipole-active state), 3.4780 eV ( $E_2$ , dipole-forbidden state), and 3.551 eV ( $E_3$ , dipole-active state), respectively [5]. Using these energy values, we fitted the PL spectra using Lorentzian functions, shown as solid red, blue, and green lines, respectively, in Figs. 1A and 1B. The fitted profiles were used to determine near/far ratios, i.e., the ratio between the peak intensities of each near/far spectrum (Table 1). The peak intensity of  $E_2$  increased drastically as the fiber probe approached the ZnO QDs, whereas the peak intensity of  $E_1$  remained constant. The increase in the peak intensity of  $E_3$  was due to the higher excitation photon energy of 3.81 eV.

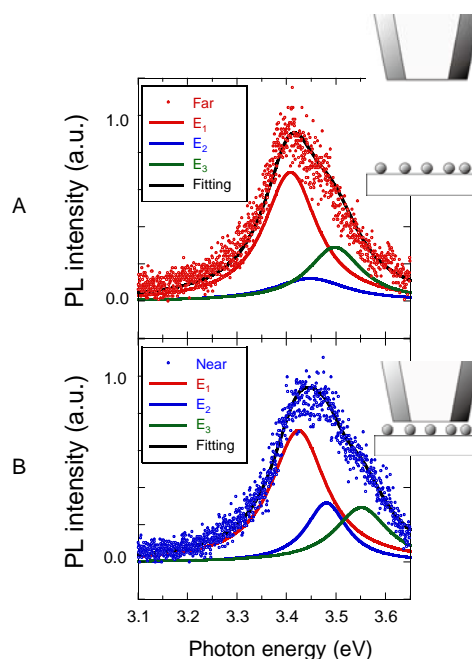


**Figure 1** : Far-field (A, red open circles) and near-field (B, PL spectra of ZnO QDs). The respective separation between the fiber and ZnO QD was (a) 1  $\mu\text{m}$  and (b) 5 nm, respectively.

**Table 1** : The ratio between near-field and far-field intensity.

	Far (Fig. 1A)	Near (Fig. 1B)	Near/Far ratio
$E_1$	0.78	0.72	0.92
$E_2$	0.12	0.31	2.58
$E_3$	0.18	0.29	1.61

In conclusion, we achieved direct observation of emission from an optically forbidden level in ZnO QDs. By introducing a near-field fiber probe in close proximity to the QDs, we observed increased emission intensity from the dipole-forbidden. Because the decay time of the dipole-forbidden state is longer than that of the dipole-active state by  $10^6$ , the dipole-forbidden state can be used to realize novel devices such as optical buffer memory, and signal-transmission devices.

### References

- [1] M. Ohtsu et al., IEEE J. Select. Top. Quant. Electron., **14**, 1404 (2008).
- [2] K. Mukai et al., J. Phys. Chem. B, **103**, 1 (1999).
- [3] Y. Liu et al., Nanotechnology, **22**, 215605 (2011).
- [4] L. Zhang et al., Appl. Mat. Inter., **2**, 1769 (2010).
- [5] N. Sakakura and Y. Masumoto, Phys. Rev. B, **56**, 4051 (1997).

# Alternative Smoothing Techniques to Mitigate EUV Substrate Defectivity

R. Teki<sup>1\*</sup>, A. John Kadaksham<sup>1</sup>, M. House<sup>1</sup>, J. Harris-Jones<sup>1</sup>, A. Ma<sup>1</sup>, S. V. Babu<sup>2</sup>, A. Hariprasad<sup>2</sup>, P. Dumas<sup>3</sup>, R. Jenkins<sup>3</sup>, J. Provine<sup>4</sup>, A. Richmann<sup>5</sup>, J. Stowers<sup>6</sup>, S. Meyers<sup>6</sup>, U. Dietze<sup>7</sup>, T. Kusumoto<sup>8</sup>, T. Yatsui<sup>9</sup>, M. Ohtsu<sup>9</sup>, F. Goodwin<sup>1</sup>

<sup>1</sup> SEMATECH, Albany, New York, USA

<sup>2</sup> Clarkson University, Clarkson, New York, USA

<sup>3</sup> QED Technologies, Rochester, New York, USA

<sup>4</sup> Stanford University, Stanford, California, USA

<sup>5</sup> Fraunhofer Institute of Laser Technology, Aachen, Germany

<sup>6</sup> Inpria, Corvallis, Oregon, USA

<sup>7</sup> HamaTech, Sternenfels, Germany

<sup>8</sup> Itochu Corporation, Osaka, Japan

<sup>9</sup> Nano-photonics Engineering Organization, Tokyo, Japan

## ABSTRACT

The majority of extreme ultraviolet (EUV) lithography mask blank defects originate from chemical mechanical polishing (CMP) of the substrate. The fact that CMP has not yet been able to yield EUV substrates with low defect counts highlights the challenges of polishing doped fused silica surfaces. Here we investigate alternative techniques based on processing either the substrate or coatings of amorphous silicon thin films and inorganic metal oxides. In particular, we evaluate a novel polymer-based non-abrasive a-Si CMP process, a photo-induced dry etching of substrate protrusions, a smoothing coat of spin-on or capillary coated Inpria resist solution, CO<sub>2</sub> laser polishing of the substrate surface, and annealing an a-Si thin film surface in reduced atmospheres. Although CMP still remains the best process with respect to overall process integration, these techniques have the potential to support CMP in solving the substrate defectivity issue and help pave the way to commercializing EUV mask blanks.

**Keywords:** EUV, defectivity, CMP, a-Si thin film, Inpria coating, fused silica, doped fused silica, smoothing

## 1. INTRODUCTION

The defectivity of EUV mask blanks poses one of the main obstacles in the realization of EUV lithography<sup>[1]</sup>. The majority (>80%) of defects—mostly pits and scratches, with some embedded particles—are on the substrate, all of which originate from CMP and cleaning<sup>[2]</sup>. Over the past few years, mask suppliers have been able to gradually reduce CMP-induced substrate defectivity, but the defect numbers are still too high<sup>[3]</sup>. Note that numerous defects do not show up during substrate inspection (at 40 nm SiO<sub>2</sub> detection sensitivity), but are detected only after they are decorated by multilayer (ML) deposition. Printability simulations have shown that pit/bump defects need to be less than 1 nm deep/high to be unprintable<sup>[4]</sup>. The fact that CMP has not yet been able to yield EUV substrates with low substrate defect counts highlights the challenges of polishing quartz (Qz) which is undoped fused silica and low thermal expansion material (LTEM) or ultra-low expansion (ULE) glass which are both titania doped fused silica substrates. Cleaning the substrates to remove particles simply adds to the pit defect count, primarily as a result of the physical impact of megasonic-induced cavitation on the substrate surface<sup>[5]</sup>. Hence to mitigate substrate defects, there is an urgent need to investigate alternative techniques that can help solve the EUV substrate defectivity issue. We looked at some options based on processing either the substrates or coatings of vapor-deposited silicon films and inorganic metal oxides from

---

\* [Ranganath.Teki@sematech.org](mailto:Ranganath.Teki@sematech.org) ; Phone: (518) 649-1058; Fax: (518) 619-1344

solution. These techniques have the potential to complement CMP find a route to obtain pit-, particle-, and scratch-free EUV substrates with a high enough yield to help pave the way to EUV mask blank commercialization.

## 2. CURRENT SUBSTRATES: QUALITY AND ISSUES

An analysis of ML deposited substrates at SEMATECH shows that blank defects larger than roughly 70 nm size are dominated by particles and ones smaller than 70 nm by pits and scratches. The defect ratio changes from 36% pits and scratches in the range of 100–150 nm to 90% pits and scratches in the range of 43–50 nm, indicating an exponential increase in defects arising from the substrate as defect size become smaller. Moreover most of these small pits and scratches do not show up during substrate inspection (at 40 nm SiO<sub>2</sub> sensitivity) but become visible after being enlarged by ML deposition. This makes it more difficult to screen substrates with high defectivity until after the ML deposition, which negatively affects the yield of good mask blanks.

	Average RMS roughness (nm)		ML Defectivity @ 50 nm (scaled)		Avg. increase in (pit+scratch) count after ML deposition @ 50 nm
	Substrate	ML blank	Scratches	Pits	
Qz A	0.10	0.16	1y	1z	8x
Qz B	0.07	0.13	1.3y	1.9z	10x

Table 1: Effect of surface roughness on mask blank defectivity for two Qz substrates.

The defectivity of substrates also seems to depend on the extent of polishing or the final surface roughness. The trend suggests that defectivity increases when the surface is polished to lower roughness levels. Table 1 shows that the ML deposition increases the surface root mean square (RMS) roughness by approximately 0.06 nm from the initial value. A blank with 0.13 nm RMS roughness has on average 30% more scratches and 90% more pits (at 50 nm SiO<sub>2</sub> sensitivity) than a blank with 0.16 nm RMS roughness. Although these ML blank roughness values are close to the roughness specification of 0.15 nm RMS given by SEMI for the exposure tool<sup>[6]</sup>, they are far from the roughness levels needed for inspection tools (see Table 2). The Lasertec inspection tools require about 0.05 nm RMS values for 33 nm SiO<sub>2</sub> sensitivity<sup>[7]</sup>; these specifications will be even more stringent for smaller defects. Also, the blank roughness needed to meet the line edge roughness (LER) targets for the 16- and 22-nm nodes according to the International Technology Roadmap for Semiconductors (ITRS) is also 0.05 nm RMS<sup>[8]</sup>. It can be expected that achieving these lower roughness levels will further increase substrate defectivity. So current substrate polishing methods seem unable to simultaneously obtain both the roughness and defectivity specifications for mask blanks, which is an impediment to commercializing EUV lithography.

	Roughness Specification	Notes
Exposure tool	≤ 0.15 nm RMS	$\lambda_{\text{spatial}} \leq 10 \mu\text{m}$
Inspection tool	≤ 0.05 nm RMS	For 33 nm sensitivity
LER target	≤ 0.05 nm RMS	For 22- and 16-nm nodes

Table 2: ML blank roughness levels required to meet exposure, inspection, and LER specifications

The defectivity levels shown in Table 1 are on undoped Qz substrates, and it is known that doping makes considerable changes not just to the coefficient of thermal expansion, but also to other material properties. We compared surface roughness and nano-indentation hardness values, measured using scanning probe microscopy, for doped and undoped substrates. For both suppliers, the doped (LTEM/ULE) substrates were slightly rougher and harder than the undoped (Qz) substrates. TiO<sub>2</sub> doping increases material hardness, which in turn makes it more difficult to polish the doped substrates to the same roughness levels as Qz. The doped substrates also have higher incoming defectivity (by 40%) in terms of pits and scratches. Since doping lowers the removal rate and because pits and scratches are continuously being created and etched away during CMP, more pits and scratches are left on the doped substrates. Also, Qz substrates being

softer are likely to deform and absorb some of the excess pad pressure and form fewer pits and scratches. Moreover, doped substrates are more susceptible to pit creation by megasonic cleaning (almost double that of Qz) because of the greater sub-surface damage<sup>[9]</sup> (SSD) induced on the harder material at the same CMP pressures. This implies that achieving a surface roughness of 0.05 nm RMS on LTEM/ULE substrates by CMP is going to be an even more difficult challenge than on Qz and hence, alternative techniques that can help come closer to both the roughness and defectivity requirements are urgently needed.

### 3. ALTERNATIVE TECHNIQUES: DISCUSSION AND RESULTS

More than 40 different techniques in the existing literature, some more mainstream than others, were examined for their capability to smooth defects,. Also prior work done at SEMAETCH on pit smoothing methodologies was revisited<sup>[10]</sup>. Since the surface finish and defectivity requirements for EUV mask blanks are far more aggressive than other current applications such as optical lenses or magnetic heads, most of the techniques did not qualify for EUV. We selected and classified the techniques based on materials that the semiconductor industry is already familiar with: current substrates, Si thin films, and Inpria inorganic resist coatings. Table 3 outlines the main categories, the materials, the technologies, and their advantages and disadvantages.

Category	Material	Strategy	Concept	Technology	Main Pros & Cons
Substrate based options	Qz/ ULE/ LTEM	Process improvement	Alternative polishing technique	MRF polishing	✓ No normal forces, only shear ✓ Less sub-surface damage X Final surface quality (roughness)
			Photo-induced dry etching	Dressed-photon nano-polishing	✓ Non-contact etching X Self-limiting process X Defectivity
		Mitigation and/or repair	Reflow substrate surface	CO <sub>2</sub> laser polishing	✓ Low surface damage X Narrow process window X Final surface quality (waviness)
Silicon based options	a-Si thin films	Process improvement	CMP without using slurry particles	Non-abrasive CMP of a-Si thin film	✓ No abrasive slurry particles ✓ Less likely to create pits/scratches X Cleaning of a-Si layer
		Mitigation and/or repair	Annealing induced migration	Annealing of a-Si thin films	✓ Low surface damage X Narrow process window X Final surface quality
Inorganic coating based options	Inpria smoothing layer	Mitigation and/or repair	Deposit inorganic coating to smooth over defects	Spin coating	✓ Potential to smooth pits X Defectivity
				Capillary coating	✓ Potential to smooth pits and particles X Defectivity
				Template smoothing	✓ Replication of defect map ✓ Champion plate can be template X Uniformity, defectivity

Table 3: Summary of the selected alternative techniques with their concept and advantages/disadvantages

To qualify these alternative techniques, we needed to first determine the parameters for our evaluation. Three main parameters were chosen: (i) surface roughness, (ii) defectivity, and (iii) defect smoothing power. Smoothing power gives a numerical estimation of how much a particular defect has been smoothed; it basically compares the defect aspect ratio

(AR) before and after the smoothing process. Upon smoothing, both pits and particles will show a decrease in depth or height and an increase in their full-width half maxima (FWHM). The AR of the defect is defined as its FWHM divided by its depth or height. The smoothing power (SP) is defined as the ratio of the defect's AR after and before smoothing. A SP of 1 therefore implies no smoothing, since the aspect ratio has remained unchanged; a SP of  $\infty$  implies perfect smoothing, since the depth or height of the defect has been reduced to 0. Hence the higher the SP, the more effective the technique is in making the defects shallower and wider, thus making them less likely to print<sup>[11]</sup>.

$$\text{Aspect ratio (A.R.)} = \frac{\text{full width half maximum}}{\text{depth or height}}$$

$$\text{Smoothing power (S.P.)} = \frac{(\text{Aspect ratio})_{\text{post}}}{(\text{Aspect ratio})_{\text{pre}}}$$

In the following section the principles behind the individual techniques and their evaluation results are discussed – starting with substrate-based techniques, followed by silicon-based and then inorganic coating-based techniques.

### 3.1 SUBSTRATE BASED TECHNIQUES

#### 3.1.1 Dressed-photon nanopolishing

Dressed-photon nanopolishing (DPNP) is a novel dry etching process that etches based on surface curvature<sup>[12]</sup>. In this technique,  $\text{Cl}_2$  gas is used as an etchant and a continuous wave (CW) laser ( $\lambda = 532 \text{ nm}$ ) is used as a light source to dissociate the  $\text{Cl}_2$ . Since its photon energy is lower than the absorption band edge energy of  $\text{Cl}_2$  ( $\lambda_{\text{abs}} = 400 \text{ nm}$ ), conventional photo-etching over the entire substrate (fused silica) surface is avoided. However, when the substrate surface has nanometer scale protrusions, depending on its roughness, a strong optical near-field is generated at the edge of the protrusion<sup>[13]</sup>. Since the optical near-field has a steep spatial gradient, a higher molecular vibrational state is excited in the  $\text{Cl}_2$  molecule by a non-adiabatic photochemical reaction<sup>[14]</sup>. As a result,  $\text{Cl}_2$  is selectively photo-dissociated only over these protrusions and the activated  $\text{Cl}^*$  radicals etch away the protrusions on the substrate. The advantage of this process is that it is self-limiting, since the etching will automatically stop when the surface becomes sufficiently flat so that the optical near-field disappears. This technique is also believed to work for pit-type defects, since the edge of the pit also appears as a surface protrusion to the etchant gas (Figure 1, left). This will tend to make the pits wide (flat) enough so that they are hopefully rendered unprintable.

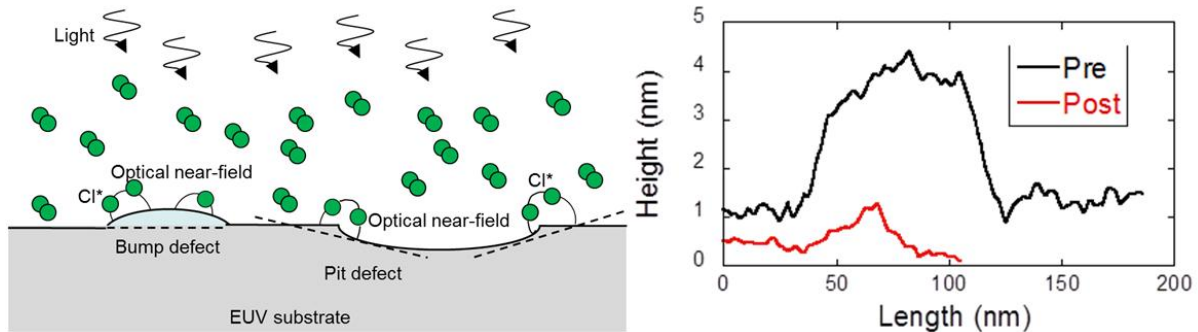


Figure 1: Schematic showing the principle of DPNP on substrate bumps and pits (left). AFM data showing that DPNP was able to etch a bump initially 4 nm high to < 1 nm on a LTEM substrate (right).

One of the first results of this technique is shown in Figure 1 on the right, where a 4 nm high bump on a LTEM substrate was etched to 0.9 nm. Moreover, the average surface roughness of the LTEM surface decreased from 0.067 nm to 0.052 nm. Further experiments are being conducted to evaluate the effect of DPNP on pit-type and other particle-type defects. This technique is particularly suitable to etch embedded or hard to remove particles caused by CMP on the substrate. Currently such particles can be removed only by aggressive cleaning, which also creates additional pits.



### 3.1.2 Magneto-rheological fluid (MRF) polishing

MRF polishing is based on a magnetically-sensitive “smart fluid” that changes viscosity in milliseconds when exposed to a magnetic field<sup>[15]</sup>. The MR fluid temporarily stiffens and conforms to the surface of the component being polished (Figure 2, right). This allows geometries of almost any shape to be polished easily and controllably. One of the advantages of MRF polishing is that the fluid is very stable and does not show wear like a traditional polishing tool; hence the first and last surfaces will be polished equally. Since the material removal rate does not change, the final output can be accurately predicted. Moreover, MRF can be numerically controlled with precision workstations and sophisticated computer algorithms to ensure that the polishing is deterministic and accurate<sup>[16]</sup>. This makes MRF particularly suited for achieving flatness specifications for EUV, and sub-50 nm peak-to-valley flatness has already been demonstrated on EUV substrates using MRF<sup>[17]</sup>. One distinct advantage MRF has over CMP is that the removal is based on a shearing mechanism and applies no normal load, thus eliminating any SSD to the material<sup>[18]</sup>.

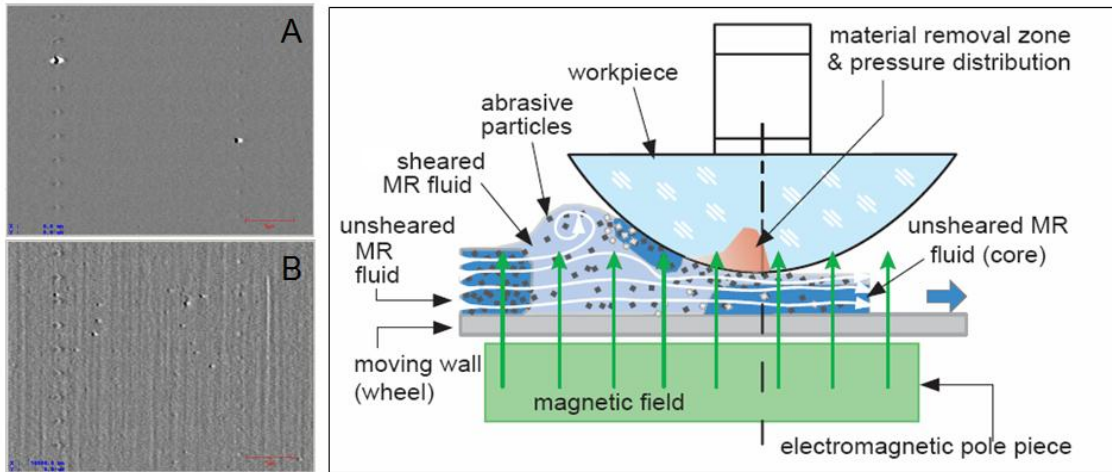


Figure 2: M1350 scans of (A) unpolished substrate and (B) MRF-polished substrate showing the characteristic grooves made by MRF polishing (left). Schematic showing the principle of MRF polishing (right, courtesy of QED Technologies).

One Qz and one LTEM substrate were sent to QED Technologies, where different MRF polishing conditions were used on the substrates. MRF-polished plates were found to be inspectable on the Lasertec M1350 tool (a multi-beam 488 nm wavelength laser confocal mask inspection system with a 70 nm SiO<sub>2</sub> sensitivity), although the characteristic grooves made by MRF polishing are clearly visible (Figure 2, left image B) as compared to a unpolished surface (Figure 2, left image A). A final CMP touching process would still be needed after MRF polishing to remove the grooves, but the advantage here is that the MRF polishing would remove the damaged layers from the previous polishing steps without creating additional SSD. Consequently, the subsequent CMP process would add fewer pits and scratches. Further work is underway to explore the potential of MRF polishing for achieving both roughness and flatness specifications.

### 3.1.3 CO<sub>2</sub> laser polishing

Laser polishing of glass by surface remelting is similar to conventional flame polishing, but since a laser can be controlled more precisely than a flame, laser polishing results in better surface qualities. Due to the high absorption coefficient, CW CO<sub>2</sub> lasers with a wavelength of  $\lambda = 10.6 \mu\text{m}$  are used<sup>[19]</sup>. The laser radiation is used to heat up the surface of the substrate, while making sure that evaporation is avoided, because otherwise material would be removed and a dent would be created. The temperature needs to be high enough to sufficiently reduce the viscosity of the glass to allow material to reflow from the peaks to the valleys. The most important process parameters are the interaction time and the intensity. The longer the interaction time and lower the intensity, the less roughness after laser polishing, but the longer the processing time<sup>[20]</sup>. Laser polishing has been shown to repair damaged fused silica optics by localized treatment<sup>[21]</sup>.

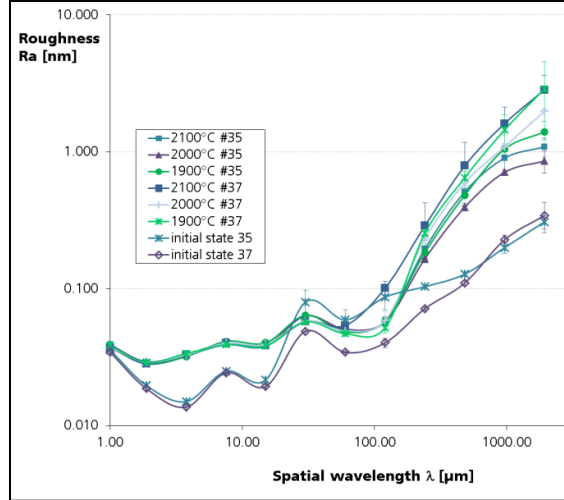


Figure 3: Average roughness with spatial wavelength for unprocessed and laser-processed Qz and LTEM substrates.

One Qz and one LTEM substrate were tested at Fraunhofer Institute for Laser Technology. The substrates were preheated to  $\sim 1000^{\circ}\text{C}$ , and then exposed to a  $\text{CO}_2$  laser to achieve temperatures of  $2100^{\circ}\text{C}$ ,  $2000^{\circ}\text{C}$ , and  $1900^{\circ}\text{C}$  in the interaction zone of the laser beam and the material, as measured by a pyrometer. It was found that the micro-roughness ( $\lambda_{\text{spatial}} < 100 \mu\text{m}$ ) was not affected, although the waviness ( $\lambda_{\text{spatial}} > 100 \mu\text{m}$ ) increased considerably (Figure 3). More experiments will be done with lower processing temperatures to determine whether the increase in waviness can be reduced to acceptable levels.

## 3.2 SILICON THIN FILM BASED TECHNIQUES

### 3.2.1 Non-abrasive CMP of a-Si thin films

Most pits and scratches on the substrate are believed to arise from the abrasive slurry particles used in CMP<sup>[22]</sup>. These particles get trapped between the surface irregularities of the polishing pad and the substrate and the excess local pressure causes them to dent or scratch the substrate. One way to remove the pits and scratches is to not use slurry particles. Currently, there is no CMP technique to polish silica substrates without slurry particles. Recently a non-abrasive CMP process for polishing poly-Si was developed at Clarkson University, which uses only a polymer to polish the material<sup>[23]</sup>. We decided to apply the same CMP process to polish a-Si thin films, which can be deposited on EUV substrates using the current ion-beam deposition (IBD) tools used to deposit the MoSi multilayers. The idea would be to clean the substrate of any particle-type defects, deposit a thin (i.e., 50-100 nm thick) a-Si film, and then CMP the a-Si layer down below the depth of the largest pit decorated from the substrate. The key is not creating any new pits and scratches in the polymeric CMP process. The post-CMP cleaning of the a-Si layers is similar to the current ML blank cleaning methodologies.

The mechanism of CMP removal is based on using a polymer such that the Si-Si bond is weaker than the bonds made by the polymer with the Si surface and with the polishing pad. In the process, polymer molecules bind to the a-Si surface and are pulled by the polishing pad with the help of a bridging attraction<sup>[24]</sup>. Among the average bond energies of silicon with several different atoms, the Si-Si bond is the weakest. Hence, the underlying Si-Si bonds are more easily broken than the binding between the polymer and the pad as well as the Si-N/Si-O bonds formed between the surface atoms of a-Si and the end atoms of polymer<sup>[25]</sup>. They are the first to rupture under the applied pressure and shear of the CMP process, removing a significant amount of a-Si (Figure 4, left).

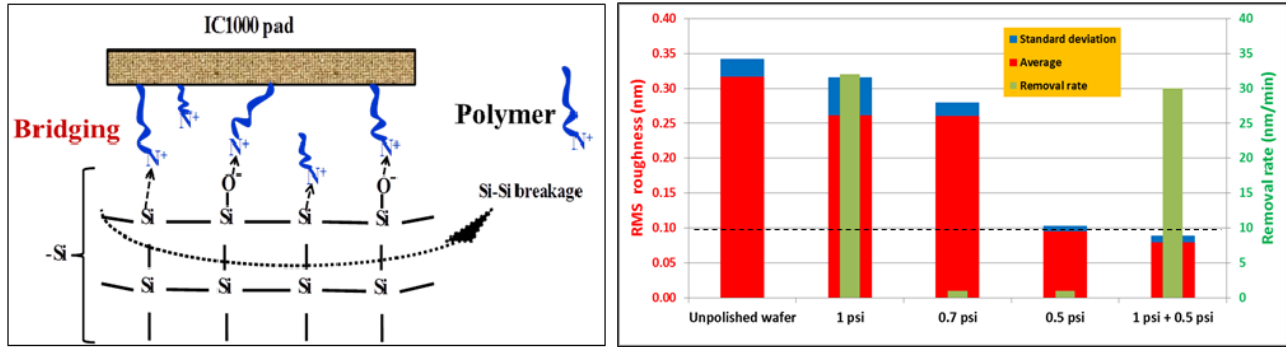


Figure 4: Schematic showing the removal mechanism of Si by polymer-based CMP (left). Chart showing final RMS roughness and corresponding removal rates for different polishing pad pressures (right).

All the initial experiments were done on 8" Si wafers coated with 1 μm thick a-Si thin film obtained from WRS Materials. The first challenge was to see whether the polymeric CMP could reach the surface roughness levels needed for EUV substrates. The polymer used was polyethylene-imine (PEI), and the following process parameters were varied: polishing pad (IC 1000, Politex), pad pressure (0.25 to 1.0 psi), rotation speed (15/15, 60/60 rpm), and polishing time (1–5 minutes). It was found that the final surface roughness depended most strongly on the pad pressure (Figure 4, right). Higher pad pressures produced greater surface roughness but also faster removal rates, while lower pressures produced a better surface finish but with slower removal rates. The optimal process was found to consist of initially polishing at 1 psi pressure to remove sufficient material thickness and then lowering the pressure to 0.5 psi to smooth the surface. Any lower pressure led to process instabilities. A surface roughness of sub-0.1 nm RMS was achieved using this process. The next step will be to transfer this CMP process to a-Si thin films coated on EUV substrates and evaluate the roughness and defectivity on the surface.

### 3.2.2 Annealing-induced Si migration

Silicon surface migration under suitable annealing conditions is known to lower the chemical potential associated with the curvature of a surface, which results in atomic level smoothing of surface asperities<sup>[26]</sup>. The surface roughness of polished Si(110) wafers was shown to reduce from ~0.21 down to ~0.05 nm RMS on high-temperature annealing in Ar atmospheres with H<sub>2</sub> as the cooling gas<sup>[27]</sup>. The migration rate depends exponentially on temperature, while the total amount of migration is related to the product of the annealing temperature and time. The idea is to deposit a thin a-Si thin film on EUV substrates using the current IBD tools used to deposit MoSi multilayers and then anneal the substrate to reflow the a-Si surface just enough to smooth out any bumps or pits on the surface.

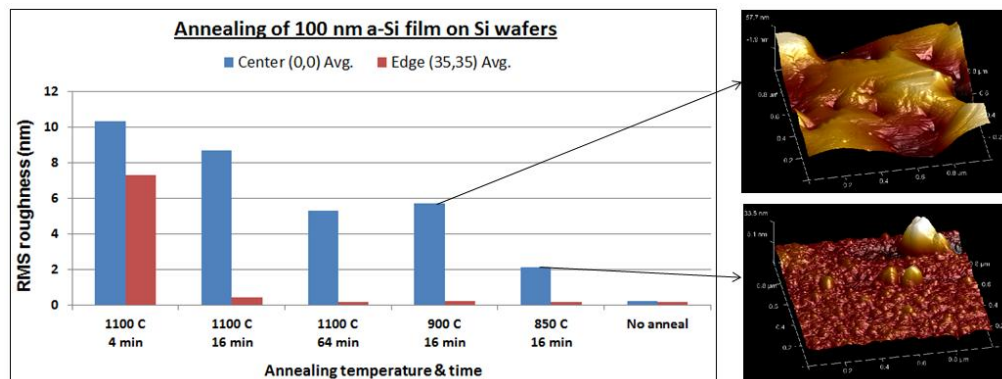


Figure 5: Chart showing RMS roughness values of annealed a-Si coated wafers for different temperatures and times.

This work was done in collaboration with researchers at Stanford University. Five 100 nm a-Si deposited 4” Si wafers obtained from Hionix were annealed at 1100 °C in 10 Torr of H<sub>2</sub> for times ranging from 4 to 64 minutes. The roughness before annealing ranged from 0.15–0.25 nm RMS. After annealing, the roughness increased significantly in the center of the wafer (~8 nm RMS) while it remained low at the edge, indicating that the a-Si thin film was flowing and accumulating in the center of the wafer (a sign that the annealing conditions were too aggressive). The wafers were then exposed to five different annealing temperatures between 850-1100 °C for 16 minutes each. The roughness post-annealing was still too high, but did come down to ~2 nm RMS for a temperature of 850 °C, as evidenced by the surface morphology (Figure 5). Further experiments are underway to test lower temperatures at which the roughness would not increase but any pits or bumps would still be smoothed.

### 3.3 INPRIA COATING BASED TECHNIQUES

Inpria inorganic metal oxide thin films can be coated from solution and form atomically dense and smooth films upon baking at a certain temperature<sup>[28]</sup>. They easily pass the vacuum outgassing tests and are used as resists for EUV lithography. Last year, 16 nm half pitch line and space patterns were demonstrated on these resists using EUV exposure<sup>[29]</sup>.

One known issue with the Inpria solutions is their high particle counts. Currently the solution particle levels (~45,000 spin coated over 132x132 mm<sup>2</sup>) are much higher than the particle levels of the de-ionized water used in cleaning. Initially the coating solution was prepared at concentrated levels and later diluted to achieve a suitable film thickness. Later, when the solution was prepared directly at the required dilution the particle counts showed a 30-fold drop. This indicated that the preparation method, dilution and possibly shelf life impact the defectivity. The solutions are currently made from store bought chemicals and not filtered. It is believed that sub-50 nm filtration will bring the defectivity to tolerable levels for EUV. We used an aluminum-oxide based solution<sup>[30]</sup> and evaluated two different coating techniques—spin coating and capillary coating—for their roughness and smoothing power only, while keeping in mind that the defectivity must be reduced for the technique to be feasible.

#### 3.3.1 Inpria spin coating

The AlO-based resist solution was spin-coated on a HamaTech feasibility tool and subsequently baked on a hot plate. In spin coating the smoothing power depends on the coating thickness, which can be controlled by the spin coating speed. For an 8 nm thick coating, the smoothing power was 1.65, and for a 70 nm coating, the smoothing power was 5.5. For comparison, the typical smoothing power for a 350 nm thick MoSi film stack deposited in the IBD tool is about 2.3<sup>[31]</sup>.

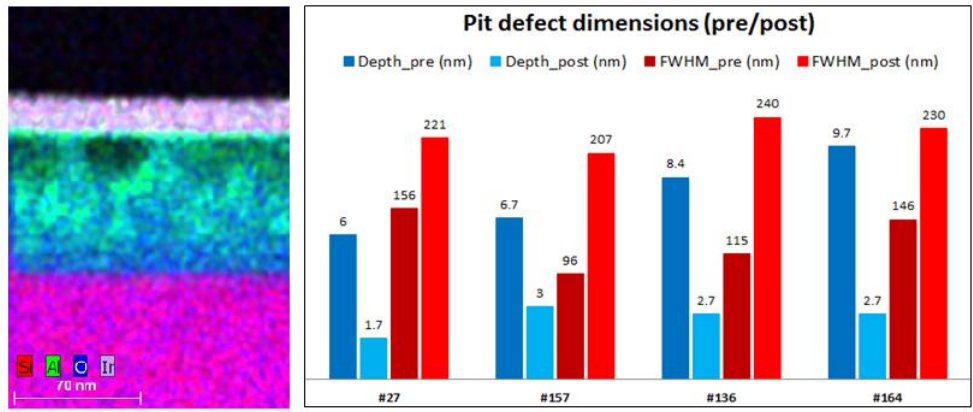


Figure 6: High resolution energy dispersive cross-section image of AlO-based coating (left). Chart showing the decrease in depth and increase in FWHM for 4 pit-type defects upon spin coating (right).

Smoothing power was determined by taking AFM pre-/post-scans on selected pit defects. Four punchmarks were made in a diamond shape at a distance of 5 μm from the defect. First 6x6 μm<sup>2</sup> scans were taken to determine the defect

location relative to the pointed edges of the punch mark. Then zoomed-in scans of the defects were taken, which enabled their depth/height and FWHM to be determined. The same procedure was repeated after spin coating while checking the pre-scan to ensure the same defect (location) was being analyzed. The chart in Figure 6 (right) shows the pre-/post-depth and FWHM of four pit-type defects. It can be seen that the depths (in blue) decreased and the FWHMs (in red) increased. The average SP calculated for these defects is 5.5. High resolution transmission electron microscope (TEM) cross-section images were taken to determine the thickness of the coating. Figure 6 (left) shows the energy dispersive spectroscopy micrograph of the coating cross-section, indicating that the coating is aluminum-oxide-based.

Although spin coating works well for pits, it is expected to leave radial comet-like tails for particles during smoothing. Also the final surface roughness, smoothing power, and coating thickness are interrelated; slower spin speeds are expected to produce thicker coatings and better smoothing, but also increase the surface roughness. Further experiments are underway to determine the optimal conditions for spin coating and to reduce the defectivity of the solution.

### 3.3.2 Inpria capillary coating

Capillary (or meniscus) coating is a novel technique based on the principle of the capillary effect<sup>[32]</sup>. The coating thickness and finish mainly depend on the surface energy at the interface of the coating liquid and the substrate surface. In capillary coating, the solution from a reservoir rises up between two parallel sheets due to capillary forces and flows up out of the nozzle (Figure 7, left). The substrate surface to be coated is placed a fraction of a millimeter above the nozzle and translated horizontally relative to the nozzle. When the meniscus atop the nozzle intersects the substrate, the solution attaches to the substrate surface by capillary forces, depending on surface wettability. As the relative motion continues, a thin film becomes entrained on the surface<sup>[33]</sup>. The fluid dynamics that control the entrained film thickness are similar to those for dip coating, and controlling the way the film dries after it is applied is an essential step in ensuring film uniformity. A distinct advantage of capillary coating is its efficient use of the fluids. It provides nearly 100% utilization of a coating solution, and with in-line filtration its lifetime is extremely long. Unlike spin coating, it has the potential to uniformly smooth both pit and particle defects as well as produce more controllable coatings.

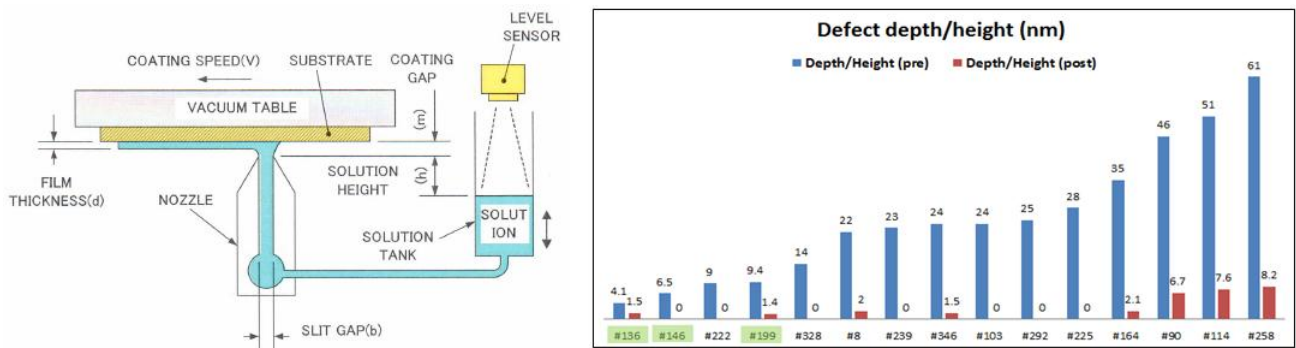


Figure 7: Schematic of capillary coating technique (left, courtesy of Itochu). Chart showing defect depth/height before and after capillary coating for selected pits and particles (right).

Capillary coating was evaluated on a cap coating tool made by Hirano Tecseed Co., Japan, using the capillary coating technology licensed from HamaTech, Germany. The chart in Figure 7 (right) shows the depth/height before and after capillary coating for specific defects. The three pits are highlighted by a green box. Capillary coating seems to cover up particles up to ~28 nm high for an 83 nm thick coating. A value of 0 indicates that the defect was not found in the 6x6  $\mu\text{m}^2$  AFM post-scan, either because the defect was sufficiently smoothed or because the particle somehow moved from its initial location during processing. The average smoothing power calculated for only those defects that could be accounted for before and after with any doubt (and excluding pit #146, infinite) was determined to be ~8.2. The RMS roughness went from 0.08 nm on the substrate to 0.14 nm on the coated metal oxide film. More experiments are planned to determine the optimal process conditions that would provide the maximum smoothing with the least increase in surface roughness.

## 4. SUMMARY

The current substrate polishing processes appear unable to simultaneously reach the roughness and defectivity levels required for the commercialization of EUV lithography. Polishing LTEM/ULE substrates is more challenging than Qz substrates because of the doping and other related factors. We have investigated alternative techniques based on substrate, silicon thin film, and inorganic metal oxide coating by evaluating roughness, defectivity, and substrate smoothing for each technique. CMP is still the best mainstream method currently available with respect to overall process integration, but it can potentially be used in combination with the above techniques to get down to the required specifications. For example, it can be used in combination with MRF polishing to reduce the extent of sub-surface damage, or it can be used in combination with DPNP to etch embedded or hard to remove particles. Further work is required to refine the current techniques; evaluate their defectivity, roughness, and smoothing; and verify final proof of concept by obtaining printability data on the actinic inspection tool.

## ACKNOWLEDGEMENTS

This work involved multiple collaborations with researchers from academia and industry all across the world. I would like to express my gratitude to the following people for facilitating this work: T. Murakami from Nano-photonics Engineering Organization, Japan; K. Kato from TEXMAC Inc., NC; A. Grenville from Inpria, OR; C. McFee from QED Technologies, NY; and Y. Zhang, W. Koolen-Hermkens from HamaTech, Germany.

I would also like to thank the following folks at SEMATECH for helping with the AFM and TEM measurements: T. Owen, J. Underwood, B. Halliday, M. Maloney, N. Lethbridge, L. Gwenden, E. Maillet, E. Stinzianni, and T. Chakroborty.

## REFERENCES

- [1] Huh S.-M., Rastegar, A. Wurm, S., Goldberg, K., Mochi I., Nakajima, T., Kisimoto, M. and Komakine M., "Study of real defects on EUV blanks and a strategy for EUV mask inspection", 26th European Mask and Lithography Conference Proc. SPIE **7545** (2010)
- [2] Rastegar, A., Eichenlaub, S., Kapila, V., John Kadaksham, A. and Marmillion, P., "Sub 50 nm cleaning-induced damage in EUV mask blanks", Proc. SPIE **6921**, 692120 (2008)
- [3] Hirabayashi, Y., "Development status of EUVL blank and substrate", Proc. SPIE **8166**, 81663T (2011)
- [4] Gullikson, E. M., Cerjan, C., Stearns, D. G., Mirkarimi, P. B. and Sweeney, D. W., "Practical approach for modeling extreme ultraviolet lithography mask defects", J. Vac. Sci. Technol. B **20**, 81 (2002)
- [5] Rastegar, A., Eichenlaub, S., Goncher, K. and Marmillion, P., "A study of damage mechanisms during EUV mask substrate cleaning", Proc. SPIE **6283**, 628301 (2006)
- [6] SEMI P37-1102: Specification for extreme ultraviolet lithography mask substrates
- [7] Internal communication with Lasertec
- [8] Naulleau, P. P., George, S. A. and McClinton, B. M., "Mask roughness and its implications for LER at the 22- and 16-nm nodes", Proc. Of SPIE **7636**, 76362H-1 (2010)
- [9] Trogolo, J. A. and Rajan, K., "Near surface modification of silica structure induced by chemical/mechanical polishing", J. Mater. Sci. **29**, 4554 (1994)
- [10] Rastegar, A. and Lee, B.-H. "Substrate pit reduction strategies for the 22 nm and 16 nm half-pitch nodes", Technology Transfer #10125132A-ENG (2010)
- [11] Kwon, H. J., Harris-Jones, J., Teki, R., Cordes, A., Nakajima, T., Mochi, I., Goldberg, K. A., Yamaguchi, Y., Kinoshita, H., "Printability of native blank defects and programmed defects and their stack structures", Proc. SPIE **8166**, 81660H (2011)
- [12] Yatsui, T., Nomura, W., Ohtsu, M., Hirata, K. and Tabata, Y., "Realization of an ultra-flat silica surface with angstrom-scale average roughness using nanophotonic polishing", Proc. Lasers and Electro-optics **20**, 1 (2008)

- [13] Kawazoe, T., Kobayashi, K., Takubo, S. and Ohtsu, M., "Nonadiabatic photodissociation process using an optical near field", *J. Chem. Phys.* **122**, 024715 (2005)
- [14] Yonemitsu, H., Kawazoe, T., Kabayahis, K., Ohtsu, M., "Nonadiabatic photochemical reaction and application to photolithography", *J. Luminescence* **122-123**, 230 (2007)
- [15] Golini D., Kordonski, W. I., Dumas P. and Hogan, S. J., "Magnetorheological finishing (MRF) in commercial precision optics manufacturing", *Proc. SPIE* **3782**, 80 (1999)
- [16] Pollicove, H. and Golini, D., "Deterministic manufacturing processes for precision optical surfaces", *Key Engineering Materials* **238-239**, 53 (2003)
- [17] Tricard, M., Golini, D., DeMarco, M. and Mooney, T., "High precision polishing of EUV photoblanks with magneto-rheological finishing (MRF)", *EUVL Symposium* (2002)
- [18] Li, Y., Liu, Z., Xie, R., Wang, J. and Xu, Q., "The surface layer of fused silica finished by various polishing techniques", *Symposium on Photonics and Optoelectronics* (2010)
- [19] Heidrich, S., Willenborg, E. and Richmann, A., "Development of a laser based process chain for manufacturing freeform optics", *Physics Procedia* **12**, 519 (2011)
- [20] Reinhart, P. (Ed.), [*Tailored Light 2, Laser Application Technology*], Springer, New York & Heidelberg, 196-202 (2011)
- [21] Mendez, E., Nowak, K. M., Baker, H. J., Villarreal, F. J. and Hall, D. R., "Localized CO<sub>2</sub> laser damage repair of fused silica optics", *Appl. Opt.* **45**, 5358 (2006)
- [22] Choi, J.-G., Prasad, Y. N., Kim, I.-K., Kim, I.-G., Kim, W.-J., Busnaina, A. A. and Park, J.-G., "Analysis of scratches formed on oxide surface during chemical mechanical planarization", *J. Electrochem. Soc.* **157**, H186 (2010)
- [23] Penta, N. K., Dandu Veera, P. R. and Babu, S. V., "Role of Poly(diallyl-dimethyl-ammonium chloride) in selective polishing of polysilicon over silicon dioxide and silicon nitride films", *Langmuir* **27**, 3502 (2011)
- [24] Penta, N. K., Matovu, J. B., Dandu Veera, P. R., Krishnan, S. and Babu, S. V., "Role of polycation adsorption in poly-Si, SiO<sub>2</sub> and Si<sub>3</sub>N<sub>4</sub> removal during chemical mechanical polishing: effect of polishing pad surface chemistry", *Colloids & Surfaces A: Physiochem. Eng. Aspects* **388**, 21 (2011)
- [25] Penta, N. K., Dandu Veera, P. R. and Babu, S. V., "Charge density and pH effects on polycation adsorption on Poly-Si, SiO<sub>2</sub>, and Si<sub>3</sub>N<sub>4</sub> films and impact on removal during chemical mechanical polishing", *ACS Appl. Mater. Interfaces* **3**, 4126 (2011)
- [26] Kant, R., Ferralis, N., Provine, J., Moboudian, R. and Howe T. R., "Experimental investigation of silicon surface migration in low pressure nonreducing gas environments", *Electrochem. Solid-State Lett.* **12**, H437 (2009)
- [27] Araki, K., Isogai, H., Takeda, R., Izunome, K., Matsushita, Y. and Zhao, X., "Effect of hydrogen termination on surface roughness variation of Si(110) by reflow oxidation during high-temperature Ar annealing", *Jpn. J. Appl. Phys.* **49**, 085701 (2010)
- [28] Anderson, J. T., Munsee, C. L., Hung, C. M., Phung, T. M., Herman, G. S., Johnson, D. C., Wager, J. F. and Keszler, D. A., "Solution-processed HafSO<sub>x</sub> and ZircSO<sub>x</sub> inorganic thin-film dielectrics and nanolaminates", *Adv. Funct. Mater.* **17**, 2117 (2007)
- [29] Stowers, J., Telecky A. and Grenville, A., "Imageable oxides: new solutions for resist", *EUVL Symposium* (2010)
- [30] Meyers, S. T., Anderson, J. T., Hong, D., Hung C. M., Wager, J. F. and Keszler, D. A., "Solution-processes aluminum oxide phosphate thin-film dielectrics", *Chem. Mater.* **19**, 4023 (2007)
- [31] Harris-Jones, J., Teki, R., Jindal, V. and Kearney, P., "Smoothing pits on EUV mask blanks by ion-beam deposition", *EUVL Symposium* (2011)
- [32] Bhattacharya, S. K., Moon, K. S. and Tummala, R. R., "Meniscus coating: a low-cost polymer deposition method for system-on-package (SOP) substrates", *IEEE trans. on Electronics Packaging Manufacturing* **26**, 110 (2003)
- [33] Krauss, C., Dietze, U., Xu, F., Koepernik, C., Dress, P., Voehringer, P., Irmischer, M. and Szekeresch, J., "STEAG HamaTech Resist Coater ASR5000 - tool concept and process results", *Proc. SPIE* **4889**, 684 (2002)

# Dressed Photon Technology for Novel Devices and Fabrications

Motoichi Ohtsu

Graduate School of Engineering, the University of Tokyo, Tokyo 113-8656, Japan,  
also with Nanophotonics Research Center, The University of Tokyo, Tokyo 113-8656, Japan

ohtsu@ee.t.u-tokyo.ac.jp

**Abstract** — This paper reviews the theoretical picture of dressed photons used to describe the electromagnetic interactions between nanometric particles located in close proximity to each other. The coupling between a dressed photon and multi-mode coherent phonons is also presented, revealing the presence of a novel phonon-assisted process in light-matter interactions. Applications of this novel process to qualitatively innovative fabrication technologies and energy conversion devices are demonstrated.

**Keywords** —dressed photon, optical near-field, phonon, etching, energy conversion

## I. INTRODUCTION

Nanophotonics, proposed by the author in 1993 [1–3], is a novel optical technology that utilizes the electromagnetic fields localized in nanometric space. These fields have been named optical near-fields due to their non-propagating features. Nanophotonics enables the realization of qualitative innovations in optical devices, fabrication techniques, energy conversion, and hierarchical systems by exploiting the novel functions and phenomena enabled by optical near-field interactions that would otherwise be impossible if only conventional propagating light were used. Advancing these innovations has required a deeper understanding of optical near-fields. The theoretical picture of *dressed photons* has been proposed to describe the electromagnetic interactions between nanometric particles located in close proximity to each other, giving birth to a new field known as dressed photon technology. This article reviews the unique features of dressed photons and demonstrates examples of the qualitative innovations that can be achieved [4].

## II. PRINCIPLES

The optical near-field is a virtual cloud of photons that always exists around an illuminated nanometric particle. A naïve wave-optical picture of the optical near-field has been given [5]. This picture, however, is not adequate for use as a theoretical basis for realizing qualitative innovations; to do so requires a quantum optical approach and quantum field theory. A real photon (also called a

free photon, i.e., conventional propagating scattered light) can be emitted from an electron in an illuminated nanometric particle. Independently of the real photon, another photon is emitted from this electron and can be re-absorbed within a short duration. This photon is nothing more than a virtual photon, and its energy is localized at the surface of the nanometric particle. Since the virtual photon remains in the proximity of the electron, it can couple with the electron in a unique manner. This coupled state, called a dressed photon, is a quasi-particle from the standpoint of photon energy transfer. The dressed photon is not the free photon but the photon that carries the material excitation energy. The dressed photon has been theoretically described by assuming a multipolar quantum electrodynamic Hamiltonian in a Coulomb gauge and single-particle states in a finite nano-system [6]. After a unitary transformation and some simple calculations, the creation and annihilation operators of the dressed photon are expressed as the sum of the operators of the free photon and an electron-hole pair.

The real system is more complicated because the nanometric subsystem (composed of the nanometric particles and the dressed photons) is buried in a macroscopic subsystem composed of the macroscopic substrate material and the macroscopic incident and scattered light fields. A novel theory was developed to avoid describing all of the complicated behaviors of these subsystems rigorously, since we are interested only in the behavior of the nanometric subsystem. In this theory, the projection operator method is effectively employed for describing the quantum mechanical states of the system [7]. As a result of this projection, the local electromagnetic interaction in the nanometric subsystem is expressed by a screened potential using a Yukawa function, which represents the dressed photons around the nanometric particles. The decay length of this potential is equivalent to the particle size.

A real nanometric material is composed not only of electrons but also of a crystal lattice. In this case, after a dressed photon is generated on an illuminated nanometric particle, its energy can be exchanged with the crystal lattice. By this exchange, the crystal lattice can excite the vibration mode coherently, creating a multi-mode coherent phonon state. As a result, the dressed photon and



the coherent phonon can form a coupled state. The creation operator of this quasi-particle, representing the coupled state, is expressed as the product of the creation operator of the dressed photon and a displacement operator of the phonon, which represents the creation of the coherent phonon state [8,9]. This coupled state (the dressed photon carrying the coherent phonon energy, or DP-CP for short) is a quasi-particle and is generated only when the particle size is small enough to excite the crystal lattice vibration coherently.

### III. FABRICATION TECHNOLOGIES

Novel fabrication technologies have been developed utilizing dressed photons. Methods of smoothing surfaces are reviewed in this section, which are high-throughput fabrication technologies because neither a fiber probe nor a photomask are required. The key to these methods is to exploit the fact that DP-CPs can always be generated on a nanometrically rough material surface when it is illuminated with propagating light. The generated DP-CPs cause smoothing of locally rough parts, which then become flat, and the smoothing stops spontaneously because DP-CPs are no longer generated. Thus, they are called self-proceeding processes. Two methods are reviewed in the following.

(1) Etching [10]: Substrates with ultra-flat surfaces of sub-nm roughness are required for various applications, including the manufacture of high-quality, extreme-UV optical components, high-power lasers, ultra-short-pulse lasers, and future optical devices with dimensions at the sub-100-nm scale. It is estimated that the required surface roughness,  $R_a$ , will be less than 0.1 nm [11]. Conventionally, chemical-mechanical polishing (CMP) has been used to flatten the surface [12]. However, CMP has difficulties in reducing  $R_a$  to less than 0.2 nm because the polishing pad roughness is as large as  $10\ \mu\text{m}$ , and the diameters of the polishing particles in the slurry are as large as 100 nm. In addition, polishing causes scratches or digs due to the contact between the polishing particles and/or impurities in the slurry and the substrate. To solve these problems, phonon-assisted photochemical etching was developed for smoothing the surface of glass. In this process, a quartz glass substrate with nanometric surface roughness is installed in a vacuum chamber filled with gaseous  $\text{Cl}_2$  molecules. Although the absorption band edge wavelength of these molecules is 400 nm, green propagating light with a wavelength as long as 532 nm is used for photochemical etching. The  $\text{Cl}_2$  molecules remain stable above the flat glass surface because of the absence of DP-CPs. However, when DP-CPs are generated at the tips of bumps on the illuminated rough surface, by the exchange of DP-CPs between the bumps and the  $\text{Cl}_2$  molecules, the  $\text{Cl}_2$  molecules are dissociated (as in Subsection 4.1) to produce Cl radicals, which etch the tips of the bumps. By this phonon-assisted process, the photochemical etching starts spontaneously to remove the bumps when the glass surface is illuminated with

incident propagating light, and it stops spontaneously when the glass surface becomes so flat that DP-CPs are no longer generated.

As shown in Fig. 1, the magnitude of the roughness,  $R_a$ , evaluated by atomic force microscopic measurements, decreased to 0.13 nm after 30 minutes of photochemical etching. In order for *in situ* real-time monitoring of the change in surface roughness during the photochemical etching, red CW laser light (wavelength = 633 nm) was radiated onto the substrate surface in addition to the green CW laser light used for etching, and the scattered red light intensity was monitored [13]. As shown in Fig. 1, the monitored results are consistent with the results of the  $R_a$  measurements.

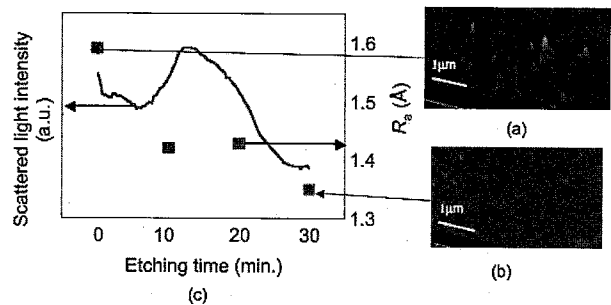


Fig. 1. Results of phonon-assisted photochemical etching of a glass substrate surface. (a), (b) AFM images of the glass surfaces before and after the etching. (c) Relation between the etching time, the surface roughness,  $R_a$ , and scattered light intensity.

After the photochemical etching, high-reflectivity films were coated on the glass substrate to produce a mirror suitable for high-power lasers [14]. Its laser damage threshold was evaluated by shooting the mirror with 355 nm laser pulses, which is a standard evaluation method. The damage threshold was  $14.0\ \text{J}/\text{cm}^2$ , which was 1.7 times higher than that of a mirror made from a conventional CMP substrate.

The methods reviewed above can be applied not only to planar substrates but also to convex and concave substrates. They can also be applied to the inner surface of a cylinder if it can be illuminated by propagating light. Side-walls of the corrugations of a diffraction grating pattern in soda lime glass have been also polished with this technique [15]. Furthermore, they can be applied also to a variety of materials, such as glasses, crystals, ceramics, metals, plastics, and so on. They can be used to polish surfaces of magnetic disks, photomasks for high-resolution photolithography, and so on.

(2) Desorption [16]: Transparent polycrystalline ceramics are attracting interest for applications in optical technology [17–20], particularly for use as gain media for solid state lasers or optical windows [21–24]. To realize higher lasing efficiency or to reduce the scattering loss in optical windows, it is necessary to decrease the surface roughness. To meet this requirement, CMP is difficult to apply to polycrystalline ceramics because of their anisotropic interaction with the polishing medium. A key problem with CMP is that it may cause scratches because

of collisions with the abrasive grains in the slurry. Furthermore, CMP may cause bumps on the surface, due to the difference in etching rates between adjacent grains and the polycrystal. To solve these problems, phonon-assisted desorption has been developed for smoothing the surface of transparent alumina ( $\text{Al}_2\text{O}_3$ ), which is a hard polycrystalline ceramic, with the aim of fabricating low-loss gain media for ceramic lasers to be used in laser-driven spark plugs for the ignition systems in automobile engines [24]. It is expected that the surface roughness, including the scratches formed in the preliminary grinding by diamond abrasive grains, will be repaired by sputtering  $\text{Al}_2\text{O}_3$  particles and phonon-assisted desorption. For this purpose,  $\text{Al}_2\text{O}_3$  particles are deposited on the substrate by RF sputtering. The substrate is illuminated with visible light (power density,  $400 \text{ mW/cm}^2$ ) whose wavelength (473 nm) is longer than that of the absorption band edge wavelength (260 nm) of the  $\text{Al}_2\text{O}_3$  particles. By this illumination, DP-CPs are generated on the ridges of the scratches, which causes the  $\text{Al}_2\text{O}_3$  particles to be activated, increasing the migration length, or which causes them to be desorbed from the ridges. By this phonon-assisted process, the deposition at the ridges is suppressed, whereas the bottoms of the scratches are filled by the  $\text{Al}_2\text{O}_3$  particles, and finally, the scratches are repaired. Experimental results are shown in Fig. 2, which shows a drastic change in the surface profile. Statistical analysis using a Hough transform revealed that the average width of the scratches decreased from 128 nm to 92 nm using this method. The average depth decreased from 3 nm to 1 nm.

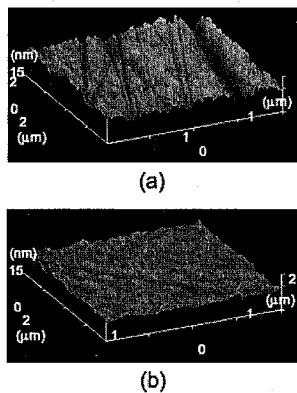


Fig. 2. AFM images of alumina substrate surface before (a) and after (b) RF sputtering under visible light illumination.

#### IV. ENERGY CONVERSION

This section reviews novel method of conversion from optical to optical energies by using DP-CPs. Frequency up-conversion of infrared light is advantageous for many applications, such as expanding the effective bandwidth of photodetectors or imaging sensors. Although second harmonic generation (SHG) [25] and phosphorescence using a multistep transition [26] are popular alternatives, SHG requires high-power, coherent light or a built-up cavity for high efficiency, and phosphorescence suffers

from problems with saturation of the emitted light intensity. To increase the frequency up-conversion efficiency and to avoid these problems, a novel optical energy up-conversion method has been realized by using powdery grains of DCM organic dye molecules as a test specimen [27]. Although the absorption band-edge wavelength of the DCM is as short as 670 nm, the grains are illuminated by near infrared-light of 805 nm-wavelength. This illumination generates DP-CPs at the edges of the grains, which are then exchanged between adjacent grains. As a result of this exchange, an electron in an adjacent grain is excited by a phonon-assisted process and then emits photons whose energies are higher than that of the incident light due to the contribution of the phonon energy.

Curve A in Fig. 3 shows the spectral profile of the frequency up-converted light. For comparison, curve B is the spectral profile of the conventional fluorescence excited by the 402 nm-wavelength light. The spectral profiles show similar shapes in the wavelength range shorter than 660 nm, which means that the up-converted light is emitted from the electrons in the same excited state as that involved in emitting the fluorescence. The spectral intensity of curve A in the longer wavelength range is as high as that of its spectral peak, which means that the longer wavelength light is emitted from a long-lived electronic excited state to which the electron relaxes after the phonon-assisted excitation. Inset images in this figure show optical microscope images of the frequency up-converted light and conventional fluorescence. The lower image shows an inhomogeneous spatial distribution of the emitted light intensity because the light was emitted selectively from the edges of the grains, showing the phonon-assisted process due to the DP-CPs. In the upper image, the spatial distribution of the fluorescence intensity is homogenous, in contrast to that of the lower image. Figure 4(a) shows the relation between the incident photon flux used for excitation and the frequency up-converted photon flux emitted from the DCM. Experimental results are presented for the wavelength components of 650 nm and 690 nm, to which the curve of the second order was least-squares fitted. The fitted results are represented by solid curves A and B. These curves show that the frequency up-conversion is due to the two-step excitation by the DP-CPs [28]. The curve A in Fig. 4(b) shows the relation between the incident light power density and the efficiency of the frequency up-conversion. For comparison, the line B shows the efficiency of conventional second harmonic generation from a popular KDP crystal, which has the same optical thickness as that of the powdery grains of DCM. It is easily found that the efficiency of the frequency up-conversion is more than 100 times greater than that of the second harmonic generation for an incident light power density lower than  $1 \text{ W/cm}^2$ . By increasing the incident light power density, the second-step excitation of the phonon-assisted process becomes dominant, and thus, the conversion efficiency increases in proportion to the

incident light power density. Therefore, the conversion efficiency remains higher than that of the second harmonic generation even at higher incident power density.

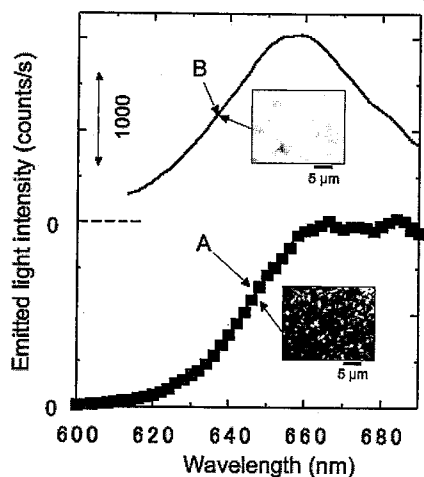


Fig. 3. Spectral profiles of frequency up-converted light. Curve A is the spectrum obtained by applying near-infrared light with a wavelength of 805 nm. Curve B is the conventional fluorescence spectrum. The inset photos show optical microscope images of the up-converted light and conventional fluorescence.

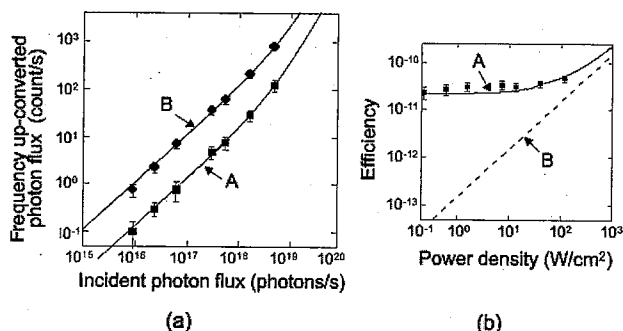


Fig. 4. Frequency up-converted light intensity and the efficiency of conversion. (a) Relation between the incident photon flux and the frequency up-converted photon flux. Curves A and B represent the intensity of the wavelength components of 650 nm and 690 nm, respectively. (b) Efficiency of the frequency up-conversion as a function of the incident light power density (curve A). For comparison, the efficiency of the second harmonic generation from a KDP crystal is also shown (line B).

It has been found that non-degenerate two-step excitation can also emit higher-frequency light by using two mutually independent light beams with different wavelengths [29]. Using this excitation, a novel system for optical pulse shape measurement has been developed: Due to the two non-degenerate optical pulses, the DCM is excited by the two-step phonon-assisted process. By measuring the emitted light intensity with a conventional visible-light photodetector as a function of the time delay of the reference optical pulse incidence, the optical pulse shape to be measured can be acquired. Using the DCM, the optical pulse shape of 800 nm-wavelength was measured with a temporal resolution of 0.8 ps, which was

limited by the lifetime of the intermediate state involved in the two-step excitation. The measured optical pulse shape has low jitter because the measurement system employs only optical processes, unlike the conventional streak-camera system employing electro-optical processes. By using other commercially available dye molecules, such as Coumarin, the measurable wavelength range can be extended to 1.3–1.55  $\mu\text{m}$  with a temporal resolution of 0.8 ps, which enables optical pulse shape measurement for optical fiber transmission systems.

## CONCLUSION

Dressed photons have allowed the realization of qualitative innovations in optical technologies, i.e., enabling novel optical devices, fabrication technologies, energy conversion, and hierarchical systems that would be unrealizable if only conventional propagating light were used. For example, in the case of fabrication technologies, it should be noted that large, expensive, high-power-consumption, short-wavelength light sources are not required, and the fabrication equipment has low power consumption. The phonon-assisted photochemical etching does not involve the use of rare-earth metals, in contrast to the conventional CMP method which uses a large amount of  $\text{CeO}_2$ , a typical rare-earth metal, for polishing quartz glasses. These notable features, realized by using dressed photon technology, are advantageous for energy saving and environmental protection for future society.

## REFERENCES

- [1] M. Ohtsu, T. Kawazoe, T. Yatsui, and M. Naruse, "Nanophotonics: Application of Dressed Photons to Novel Photonic Devices and Systems," *IEEE J. Selected Topics in Quantum Electron.*, vol.14, no.6, pp.1404-1417, December 2008.
- [2] M. Ohtsu, K. Kobayashi, T. Kawazoe, T. Yatsui, and M. Naruse, *Principles of Nanophotonics*, Florida, Taylor & Francis, 2008.
- [3] M. Ohtsu (ed.), *Progress in Nano-Electro-Optics V*, Berlin, Springer, 2006.
- [4] M. Ohtsu (ed.), *Progress in Nanophotonics 1*, Berlin, Springer, 2011.
- [5] Y. Leviatan, "Study of near-zone fields of a small aperture," *J. Appl. Phys.*, vol.60, no. 5, pp.1577-1583, September 1986.
- [6] K. Kobayashi, S. Sangu, H. Ito, and M. Ohtsu, "Near-field optical potential for a neutral atom," *Phys. Rev. A*, vol.63, no.1, 013806, January 2001.
- [7] M. Ohtsu and K. Kobayashi, *Optical Near Fields*, Berlin, Springer, 2004.
- [8] Y. Tanaka and K. Kobayashi, "Optical near field dressed by localized and coherent phonons," *Journal of Microscopy*, vol.229, part.2, pp.228-232, March 2008.
- [9] A. Sato, Y. Tanaka, F. Minami, and K. Kobayashi, "Photon localization and tunneling in a disordered nanostructure," *J. Luminescence*, vol.129, pp.1718-1721, 2009.

- [10] T. Yatsui, K. Hirata, W. Nomura, Y. Tabata, and M. Ohtsu, "Realization of an ultra-flat silica surface with angstrom-scale average roughness using nonadiabatic optical near-field etching," *Appl. Phys. B*, vol.93, no.5, pp.55-57, August 2008.
- [11] B. Wu and A. Kumar, "Extreme ultraviolet lithography: A review," *J. Vac. Sci. Technol. B*, vol.25, no.6, pp.1743-1781, November 2007.
- [12] L.M. Cook, "Chemical processes in glass polishing," *J. Non-Cryst. Solids*, vol.120, pp.152-171, 1990.
- [13] T. Yatsui, K. Hirata, Y. Tabata, W. Nomura, T. Kawazoe, M. Naruse, and M. Ohtsu, "In situ real-time monitoring of changes in the surface roughness during nonadiabatic optical near-field etching," *Nanotechnology*, vol.21, no.35, 355303, August 2010.
- [14] K. Hirata, in: Proceedings of the 2011 Photonics West, San Francisco, CA, USA, 22-27 January 2011, vol. 7921, (SPIE, Bellingham, 2011) pp.79210M1-13.
- [15] T. Yatsui, K. Hirata, Y. Tabata, Y. Miyake, Y. Akita, M. Yoshimoto, W. Nomura, T. Kawazoe, M. Naruse, and M. Ohtsu, "Self-organized near-field etching of the sidewalls of glass corrugations," *Appl. Phys. B*, vol.103, no.3, pp.527-530, June 2011.
- [16] W. Nomura, T. Yatsui, Y. Yanase, K. Suzuki, M. Fujita, A. Kamata, M. Naruse, and M. Ohtsu, "Repairing nanoscale scratched grooves on polycrystalline ceramics using optical near-field assisted sputtering," *Appl. Phys. B*, vol.99, no.1-2, pp.75-78, April 2010.
- [17] A. Ikesue and I. Furusato, "Fabrication of Polycrystalline, Transparent YAG Ceramics by a Solid-State Reaction Method," *J. Am. Ceram. Soc.*, vol.78, no.1, pp.225-228, 1995.
- [18] A. Ikesue, T. Kinoshita, K. Kamata, and K. Yoshida, "Fabrication and Optical Properties of High-Performance Polycrystalline Nd:YAG Ceramics for Solid-State Lasers," *J. Am. Ceram. Soc.*, vol.78, no.4, pp.1033-1040, April 1995.
- [19] J. Lu, J. Son, M. Prabhu, J. Xu, K. Ueda, H. Yagi, T. Yanagitani, and A. Kudryashov, "High-Power Nd:Y<sub>3</sub>Al<sub>5</sub>O<sub>12</sub> Ceramic Laser," *Jpn. J. Appl. Phys.*, vol.39, no.1B, L1048-L1050, October 2000.
- [20] N. Tanaka, "Transparent Ceramics," *Bull. Ceram. Soc. Jpn.*, vol.38, no.12, pp.967-969, December 2003.
- [21] A. Krell, P. Brank, H. Ma, and T. Hutzler, "Transparent Sintered Corundum with High Hardness and Strength," *J. Am. Ceram. Soc.*, vol.86, no.1, pp.12-18, January 2003.
- [22] J. Lu, K. Ueda, H. Yagi, T. Yanagitani, Y. Akiyama, and A.A. Kaminskii, "Neodymium doped yttrium aluminium garnet (Y<sub>3</sub>Al<sub>5</sub>O<sub>12</sub>) nanocrystalline ceramics- a new generation of solid state laser and optical materials," *J. Alloys Compd.*, vol.341, pp.220-225, 2002.
- [23] A. Ikesue, "Polycrystalline Nd:YAG ceramics lasers," *Opt. Mater.*, vol.19, pp.183-187, 2002.
- [24] D. Graham-Rowe, "Lasers for engine ignition," *Nature Photonics*, vol.2, 515517, September 2008.
- [25] A. Yariv, *Introduction to Optical Electronics*, 1<sup>st</sup> ed., New York, Holt: Rinehart and Winston, 1985.
- [26] P.W. Atkins, *Physical Chemistry*, 6<sup>th</sup> ed., Oxford, Oxford Univ. Press, 1998.
- [27] T. Kawazoe, H. Fujiwara, K. Kobayashi, and M. Ohtsu, "Visible light emission from dye molecular grains via infrared excitation based on the nonadiabatic transition induced by the optical near field," *IEEE J. Selected Topics in Quantum Electron.*, vol.15, no.5, pp.1380-1386, September 2009.
- [28] H. Fujiwara, T. Kawazoe, and M. Ohtsu, "Nonadiabatic multi-step excitation for the blue-green light emission from dye grains induced by the near-infrared optical near-field," *Appl. Phys. B*, vol.98, no.2-3, pp.283-289, February 2010.
- [29] H. Fujiwara, T. Kawazoe, and M. Ohtsu, "Nonadiabatic nondegenerate excitation by optical near-field and its application to optical pulse-shape measurement," *Appl. Phys. B*, vol.100, no.1, pp.85-91, January 2010.

# Self-assembled QD based nanophotonic device

**Takashi Yatsui, Hiroyuki Fujita\*, Motoichi Ohtsu**

School of Engineering, University of Tokyo, Bunkyo-ku, Tokyo, 113-8656 Japan

\* Institute of Industrial Science, University of Tokyo, Meguro-ku, Tokyo, 153-8505 Japan

## ABSTRACT

This paper reviews recent progress of nanophotonic device using self-assembled quantum dots (QDs). We developed a self-assembly method that aligns nanometre-sized QDs into a straight line along which photonic signals can be transmitted by optically near-field effects.

## 1. INTRODUCTION

Innovations in optical technology are required for the development of future information processing systems, which includes increasing the integration of photonic devices by reducing their size and levels of heat generation. To meet this requirement, we proposed nanophotonic signal transmission (NST) devices that consist of semiconductor quantum dots (QDs) [1,2]. These NST devices operate using excitons in QDs as the signal carrier, due to optical near-field interactions between closely spaced QDs. The exciton energy transfers to another QD when the exciton energy levels are resonant and, therefore, the optical beam spot may be decreased to be as small as the QD size. To produce the NST device, a new technique is required for positioning and alignment of QDs with precise separation.

## 2. SELF-ASSEMBLY OF QDs ALONG DNA

Figure 1 illustrates our approach for the development of a self-assembling NST device with angstrom-scale controllability in spacing among QDs using silane-based molecular spacers and DNA [3]. First, ZnO QDs 5 nm

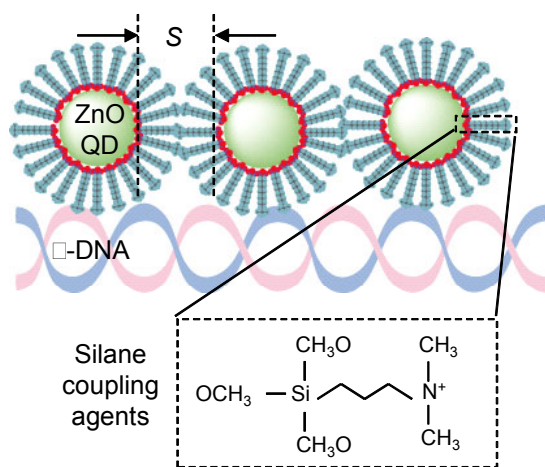


Fig. 1 Schematic of ZnO QD alignment along the  $\lambda$  DNA. S: separation between QDs

diameter in diameter were synthesized using the Sol-Gel method [4]. Then, the surfaces of QDs were coated with a silane coupling agent 0.6 nm in length. The function of the agent is to maintain the spacing between QDs, and to be adhesive to anionic DNA, due to its cationic nature. We used  $\lambda$  DNA (stretched length = 16  $\mu$ m) as a template, and when the QDs are mixed, the QDs are self-assembled onto the DNA by electrostatic interactions. Dense packing of the ZnO QDs along the DNA was obtained, as shown by transmission electron microscopy (TEM) (Fig. 2(a)). The separation between QDs ( $S$ ) was determined by TEM and shown to be 1.2 nm, which was in good agreement with twice the length of silane coupling agents (Fig. 2(d)). Such a high density of packing, despite the electrostatic repulsion between ZnO QDs, was due to the quaternary ammonium group of the silane coupling agent [3].

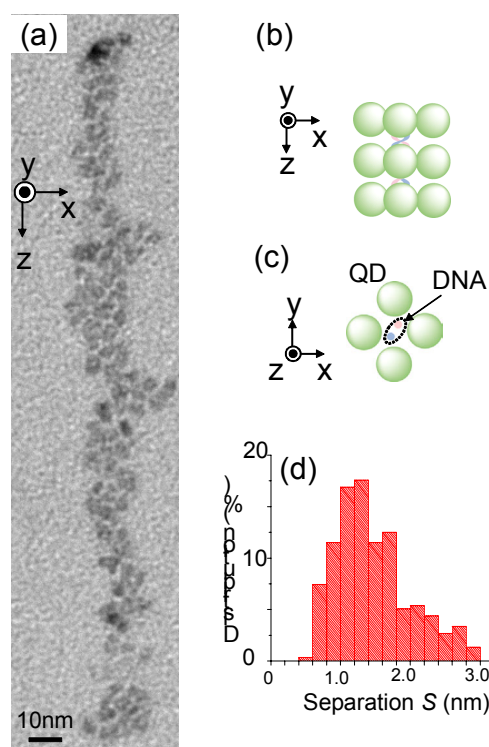
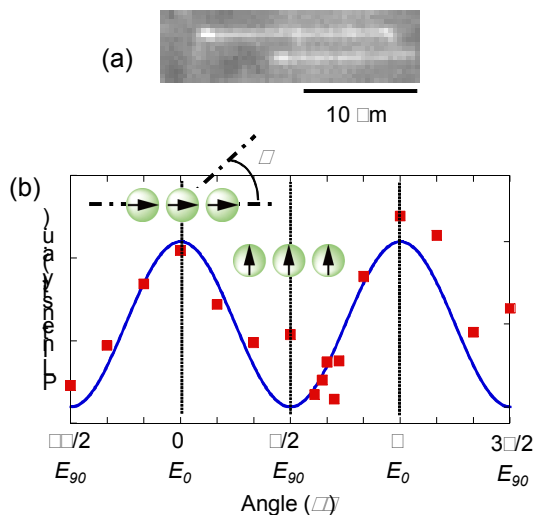


Fig. 2 TEM analysis of fabricated ZnO QDs. (a) Typical TEM pictures of the ZnO QDs. (b) and (c) Schematic of QD alignment. (d) ZnO QD diameter distribution.

### 3. NEAR-FIELD ENERGY TRANSFER ALONG THE QD CHAINS

To observe the optical properties of the aligned ZnO QDs, the DNA with QDs was stretched and straightened on the silicon substrate using combing technique [5], where the silicon substrate was terminated with silane coupling agent and the anionic DNA was adsorbed on the cationic silicon substrate. We obtained the isolated chain of ZnO QDs (see Fig. 3(a)). From the polarization dependence of photoluminescence (PL) at a wavelength of 350 nm (Fig. 3(b)), corresponding to the ground state of 5-nm ZnO QDs, the strong PL emission was obtained by excitation of parallel polarization along the QD chains ( $E_0$ ). Previous studies on the excitation polarization dependence of nanorods [6] indicated that the PL under parallel excitation ( $E_0$ ) is much greater than that under perpendicular polarization ( $E_{90}$ ), due to the absorption anisotropy. Similar polarization dependence was observed in our chained structure. It is possible that the dipoles between adjacent QDs are coupled with optical



**Fig. 3 TEM analysis of fabricated ZnO QDs. (a) Stretched ZnO QD chain along the  $\lambda$  DNA. (b) Incident light polarization dependence of PL intensity. A 4th-harmonic, Q-switched Nd:YAG laser ( $\lambda = 266$  nm) was used to excite the ZnO QDs.  $\theta$ : Polarization angle with respect to the direction along the QD chains.**

near-field interaction, and QD chains have large dipolar strength (see Fig. 3(b)), indicating that they act as an NST device along the chained QDs.

### 4. SUMMARY

As optical near-field energy can transmit through the resonant energy level, NST devices have a number of potential applications, such as wavelength division multiplexing using QDs of different sizes.

### REFERENCES

- [1] M. Ohtsu, T. Kawazoe, T. Yatsui, M. Naruse, "Nanophotonics: Application of dressed photons to novel photonic devices, and systems," IEEE J. Select. Top. Quant. Electron. Vol. 14, No. 8, pp.1404-1417 (2008).
- [2] T. Yatsui, Y. Ryu, T. Morishima, W. Nomura, T. Kawazoe, T. Yonezawa, M. Washizu, H. Fujita, and M. Ohtsu, "Self-assembly method of linearly aligning ZnO quantum dots for a nanophotonic signal transmission device," Appl. Phys. Lett., Vol. 96, No.13, 133106 1-3 (2010).
- [3] T. Yonezawa, S. Onoue, N. Kimizuka, "Metal Coating of DNA Molecules by Cationic, Metastable Gold Nanoparticles," Chem. Lett., Chem. Lett. Vol. 31, pp.1172-1173 (2002).
- [4] E.A. Meulenkaamp, "Synthesis and Growth of ZnO Nanoparticles," J. Phys. Chem. B Vol. 102, No. 29, pp 5566-5572 (1998).
- [5] H. Oana, M. Ueda, M. Washizu, Biochem. Biophys. Research Commun. Vol. 265, Issue 1, pp. 140-143 (1999).
- [6] J. Wang, M. S. Gudiksen, X. Duan, Y. Cui, C.M. Lieber, "Highly Polarized Photoluminescence and Photodetection from Single Indium Phosphide Nanowires," Science Vol. 293, No. 5534, pp. 1455-1457 (2001).

## Nanophotonic system based on localized and hierarchical optical near-field processes

M. Naruse<sup>1,2</sup>, N. Tate<sup>2,3</sup>, M. Ohtsu<sup>2,3</sup>

<sup>1</sup> National Institute of Information and Communications Technology, Koganei, Tokyo 184-8795, Japan

<sup>2</sup> The University of Tokyo, Nanophotonics Research Center, Tokyo 113-8656, Japan

<sup>3</sup> The University of Tokyo, Dept. Electrical Eng. & Info. Sys., Tokyo 113-8656, Japan

email: [naruse@nict.go.jp](mailto:naruse@nict.go.jp)

### Summary

To break through the diffraction limit and achieve novel functionalities and energy saving at a smaller scale, a deeper understanding of light–matter interactions on the nanoscale is indispensable. Here we demonstrate nanophotonic systems exploiting localized and hierarchical optical near-field processes on the nanoscale.

### Introduction

Conventional optical sciences and technologies are based on light propagation in a medium. As a result, it is generally impossible, for example, to shrink the size of an optical light spot beyond the diffraction limit imposed by the wave properties of propagating light. Also, the functional behavior of propagating light is quite limited. Therefore, it is fundamentally important to shift the physical fundamentals from propagating light to nanometer-scale light–matter near-field interactions [1]. By treating the optical near-field as a quasi-particle called a dressed photon, meaning that photon is dressed by material excitations on the nanoscale [1], optical near-field interactions provide unique physical processes, such as optical energy transfer involving energy levels that are optically forbidden conventionally and hierarchical properties. These phenomena cannot be achieved or even explained based on propagating light. We demonstrate nanophotonic systems, both theoretically and experimentally, by exploiting these unique optical near-field processes on the nanoscale in order to extract added-value or novel functionalities, as schematically shown in Fig. 1.

### Nanophotonic System Based on Localized Energy Transfer

Optical near-field interactions associated with nanoscale materials, such as quantum dots, are described by a Yukawa-type potential. This picture has revealed that the interaction between two quantum dots via optical near-fields, even though it involves dipole-forbidden energy levels, results in unidirectional energy transfer by an energy dissipation process occurring in the larger dot [1,2] (Fig. 1(a)). For system-level applications, various signal processing functions, such as logic gates, summation, and broadcast, have been demonstrated [2-4]. It should be noted that the lower bound of the energy dissipation required in such localized energy transfer is about  $10^4$  times lower than the bit flip energy in an electrically wired device [5]. Also, we investigated efficient and modulatable optical energy transfer in multiple-quantum-dot structures by introducing a network of optical near-field interactions. With a density-matrix–based formalization of inter-dot optical near-field interactions, our theoretical approach reveals efficient, robust, and modulatable optical energy transfer and shows good agreement with experimental observations [6,7].

## Nanophotonic System Based on Hierarchy in Optical Near-Field

Optical near-field interactions at the nanoscale are scale-dependent, or hierarchical, meaning that interactions behave differently depending on the physical scale involved [8]. We have developed the theoretical basis of part of this behavior based on angular spectrum analysis [9] (Fig. 1(b)). In addition, optical near-fields could behave differently depending on the nanostructures involved, while keeping the macro-scale optical response functions constant. We experimentally demonstrated a “hierarchical hologram” based on this principle, where three-dimensional images are observed in the far-field, while including hidden information by engineering the shape of the hologram on the nanoscale, information which is only retrievable via optical near-fields [10].

### Conclusions

We have been demonstrating nanophotonic systems based on localized and hierarchical optical near-field processes, which are unachievable with conventional propagating light, to implement novel functionalities. Together with further theoretical [1,9] and experimental advancements [2] of light–matter interactions on the nanoscale, we seek to further advance nanophotonic systems.

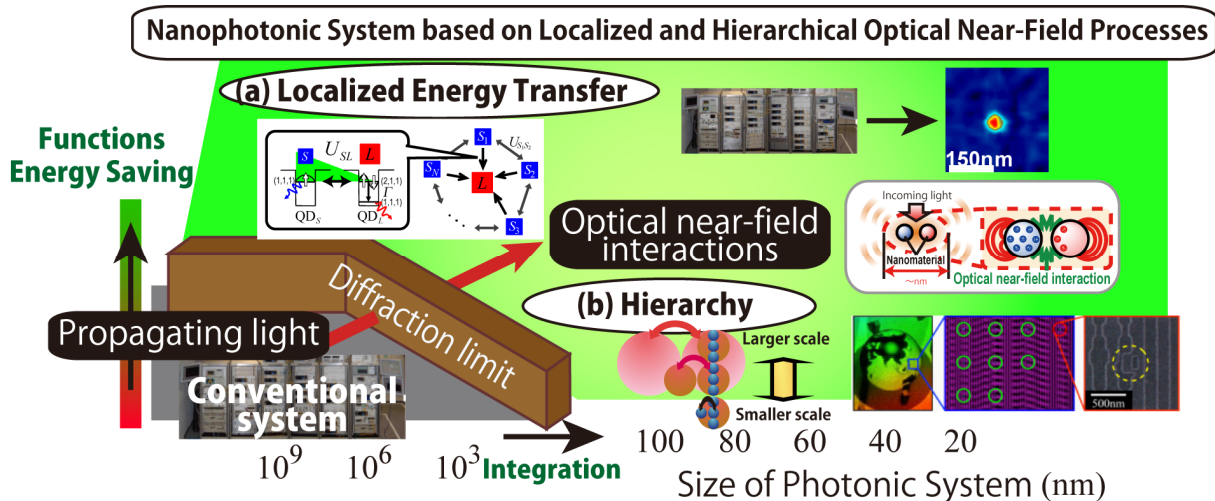


Fig. 1. Nanophotonic system based on optical near-field processes: (a) Systems based on energy transfer between quantum nanostructures via optical near-field interactions and (b) systems based on hierarchical properties of optical near-fields

### References

- [1] M. Ohtsu, et al., *IEEE J. Sel. Top. Quantum Electron.*, **8**, 839, 2002
- [2] T. Kawazoe, et al., *Appl. Phys. B*, **103**, 537, 2011
- [3] M. Naruse, et al., *Opt. Lett.*, **30**, 201, 2005
- [4] M. Naruse, et al., *Opt. Express*, **14**, 306, 2006
- [5] M. Naruse, et al., *Opt. Express*, **18**, A544, 2010
- [6] M. Naruse, et al., *Phys. Rev. B*, **80**, 125325, 2009
- [7] N. Tate, et al., *Opt. Express*, in press
- [8] M. Naruse, et al., *Opt. Express*, **13**, 9265, 2005
- [9] T. Inoue and H. Hori, Quantum theory of radiation in optical near field based on quantization of evanescent electromagnetic waves using detector mode, in *Progress in Nano-Electro-Optics IV*, ed, M. Ohtsu, (Springer Verlag, Berlin, 2005)
- [10] N. Tate, et al., *Optics Express*, **18**, 7497, 2010



## Dressed photon technology

M. Ohtsu\*

Department of Electrical Engineering and Information Systems,  
Graduate School of Engineering, The University of Tokyo  
2-11-16 Yayoi, Bunkyo-ku, Tokyo 113-8656, Japan  
e-mail: ohtsu@ee.t.u-tokyo.ac.jp

\* also with Nanophotonics Research Center, The University of Tokyo

Nanophotonics, proposed by M. Ohtsu in 1993 [1-4], is an innovative science and technology that utilizes dressed photons (conventionally called optical near fields), which are virtual photons carrying a material excitation in nanometric space. Sometimes, plasmonics, photonic crystals, and quantum dot technology are also included in the category of nanophotonics, even though they are conventional wave-propagation optical technologies based on interactions between real photons in metals, materials with periodic structures, and quantum dots, respectively. However, it should be noted that dressed photons and real photons are different and incompatible types of quasi-particles. In order to make these differences, as well as the advantages of nanophotonics, more clearly understood, nanophotonics should instead be called *Dressed Photon Science and Technology*.

This presentation reviews the principles of generation and detection of the dressed photon, which is a quasi-particle representing the coupled state of a photon and an electron in nanometric space. After the possibility of coupling with multi-mode phonons is discussed, some novel fabrication technologies that exploit the unique features of dressed photons are demonstrated. They are: (1) High-resolution photolithography using a green light-emitting diode as a light source, and its application to fabricating soft X-ray optical devices. (2) Self-proceeding photochemical etching for realizing an ultra-flat glass surface with a roughness as low as 0.1 nm for fabricating laser mirrors with a high damage threshold. (3) Annealing of bulk Si crystals, and its application to fabricating high-efficiency light emitting devices. These applications demonstrate that dressed photon technology has realized qualitative innovations in optical technology that would otherwise be impossible using conventional propagating light. The future outlook of this novel technology will be presented.

### References

- [1] M. Ohtsu, T. Kawazoe, T. Yatsui, and M. Naruse, *IEEE J. Selected Topics in Quantum Electron.*, **14**, 1404 (2008)
- [2] M. Ohtsu, K. Kobayashi, T. Kawazoe, T. Yatsui, and M. Naruse, "Preface", in *Principles of Nanophotonics*, (Taylor & Francis, Florida, 2008), pp.ix-x
- [3] M. Ohtsu, Preface to Volume V, in *Progress in Nano-Electro-Optics V*, ed. by M. Ohtsu, (Springer, Berlin, 2006), pp.VII-VIII
- [4] M. Ohtsu(ed.), *Progress in Nanophotonics I*, (Springer-Verlag, 2011), pp.58.

# Nanophotonic fabrication using a dressed photon

T. Yatsui<sup>1, 2</sup>, W. Nomura<sup>1</sup>, & M. Ohtsu<sup>1</sup>

1  THE UNIVERSITY OF TOKYO

2  Advanced Carbon Technology Research and Development Program



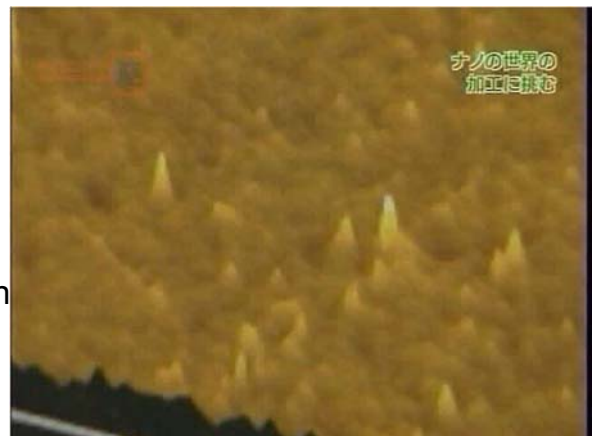
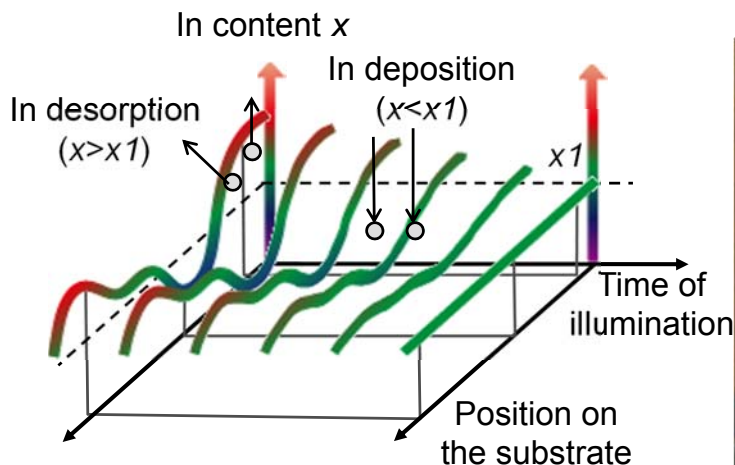
1/36



## Topics to be presented



- Increasing spatial homogeneity
- Realizing ultra-flat surface in Å scale
  - Using near-field desorption
  - Using near-field etching



2/36



# Acknowledgments



- In content controlling  
K. Ito & H. Kawamura  
Dr. M. Mizumura



- Nano-wall substrate  
Y. Miyake, Y. Akita, & Prof. M. Yoshimoto



- Near-field desorption  
Dr. Y. Yanase, M. Fujita, K. Suzuki, & A. Kamata | COVALENT |

- Near-field etching  
K. Hirata, T. Morimoto & Y. Tabata



- Ohtsu Research Group @ UT



- ¥



# To go beyond the diffraction limit



Optical  
near fields



- Non-propagating (Localized on the material surface)
- Size of localization = material size  
(independent of the wavelength)  $\ll$  wavelength

- E. H. Synge (1928), "A suggested method for extending microscopic resolution into the ultra-microscopic region."
- H. A. Bethe (1944), "Theory of diffraction by small holes."



Visible light ( $h\nu$ )

Nanoparticle

Phonon

Free photon ( $h\nu$ )

e-h pair

Dressed photon (DP,  $h\nu_{DP}$ )

Coupled state of DP & phonon ( $h\nu_{DP-ph}$ )

$h\nu < h\nu_{DP} < h\nu_{DP-ph}$

Energy up-conversion

$$\tilde{a}_{\vec{k}\lambda} = \hat{a}_{\vec{k}\lambda} - iN_{\vec{k}} \sum_{\substack{\alpha>f \\ \beta<F}} \left\{ \rho_{\alpha\beta\lambda}^* (\vec{k}) \hat{A}_{\alpha\beta} + \rho_{\beta\alpha\lambda}^* (\vec{k}) \hat{A}_{\alpha\beta}^\dagger \right\}$$

$$\tilde{a}_{\vec{k}\lambda}^\dagger = \hat{a}_{\vec{k}\lambda}^\dagger + iN_{\vec{k}} \sum_{\substack{\alpha>f \\ \beta<F}} \left\{ \rho_{\alpha\beta\lambda} (\vec{k}) \hat{A}_{\alpha\beta}^\dagger + \rho_{\beta\alpha\lambda}^* (\vec{k}) \hat{A}_{\alpha\beta} \right\}$$

$$\hat{\alpha}_i = \tilde{a}_i \left\{ \sum_{p=1}^N \frac{\chi_{i,p}}{\Omega_p} \exp(\hat{b}_p^\dagger - \hat{b}_p) \right\}$$

$$\hat{\alpha}_i^\dagger = \tilde{a}_i^\dagger \left\{ \sum_{p=1}^N \frac{\chi_{i,p}}{\Omega_p} \exp(\hat{b}_p^\dagger - \hat{b}_p) \right\}$$

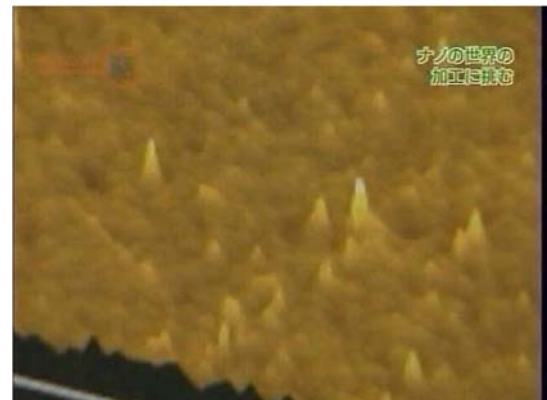
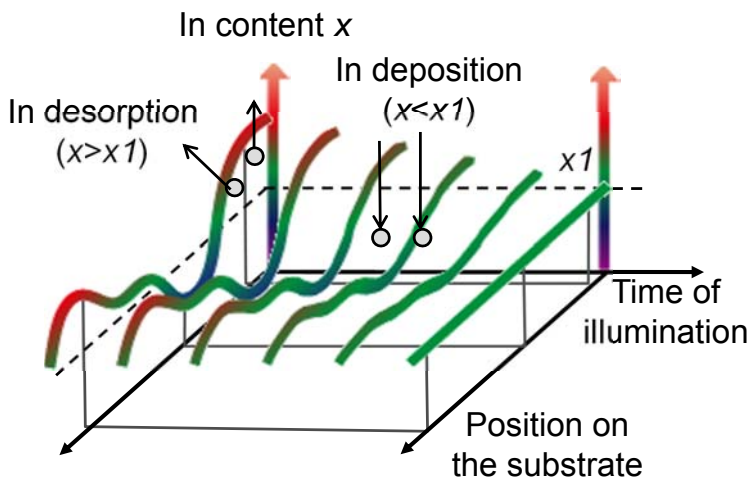
Coherent state of phonon

K. Kobayashi, et al., PRA, **63**, 013806 2001

K. Kobayashi et al., Physica E **40**, 297 (2007)



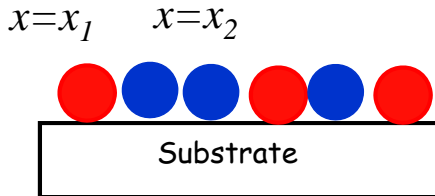
- Increasing spatial homogeneity
- Realizing ultra-flat surface in Å scale
  - Using near-field desorption
  - Using near-field etching



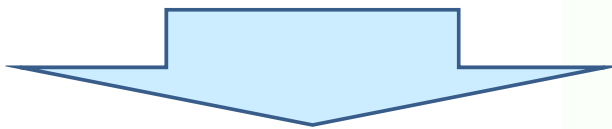


The control of LED color is important in many applications, including the generation of white light and in optical communications

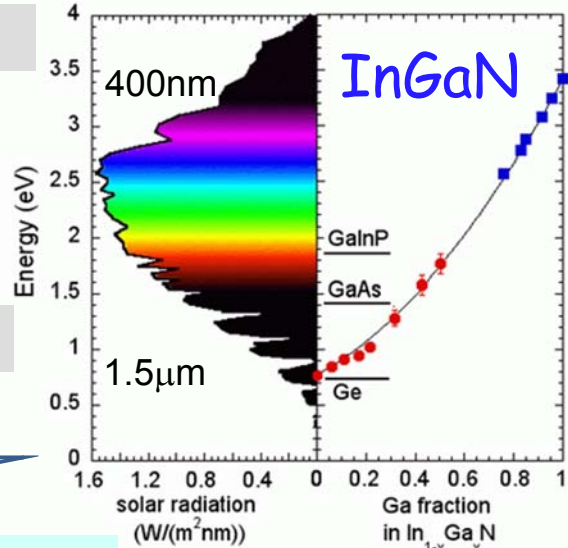
Low spatial uniformity of In



Low color-rendering index

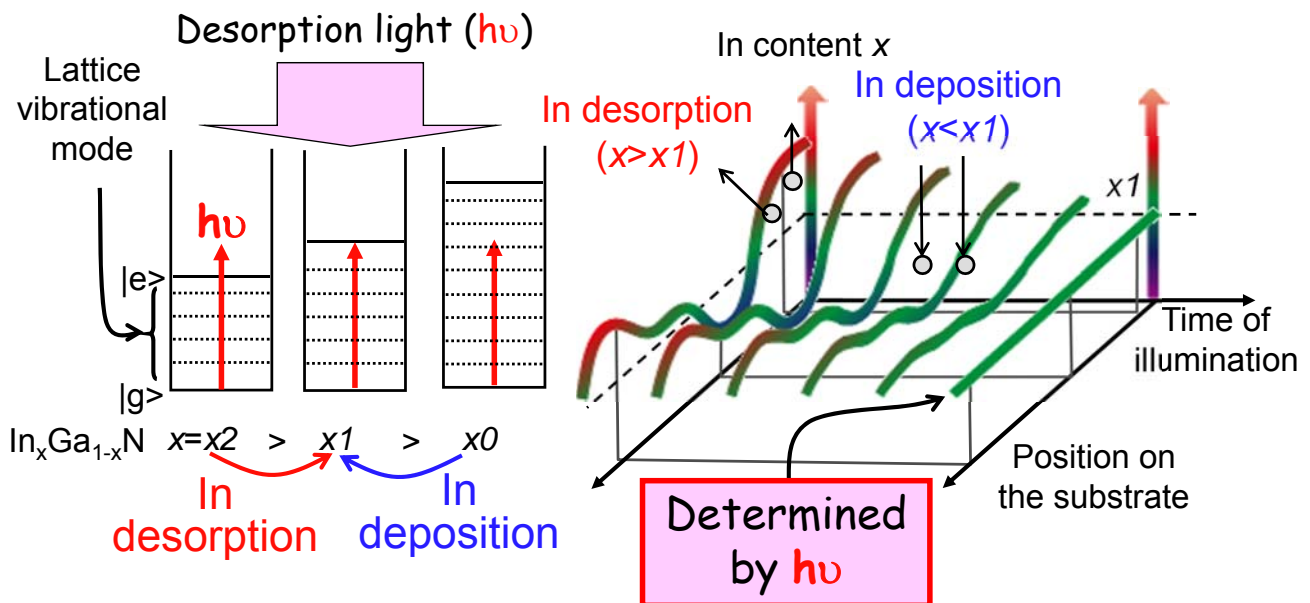


Increasing spatial homogeneity



<http://emat-solar.lbl.gov/>

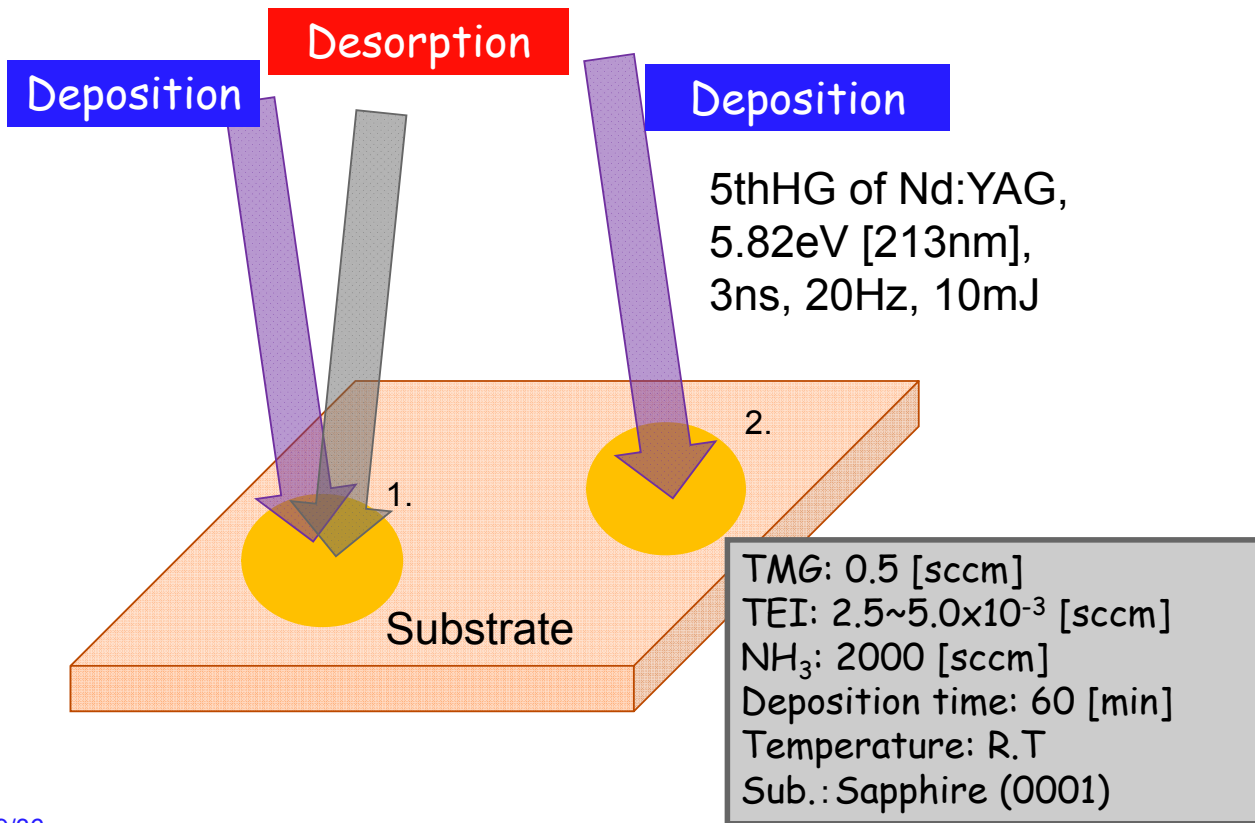
7/36



The growth is governed by a trade-off between In deposition ( $x < x_1$ ) & In desorption ( $x > x_1$ )

T. Yatsui et al., Appl. Phys. B, 97, 375-378 (2009)

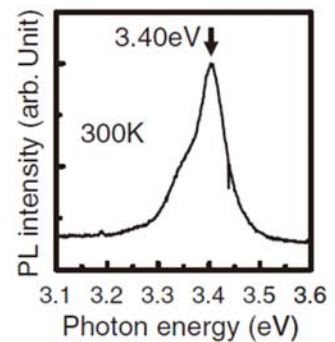
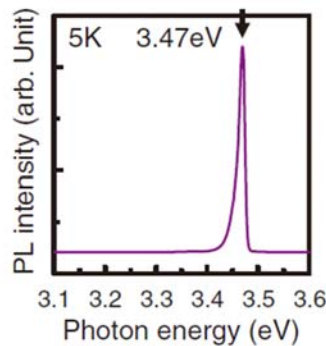
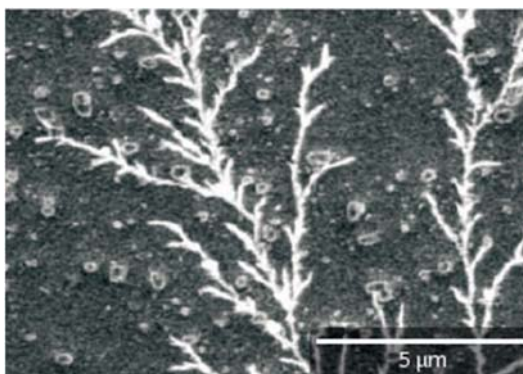
8/36



9/36

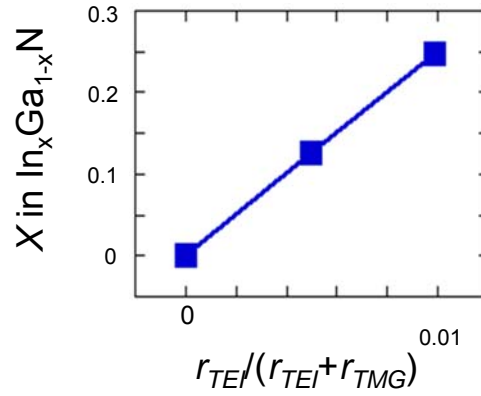
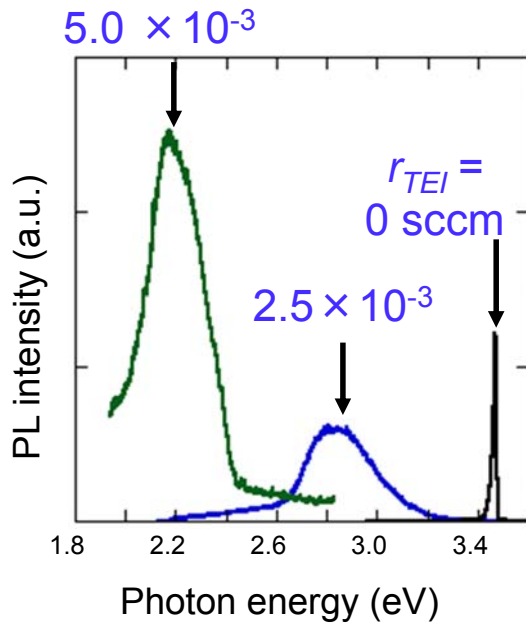


## UV-emitting GaN fabricated "at room temperature"



Nature Photo. **3**, 252 (2009)  
 Appl. Phys. Exp. **2**, 031004 (2009)  
 Appl. Phys. Exp. **1**, 061102 (2008)  
 Appl. Phys. Lett. **85**, 3059 (2004)

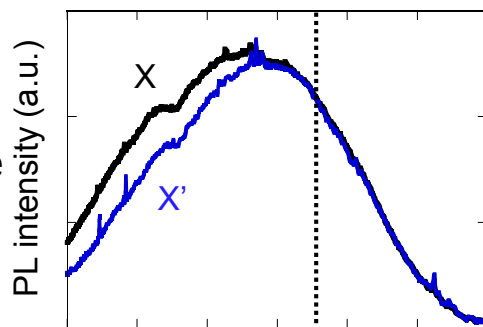
10/36



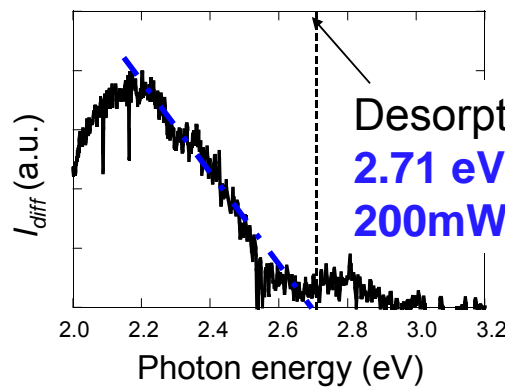
11/36



X: Deposition alone  
 X': Depo. + Deso.



X: X-X'

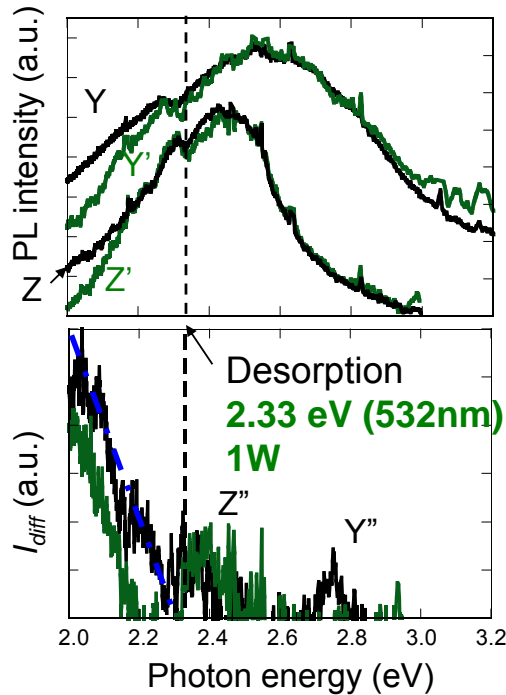


Resulting in a film with a more spatially uniform of In content

12/36



Y&Z: Depo. alone  
Y'&Z': Depo.  
+ Deso.



TMG:0.5sccm,  
NH<sub>3</sub>:2000sccm  
Y: TEI:2.5 × 10<sup>-3</sup>sccm  
Z: TEI:5.0 × 10<sup>-3</sup>sccm

Y'':Y-Y'  
Z'':Z-Z'

Controlled by the photon energy of the desorption

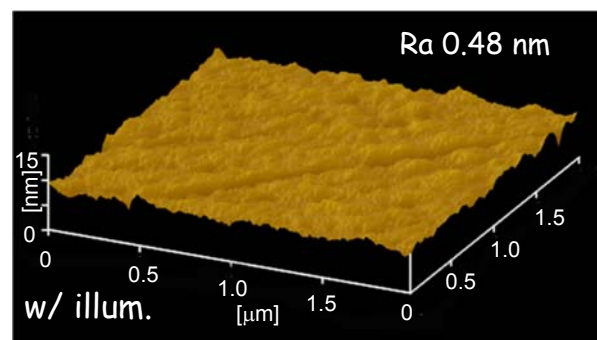
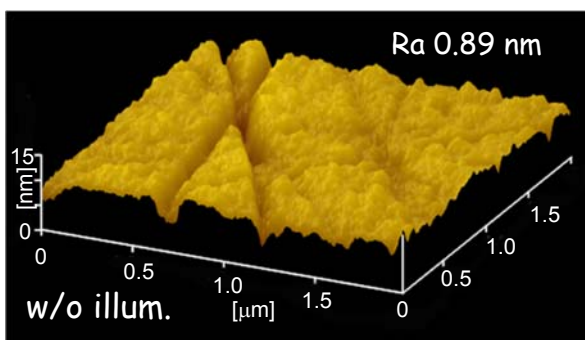
T. Yatsui et al., Appl. Phys. B, 97, 375-378 (2009)



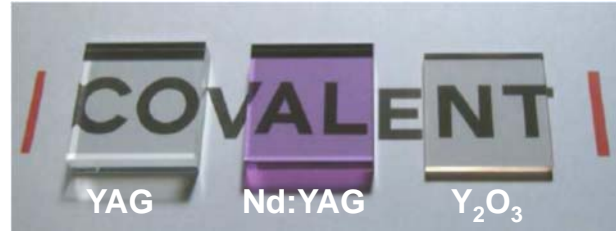
## Topics to be presented



- Increasing spatial homogeneity
- Realizing ultra-flat surface in Å scale
- Using near-field desorption
- Using near-field etching

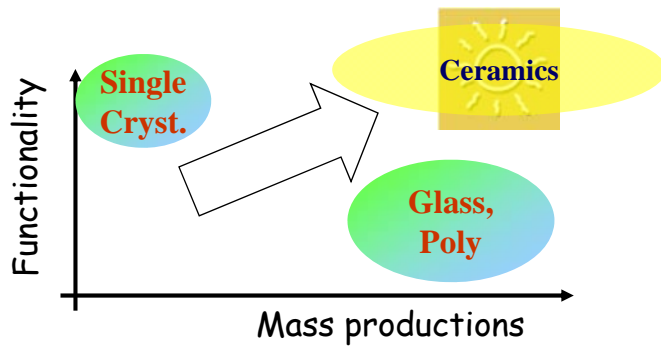






Optical transmission loss comparable to single crystals

Solid state lasers, optical windows & spark plug



Annual review 2009 of Prof. T. Taira's Group

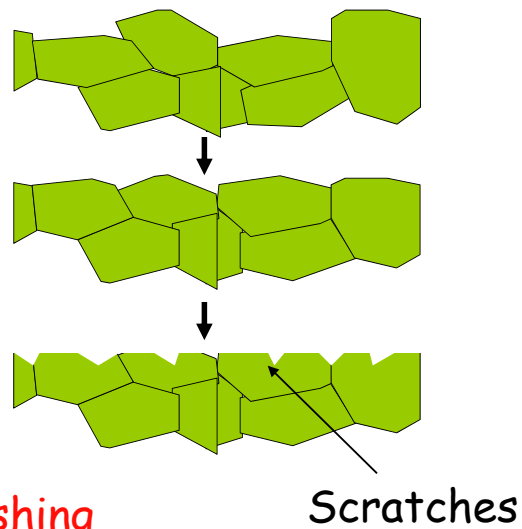


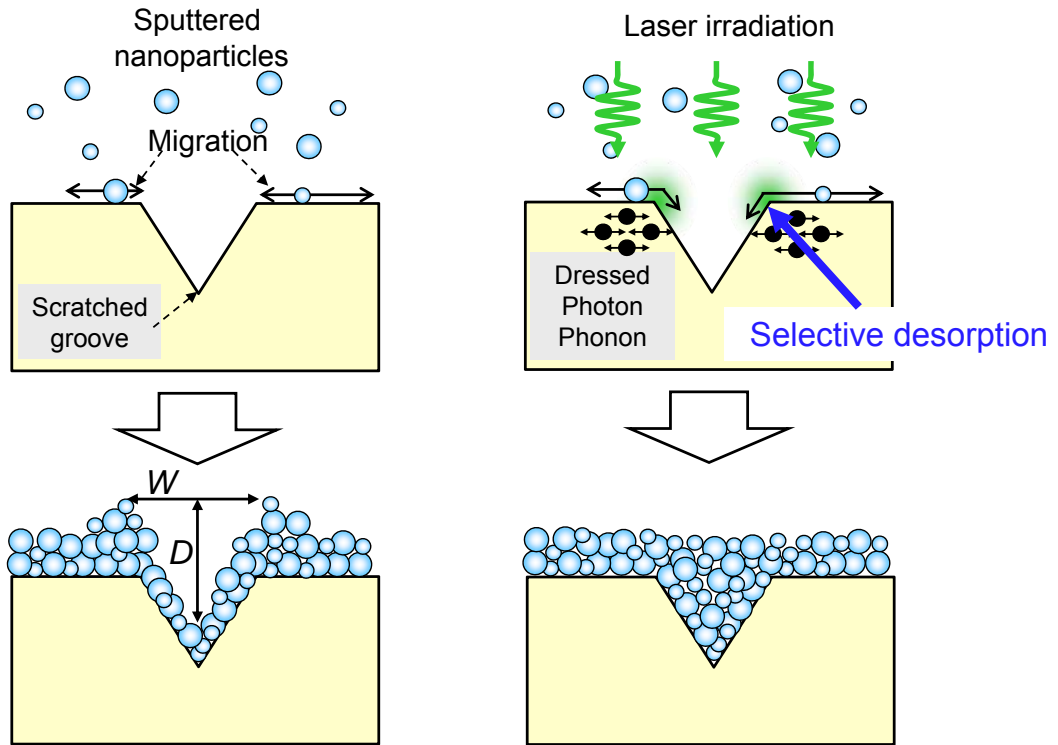
## Present process

(1) Sinter  
Ra > 1µm

(2) Rough Polishing  
Ra < 1µm

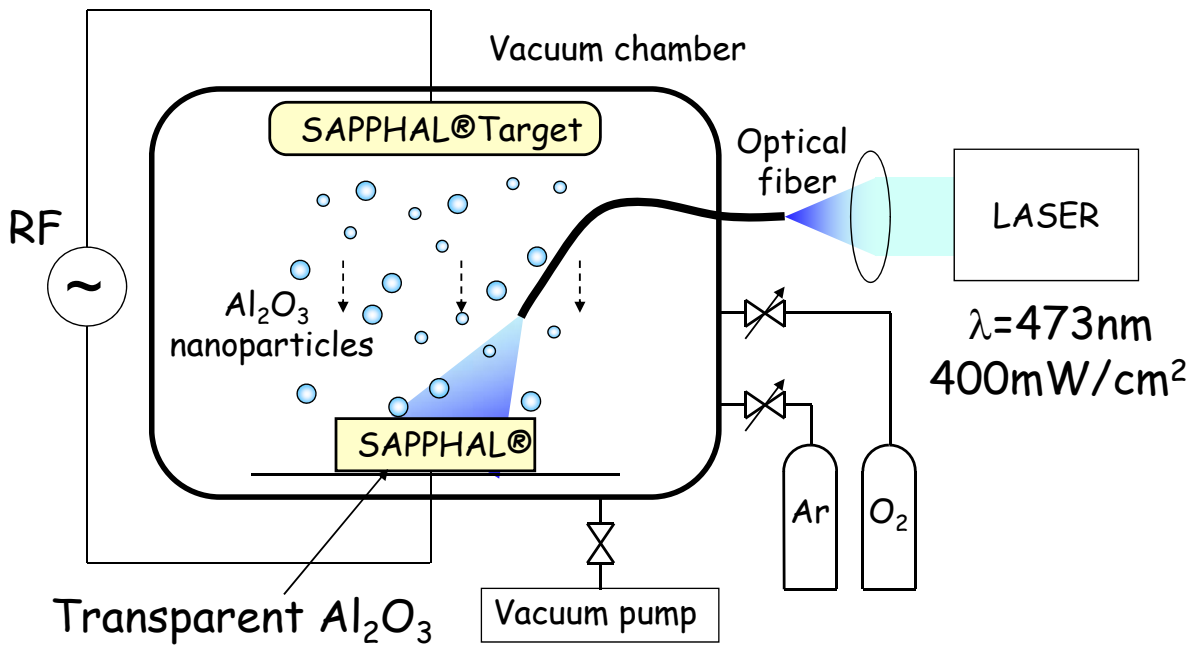
(3) Polishing with diamond slurries using  
**Chemical-Mechanical Polishing**  
Ra < 5nm





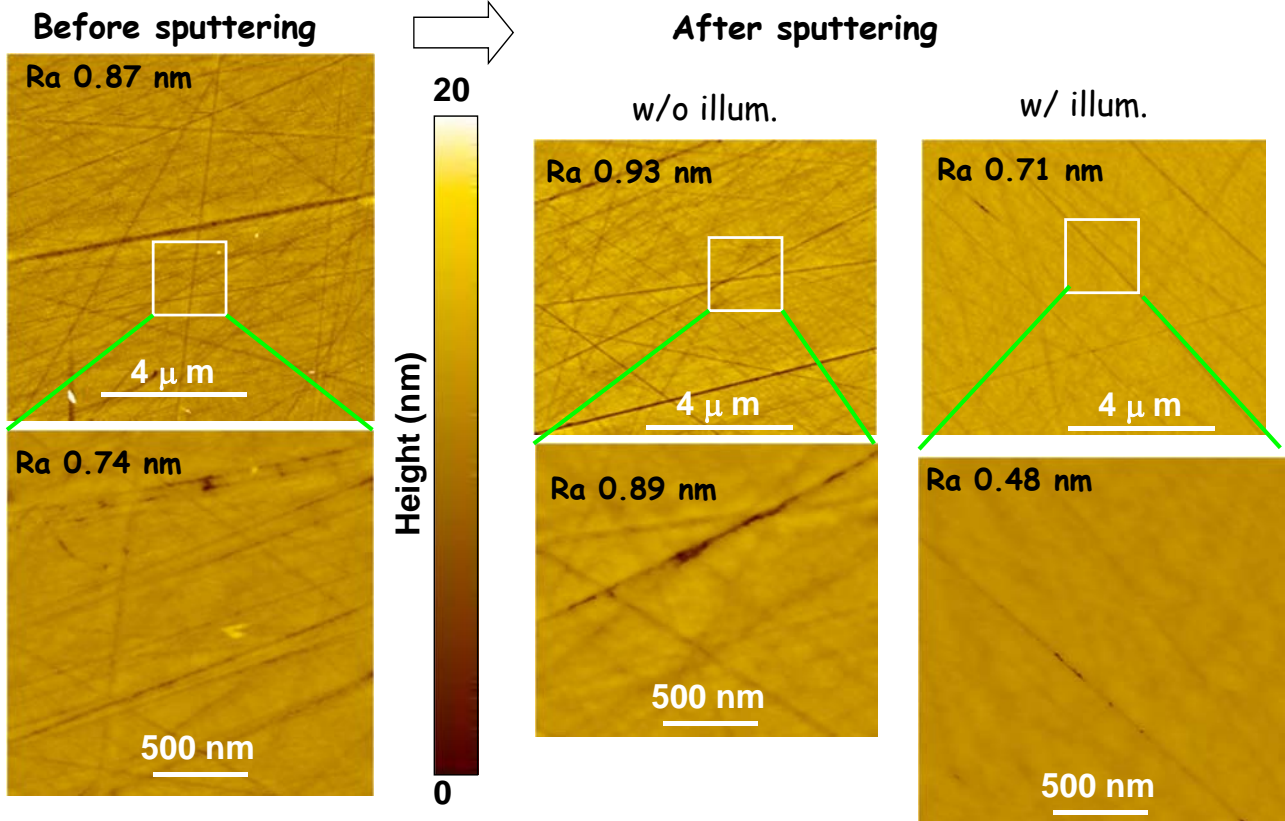
T. Yatsui et al., Nano Lett. 5, 2548 (2005)

17/36

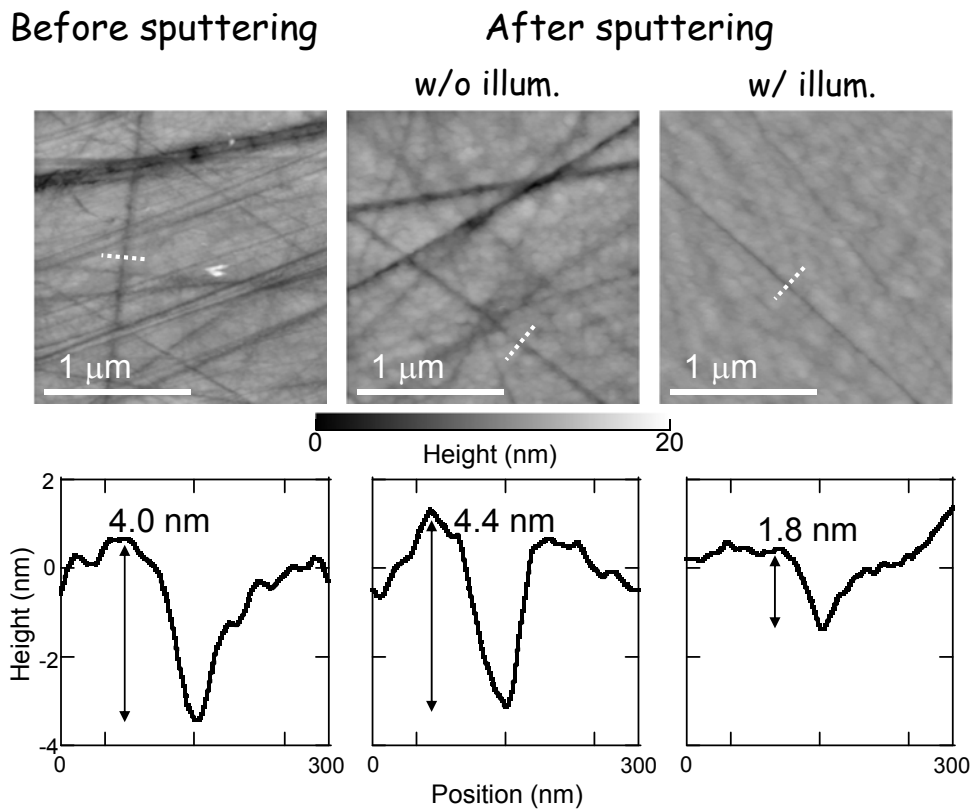


Absorption band edge energy of  $Al_2O_3 \sim \lambda = 250 \text{ nm}$

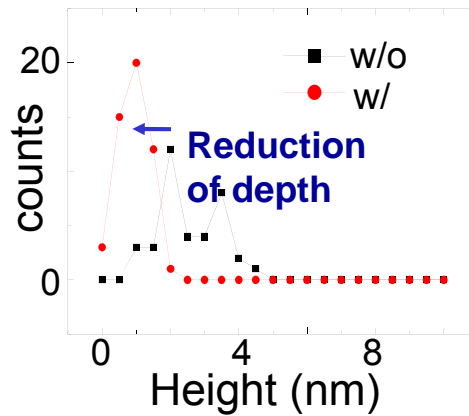
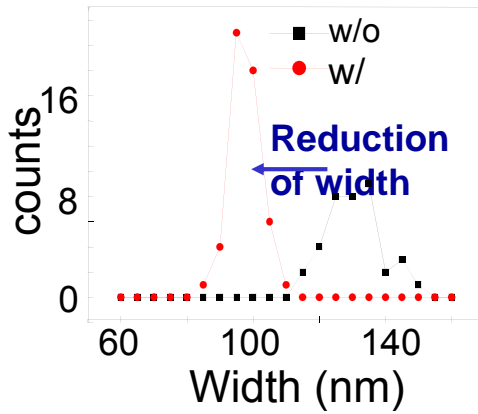
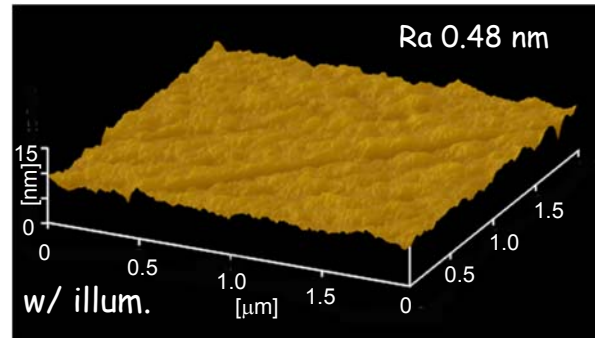
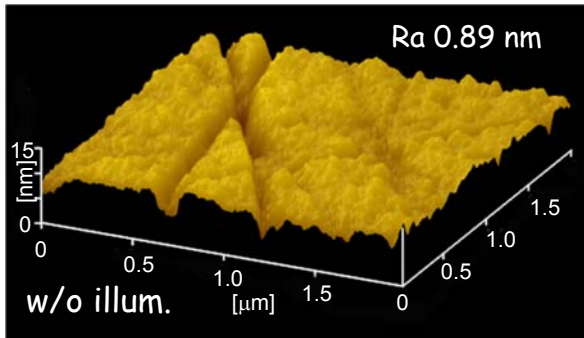
18/36



19/36



20/36

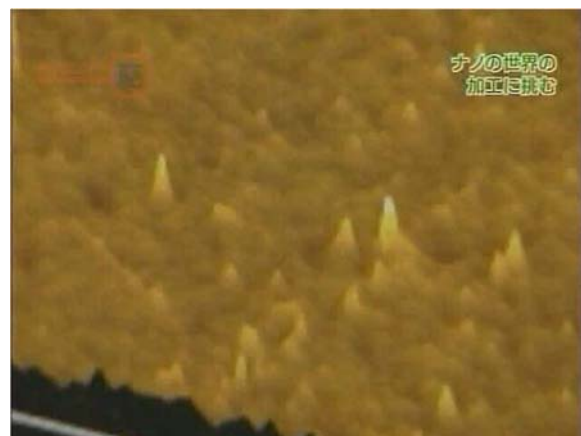


21/36

W. Nomura et al., Appl. Phys. B, 99, 75 (2009)



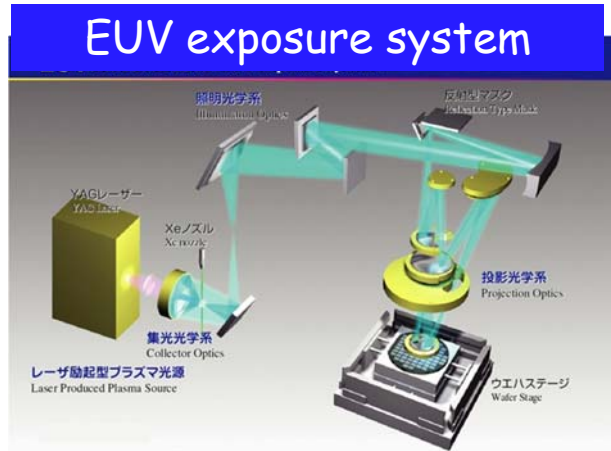
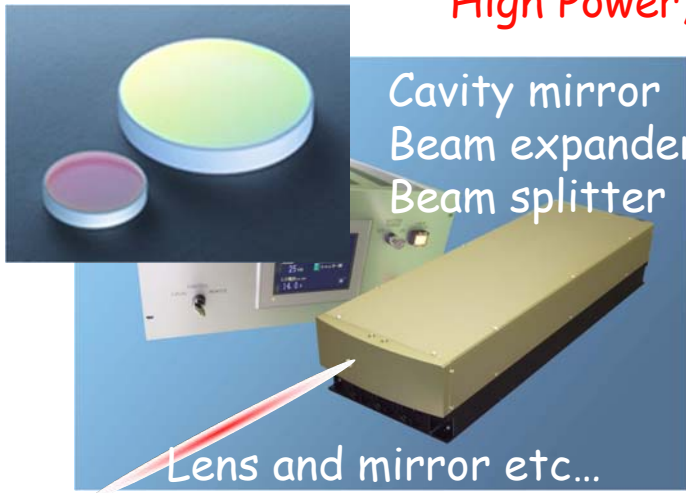
- Increasing spatial homogeneity
- Realizing ultra-flat surface in Å scale
  - Using near-field desorption
  - Using near-field etching



22/36



Ultra-flat sub. with sub-nm roughness:  
High Power, fs pulse, EUV, HDD, etc...



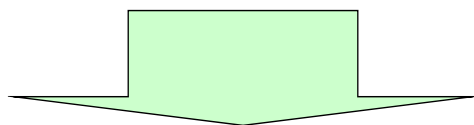
<http://www.euva.or.jp/>

Requirement of ultra flat surface with **Ra < 1A**  
for the reduction of scattering loss

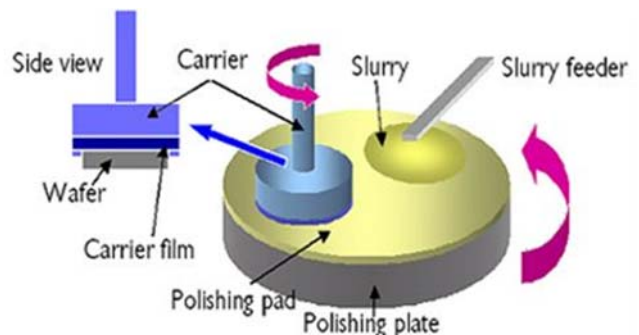
23/36



Galileo Galilei  
1564- 1642



Chemical-Mechanical polishing  
lower limit of Ra ~ **2A**  
Pad roughness ~ 10μm



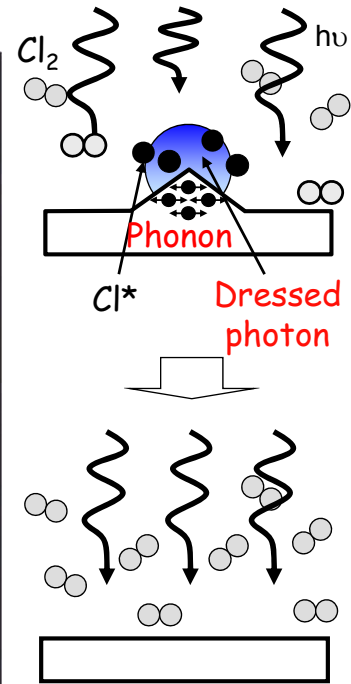
<http://chemelab.ucsd.edu/>

24/36

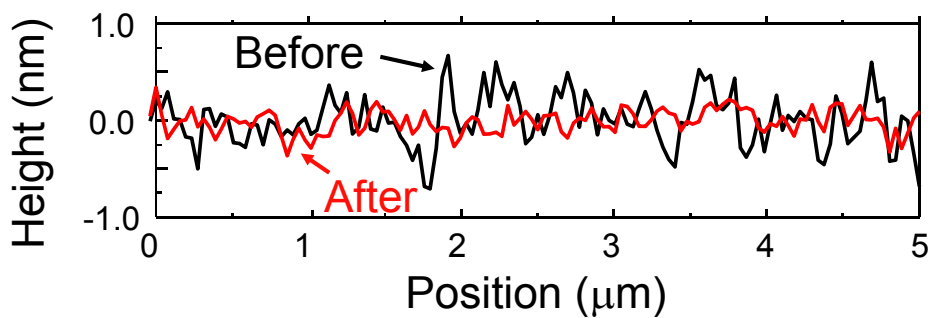
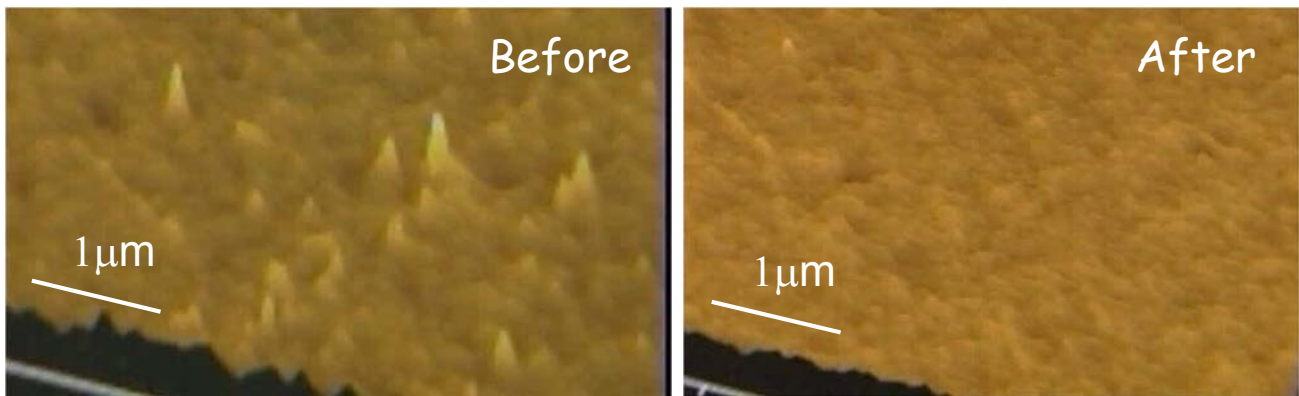


$\lambda=532\text{nm}$

Absorption edge of  $\text{Cl}_2 \sim \lambda=400\text{nm}$

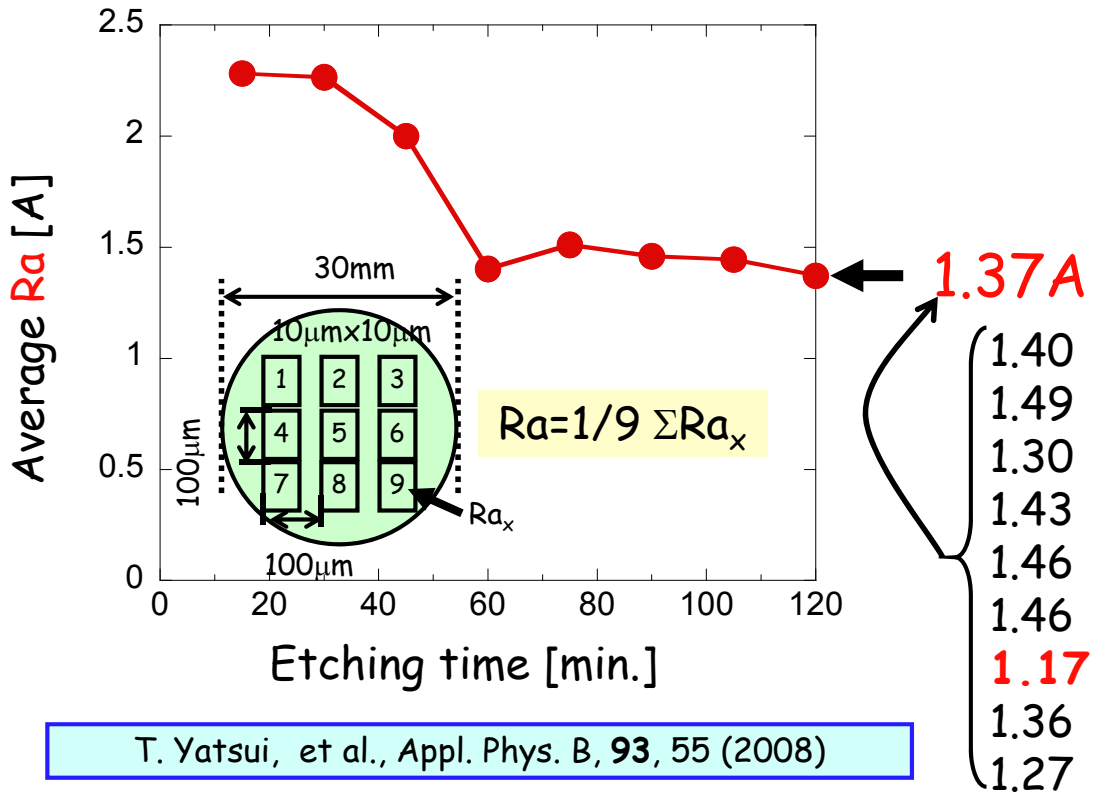


- $\text{Cl}_2$  is selectively photodissociated at the protrusions
- The activated Cl atoms etch away the protrusions
- 25/36 ➢ NF etching automatically stop when the substrate become sufficiently flat





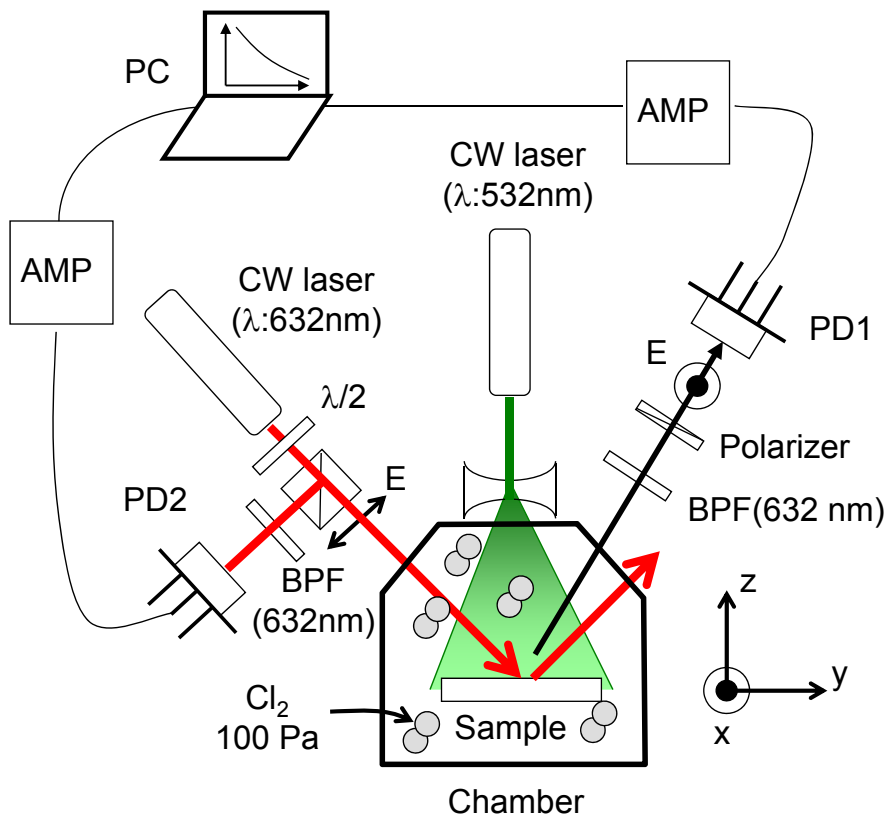
# Time dependence of average Ra



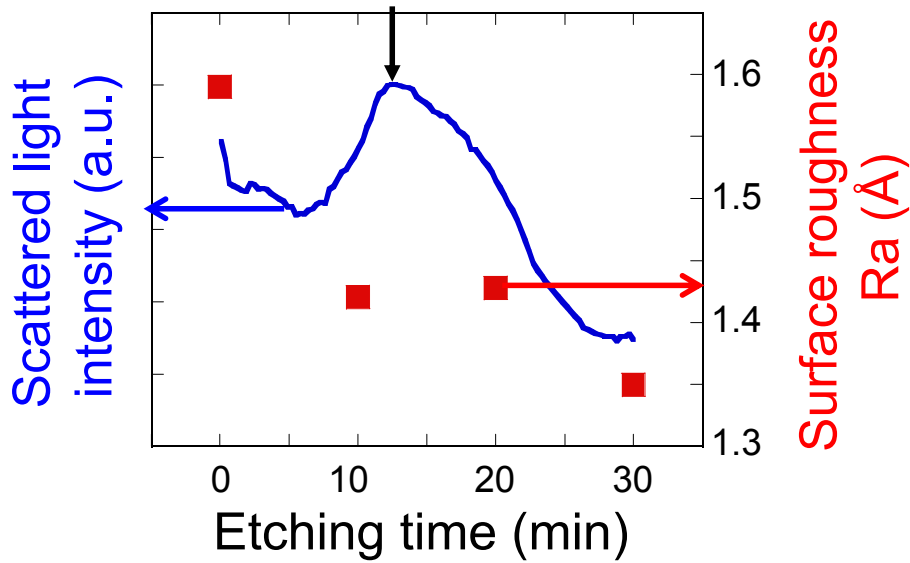
27/36



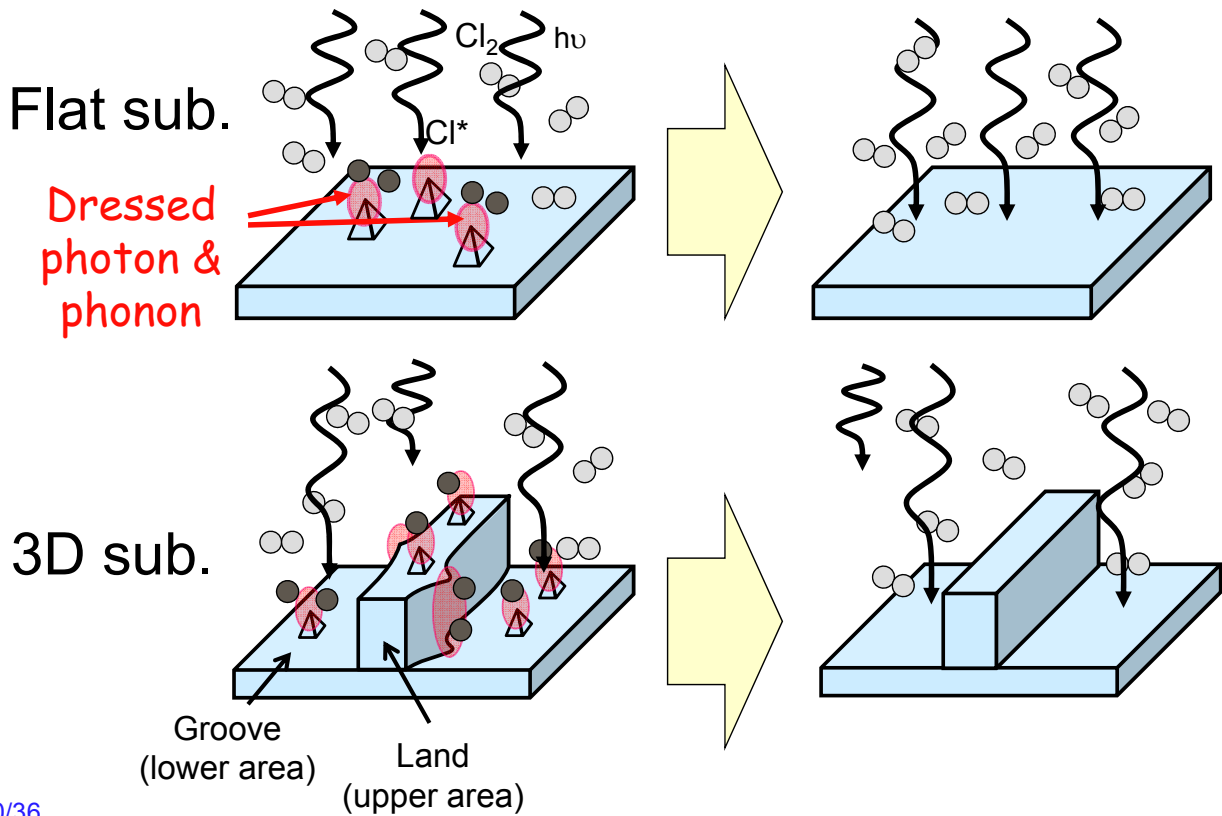
# In situ real-time monitoring of changes in surface roughness



28/36



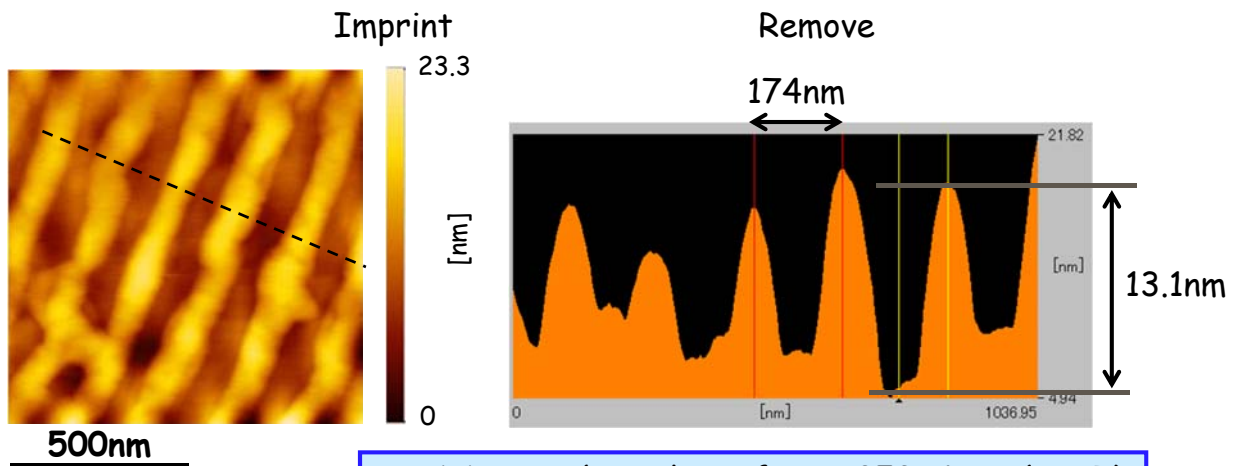
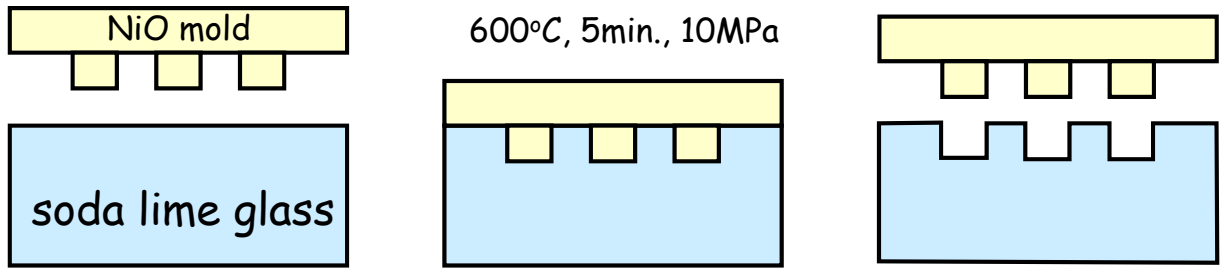
T. Yatsui et al., *Nanotechnology* **21**, 355303 (2010)  
<http://nanotechweb.org/cws/article/lab/43766>







# Nano-wall substrate



S. Akiba *et al.*, *Appl. Surf. Sci.* **253**, 4512 (2007)

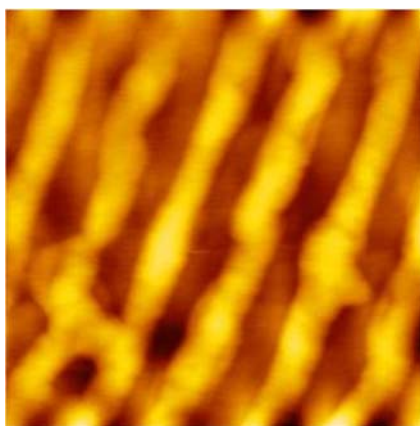
31/36



# Near-field etching on nano-wall substrate

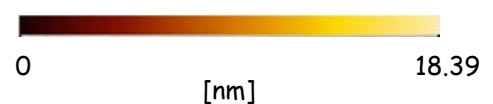
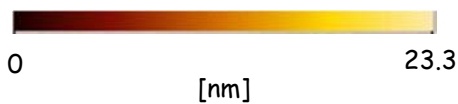
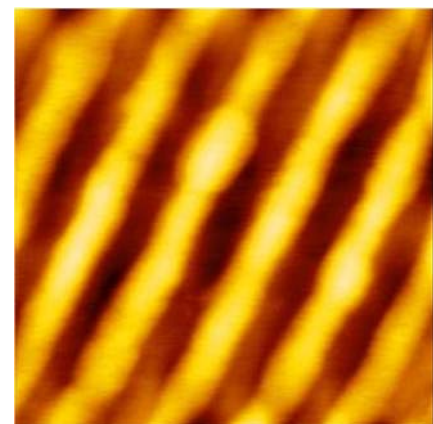


Before



Flow rate: 100sccm  
 Cl<sub>2</sub> press.: 100Pa  
 Wavelength: 532nm  
 Laser intensity: 2W  
 Etching time: 30min

After



32/36



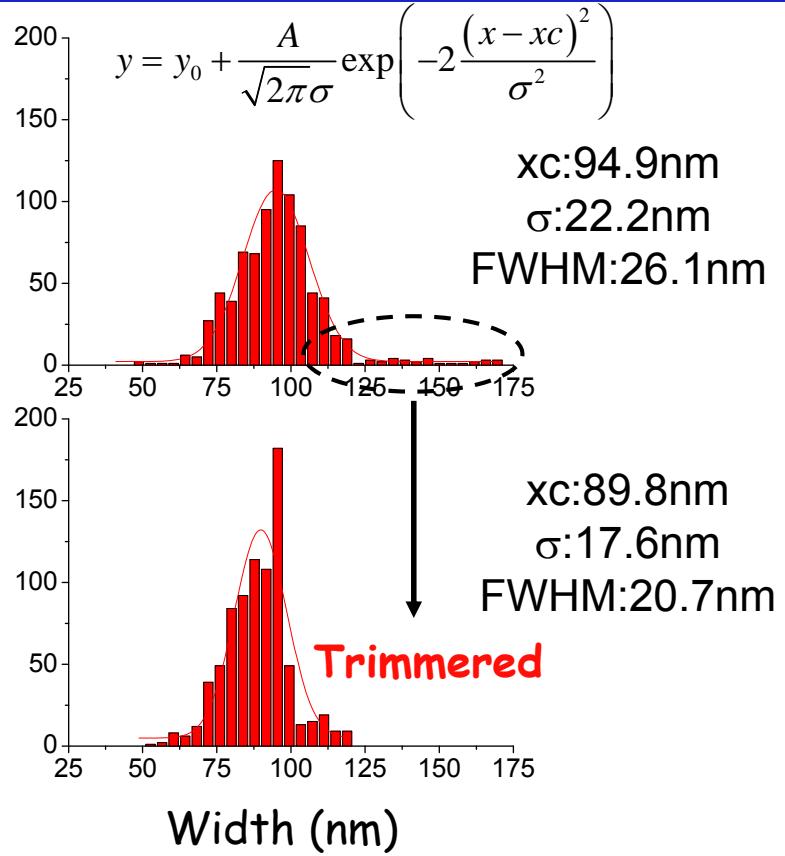
# Near-field etching on nano-wall substrate



Before



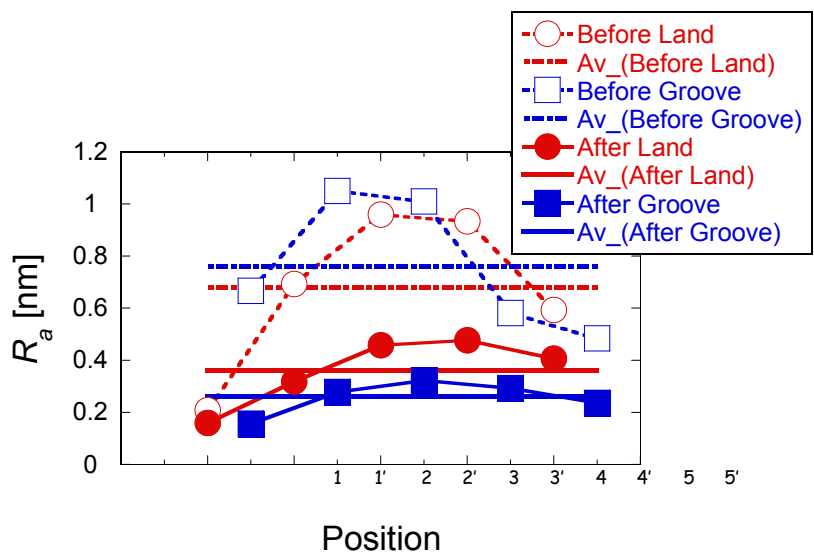
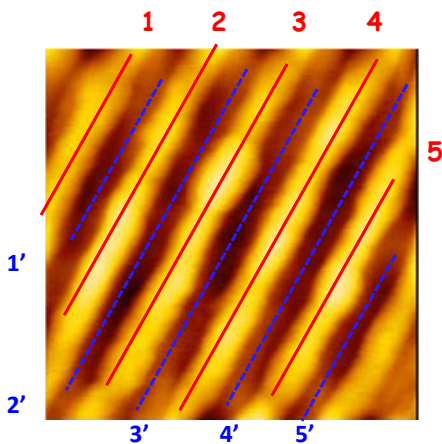
After



33/36

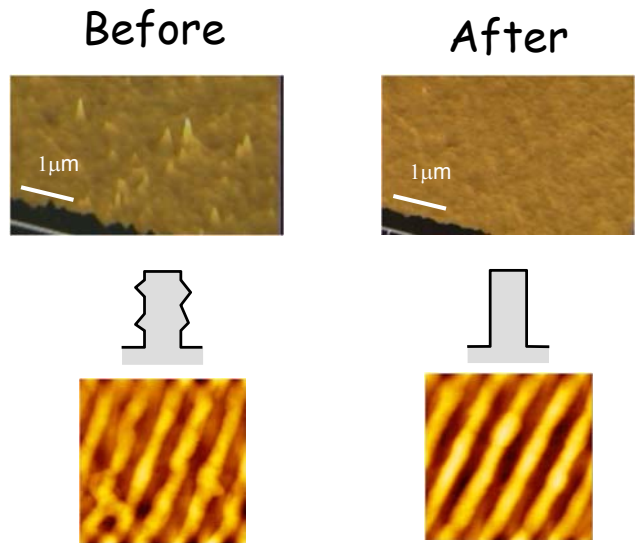
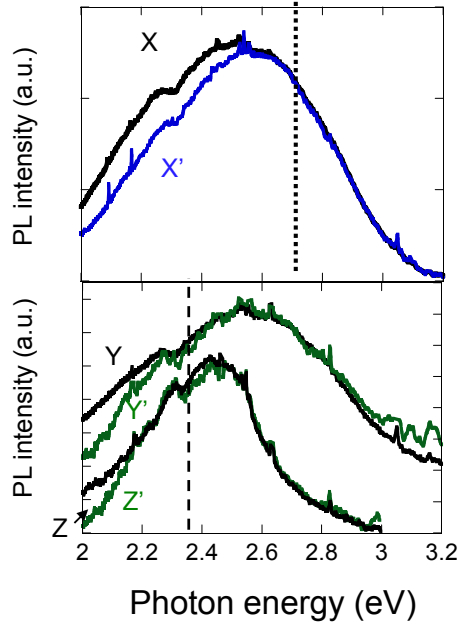


# Near-field etching on nano-wall substrate



T. Yatsui, et al., Appl. Phys. B, 103, 527 (2011)

34/36



➤ Applicable to **MOCVD**, **MBE**, **PLD** & other materials (**InGaAs**)

➤ Applicable to various structure: convex & concave lens, hollow structure, etc...

35/36

Thanks a lot!



For more information: Takashi Yatsui  
 yatsui@ee.t.u-tokyo.ac.jp  
 www.lux.t.u-tokyo.ac.jp/index.html

## Efficient light emitting diodes using indirect-transition semiconductors driven by dressed photons

T. Kawazoe and M. Ohtsu

Dept. Electrical Eng. and Information Systems, the Univ. of Tokyo,  
also with Nanophotonics Research Center, the Univ. of Tokyo  
2-11-16 Yayoi, Bunkyo-ku, Tokyo 113-8656, Japan  
Email: kawazoe@ee.t.u-tokyo.ac.jp

At present, semiconductor light emitting diodes (LEDs) are fabricated by using direct-transition semiconductors (DTSs), *e.g.*, InGaAs, AlGaInP, InGaN, and so on. This is because the emission efficiency of indirect-transition semiconductors (ITSs), *e.g.*, Si, GaP and so on, is much lower than that of DTSs. However, dressed photon (DP) technology [1] is able to increase the emission efficiency of ITSs. Since DPs are strongly coupled with phonons with large wave numbers, the wave number conservation law does not govern the electron transition probability in ITSs. Recently, we have demonstrated an efficient, bulk Si LED driven by DPs generated at the inhomogeneous domain boundary of a dopant in the p–n junction [2].

There are two processes in fabricating a DP device (*e.g.*, LED) using an ITS: (1) Forward current is applied to the ITS substrate containing the p–n junction to diffuse the dopant, whose spatial density fluctuates, by Joule heating to construct a domain boundary that acts as a DP generator. (2) During process (1), the p–n junction is irradiated with laser light to stabilize the DP generator by stimulated emission, which decreases the Joule heating. This stimulated emission stops diffusion of the dopant once the shape of the domain boundary is suitable for generating DPs. This is because the Joule heating is regulated by the stimulated emission. The efficiency of spontaneous emission is proportional to that of the stimulated emission. Therefore, as a result of competition between the deformation by process (1) and the solidification of the domain boundary by process (2), many “radiative” relaxation paths are formed via DPs in the p–n junction. Because DPs are not governed by the wave number conservation law, the LEDs fabricated by these processes are efficient, even though they use ITSs.

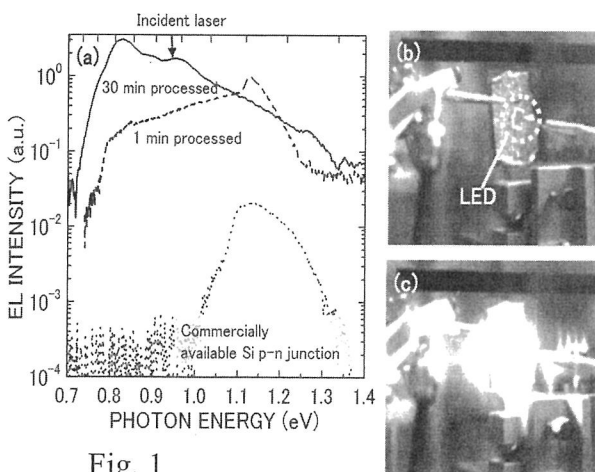


Fig. 1

Figure 1(a) shows the electroluminescence (EL) spectra of unprocessed and processed Si LEDs. The EL intensity of the processed Si LED (solid line) was about 100 times stronger than that of the unprocessed Si LED. The EL photon energy shifted toward that of the laser light used ( $\hbar\omega = 0.95$  eV). Figures. 1(b) and (c) show infrared photographs of the external appearance of the processed device with and without currents ( $4.2$  A/cm<sup>2</sup>) at

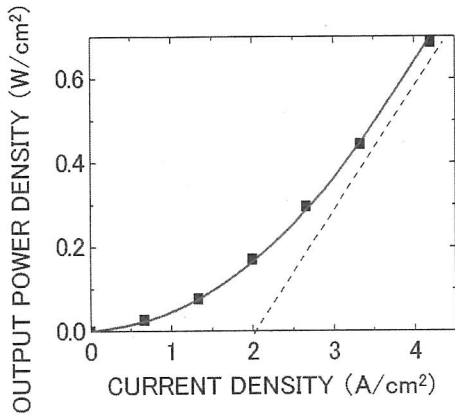


Fig. 2

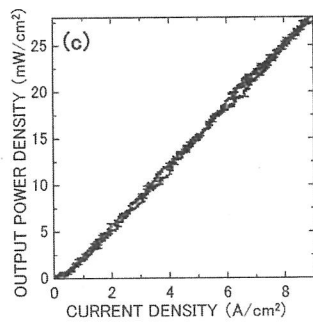
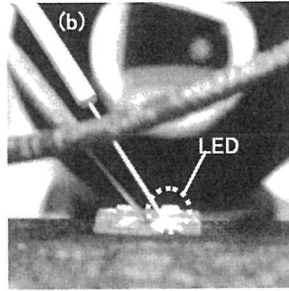
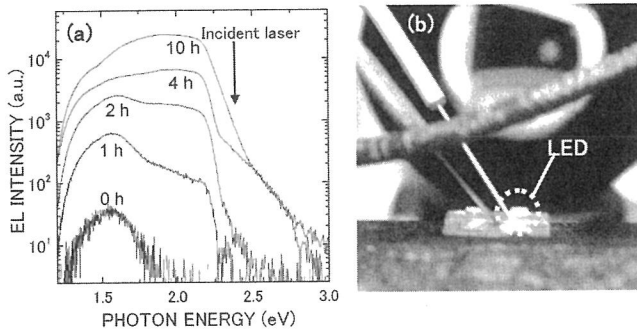


Fig. 3

room temperature under room lighting.

Figure 2 shows the current density dependence of the optical output power density in the energy region higher than the photon energy  $\hbar\omega = 0.73$  eV. The measured values were fitted by the quadratic curve shown by the solid line. This is because the two-photon spontaneous emission process [2] is dominant. When the current density was  $4.0$  A/cm<sup>2</sup>, the external quantum efficiency (QE) was 15%, which is as high as that of a commercial LED.

Figure 3(a) shows the EL spectra from unprocessed (0 hour) and processed (1–10 hours) GaP LEDs. The EL intensity of the 10-hour processed GaP LED was about 1000 times stronger than that of the unprocessed LED. The EL photon energy shifted toward that of the laser light used ( $\hbar\omega = 2.33$  eV).

Figure 3(b) shows a visible-light photograph

of the external appearance of the device with a current density of  $8.9$  A/cm<sup>2</sup> at room temperature under room lighting.

Figure 3(c) shows the current density dependence of the optical output power density. The output power density linearly increased with increasing current density. This is because the single-photon spontaneous emission process [2] is dominant. When the current density was  $8.0$  A/cm<sup>2</sup>, the external QE was 0.2%, which is considerably high for an ITS. We estimated that the QE may reach

more than 10% by improving the electrodes, making this GaP LED a promising device to resolve the “green gap” problem.

In the presentation, other applications of the fabrication process and fabricated devices will be also described, *e.g.*, ZnO LEDs, Si lasers, and pulse generators.

[1] M. Ohtsu, et al., IEEE J. Sel. Top. Quantum Electron. **14**, 1404 (2008).

[2] T. Kawazoe, M.A. Mueed, and M. Ohtsu, Appl. Phys. B, **104**, P747 (2011).



**Tadashi Kawazoe.** He received the degree of Ph.D. in physics from University of Tsukuba, Tsukuba, Japan, in 1996, respectively. In 1996, he joined the faculty of Engineering, Yamagata University, Japan, as a research associate. In 2000, he has been with Japan Science and Technology Corporation, Japan. In 2007, he joined the University of Tokyo as a projected associated professor and as a projected researcher since 2011. Dr. Kawazoe is a member of the Japan Society of Applied Physics and the Physical Society of Japan.

## Emission from a dipole-forbidden energy state in ZnO quantum dots induced by the near-field interaction

T. Yatsui<sup>1</sup>, M. Tsuji<sup>1</sup>, Y. Liu<sup>1</sup>, T. Kawazoe<sup>1</sup>, A. Neogi<sup>2</sup>, and M. Ohtsu<sup>1</sup>

<sup>1</sup> School of Engineering, the University of Tokyo, Japan

2-11-16 Yayoi, Bunkyo-ku, Tokyo 113-8656, Japan

<sup>2</sup> Department of Physics, University of North Texas, Denton, Texas 76203

Email: yatsui@ee.t.u-tokyo.ac.jp

To reduce the size of photonic devices below the diffraction limit, we have proposed nanophotonic devices<sup>1</sup> that consist of semiconductor quantum dots (QDs). In a nanophotonic device, the dipole-forbidden energy-transition<sup>2</sup> can reduce the size of device beyond the diffraction limit of light and achieve the unidirectional energy transfer, which is unattainable in conventional photonic devices. The dipole-forbidden energy transition originates from an exchange of the virtual photons between the resonant energy states. The use of virtual photons activates dipole-forbidden energy state. Although emission from the dipole-forbidden energy state cannot be detected in the far field, it can be utilized when the nanoparticle and detector are in close proximity. Here, we report direct observation of emission from an optically forbidden level in ZnO QDs using the near-field interaction induced by a fiber probe.

ZnO colloidal QD was synthesized using sol-gel method<sup>3</sup>. The average diameter of fabricated ZnO QD was 4 nm. The synthesized ZnO QDs were dispersed uniformly over a sapphire substrate. The red open circles in Fig. 1A and the blue open circles in Fig. 1B represent the far-field and near-field spectra which were obtained with the probe-to-sample distance of 6  $\mu\text{m}$  and 5nm, respectively.

To observe the changes between far- and near-field spectra, we considered the quantized energy levels in ZnO QDs. QDs synthesized by the sol-gel method are known to be spherical, although the crystalline structure of ZnO QDs is wurtzite<sup>4</sup>. In the present study, the QD shape was assumed to be spherical with radius  $R$ , and the quantized energy levels were calculated as 3.423 eV ( $E_1$ , dipole-active state), 3.4780 eV ( $E_2$ , dipole-forbidden state), and 3.551 eV ( $E_3$ , dipole-active state), respectively<sup>5</sup>. Using these energy values, we fitted the PL spectra using Lorentzian functions, shown as solid red, blue, and green lines, respectively, in Figs. 1A and 1B. The fitted profiles were used to determine near/far ratios, i.e., the ratio between the peak intensities of each near/far spectrum (Table 1). The peak intensity of  $E_2$  increased drastically as the fiber probe approached the ZnO QDs, whereas the peak intensity of  $E_1$  remained constant. The increase in the peak intensity of  $E_3$  was due to the higher excitation photon energy of 3.81 eV.

In conclusion, we achieved direct observation of emission from an optically forbidden level in ZnO QDs. By introducing a near-field fiber probe in close proximity to the QDs, we observed increased emission intensity from the dipole-forbidden. Because the decay time of the dipole-forbidden state is longer than that of the dipole-active state by  $10^6$ , the dipole-forbidden state can be used to realize novel devices such as optical buffer memory, and signal-transmission devices.

**Acknowledgment.** This work was partially supported by The University of Tokyo Global COE Program “Secure-Life Electronics” MEXT, a Grant-in-Aid for Young Scientists (A), JSPS, and a Research Grant (Basic Research) from the TEPCO memorial foundation.

**Reference** [1] M. Ohtsu *et al.*, *IEEE J. Select. Top. Quant. Electron.*, **2008**, *14*, 1404. [2] K. Mukai *et al.*, *J. Phys. Chem. B*, **1999**, *103*, 1. [3] Y. Liu *et al.*, *Nanotechnology*, **2011**, *22*, 215605. [4] L. Zhang *et al.*, *Appl. Mat. Inter.*, **2010**, *2*, 1769. [5] N. Sakakura and Y. Masumoto, *Phys. Rev. B* **1997**, *56*, 4051



**Takashi Yatsui** was born in Tokyo, Japan, on January 21, 1972. He received his B.E. degree from Keio University, Tokyo, Japan in 1995 and M.E. and D.E. degrees from Tokyo Institute of Technology, Tokyo, Japan in 1997 and 2000, respectively.

From 1999 to 2000, he was a Research Fellow of the Japan Society for the Promotion of Science. From 2000 to 2008, he was a Researcher at the Japan Science and Technology Agency, Tokyo. In 2008, he joined the University of Tokyo as an Associate Professor. His current research interests include nanofabrication using optical near-field and its application to nanophotonics.

Dr. Yatsui received the Excellent Research Presentation award from the Japan Society of Applied Physics in 2000, Tejima Doctoral Dissertation Award from the Tejima Foundation in 2001, and the Gottfried Wagener Prize 2010.

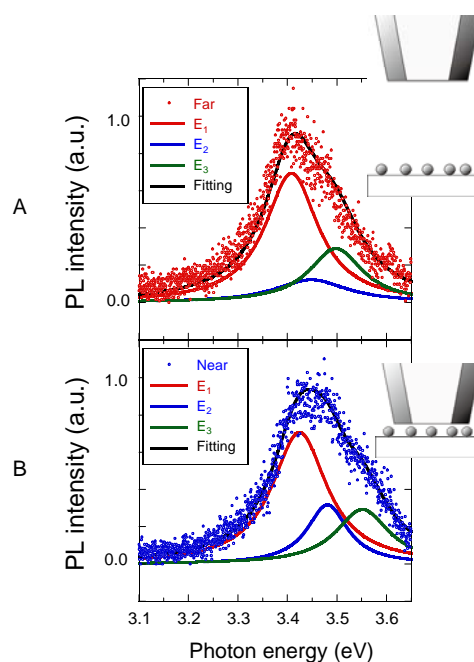


Fig. 1. Far-field (A, red open circles) and near-field (B, blue open circles) PL spectra of ZnO QDs. The respective separation between the fiber and ZnO QD was (a) 1  $\mu\text{m}$  and (b) 5 nm, respectively.

Table 1 The ratio between near-field and far-field intensity.

	Far (Fig. 1A)	Near (Fig. 1B)	Near/Far ratio
$E_1$	0.78	0.72	0.92
$E_2$	0.12	0.31	2.58

### Notes:

### Abstract Summaries:

#### **The Magic of the Dressed Photon (OP4)**

*Motoichi Ohtsu*

This presentation reviews the principles of generation and detection of the dressed photon, which is a quasi-particle representing the coupled state of a photon and an electron in nanometric space. After the possibility of coupling with multi-mode photons is discussed, some novel fabrication technologies that exploit the unique features of dressed photons are demonstrated. They are: (1) High-resolution photolithography using a green light-emitting diode as a light source, and its application to fabricating soft X-ray optical devices. (2) Self-proceeding photochemical etching for realizing an ultra-flat glass surface with a roughness as low as 0.1 nm for fabricating laser mirrors with a high damage threshold. (3) Annealing of bulk Si crystals, and its application to fabricating high-efficiency light emitting devices. These applications demonstrate that dressed photon technology has realized qualitative innovations in optical technology that would otherwise be impossible using conventional propagating light. The future outlook of this novel technology will be presented.



## STOCHASTIC MODELING OF MORPHOLOGY FORMATION BY A PHONON-ASSISTED OPTICAL NEAR-FIELD PROCESS

M. Naruse<sup>1</sup>, T. Kawazoe<sup>2</sup>, T. Yatsui<sup>2</sup>, N. Tate<sup>2</sup>, and M. Ohtsu<sup>2</sup>

<sup>1</sup>National Institute of Information and Communications Technology,  
4-2-1 Nukui-kita, Koganei, Tokyo 184-8795, Japan.

<sup>2</sup>Department of Electrical Engineering and Information Systems and Nanophotonics Research Center,  
School of Engineering, The University of Tokyo, Tokyo 113-8656, Japan  
E-mail: naruse@nict.go.jp

We previously reported in [1] that by depositing an Ag electrode on a photovoltaic device composed of P3HT and ZnO under light illumination (wavelength = 660 nm) while reversely biasing the P3HT/ZnO pn junction, a unique granular Ag film was formed, as shown in Fig. 1(a) (the conditions are summarized in the inset of Fig. 1(b)). This Ag film generated a photocurrent at wavelengths as long as 670 nm, which is longer than the long-wavelength cutoff  $\lambda_c$  (= 570 nm) of P3HT. We consider that such an effect originates from a phonon-assisted process induced by an optical near-field. In this study, we analyzed the morphological character of the Ag clusters and built a stochastic model in order to understand the principles behind the formation process, and to optimize device performance in future. Fig. 1(b) represents the incidence pattern as a function of the size of Ag clusters, obtained by analyzing the SEM images in Fig. 1(a). A number of small clusters were observed in cases (ii) and (iii), but some of them were large. Also, as depicted by arrows in Fig. 1(b), the incidence increased at a particular cluster size. Also note that the increase appeared at a larger size with smaller light irradiation. As a stochastic model, we calculate what we call the “pseudo footprint”, denoted by  $S$  hereafter, in each square grid cell, corresponding to the sum of the areas of its eight neighbors. For example,  $S$  is equal to 20 for the point  $P$  in the example in Fig. 1(c).  $S$  represent the physical effects of the light irradiation and the electrical bias voltage. If the calculated value of  $S$  is smaller than a threshold  $Z$ , an arriving particle is able to land on the point  $P$ ; in contrast, if  $P$  is occupied, the arriving particle will sit in a free, randomly chosen neighbor, representing a diffusion process. If  $S$  is larger than  $Z$ , the arriving particle is deflected outside the system, representing repulsion between the arriving positively charged Ag particle and the positively charged clusters on the surface due to the reverse bias. By iteratively applying such a stochastic process, a variety of spatial patterns were generated. The stochastic properties, that is to say, the incidence pattern, converged to the profile shown in Fig. 1(d). The incidence pattern exhibited different characters depending on the threshold value ( $Z = 5, 10, 20$ ): with larger  $Z$ , the area of the cluster yielding the peak incidence shifted towards a larger value, which agrees with the experimentally observed character in Fig. 1(b), where larger optical light irradiation produces smaller clusters.

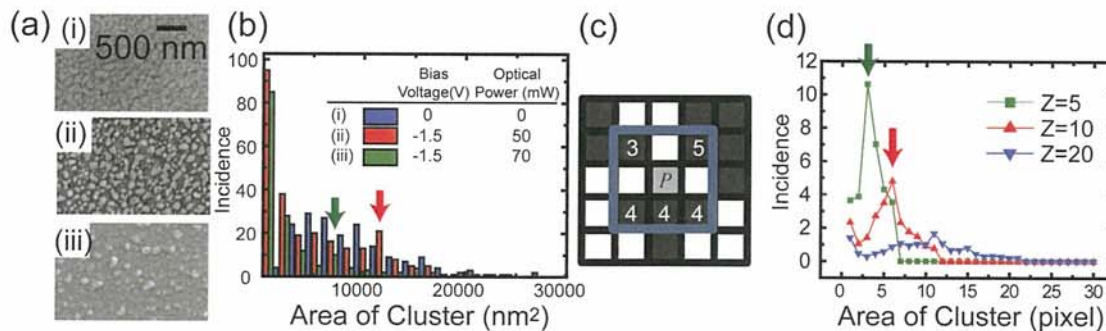


Fig. 1: (a) SEM images of Ag surfaces on P3HT. (b) Image analysis of surfaces (i), (ii), and (iii) in (a). (c) Stochastic modeling. (d) Converged incidence patterns of clusters for different thresholds  $Z$ .

**References** [1] S. Yukutake, et al., Appl. Phys. B **99**, 415-422 (2010).

## CONTROLLING THE SIZE AND VARIANCE OF ZNO QUANTUM DOT DIAMETER USING PHOTO-ASSISTING SOL-GEL METHOD

*Y. Liu, T. Yatsui, T. Kawazoe, and M. Ohtsu*

*Department of Electrical Engineering and Information Systems, School of Engineering, the University of Tokyo, Tokyo 113-8656, Japan*

*E-mail: [ryu@nanophotonics.t.u-tokyo.ac.jp](mailto:ryu@nanophotonics.t.u-tokyo.ac.jp)*

Recently, techniques involving ZnO quantum dots (QDs) have been used to produce nanophotonic devices [1]. To achieve high-performance nanophotonic devices, it is necessary to decrease ZnO QD size variance to resonate the discrete exciton energy level of QDs. However, in conventional sol-gel ZnO QD synthesis, QD size variance exceeds 20%. To reduce size variance, it is necessary to reduce the size of large QDs and increase the size of small QDs. We found that it was possible to reduce the size of large ZnO QDs using the photon-assisted sol-gel method with a continuum-wave He-Cd light ( $\lambda = 325$  nm). Because the irradiated light was shorter than the absorption band edge wavelength of ZnO ( $\lambda_{ab}(\text{ZnO}) = 380$  nm), illumination induced the oxidation-reduction process, etching the ZnO QDs. Thus, we decreased the size of large QDs and reduced variance from 23 to 17% [2].

To increase the size of small QDs, we irradiated the ZnO QDs with 660-nm light, which is longer than  $\lambda_{ab}(\text{ZnO})$ . Wavelengths longer than  $\lambda_{ab}(\text{ZnO})$  did not induce etching because no ZnO QD carriers were excited; however, the dressed photons in ZnO QDs were excited [3]. Thus, when the ZnO precursors were in close proximity to the QDs, the excited dressed photons accelerated ZnO deposition onto QDs. To confirm this, we performed QD growth with 660-nm irradiation using the sol-gel method. Figure 1 shows the growth-time dependence of ZnO QD size; irradiation with 660-nm light during growth resulted in increased QD size. Further reduction in ZnO QD size variance can be achieved using a combination of etching and deposition.

### Reference:

- [1] T. Yatsui *et al.*, APL **96**, 133106 (2010).
- [2] Y. Liu *et al.*, Nanotech. **22**, 215605 (2011).
- [3] M. Ohtsu *et al.*, IEEE JSTQE, **14**, 1404 (2008)

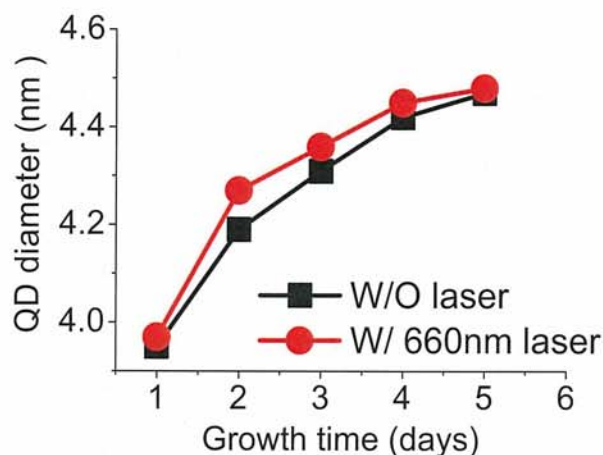


Fig. 1 Growth-time dependence of ZnO QD diameter.

## NANOPHOTONIC DROPLET: AUTONOMOUS CAPSULATION OF SORT-SELECTIVE QUANTUM DOT PAIRS BASED ON PHONON-ASSISTED PROCESS

N. Tate<sup>1</sup>, Y. Liy<sup>1</sup>, T. Kawazoe<sup>1</sup>, M. Naruse<sup>1,2</sup>, T. Yatsui<sup>1</sup> and M. Ohtsu<sup>1</sup>

<sup>1</sup>The University of Tokyo, <sup>2</sup>National Institute of Information and Communications Technology  
tate@nanophotonics.t.u-tokyo.ac.jp

Nanophotonic devices utilizing optical near-field interactions induced between multiple nanometer-scale materials can realize several novel functions, such as logic gates and energy guides [1]. Here we propose a technique for autonomous encapsulation of quantum dot (QD) pairs at the submillimeter scale as *nanophotonic droplets* by utilizing a phonon-assisted optical near-field process via optical near-fields. This technique can efficiently induce optical near-field interactions between selected QDs, as well as the associated optical response. We experimentally formed a nanophotonic droplet containing ZnO and CdSe/ZnS QDs in a cured UV-curable polymer and verified the encapsulation process and the photoresponse characteristics of the nanophotonic droplets.

For an experimental demonstration, we used commercially available CdSe/ZnS QDs (*Ocean Optics*; absorption peak wavelength  $\lambda_{AB} = 600$  nm; emission peak wavelength  $\lambda_{EM} = 610$  nm) and ZnO QDs ( $\lambda_{AB} = 360$  nm;  $\lambda_{EM} = 365$  nm) that we prepared by sol-gel synthesis. The QDs were mixed with a UV-curable polymer (NORLAND NOA65; absorption edge wavelength: 350 nm) and were encapsulated to form nanophotonic droplets by irradiating them with 457 nm assisting light. These experimental conditions fulfilled specific energy conditions for the autonomous encapsulation process. Figure 1(a)

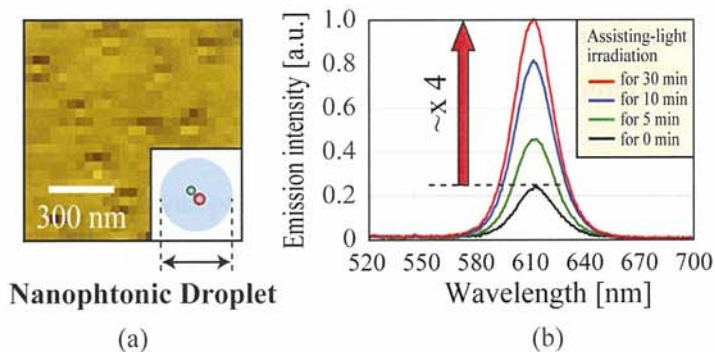


Fig. 1: (a) Schematic diagram of formation of nanophotonic droplet and its AFM image after 10 minutes irradiation with assisting light ( $\lambda = 457$  nm). (b) Emission spectra (325 nm excitation light) of several samples formed with various assisting-light irradiation times.

shows an AFM image of the nanophotonic droplets, which was spin-coated on a Si substrate. In order to verify the photoresponse characteristics of each sample, we measured the emission spectra with 325 nm excitation lights. As shown in Fig1(b), depending on the irradiation time of the assisting light, the emission intensity, which was derived from the CdSe/ZnS QDs, was successfully increased. The result indicates that ZnO QDs and CdSe/ZnS QDs in the nanophotonic droplets were closely positioned each other to induce preferable energy transfer between close QDs.

In our approach, several types of nanophotonic droplets realizing various optical functions can be formed by controlling the encapsulation parameters, such as the types and numbers of materials, the intensity and irradiation time of the assisting light, Brownian motion activity, and so on. Variation of these parameters will be directly revealed in the optical input–output relations of the nanophotonic droplets. Our concept will be important not only for high-quantum-efficiency optical devices, but also for devices that interface between nano- and macro-scale phenomena. Modifying the nanophotonic droplets will allow them to be used for other application fields, such as sensor elements and display elements.

### Reference:

[1] M. Ohtsu et al., *Principle of Nanophotonics* (Taylor & Francis, London, 2008).

## NUMERICAL SIMULATION FOR NON-ADIABATIC OPTICAL NEAR-FIELD ETCHING

Y. Fujiyoshi<sup>1\*</sup>, M. Haraguchi<sup>1</sup>, T. Okamoto<sup>1</sup>, T. Yatsui<sup>2</sup>, M. Ohtsu<sup>2</sup>, K. Hirata<sup>3</sup>, Y. Tabata<sup>3</sup>

<sup>1</sup>Department of Optical System and Technology, The University of Tokushima  
Minami jousanjima 2-1, Tokushima 770-8506, Japan

<sup>2</sup>Department of Electrical Engineering and Information Systems, School of Engineering,  
The University of Tokyo, 2-11-16 Yayoi, Bunkyo-ku, Tokyo 113-8656, Japan

<sup>3</sup>Sigma Koki Co. Ltd., 1-19-9 Midori, Sumida-ku, Tokyo 130-0021, Japan  
fujiyosi@opt.tokushima-u.ac.jp

Recently, non-adiabatic optical near-field etching [1] has been proposed as a new method providing an ultra-flat-surface substrate with sub-nm scale roughness. In order to reveal the optimal experimental conditions, it is required to develop a simulation method. Therefore, we have proposed already a simulation program for non-adiabatic near-field etching [2]. However, we did not consider the characteristics of optical near-field and phonon coupling, called the dressed-photon. Which allow etching only at a projection of the surface. In order to find the variation of the etched surface, we employed a step structure as an initial shape of the surface, as shown in Fig. 1(a). The height of the step is set a value in the range from 0 nm to 10 nm. After etching, we have never obtained a flattened surface without considering the characteristics of the dressed-photon, shown in Fig. 1 (b). On the other hand, we have obtained more flattened surface than before by using new program taking into account the characteristic of the dressed-photon, as shown in Fig. 1(c).

This work was partially supported by NEDO under the program of Strategic Development on Rationalization Technology using Energy.

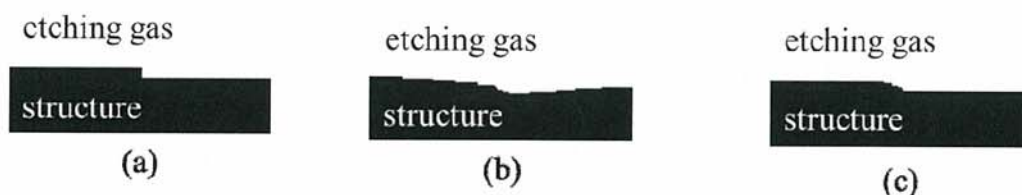


Fig 1 The surface shape of the initial structure (b) The surface shape of the after etching not considered the characteristics of dressed-photon (c) The surface shape after etching when considered the characteristics of dressed-photon

[1] T. Yatsui, K. Hirata, W. Nomura, Y. Tabata, and M. Ohtsu, *Appl. Phys. B* 93, 55 (2008).

[2] Y. Fujiyoshi, Technical digest of APNFO-7, P182 (2009).

## Long-range optical energy transfer between randomly distributed resonant quantum dots

Wataru Nomura<sup>1</sup>, Takashi Yatsui<sup>1</sup>, Tadashi Kawazoe<sup>1</sup>, Makoto Naruse<sup>2,1</sup>, Motoichi Ohtsu<sup>1</sup>  
<sup>1</sup>School of Engineering, The University of Tokyo, and The Nanophotonics Research Center, The University of Tokyo, Bunkyo-ku, Tokyo, 113-8656, Japan  
<sup>2</sup>National Institute of Information and Communications Technology, 4-2-1 Nukui-kita, Koganei, Tokyo 184-8795, Japan  
 e-mail: nomura@nanophotonics.t.u-tokyo.ac.jp

An exciton in one of a set of closely distributed quantum dots (QDs) is transferred to the nearest QD with resonant energy levels via an optical near-field interaction [1]. We have previously confirmed micrometer-scale energy transfer between randomly dispersed QDs based on optical near-field interactions [2]. In the present study, we successfully observed the output emission after long-range energy transfer between resonant QDs and verified that this transfer was based on optical near-field interactions by comparing the result with that obtained from a non-resonant QD pair.

We employed three types of CdSe/ZnS core-shell QDs, designated as QDS, QDM, and QDL, whose emission wavelengths were 538 nm, 545 nm, and 585 nm, respectively. The ground state of the exciton in QDS was resonant with the first excited state in QDL. On the other hand, QDM was not resonant with QDL. As a *resonant sample*, we dispersed QDSs and QDLs in two orthogonal paths on a SiO<sub>2</sub> substrate by e-beam lithography and a lift-off process, as shown in Fig. 1. The width of the QDS path was 200 nm. For comparison, we also prepared a *non-resonant sample* using QDMs and QDLs in the same process.

The output emissions from these two samples were evaluated by using a HeCd-excitation laser and an EMCCD camera with a band-pass filter ( $\lambda = 590 \pm 5$  nm). QDS or QDM was irradiated with a spot of excitation laser light, which was a distance  $L$  away from intersection with the QDL path. Figure 2 shows the observed emission from QDL in the (a) resonant and (b) non-resonant samples, at  $L = 5$   $\mu$ m. The resonant sample showed an intensity at the intersection 7.5 times higher than the non-resonant sample. By evaluating the dependency of the output signal on  $L$  in the resonant sample, the energy transfer length of the resonant sample was estimated to be 6.2  $\mu$ m, which agreed well with the calculated results in our previous work [2].

### Acknowledgement

This work was supported by The New Energy and Industrial Technology Development Organization (NEDO) Special Courses: A comprehensive activity for personnel training and industry-academia collaboration based on NEDO projects.

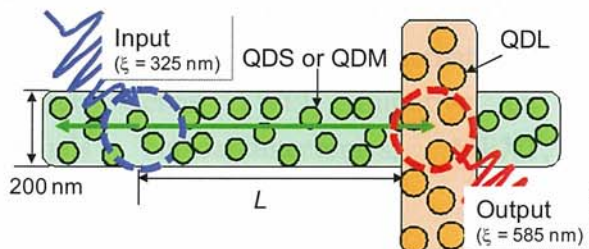


Fig. 1 Schematic diagram of fabricated sample and experimental conditions. Blue and red dashed circles indicate input and output ports, respectively.

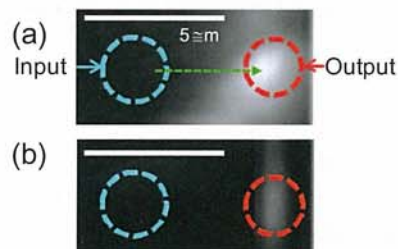


Fig. 2 CCD image of emission from QDL in (a) resonant and (b) non-resonant samples, respectively.

### References

- [1] M. Ohtsu et al., IEEE J. Selec. Top. Quant. Electron. **14**, 1404 (2008)
- [2] W. Nomura, T. Yatsui, T. Kawazoe, M. Naruse, and M. Ohtsu : Appl. Phys. B **100**, 181 (2010)

# [III] REVIEW PAPERS



# ナノ領域の光と物質との相互作用を用いた新機能デバイス

Innovative Optical Functional Devices by Dressed Photon Interactions

成瀬 誠 川添 忠 大津元一

## 1. はじめに

ナノ寸法での光と物質の相互作用を活用する技術の進展が著しく<sup>(1)</sup>、近年の材料技術や分析技術等の急速な進歩を受けて、光デバイスの単なる微細化にとどまらず広範な応用展開が技術ロードマップ<sup>(2)</sup>でも展望されるようになった。特にナノ物質近傍の近接場光<sup>(用語)</sup>を用いることで、従来の光（伝搬光）に不可避の回折限界が打破され光の微小化が実現された。更に、近接場光とはナノ寸法において光子と物質中の励起が結合した場であり、物質励起の衣をまとった光子（dressed photon, ドレスト光子<sup>(用語)</sup>）と捉えることで、光の微小化にとどまらない機能が可能になった<sup>(3)</sup>。本稿は、ドレスト光子に基づいた、①「配線型」から「励起移動型」へのデバイス基本構造の転換、並びに②波長変換・受発光デバイスという2個の具体例に大きく整理しつつ、最近のデバイスの実現例及び情報通信や環境・エネルギーなどの応用から見た顕著な特徴にも触れながら現状と今後を展望する。

従来の光（伝搬光、通信波長でおよそ1.5 μm）は、ナノ寸法の物質よりも十分に大きいため、物質に対しては通常は一樣に作用すると考える。この近似は長波長近似と呼ばれ、従来、差し当たって問題になることはなかった。しかし、ナノ寸法の局所領域には、ナノ寸法の物質に局在したドレスト光子があり、長波長近似が妥当ではなくなり、従来は禁制されていた過程もドレスト光子では許容されることがある<sup>(3)</sup>。2. では従来のデバイ

スとの差異を踏まえながら、ドレスト光子に基づいたデバイスの原理と最近の進展を示す。更に、ドレスト光子は格子振動（フォノン）と結合することも可能であり、ナノ寸法での物質の形状や寸法によっては入力となる伝搬光の光子エネルギーよりも大きなエネルギー状態へ物質中の電子を励起できる。これを本稿では「ドレスト光子によるフォノン援用過程」と呼ぶ。3. 及び4. ではこの過程を用いた光デバイスの例を示す。

## 2. ドレスト光子によるデバイス基本構造の転換

グリーンな情報通信技術の実現に向け光技術への期待は高いが、従来、その要点は、光電変換を可能な限り省略し、電気的処理に不可避の電力消費を削減することにある<sup>(4)</sup>。このことは同時に、電子技術が主たる役割を担っているデータ処理については、従来の光技術が不十分であり、また電子技術がエネルギー消費削減の危機を迎えていることの表出でもある。この問題を根本から解決するには、信号の輸送に必要な最小エネルギー散逸が何によって支配されるかという基本原理に立ち返る必要がある。ナノ寸法における光と物質の相互作用を用いた技術は「配線型から励起移動型へ」というデバイスの基本構造の転換を可能にし、このことが多くの価値を産み出す。励起移動型デバイスの機能と性質を図1の模型で掘り下げる。半径が $R_S$ 及び $R_L=1.43R_S$ である球形の量子ドット $QD_S$ 及び $QD_L$ が近接配置されたシステムにおいて、 $QD_S$ の(1,0)準位(図1(a)のS)に存在する励起子は近接場光相互作用を介して伝搬光では禁制されていた $QD_L$ の(1,1)準位(同図 $L_2$ )へ遷移できる<sup>(1)</sup>。 $QD_L$ では(1,1)準位の下方に(1,0)準位(同図 $L_1$ )が存在し、上準位から下準位への緩和は量子ドット間の相互作用時間よりも相対的に速いので $QD_L$ に移動した励起子は下準位に緩和する。このような一方の励起移

成瀬 誠 正員 独立行政法人情報通信研究機構光ネットワーク研究所

E-mail naruse@nict.go.jp

川添 忠 東京大学大学院工学系研究科電気系工学専攻

E-mail kawazoe@ee.t.u-tokyo.ac.jp

大津元一 正員 東京大学大学院工学系研究科電気系工学専攻

E-mail ohtsu@ee.t.u-tokyo.ac.jp

Makoto NARUSE, Member (Photonic Network Research Institute, National Institute of Information and Communications Technology, Koganei-shi, 184-8795 Japan), Tadashi KAWAZOE, Nonmember, and Motoichi OHTSU, Member (School of Engineering, The University of Tokyo, Tokyo, 113-8656 Japan).

電子情報通信学会誌 Vol.95 No.4 pp.330-334 2012年4月

©電子情報通信学会 2012

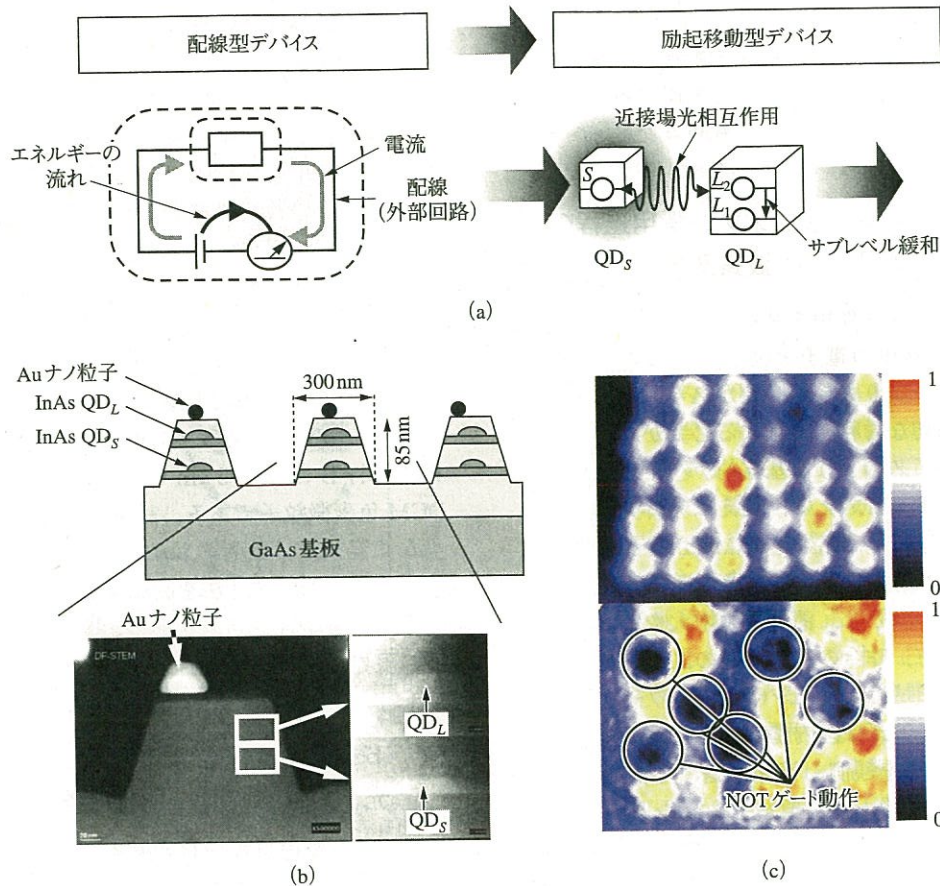


図1 励起移動型デバイスの基本構造と実現例 (a)ドレスト光子によるデバイスの基本構造の転換:「配線型」から「励起移動型」へ。(b),(c)大小の量子ドットを2層に積層したデバイスの断面図(b)とその二次元アレーの動作(c)。図(c)は二次元アレー中のNOT論理素子からの出力光強度分布を表し、上図は入力信号なし、下図は入力信号ありの場合の顕微分光による評価。

動に必要なエネルギー散逸は、行き先となる量子ドット  $QD_L$  の上準位から下準位へのサブレベル緩和に相当する。一方、電気配線を必要とする電子デバイスにおける必要エネルギー散逸は、電子デバイス自身の性質ではなくそれを取り巻く外部回路が決定付けている。そのため、外部回路でのエネルギー散逸を傍受することで内部回路の秘密情報を読み出し得るというセキュリティ上の重要な問題も生じる<sup>(5)</sup>。これに対し励起移動型デバイスでは、理論上はCMOS論理におけるビット反転に必要

### 用語解説

**近接場光** 物質に誘起される振動電界のうち、遠方に伝搬せず減衰する成分。光の回折限界よりも微細な寸法にも存在することから、高分解能の顕微鏡(近接場光顕微鏡)などに応用されている。

**ドレスト光子** ナノ寸法の微小領域では光(近接場光)は物質中の電子やフォノンと結合とし、これを「物質励起の衣をまとった光(ドレスト光子)」という準粒子として捉える描像。伝搬光では禁制されていたエネルギー準位への遷移や、物質中のフォノンとの結合を介した遷移を系統的に説明可能とし、本稿で紹介されている光デバイス機能のほか、光加工などに応用されている。

なエネルギー散逸のおよそ  $10^{-4}$  倍となり得る<sup>(6)</sup>。このような励起移動型デバイスの構造並びに効率の高さは、光合成系におけるエネルギー輸送にも類似しており、ナノ寸法の複雑システムが創発するシステム機能としても考えることができる<sup>(7)</sup>。

さて、励起移動の行き先となるエネルギー準位が存在するか否か、また、エネルギー準位が存在する場合にも、その準位が占有されるか否かによって励起移動の振舞いに違いが生じる。この特徴を利用することでANDゲート等の基本論理素子を実現できる<sup>(1),(3)</sup>。実験的には、量子ドットの寸法・間隔をいかに制御するか、更には出力信号をいかに効率的に外部に取り出すかが、特に室温動作という実用上のポイントになる。最近、分子線エピタキシーにより位置と寸法の制御された量子ドット形成プロセスを最適化することで、室温動作するデバイスの二次元アレーが実現した<sup>(8)</sup>。図1(b)にデバイス断面、図1(c)に二次元に配列されたデバイス動作の概観を示す。また、何らかの要因によってドレスト光子を媒介とする相互作用が欠損した場合にも、相互作用できる量子ドットがその近傍に存在すれば、光励起は自律的にう回動作することも特徴といえる(自律性・ロバスト



性)<sup>(9),(10)</sup>。また、信号処理に限らず、エネルギーの集光<sup>(11)</sup>、パルス発振<sup>(12)</sup>など新たな機能構築への展開が図られているほか、自律動作等に注目し生体ナノマシンへの展開を検討している研究グループもある<sup>(13)</sup>。

### 3. ドレスト光子によるフォノン援用過程の光デバイス応用——①波長変換——

通常、光と物質を相互作用させるには入力となる光子のエネルギーが物質中の電子を励起するためのバンドギャップエネルギーより大きい必要がある、利用する光の波長に応じて適切な材料を選択する必要がある。この原則は受発光デバイスのような基本的デバイスの革新に際し根本的なハードルといえる。例えば赤外光センサの課題を取り上げてみる。InGaAs や MCT などを用いた赤外光センサが普及しているが、大きな暗電流雑音低減のため冷却機構を必要とし、消費電力増大や装置大型化を招いていた。一方、昨今の環境問題の高まりを受け赤外光センサの適応領域は環境センサネットワークなどへと広がりつつある。例えば国内携帯電話大手は全国規模で花粉や CO<sub>2</sub> 濃度等を観測し情報配信する計画の試験運用を開始している<sup>(14)</sup>。また環境センシング自体も省エネに有用とされている<sup>(15)</sup>。このようなシステムは大規模化が必至であり光センサの省エネ化は急務といえるが上記のように基本的限界があった。

この問題のブレイクスルーとなるのがドレスト光子によるフォノン援用過程である。後述のようにナノ寸法の物質の形状に依存して発生するドレスト光子を介して入力となる赤外光を波長の短い可視光に変換する。可視光に変換されれば、冷却不要で安価で小形な Si フォトダイオード等との組合せが可能になる。

フォノン援用過程を用いた赤外光→可視光の変換原理の例を図 2(a) に示す<sup>(16)</sup>。用いる材料は有機色素微粒子で、ナノ寸法の形状を有する。これに赤外光が入射する

とナノ寸法物質の突起部などの形状に依存してドレスト光子が生じる。ドレスト光子は微粒子中の分子振動(フォノン)を励起することができる。この状態(基底状態の電子と励起状態にあるフォノン)を中間状態にして、更に赤外光の入射によって物質中の電子は励起状態に至り、その後、再結合して可視光が発生する。図 2(b) に DCM 色素微粒子を用いた、フォノン援用過程による赤外光→可視光変換の実験例を示す。試料 A は微粒子の平均寸法が 1 μm 以下であり、波長 800 nm の赤外光を入射すると波長約 660 nm の可視光が生じる。図 2(b) は試料 A の SEM 像及び試料表面の可視発光部を画像化したものである。白色部が可視発光部を示す。一方、試料 B は長さ 5 μm のロッド形状を有する同様の DCM 色素微粒子である。試料 A に比べて可視発光部が少なく変換量は前者のおよそ 1/10 にすぎない。このように物質の形状・寸法を制御することでドレスト光子とフォノンを結合させ、フォノン援用過程によって従来技術の限界を打破することができる。

### 4. ドレスト光子によるフォノン援用過程の光デバイス応用——②受発光デバイス——

フォノン援用過程は発光素子への応用も可能になっている。従来、間接遷移形の半導体は原則として発光効率が著しく低い。このため、例えば、導波路や分波などの光デバイスは安価な Si で実現されても、光源は複雑なヘテロ構造を有した外部光源との組合せとする構成が典型であった。ドレスト光子によるフォノン援用過程によれば、先の例と同じく、物質中のフォノンが励起された中間状態を介して電子励起を実現し、結果として、例えば Si においても発光を実現できる。文献(17)ではバルクの n 形 Si にボロンを打ち込み p 形としてホモ接合構造を形成し長波長帯 (0.9~1.7 μm) において 1.1 W (投入電力 10 W) という高輝度・高効率で LED として

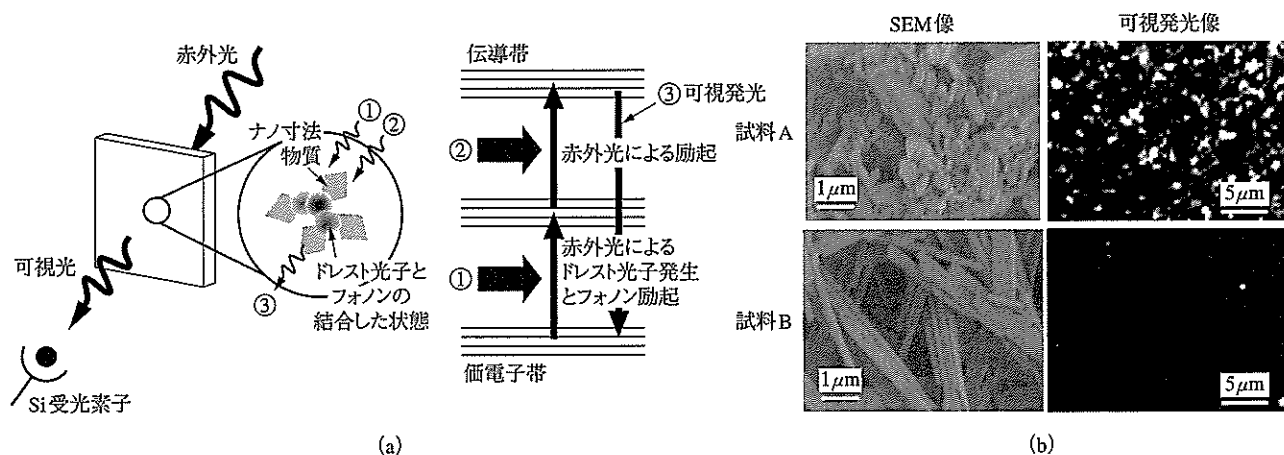
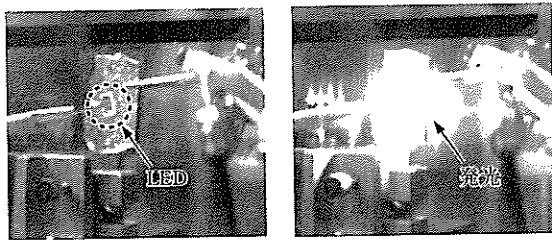
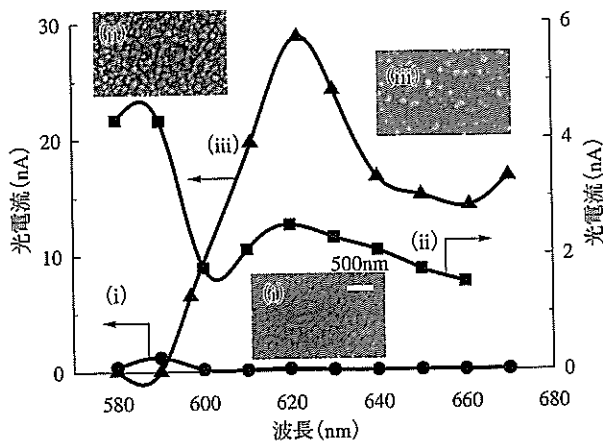


図 2 ドレスト光子によるフォノン援用過程 (a)赤外光→可視光変換の模式図。(b)物質の形状・寸法に依存するフォノン援用過程。微細構造を含む試料 A では可視発光が多く生じているが微細構造を含まない試料 B ではほとんど生じていない。



(a)



(b)

図3 フォノン援用過程を用いた受発光デバイス (a)ドレスト光子によるホモ接合構造を持つバルクシリコン結晶からの発光。シリコンの光援用アニールにより通信波長帯でLED発光している。(b)ドレスト光子による受光デバイスの感度の拡大。(i),(ii),(iii)はAg電極作製時の逆バイアス電圧、照射光パワーがそれぞれ(0 V, 0 mW), (-1.5 V, 50 mW), (-1.5 V, 70 mW)の場合。挿入図はAg電極表面のSEM像。(ii),(iii)ではP3HTの吸収端波長である約570 nmよりも長波長帯において光電流が生じている。

発光させることに成功している(図3(a))。微分外部電力変換効率は5.0%、微分外部量子効率40%に達している。この発光は実フォノン準位を介した2段階励起によることが確認されている。このデバイスでは、作製過程において順バイアス印加時のジュール熱を用いたアニールによりSi中のボロンを拡散させるが、その際に発光を発現させたい波長の光を同時に照射することがポイントとなっている(実験では波長 $1.3\mu\text{m}$ の光を光量 $10\text{ W/cm}^2$ で照射)。実際、発光スペクトルピーク波長はSiのバンドギャップエネルギーではなく照射光の波長に相当する。このようにフォノン援用過程による効果を最大化するには、作製時にもフォノン援用過程を用いて狙いの機能を誘導するという、いわば「循環型の考え方」の有効性が示唆される。このような作製プロセスは、システムの形態と制御を同時に考慮することによって、所望の機能をより効率的に実現する技術として注目を集めている「モルフォロジカルコンピューティング」<sup>(18)</sup>と呼ばれる概念が、ナノ寸法において具現したものと見ることもでき、更なる適応領域の広がりが期待さ

れる。

同様の概念に基づき、文献(19)では有機薄膜太陽電池のAg電極作製工程において、光の照射と電圧印加を併用することで、電極表面に特徴的モルフォロジーを生じさせ、従来は感度のなかった長波長域で受光感度を発現させることに成功している。具体的には、P3HT (poly(3-hexylthiophene))を材料とした有機薄膜発電デバイス上への電極作製プロセスで、逆バイアスをかけ、かつ光を照射しながら電極材料であるAgのスパッタリングを行う。ここで、照射する光の波長をP3HTの光吸収端波長である約570 nmよりも長波長の660 nmに設定する。すなわち伝搬光に対してはP3HTが透明である波長の光を照射する。このときP3HTにおいて前章と同じ原理でフォノン援用の電子励起が起きるが、逆バイアスのため電子正孔対は分離し正孔は堆積したAg電極表面に引きつけられ表面は正に帯電する。一方RFスパッタリングで堆積するAgも正に帯電しているためAg電極表面の帯電部から斥力を受け、正孔の少ないAg電極領域に優先的に堆積する。この結果、Ag電極の表面は上記のフォノン援用過程を反映した特徴的モルフォロジーに至る。このようにして作製されたデバイスは、通常のP3HTでは感度を有さない長波長の光に対して感度を示し、作製時に用いた光の波長(660 nm)近辺において最大感度を示す(図3(b))<sup>(19)</sup>。

フォノン援用光過程の素過程を、物質の幾何学的構造などを含めて包括的に解明するのは今後の課題といえるが、ドレスト光子とフォノンの結合の一次元理論モデル<sup>(20)</sup>、物質の形状・そこに発生するドレスト光子・並びに系に流出入するエネルギーを考慮した確率モデルに基づいた自己組織臨界現象に類似したモルフォロジー形成過程<sup>(21)</sup>が理論的に解明されている。また、フランスの研究グループは実験的素過程解明に向けてナノ寸法におけるフォノンの効果を直接的に評価分析する実験を示している<sup>(22)</sup>。なお、波長変換や受発光デバイスなどがナノ寸法での物質の形状・配置制御で実現され得ることは、レアメタルなどの稀少材料を必要とせずと同等の機能が達成できることに相当し、原料採取、製造、使用、廃棄まで含め製品が経験する全行程を通じての環境負荷を問う、ライフサイクルアセスメント(LCA)と呼ばれる環境影響評価手法の立場からも効果が高いと期待できる。

## 5. まとめ

物質励起の衣をまとった光子であるドレスト光子の概念を踏まえ、最近の事例を参照しながら光デバイスの新機能を解説した。ナノ領域の光と物質の相互作用は、情報通信、ライフサイエンス・健康、照明・ディスプレイ、セキュリティ、環境・エネルギー、加工などの広い

分野に及ぶ基盤技術であり、様々な応用との接点を柔軟に考慮することはもちろんのこと、材料からシステムまで多様な視点に基づいた分野融合的接近がますます重要となっている。本稿でも触れているように、従来の光技術には回折限界という空間軸に関わる限界、バンドギャップエネルギーに代表されるエネルギー軸上の限界等があり、また、適応先となる応用が抱えている構造的課題もある。震災を経て科学技術や理工学を改めて見つめ直す必要のある昨今、ナノ寸法の光と物質の相互作用の本質を探求し、今後の発展を真剣に見据えていく必要がある。

謝辞 本稿の掲載の内容は情報通信研究機構関連各位、東京大学大津研究室の職員・学生各位並びに産学連携研究に参画頂いている企業等の関連各位との共同成果による。

## 文 献

- (1) M. Ohtsu, K. Kobayashi, T. Kawazoe, S. Sangu, and T. Yatsui, "Nanophotonics: design, fabrication, and operation of nanometric devices using optical near fields," *IEEE J. Sel. Top. Quantum Electron.*, vol. 8, no. 4, pp. 839-862, 2002.
- (2) MONA consortium. A European roadmap for photonics and nanotechnologies, 2008, National Research Council, Nanophotonics: Accessibility and Applicability, National Academies Press, Washington, D.C., 2008 など.
- (3) M. Ohtsu, T. Kawazoe, T. Yatsui, and M. Naruse, "Nanophotonics: Application of dressed photons to novel photonic devices, and systems," *IEEE J. Sel. Top. Quantum Electron.*, vol. 14, no. 6, pp. 1404-1417, 2008.
- (4) 佐藤健一, "持続的発展可能な情報通信ネットワークと光ネットワーク技術の役割," *信学誌*, vol. 93, no. 8, pp. 654-658, Aug. 2010.
- (5) M. Naruse, H. Hori, K. Kobayashi, and M. Ohtsu, "Tamper resistance in optical excitation transfer based on optical near-field interactions," *Opt. Lett.*, vol. 32, no. 12, pp. 1761-1763, 2007.
- (6) M. Naruse, H. Hori, K. Kobayashi, P. Holmström, L. Thylén, and M. Ohtsu, "Lower bound of energy dissipation in optical excitation transfer via optical near-field interactions," *Opt. Express*, vol. 18, no. 104, pp. A544-A553, 2010.
- (7) N. Johnson, *Simply Complexity*, Oneworld Publications, Oxford, 2007.
- (8) T. Kawazoe, M. Ohtsu, S. Aso, Y. Sawado, Y. Hosoda, K. Yoshizawa, K. Akahane, N. Yamamoto, and M. Naruse, "Two-dimensional array of room-temperature nanophotonic logic gates using InAs quantum dots in mesa structures," *Appl. Phys. B*, vol. 103, no. 3, pp. 537-546, 2011.
- (9) M. Naruse, T. Kawazoe, R. Ohta, W. Nomura, and M. Ohtsu, "Optimal mixture of randomly dispersed quantum dots for optical excitation transfer via optical near-field interactions," *Phys. Rev. B*, vol. 80, 125325, 2009.
- (10) M. Naruse, K. Leibnitz, F. Peper, N. Tate, W. Nomura, T. Kawazoe, M. Murata, and M. Ohtsu, "Autonomy in excitation transfer via optical near-field interactions and its implications for information networking," *Nano Comm. Networks*, vol. 2, no. 4, pp. 189-195, 2011.
- (11) K. Akahane, N. Yamamoto, M. Naruse, T. Kawazoe, T. Yatsui, and M. Ohtsu, "Energy transfer in multi-stacked InAs quantum dots," *Jpn. J. Appl. Phys.*, vol. 50, 04DH05, 2011.
- (12) M. Naruse, H. Hori, K. Kobayashi, T. Kawazoe, and M. Ohtsu, "Optical pulsation mechanism based on optical near-field interactions," *Appl. Phys. B*, vol. 102, no. 4, pp. 717-723, 2011.
- (13) C. Pistol, C. Dwyer, and A.R. Lebeck, "Nanoscale optical computing using resonance energy transfer logic," *IEEE Micro*, vol. 28, no. 6, pp. 7-18, 2008.
- (14) NTT ドコモ, 報道発表資料, 2009年11月25日, [http://www.nttdocomo.co.jp/info/news\\_release/page/091125\\_00.html](http://www.nttdocomo.co.jp/info/news_release/page/091125_00.html)

- (15) 南 正輝, 川村龍太郎, 森川博之, 平原正樹, "省電力志向新世代ネットワーク," *信学論 (B)*, vol. J92-B, no. 4, pp. 605-614, April 2009.
- (16) T. Kawazoe, H. Fujiwara, K. Kobayashi, and M. Ohtsu, "Visible light emission from dye molecular grains via infrared excitation based on the nonadiabatic transition induced by the optical near field," *IEEE J. Sel. Top. Quantum Electron.*, vol. 15, no. 5, pp. 1380-1386, 2009.
- (17) T. Kawazoe, M.A. Mueed, and M. Ohtsu, "Highly efficient and broadband Si homojunction structured near-infrared light emitting diodes based on the phonon-assisted optical near-field process," *Appl. Phys. B*, vol. 104, no. 4, pp. 747-754, 2011.
- (18) C Paul, "Morphological computation: A basis for the analysis of morphology and control requirements," *Robot. Auton. Syst.*, vol. 54, no. 8, pp. 619-630, 2006.
- (19) S. Yukutake, T. Kawazoe, T. Yatsui, W. Nomura, K. Kitamura, and M. Ohtsu, "Selective photocurrent generation in the transparent wavelength range of a semiconductor photovoltaic device using a phonon-assisted optical near-field process," *Appl. Phys. B*, vol. 99, no. 3, pp. 415-422, 2010.
- (20) Y. Tanaka and K. Kobayashi, "Spatial localization of an optical near field in one-dimensional nanomaterial system," *Physica E*, vol. 40, no. 2, pp. 297-300, 2007.
- (21) M. Naruse, T. Kawazoe, T. Yatsui, N. Tate, and M. Ohtsu, "A stochastic modeling of morphology formation by optical near-field processes," *Appl. Phys. B*, vol. 105, no. 4, pp. 185-190, 2011.
- (22) S. Sauvage, A. Driss, F. Réveret, P. Boucaud, A. Dazzi, R. Prazeres, F. Glotin, J.-M. Ortéga, A. Miard, Y. Halioua, F. Raineri, I. Sagnes, and A. Lemaître, "Homogeneous broadening of the S to P transition in InGaAs/GaAs quantum dots measured by infrared absorption imaging with nanoscale resolution," *Phys. Rev. B*, vol. 83, no. 3, 035302, 2011.

(平成 23 年 11 月 2 日受付 平成 23 年 12 月 4 日最終受付)

なるせ まこと  
成瀬 誠 (正員)



1994 東大・工・計数卒。1999 同大学院博士課程了。博士 (工学)。東大リサーチ・アシリエイト, 助手を経て 2002 から情報通信研究機構。2003 から主任研究員。光システム, ナノフォトニクス, 情報ネットワーク等の研究に従事。2001~2005 科学技術振興機構さきがけ業務, 2006~2011 東大客員准教授業務。2008 光論文賞等受賞。

かわざお なるし  
川添 忠



1990 筑波大・理・物理卒。1996 同大学院博士課程了。博士 (理学)。山形大助手, 科学技術振興機構研究員などを経て, 現在東大主幹研究員。ナノフォトニクスの研究に従事。

おつ ともいち  
大津 元一 (正員)



1978 東工大大学院理工学研究科電子物理工学専攻博士後期課程了。同大学助手等を経て 1991 同大学院総合理工学研究科教授, 2004 から東大大学院工学系研究科電子工学専攻教授。2008 同大学院工学系研究科総合研究機構ナノフォトニクス研究センター長業務。1993~1998 神奈川科学技術アカデミー「大津フォトン制御」, 1998~2003 科学技術振興機構 ERATO「局在フォトン」プロジェクト, 2002~2006 NEDO「大容量光ストレージ技術の開発」, 2006~2010 NEDO「ナノフォトニクス総合的展開」, 2006~2010 NEDO「低損失オプティカル新機能部材技術開発」等の総括責任者を歴任。Julius Springer Prize for Applied Physics (2009), 本会業績賞 (2007), 井上春成賞 (2005), 紫綬褒章 (2004), 日本 IBM 科学賞 (1998) 等各受賞。

# 総論

東京大学  
大津元一

## 1 はじめに

従来の光技術は伝搬光と物質との相互作用を利用して発光・受光デバイスを開発し、それらを情報の記録，伝送，表示，さらには加工，照明，計測等の多様な分野に応用してきた。しかし昨今はデバイスの微小化<sup>1)</sup>，消費エネルギーの低減化<sup>2,3)</sup>，加工の高分解能化<sup>4)</sup>などの社会的要求が高まっている。さらにその上，希少資源（レアメタル）の使用量削減・駆逐<sup>5)</sup>，セキュアライフ<sup>6,7)</sup>などの問題の解決にも寄与することが求められている。しかし従来の光技術ではこれらの問題を解決することが困難になってきており，その原因は光子と物質とを独立に考える既存の光学原理に立脚していることによる。

その問題を解決するため，既存の原理とは異なる考え方にに基づき，光子と物質とがナノ寸法領域で結合した状態を利用する技術が進展している。この結合状態は近接場光と呼ばれてきたが<sup>8)</sup>，これはナノ寸法領域における光・物質相互作用とそれに伴うエネルギー移動を議論するには不十分である。この議論を進める為，さらには上記の応用システムを設計する為，この結合状態はドレスト光子（Dressed photon. 以下DPと略記）と呼ばれる準粒子とみなされるようになり<sup>9)</sup>，その結果ドレスト光子工学と称する技術が発展している。

DPはさらに多モードのフォノンとも結合し，ドレスト光子フォノン（以下DPPと略記）と呼ばれる準粒子も形成する。これを光技術に利用した場合，次の変革がもたらされ，上記の問題が次々と解決されるようになった。

- (1) DPPは伝搬光の光子より高いエネルギーをもつので，エネルギー上方変換が実現する。
- (2) 伝搬光に反応しない物質がDPPには反応するので，新しい発光・受光デバイス，エネルギー変換デバイスが実現する。
- (3) DPPにより自己組織的な微細加工ができるので，レアアース研磨剤などが不要の物質表面処理加工，物質組成均一化技術が実現する。
- (4) DPPは空間的階層性を示すので，情報セキュリティデバイスが実現する。

DP，DPPはナノ寸法の凹凸，組成不均一性を有する物質部位に必ず発生するので，これらを使う技術は普遍的である。従って従来の光技術の多くの分野を置き換え，かつこれらの分野で不可能だった機能を可能とする質的変革をもたらしている。本特集ではこの技術の実用化の事例について紹介する。特に環境，エネルギー，セキュアライフの観点から技術開発の例を紹介する。

## 2 技術開発の例

本特集で解説される事例を含め，最近の技術開発の例を列挙すると次のようになる。

なお，注番号は各々（注1）NEDO低損失オプティカル新機能部材技術開発事業（H18～H22年度），（注2）NEDOエネルギー使用合理化技術先導の開発事業（H20～H22年度），（注3）NEDO挑戦研究開発事業（H21～H23年度），（注4）NEDO先導研究開発事業（H22～H24年度）により産学連携で技術開発されたことを意味する。

その一部は既に市販され、または製品化の為の調整が進んでいる。

(1) デバイス

1. 間接遷移型半導体の発光・受光デバイス：光ファイバ通信波長帯で発光する高効率・高出力シリコン発光ダイオードが開発されている（図1(a)）<sup>10)</sup>。シリコンは無害、かつ資源枯渇の心配のない材料であることから環境、資源、エネルギー問題の解決に寄与する。他の間接遷移型半導体により可視域での発光も可能であることから通信のみでなくディスプレイ、太陽電池などへの応用が期待されている。
2. 低損失偏光制御板（注1）：赤、緑、青色光に対し

高い透過効率と消光比を有するデバイスが開発されている。高効率であることからエネルギー問題の解決に寄与する。ディスプレイ装置などへの応用が期待されている。

3. ナノ光論理ゲート（注1）：室温動作の論理ゲートデバイスの2次元配列アレイが開発されている（図1(b)）<sup>11)</sup>。デバイスユニット寸法は一辺200～300 nm、消費電力はCMOS論理ゲートデバイスの $10^{-4}$ である。低消費電力であることからエネルギー問題の解決に寄与する。光インターコネクション、ディスプレイ、エネルギー変換などへの応用が期待されている。
4. 情報セキュリティデバイス：ホログラムにナノ寸

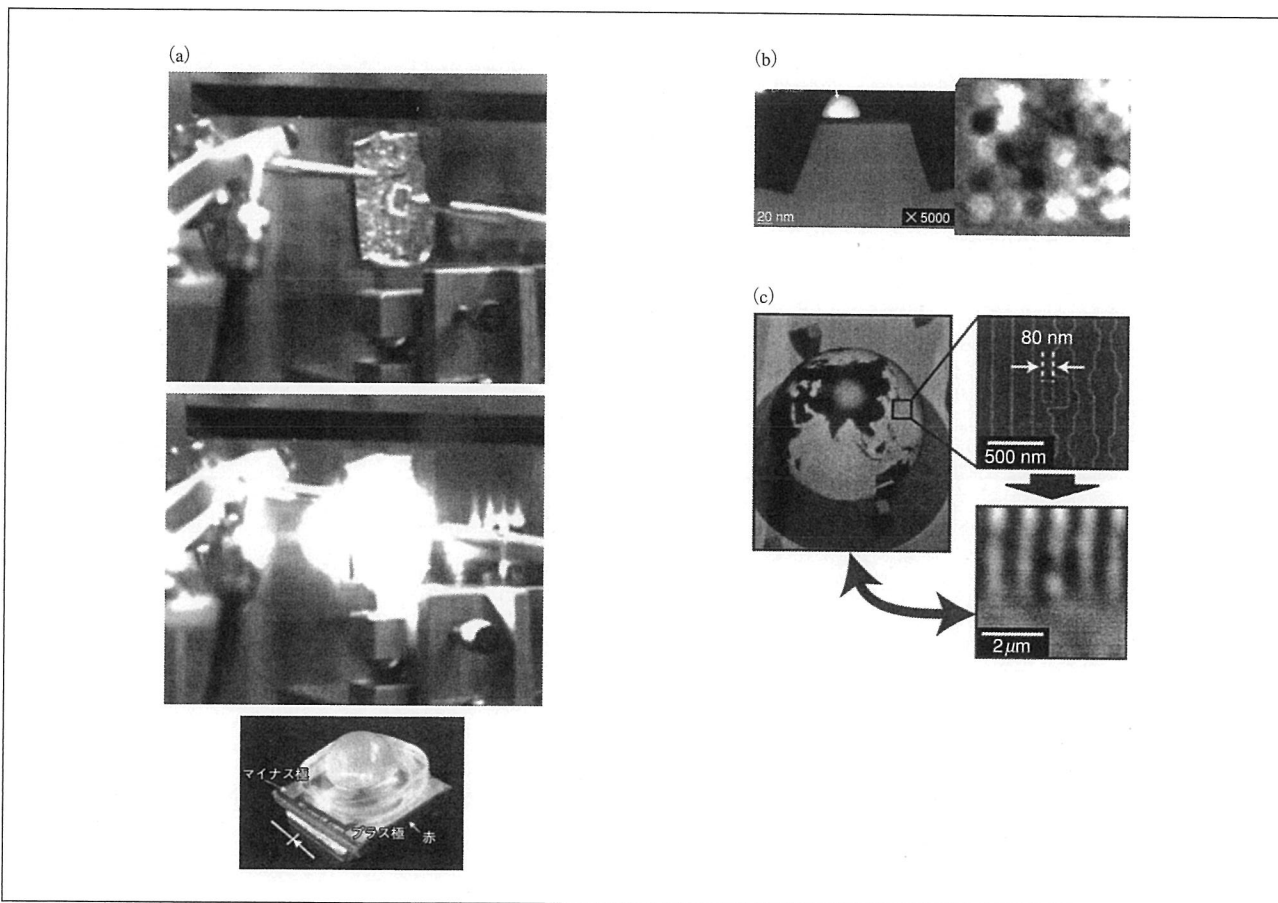


図1 デバイスの例。

(a) シリコン発光ダイオード（上図：デバイス外観。中図：発光スポット。下図：試供品モジュール外観）。(b) ナノ光論理ゲート（左図：断面SEM像。右図：2次元アレイからの出力光スポット）。(c) ナノホログラム（左図：ホログラム全体像。右上図：ナノパターンSEM像。右下図：ナノパターン近接場光学顕微鏡像）。

法パターンを記録したデバイスが開発されている (図1(c))<sup>12)</sup>。セキュアライフの問題の解決に寄与し、情報セキュリティシステムなどへの応用が期待されている。

(2) 加工

1. 物質の表面平坦化, 組成均一化 (注2, 3) : ガラス, プラスチック, セラミック, 結晶などの表面研磨技術が開発されている (図2(a))<sup>13)</sup>。石英ガラスの場合面粗さは1.3 Å程度まで減少している。この技術は光化学エッチング法でありCeO<sub>2</sub>のよう

なレアメタル研磨剤を使わないことから環境, エネルギー問題の解決に寄与する。光学素子, 光ディスク, 磁気ディスク, ディスプレイパネル, リソグラフィ用フォトマスク表面研磨などへの応用が期待されている。

2. リソグラフィ : 4インチ寸法にわたり一括加工で最小線幅50 nmが可能な自動化装置が開発されている (図2(b))。光源は可視域発光ダイオード1つであり装置の消費電力が小さく, かつ装置が小型であることからエネルギー問題の解決に寄与する。すでに軟X線用の回折格子, フレネルゾーンプレート<sup>14)</sup>などの素子, Si導波路アレイ, さらに上記(1)2のデバイスの作製などに使われており, デスクトップ型装置も実現している。

(3) システム

1. 光周波数上方変換 (注4) : 光ファイバ通信波長帯の近赤外光を可視光へ変換するシステムが開発されている。赤外光検出器の冷却装置などが不要となるためエネルギー問題の解決に寄与する。光パルス形状評価装置などへの応用が期待されている<sup>15)</sup>。

2. マイクロ・ナノ流体システム : 微小流体システムの加工などにもDPPが利用されている。使用流体量が著しく節減されることからエネルギー問題の解決に寄与する。バイオ, 医用, 化学などの微小流体システムへの応用が期待されている。

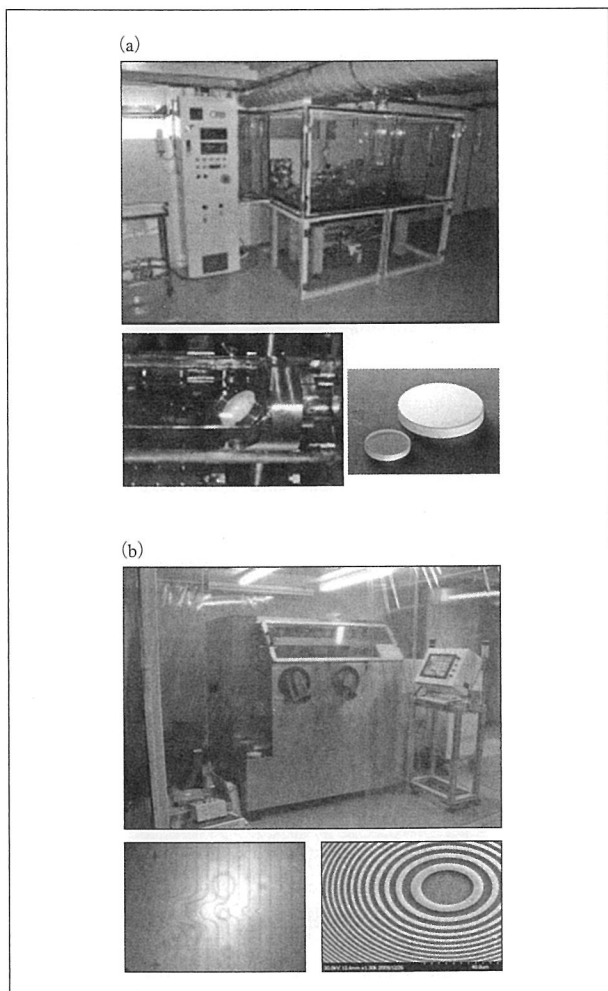


図2 加工装置の例。

(a) 表面平坦化装置 (上図: 装置全体, 下左図: 装置中心部拡大図, 下右図: 研磨例としてのレーザー鏡用基板)。 (b) リソグラフィ装置 (上図: 装置全体, 下左図: 加工例としてのシリコン導波路アレイ, 下右図: 加工例としての軟X線用フレネルゾーンプレート)。

3 おわりに

ドレスト光子工学はデバイス, 加工, システムの多岐にわたり応用されているが, これは本技術が今後の社会を支える基盤技術であることの証左といえる。これにより既存の光技術が抱える問題が解決したのみに留まらず, 既存技術では不可能な機能を有するデバイス, 加工, システムが創出された。今後はこのような質的変革をさらに推進すべきであり, またその為の大きな可能性が随所に現れている。

参考文献

- 1) 2005 communications technology roadmap on Silicon Microphotonics <http://mpc-web.mit.edu/>

2) D. C. Kilper, D. Neilson, D. Stiliadis, D. Suvakovic, S. Goyal, "Fundamental limits on energy use in optical networks," in Proceedings of 36th European Conference and Exhibition on Optical Communication (ECOC), 2010, pp. 1-6.

3) M. Naruse, H. Hori, K. Kobayashi, P. Holmstrom, L. Thylen, and M. Ohtsu, "Lower bound of energy dissipation in optical excitation transfer via optical near-field interactions," Opt. Express **18**, A544 (2010)

4) C. Wagner and N. Harned, Nature Photonics **4**, 24 (2010)

5) Y. Kato, K. Fujinaga, K. Nakamura, Y. Takaya, K. Kitamura, J. Ohta, R. Toda, T. Nakashima, and H. Iwamori, Nature Geoscience **4**, 535 (2011)

6) 松本 勉, 応用物理 **80**, 0030 (2011)

7) M. Naruse, H. Hori, K. Kobayashi, and M. Ohtsu, Opt. Lett. **32**, 1761 (2007)

8) M. Ohtsu, K. Kobayashi, T. Kawazoe, M. Naruse, *Principles of Nanophotonics*, CRC Press, Boca Raton, 2008

9) M. Ohtsu, *Progress in Nanophotonics I*, ed. by M. Ohtsu, Springer-Verlag, Heidelberg, 2011, pp. 1-58.

10) T. Kawazoe, M. A. Mueed, M. Ohtsu, Appl. Phys. B **103**, 537 (2011)

11) T. Kawazoe, M. Ohtsu, S. Aso, Y. Sawado, Y. Hosoda, K. Yoshizawa, K. Akahane, N. Yamamoto, M. Naruse, Appl. Phys. B **103**, 537 (2011)

12) N. Tate, M. Naruse, T. Yatsui, T. Kawazoe, M. Hoga, Y. Ohyagi, T. Fukuyama, M. Kitamura, M. Ohtsu, Opt. Exp. **18**, 7497 (2010)

13) T. Yatsui, K. Hirata, W. Nomura, Y. Tabata, M. Ohtsu, Appl. Phys. B **93**, 55 (2008)

14) T. Kawazoe, T. Takahashi, M. Ohtsu, Appl. Phys. B **98**, 5 (2010)

15) H. Fujiwara, T. Kawazoe, M. Ohtsu, Appl. Phys. B **100**, 85 (2010)

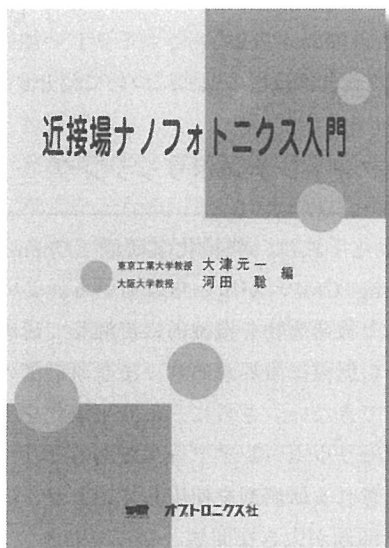
■ Overview

■ Motoichi Ohtsu

■ Graduate School of Engineering and Nanophotonics Research Center, University of Tokyo

オオツ モトイチ

所属：東京大学大学院 工学系研究科及びナノフォトニクス研究センター 教授



## 近接場ナノフォトニクス入門

- 編者：大津 元一、河田 聡
- 体裁：B5判 140頁 ● 刊行：2000年4月
- ISBN：978-4-900474-83-3
- 定価：5,250円（本体5,000円+税）

- 第1部 基礎編
- 第2部 理論編
- 第3部 要素技術編
- 第4部 応用のための参考文献集編

光のオンライン書店

<http://shop.optronics.co.jp/>

クレジット・代金引換・コンビニ払い

光のオンライン書店

検索



# バルク結晶シリコンを用いた高効率・高出力発光ダイオード

東京大学  
川添 忠，大津元一

## 1 はじめに

発光ダイオード (LED) の発光波長の値は用いられる半導体のバンドギャップエネルギー  $E_g$  の値によって決まる。すなわち例えば光ファイバ通信波長帯を含む  $1.0 \mu\text{m}$  ~  $1.7 \mu\text{m}$  の近赤外LEDを実現するには InGaAsP が用いられている<sup>1,2)</sup>。これは直接遷移型半導体であり，その発光の高効率化のためには InP 基板上にエピタキシャル成長された InGaAsP 活性層と InP キャリア閉じ込め層とを用いた複雑なダブルヘテロ構造を使う必要がある。この場合，InP は高い毒性を持つこと<sup>3)</sup>，In が希少資源 (レアメタル) であることが問題である。一方，シリコン (Si) は毒性が低く，資源枯渇の心配のない半導体であるが間接遷移型なので発光効率が低い。従ってこれまで，LED に用いる材料としては不適当と考えられてきた。しかし環境問題への関心の高まりから，最近では Si を用いた発光素子が研究されるようになった。たとえば可視光領域では多孔質 Si<sup>4)</sup>，Si と SiO<sub>2</sub> の超格子構造<sup>5,6)</sup>，SiO<sub>2</sub> 中の Si ナノ凝集粒子<sup>7)</sup> が用いられ，赤外光領域では Er ドープ Si<sup>8)</sup>，Si-Ge<sup>9)</sup> が用いられている。これらは間接遷移型の半導体を直接遷移型に近づけるための電子状態の制御という共通の手法に基づいている。しかしそれらの発光効率は依然として低く，例えば Si のサブバンドギャップ遷移<sup>10)</sup> を利用した LED の外部量子効率，電力変換効率は各々 0.5%，0.8% である。

我々はこれらの材料工学的な既存手法ではなく，光子とナノ寸法物質励起の結合した準粒子であるドレスト光

子 (以下 DP と略記) の新原理にもとづきバルク結晶 Si による高効率・高出力 LED を世界に先駆けて作製した<sup>11)</sup>。すなわち，DP を用いたナノ寸法物質間での光子と電子系の関与する相互作用にはフォノンが介在可能であること<sup>12)</sup> を利用し，Si 結晶にこのフォノンを援用したアニールを施し，間接遷移型半導体である Si をあたかも直接遷移型半導体であるかのように変化させた。本稿では本特集の主旨である「ドレスト光子，環境，エネルギー」に合わせ，表題の話題を概説する。

## 2 発光の原理とデバイス作製方法

DP とフォノンとが結合する性質に起因するフォノン援用過程<sup>13)</sup> を用いると  $E_g$  より小さい光子エネルギーを持つ光が入射した場合でも電子正孔対が生成される。なぜなら DP とフォノンとが結合した準粒子は，電気双極子禁制なフォノン準位への遷移を経由して価電子帯中の電子を伝導帯に励起させることが可能だからである。この現象を利用し，本特集の他記事でも紹介されている加工技術，波長変換などが開発され，それらの一部はすでに実用化されている。

この励起の逆過程として二段階の自然放出過程が存在する<sup>14)</sup>。これにより発生した DP の一部は伝搬光に変換され観測されるので，電流注入によって電子を励起すれば LED が実現する。また，このデバイスの発光波長は  $E_g$  ではなく，pn 接合近傍にある DP の光子エネルギーに依存する。良く知られているように，間接遷移型半導体が伝搬光を自然放出するにはフォノンが必要である。な



ぜなら、この自然放出のためには波数が保存しなければならないからである。しかしDPでは光子が多モードのフォノンと強く結びつき、波数保存則を満たす多数のモードを持つので<sup>13, 15)</sup>、DPによる自然放出の確率は非常に大きい。また、このフォノン援用過程は二段階の誘導放出過程も可能にする。

既存のLEDには半導体基板上にCVD法等で成長させた結晶が用いられている。これに対し本方法ではDPによる二段階フォノン援用過程を二回使う。その第一はもちろんデバイスを動作させ自然放出光を得るためであり、その結果は次節で示される。第二はこのデバイスを作製するため、すなわち高効率の自然放出に適したドーパント濃度の空間分布を自己組織的に制御するためである。以下ではこの第二の使用法について記す。

デバイス作製のための基板にはヒ素 (As) がドーパされたn型Si結晶を用いた。この基板にイオン打ち込み法によってさらにボロン (B) をドーパし、p層を作製した。その後、p層側にITOを、n基板側にAlを各々堆積し、これらを電極として用いた。その後これらの電極付きのSi基板を一辺数mmの寸法に切り出して一つのデバイスとした。

DPの発生効率を向上させるため、デバイスを順方向電流によってアニールしBを拡散させた。するとBの空間分布は電流による発熱のために変化し微小な不均一領域境界を生ずる。このアニールの際、結晶に光を照射する。するとこの光により効率よくDPが発生する境界部位において、順方向電流によって反転分布を形成しているpn接合部の電子と正孔の一部は誘導放出により伝搬光に変換され、発生した光はデバイス外部に放出される。その結果、DPが発生した部位のエネルギーの一部は光として散逸され温度が下がり、Bの拡散が抑制される。他方DPの発生効率の低い部位はBの拡散が続く。最終的にはpn接合部全体がDP発生に適したB分布をもつ定常状態に自己組織的に達する。なおSiは間接遷移型半導体であるので通常的光子では誘導放出が期待できず、このようなアニール過程は生じないため、この過程にはDPが不可欠である。

実際のアニールでは、Siの $E_g (= 1.12 \text{ eV})$ <sup>16)</sup>よりも小さい光子エネルギー ( $h\nu_{\text{anneal}} = 0.95 \text{ eV}$  : 波長  $1.30 \mu\text{m}$ )

のレーザー光 (光パワー密度  $10 \text{ W/cm}^2$ ) をITO電極側より照射した。この光はSiに吸収されることなく結晶中を伝搬し、Bの不均一分布<sup>17)</sup>の領域の境界にDPを発生する。実際にアニールのための順方向電流を注入すると、その直後結晶表面温度は室温から約  $155^\circ\text{C}$  へと上昇したが、誘導放出の為に直ちに約  $140^\circ\text{C}$  に低下し、その後数分でほぼ定常状態に達した。

### 3 デバイスの発光特性

非バイアス時と順方向バイアス時のデバイスの外観を室温・蛍光灯照明下にて撮影した写真を各々図1(a), (b)に示す。(b)では強い発光が確認される。この時の投入電力は  $11 \text{ W}$  であり、発光パワーは  $1.1 \text{ W}$  に達した。図1(c)はデバイス封止後にコリメート用レンズが付加された試供品モジュールの外観である<sup>18)</sup>。よく知られているように、既存の方法で作られた市販のSiフォトダイオードもわずかながら発光する。そこで比較のため、バイアス電流密度  $0.2 \text{ A/cm}^2$  の時の市販のSiフォトダイオードからの微弱な発光スペクトルを図2の曲線Aに示す。この図では発光スペクトルが $E_g$ よりも高エネルギー側に分布している<sup>10)</sup>。これはSiの間接遷移型バンド構造の中でのフォノン散乱による。

これに対し図2の曲線B~Dは1分間、7分間、30分間のアニールにより作られたデバイスの発光スペクトルである。バイアス電流密度は  $1.5 \text{ A/cm}^2$  である。曲線Aとは異なり、発光スペクトルは $E_g$ より低エネルギー側に広がっている。  $0.8 \text{ eV}$  より低エネルギー領域での発光スペクトル強度の減少は光検出器の感度限界に起因する。アニール時間の増加とともに発光強度が著しく増加し、発光ピークは長波長側にシフトしている。曲線Dに示すように30分間のアニールにより作られたデバイスではもはや $E_g$ の位置に明瞭な発光ピークは存在せず、その代わりにアニールの際に照射した光の光子エネルギー  $h\nu_{\text{anneal}}$  に相当する領域にピーク (図中の下向き矢印) が現れている。これは照射光によってDPが発生しアニールの進行が抑制され、かつ発光波長が  $h\nu_{\text{anneal}}$  により制御されたことを意味する。このことから本技術は既存材料を使いつつも所望の発光波長が得られることがわかる。これは

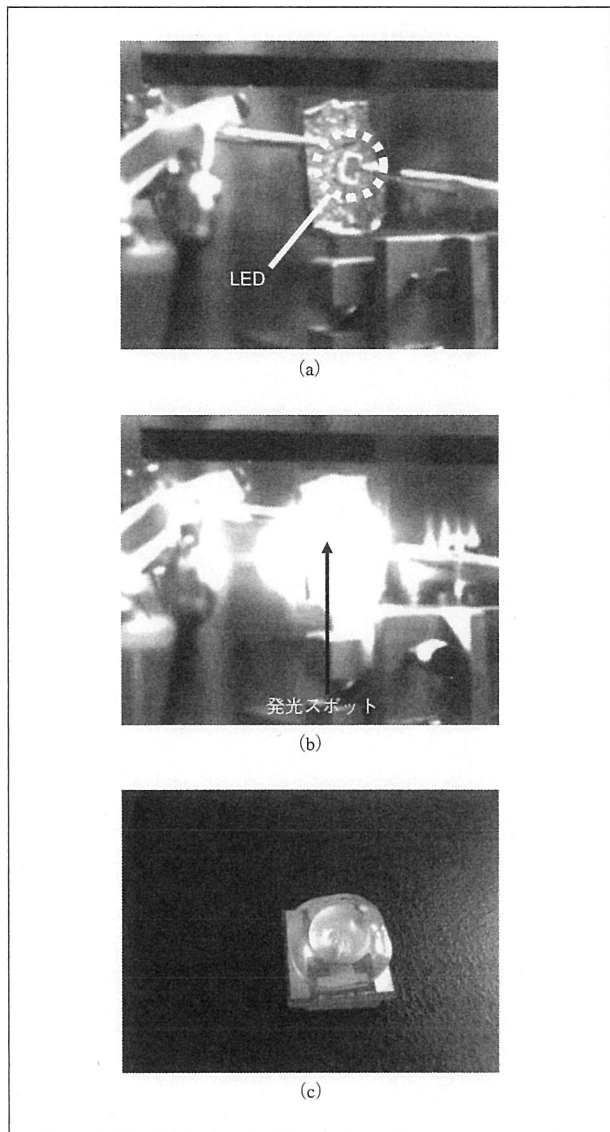


図1 デバイスが室温で発光する様子を蛍光灯照明下にて赤外線カメラで撮影した写真。(a) 電流密度  $I_0=0$ 。(b) 電流密度  $I_0=4.2 \text{ A/cm}^2$ 。(c) 試供品モジュール外観。

光・物質融合工学と称すべき手法で、従来の材料工学的手法とは異なる。

30分間のアニールにより作られたデバイスに関し、注入電流密度と出力光パワー密度との関係を測定した結果を図3に示す。これは光子エネルギーが0.73 eV以上の発光成分から求めた結果である。従来のLEDでは出力光パワー密度は注入電流密度に比例するが、本デバイスでは実線の曲線からわかるように注入電流密度の二乗に

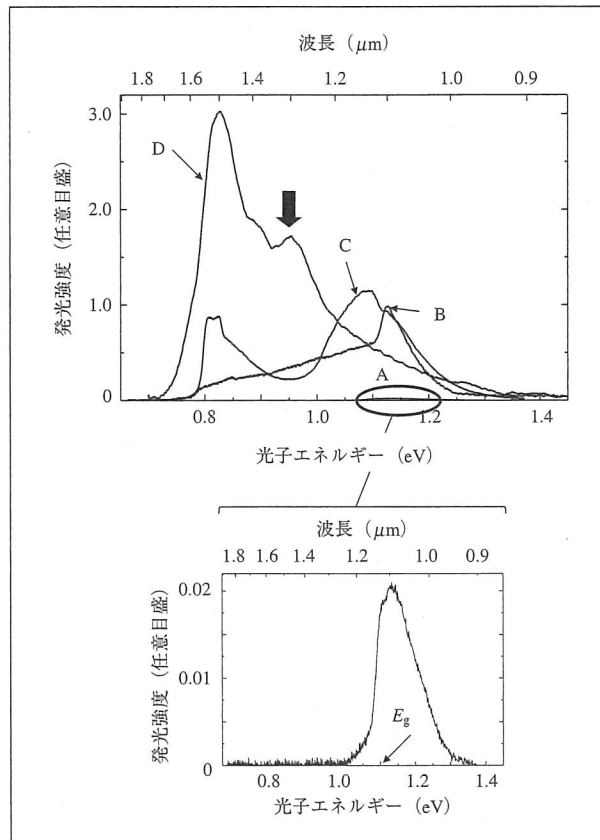


図2 発光スペクトル。曲線A：市販のSiフォトダイオードの発光スペクトル。曲線B～D：作製したデバイスの発光スペクトル。アニール時間1分 (B)、7分 (C)、30分 (D)。

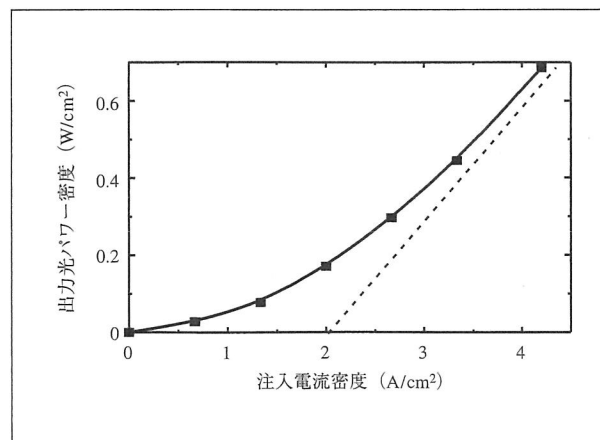


図3 注入電流密度  $I_0$  と発光パワー密度  $P_0$  との関係。■印は光子エネルギー0.73 eV以上の領域の発光の全パワー密度の測定結果。実線の曲線は2次曲線  $P_0=0.04 \times I_0^2$  を表す。破線の傾きは微分外部量子効率40%に相当。

比例している。これは主たる発光過程がフォノン準位を介した二段階遷移であり一電子注入により二光子が発生した事を示している。なお注入電流密度 $4.0 \text{ A/cm}^2$ の時、外部量子効率 $15\%$ であった。また、注入電流密度が $3.0 \sim 4.0 \text{ A/cm}^2$ の時の微分外部量子効率は $40\%$ であった。

本方法で用いた高抵抗率のSi基板の厚みを薄くすれば電力効率はさらに増加する。また電流密度はさらに高くできるので、より高効率・高出力のLEDが実現すると考えられる。

## 4 おわりに

筆者らはSi中のBの不均一領域境界に発生するDPが駆動する誘導放出を利用し、電流注入によるアニールを制御して、高効率・高出力のLEDを世界に先駆けて作製した。このデバイスはBの不均一領域境界に発生するDPによる二段階フォノン援用過程によって発光する。単純なホモ接合構造のバルク結晶Siを用いたにも拘らず、全光パワーは $1.1 \text{ W}$ に達した。また外部量子効率は $15\%$ 、微分外部量子効率は $40\%$ であった。本技術はSi以外の間接遷移型半導体、さらにまた直接遷移型半導体にも適用可能であるため、本稿のような近赤外域のみでなく可視域のLEDも作製できる。これにより表示、照明システムの省エネルギー化のみでなくそこで使われている半導体材料のレアメタル駆逐、3R問題 (Reduce, Reuse, Recycle) の解決などにつながる事が期待される。

### 参考文献

- 1) T. P. Lee, C. A. Burus, A. G. Dentai, IEEE J. Quantum Electron. **17**, 232 (1981)
- 2) R. A. Milano, P. D. Dapkus, G. E. Stillman, IEEE Tran., Electron Devices **29**, 266 (1982)
- 3) National toxicology program: NTP technical report on the toxicology and carcinogenesis studies of indium phosphide (CAS No. 22398-80-

7)in F344/N rats and B6C3F1 mice (inhalation studies), NTP TR 499, (U. S. Department of health and human services, Public Health Service, National Institute of Health, 2001)

- 4) K. D. Hirschman, L. Tysbekov, S. P. Duttagupta, P. M. Fauchet, Nature **384**, 338 (1996)
- 5) Z. H. Lu, D. J. Lockwood, J.-M. Baribeau, Nature **378**, 258 (1995)
- 6) L. Dal Negro, R. Li, J. Warga, S. N. Basu, Appl. Phys. Lett. **92**, 181105 (2008)
- 7) T. Komoda, Nucl. Instrum. Methods B **96**, 387 (1995)
- 8) S. Yerci, R. Li, L. Dal Negro, Appl. Phys. Lett. **97**, 081109 (2010)
- 9) S. K Ray, S. Das, R. K Singha, S. Manna, A. Dhar, Nanoscale Research Lett. **6**, 224 (2011)
- 10) M. A. Green, J. Zhao, A. Wang, P. J. Reece, M. Gal, Nature **412**, 805 (2001)
- 11) T. Kawazoe, M. A. Mueed, M. Ohtsu, Appl. Phys. B **104**, 747 (2011)
- 12) M. Ohtsu, T. Kawazoe, T. Yatsui, M. Naruse, IEEE J. Selected Topics in Quantum Electron. **14**, 1404 (2008)
- 13) T. Kawazoe, K. Kobayashi, S. Takubo, M. Ohtsu, J. Chem. Phys. **122**, 024715 (2005)
- 14) S. Yukutake, T. Kawazoe, T. Yatsui, W. Nomura, K. Kitamura, M. Ohtsu, Appl Phys B **99**, 415 (2010)
- 15) Y. Tanaka, K. Kobayashi, Physica E **40**, 297 (2007)
- 16) R. J. Van Overstraeten, R. P. Mertens, Solid State Electron. **30**, 1077 (1987)
- 17) J. A. Van den Berg, D. G. Armour, S. Zhang, S. Whelan, H. Ohno, T.-S. Wang, A. G. Cullis, E. H. J. Collart, R. D. Goldberg, P. Bailey, T. C. Q. Noakes, J. Vac. Sci. Technol. B **20**, 974 (2002)
- 18) (特)ナノフォトンクス工学推進機構カタログ「ドレスト光子を利用したプリリアント・シリコン発光素子」, (特)ナノフォトンクス工学推進機構, 東京, 2011

### ■ A high-efficiency and high-power light emitting diode by a bulk Si crystal

■① Tadashi Kawazoe, ② Motoichi Ohtsu

■①② Graduate School of Engineering and Nanophotonics Research Center, University of Tokyo

①カワゾエ タダシ

所属：東京大学大学院 工学系研究科及びナノフォトンクス研究センター 特任研究員 (主幹研究員)

②オオツ モトイチ

所属：東京大学大学院 工学系研究科及びナノフォトンクス研究センター 教授

# 電子情報 通信学会誌

THE JOURNAL OF THE INSTITUTE OF ELECTRONICS,  
INFORMATION AND COMMUNICATION ENGINEERS

本会のWWWホームページ  
<http://www.ieice.org>

## 小特集 ナノデバイス

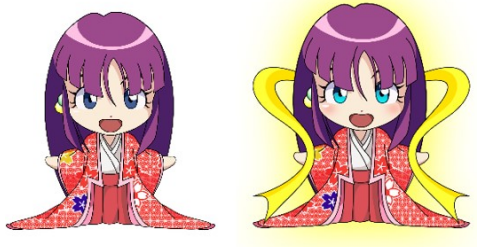
- ・オンライン手書き文字認識の最新動向
- ・エレクトロマイグレーション

**4** 平成24年4月  
APRIL  
Vol.95 No.4

THE INSTITUTE OF ELECTRONICS, INFORMATION  
AND COMMUNICATION ENGINEERS

**ieice** 一般社団法人  
電子情報通信学会

## [IV] PUBLISHED BOOKS



Gyu-Chul Yi

Editor

# Semiconductor Nanostructures for Optoelectronic Devices

Processing, Characterization  
and Applications

With 221 Figures



Springer

## *Editor*

Gyu-Chul Yi

Seoul National University, Department of Physics  
Gwanak-ro 599, 151-747 Seoul  
Korea, Republic of (South Korea)  
gyuchul.yi@gmail.com

## *Series Editors:*

Professor Dr. Phaedon Avouris  
IBM Research Division  
Nanometer Scale Science & Technology  
Thomas J. Watson Research Center  
P.O. Box 218  
Yorktown Heights, NY 10598, USA

Professor Dr. Bharat Bhushan  
Ohio State University  
Nanotribology Laboratory  
for Information Storage  
and MEMS/NEMS (NLIM)  
Suite 255, Ackerman Road 650  
Columbus, Ohio 43210, USA

Professor Dr. Dieter Bimberg  
TU Berlin, Fakultät Mathematik/  
Naturwissenschaften  
Institut für Festkörperphysik  
Hardenbergstr. 36  
10623 Berlin, Germany

Professor Dr., Dres. h.c. Klaus von Klitzing  
Max-Planck-Institut  
für Festkörperforschung  
Heisenbergstr. 1  
70569 Stuttgart, Germany

Professor Hiroyuki Sakaki  
University of Tokyo  
Institute of Industrial Science  
4-6-1 Komaba, Meguro-ku  
Tokyo 153-8505, Japan

Professor Dr. Roland Wiesendanger  
Institut für Angewandte Physik  
Universität Hamburg  
Jungiusstr. 11  
20355 Hamburg, Germany

NanoScience and Technology ISSN 1434-4904

ISBN 978-3-642-22479-9

e-ISBN 978-3-642-22480-5

DOI 10.1007/978-3-642-22480-5

Springer Heidelberg Dordrecht London New York

Library of Congress Control Number: 2011941807

© Springer-Verlag Berlin Heidelberg 2012

This work is subject to copyright. All rights are reserved, whether the whole or part of the material is concerned, specifically the rights of translation, reprinting, reuse of illustrations, recitation, broadcasting, reproduction on microfilm or in any other way, and storage in data banks. Duplication of this publication or parts thereof is permitted only under the provisions of the German Copyright Law of September 9, 1965, in its current version, and permission for use must always be obtained from Springer. Violations are liable to prosecution under the German Copyright Law.

The use of general descriptive names, registered names, trademarks, etc. in this publication does not imply, even in the absence of a specific statement, that such names are exempt from the relevant protective laws and regulations and therefore free for general use.

Printed on acid-free paper

Springer is part of Springer Science+Business Media ([www.springer.com](http://www.springer.com))

# Preface

The goal in nanotechnology is to make high-performance nanodevices. For nanodevice fabrications, novel *bottom-up* approach, fabricating devices and systems by hierarchical assembly or controlled growth of nanoscale materials, has attracted tremendous interest. Because this bottom-up method allows single-crystalline nanostructure growth on a variety of substrates, the bottom-up method has been used to prepare high-quality nanomaterials even on amorphous glass, plastic, and graphene substrates. In the bottom-up approach, one-dimensional (1D) semiconductor nanostructures, including nanorods, nanowires, nanobelts, and nanotubes, are vital components for fabricating optoelectronic and photonic nanodevices. In particular, 1D semiconductor nanostructures such as nanowires, nanorods, and nanotubes open up significant opportunities for the fabrication of high-performance optoelectronic nanodevice. For the fabrication of high-efficiency optoelectronic devices including light-emitting diodes (LEDs) and solar cells, 1D heteroepitaxial nanostructures with well-defined crystalline interfaces must be essential building blocks since embedding quantum structures in individual nanostructures would enable novel physical properties such as quantum confinement to be exploited, such as the continuous tuning of spectral wavelength by varying the well thickness. Sophisticated optoelectronic nanodevices can be readily fabricated by composition and doping controls of semiconductor nanostructures. Furthermore, nanodevices based on vertically ordered 1D nanostructures permit extremely small size and ultrahigh density. Here, this book introduces the current status of semiconductor nanostructures for optoelectronic devices and outlines the processing and characterizations of semiconductor nanostructures and their optoelectronic device applications.

In Chaps. 1–6, current research activities related to the synthesis of 1D semiconductor nanostructures by various growth methods and their optoelectronic device applications are reviewed. Chapter 1 provides an overview of vapor–liquid–solid growth process, which has widely been employed for preparation of semiconductor nanowires. Using this technique, Si, Ge, GaAs, InP, GaP, ZnO, and GaN nanowires have been synthesized and several nanodevices including



p–n junction semiconductor nanowire LEDs and solar cells have been fabricated. In Chaps. 2 and 3, catalyst-free metal-organic vapor phase epitaxy to prepare high purity semiconductor nanostructures is introduced. Here, the processes to control positions, conductivities, and compositions of nanostructures for fabricating coaxial nanostructure LEDs are also described. Chapter 4 describes synthesis methods and characteristics of AlN nanostructures for UV optoelectronic device applications. Chapter 5 reviews the research progress on the controlled synthesis of a wide variety of nanowire heterostructures such as branched heterostructures, which includes solution phase and template-based methods. Meanwhile, the semiconductor nanostructures can be hybridized with graphene, which has recently been attracting much attention as a novel nanomaterial system for flexible optoelectronic devices as details are described in Chap. 6.

In Chaps. 7 and 8, structural and optical characterizations of semiconductor nanomaterials and nanostructures are reviewed. Chapter 7 introduces research on structural properties of ZnO and GaN nanostructures using X-ray absorption fine structure. As described in Chap. 8, optical properties of semiconductor nanostructures were investigated using luminescence characterization techniques, which are nondestructive, nonintrusive, and sensitive to the presence of defects or impurities in nanomaterials.

The last three chapters describe nanodevice applications of 1D semiconductor nanostructures. In Chap. 9, lasing characteristics of single and assembled nanowires are reviewed. Chapter 10 introduces near-field optical evaluation and the use of nanorod quantum structures for nanophotonic devices such as a nanophotonic gate. Finally, Chap. 11 presents the overview of nanowire solar cell studies, and integration strategies for practical device applications.

This book entitled “Semiconductor Nanostructures for Optoelectronic Devices – Processing, Characterization and Applications” is being introduced to review the recent works in the field of 1D nanomaterials and their optoelectronic device applications. Each chapter is written by leading scientists in the relevant field. Thus, I hope that high-quality scientific and technical information is provided to students, scientists, and engineers who are, and will be, engaged in fabrications of semiconductor nanostructures and their optoelectronic device applications.

I extend my acknowledgment to Dr. Claus Ascheron of Springer-Verlag for his guidance and suggestions.

Seoul  
Republic of Korea

*Gyu-Chul Yi*

# Contents

<b>1</b>	<b>Vapor-Liquid-Solid Growth of Semiconductor Nanowires</b> .....	<b>1</b>
	Heon-Jin Choi	
1.1	Introduction .....	1
1.2	VLS Mechanism for One-Dimensional Crystal Growth .....	3
1.2.1	Requirements for Metal Catalyst .....	5
1.2.2	Phase Diagram .....	6
1.2.3	Kinetics and Rate-Determining Step .....	8
1.2.4	Size of the Metal Catalyst .....	9
1.3	Growth of Nanowires by the VLS Mechanism and Current Issues for Optoelectronics .....	10
1.3.1	Growth of Semiconductor Nanowires by the VLS Mechanism .....	10
1.3.2	Issues Associated with the VLS Mechanism for Optoelectronics .....	11
1.4	Devices Based on the VLS Mechanism .....	27
1.5	Summary and Perspectives .....	33
	References .....	35
<b>2</b>	<b>Catalyst-Free Metal-Organic Vapor-Phase Epitaxy of ZnO and GaN Nanostructures for Visible Light-Emitting Devices</b> .....	<b>37</b>
	Chul-Ho Lee and Gyu-Chul Yi	
2.1	Introduction .....	37
2.2	Catalyst-Free MOVPE of ZnO Nanorods .....	39
2.3	Position-Controlled Growth of ZnO and GaN Nanostructures .....	46
2.4	Light-Emitting Device Applications .....	53
2.5	Conclusions and Perspectives .....	62
	References .....	63

<b>3</b>	<b>III–V Semiconductor Nanowires on Si by Selective-Area Metal-Organic Vapor Phase Epitaxy</b> .....	67
	Katsuhiro Tomioka and Takashi Fukui	
3.1	Introduction .....	67
3.2	Optical Application of Semiconductor NWs .....	69
3.3	Growth of NWs by Selective-Area Metal-Organic Vapor Phase Epitaxy .....	71
3.3.1	Process of SA-MOVPE for NW Growth .....	72
3.3.2	Crystal Shape in SA-MOVPE .....	73
3.3.3	Growth of Core-Shell Structures .....	76
3.4	Heteroepitaxy of III–V NWs on Si Substrate .....	77
3.4.1	Basic Concept for Selective-Area Growth of III–V NWs on Si .....	79
3.4.2	Selective-Area Growth of InAs NWs on Si .....	81
3.4.3	Selective-Area Growth of GaAs NWs on Si .....	85
3.4.4	Size Dependence of the GaAs NW Growth on Si .....	86
3.4.5	Growth of GaAs/AlGaAs Core-Shell NWs on Si .....	88
3.5	Fabrication of III–V NW-based LEDs on Si Surface .....	89
3.5.1	Growth of AlGaAs/GaAs/AlGaAs Double-Heterostructures in CMS NWs on Si .....	90
3.5.2	Fabrication of CMS NW-Based LEDs on Si .....	90
3.5.3	GaAs/GaAsP CMS Structure and Multi-Quantum well Layers for Laser Diodes .....	93
3.6	Summary .....	96
	References .....	97
<b>4</b>	<b>Synthesis and Properties of Aluminum Nitride Nanostructures</b> .....	103
	Daniel S.P. Lau and X.H. Ji	
4.1	Introduction .....	103
4.1.1	Overview .....	103
4.1.2	Properties of AlN .....	104
4.2	Synthesis of AlN Nanostructures .....	105
4.2.1	Vapor–Liquid–Solid Growth .....	106
4.2.2	Vapor–Solid Growth .....	109
4.3	Doping of AlN Nanostructures .....	117
4.4	Physical Properties of AlN Nanostructures .....	120
4.4.1	Structural Properties Raman Spectra .....	120
4.4.2	Optical Properties of AlN Nanostructures .....	123
4.4.3	Ferromagnetic Properties .....	129
4.5	Concluding Remarks and Perspectives .....	132
	References .....	133
<b>5</b>	<b>Semiconductor Nanowire Heterostructures: Controlled Growth and Optoelectronic Applications</b> .....	137
	Chuanwei Cheng and Hong Jin Fan	
5.1	Introduction .....	137

5.2	Synthesis of Semiconductor NW Heterostructures .....	139
5.2.1	Segmented NW Heterostructures .....	139
5.2.2	Coaxial and Core/Multishell Semiconductor NW Heterostructures .....	145
5.2.3	Branched Semiconductor NW Heterostructures .....	150
5.3	Applications of Semiconductor NW Heterostructures .....	156
5.3.1	Optical Properties.....	156
5.3.2	Photovoltaics and Photoelectrochemical Water Splitting .....	157
5.3.3	Photodetectors .....	160
5.4	Conclusions and Perspective.....	162
	References.....	163
<b>6</b>	<b>Hybrid Semiconductor Nanostructures with Graphene Layers</b> .....	<b>167</b>
	Won Il Park, Jung Min Lee, Dong Hyun Lee, and Gyu-Chul Yi	
6.1	Introduction.....	167
6.2	Graphene: 2D Materials for Transparent Conducting Layers .....	169
6.2.1	Physical Properties of Graphene .....	169
6.2.2	Synthesis and Application of Graphene .....	171
6.3	Hybrid Semiconductor Nanostructures with Graphene: 0D–2D, 1D–2D, and 2D–2D Hybrids.....	175
6.3.1	Hybrid Lamellar Composites: 2D–2D Hybrids .....	175
6.3.2	Nanoparticle–Graphene Hybrids: 0D–2D Hybrids .....	177
6.3.3	Nanorod–Graphene Hybrids: 1D–2D Hybrids.....	177
6.4	1D–2D Nanorod–Graphene Hybrids for Electronics and Optoelectronics .....	179
6.4.1	Vertical 1D Nanostructures on 2D Graphene.....	180
6.4.2	2D Graphene on Vertical 1D Nanostructures.....	183
6.4.3	Multistage Hybrid Nanoarchitectures: Pillared Graphene.....	186
6.4.4	Application of 1D–2D Hybrids for Electronics and Optoelectronics .....	187
6.5	Conclusions .....	192
	References.....	193
<b>7</b>	<b>Microstructural Properties of Nanostructures</b> .....	<b>197</b>
	Sang-Wook Han	
7.1	Introduction.....	197
7.2	X-ray Absorption Fine Structure .....	199
7.3	ZnO Nanoparticles .....	203
7.4	ZnO Nanorods .....	209
7.5	Coaxial GaN/ZnO Nanorods.....	212
7.6	ZnO Nanorods on GaN and $Al_2O_3$ Substrates.....	215
7.7	Conclusions.....	221
	References.....	222

<b>8</b>	<b>Luminescence Characterizations of Semiconductor Nanostructures</b> .....	225
	Jinkyong Yoo	
8.1	Introduction .....	225
8.2	Radiative Recombination in 1D Semiconductor Nanostructures .....	226
8.3	Luminescence Characterizations of 1D Semiconductor Nanostructures .....	228
	8.3.1 Local Probe Techniques .....	228
	8.3.2 Luminescent Characteristics of Semiconductor Nanostructures .....	234
8.4	The Limit of Luminescence Characterizations .....	246
8.5	Summary .....	248
	References .....	249
<b>9</b>	<b>Lasing Characteristics of Single and Assembled Nanowires</b> .....	251
	S.F. Yu	
9.1	Introduction .....	251
9.2	Lasing Characteristics of Single Nanowires .....	252
	9.2.1 Feedback Mechanism of Single-Nanowire Lasers .....	253
	9.2.2 Modal Characteristics of Nanowires with Different Geometries .....	255
	9.2.3 Near-and Far-Field Profiles .....	260
	9.2.4 Criteria to Achieve Stimulated Emission .....	262
9.3	Lasing Characteristics of Assembled Nanowires .....	263
	9.3.1 What is a Random Laser? .....	263
	9.3.2 Feedback Mechanism of Random Lasers .....	264
	9.3.3 Formation of Random Cavities Using Assembled Nanowires .....	266
	9.3.4 Criteria to Achieve Stimulated Emission .....	270
9.4	Single and Assembled Nanowires Laser Diodes .....	272
	9.4.1 Single-Nanowire Electrically Driven Lasers .....	272
	9.4.2 Electrically Pumped Nanowire Array Lasers .....	272
9.5	Conclusion and Discussion .....	275
	References .....	277
<b>10</b>	<b>Nanophotonic Device Application Using Semiconductor Nanorod Heterostructures</b> .....	279
	Takashi Yatsui, Gyu-Chul Yi, and Motoichi Ohtsu	
10.1	Introduction .....	279
10.2	ZnO Nanorod Heterostructure for Nanophotonic Device .....	280
10.3	Near-Field Evaluation of Isolated ZnO Nanorod Single-Quantum-Well Structure for Nanophotonic device .....	280
10.4	A Nanophotonic AND-Gate Device Using ZnO Nanorod Double-Quantum-Well Structures .....	286
10.5	Conclusions .....	294
	References .....	295

**11 Semiconductor Nanowires for Solar Cells** ..... 297  
 S.T. Picraux, J. Yoo, I.H. Campbell, S.A. Dayeh,  
 and D.E. Perea

11.1 Introduction ..... 297

11.2 Key Concepts ..... 300

11.3 Nanowire Fabrication ..... 302

11.4 Overview of Nanowire Solar Cell Studies ..... 303

11.5 Enhanced Optical Absorption in Nanowire Arrays ..... 310

    11.5.1 Basic Principles of NW Array Optics ..... 311

    11.5.2 Experimental Demonstrations of Increased  
         Absorption ..... 314

11.6 Optoelectronic Properties of Radial Nanowire Diodes ..... 316

11.7 Solar Cell Performance: Combined Optical  
 and Electrical Properties ..... 320

11.8 Integration Strategies for Nanowire Solar Cells ..... 322

    11.8.1 General Approaches ..... 322

11.9 Conclusions ..... 326

References ..... 326

**Index** ..... 329

# Contributors

**Ian H. Campbell** Center for Integrated Nanotechnologies, Los Alamos National Laboratory, Los Alamos, NM 87545, USA, [campbell@lanl.gov](mailto:campbell@lanl.gov)

**Chuanwei Cheng** Department of Physics, Tongji University, 1239 Siping Road, 200092, Shanghai City, China, [cwcheng@tongji.edu.cn](mailto:cwcheng@tongji.edu.cn)

**Heon-Jin Choi** Department of Materials Science and Engineering, Yonsei University, 50 Yonsei-ro, Seodaemun-gu, Seoul 120-749, Korea, [hjc@yonsei.ac.kr](mailto:hjc@yonsei.ac.kr)

**Shadi A. Dayeh** Center for Integrated Nanotechnologies, Los Alamos National Laboratory, Los Alamos, NM 87545, USA, [shadi@lanl.gov](mailto:shadi@lanl.gov)

**Hong Jin Fan** Division of Physics and Applied Physics, School of Physical and Mathematical Sciences, Nanyang Technological University, 21 Nanyang Link, 637371, Singapore, [FANHJ@ntu.edu.sg](mailto:FANHJ@ntu.edu.sg)

**Takashi Fukui** Graduate School of Information Science and Technology, Research Center for Integrated Quantum Electronics (RCIQE), Hokkaido University, Kita 14, Nishi 9, Kita-ku, Sapporo, Japan, [fukui@rciqe.hokudai.ac.jp](mailto:fukui@rciqe.hokudai.ac.jp)

**Sang-Wook Han** Department of Physics Education, Chonbuk National University, 567 Baekje-daero, Deokjin-gu, Jeonju-si, Jeollabuk-do 561-756, Korea, [shan@jbnu.ac.kr](mailto:shan@jbnu.ac.kr)

**Xiao Hong Ji** School of Materials Science and Engineering, South China University of Technology, Wushan RD., Tianhe District, Guangzhou, P.R.China, 510641 [jxhong@scut.edu.cn](mailto:jxhong@scut.edu.cn)

**Daniel S. P. Lau** Department of Applied Physics, The Hong Kong Polytechnic University, Hung Hom, Kowloon, Hong Kong, P.R. China, [apsplau@polyu.edu.hk](mailto:apsplau@polyu.edu.hk)

**Chul-Ho Lee** Department of Materials Science and Engineering, POSTECH, San31, Hyoja-dong, Nam-gu, Pohang, Gyungbuk, Korea, [chulholee@gmail.com](mailto:chulholee@gmail.com)

**Dong Hyun Lee** Department of Material Science and Engineering, Hanyang University, 222 Wangsimni-ro, Seongdong-gu, Seoul 133-791, Korea, [azaleaz@hanyang.ac.kr](mailto:azaleaz@hanyang.ac.kr)

**Jung Min Lee** Department of Material Science and Engineering, Hanyang University, 222 Wangsimni-ro, Seongdong-gu, Seoul 133-791, Korea, [dlwjalds2929@naver.com](mailto:dlwjalds2929@naver.com)

**Motoichi Ohtsu** School of Engineering, University of Tokyo, 2-11-16 Yayoi Bunkyo-ku, 113-8656 Tokyo, Japan, [ohtsu@ee.t.u-tokyo.ac.jp](mailto:ohtsu@ee.t.u-tokyo.ac.jp)

**Won Il Park** Department of Material Science and Engineering, Hanyang University, 222 Wangsimni-ro, Seongdong-gu, Seoul 133-791, Korea, [wipark@hanyang.ac.kr](mailto:wipark@hanyang.ac.kr)

**Daniel E. Perea** Center for Integrated Nanotechnologies, Los Alamos National Laboratory, Los Alamos, NM 87545, USA, [d-perea@lanl.gov](mailto:d-perea@lanl.gov)

**S. Tom Picraux** Center for Integrated Nanotechnologies, Los Alamos National Laboratory, Los Alamos, NM 87545, USA, [picraux@lanl.gov](mailto:picraux@lanl.gov)

**Katsuhiko Tomioka** Graduate School of Information Science and Technology, Research Center for Integrated Quantum Electronics (RCIQE), Hokkaido University, Kita 14, Nishi 9, Kita-ku, Sapporo, Japan

Japan Science and Technology Agency (JST), PRESTO, Kawaguchi, Japan, [tomioka@rciqe.hokudai.ac.jp](mailto:tomioka@rciqe.hokudai.ac.jp)

**Takashi Yatsui** School of Engineering, University of Tokyo, 2-11-16 Yayoi Bunkyo-ku, 113-8656 Tokyo, Japan, [yatsui@ee.t.u-tokyo.ac.jp](mailto:yatsui@ee.t.u-tokyo.ac.jp)

**Gyu-Chul Yi** National Creative Research Initiative Center for Semiconductor Nanostructures, Department of Physics and Astronomy, Seoul National University, 599 Gwanak-ro, Gwanak-gu, Seoul 151-747, Korea, [gyuchul.yi@gmail.com](mailto:gyuchul.yi@gmail.com)

**Jinkyung Yoo** Center for Integrated Nanotechnologies, Los Alamos National Laboratory, Los Alamos, NM 87545, USA, [trip297@gmail.com](mailto:trip297@gmail.com)

**Siu Fung Yu** Department of Applied Physics, The Hong Kong Polytechnic University, Hung Hom, Kowloon, Hong Kong, P.R. China, [Siu.Fung.Yu@inet.polyu.edu.hk](mailto:Siu.Fung.Yu@inet.polyu.edu.hk)



## 19. Nanooptics

Nanooptics deals with optical near fields, the electromagnetic fields that mediate the interaction between nanometric particles located in close proximity to each other. The optical near field mediates this interaction, whose energy is localized around the nanometric particles like an electron cloud around an atomic nucleus. Its decay length is proportional to the particle size. This chapter is primarily a review of nanophotonics, a leading branch of nanooptics, which is the technology utilizing the optical near field. The true nature of nanophotonics is to realize qualitative innovation in photonic devices, fabrications, and systems by utilizing novel functions and phenomena caused by optical near field interactions, which are impossible as long as conventional propagating light is used. As evidence of such qualitative innovation, this chapter describes novel nanophotonic devices, fabrication techniques, energy conversions, systems, and extensions related to science.

19.1	<b>Basics</b> .....	1335
19.1.1	The Photonic Crystal .....	1335
19.1.2	Plasmonics .....	1336
19.1.3	Silicon Photonics .....	1336
19.1.4	Quantum Dot Laser .....	1336

### 19.1 Basics

Nanooptics deals with the light generated in or on nanometer-sized particles. It has been applied to open an innovative field of technology, i. e., *nanophotonics*, in order to develop novel photonic devices, fabrication techniques, energy conversions, and systems, as proposed by *Ohtsu* [19.1]. Nanophotonics is a means, for example, to reduce the size of photonic devices, improve the resolution of optical fabrications, and increase the storage density of optical disc memories. However, the diffraction limit of light impedes the attainment of these improvements.

19.2	<b>Principles of Nanophotonics</b> .....	1336
19.3	<b>Nanophotonic Devices</b> .....	1338
19.3.1	Basic Devices .....	1339
19.3.2	Input and Output Terminals .....	1342
19.3.3	Unique Features and Application to Information Processing Systems ..	1343
19.4	<b>Nanophotonic Fabrication</b> .....	1344
19.4.1	Photochemical Vapor Deposition ....	1344
19.4.2	Photolithography .....	1345
19.4.3	Self-Organized Smoothing .....	1347
19.5	<b>Nanophotonic Energy Conversion</b> .....	1350
19.5.1	Optical/Optical Energy Up-Conversion .....	1350
19.5.2	Optical/Electrical Energy Up-Conversion .....	1351
19.6	<b>Hierarchy in Nanophotonics and Its Applications</b> .....	1353
19.6.1	Propagating Light and Optical Near-Field Interactions	1353
19.6.2	Hierarchy in the Subwavelength Regime .....	1353
19.6.3	Shape-Engineered Nanostructures for Hierarchy .....	1353
19.7	<b>Industrial Applications of Nanophotonics</b>	1354
19.8	<b>Summary</b> .....	1355
	<b>References</b> .....	1355

Considering photonic devices, the technologies listed below have recently been developed, which bear some resemblance to nanophotonics. Nevertheless, they cannot reduce the size of these devices beyond the diffraction limit.

#### 19.1.1 The Photonic Crystal

This is a filter device [19.2] used to control optical interference and light scattering by installing a subwavelength-sized periodic structure in the device

# Springer Handbook of Lasers and Optics

The **Springer Handbook of Lasers and Optics** provides fast, up-to-date, comprehensive and authoritative coverage of the wide fields of optics and lasers. It is written for daily use in the office or laboratory and offers explanatory text, data, and references needed for anyone working with lasers and optical instruments.

This second edition features numerous updates and additions. Especially four new chapters on **Fiber Optics, Integrated Optics, Frequency Combs, and Interferometry** reflect the major changes. In addition, chapters **Optical Materials and Their Properties, Optical Detectors, Nanooptics, and Optics far Beyond the Diffraction Limit** have been thoroughly revised and updated.

The now 25 chapters are grouped into four parts which cover basic principles and materials, fabrication and properties of optical components, coherent and incoherent light sources, and, finally, selected applications and special fields such as terahertz photonics, x-ray optics and holography.

Each chapter is authored by respected experts and contains the basic principles, applications and latest information in the field. Among the subjects covered are geometrical and wave optics, linear and nonlinear optics, optical materials and components, detectors, incoherent and all essential types of coherent light sources, generation of ultrashort pulses, spectroscopic techniques, laser safety as well as current trends in such modern areas as quantum optics, femto- and attosecond physics, and nanooptics as well as optics beyond the diffraction limit.

The handbook is written and compiled for physicists, engineers and other scientists at universities and in industrial research who develop and use optical techniques.

**With a Foreword by Nobel Laureate T.W. Hänsch.**

ISBN 978-3-642-19408-5



9 783642 194085

## Key Topics

- Basic optics principles
- Coherent and incoherent light sources
- Spectroscopies and attophysics
- Optical materials and their properties
- Fabrication and properties of optical components
- Fiber optics, integrated optics, frequency combs, and interferometry
- Selected applications and special fields: Nanooptics, quantum optics, x-ray optics, terahertz photonics, and holography

## Features

- Contains over 1000 two-color illustrations
- Includes over 120 comprehensive tables with properties of optical materials and light sources
- Emphasizes physical concepts over extensive mathematical derivations. Chapters with summaries, detailed index
- Delivers a wealth of up-to-date references.



**Springer**  
**Handbook** *of*

*Träger*  
*Editor*

*2nd Edition*

 Springer

---

# **HOLOGRAMS – RECORDING MATERIALS AND APPLICATIONS**

---

Edited by **Izabela Naydenova**

**INTECHWEB.ORG**

## **Holograms – Recording Materials and Applications**

Edited by Izabela Naydenova

### **Published by InTech**

Janeza Trdine 9, 51000 Rijeka, Croatia

### **Copyright © 2011 InTech**

All chapters are Open Access distributed under the Creative Commons Attribution 3.0 license, which permits to copy, distribute, transmit, and adapt the work in any medium, so long as the original work is properly cited. After this work has been published by InTech, authors have the right to republish it, in whole or part, in any publication of which they are the author, and to make other personal use of the work. Any republication, referencing or personal use of the work must explicitly identify the original source.

As for readers, this license allows users to download, copy and build upon published chapters even for commercial purposes, as long as the author and publisher are properly credited, which ensures maximum dissemination and a wider impact of our publications.

### **Notice**

Statements and opinions expressed in the chapters are these of the individual contributors and not necessarily those of the editors or publisher. No responsibility is accepted for the accuracy of information contained in the published chapters. The publisher assumes no responsibility for any damage or injury to persons or property arising out of the use of any materials, instructions, methods or ideas contained in the book.

**Publishing Process Manager** Silvia Vlase

**Technical Editor** Teodora Smiljanic

**Cover Designer** Jan Hyrat

**Image Copyright** Daniela Illing, 2011. Used under license from Shutterstock.com

First published October, 2011

Printed in Croatia

A free online edition of this book is available at [www.intechopen.com](http://www.intechopen.com)  
Additional hard copies can be obtained from [orders@intechweb.org](mailto:orders@intechweb.org)

Holograms – Recording Materials and Applications, Edited by Izabela Naydenova  
p. cm.

978-953-307-981-3

---

# Contents

---

## **Preface IX**

### **Part 1 Holographic Recording Materials 1**

- Chapter 1 **Ionic Liquids in Photopolymerizable Holographic Materials 3**  
Hechun Lin and Peter W. de Oliveira
- Chapter 2 **Norland Optical Adhesive 65<sup>®</sup> as Holographic Material 23**  
J.C. Ibarra, L. Aparicio-Ixta,  
M. Ortiz-Gutiérrez and C.R. Michel
- Chapter 3 **Light-Sensitive Media-Composites for Recording Volume Holograms Based on Porous Glass and Polymer 45**  
O.V. Andreeva and O.V. Bandyuk
- Chapter 4 **Digital Holographic Recording in Amorphous Chalcogenide Films 71**  
Andrejs Bulanovs
- Chapter 5 **Azobenzene-Containing Materials for Hologram 95**  
Haifeng Yu and Takaomi Kobayashi
- Chapter 6 **Holography Based on the Weigert's Effect 117**  
Zurab V. Wardosanidze
- Chapter 7 **Holographic Image Storage with a 3-Indoly-Benzylfulgimide/PMMA Film 145**  
Neimule Menke and Baoli Yao
- Chapter 8 **Three-Dimensional Vector Holograms in Photoreactive Anisotropic Media 179**  
Tomoyuki Sasaki, Akira Emoto,  
Kenta Miura, Osamu Hanaizumi,  
Nobuhiro Kawatsuki and Hiroshi Ono

**Part 2 Holographic Data Storage 197**

- Chapter 9 **Diffraction Property of  
Collinear Holographic Storage System 199**  
Yeh-Wei Yu and Ching-Cherng Sun

- Chapter 10 **Theory of Polychromatic  
Reconstruction for Volume Holographic Memory 219**  
Ryushi Fujimura, Tsutomu Shimura and Kazuo Kuroda

**Part 3 Holographic Devices 255**

- Chapter 11 **Application of Holograms in WDM  
Components for Optical Fiber Systems 257**  
Alfredo Martín Mínguez and Paloma R. Horche

- Chapter 12 **Polarization-Selective Substrate-Mode Volume  
Holograms and Its Application to Optical Circulators 283**  
Jing-Heng Chen, Kun-Huang Chen and Der-Chin Su

- Chapter 13 **Holographic Synthesis of  
Diffraction Free Beams and Dark Hollow Beams 305**  
G. Martínez Niconoff, P. Martínez Vara,  
J. Muñoz Lopez and A. Carbajal Dominguez

**Part 4 Holograms in Security Applications 315**

- Chapter 14 **Optimization of Hologram for Security Applications 317**  
Junji Ohtsubo

- Chapter 15 **Nanophotonic Hierarchical Holograms: Demonstration  
of Hierarchical Applications Based on Nanophotonics 341**  
Naoya Tate, Makoto Naruse, Takashi Yatsui,  
Tadashi Kawazoe, Morihisa Hoga, Yasuyuki Ohyagi, Yoko Sekine,  
Tokuhiko Fukuyama, Mitsuru Kitamura and Motoichi Ohtsu

**Part 5 Signal Processing 357**

- Chapter 16 **Photonic Microwave Signal  
Processing Based on Opto-VLSI Technology 359**  
Feng Xiao, Kamal Alameh and Yong Tak Lee

Motoichi Ohtsu

*Editor*

# Progress in Nanophotonics 1

With 184 Figures

 Springer



# Contents

<b>1 Nanophotonics: Dressed Photon Technology for Qualitatively Innovative Optical Devices, Fabrication, and Systems</b> .....	1
Motoichi Ohtsu	
1.1 Introduction .....	1
1.2 Background and Principles .....	2
1.3 Fiber Probes, Sensing Systems, and 1 Tb in. <sup>-2</sup> -Density Magnetic Storage Systems .....	6
1.4 Nanophotonic Devices .....	9
1.4.1 Basic Devices .....	9
1.4.2 Input and Output Terminals .....	17
1.4.3 Unique Features and Application to Information Processing Systems .....	20
1.5 Nanophotonic Fabrication .....	24
1.5.1 Photochemical Vapor Deposition .....	24
1.5.2 Photolithography .....	28
1.5.3 Self-Organized Smoothing .....	35
1.6 Nanophotonic Energy Conversion .....	44
1.6.1 Optical/Optical Energy Up-Conversion .....	44
1.6.2 Optical/Electrical Energy Up-Conversion .....	48
1.7 Nanophotonic Systems and Their Evolution to Related Sciences .....	53
1.8 Summary .....	54
References .....	55
<b>2 Probe-Free Nanophotonic Systems: Macro-Scale Applications Based on Nanophotonics</b> .....	59
Naoya Tate, Makoto Naruse, and Motoichi Ohtsu	
2.1 Introduction .....	59
2.2 Probe-Free Nanophotonic Systems .....	61

2.3	Nanophotonic Matching as Macro-Scale Observation .....	63
2.3.1	Macro-Scale Observation .....	63
2.3.2	Quadrupole–Dipole Transform .....	63
2.3.3	Nanophotonic Matching .....	65
2.3.4	Experimental Demonstration .....	67
2.3.5	Outlook .....	70
2.4	Nanophotonics-Induced Phase Transition as Magnified-Transcription .....	72
2.4.1	Magnified-Transcription of Optical Near-Fields .....	72
2.4.2	Photoinduced Phase Transition .....	73
2.4.3	Experimental Demonstrations .....	74
2.4.4	Outlook .....	77
2.5	Nanophotonic Hierarchical Hologram .....	77
2.5.1	Background .....	77
2.5.2	Basic Concept .....	78
2.5.3	Nanophotonic Code .....	81
2.5.4	Numerical Evaluations .....	82
2.5.5	Experimental Demonstration .....	85
2.5.6	Outlook .....	89
2.6	Summary .....	90
	References .....	91
<b>3</b>	<b>Self-Formation of Semiconductor Quantum Dots</b> .....	<b>93</b>
	Koichi Yamaguchi	
3.1	Introduction .....	93
3.2	Stranski–Krastaov Growth of Quantum Dots .....	94
3.3	Uniform Formation of Quantum Dots .....	96
3.3.1	Self Size-Limiting Growth of Uniform InAs/GaAs Quantum Dots .....	96
3.3.2	Capping Growth of Uniform InAs/GaAs Quantum Dots .....	100
3.3.3	Closely-Stacked Growth of Uniform InAs/GaAs Quantum Dots .....	103
3.4	Control of Quantum Energy Level .....	106
3.5	Density Control of Quantum Dots .....	109
3.5.1	Sb-Mediated Growth of High-Density InAs/GaAs Quantum Dots .....	109
3.5.2	Intermittent Growth of Low-Density InAs/GaAs Quantum Dots .....	113
3.6	Quantum Dot Array .....	116
3.6.1	Vertical Array of InAs/GaAs Quantum Dots .....	116
3.6.2	In-Plane Arrays of InAs/GaAs Quantum Dots .....	118
3.7	Conclusion .....	123
	References .....	123

<b>4</b>	<b>Near-Field Optical Imaging of Plasmon Wavefunctions and Optical Fields in Plasmonic Nanostructures</b> .....	127
	Kohei Imura and Hiromi Okamoto	
4.1	Introduction .....	127
4.2	Optical Properties of Nanoparticles .....	128
4.2.1	Optical Properties of Ensemble of Nanoparticles .....	131
4.3	Plasmon Wavefunctions .....	133
4.4	Principle of Wavefunction Visualization .....	133
4.5	Near-Field Optical Microscope .....	135
4.5.1	Instrumentation of Near-Field Optical Microscope .....	135
4.5.2	Time-Resolved and Non-Linear Measurements .....	137
4.6	Photonic Local Density-of-States Calculation .....	138
4.7	Near-Field Transmission Measurements .....	139
4.7.1	Near-Field Transmission Measurement of Spherical Gold Nanoparticles .....	140
4.7.2	Near-Field Transmission Measurement of Gold Nanorods .....	141
4.8	Time-Resolved Measurement .....	145
4.9	Non-Linear Measurements .....	148
4.9.1	Gold Nanorods .....	149
4.9.2	Gold Nanoplates .....	151
4.9.3	Dimeric Nanoparticles .....	152
4.9.4	Larger Assemblies of Nanoparticles .....	154
4.10	Summary .....	156
	References .....	157
<b>5</b>	<b>Simple Approaches for Constructing Metallic Nanoarrays on a Solid Surface</b> .....	161
	Hidenobu Nakao	
5.1	Introduction .....	161
5.2	Assembling MNPs in One Dimension .....	162
5.2.1	Chemical Self-Assembly .....	162
5.2.2	Physical Means .....	164
5.2.3	Template-Assisted Assembly .....	166
5.3	Highly Aligned DNA as Templates for 1D Assembly of MNPs .....	166
5.3.1	Stretching and Aligning DNA Molecules on Surfaces .....	167
5.3.2	Assembling AuNPs onto Aligned DNA Molecules .....	170
5.4	Fabrication and Patterning of Metallic Nanoarrays with Long-Range Order .....	176
5.4.1	Preparation of Longer Metallic Nanoarrays with DNA Nanofibers .....	177
5.4.2	Transfer Printing of Metallic Nanoarray .....	181
5.5	Conclusions .....	182
	References .....	184

<b>6 Assembly and Immobilization of Metal Nanoparticles</b> .....	189
Nao Terasaki and Tetsu Yonezawa	
6.1 Introduction .....	189
6.2 Preparation of Metal Nanoparticles .....	190
6.2.1 Preparation of Metal Nanoparticles by Chemical Reduction .....	190
6.3 Assembly Formation .....	194
6.3.1 Two Dimensional Assembly Formation of Nanoparticles by Simple Evaporation of Dispersions .....	195
6.3.2 Two Dimensional Arrays Formation on Liquid–Liquid Interfaces .....	197
6.3.3 Direct Preparation of Nanostructures on a Substrate .....	198
6.3.4 Control of Nanoparticle Assembly by Stabilizing Reagents .....	198
6.3.5 Nanoparticle Assembly with Templates .....	206
6.4 Conclusions .....	228
References .....	229
<b>Index</b> .....	233

Nano-Optics and Nanophotonics

Motoichi Ohtsu *Editor*

# Progress in Nanophotonics 1

 Springer